NIST UNITED STATES DEPARTMENT OF COMMERCE
NATIONAL INSTITUTE OF STANDARDS AND TECHNOLOGY

NISTIR 3944

MATERIALS STUDIES FOR MAGNETIC FUSION ENERGY APPLICATIONS AT LOW TEMPERATURES - XIII

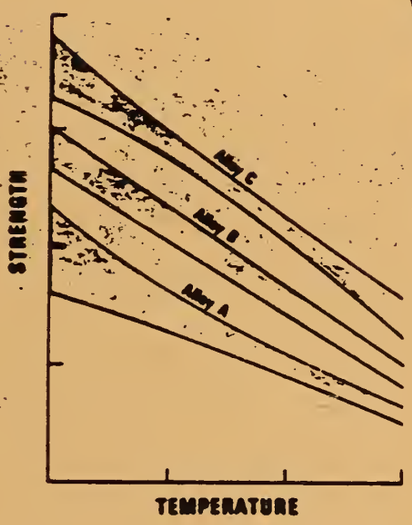

NISTIR 3944

MATERIALS STUDIES FOR MAGNETIC FUSION ENERGY APPLICATIONS AT LOW TEMPERATURES - XIII

Edited by

R.L. Tobler and R.P. Reed
National Institute of Standards and Technology
Boulder, Colorado 80303-3328

September 1990

Prepared for

Department of Energy
Office of Fusion Energy
Washington, D.C. 20545

U.S. DEPARTMENT OF COMMERCE, Robert A. Mosbacher, Secretary
NATIONAL INSTITUTE OF STANDARDS AND TECHNOLOGY, John W. Lyons, Director

CONTENTS

WELDING

TEST STANDARDS

SUMMARY

This report contains the results of research to determine the properties of materials that may be used in cryogenic structures for the superconducting magnets of magnetic fusion energy power plants and prototypes. This research facilitates their design and development. The program was developed jointly by the staffs of the National Institute of Standards and Technology and the Office of Fusion Energy of the Department of Energy; it is managed by NIST and sponsored by DOE. The research is conducted at NIST and at other laboratories through cooperative agreements with NIST. Some research, such as the development of test standards, is partially funded by NIST through its own base research programs. Cooperative research at other laboratories is performed by their own funding.

Research results for 1989/90 are presented in technical papers under four headings that reflect the main program areas: Structural Alloys, Welding, Test Standards and Technology Transfer. Objectives and research highlights are summarized in the introduction to each program area.

This report also includes an Appendix consisting of two papers with data for a ferritic steel and four aluminum alloys. That research was funded primarily by other programs but the information is of interest to magnetic fusion energy applications.

NOTE: Certain commercial equipment, instruments, or materials are identified in this report to specify the experimental procedure adequately. In a few instances, company names are used to identify the source of specific research. In no case does such identification imply recommendation or endorsement by the National Institute of Standards and Technology, nor does it imply that the material or equipment identified is necessarily the best available for the purpose.

ORGANIZATIONAL CONTACTS

Specific technical questions may be directed to the following people, who contributed to major aspects of the program during the fiscal year of 1990.

Department of Energy, Office of Fusion Energy, Washington, D.C. 20545

Program Monitor	M. Cohen	(301) 353-4952

National Institute of Standards and Technology, Boulder, CO 80303

Program Manager	R.L. Tobler	(303) 497-3421
	R.P. Reed (to Feb 90)	(303) 497-3870
Structural Alloys	P.T. Purtscher	(303) 497-5789
	R.P. Reed	(303) 497-3870
	N.J. Simon	(303) 497-3687
	R.L. Tobler	(303) 497-3421
	R.P. Walsh	(303) 497-3818
Welding	C.N. McCowan	(303) 497-3699
	T.A. Siewert	(303) 497-3523
Technology Transfer	E.S. Drexler	(303) 497-5350
	N.J. Simon	(303) 497-3687
Test Standards	R.P. Reed	(303) 497-3870
	R.L. Tobler	(303) 497-3421

PROGRAM DESCRIPTION

The overall objective of the program is to assist in the design, construction, and safe operation of magnetic fusion energy (MFE) systems that use cryogenic components, especially superconducting magnets. The specific steps taken to achieve this objective are: (1) evaluation of the materials research needs specific to MFE devices; (2) research programs to acquire the necessary data; and (3) effective materials technology transfer by rapid dissemination of the data to potential users through personal contacts, publications, and workshops.

Efforts directed at the first specific objective began with the publication of the "Survey of Low Temperature Materials for Magnetic Fusion Energy" in March 1977. A publication updating part of this survey, "Structural Alloys for Superconducting Magnets in Fusion Energy Systems," was included in Volume IV (1981) of this series. In Volume VI (1983), reviews of the properties of austenitic stainless steels and of their elastic constants also contributed to this objective. Through interactions with low-temperature design, construction, and measurement programs, such as the Large Coil Project (LCP), the Compact Ignition Tokamak (CIT), and the International Thermonuclear Experimental Reactor (ITER), we are aware of new problems as they arise. This year's report contains results of continued research on stainless steels in support of ITER designs.

Research projects contributing to the second objective are described in the technical papers. Again, research toward the establishment of test standards was emphasized.

The third objective is satisfied, in part, by these annual reports and by the series of workshops on Cryogenic Structural Materials. Since 1982, handbook pages presenting the available data for specific materials have been distributed to members of the magnetic fusion energy community who are involved with low-temperature materials.

STRUCTURAL ALLOYS

STRUCTURAL ALLOYS PROGRAM

LEADER: R.P. Reed
CONTRIBUTORS: P.T. Purtscher, N.J. Simon, R.L. Tobler, R.P. Walsh

OBJECTIVES:

- Development of strong, tough structural alloys for use in superconducting magnets
- Development of strong, fatigue-resistant structural alloys for use in pulsed superconducting magnets
- Development of effective codes and standards for low-temperature property measurements and structural design

RESEARCH HIGHLIGHTS:

- Selective mechanical property tests of specific candidate alloys for magnet applications were carried out. These include tension, fracture toughness, and fatigue crack growth tests of JK1 (modified 316LN alloy) for superconducting conduit; fatigue crack growth and threshold fatigue tests for AISI 316LN and related alloys for magnet cases; and creep tests of copper for conductor and stabilizer applications.

- A computer-controlled test apparatus was used to measure fatigue crack growth rates and threshold stress intensity factors for austenitic stainless steels at room temperature, 76, and 4 K. Long-crack thresholds were determined using a decreasing ΔK technique and the database at 4 K was augmented by tests of 6 alloys. A simulation technique was also developed and used to characterize the behavior of short cracks. Short-crack simulation tests of JK1 conduit steel are reported and tests of other austenitic stainless steels are in progress to develop a comprehensive database.

- Selected papers in this section describe various effects (strain rate, load control, processing, composition, test temperature, and stress state) on the mechanical behavior of stainless steels. These studies impact cryogenic technology by improving our understanding of material behavior; they contribute to a potential lowering of material costs, and to resolution of technical points regarding the development of cryogenic test standards and design codes.

SUMMARY OF MECHANICAL PROPERTY MEASUREMENTS OF STRUCTURAL ALLOYS

Alloy Designation	Country of Supplier	Tensile 295-4 K	Elastic 295-4 K	Fracture Toughness 295, 76, 4 K	Fatigue Crack Growth Rate 295, 76, 4 K	Fatigue S-N 4 K	Report Volume* (page)
AUSTENITIC STEELS							
Fe-5Cr-25Mn-0.2C	Japan	VII					VII (65)
Fe-5Cr-26Mn	Japan		VI				VI (181)
Fe-13Cr-19Mn	USSR		III		VI		III (79) VI (41)
Fe-13Cr-22Mn-0.2N	Japan	VI		XII			VII (65) XII (239)
Fe-16Cr-8Ni-8Mn	U.S.	VIII		VIII			VIII (151,181)
Fe-16Cr-28Ni	P.R. China		XII				XII (141)
Fe-17Cr-18Mn-0.5N	U.S.	VII, VIII		VIII			VII (65) VIII (181)
Fe-17Cr-9Ni-8Mn	U.S.		III				III (91)
Fe-17Cr-13Ni-2Mo 316	U.S.	I,II, III,IV VI,VIII, IX,X,XI	VI	I,II, VIII, IX,X,XI	II,VIII, IX	I	I (15,71) II (79) III (49,105,117) IV (147) V (185) VI (157) VIII (181,209,251) IX (15,27,43) X (77) XI (71)
Fe-17Cr-13Ni-2Mo 316LN	U.S.	II,IX,XI		II,IX,XI	II		II (79) IX (15,27,53) XI (71,103)
Fe-18Cr-(11-14)Ni-(0-4)Mo 316LN	U.S.	X	X	X			X (9,31,43,55)
Fe-18Cr-3Ni-13Mn	U.S.	I,VI, VIII,XI	III	I,VIII,XI, XII	I,VI,VII		I (93) III (91) VI (53) VII (85) VIII (167,219) XI (89) XII (239)
Fe-18Cr-8Ni-(0.6)Mn	U.S.		X				X (67)
Fe-19Cr-(6-15)Ni-4Mn-(0.1-0.3)N	USSR	VIII,XI		VIII,IX,XI			VIII (123) IX (53) XI (113)
Fe-19Cr-9Ni-304 (cont'd on next page	U.S.	I,II, III,	I,II III,	I,II, III,	II,III,IV		I (15,71,213) II (79,149,175) III (15,91,105,117)

*MATERIALS STUDIES FOR MAGNETIC FUSION ENERGY APPLICATIONS AT LOW TEMPERATURES: NBSIR 78-884(I); NBSIR 79-1609 (II); NBSIR 80-1625 (III); NBSIR 81-1645 (IV); NBSIR 82-1667 (V); NBSIR 83-(VI); NBSIR 84-3000 (VII); NBSIR 85-3025 (VIII); NBSIR 86-3050 (IX); NBSIR 87-3067 (X); NBSIR 88-3082 (XI); NISTIR 89-3931.

Designation	Country of Supplier	Tensile 295-4 K	Elastic 295-4 K	Fracture Toughness 295,76,4 K	Fatigue Crack Growth Rate 295, 76, 4 K	Fatigue S-N 4 K	Report Volume* (page)
AUSTENITIC STEELS							
Fe-19Cr-9Ni 304 , cont'd	U.S.	IV,VI VII,IX,X	IV,VIII	IV,IX, X	IV		IV (37,101,203, 215,227) V (71) VI (73) VII (13,47,75,157) IX (27) X (77)
Fe-19Cr-9Ni 304L	U.S.	II,III, IV,VIII, IX,X	I,II,IV	II,IV, VIII,IX	III,IV, VIII		I, (213) II (79,123,175) IV (37,101,131, 215,302) VIII (181,229,251) IX (27,141) X (9)
Fe-19Cr-9Ni-(1-10)Mn	U.S.	IV,V, VIII	V	IV,V,VIII, IX			IV (77) V (15,59,189) VIII(181) IX (53)
Fe-19Cr-9Ni-N 304N	U.S.	I,III, IV,IX	IV	I,III,IV, IX	I,III,IV		I (93) III (15) IV (37,101,203, 215) IX (27)
Fe-19Cr-9Ni-N 304LN	U.S.	II,III, IV,V,VI VIII,IX	IV,VIII	II,III,IV, VIII,IX	II,III,IV, VIII		II (35,79) III (15) IV (37,101,203) V (29) VI (113) VIII(181,207,229) IX (150)
Fe-19Cr-10Ni-(0.03-0.29)N-(0.03-0.09)C	U.S.	II,VIII,	VIII,IX, XI,XII	III,VIII,	III		III (15) VIII(145,181) IX (159) XI (131) XII (169,177)
Fe-(14-19)Cr-19Mn	Switzerland		XII				XII (159)
Fe-20Cr-7Ni-8Mn 216	U.S.	VIII		VIII			VIII(151,181)
Fe-20Cr-8Ni-2Mn 304HN	U.S.	VIII		VIII			VIII(151,181)
Fe-20Cr-16Ni-6Mn	USSR	V,VI	V				V (29,213) VI (113)
Fe-21Cr-6Ni-9Mn	U.S.	I,VIII	III,IV, XII	I,VIII		I	I (15,71) III (91) VI (157) VIII(151,181) IX (95) X (9) XII (141)
Fe-21Cr-(6-12)Ni-9Mn	P.R. China		XII				XII (141,153)

(cont.d on next page)

*MATERIALS STUDIES FOR MAGNETIC FUSION ENERGY APPLICATIONS AT LOW TEMPERATURES: NBSIR 78-884 (I): NBSIR 79-1609 (II); NBSIR 80-1627 (III); NBSIR 81-1645 (IV); NBSIR 82-1667 (V); NBSIR 83-1690 (VI); NBSIR 84-3000 (VII); NBSIR 85-3025 (VIII); NBSIR 86-3050 (IX); NBSIR 87-3067 (X); NBSIR 88-3082 (XI); NISTIR 89-3931.

SUMMARY OF MECHANICAL PROPERTY MEASUREMENTS OF STRUCTURAL ALLOYS, continued

Alloy Designation	Country of Supplier	Tensile 295-4 K	Elastic 295-4 K	Fracture Toughness 295, 76, 4 K	Fatigue Crack Growth Rate 295, 76, 4 K	Fatigue S-N 295, 4 K	Report, Volume (page)
Fe-21Cr-12Ni-5Mn	U.S.	I,II	III,XII	I,II	I,II		I (93) II (79) III (91) XII (141)
Fe-25Cr-21Ni 310	U.S.	V,VI, VII, VIII, IX,X	III,VI	V,VIII			III (105,117) V (71,145) VI (73) VII (65)
Fe-19Ni-9Co 200-300 grades	U.S.		IV				IV (237)
Reviews of austenitic steels		IV,V,VI XI,XII	IV,V,VI XI,XII	IV,V,VI, XI,XII	IV, V,VI, VII	IV,VI	IV (17,257) V (171) VI (11,127,157) VII (103) XI (3,47) XII (9,45,71,93)
ALUMINUM ALLOYS							
Al-0.6Fe-0.2Cu-0.1Si 1100	U.S.	IX					IX (107)
Al-2.7Cu-2.2Li 2090	U.S.	XII	X			XII	X (163) XII (131)
Al-6Cu-0.2Mn 2219	U.S.	XII	II	II	II	II,XII	II (19) XII (131)
Al-4Mg 5083-0	U.S.	IV				II	II (35) IV (185)
Al-5.6Zn-2.5Mg-1.6Cu 7075	U.S.	XII				XII	XII (131)
Al-5.7Zn-2.3Mg-1.5Cu 7475	U.S.	XII				XII	XII (131)
COPPER ALLOY							
99.99Cu-Ag C10100, C10200	U.S.	IX,XI					IX (95,107) XI (147)
99.5Cu-Ag C10400	U.S.	X	X			X	X (83,127,139)
99.75Cu-Ag C15500	U.S.	X	X			X	X (83,127,139, 151)
97.6Cu-Ag-0.3CBe C17510	U.S.	X					X (83)
99.95(Cu+Fe)-18Cr-13Mn-3Ni-0.37N (laminate)	U.S.	XI					XI (159)
SUPERCONDUCTORS							
Nb-45Ti	U.S.		III				III (133)

*MATERIALS STUDIES FOR MAGNETIC FUSION ENERGY APPLICATIONS AT LOW TEMPERATURES: NBSIR 78-884 (I); NBSIR 79-1609 (II); NBSIR 80-1627 (III); NBSIR 81-1645 (IV); NBSIR 82-1667 (V); NBSIR 83-1690 (VI); NBSIR 84-3000 (VII); NBSIR 85-3025 (VIII); NBSIR 86-3050 (IX); NBSIR 87-3067 (X); NBSIR 88-3082 (XI); NISTIR 89-3931.

MECHANICAL PROPERTIES OF A SUPERCONDUCTOR CONDUIT PROPOSED FOR ITER MAGNETS

R.L. Tobler, R.P. Walsh, C.N. McCowan and R.P. Reed
Materials Reliability Division
National Institute of Standards and Technology
Boulder, CO 80303

A conduit for superconductor cables was tested to evaluate its suitability for International Thermonuclear Experimental Reactor magnets at liquid helium temperature. The conduit material, JK1, is a 316LN alloy modified by the addition of 0.05% Nb. Tension, fatigue, and fracture toughness measurements are reported. A short crack simulation technique was used to measure fatigue crack growth rates and thresholds. At 4 K, the alloy's yield strength after heat treatment exceeds the targeted 1200 MPa, but its toughness (J_{Ic} = 40 kJ/m^2 for the T-L orientation) is lower than desired or expected from alloy development studies. Metallurgical differences between rolled plate and formed conduit, or between research grade and commercial processing could account for the difference in toughness.

INTRODUCTION

High-field superconducting magnets use A15 type superconductors in austenitic alloy conduit sheaths. The conduit sheaths protect the superconductor cables and also contain the liquid helium coolant at 4 K. The cable components and conduit are heated together during fabrication at temperatures around 700°C. This heat treatment reacts the Nb and Sn elements to produce the superconducting compound Nb_3Sn. It also ages the conduit and adversely affects its mechanical properties.

The mechanical properties of austenitic stainless steels that are proposed as conduit materials are degraded during aging by sensitization (carbide precipitation). Precipitation of $M_{23}C_6$ carbides on grain boundaries is particularly deleterious. One method to combat this problem is to add small amounts of Nb to retard the rate of carbide formation.

After testing laboratory plates, Shimada and Tone [1,2] decided that alloy 316LN + 0.05% Nb offers better prospects than 304LN + 0.05% Nb or 22Mn steel + 0.05% Nb. Despite some carbide and nitride precipitation during aging, 316LN + 0.05% Nb retained a transgranular fracture mechanism at 4 K. The alloy was designated JK1 and selected for further study. Recently, JK1 conduit was manufactured and proposed for International Thermonuclear Experimental Reactor (ITER) magnets. In this paper, we report mechanical property measurements for that conduit. Included are tension, fatigue, and fracture toughness measurements at selected temperatures (295, 76, and 4 K) before and after heat treatment.

MATERIAL AND SPECIMENS

Material was received in the form of a seamless rectangular tube with the geometry shown in Fig. 1. In the as-received condition there is some residual cold work from the extrusion process. As shown in Table 1, the chemical composition is equivalent to plate compositions tested earlier.

Table 1. Chemical compositions of JK1 conduit (tested in this study) and JK1 research plate materials [1,2].

Material	Cr	Ni	Mn	C	Mo	N	Nb	Si	S	P
conduit	17.2	12.3	1.32	0.009	1.96	0.17	0.051	0.12	0.004	0.003
plate[1]	17.17	12.14	1.48	0.010	2.03	0.19	0.055	0.10	0.0014	0.003
plate[2]	17.12	12.45	1.26	0.010	1.98	0.198	0.049	0.12	0.005	0.007

The material was tested in the as-received (cold worked) and aged conditions. To heat treat the material in laboratory furnaces, the 1 m long stock was sectioned into 0.3 m lengths, heated in an argon atmosphere at 650°C for 180 h, and furnace cooled. This 650°C, 180 h treatment is specified for the superconductor in ITER magnets.

Test specimens and dimensions are shown in Fig. 2. Flat specimens (rectangular cross section) for tension tests were machined with their loading axes in longitudinal or transverse orientations relative to the extrusion direction or conduit length. Compact specimens for fracture mechanics tests were machined in both the T-L and L-T orientations as defined by ASTM Methods E 399-83. The specimen thicknesses were full size, that is, identical to the thickness of the conduit wall; no machining was performed on the specimen faces.

The microstructure of the conduit was examined before and after heat treatment. Representative features after heat teatment are shown in Figs. 3 and 4. In Fig. 3, the grain boundaries are heavily decorated with precipitates. Rod-shaped inclusions were observed in as-received material and are also visible in the lower right portion of Fig. 3. Figure 4, produced at lower magnification and with a different etchant, reveals banding (alternate light and dark regions extending across many grains), which is evidence of a deformed structure, chemical inhomogeneity, or both.

PROCEDURE

Tension tests were conducted using a screw-driven universal machine at a nominal strain rate of 2.5×10^{-4} s^{-1}. The yield strength at 0.2% plastic strain was measured using a 25.4 mm gage length, clip-on extensometer. The cryogenic apparatus was described before [3].

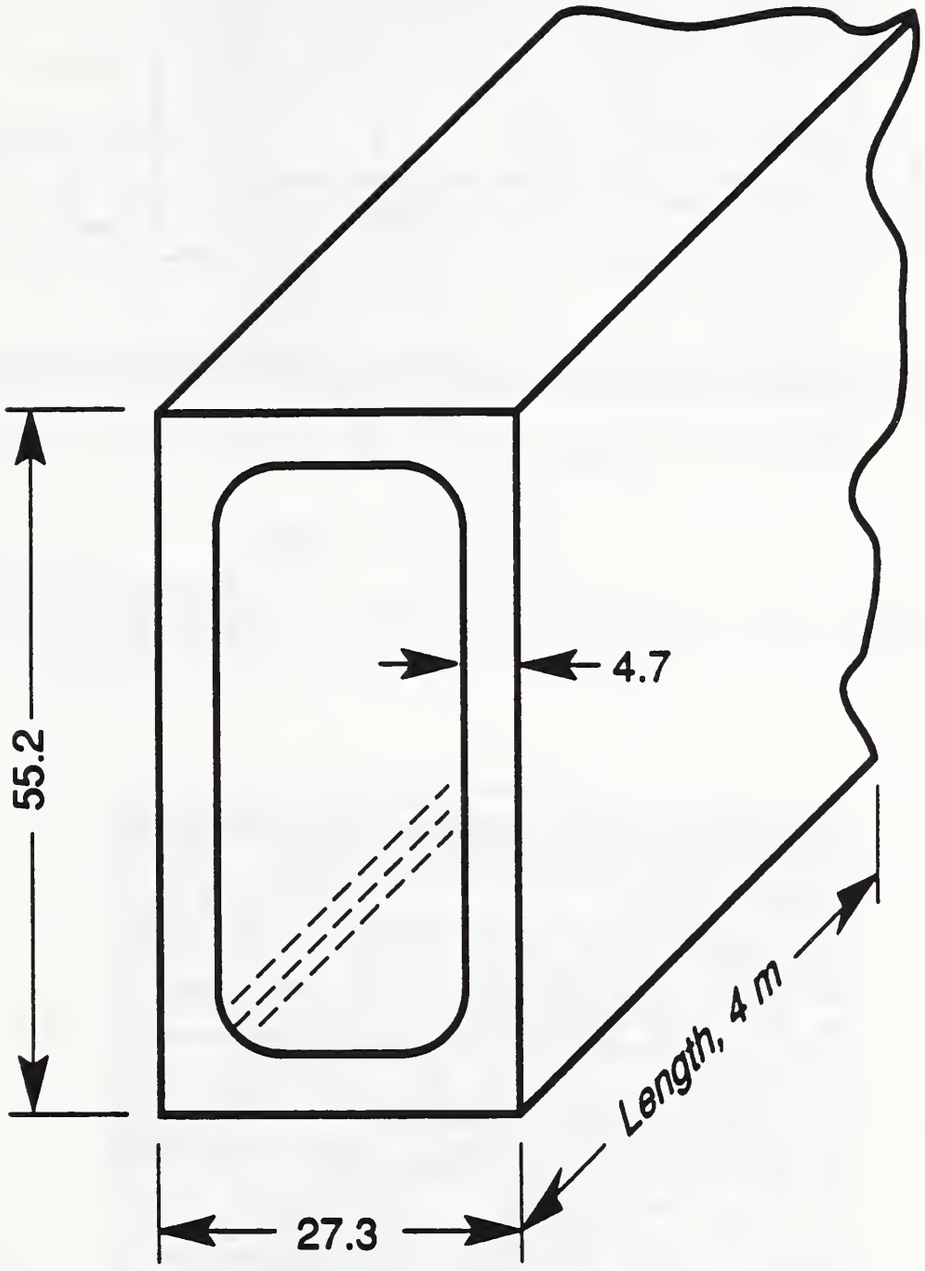

Figure 1. JK1 conduit geometry and dimensions, as-received. The dimensions are in mm, except for length which is m.

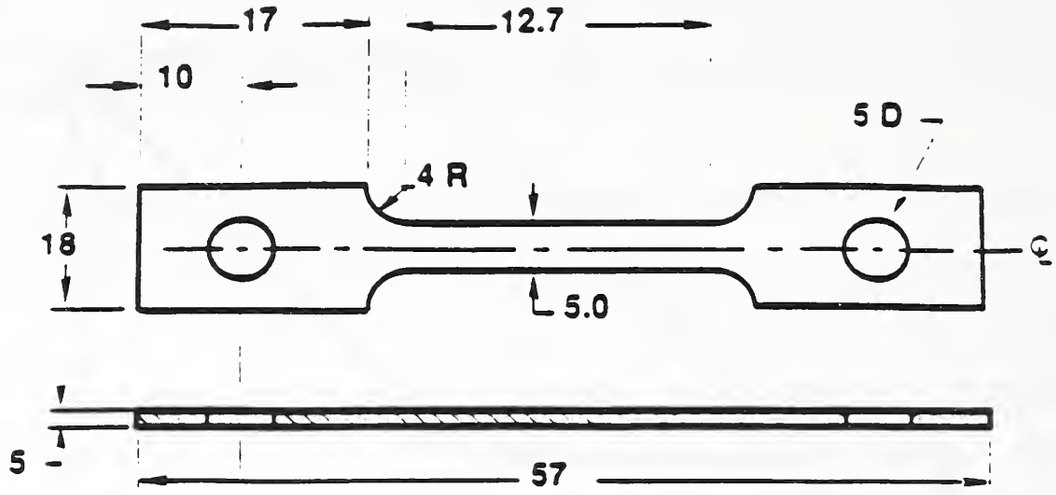

Note:
All dimensions in mm
Tolerance ± 0.1 mm
Not to scale

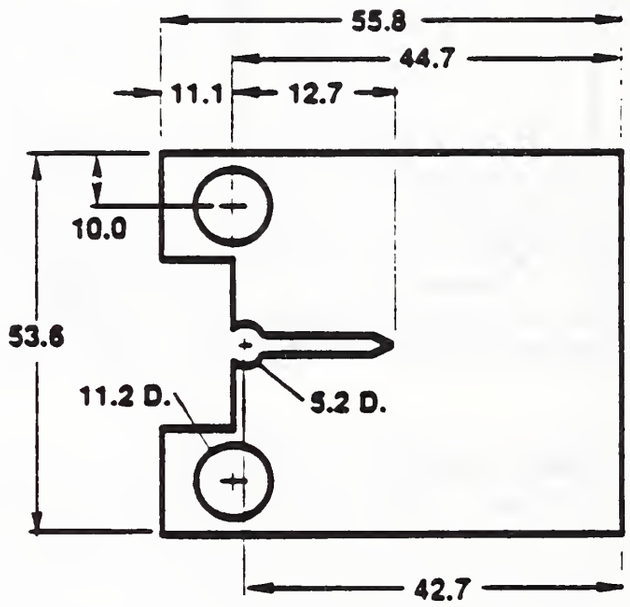

Figure 2. Test specimen geometries used in this study. The flat tension (A) and compact specimen (B) thicknesses are 4.7 mm, equal to the conduit wall thickness.

Figure 3. Precipitates (presumably carbides) and inclusions in the JK1 conduit microstructure after aging at 650°C for 180 h (1000x).

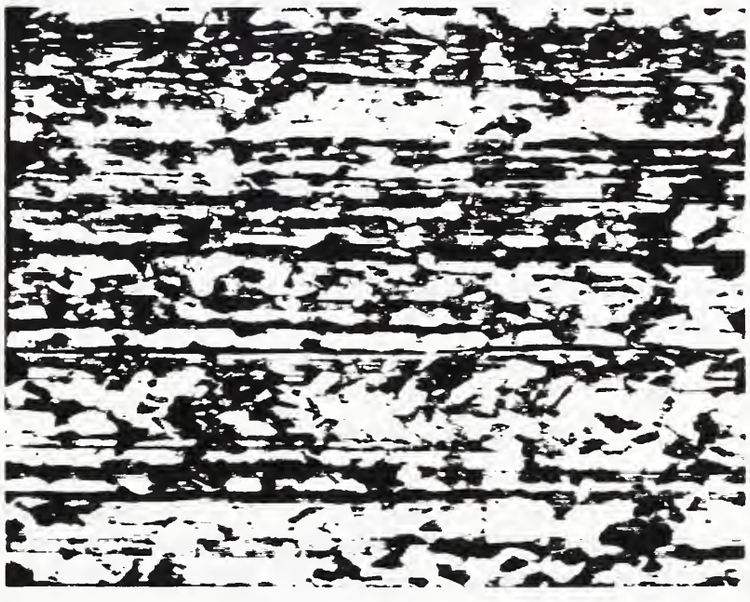

Figure 4. Banding in the JK1 conduit microstructure after aging at 650°C for 180 h (50x).

Fatigue and fracture toughness tests used a servohydraulic machine. The toughness was measured at 4 K after each specimen was fatigue cracked in liquid nitrogen at 76 K. Liquid nitrogen is less expensive than liquid helium, and it ensures a much smaller plastic zone at the crack tip than the alternative of precracking at room temperature. The maximum fatigue stress intensity factor at the crack tip did not exceed 33 $MPa \cdot m^{\frac{1}{2}}$, the minimum-to-maximum stress intensity factor ratio, R, was constant at 0.1, and the loads during fatigue were less than 40% of the limit loads for fracture at 4 K. The value of J_{Ic} was measured using the single-specimen unloading compliance technique with computer-aided data reduction [4], and J_{Ic} was defined and measured according to the ASTM E 813-81 method.

Fatigue crack growth rates were measured using the short crack simulation described by Herman, Hertzberg, and Jaccard [5]. This differs from the decreasing ΔK technique used in all previous cryogenic work [6-8]. In the short crack simulation, the maximum fatigue stress intensity factor, K_{max}, is maintained constant while K_{min} is progressively increased. The initial conditions for this study are $K_{max} = 35\ MPa \cdot m^{\frac{1}{2}}$ and $R = 0.1$. ΔK is subsequently reduced to near-threshold levels and R increases typically to 0.9. Using this technique for JK1, we measured fatigue crack growth rates spanning three orders of magnitude. Cycle frequency varied between 10 and 70 Hz depending on ΔK; higher frequencies were selected at lower ΔK to shorten the time for measurements near the fatigue crack growth threshold. The apparatus for fatigue crack growth threshold tests is described elsewhere [7].

The procedure for calculating fatigue crack growth rates was as follows. The crack was allowed to grow for an increment, typically 0.25 mm, and the rate was calculated:

$$\Delta a/\Delta N = (a_2 - a_1)/(N_2 - N_1). \qquad (1)$$

The fatigue loads were then changed for measurements at a lower ΔK value. The new ΔK was calculated from [7]

$$\Delta K = \Delta K_o \exp[C(a - a_o)], \qquad (2)$$

where ΔK = instantaneous stress intensity factor range,
ΔK_o = the initial stress intensity factor range,
a = the instantaneous crack length,
a_o = the final crack length, and
C = the stress intensity gradient,

$$C = \frac{1}{K}\frac{dK}{da}. \qquad (3)$$

The selected value of C was typically 0.3 or 0.4 mm^{-1}.

RESULTS

Tension Tests

The tensile property measurements at 295, 76, and 4 K are listed in Table 2 (longitudinal orientations) and Table 3 (transverse orientations). The data show that the JK1 conduit, before and after aging, has acceptable ductility. The room temperature (295 K) ductility is slightly improved by aging, whereas the cryogenic ductility (at 76 and 4 K) is slightly degraded. The yield and ultimate tensile strengths increase strongly at cryogenic temperatures as shown by the results for longitudinal specimens plotted in Fig. 5. At 4 K, the yield strength exceeds 1200 MPa in both the as-received and aged conditions. Aging systematically lowers the yield strength at each temperature by a modest amount.

Table 2. Tensile property measurements for JK1 conduit specimens in the longitudinal orientation.

Temperature (K)	Condition	Specimen No.	YS (MPa)	UTS (MPa)	EL (%)	RA (%)	E (GPa)
295	As-received	1.	889	987	30	65	188
		2.	725	810	42	68	191
		Avg.	807	898	36	66	190
	Aged	1.	680	932	29	75	174
		2.	649	826	42	82	203
		Avg.	664	879	36	78	188
76	As-received	1.	1301	1555	51	64	201
		2.	1351	1589	46	65	202
		Avg.	1326	1572	48	64	202
	Aged	1.	1247	1555	33	43	204
		2.	1096	1435	26	43	206
		Avg.	1172	1445	30	43	205
4	As-received	1.	1282	1713	49	48	200
		2.	1427	1822	44	63	204
		Avg.	1354	1768	46	56	202
	Aged	1.	1237	1780	37	53	200
		2.	--	1738	38	53	198
		Avg.	1237	1759	38	53	199

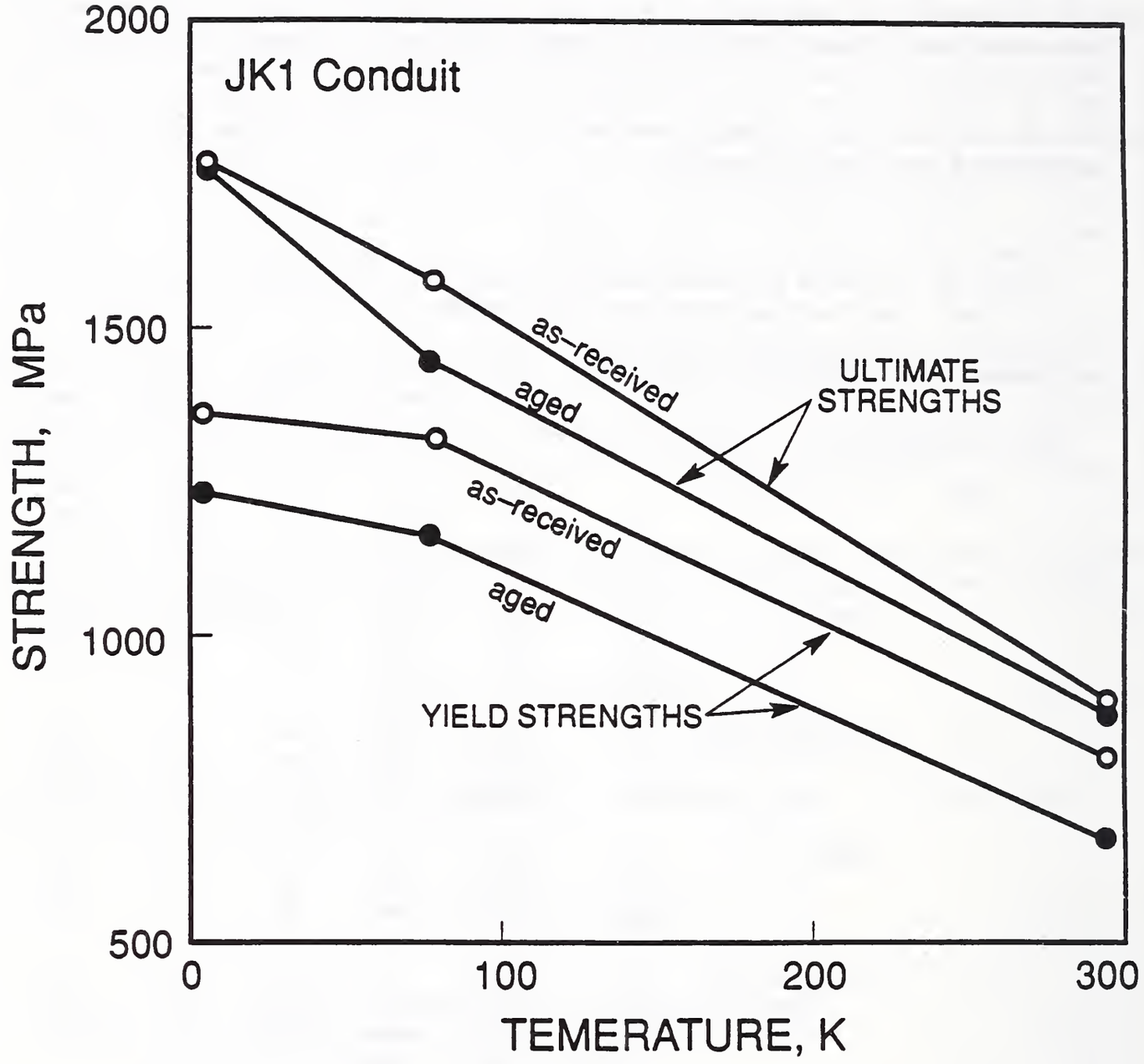

Figure 5. Yield and ultimate strengths in the as-received (cold worked) and aged conditions.

Table 3. Tensile property measurements for JK1 conduit specimens in the transverse orientation.

Temperature (K)	Condition	Specimen No.	YS (MPa)	UTS (MPa)	EL (%)	RA (%)	E (GPa)
295	Aged	1.	NA	786	48	84	NA
		2.	NA	782	48	86	NA
		Avg.		784	48	85	
76	Aged	1.	NA	1426	62	84	NA
		2.	1078	1442	65	85	217
		Avg.		1434	64	84	
4	Aged	1.	NA	1677	44	68	NA
		2.	NA	1651	47	67	NA
		Avg.		1664	46	68	

Fracture Toughness

Table 4 lists the J_{Ic} measurements at 4 K. Tests in the T-L orientation were performed in the as-received and aged conditions to show the effect of heat treatment. Two tests were performed for each condition. The average values at 4 K show that J_{Ic} is reduced from 82 kJ/m^2 in the as-received condition to 40 kJ/m^2 in the aged condition.

The effect of specimen orientation was evaluated (using aged material) by comparing two tests in the T-L orientation and two in the L-T orientation. Table 4 shows a measurable difference in the average J_{Ic} values: 72 kJ/m^2 for the L-T orientation and 40 kJ/m^2 for the T-L orientation. This is consistent with the behavior of commercial rolled stainless steel plates in that L-T orientations are usually tougher than T-L orientations.

The fracture surfaces of aged compact specimens tested at 4 K were examined with a scanning electron microscope. In general, the fracture surfaces are ductile and rough. For example, Fig. 6 features an aged specimen in the T-L orientation tested at 4 K. The morphology consists of a mixture of elongated troughs and small dimples. The troughs are oriented in the same direction as the bands shown in Fig. 4. Figures 6A and 6B at magnifications of 30 and 100x show the zone of crack growth produced during the J test. Elongated troughs extend from the fatigue crack front in the direction of crack growth. Figures 6C and 6D show small dimples that formed between the troughs. At 1000 and 3000x, rod-shaped inclusions are visible near the center of the troughs. The same rod-shaped inclusions were cited in Fig. 3. Energy Dispersive Analysis of X-rays (EDAX) indicates they may be sulfides.

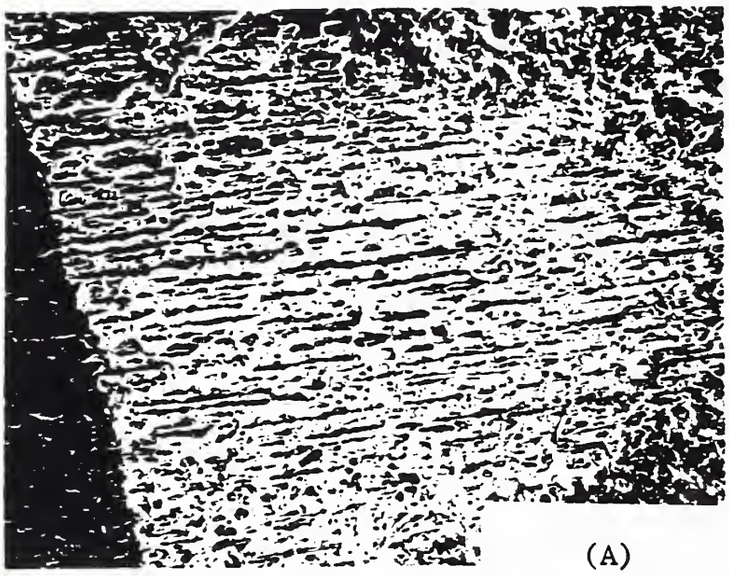

(A)

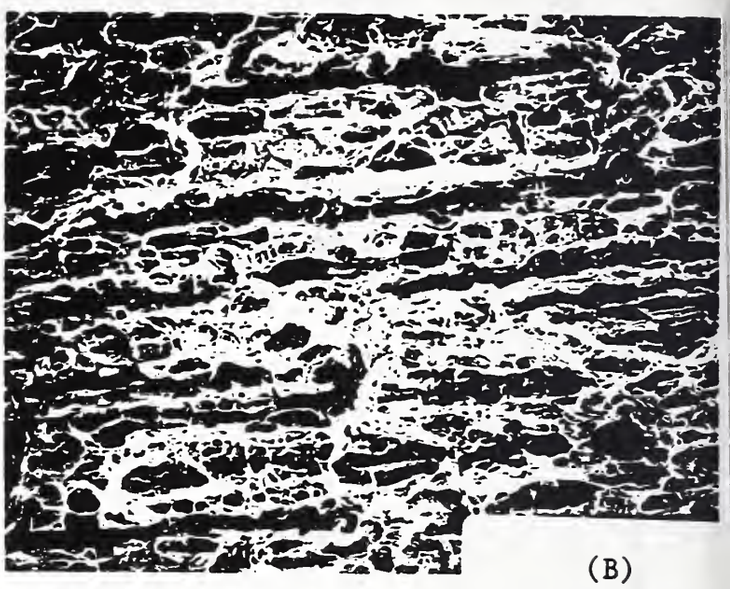

(B)

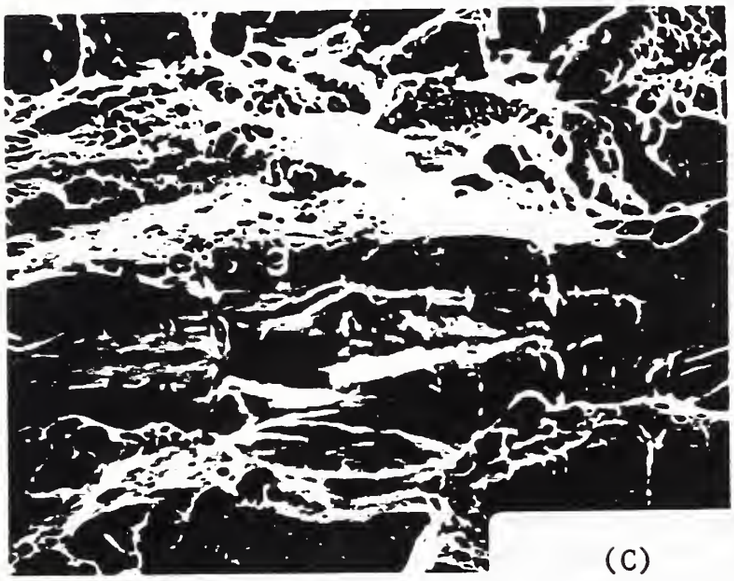

(C)

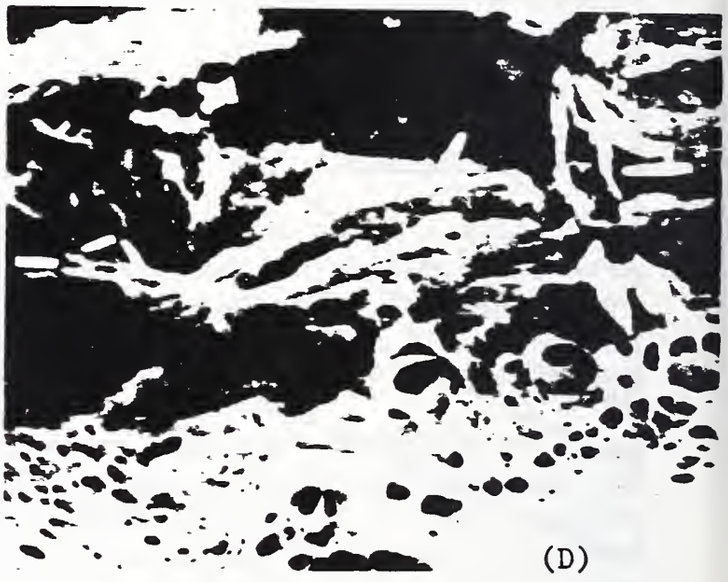

(D)

Figure 6. Fracture surface appearance of JK1 compact specimen in the T-L orientation after J-testing at 4 K:
(A) triangular zone of crack extension a (30x), and
(B) enlargement, showing longitudinal troughs (1000x).
(C) enlargement, showing regions of fine dimples adjacent to the troughs, along with rod-shaped inclusions within the troughs (1000x).
(D) enlargement of above (3000x).

Table 4. Fracture toughness measurements for JK1 conduit at 4 K.

Specimen No.	Orientation	Condition	J_{Ic} (kJ/m^2)	$K_{Ic}(J)^a$ (MPa·m$^{1/2}$)
1	T-L	As-received	120	155
2	T-L	As-received	45	95
avg.			82	125
3	T-L	Aged	38	88
4	T-L	Aged	43	93
5	T-L	Aged	40	90
avg.			40	90
6	L-T	Aged	70	118
7	L-T	Aged	75	122
avg.			72	120

a $K_{Ic}(J)$, an estimate of K_{Ic}, is calculated from $(E \cdot J_{Ic})^{1/2}$.

Fatigue Crack Growth Tests

Fatigue crack growth rates for JK1 were measured at 295 and 4 K. Room temperature results are shown in Fig. 7. The rates range from 10^{-7} to 10^{-10} m/cycle, for ΔK between 36 and 3 MPa·m$^{1/2}$. There is no measurable effect of specimen orientation (T-L vs. L-T), judging from the data for material in the aged condition. Based on data for the L-T orientation, aging does affect the fatigue crack growth rates for this alloy, but only at relatively high ΔK. At these higher values of ΔK (which correspond to low R ratios in this study), the rates after aging are lower than those for as-received material. At low ΔK (higher R ratios), the effect of heat treatment is either nonexistent or too small to be detected beyond the scatter of measurements. Therefore a single trend line at low ΔK in Fig. 7 represents all the data at 295 K. Following common convention, the threshold ΔK_{th} can be defined operationally as the value of ΔK that corresponds to a crack growth rate of 10^{-10} m/cycle. Then, extrapolation of the data of Fig. 7 indicates that ΔK_{th} is approximately 3 MPa·m$^{1/2}$ for JK1 in both the as-received and aged conditions at 295 K.

The fatigue crack growth rates measured at 4 K are plotted in Fig. 8. As is the case at 295 K, there is no measurable effect of specimen orientation (T-L vs. L-T) for specimens in the aged condition. Also, an effect of heat treatment (as-received condition vs. aged condition) is discernable only at ΔK higher than 10 MPa·m$^{1/2}$. Below 10 MPa·m$^{1/2}$, as threshold is approached, the data for the as-received and aged conditions merge into one trend line and extrapolation gives $\Delta K_{th} \approx 3$ MPa·m$^{1/2}$, which is equivalent to the result obtained at 295 K.

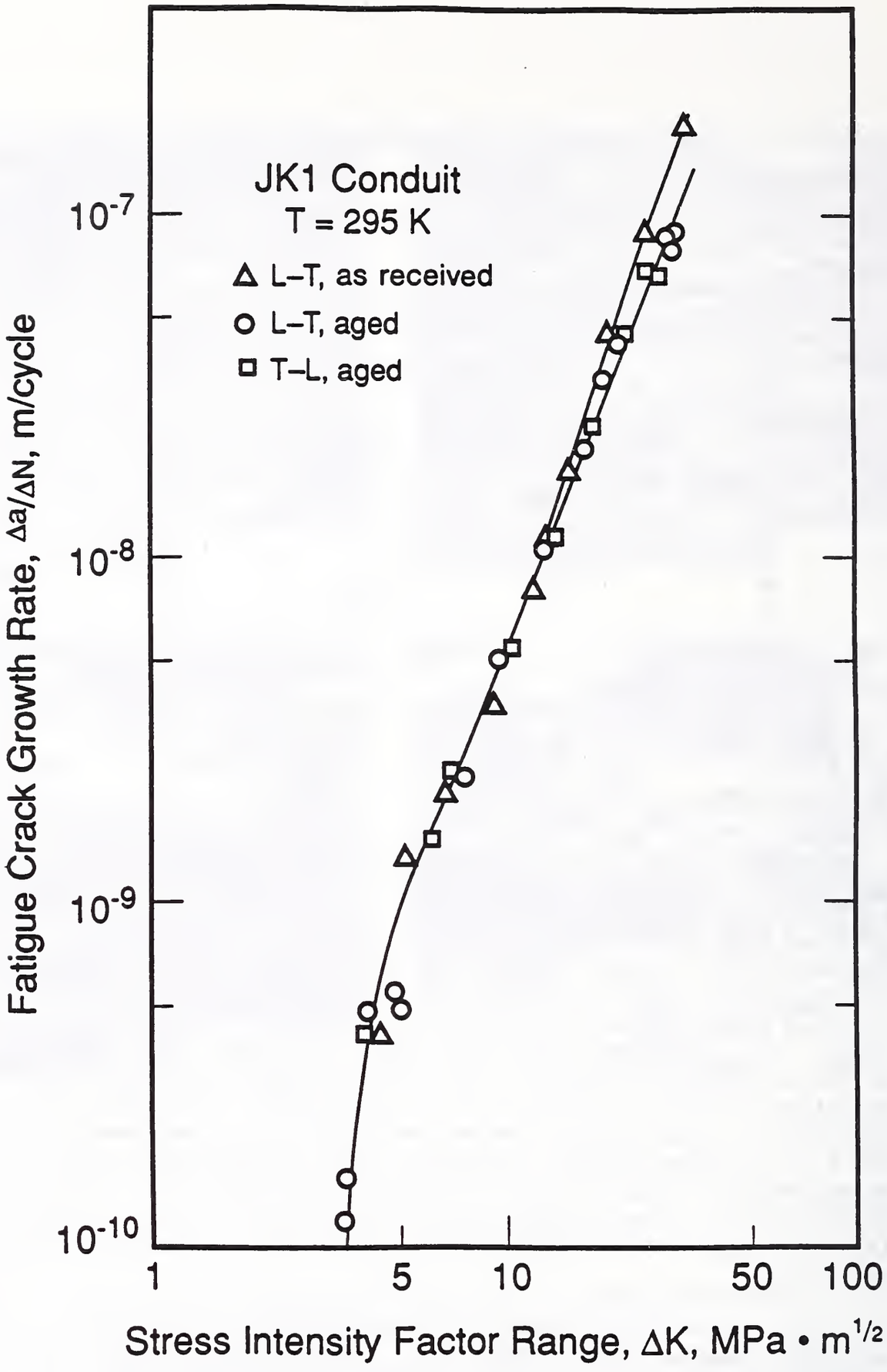

Figure 7. Fatigue crack growth rates for JK1 conduit at 295 K.

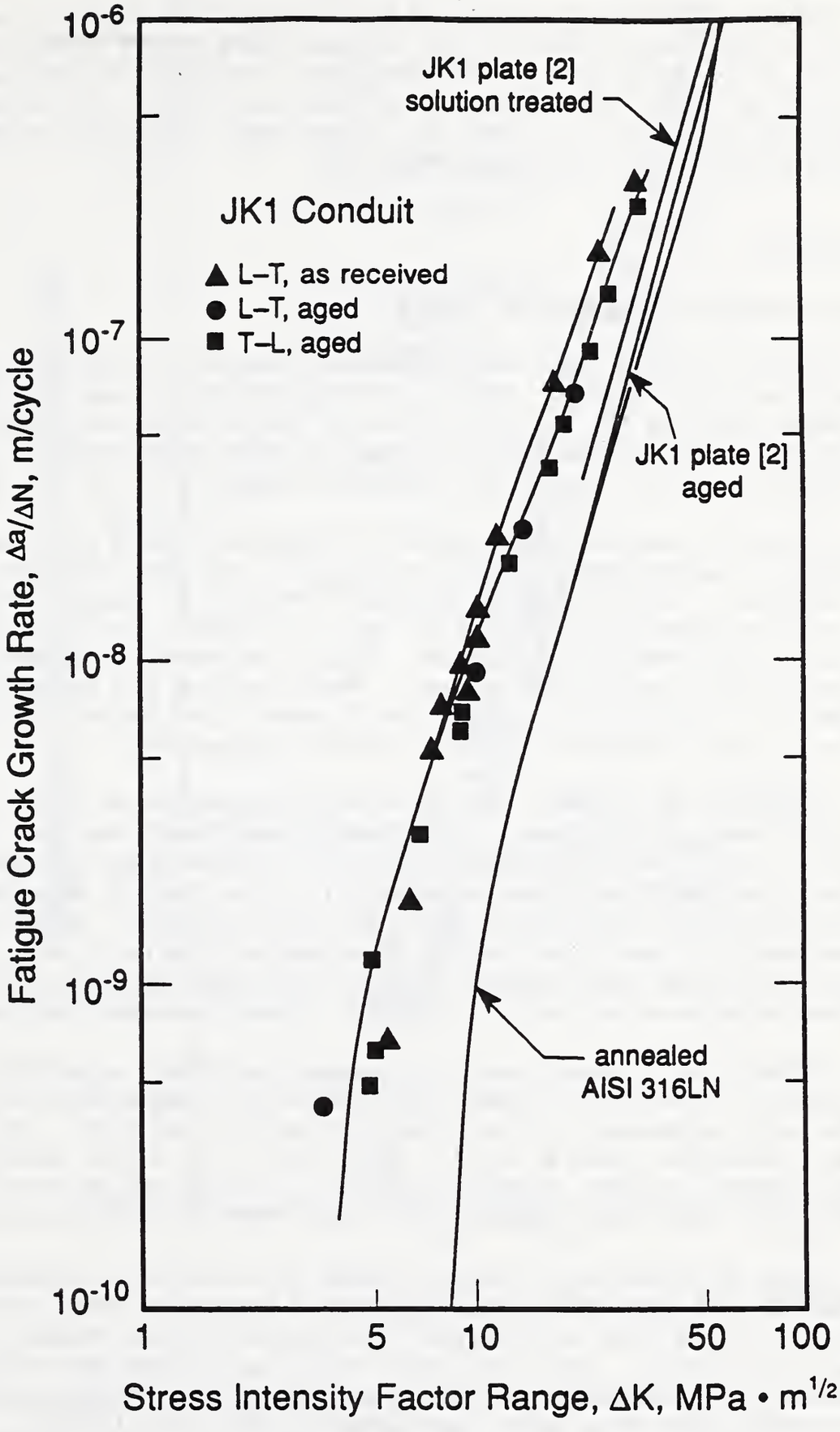

Figure 8. Fatigue crack growth rates for JK1 conduit and other materials at 4 K.

Figure 9 compares the data of the two previous figures, emphasizing the effect of test temperature on the fatigue crack growth rates for this alloy. The data are clearly temperature dependent at higher ΔK, but not at lower ΔK. At higher ΔK where the temperature effect does exist, the rates at 4 K are higher than at 295 K. At lower ΔK, below about 7 MPa·m$^{\frac{1}{2}}$, the effect of temperature becomes indistinguishable.

DISCUSSION

Static Mechanical Properties at 4 K

Figure 5 showed that heat treatment lowered the yield strength of the as-received JK1 conduit. This is attributable to a recovery effect: heat treatment relieved the plastic strain in the as-received conduit and consistently reduced the yield strength at each temperature by about 140 MPa. The aged alloy still meets the targeted strength of 1200 MPa or more at 4 K.

Figure 10 compares the conduit with plates tested previously [1,2]. Toughness is approximated by $K_{Ic} = (E \cdot J_{Ic})^{\frac{1}{2}}$ and data for the T–L orientation are compared. A K_{Ic} value of 150 MPa·m$^{\frac{1}{2}}$ or more is desired for the conduit [1], but the measured toughness is lower than that, and lower than levels previously achieved by JK1 plates. Thus, the hoped-for properties were not realized in the commercial product. Understanding the factors that determine toughness is critical for product development, and factors influencing the toughness are considered in the following discussion.

First, it is unlikely that specimen preparation or size can account for the difference in toughness. The conduit specimens were full sized, and machining tools never touched the planar surfaces. Our specimens were thinner than the 25 mm plate specimens [1], but the J_{Ic} measurements are valid according to the Method E 813-81 size criterion. Moreover, the effect of specimen size has been studied in stainless steels at 4 K. Typically, thinner specimens give slightly higher, not lower toughness [9] so smaller specimen size does not help to explain a lower measured toughness.

Differences in measurement techniques represent a potential influence on J_{Ic} results. However, a recent interlaboratory comparison revealed no bias in the test techniques at the laboratories involved [10]. The older method of data reduction (ASTM E 813-81) gives lower J_{Ic} values than the current method (ASTM E 813-88), simply because of a change in the definition of J_{Ic}. The Fig. 10 comparison, however, is based consistently on Method E 813-81.

The most significant factors appear to be material processing and heat treatment. The data for plates in Fig. 10 represent tests performed on 90 kg laboratory heats that were forged from ingots and hot-rolled at 1050°C into 28-mm-thick plates. The plates were solution-treated and then aged at 700°C for short (75 h) or long (200 h) time. Our specimens with a tube processing history were aged at a lower temperature (650°C) for 180 h.

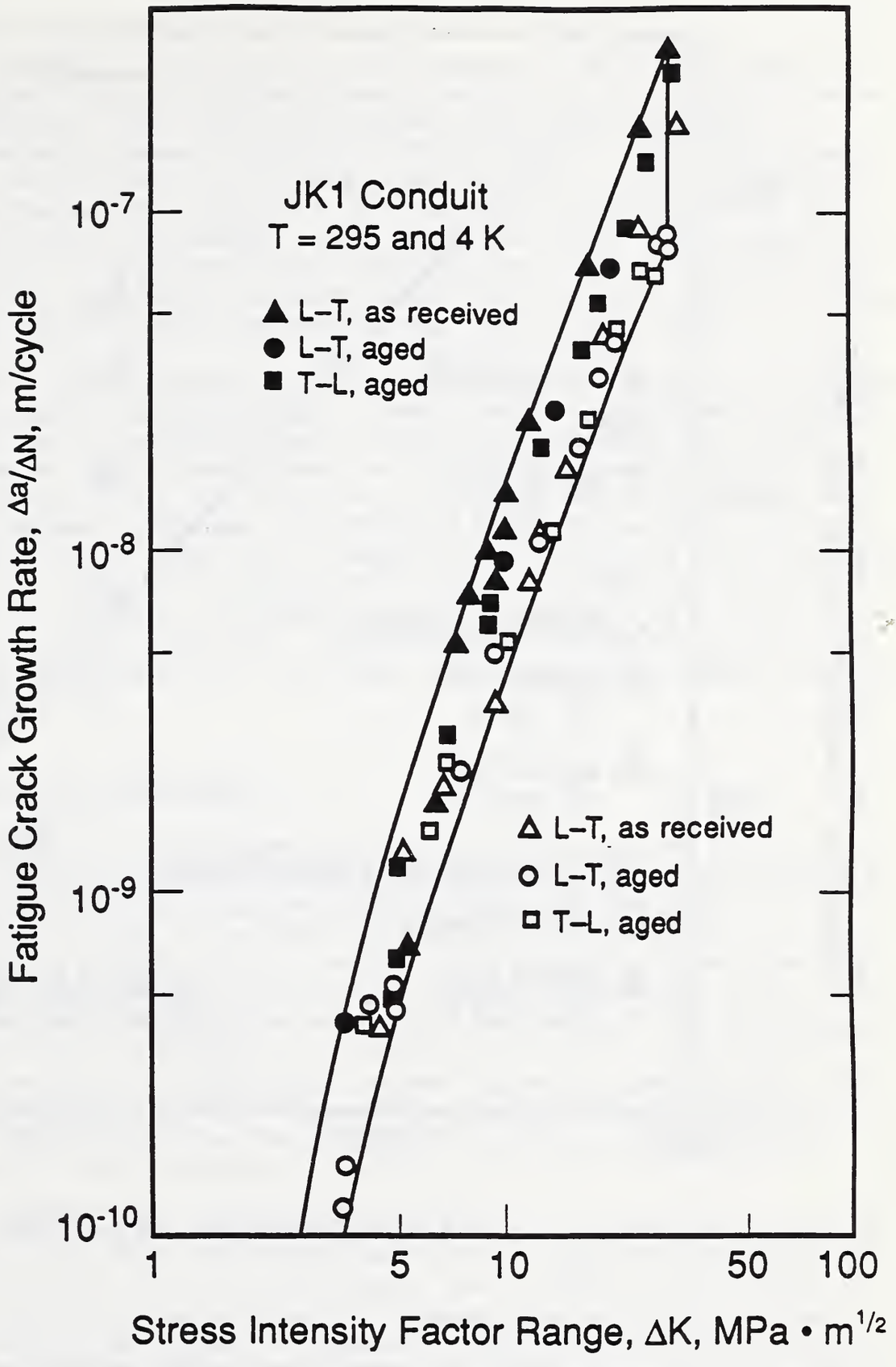

Figure 9. Comparison of fatigue crack growth rate measurements for JK1 conduit using the short crack simulation technique (295 and 4 K). The scatterband encompasses all measurements regardless of ondition, specimen orientation, and temperature.

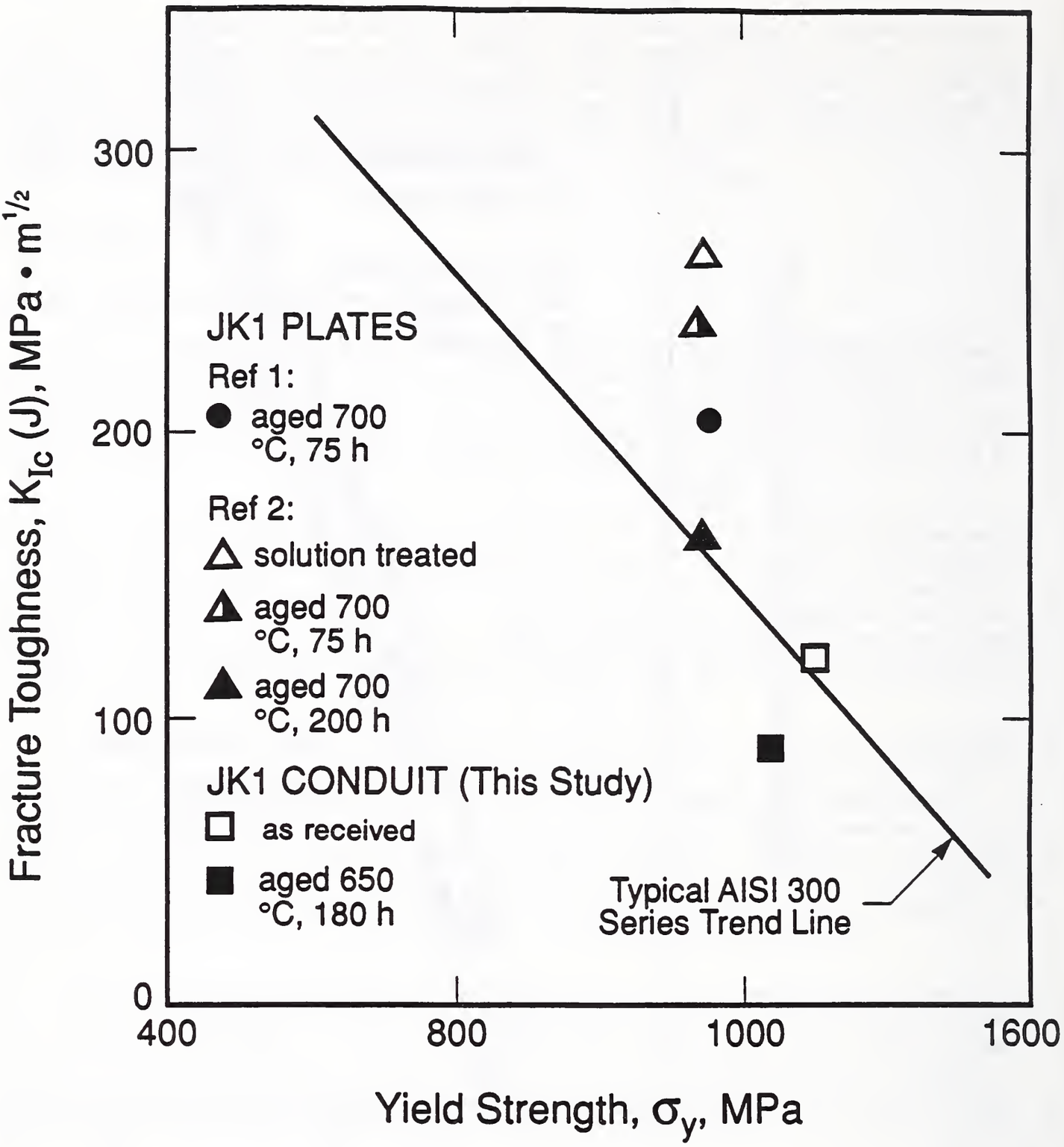

Figure 10. Strength–toughness comparison for JK1 conduit and plates in relation to the trendline for commercial austenitic stainless steel plates at 4 K.

Processing strongly influences the performance of JK1. Even small amounts of cold-working can be deleterious to properties after aging because defects (dislocations) that accelerate diffusion and grain boundary precipitation during subsequent aging are introduced [1]. Long aging times are detrimental because they allows more time for precipitation. From plate studies, the toughness after aging for 75 h is not much different than the solution-treated condition; however, after aging for 200 h, the toughness falls signifiantly and approaches the levels measured in this study for conduit. Therefore, the lower toughness of JK1 in this study might be due to a combination of residual cold work and a long (180 h) aging time.

From a metallurgical viewpoint, the mechanism of the toughness reduction for the conduit remains unidentified. A more complete understanding would require a separation of variables that is beyond the scope of the present study. The complex JK1 microstructure features inclusions, precipitates, and chemical inhomogeniety. In principle, any or all of these factors can contribute to a reduced toughness. We observed no grain boundary facets on the 4-K fracture surfaces (Fig. 6), so apparently the level of grain boundary precipitation after aging is insufficient to cause intergranular fracture in this material at 4 K. The low toughness cannot, therefore, be ascribed simply to grain boundary conditions. The rod-shaped inclusions might contribute to low toughness if at relatively low strains they debond from the matrix and produce voids.

Fatigue Crack Growth at 295 and 4 K

Figure 8 compared our measurements of fatigue crack growth rate with Shimada's [2]. Shimada used the conventional decreasing ΔK procedure with a constant stress ratio of 0.1. His results for JK1 plate are nearly equivalent to NIST results for an AISI 316LN alloy [11] (see Fig. 8) obtained by the same method. In this study of the conduit, we measured the rates at constant K_{max} and the stress ratio changed continuously from 0.1 to 0.9 as ΔK was lowered. Higher rates of fatigue crack growth are expected at the higher stress ratios in this study. At $\Delta K = 36$ MPa·m$^{\frac{1}{2}}$ and $R = 0.1$, however, our rates for the conduit still exceed those for plates of JK1 and AISI 316LN. We conclude that the rates of crack growth for the conduit in this study are higher than those for AISI 316LN or JK1 plates because of material as well as test differences.

Previously published fatigue crack growth rates for austenitic steels at cryogenic temperatures apply for long cracks [6,7]. When the conventional procedure is used for long-crack measurements near threshold the results at low R are influenced by crack closure [6] whereas tests at high R are not. Crack closure reduces the nominal ΔK applied, contributing to lower rates at a given ΔK and higher thresholds at 10^{-10} m/cycle. The technique used in the present study ensures a high R ratio near the threshold. The ΔK_{th} measurements are then conservative, and the da/dN-vs.-ΔK data at 295 and 4 K approximate short crack growth rates at these temperatures [5]. It is accepted that short cracks in structures will grow at rates faster than predicted from long-crack data. Therefore, designers of superconducting machinery may choose to base their design calculations on data produced by the short crack simulation technique employed in this study.

SUMMARY AND CONCLUSIONS

A newly developed conduit sheath material was characterized with respect to its mechanical properties. The material is 316LN, which contains 0.05%Nb to retard carbide precitation during aging. The property measurements at 4 K pertain directly to proposed ITER magnet designs.

The measurements of fatigue crack growth rate in this study used a relatively new (constant K_{max}) technique that can be used for conservative design against failure by fatigue. We believe these data are the first of their kind available for any material at 4 K; all previous cryogenic data reported in the literature were obtained using the conventional decreasing ΔK technique at a constant stress ratio, typically R = 0.1. Essentially, the present results simulate the behavior of short cracks that are of practical concern in conduit applications.

The yield strength of the JK1 conduit exceeds the targetted 1200 MPa at 4 K, but its fracture toughness (J_{Ic} = 40 kJ/m^2) is lower than anticipated from earlier research and development reports. The results suggest that it may be more difficult to achieve the hoped-for mechanical properties in commercial products. Our experience here also underlines the importance of establishing cryogenic material specifications and test standards, and specifying fracture toughness minimums or verification testing for critical materials in the procurement stage.

ACKNOWLEDGMENT

The test material was provided by N. Mitchell of the International Thermonuclear Experimental Reactor and the NET research teams, Garching, West Germany. The research was sponsored solely by the U.S. Department of Energy, Office of Fusion Energy.

REFERENCES

1. M. Shimada and S. Tone, Effects of niobium on cryogenic mechanical properties of aged stainless steels, in: Adv. Cryo. Eng., Vol. 34, Plenum, New York, 1988, pp. 131-139.

2. M. Shimada, Fatigue crack growth rate at 4 K of aged austenitic stainless steels, in: Adv. Cryo. Eng., Vol. 36, Plenum, New York, to be published.

3. D.T. Read and R.L. Tobler, Mechanical property measurements at low temperatures, in: Adv. Cryo. Eng., Vol. 28, Plenum, New York, 1982, pp. 17-28.

4. R.L. Tobler, D.T. Read, and R.P. Reed, Strength/toughness relationship for strengthened AISI stainless steels at 4 K, in: Fracture Mechanics: Thirteenth Conference, ASTM STP 743, R. Roberts, Ed., Amer. Soc. Test. Maters., Philadelphia, 1981, pp. 250-268.

5. W.A. Herman, R.W. Hertzberg, and R. Jaccard, A simplified laboratory approach for the prediction of short crack behavior in engineering structures, Fat. Fract. Eng. Maters. Structs., Vol. 11, No.4, 1988, pp. 303-320.

6. P.K. Liaw and W.A. Logsdon, Fatigue crack growth threshold at cryogenic temperatures: a review, Eng. Fract. Mechs., Vol. 22, 1985, pp. 585-594.

7. R.L. Tobler and Y.W. Cheng, Automatic near-threshold fatigue crack growth rate measurements at liquid helium temperature, Int. J. Fat., Vol. 7, No. 4, 1985, pp. 191-197.

8. R.L. Tobler and Y.W. Cheng, Midrange fatigue crack growth data correlations for structural alloys at room and cryogenic temperatures, in: Fatigue at Low Temperatures, ASTM STP 857, R.I. Stephens, Ed., Amer. Soc. Test. Maters., Philadelphia, 1985, pp. 3-30.

9. M. Shimada, R.L. Tobler, T. Shoji, and H. Takahashi, Size, side-grooving, and fatigue precracking effects on J-integral test results for SUS 304 stainless steel at 4 K, in: Adv. Cryo. Eng., Vol. 34, Plenum, New York, 1988, pp. 251-258.

10. H. Nakajima, K. Yoshida, S. Shimamoto, R.L. Tobler, P.T. Purtscher, and R.P. Reed, Round robin tensile and fracture test results for an Fe-22Mn-13Cr-5Ni austenitic stainless steel at 4 K, Adv. Cryo. Eng., Vol. 34, Plenum, New York, 1988, pp. 241-249.

11. R.L. Tobler, Near-Threshold Fatigue Crack Growth Rate Measurements for Austenitic Stainless Steels at 4 K, in this volume.

NEAR-THRESHOLD FATIGUE CRACK GROWTH OF AUSTENITIC STAINLESS STEELS AT CRYOGENIC TEMPERATURES

R.L. Tobler

Materials Reliability Division
National Institute for Standards and Technology
Boulder, Colorado 80303

Measurements of fatigue crack growth rate are reported for 5 austenitic stainless steels at room and cryogenic temperatures (76 or 4 K). The alloys evaluated in this study were AISI 316, 316LN, 304L, 304LN, and 304HN. The rate measurements span the range 10^{-6} to 10^{-10} m/cycle, and threshold stress intensity factors are identified at 10^{-10} m/cycle. The apparent thresholds for the 5 steels range between 6.5 and 10.5 MPa·$m^{\frac{1}{2}}$ and vary slightly with material and temperature. The effective thresholds (that is, the apparent thresholds corrected for crack closure) are uniformly lower than the apparent thresholds and range between 4 and 7 MPa·$m^{\frac{1}{2}}$. At 4 K the thresholds increase moderately with yield strength which ranges from 610 to 1270 MPa for these alloys.

INTRODUCTION

Fatigue crack growth rates and threshold stress intensity factors are relevant to superconducting magnet design because they can be used to predict safe operating conditions and lifetimes. Typically, fatigue crack growth rates (da/dN) are plotted versus the stress intensity factor range (ΔK); the data on log–log coordinates define a curve that may be divided into 3 stages: very low rates approaching threshold values, intermediate rates of growth, and high rates approaching instability.

In Stage I (low ΔK) the crack growth rates diminish and approach an asymptote called the threshold, ΔK_{Th}. Measurements near threshold are time consuming and difficult to perform, so few data are available in this stage. Liaw and Logsdon [1] reviewed these data in 1985. In Stage II (intermediate ΔK) the measurements are easier and can be completed in relatively short time; consequently the database for cryogenic materials in Stage II is larger than in the other stages. Those data were reviewed by Tobler and Cheng [2], also in 1985. In Stage III (high ΔK), the crack growth rates for materials accelerate as ΔK approaches the upper critical limit of fracture toughness. This third stage is seldom studied because the crack growth rates are too high for practical applications.

Owing to measurement difficulties the Stage I database for stainless steels at cryogenic temperatures remains quite limited. All the problems associated with room temperature testing, and more, are present in high-cycle cryogenic testing. The cost and complexity of testing, as well as material variability, is greater at cryogenic temperatures. Good experimental technique is important, and automatic testing with computers to acquire data in a reasonable time. Liaw and co-workers [3,4] designed a fully automatic fatigue apparatus and report data for aged Fe-29Ni-14Cr-1.2Mo austenitic stainless steel and its welds at 297, 97, and 4 K. They used a servohydraulic, computer-controlled test machine, conventional fracture mechanics specimens, and a compliance technique. Later, we adopted their method and evaluated 3 austenitic stainless steels at 4 K [5,6].

At the time of their review, Liaw and Logsdon found data for only one austenitic stainless steel: AISI 304. Austenitic alloys, especially the stainless steels, are important candidates for cryogenic magnet applications in fusion energy. Therefore our purpose is to increase the data available for these materials. This paper presents the initial results for long cracks in five commercial 300 series stainless steels. Short crack behavior in these alloys is the subject of a later paper.

PROCEDURES

Experimental Apparatus

The apparatus pictured in Fig. 1 is an automatic test system that allows continous testing, data collection, and load adjustments to be performed by computer without the assistance of a machine operator. Automatic testing minimizes time and reduces data scatter, owing to higher precision in crack length measurement and better control of data point spacing. The automatic procedure is relatively easy to implement with minimal operator training, and it eliminates subjective interpretation and operator bias.

The system consists of a 100-kN servohydraulic test machine and cryostat, a programmable digital oscilloscope, a programmable arbitrary waveform generator, a minicomputer and an automatic liquid helium refill system. The servohydraulic machine has an inverted stage with its actuator above the cryostat. The system includes a servo control system with two DC conditioners, a valve drive, a signal amplifier, and a load cell. The fatigue cycle counts are calculated by computer from the test frequency and elapsed time. A programmable arbitrary-waveform generator is used since the applied loads vary with time. The specimen is pinned at the bottom of the load frame and enclosed during cryogenic tests in a vacuum-insulated stainless steel Dewar. Nonmetallic materials of low thermal conductivity are used to reduce the steady state heat leak into the dewar. The cryostat design and associated instrumentation are described elsewhere in detail [6].

An automatic refill system, shown in Fig. 2, keeps the specimen fully submerged in liquid helium for continous 24-h operation. The components include a 305-mm superconducting liquid-level detector, a level controller, a conventional three-way solenoid value, a pressurized helium gas cylinder, and

a 500-l liquid helium supply Dewar. A vacuum-jacketed flexible copper transfer line connects the supply Dewar to the cryostat. The liquid helium in the cryostat is monitored by the detector, which is attached to one of the load frame columns. The desired minimum and maximum level limits are set on the controller, and they trigger the solenoid valve that regulates liquid helium transfer.

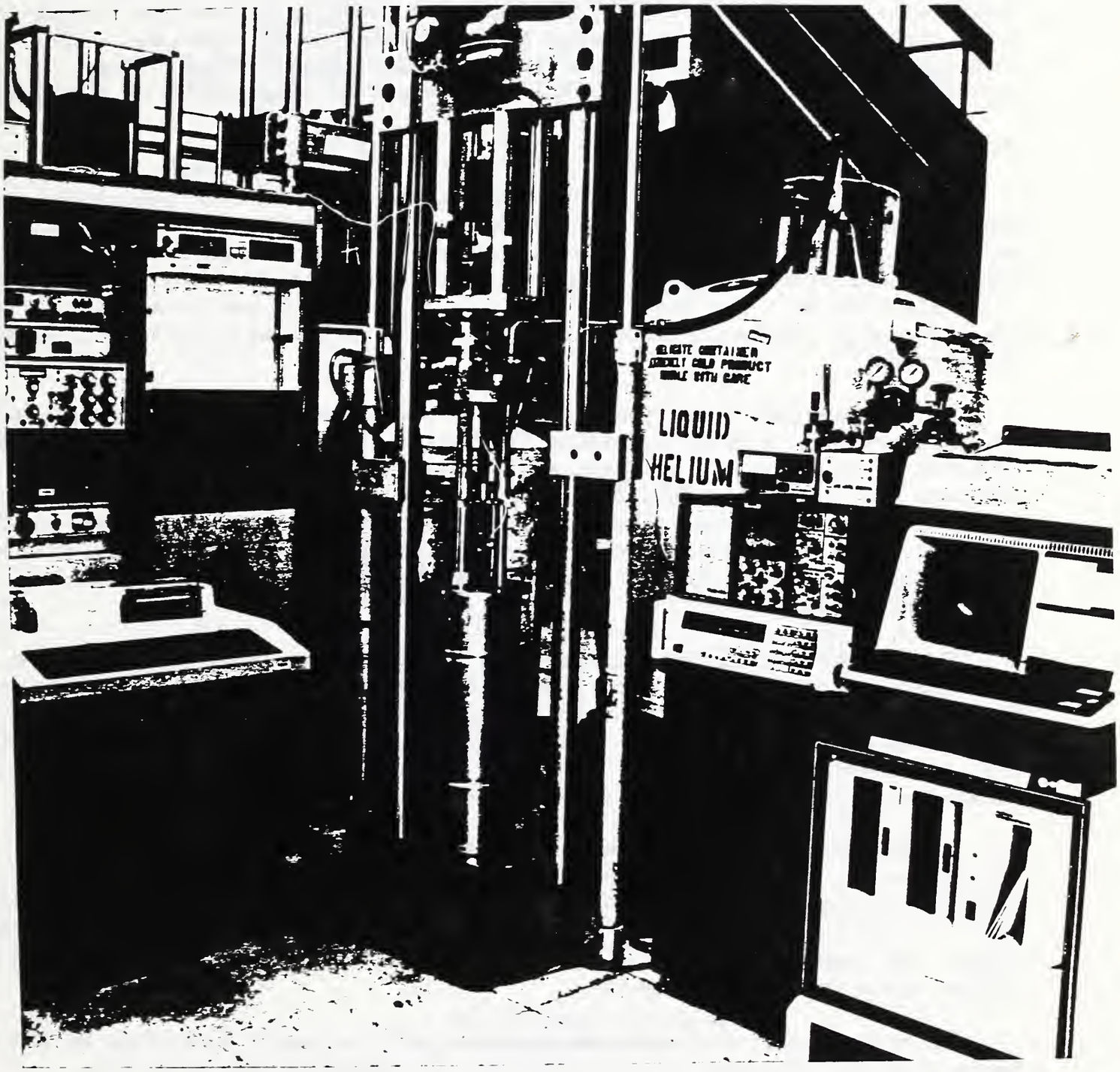

Figure 1. Computer-controlled fatigue test system.

Specimen Geometry and Clip Gage

The compact specimen used in this study is shown in Fig. 3. The specimen width (W) is 76.2 mm and the thickness (B) is 6.4 mm. The relatively large W/B ratio of 12 provides a sizeable ligament for crack growth while minimizing the loads required. The machined notch is 22.9 mm long (a/W = 0.3) and the notch tip radius is 0.05 mm. The clip gage used in these tests is ring-shaped [7]. The gage was modified to use short beams which enable the gage to be mounted tightly, close to the specimen. This stabilizes the gage against vibration and reduces signal noise. Gage calibrations at 295, 76, and 4 K are independent of temperature to within 2%.

Test Procedure

Crack length (a) is measured by compliance with the clip gage mounted at the specimen edge. Compliance is specimen deflection per unit load, which depends on crack length for a given material and specimen geometry. The instantaneous crack length is computed using Saxena and Hudak's [8] function to within 0.04 mm. The load cell and clip gage signals are interfaced to the computer which infers the crack length once per minute and displays it on the CRT terminal.

As the specimen is fatigued under the prescribed loading conditions and cyclic frequency, a crack initiates and begins to grow. When the preselected interval (1 min) for crack length measurement is reached, the computer requests the compliance data from the oscilloscope, which instantaneously freezes the load-vs.-displacement signals in memory and transmits them to the computer. The computer fits the data to a straight line using a linear least-squares method. Correlation coefficients of 0.995 or higher are usually obtained.

Only a portion of the load-vs.-displacement curve (the part between a specified intermediate load and a value corresponding to 95% of the maximum fatigue load) is used for the compliance calculations. The specified intermediate load is typically the mean load, because this is usually larger than the crack closure loads. The upper 5% of the load is excluded to eliminate any signal noise at maximum load during high-frequency tests.

As the crack grows, the difference between the current measured crack length and the previously recorded crack length is checked against a specified value (0.5 mm), which is within the recommended values of ASTM E 647-83. If the increment of growth is equal to or greater than the specified value, the computer calculates a, N, da/dN, and ΔK. These data are stored on floppy discs for later analyses.

In this study, the loads are progressively decreased according to the decreasing-ΔK technique. The loads are calculated from the equations:

$$\Delta K = \Delta K_0 \exp[C(a-a_0)], \quad (1)$$

$$\Delta P = BW^{1/2}\Delta K/f(a/W), \text{ and} \quad (2)$$

$$P_{max} = \Delta P/(1-R), \quad P_{min} = P_{max}R, \quad (3)$$

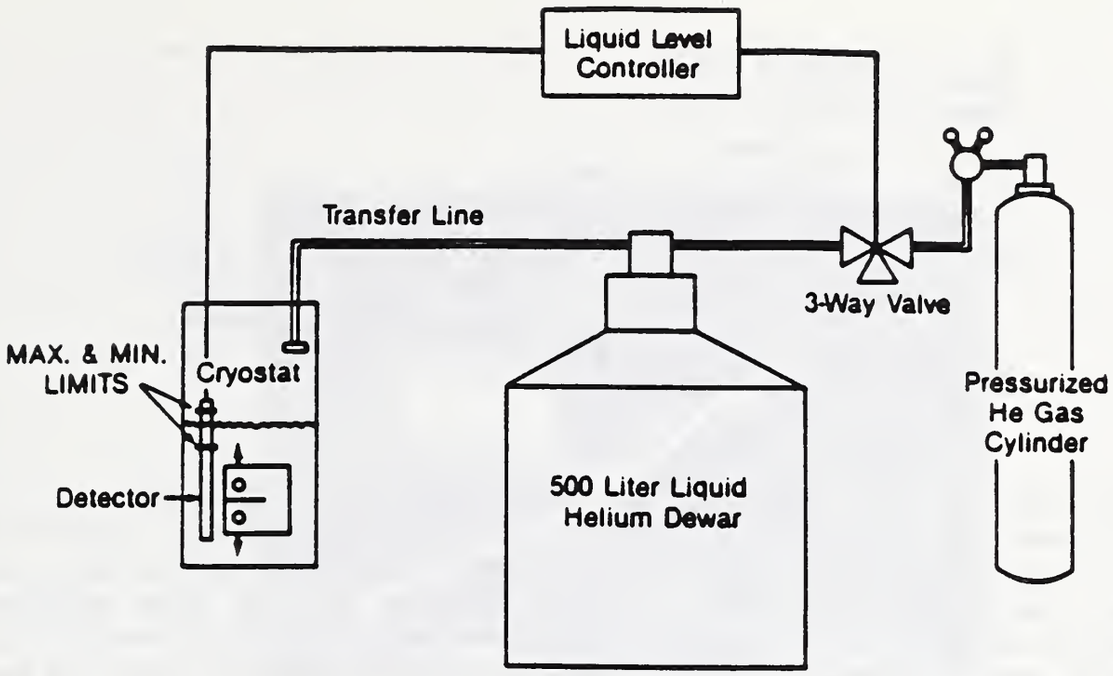

Figure 2. Schematic of automatic helium refill system.

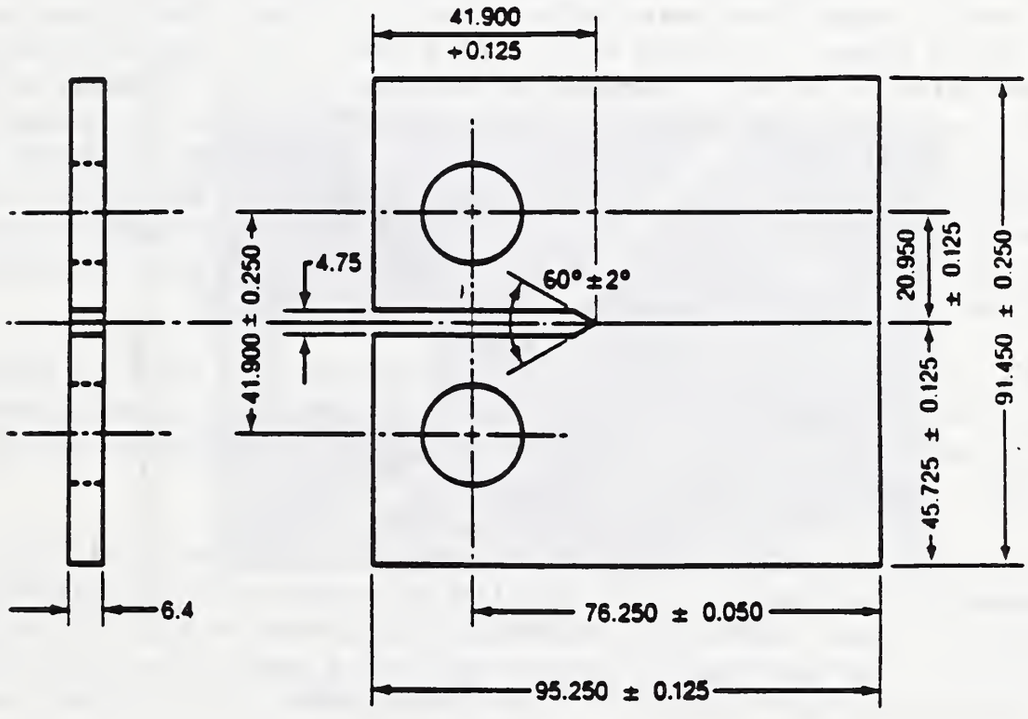

Figure 3. Fatigue test specimen.

where

P_{max} = maximum load
P_{min} = minimum load
$R = P_{min}/P_{max}$
a = current crack length
a_0 = crack length at the start of test
$f(a/W) = [2 + (a/W)][0.886 + 4.64(a/W) - 13.32(a/W)^2 + 14.72(a/W)^3 - 5.6(a/W)^4]/[1 - (a/W)]^{1.5}$
ΔK = current crack-tip stress intensity range
ΔK_0 = crack-tip stress intensity range at the start of test
C = a constant

The data were obtained in two steps. The rates from about 10^{-8} to 10^{-10} m/cycle were first measured by the decreasing ΔK technique starting at ΔK = 15 MPa·m$^{\frac{1}{2}}$ with $C = -0.08$ mm^{-1} and f = 40 Hz. After reaching ΔK_{Th} at 10^{-10} m/cycle, the test was stopped. The second data set was then measured by an increasing ΔK technique, starting again at about ΔK = 15 MPa·m$^{\frac{1}{2}}$, but with C = 0.10 mm^{-1} and f = 10 or 20 Hz. This second data set provided the rates up to about 10^{-6} m/cycle.

The sequence of operations is as follows. After each crack length measurement, the crack length is compared with the last stored crack length to ensure that a specified measurable amount of crack growth has occurred. After the crack grows a certain amount (0.13 mm), the new ΔK is calculated.

At the relatively high frequencies desired in near-threshold fatigue testing, hydraulic lag can occur. Then, the specimen is not actually subjected to the load range commanded by the computer or waveform generator. Overprogramming is sometimes necessary to overcome the problem. Automatic overprogramming is a trial-and-error process whereby the computer monitors the values of P_{max} and P_{min} through the programmable digital oscilloscope and makes necessary changes to achieve the commanded values.

During the test, point-to-point data reduction is used to calculate ΔK and da/dN from a and N. If the results of da/dN-vs.-ΔK scatter excessively, the seven-point incremental polynomial method can be used to smooth the results after the test is completed.

For simplicity in this study the da/dN-vs.-ΔK curves and ΔK_{Th} results are presented on the basis of the applied ΔK values with no corrections for crack closure. Since there are no accepted standard values of properties for these materials, no meaningful statements can be made about the accuracy of results. The measurement precision is commensurate with current practice.

Following the determination of ΔK_{Th}, a correction for crack closure is applied. Crack closure causes the cracks to remain closed for a portion of the load cycle; this portion of the load is ineffective in contributing to the driving force for crack growth. In Fig. 4, the lower segments of the bilinear load–displacement curves are associated with closure and are disregarded in the calculation of the effective ΔK. The correction factor is $(P_{max} - P_C)/(P_{max} - P_{min})$, where P_C is the load at closure; this factor multiplied times the apparent threshold gives the effective threshold.

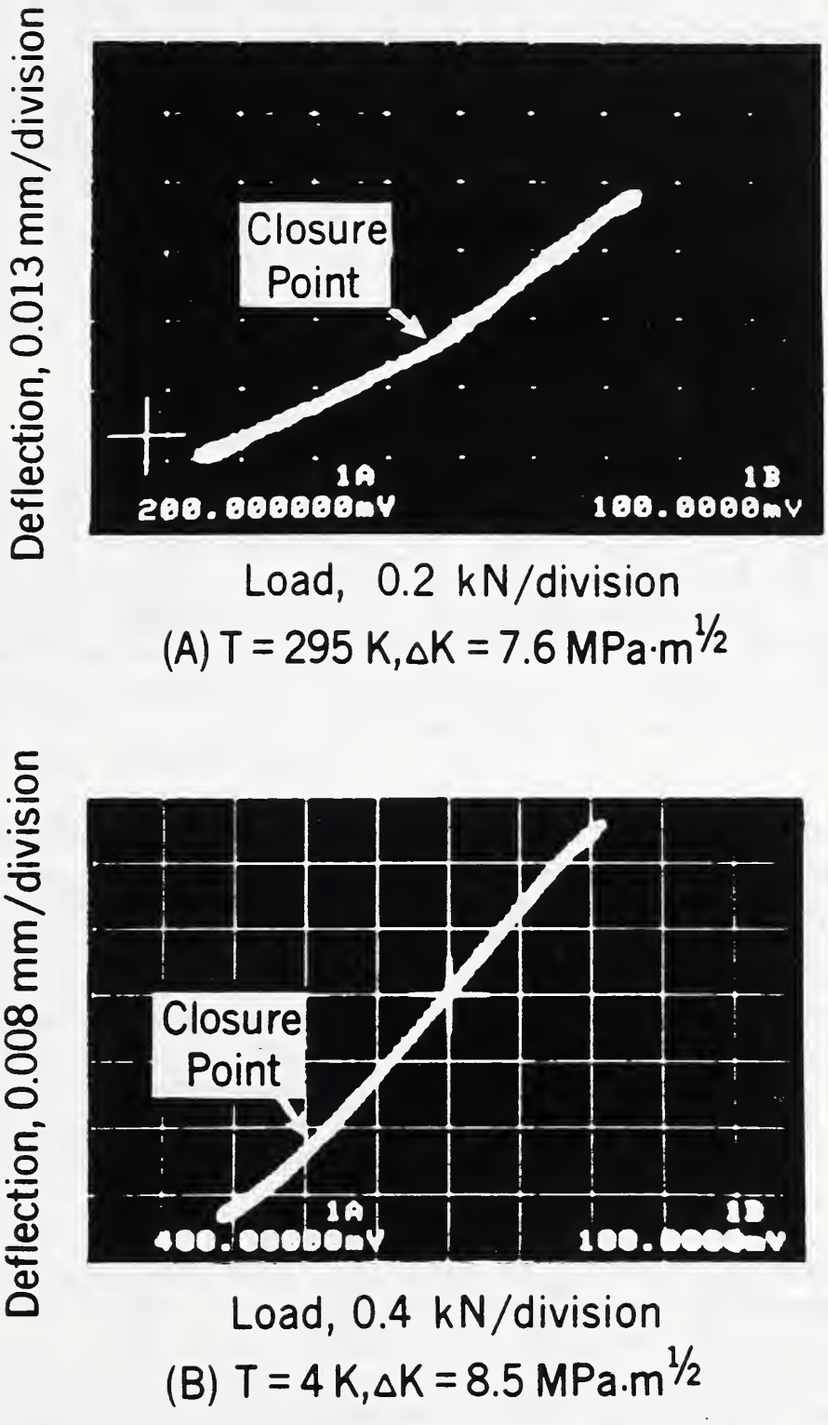

Figure 4. Load–displacement records showing evidence of crack closure.

MATERIALS

Five austenitic stainless steels were tested. The materials were plates and bars in the as-received, annealed conditions. AISI 316, 304L, and 304LN were 51, 25, and 25 mm thick plates, respectively. Specimens from these plates were machined in the T-L orientation according to the designation used in ASTM Methods E 399-83. AISI 316LN was a 457 mm diameter bar, and AISI 304 HN was a 165 mm diameter bar; the specimen orientations for these alloys were R-C and R-L, respectively. Tables 1 and 2 list the chemical compositions and selected tensile properties for each material at room temperature and 4 K.

Table 1. Composition of test materials (mass %). Balance is Fe.

Material	Cr	Ni	C	N	Mn	P	S	Si	Cu	Mo
AISI 316	17.25	13.48	0.057	0.030	1.86	0.024	0.019	0.58	--	2.34
AISI 316LN	16.71	13.83	0.029	0.100	1.84	0.021	0.008	0.33	--	2.18
AISI 304L	18.20	8.56	0.020	0.082	1.73	0.024	0.005	0.62	0.24	0.40
AISI 304LN	18.00	9.91	0.037	0.120	1.50	0.022	0.017	0.57	0.197	0.205
AISI 304HN	20.21	8.44	0.059	0.28	1.83	0.025	0.021	0.50	0.60	0.59

Table 2. Measured mechanical properties of test materials.

Material	Test temperature (K)	Yield strength (MPa)	Ultimate strength (MPa)	Elongation (%)	Reduction of area (%)
AISI 316	295	228	576	56	73
	4	711	1301	48	57
AISI 316LN	295[a]	267	551	53	76
	4	834	1364	45	53
AISI 304L	295	245	642	66	77
	4	610	1678	35	48
AISI 304LN	295	279	612	68	62
	4	745	1570	34	42
AISI 304HN	295[a]	441	765	47	73
	4	1267	1727	8	22

[a]Room temperature data are from manufacturer's mill sheet.

RESULTS

The da/dN-vs.-ΔK curves for the 5 stainless steels at selected temperatures and stress ratios are presented in Figs. 5-13. In these figures, da/dN is plotted versus the applied ΔK values without closure corrections. Following conventional methodology, the threshold is operationally defined as the value of ΔK corresponding to an average rate of 10^{-10} m/cycle. This rate corresponds to less than 1 lattice spacing per load cycle. The apparent thresholds (to the nearset 0.5 MPa.m$^{\frac{1}{2}}$) were obtained from the data plots and are listed in Tables 3 and 4, along with the effective thresholds which are from the apparent thresholds with corrections for crack closure.

AISI 316

Figure 5 shows room temperature results for AISI 316 at R = 0.1. The data trend on log–log coordinates is linear, and the rates at low ΔK do not begin to approach an asymptote at 10^{-10} m/cycle. The measurements agree well with rates reported by Read and Reed [9], who tested this same heat in Stage II at ΔK = 25 to 50 MPa·m$^{\frac{1}{2}}$. Our data at low ΔK complement their data for 25-mm thick compact specimens at 20 Hz. This indicates there is no effect of specimen thickness between 6 and 25 mm, that the Stage II linear trend for this alloy apparently extends to exceptionally low growth rates, and that true thresholds, if they exist, could be detected only by measurements at lower ΔK values than studied here.

The 4-K measurements for AISI 316 at R = 0.1 are also shown in Fig. 5. Again, the rates are in fair agreement with the previous Stage II results [10] for 25-mm thick specimens, but the data trend differs from that at 295 K. Over the broader range of ΔK the da/dN curve at 4 K shows a knee and crosses the 295-K trend line twice. Clearly, for AISI 316 at R = 0.1, reducing the temperature from 295 to 4 K increases the threshold for fatigue crack growth. The apparent ΔK_{Th} at 4 K (8.5 MPa·m$^{\frac{1}{2}}$) is slightly higher than that at 295 K (7.5 MPa·m$^{\frac{1}{2}}$). When crack closure corrections are applied, the effect of temperature on ΔK_{Th} is maintained, as shown by the effective threshold values listed in Table 3.

Fatigue crack growth at a higher stress ratio, R = 0.3, is shown in Fig. 6. This time the apparent ΔK_{Th} decreases as the test temperature is decreased from 295 to 4 K. This is the opposite of the temperature dependence shown in Fig. 5 and Table 3 for apparent thresholds at R = 0.1. As explained later this apparent reversal of the temperature dependence is due to crack closure. The effective values of ΔK_{Th} do follow the same temperature dependence at both R ratios, as shown in Table 3.

By comparing the room temperature data in Figs. 5 and 6, we see that the 295 K rates and thresholds are independent of stress ratio at R = 0.1 and 0.3. At 4 K, however, a significant effect of R ratio emerges, as shown by the data in Fig. 7. In tests at 4 K, we examined the behavior at 4 different stress ratios between 0.1 and 0.7. For the range of ΔK studied, the 4-K rates are equivalent at R = 0.3, 0.5, and 0.7, but higher than at R = 0.1. In addition, the range of Stage II is dpressed at the higher R ratios as compared to R = 0.1. ΔK_{Th} is also lower at R = 0.3, 0.5, and 0.7 than it is at 0.1.

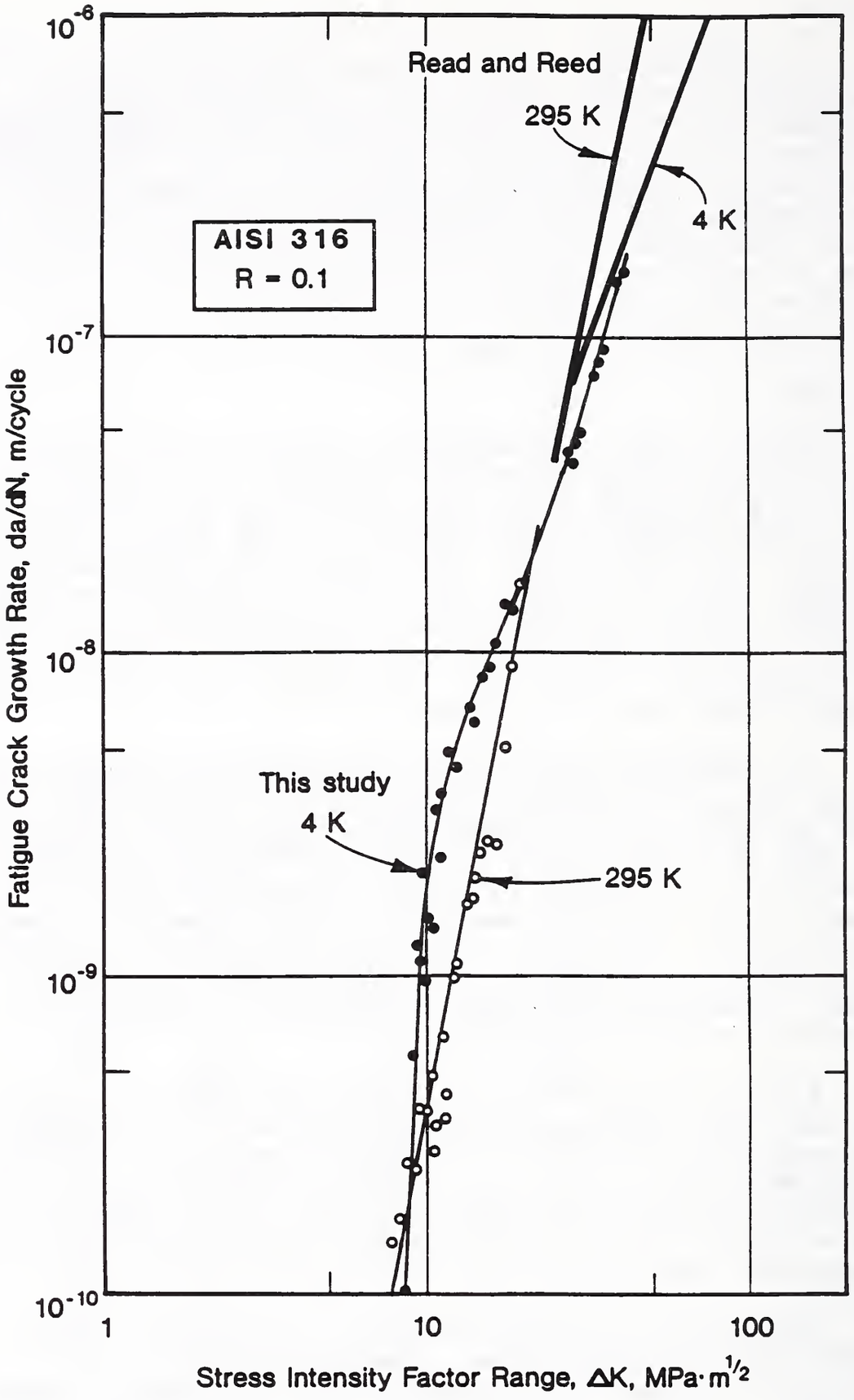

Figure 5. Fatigue crack growth rate data for AISI 316 at R = 0.1.

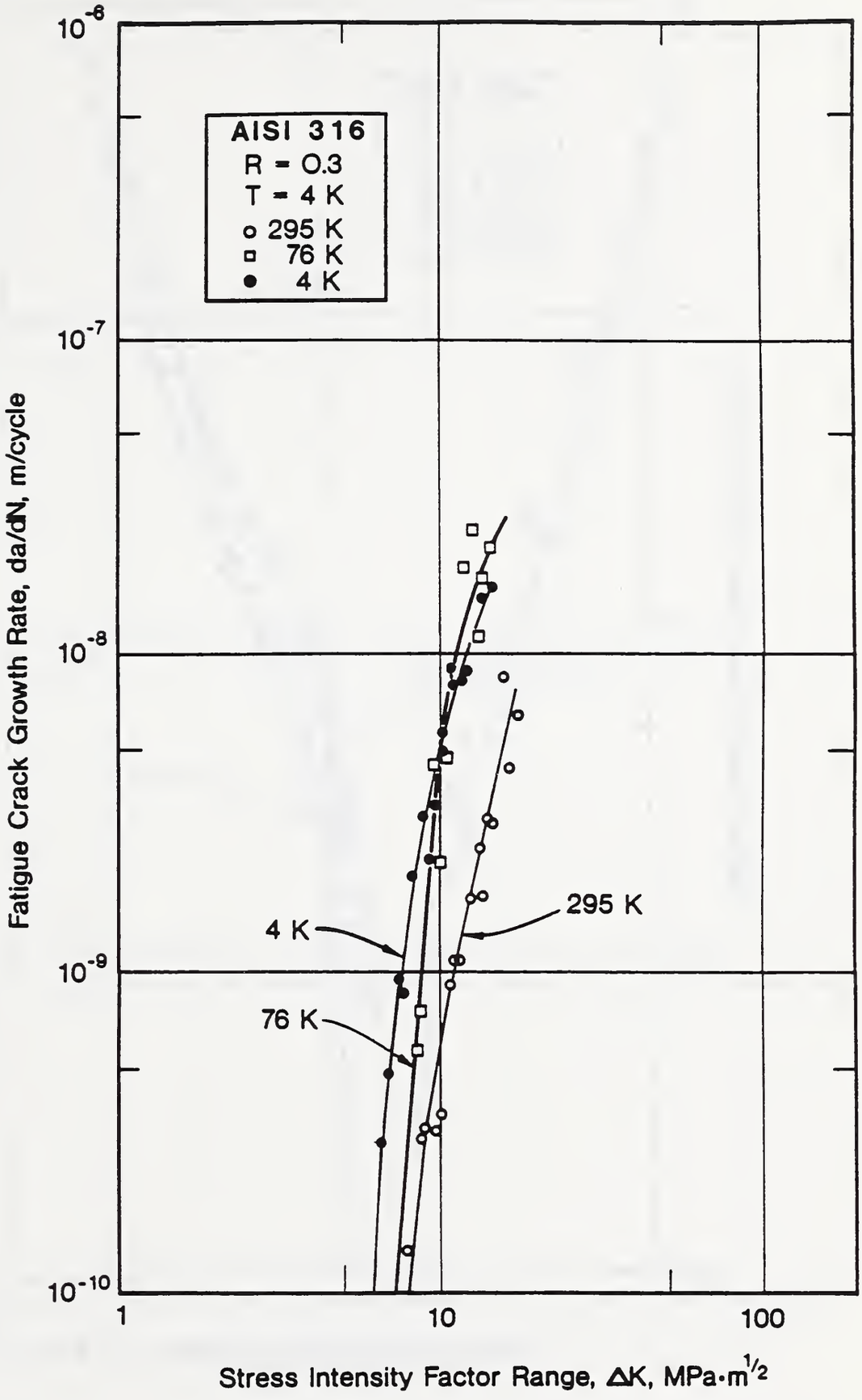

Figure 6. Fatigue crack growth rate data for AISI 316 at R = 0.3.

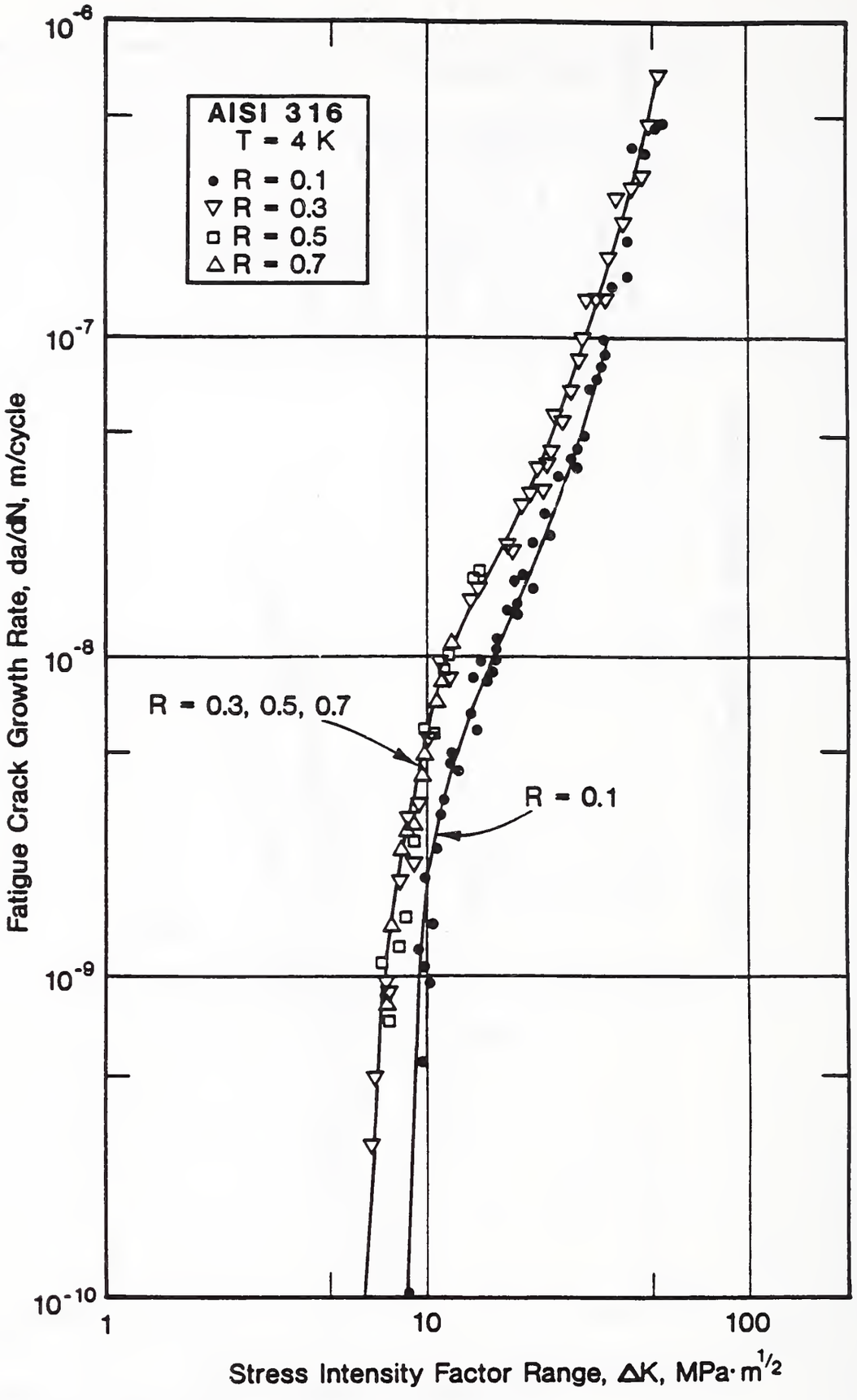

Figure 7. Fatigue crack growth rate data for AISI 316 at several stress ratios.

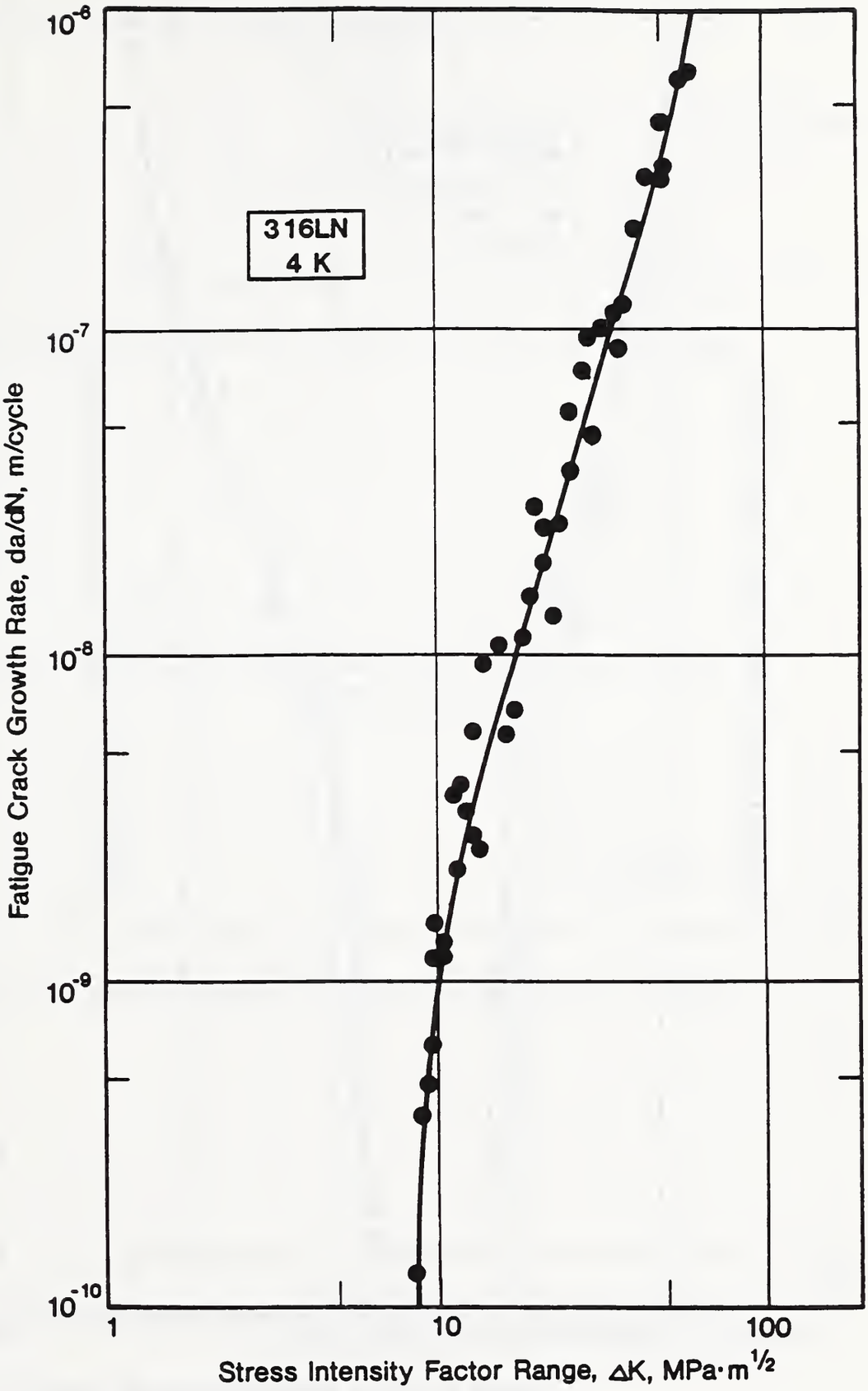

Figure 8. Fatigue crack growth rate data for AISI 316LN at R = 0.1.

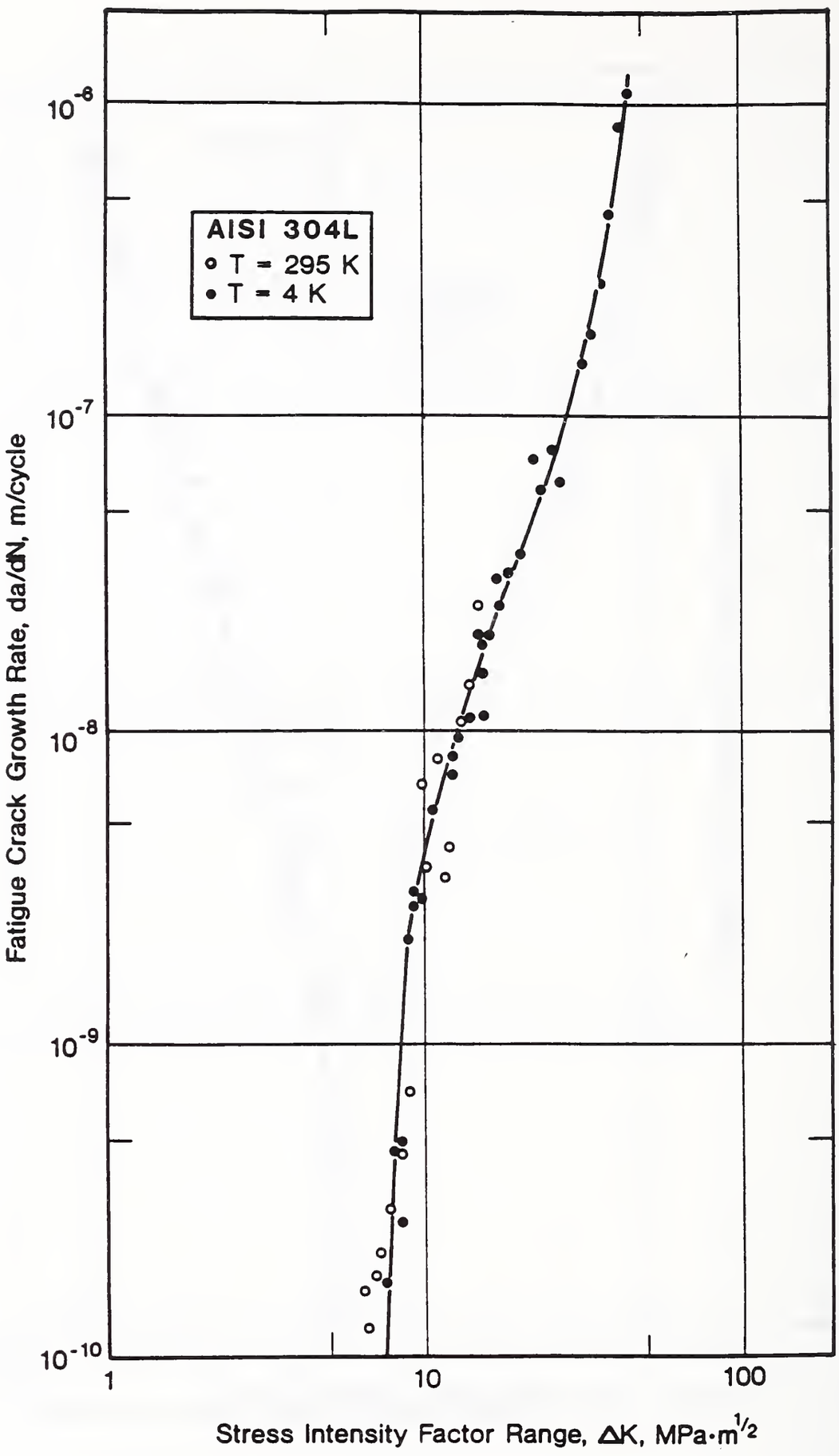

Figure 9. Fatigue crack growth rate data for AISI 304L at R = 0.1.

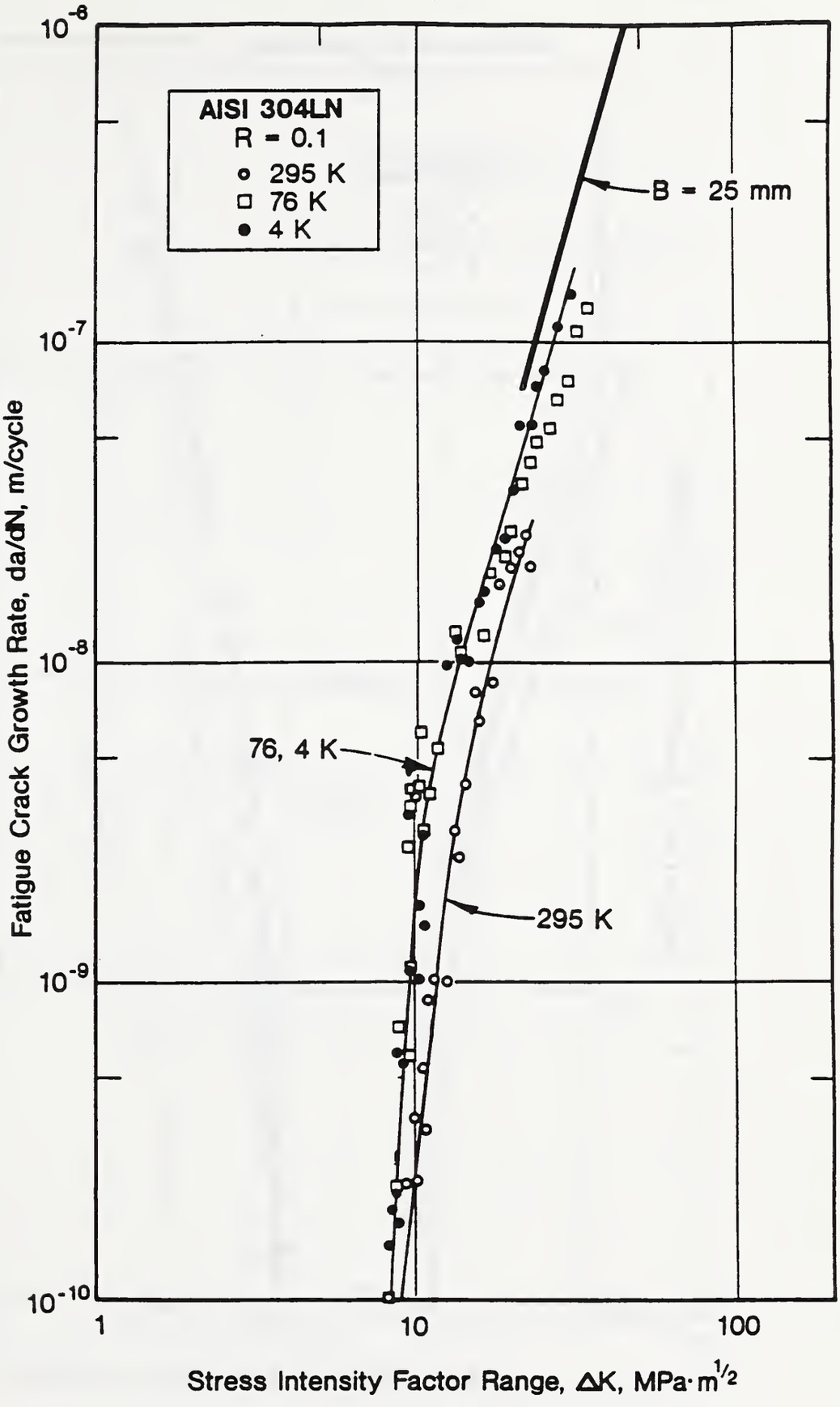

Figure 10. Fatigue crack growth rate data for AISI 304LN at R = 0.1.

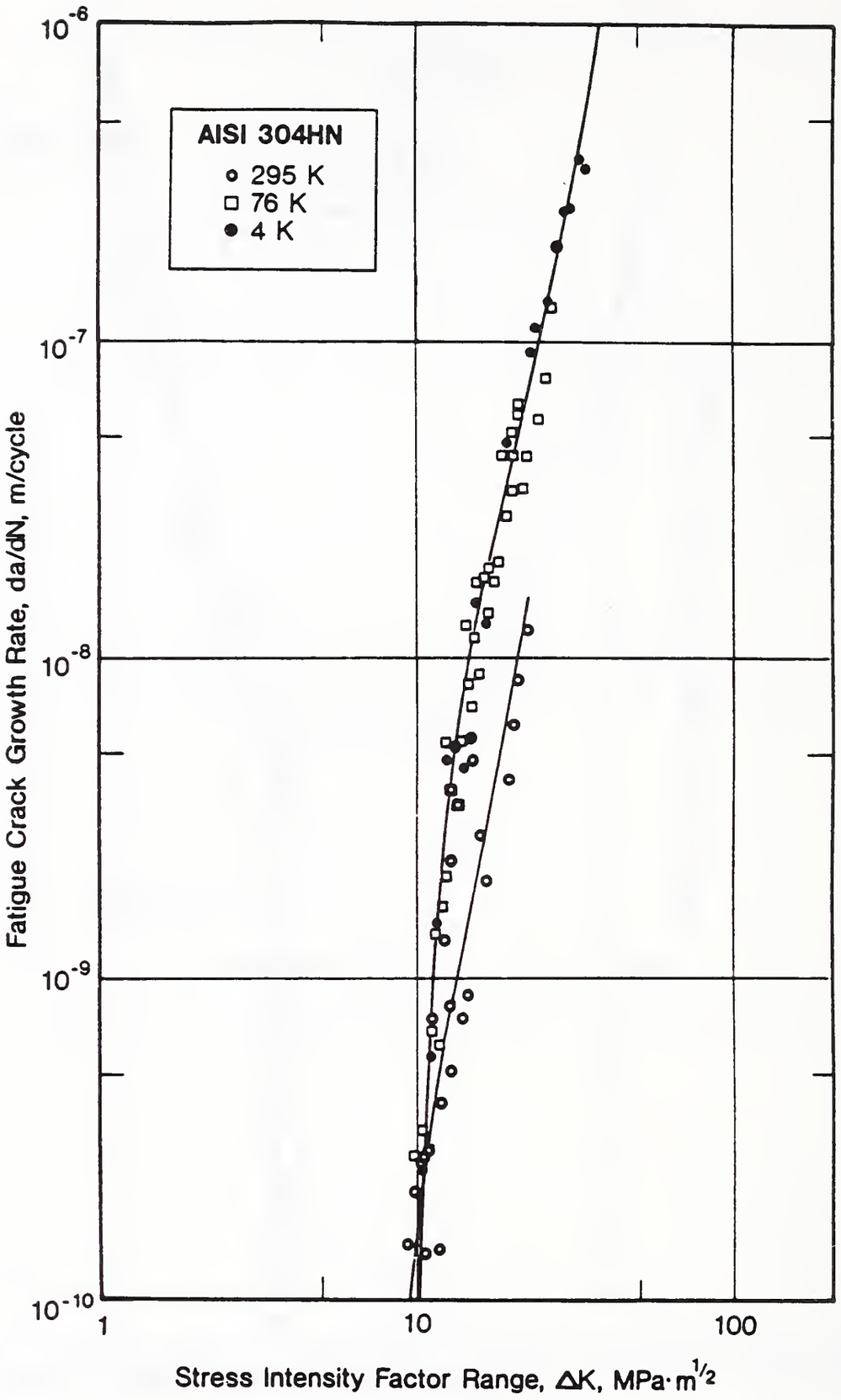

Figure 11. Fatigue crack growth rate data for AISI 304HN at R = 0.1.

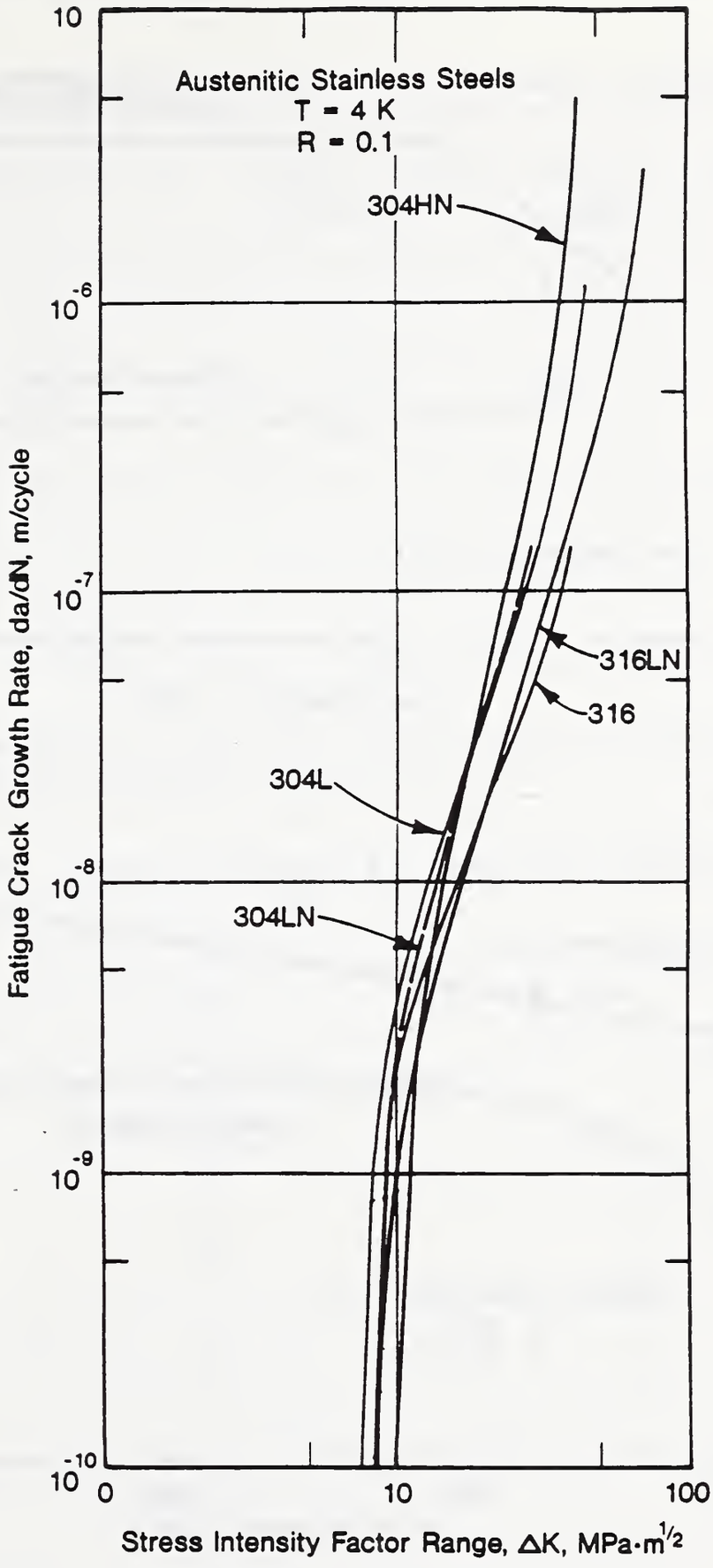

Figure 12. Fatigue crack growth rate data for 5 stainless steels at 4 K.

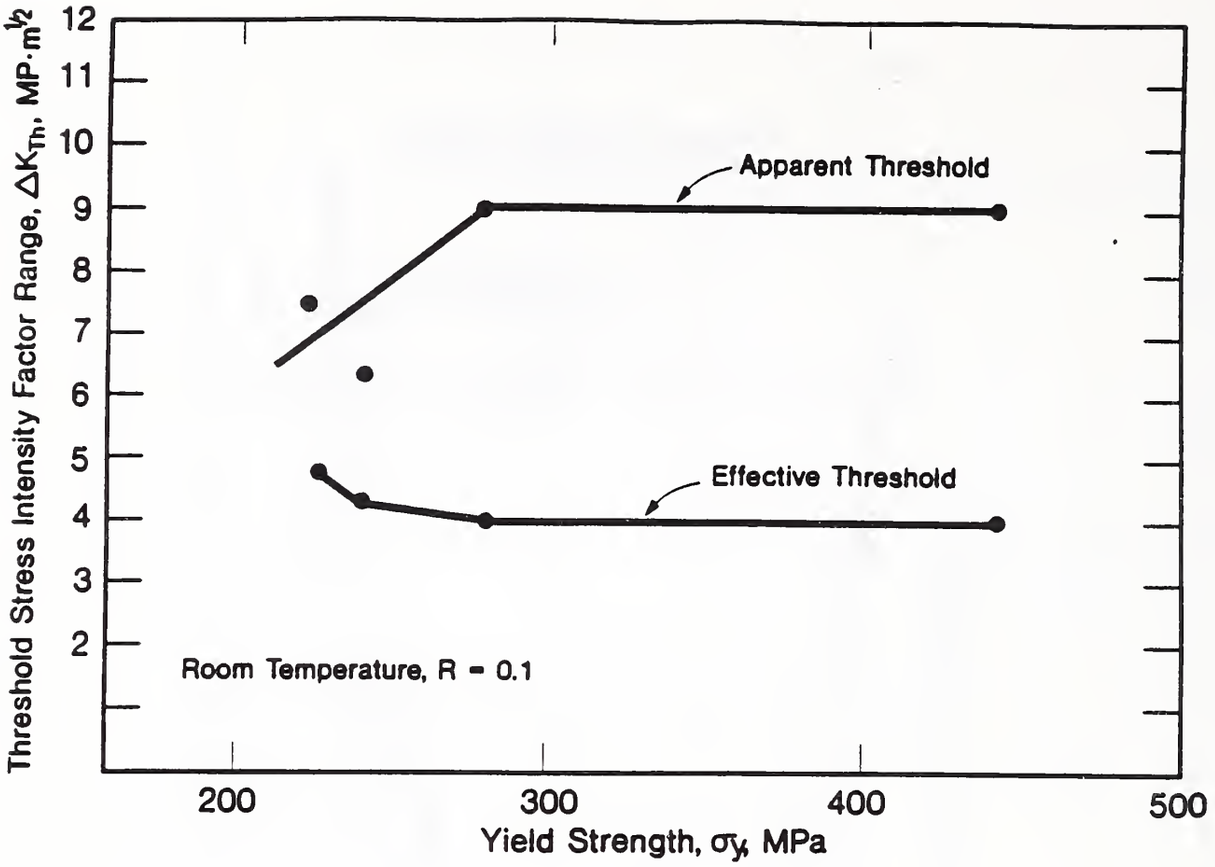

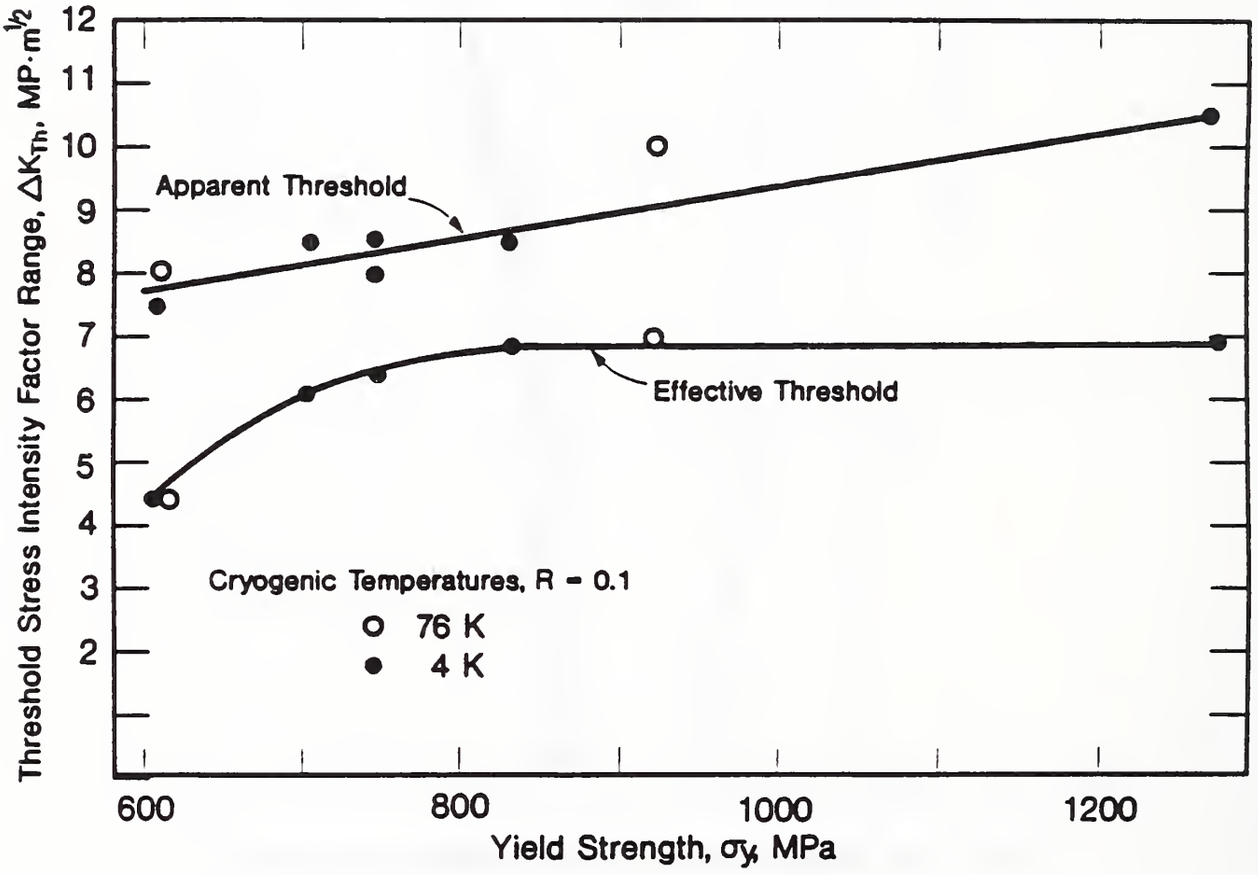

Figure 13. Dependence of fatigue crack growth thresholds on yield strength.

Table 3. Apparent and effective threshold stress intensity factors for AISI 316 stainless steel at two temperatures and two stress ratios.

Temperature (K)	Stress Ratio, R	Apparent K_{Th} ($MPa \cdot m^{1/2}$)	Effective K_{Th} ($MPa \cdot m^{1/2}$)
295	0.1	7.5	4.6
	0.3	7.5	4.6
4	0.1	8.5	6.1
	0.3	6.5	5.1

Table 4. Apparent and effective threshold stress intensity factors for 5 austentitic stainless steels at R = 0.1.

Alloy	Temperature	Apparent Threshold, K_{Th}	Effective Threshold, K_{Th}
AISI 316	295	7.5	4.6
	4	8.5	6.1
AISI 316LN	4	8.5	6.8
AISI 304L	295	6.5	4.3
	4	7.5	4.4
AISI 304LN	295	9.0	4.0
	76	8.0	4.4
	4	8.0	6.3
AISI 304HN	295	9.0	4.0
	76	10.0	7.0
	4	10.5	6.8

AISI 316LN

AISI 316LN contains less carbon and more nitrogen than AISI 316. The yield strength of AISI 316LN is consequently higher at 4 K but otherwise the two alloys have nearly equivalent mechanical properties in tension tests (Table 2). Fatigue crack growth rates for AISI 316LN were measured in liquid helium at R = 0.1, and the results are plotted in Fig. 8. The data define a curve similar to that for 316. The apparent threshold, 8.5 MPa·$m^{½}$, is equal to that for AISI 316 at T = 4 K and R = 0.1. The AISI 316LN alloy was not studied further since it behaves similarly to AISI 316.

AISI 304L

Figure 9 presents the data for AISI 304L. The 304L (and other 304-type steels) has substantially less Ni than 316 or 316LN; it also has a lower yield strength but a higher ultimate strength than 316 or 316LN. The fatigue crack growth rates for 304L at R = 0.1 were measured at 295 and 4 K and the results are shown in Fig. 9. In general, the 304L behavior is similar to that of AISI 316 and 316LN at the conditions studied: the 295 K data trend is nearly linear, the 4 K trend is sigmoidal, and the two trend lines cross twice. The ΔK_{Th} are 6.5 MPa·$m^{½}$ at 295 K and 7.5 MPa·$m^{½}$ at 4 K.

AISI 304LN

The 304LN steel of this study has 0.04% more N than the 304L, which makes it stronger than the 304L, and it has 2% more Ni which makes it more stable against phase transformation. Figure 10 presents the data for AISI 304LN at R = 0.1. The fatigue crack growth rates were measured at 295, 76, and 4 K. The rates for 304LN are similar to those for 304L over most of the ΔK range studied. The data at 295 K do not show an obvious knee at low ΔK. A gentle curve suffices to describe the trend. In stage I, the 76 and 4 K results appear to be essentially equivalent. The apparent thresholds at both these cryogenic temperatures are 8 MPa·$m^{½}$ which is lower than the 9.0 MPa·$m^{½}$ value obtained at 295 K. However, the effective threshold is higher at 4 K than at room temperature or 76 K.

AISI 304HN

AISI 304HN contains more N than any other alloy of this study. As a result, the alloy has greater strength and lower ductility than the others. The yield strength of the 304HN at 4 K is particularly high and exceeds 1200 MPa. Figure 11 presents the measurements of fatigue crack growth rates for AISI 304HN at three temperatures (295, 76, and 4 K) and R = 0.1. The apparent thresholds at each temperature are the highest reported for the 5 steels tested in this study. Again the apparent and effective thresholds increase at cryogenic temperatures. The results at 76 and 4 K are essentially equivalent, and higher than at 295 K. At 4 K the apparent and effective thresholds reach 10.5 and 6.8 MPa·$m^{½}$, respectively, and are clearly the highest values observed for any alloy in this study.

Comparison

Figure 12 compares all 5 alloys at T = 4 K and R = 0.1. Overall, the data define similarly shaped curves that fit in a relatively narrow band, with appparent thresholds ranging from 6.5 to 10.5 MPa·$m^{\frac{1}{2}}$. Some metallurgical effects are perceived in the results. For example, in stage II at ΔK = 15 MPa·$m^{\frac{1}{2}}$ or more, the rates become higher for the alloys in the 304 system than in the 316 system. Also, at the highest values of ΔK studied, the strength of alloys may be influential within each system since the rates for 316LN are lower than for 316, and the rates for 304HN are lower than for 304L or 304LN. As ΔK decreases to intermediate values, the curves for different alloys cross over. As threshold is approached, the yield strength influences the ranking of alloys. This is shown clearly in Fig. 13, where the thresholds (both apparent and effective) are plotted versus yield strength. At 295 K, the trend is insignificant because there is not a great variation in yield strengths for the 5 steels at this temperature. The effective thresholds at this temperature are equivalent for the 5 alloys. At 4 K, the dependence on yield strength is more pronounced. As shown in this figure, the apparent and effective thresholds both increase moderately with yield strength at 4 K.

DISCUSSION

Liaw and Logsdon's [1] review considered cryogenic threshold data available at the time for aluminum, copper, nickel, steels, and titanium alloys. (Only one 300 series steel, AISI 304, was referenced.) They observed that decreasing temperature generally increases the threshold. They used crack closure concepts to explain the effects of stress ratio and dislocation dynamics to explain the improvement of thresholds at cryogenic temperatures. The same principles are sufficient to rationalize the behavior of the 300 series stainless steels in the present study.

At 295 K, as shown in Fig. 5, the fatigue crack growth rates for AISI 316 follow a linear trend for at least four orders of magnitude in da/dN, and no asymptote is approached at 10^{-10} m/cycle. The 304L and 304LN alloys behaved similarly at this temperature, as shown in Figs. 9 and 10. This observation implies that no true threshold is exhibited in this range, and the operational definition of ΔK_{Th} at 10^{-10} m/cycle is evidently of limited significance for the austenitic stainless steels at room temperature. Presumably, crack growth could be measured at ΔK below the operationally defined thresholds, although the time required for such measurements by present methods would greatly increase. An average growth rate of 10^{-10} m/cycle corresponds to 1 angstrom per cycle whereas the lattice spacings for austenitic steels are a few Angstroms. Rates of crack growth less than a lattice parameter per cycle are possible, assuming that the crack grows nonuniformly, in spurts, or in highly localized areas along the crack front. Additional tests at still lower ΔK values are needed to confirm that crack growth continues at rates below 10^{-10} m/cycle for other austenitic alloys.

Stress Ratio and Crack Closure Effects

Crack closure as observed in the oscilloscope load–displacement signals figures prominently in the interpretation of our results. Closure is more pronounced in the austenitic steels at room temperature than at cryogenic temperatures. It is also more pronounced at low ΔK than at high ΔK. In the tests at 295 K near threshold, closure loads typically approached the mean load of the fatigue cycle at R = 0.1, whereas at 4 K the closure loads were much lower due to increased resistance to plastic deformation.

For AISI 316 between R = 0.1 and 0.3 we observed an effect of stress ratio at 4 K but not at 295 K. The closure load was significantly higher at 295 K than at 4 K, as shown in Fig. 3. In this case the closure and minimum loads were such that the change in stress ratio from 0.1 to 0.3 affected the effective ΔK at 4 K, but not at 295 K.

Crack closure also explains why there is no effect of stress ratio between R = 0.1 and 0.3 for AISI 316 at 295 K. At 295 K the closure load is about ½ the applied maximum loads; therefore the effective ΔK is the same at R = 0.1 and R = 0.3 (Table 3), and no stress ratio effect is observed. Stress ratio effects would be expected at R ratios above 0.5.

Crack closure also explains the effects of stress ratio found at low R at 4 K. At 4 K, rate differences are measureable between R = 0.1 and 0.3 (Fig. 6) because closure occurs at low loads; the closure load is intermediate between the minimum loads at R = 0.1 and 0.3 and that affects the effective ΔK.

Temperature Effects

Owing to closure the apparent thresholds for these alloys do not always increase with a temperature reduction from 295 to 4 K. However, when closure is taken into account, the effective thresholds are always higher at 4 K than at 295 K. Other metals and structural alloys at room and cryogenic temperatures show the same result: the effective threshold at cryogenic temperature is higher than at room temperature which is consistent with dislocation dynamics theory [1].

In general, the steels in this study behaved similarly at 4 K (Fig. 9). One reason for this is that all have similar Young's moduli. We showed that rates for a wide variety of alloys in Stage II depend strongly on Young's modulus and can be normalized on the basis of the parameter $\Delta K/E$ [2]. In Stage I also, the threshold increases with Young's modulus [10]. Young's modulus is fixed primarily by the base composition and is structure-insensitive. The 5 alloys in this study are composed primarily of iron, chromium, and nickel, and their Young's moduli are equivalent within a few percent. The general similarity of performance is therefore not surprising.

Aside from Young's modulus, other factors influence fatigue resistance. The secondary effects of yield strength were cited in Figs. 12 and 13. Austenite phase stability is potentially important. In very unstable alloys,

especially those with low C, N, and Ni contents, massive martensitic phase transformations can improve fatigue crack growth properties [11,12]. The AISI 304L steel of this study has low C but fairly high Ni and other stabilizing elements. Additional tests of still leaner 304L grade alloys are recommended to evaluate possible effects on fatigue crack growth. However, even if the effect proves to be favorable, 304L grades would not be used for fusion magnets at 4 K since high yield strength is required. High yield strengths in austenitic stainless steels is achieved primarily by nitrogen additions which also stabilize the austenite against phase transformation.

The data in this study pertain to long cracks in conventional compact laboratory specimens. To date, most cryogenic data for stages I and II have been produced for specimens containing long cracks, typically at low R, and frequencies from 4–20 Hz. The use of these data may not be appropriate in applications where short cracks are present. Room temperature studies show that short cracks do not behave like long cracks. Short cracks grow at higher rates than data from specimens with long cracks might suggest. To support proposed superconducting machinery designs, both long and short crack behavior must be characterized and understood. Therefore short crack behavior is being simulated in ongoing research at NIST and is the subject of a subsequent paper.

SUMMARY AND CONCLUSIONS

The fatigue apparatus used in this study is fully automatic. The approach allows continuous data reduction and load adjustments without an operator. Tests at 40 Hz last 4 days and nights with continuous 24-h operation. Typically, 13 million load cycles are needed for 1 threshold measurement and to measure rates of crack growth spanning the range between 10^{-6} and 10^{-10} m/cycle. Fatigue crack growth rates for 5 austenitic stainless steels are reported. The decreasing-ΔK technique was used at selected R ratios to obtain data for long cracks in laboratory specimens. Several material and test variable effects are summarized as follows:

1. The rates at 295 K for several austenitic stainless steels do not approach an asymptote at 10^{-10} m/cycle; thus crack growth will occur at lower rates, and longer tests may be needed to reach a true threshold at 295 K.

2. The effect of a temperature reduction from 295 to 4 K is to increase the effective thresholds of all 5 steels.

3. At 4 K, conventional thresholds exist near 10^{-10} m/cycle for steels tested. The operationally defined thresholds increase slightly as yield strength increases.

4. At 4 K, the apparent thresholds range between 6.5 and 10.5 MPa·$m^{\frac{1}{2}}$. The effective thresholds (the apparent thresholds corrected for crack closure) are uniformly lower and range between 4 and 7 MPa·$m^{\frac{1}{2}}$.

REFERENCES

1. P.K. Liaw, and W.A. Logsdon, Fatigue crack growth threshold at cryogenic temperatures: a review, Eng. Fract. Mechs., Vol. 22, 1985, pp. 585-594.

2. R.L. Tobler and Y.W. Cheng, Midrange fatigue crack growth data correlations for structural alloys at room and cryogenic temperatures, in: Fatigue at Low Temperatures, ASTM STP 857, R.I. Stephens, Ed., Amer. Soc. Test. Maters., Philadelphia, 1985, pp. 3-30.

3. P.K. Liaw, W.A. Logsdon, and M.H. Attaar, Automated near-threshold fatigue crack growth rate testing of JBK-75 stainless steel at cryogenic temperatures, in: Austenitic Steels at Low Temperatures, R.P. Reed and T. Horichi, Eds., Plenum, New York, 1983, p. 171-185.

4. P.K. Liaw, W.A. Logsdon, and M.H. Attaar, Cryogenic temperature near-threshold fatigue crack growth rate data for JBK-75 stainless steel, Cryogenics, Vol., 23, 1983, pp. 523-526.

5. R.L. Tobler, and Y.W. Cheng, Automatic near-threshold fatigue crack growth rate measurements at liquid helium temperature, Int. J. Fat., Vol. 7, 1985, pp. 191-197.

6. R.L. Tobler, Near-threshold fatigue crack growth behavior of AISI 316 Stainless Steel, Adv. Cryo. Eng., Vol. 32, Plenum, New York, 1986, pp. 321-327.

7. R.L. Tobler and J.A. Shepic, Design and performance of a ring-shaped clip gage for fracture mechanics testing, J. Test. and Eval., Vol. 13, No. 4, 1985, pp. 299-302.

8. A. Saxena and S.J. Hudak, Jr., Review and extension of compliance information for common crack growth specimens, Int. J. Fracture, Vol. 14, No. 5, 1978, pp. 453-468.

9. D.T. Read and R.P. Reed, Fracture and strength properties of selected austenitic stainless steels at cryogenic temperatures, in Materials Studies For Magnetic Fusion Energy Applications at Low Temperatures - II, NBSIR 79-1609, National Institute of Standards and Technology, Boulder Co, 1979, pp. 81-122.

10. P.K. Liaw, W.A. Logsdon, and M.A. Burke, Fatigue crack propagation behavior of 63Sn-37Pb solder, Scripta Metall., Vol. 23, 1989, p. 747.

11. Y. Katz, A. Bussiba, and H. Mathias, The role of induced phase transformations on fatigue processes in AISI 304L, Proceedings of the 4th European Conference on Fracture, p. 503.

12. Mei, Z., Chang, G.M., and Morris, J.W., Jr., Fatigue crack growth in metastable austenitic stainless steels, in: Cryogenic Materials, 88, Vol. 2, Structural Materials, R.P. Reed, X.X. Xing, and E.W. Collings, Eds., International Cryogenic Maters. Conference, Boulder, Co., 1988, pp. 491-500.

CREEP OF COPPER: 4 to 295 K

R.P. Reed, N.J. Simon, and R.P. Walsh

Fracture and Deformation Division
National Institute of Standards and Technology
Boulder, Colorado 80303

ABSTRACT

Creep measurements at 295, 76 and 4 K have been conducted on C10400 copper. Specimens were held under constant tensile load (dead weight) for periods of time sometimes exceeding one month. Creep data have been fitted to a series of expressions relating creep strain to time by a nonlinear least-squares procedure. The coefficients of the terms in these equations were related to applied stress levels. Primary, logarithmic, and steady-state creep ranges are discussed.

INTRODUCTION

For many cryogenic technological applications, such as the operation of a high-field superconducting magnet for long periods of time, knowledge of the creep properties of the structural reinforcements is necessary. The study of the time-dependent mechanical behavior of structural materials at low temperatures has proved very challenging. Maintenance of temperature and mechanical stability, as well as accurate recording of stress and strain over long periods of time, stretch the limits of our measurement capabilities.

The creep of metals at low temperature has been reviewed by Tien and Yen[1] and Yen et al.[2] A wide range of results are apparent from these reviews. Both logarithmic (creep strain proportional to logarithm of time) and steady-state (creep strain proportional to time) have been reported for metals at low temperatures.

Copper is used extensively as a stabilizing material for superconducting magnets and as a conductor in high field, normal-metal magnets. Thus, it is necessary to understand its creep characteristics. The creep of copper, perhaps, has been studied more than any other metal at low temperatures.[1-7] This paper reports on the creep of copper at temperatures less than 0.22 T_m (295, 76, and 4 K) and at stress levels about $10^{-3}\mu$ (25 - 60 MPa) where T_m is the melting temperature (1356 K) and μ is the shear modulus. Our study provides a basis for comparison of the results from various laboratories and for understanding the complexities of these measurements.

Advances in Cryogenic Engineering (Materials), Vol. 36
Edited by R. P. Reed and F. R. Fickett
Plenum Press, New York, 1990

Table 1. Creep Strain Expressions

(1) $\epsilon_{true} = \epsilon_o + a_1 \ln t$	(7) $\epsilon_{true} = \epsilon_o + a_1 t^{a_2} + a_3 t$
(2) $\epsilon_{true} = \epsilon_o + a_1 \ln t + a_3 t$	(8) $\epsilon_{true} = \epsilon_o + a_1 t^{a_4} + a_3 t^{a_4} + a_5 t$
(3) $\epsilon_{true} = \epsilon_o + a_1 \ln(a_2 t + 1)$	(9) $\epsilon_{true} = \epsilon_o + a_1 \ln(a_2 t + a_3)$
(4) $\epsilon_{true} = \epsilon_o + a_1 \ln(a_2 t + 1) + a_3 t$	(10) $\epsilon_{true} = \epsilon_o + a_1 \ln(a_2 t + a_3) + a_5 t$
(5) $\epsilon_{true} = \epsilon_o + a_1(1 - e^{-a_2 t}) + a_3 t$	(11) $\epsilon_{true} = \epsilon_o + a_1 \ln t + a_5 t^{a_4}$
(6) $\epsilon_{true} = \epsilon_o + a_1 t^{1/3} + a_2 t^{2/3} + a_3 t$	

EXPERIMENTAL PROCEDURES

Oxygen-free, high conductivity C10400 copper (Cu + Ag = 99.99 wt.%) wa obtained in 20-mm diameter bar stock. It was used in the annealed conditio (650°C/1 h) with a hardness of R_B = 22 and a grain size of 36 μm. Subsequently, specimens were reannealed (650°C/1 h) after undergoing creep deformation of 0.02 to 0.04 in previous tests; these specimens are called "reannealed" in the text. Average yield strengths of 25, 27, and 30 MPa were measured at 295, 76 and 4 K, respectively, for this copper.

The dead-weight loading system utilized a lever arm pivoted above the specimen. For low temperature tests a 900-mm deep superinsulated dewar with a narrow neck was used. Dewar capacity was 30 L. The test fixture consisted of a G-10CR outer compression cylinder and an inner titanium pull rod. Liquid helium boiloff without the test fixture was 0.2 L/h and with the test fixture was 0.5 L/h.

Metal-film, resistance strain gages (73Ni-20Cr alloy) were bonded to the round specimens with a low-temperature epoxy. Strain sensitivity at room and low temperature was 5×10^{-7}; instrumental and temperature drift resulted in strain readout variability over a period of one month of about $\pm 2 \times 10^{-7}$ at room temperature and about $\pm 4 \times 10^{-6}$ at 4 K. To measure variability during a test, dummy specimens were inserted in the cryostat.

Other environmental factors caused measurement inconsistencies. These included vibrations, ambient temperature variability, cryogenic liquid transfer, and the reduction of the cryogenic liquid level with time. Floor vibrations induced by other laboratory equipment led to sudden spurious jumps (~ 10^{-5}) of strain during testing. Vibrations induced specimen strain despite the use of damping pads. Ambient temperature variability led to daily cyclic patterns of strain (at the 10^{-7} level); to eliminate these thermally induced strain cycles subsequent test specimens were maintained at 303 K using resistance heaters attached to brass specimen grips. The transfer of cryogenic fluids into the dewar produced transient specimen loads of the order of 0.5 kg that were induced by the differential thermal contraction between the pull rod and compression cylinder. These transient loads, measured by strain gages on the pull-rod and compression cylinder, were not adequately compensated by the lever-arm. Similarly, the reduction of liquid level with time is thought to have led to load changes in the filament-reinforced composite cylinder from thermal contraction changes transmitted by the continuous filaments. These strain differences, again in the range of 10^{-7}, led to small uncompensated load changes on the specimen.

MODEL ANALYSIS

The creep strain after a period of elapsed time, t, is the sum of the initial strain upon loading, ϵ_o, and a time-dependent strain. Both the

Table 2. Summary of Creep Data

Temp. (K)	σ_a (MPa)	σ_a/σ_y	ϵ_o (10^{-3})	a_1 (10^{-6})	Duration (min)
295	20.20	0.81	1.704	3.192	37440
	24.90	1.00	3.269	4.153	37440
	27.00	1.08	0.709	1.67	29986
	29.96	1.20	4.726	3.44	27300
	31.40	1.26	4.873	3.15	18856
	34.00	1.36	3.131	3.663	29986
	34.10	1.36	5.575	4.254	41640
	36.40	1.46	5.647	4.297	49950
	37.60	1.50	7.031	4.871	41640
	38.00	1.52	4.083	4.371	29986
	41.00	1.64	5.596	5.111	29986
	42.20	1.69	8.208	5.845	15695
	42.40	1.70	8.031	4.232	49950
	45.10	1.80	9.116	4.49	18856
	45.30	1.81	9.032	5.672	15695
76	24.30	0.90	0.650	2.323	12591
	26.10	0.97	1.659	3.233	12591
	29.70	1.10	2.609	2.506	96600
	33.20	1.23	2.23	3.934	96600
	35.20	1.30	1.188	3.763	12591
	35.40	1.31	2.731	3.876	96600
	37.10	1.37	4.889	4.684	58894
	41.30	1.53	4.815	3.865	36345
	45.00	1.67	5.258	4.588	43455
	49.50	1.83	7.499	4.642	12820
4	30.00	1.00	2.199	0.005	1027
	30.60	1.02	0.838	0.361	21339
	32.00	1.07	3.521	0.139	1027
	34.40	1.15	2.563	0.663	21339
	35.60	1.19	3.817	1.008	1488
	37.60	1.25	2.178	0.423	21339
	41.50	1.38	5.743	0.787	18540
	43.80	1.46	4.933	0.16	3612
	44.00	1.47	5.834	0.17	1027
	47.20	1.57	3.926	0.144	1405
	48.90	1.63	8.225	1.166	6935
	60.00	2.00	17.56	2.285	6935

initial and time-dependent strain components are functions of the temperature, T, and the applied stress, σ_a. We have chosen to describe this functional dependence by first fitting a series of expressions of the creep strain as a function of time (Table 1) to individual data sets obtained at 4, 76, and 295 K for a series of σ_a values. Then, the dependence of the constants (a_i) in these expressions upon σ_a and T was determined from plots of the constants versus σ_a for the three test temperatures. The 11 expressions in Table 1 were obtained from the literature, or are generalizations of expressions for creep strain found in the literature. The creep strain expression is expected to be logarithmic [Equations (1) and (3)] when $T \leq 0.3\ T_m$. Equations (2) and (4) allow for a steady-state creep ($a_s t$, $\dot{\epsilon} = a_s$) in addition to the logarithmic creep, and Eqs. (9), (10), and (11) are further generalizations of these expressions. Equations (5) and (6) are expressions given in the literature for temperatures of the order of $0.4\ T_m$ and higher. In this temperature regime, the primary stage of creep is represented by $[a_1 (1 - e^{-a_2 t})]$ or $[a_1 t^{1/3} + a_2 t^{2/3}]$ and the secondary, or steady-state regime, by the $a_s t$ term. Equations (7) and (8) are generalizations of these expressions. The equations in Table 1 were fitted to the data sets by a nonlinear least-squares computer program. The constants a_i from the expressions that best fitted the data sets were then plotted as a function of σ_a. A linear least-squares fit was made to the data in these plots.

1177

EXPERIMENTAL RESULTS AND DISCUSSION

The results are summarized in Table 2, which includes applied stress, the ratio of the applied stress to the yield strength (σ_y), the initial strain on application of the dead weight (ϵ_o), and the coefficient for the primary creep term (a_1) from Eq. (2) in Table 1. When the data sets at 295 and 76 K were fitted to the equations in Table 1, Eq. (11) usually gave the lowest standard deviation (S.D.). In many cases, the nonlinear least squares procedure did not give a convergent result when the data set was fitted to Eq. (11); however, the S.D. of the fit was the lowest found for 12 out of 15 sets at 295 K, and for 6 out of 7 sets at 76 K (Eq. (11) was not fitted to 3 of the 76-K data sets reported in Table 2). The test duration ranged from 15 700 to 50 000 min at 295 K and from 12 600 to 96 600 min at 76 K. At 4 K, the test duration was generally much shorter (1000 to 21 300 min) and Eq. (11) was not found to give the best fit to the data sets. It is thought that Eq. (11) usually provided the best fit for data sets of longer duration because the power of $t(a_4)$ was allowed to vary; in Eqs. (2), (4) - (8), and (10), the power of t is 1.0. At the longer elapsed times, it is more likely that a different stage of creep has been entered, and therefore, a more general expression for t allows a better fit to the data. [That multiple stages of creep were present is further substantiated by the observation that in all cases, Eq. (2) was a better fit than was Eq. (1) and Eq. (4) was better than Eq.(3)]. However, because small aberrations in a data set could exert a large influence over the values of a_4 and a_5 for Eq. (11) determined in the nonlinear least-squares iterations (a_1 is slightly affected, also) the functional dependence of the constants ϵ_o and a_1 upon T and σ_a for Eq. (2) are used in our discussions.

Instantaneous Strain

On application of load there is an instantaneous specimen strain. The square root of the initial strain, ϵ_o, is a linear function of the applied stress, σ_a. This is illustrated for all temperatures in Fig. 1 and summarized in Table 2. This result is expected, since the stress-strain curves of copper are approximately parabolic and the primary strain on application of load corresponds to this relationship.

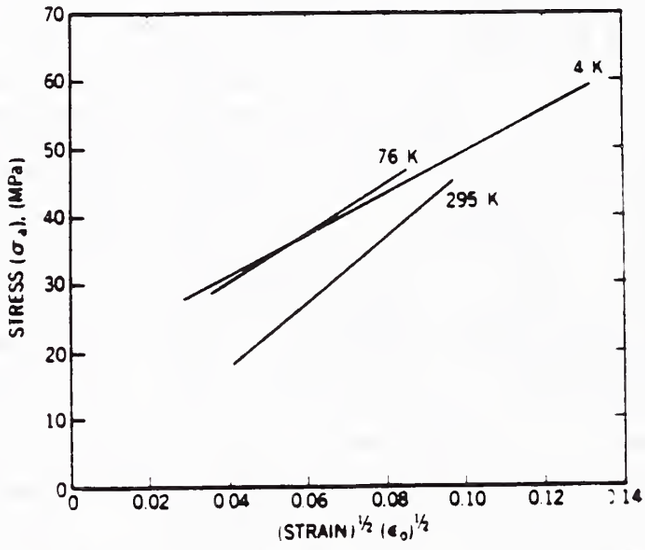

Fig. 1. Applied stress versus specimen strain (to 1/2 power) for copper at 295, 76, and 4 K.

1178

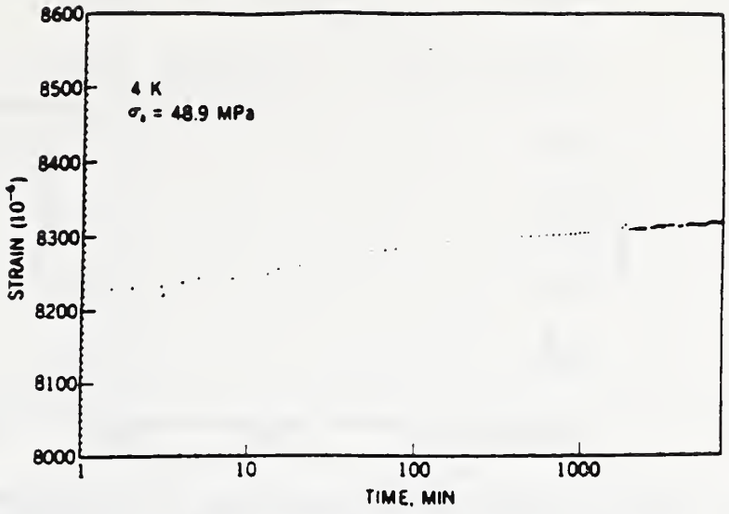

Fig. 2. Dependence of creep strain versus log time for copper under a stress of 48.9 MPa at 4 K.

Creep Behavior: General

Tests were conducted at three temperatures (4, 76, and 295 K) and at relatively low stress levels (~ $10^{-3}\mu$). When the test temperature is less than approximately 0.3 T_m, logarithmic or exhaustive creep is normally expected. (Here we define exhaustive creep as distinguished by an ever-decreasing creep rate, where the creep strain is not a linear function of the log of the time.) In our creep tests the test temperature is less than 0.22 T_m. Steady-state creep rates or a normal secondary creep stage are not expected to occur under these test conditions.[8] Yet, there have been a number of papers attempting to analyze for activation energies and to measure steady-state creep rates, even at 77 K. These include the recent studies by Yen et al.[3,5] and reviews by Tien and Yen and Yen et al.[2] emphasizing thermally activated steady-state creep processes in copper at 77 K. We found distinct creep characteristics of copper at each test temperature. However, in no case was steady-state creep detected. Results are presented and discussed separately for each test temperature.

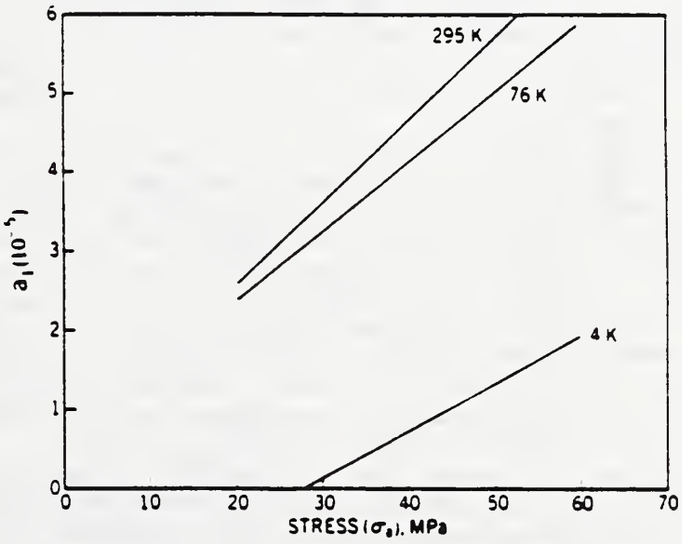

Fig. 3. Creep coefficient, a_1, versus applied stress from Eq. 2 (Table 1) for copper at 295, 76 and 4 K.

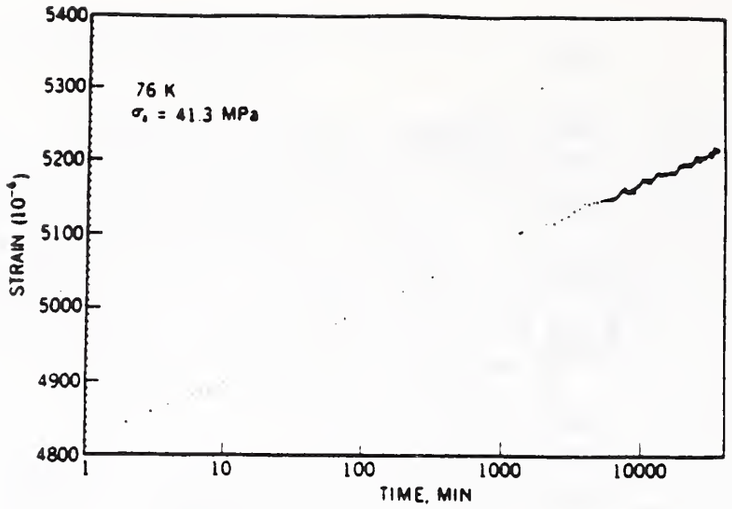

Fig. 4. Dependence of creep strain on log time for copper under a stress of 41.3 MPa at 76 K.

Creep Behavior: 4 K

Initially, the creep strain at 4 K is linearly related to the log of time. But after a brief time (usually less than 1000 min) the dependence of strain on log time decreases. This dependence is illustrated in Fig. 2. The logarithmic coefficient, a_1, from Eq. (2) (Table 1) is plotted versus applied stress (σ_a) for 4 K in Fig. 3. Compared to higher temperature coefficients, a_1 is quite low. The data of Yen et al.[3] at 4 K correspond very closely to our data where a_1 is of the order of 10^{-5}. Startsev[7] reports much higher values of a_1, of the order of 10^{-2}, for copper at

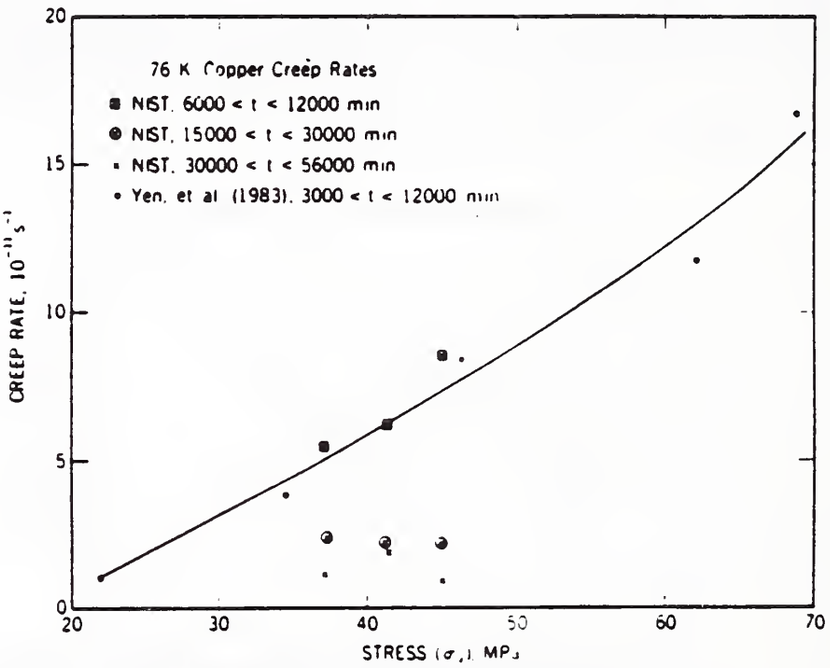

Fig. 5. Creep rates versus applied stress for copper at 76 K; effects of time interval on rates are illustrated. Data of Yen [1,3] also included.

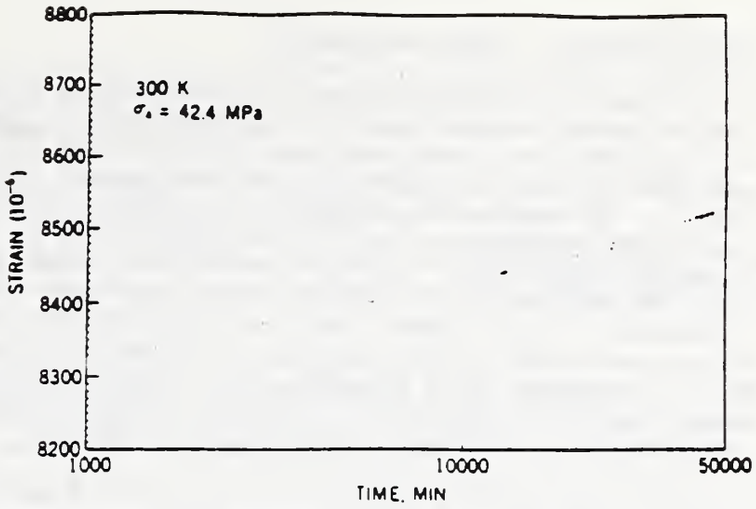

Fig. 6. Dependence of creep strain on log time for copper under a stress of 42.4 MPa at 300 K.

temperatures ranging from 1.5 to 4.2 K. The higher values led to the suggestion that dislocation tunneling played a role in low-temperature creep processes.[7]

If 4-K creep strain is plotted linearly versus time, the curves of 4-K measurements are significantly different from those at higher temperatures. A very brief transient period is noticed. The length of this transient period was less than 500 min in all tests. Owing to the diminishing creep rates with time, creep strains did not exceed 150 x 10^{-6} following the instantaneous strain, ϵ_o.

Creep Behavior: 76 K

Creep strain is linearly proportional to the logarithm of the time at 76 K within experimental uncertainties. Evidence for this dependence is shown in Fig. 4. The coefficient, a_1, for the logarithmic dependence is plotted versus applied stress in Fig. 3. While a_1 at 76 K has much the same dependence on stress as a_1 at 4 K, the magnitude of a_1 at 76 K is about 3 x 10^{-5} larger than at 4 K. The lowest stress for the Wyatt data[4] is about 62 MPa; therefore, these data are not included in this figure. However, a_1 is also lower (- 3 x 10^{-5}) than our data for high stress levels.

When creep strain at 76 K is plotted linearly versus time a larger transient region is apparent, compared to curves at 4 K. It appears that there is a linear region, corresponding to a steady-state creep rate, in each plot of strain vs. time. Yet, as illustrated in Fig. 5, careful data analyses yield ever-decreasing creep rates. In Fig. 5 the data of Yen et al.[2,3] obtained over the time interval from 3000 to 12 000 min. are plotted and joined by a curve. Our creep-rate data, obtained over the same time interval from our curves, are plotted for these specimens. They conform excellently to the Yen data. But, at longer periods of elapsed time, lower values of the creep rate are calculated and included in Fig. 5. Creep rates as low as 1 x 10^{-11} s^{-1} for stress levels above 33 MPa at 76 K have been obtained. Therefore, we conclude that there is no steady-state creep stage in copper at the stress levels used in this study. At these stress levels, the creep rate is continuing to decrease as evidenced by the linear dependence of strain on log time (Fig. 4).

Creep Behavior: Room Temperature

A typical creep curve for room temperature is shown in Fig. 6. At ambient temperatures, the curve of creep strain versus time can be portrayed as logarithmic at times less than approximately 10^4 min. A plot of a_1 obtained from Eq. (2) (Table 1) analyses versus applied stress is shown in Fig. 3. The slopes of a_1 versus σ_a (see Fig. 3) gradually decrease with decreasing temperature, and the absolute values of a_1 increase with increasing temperature. However, at elapsed times greater than about 10^4 min, the dependence of strain on time increases, relative to a logarithmic dependence. This, again, provides an opportunity for the assessment of steady-state conditions. At 300 K, the length of the transient region is longer than that of 76 K curves. Our calculated values of creep rates range from 2.5×10^{-11} to 6×10^{-11} s^{-1} over a stress range from 20 to 45 MPa at 300 K for time intervals from 20 to 50×10^3 min.

The extrapolated value of σ_a at $(\epsilon_o)^{\frac{1}{2}} = 0$ may be regarded as the elastic limit for high strain rates (σ_o). At room temperature σ_o is nearly zero; at 76 and 4 K σ_o is nearly equivalent (within data scatter), about 17.5 MPa.

Gohn and Fox[9] and Davis[10] have conducted room temperature creep tests of copper for longer periods of time (15×10^5 and 6×10^6 min respectively). The strain versus time curves of Gohn and Fox for room temperature creep tests exhibit decidedly decreasing strain rates with time. No steady-state range is observed. However, if one uses the tangent of the curve at 12×10^5 min for their data, a strain rate of 0.25×10^{-11} s^{-1} is calculated for an applied stress of 69 MPa at room temperature. Similar low creep rates may be obtained from the data of Davis at lower stress. Thus, longer periods of time lead to diminishing creep rates; steady-state conditions are not achieved at room temperature.

Engineering Strain and Creep Conditions

Finally, the strains one may expect at these three temperatures may be summarized for various stresses. At room temperature for a stress equivalent to the yield strength (30 MPa), the maximum total creep strain for 20 years service is approximately 0.02 (including $\epsilon_o = 0.004$) from our data; if the lower creep rates from longer-time data[9,10] are used, a total creep strain of less than 0.006 (including $\epsilon_o = 0.004$) is estimated. At stresses of 1.5 σ_y our rates approximately doubled; thus, a maximum extrapolated (20 years) strain would be 0.04; using the lower rate data[9,10] this strain would be reduced to 0.01.

At 76 K the creep rates are similar to room temperature, therefore the total predicted strains would reflect the difference in instantaneous strain (about 0.0035 at 76 K). At 4 K the creep rates are less but the instantaneous strain is equivalent to that observed at 76 K. Total strain for a stress level of the yield strength (37 MPa) for 20 year service would be predicted to reflect only the instantaneous strain (~ 0.0035), since the creep rate exhausts relatively quickly at 4 K.

We used Eq. (2) (Table 1) for the analyses. At 76 K and room temperature, the contribution from the a_5 term in Eq. (2) was small compared to that from the a_1 term for the typical test duration. Before 10 000 min, the contribution from the a_5 term is generally negligible, and between 10 000 and 30 000 min, the increase in creep strain due to the a_5 term is usually no more than about one-half of the increase due to the a_1 term. Beyond about 40 000 min, however, the a_5 term becomes dominant, in part because log t increases very slowly at that point compared to t. Because a_1 is smaller at 4 K, the a_5 term is important after shorter periods of elapsed time than at 76 K and room temperature.

1182

SUMMARY

The creep characteristics of 99.99% pure, oxygen-free copper (C10400) were studied at 4 and 76 K and at room temperature at stress levels between 0.7 and 1.5 of the yield strengths. Major conclusions are:

1. At all temperatures the primary stage is best described by a logarithmic dependence of creep strain on time.
2. No steady-state creep was detected at any temperature. Creep rates continued to decrease or to exhaust at each temperature as a function of time.
3. At 4 K logarithmic creep was followed by a relatively quick exhaustion of creep. At 76 K logarithmic creep continued for the duration of the tests, within the limits of experimental imprecision. At room temperature creep rates increased from the logarithmic creep of the primary stage, but did not attain steady-state conditions.
4. Total creep strains (including strain on application of the load) of less than 0.020 are predicted for $\sigma_a = \sigma_y$ at room temperature for a service time of 20 years. At 76 K a total creep strain of less than 0.019 is predicted; at 4 K, the total creep strain is less than 0.004 when $\sigma_a = \sigma_y$.

ACKNOWLEDGMENTS

This project was supported by the Office of Fusion Energy (DoE). Elizabeth S. Drexler assisted excellently in data analyses.

REFERENCES

1. J.K. Tien and C.T. Yen, "Cryogenic Creep of Copper," Adv. Cry. Eng.-Maters. 30:319-338 (1984).
2. C. Yen, T. Caulfield, J.K. Tien, L.D. Roth, and J.M. Wells, "Cryogenic Creep of Copper," Paper 8305-030, Metals/Materials Technology Series American Society for Metals, Metals Park, OH (1983).
3. C.T. Yen, "Long-Term Creep of Copper at Cryogenic Temperatures," Ph.D. Thesis, Columbia U., New York (1983).
4. O.H. Wyatt, "Transient Creep in Pure Metals," Proc. Phys. Soc. B66: 459-480 (1953).
5. C. Yen, T. Caulfield, L.D. Roth, J.M. Wells, and J.K. Tien, "Creep of Copper at Cryogenic Temperatures," Cryogenics 24:371-377 (1984).
6. V.A. Koval, V.P. Soldatov, "Jumplike Deformation of Copper and Aluminum During Low-Temperature Creep," Adv. Cry. Eng.-Maters. 26:86-90 (1980).
7. V.I. Startsev, "Low Temperature Creep of Metals," Czech. J. Phys. B 31: 115-124 (1981).
8. R.W. Evans and B. Wilshire, Creep of Metals and Alloys, The Institute of Metals, London (1985).
9. G.R. Gohn and A. Fox, "New Methods for Determining Stress-Relaxation," Matls. Res. Stds.:957-966 (1961).
10. E.A. Davis, "Creep and Relaxation of Oxygen-Free Copper," J. Appl. Mech. 10:A101-105 (1943).

STRAIN RATE EFFECT ON TENSILE PROPERTIES AT 4 K OF A VAMAS ROUND-ROBIN AUSTENITIC STEEL

R.P. Reed, R.P. Walsh and R.L. Tobler

Fracture and Deformation Division
National Institute of Standards and Technology
Boulder, Colorado USA

ABSTRACT

A high-strength austenitic steel with nominal composition Fe-25Cr-14Ni-0.37N was included in an international round-robin measurement program. Tensile and fracture toughness tests were conducted at 4 K by leading low temperature test laboratories in Japan, Europe, and the U.S. This paper reports on the effect of strain rate on displacement-controlled tensile tests at 4 K. Similar to other recent results on austenitic steels, a transition in ultimate strength was observed as a function of strain rate: at higher strain rates the strength decreased about 10%. The onset of discontinuous yielding was also strain-rate dependent. The reduction of ultimate tensile strength is associated with the change from the nucleate to film heat-transfer mechanism from the specimen surface to liquid helium.

INTRODUCTION

Low temperature test standards are now in the process of being established both in the U.S. through the ASTM E-28 committee, in Japan through JIS, and with active participation of European test laboratories. One focal group for discussion and round-robin testing leading to such standards is the Versailles Advanced Material and Standards (VAMAS) organization. This group selected a Japanese austenitic steel (Fe-25Cr-14Ni-0.37N, YUS 170) as one of their two alloys for round-robin tensile and fracture toughness tests at 4 K.[1] To complement these tests, we have extended our measurements at NIST to study the effects of strain rate at 4 K since our previous research identified a transition in ultimate strength as a function of strain rate for austenitic steels.[2] Furthermore, many laboratories in the VAMAS round robin conducted their tests at strain rates within the transition region. This paper presents the NIST measurements and discusses them in terms of round-robin test variability and future tensile-test standards.

EXPERIMENTAL CONDITIONS

The composition of the austenitic steel is Fe-25.06Cr-13.52Ni-0.76Mo-0.78Mn-1.12Si-0.015C-0.37N-0-035P-0.001S. Annealed specimens were received from the National Research Institute for Metals (Tsukuba, Japan). The

Advances in Cryogenic Engineering (Materials), Vol. 36
Edited by R. P. Reed and F. R. Fickett
Plenum Press, New York, 1990

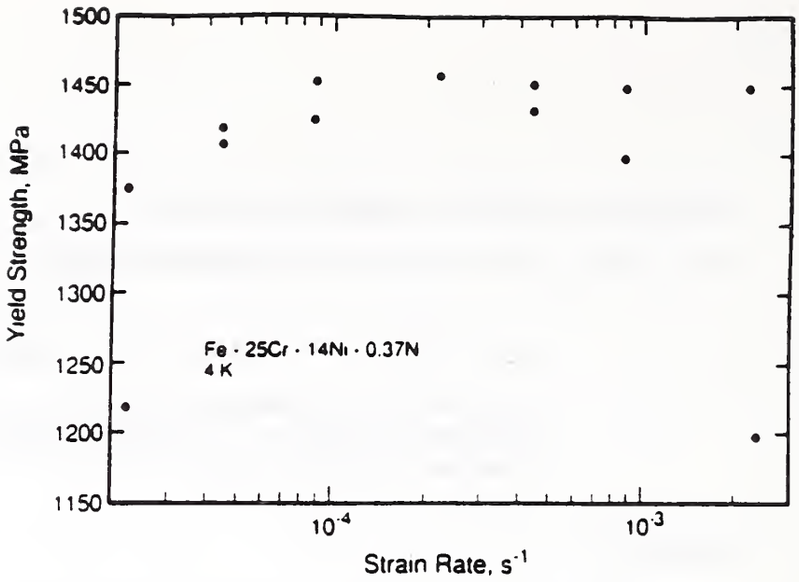

Fig. 1. Tensile yield strength at 4 K as a function of strain rate for Fe-25Cr-14Ni-0.37N austenitic steel.

average grain size was 50 μm; equiaxed grain structure was observed in all photomicrographs. Specimen diameter was 6.35 mm with a 37.5 mm gage length; total specimen length was 87.5 mm.

Tensile tests were conducted in displacement control in boiling liquid helium (4 K) using a screw-driven, commercial machine. The cryostat and clamp-on, strain-gage extensometers have been described previously.[2] Elongation was measured over the entire specimen gage length. Reported strain rates refer to the nominal rate of plastic deformation within the reduced section of the specimens.

EXPERIMENTAL RESULTS

Strain rate has little effect on the tensile yield strength at 4 K of the Fe-25Cr-14Ni-0.37N alloy as shown for thirteen tests in Fig. 1. The two data points of very low yield strengths (1200 and 1218 MPa) were closely examined. Neither metallurgical variables (such as grain size), nor measurement variables (such as irregular stress-strain curve) can explain these data. The most likely explanation is chemical inhomogeneity within the specimen gage lengths.

There is a transition in ultimate tensile strength as function of strain rate; at strain rates in excess of about $1.3 \times 10^{-4} s^{-1}$ the ultimate strength begins to decrease (Fig. 2). The ultimate strength decreases about 10% at higher strain rates and remains thereafter constant at strain rates in excess of about $4 \times 10^{-4} s^{-1}$. Elongation, as shown in Fig. 3 increases at higher strain rates ($\geq 4 \times 10^{-4} s^{-1}$). This increase is not associated with an increase in the reduction of area; reduction of area values vary from 31 to 48%, but show no trend with strain rate.

Discontinuous yielding was observed during all tensile tests at 4 K. As described in an earlier paper,[3] the initiation of discontinuous yielding in austenitic steels at 4 K is a function of strain rate; both the initiation stress and strain exhibit transitions to lower values at higher strain

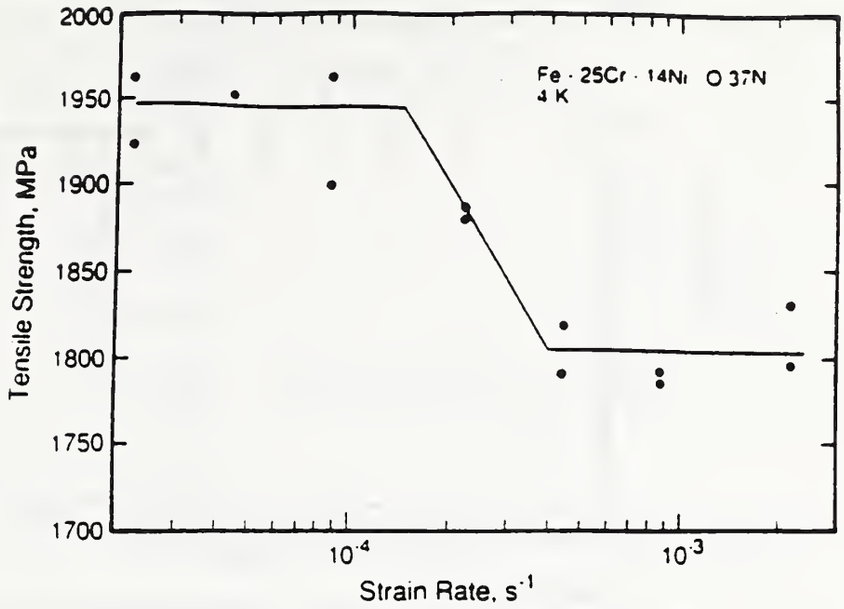

Fig. 2. Ultimate tensile strength at 4 K as a function of strain rate for Fe-25Cr-14Ni-0.37N austenitic steel.

rates. Engineering stress-strain curves at high and low strain rates are shown in Fig. 4. For the Fe-25Cr-14Ni-0.37N alloy, the stress (σ_i) and strain (ϵ_i) at initiation of discontinuous yielding are plotted in Fig. 5a and b, respectively. Similar to the other alloys, both initiation stress and strain rapidly decrease as the strain rate increases above $10^{-4}s^{-1}$.

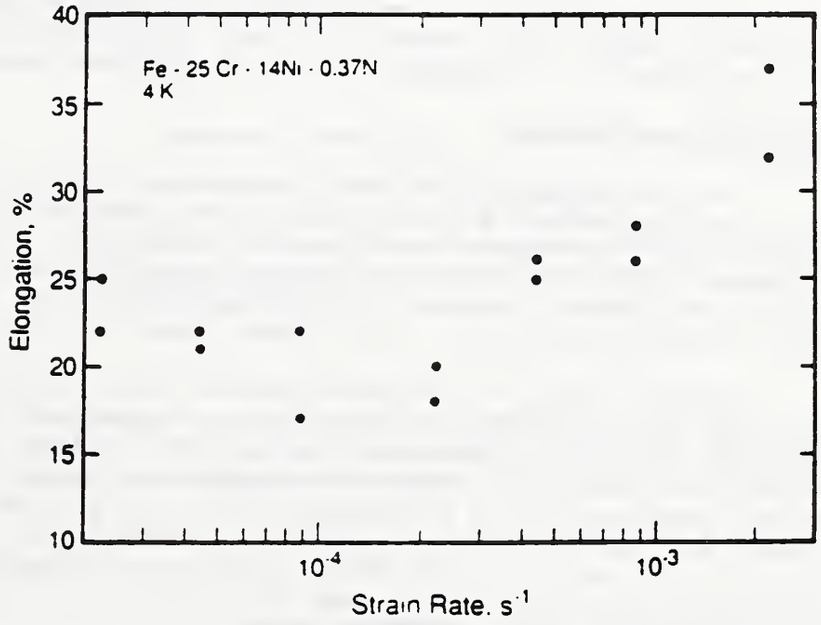

Fig. 3. Tensile elongation as a function of strain rate for Fe-25Cr-14Ni-0.37N austenitic steel.

1063

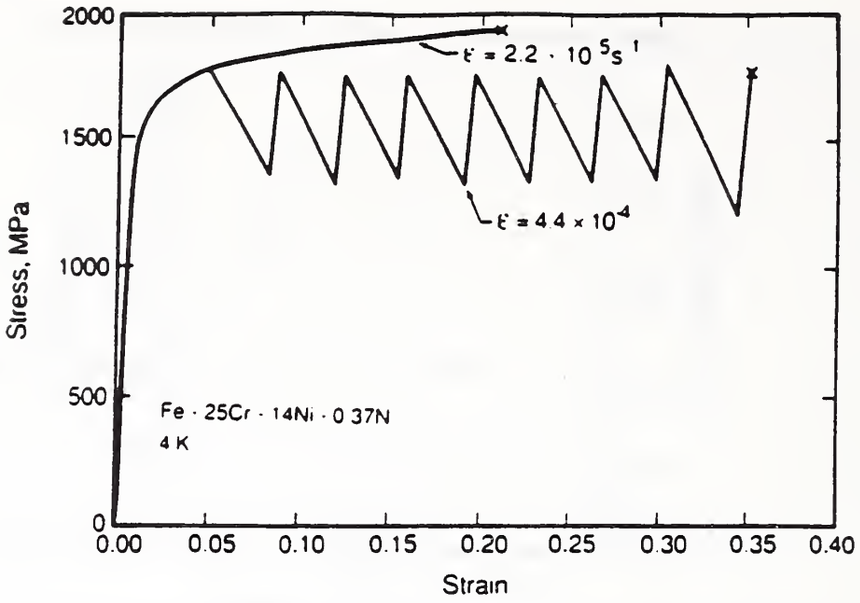

Fig. 4. Tensile stress-strain curves (engineering) of Fe-25Cr-14Ni-0.37N austenitic steel at two strain rates at 4 K.

DISCUSSION

Alloy Fe-25Cr-14Ni-0.37N is stronger than most other austenitic alloys that we have studied. It exhibits a transition of ultimate strength (σ_μ) to lower values at higher strain rates, similar to other austenitic steels. However, unlike other austenitic alloys, the transition of the ultimate strength of the Fe-25Cr-14Ni-0.37N alloy occurs at lower strain rates. The range of the strain rate in the transition region (to lower values of σ_μ) encompasses the strain rates used by most laboratories in the VAMAS round-robin tests of this alloy. Therefore, the variability of strain rates from contributing laboratories is very likely to account for much of the data variability found in the round-robin tests. We discuss the ramifications of this and present our interpretation of the divergent tensile behavior at 4 K.

Discontinuous Yielding

The sudden surge of localized catastrophic slip during tensile tests at 4 K of most structural alloys produces local temperature increases of the order of 50 K. At higher strain rates, the nature of the temperature increases change from spike-like to wave-like; that is, the strain duration of each temperature increase arising from discontinuous yields lengthens. Reed and Walsh[2] and Ogata, et al[4] report these characteristics.

As shown in Fig. 6, the stress and the strain that are associated with the onset of discontinuous yielding follow trends very similar to those of 304L, 310, and 316LN. Serrated yielding in all alloys initiates at lower values of σ_i and ϵ_i for strain rates higher than about $10^{-4} s^{-1}$. At lower strain rates there is no detectable effect on initiation; at strain rates higher than about $4 \times 10^{-4} s^{-1}$, minimum values of σ_i and ϵ_i are maintained. Therefore, a transition from higher to lower initiation stress and strain is observed over the strain rate range from 10^{-4} to $4 \times 10^{-4} s^{-1}$ for all austenitic steels that we have measured.

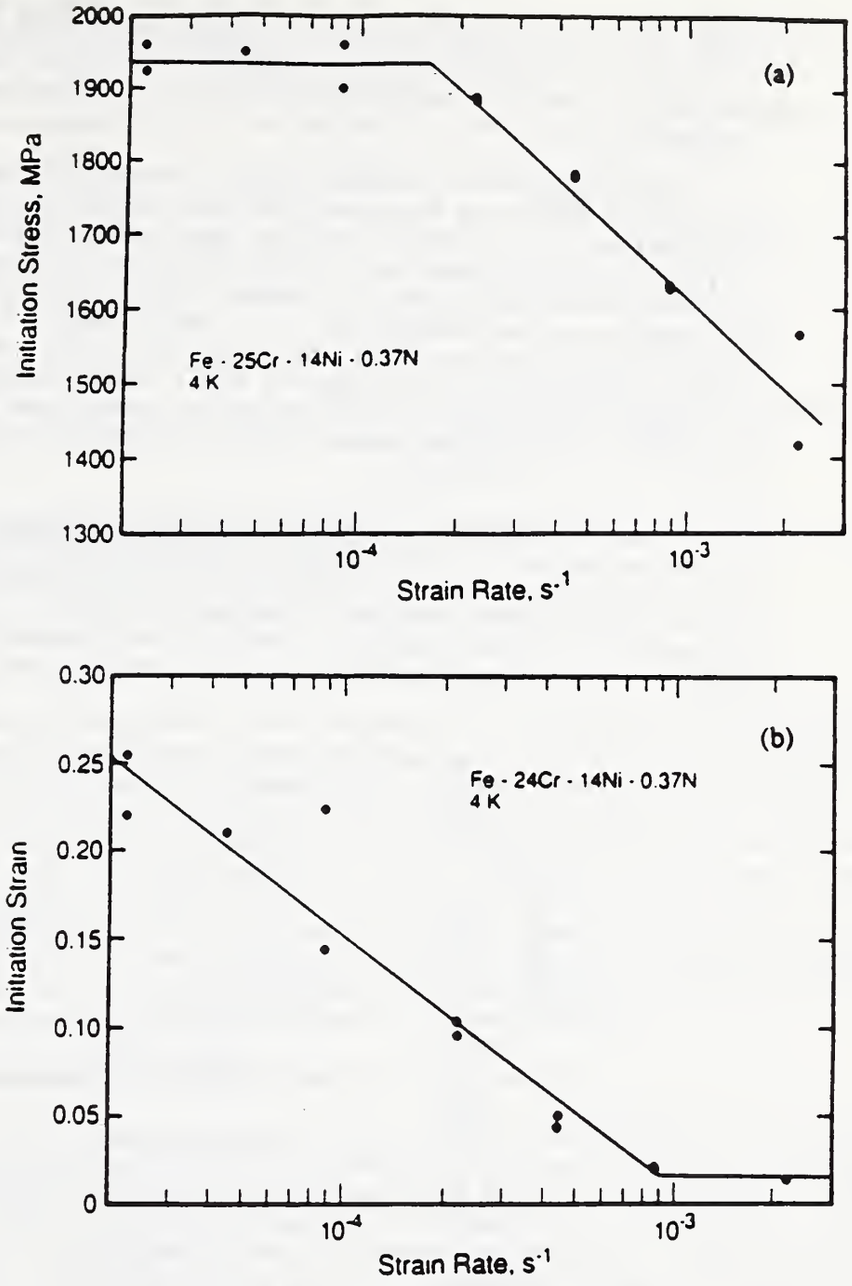

Fig. 5. The stress (a) and strain (b) corresponding to initiation of discontinuous yielding at 4 K as a function of strain rate for alloy Fe-25Cr-14Ni-0.37N.

We discuss the mechanism of discontinuous yielding in another paper of this volume.[6] The onset of discontinuous yielding is attributed to thermal instability; this produces mechanical instability resulting from localized overheating of slip bands.

Reduction of Ultimate Strength

In Fig. 7 the ultimate tensile strength at 4 K is plotted versus strain rate for the Fe-25Cr-14Ni-0.37N alloy and austenitic alloys that

were previously studied[2]. The three lower-strength alloys (304, 310, and 316LN) maintained high ultimate strengths until the strain rate exceeded $2 \times 10^{-3} s^{-1}$. Thus, in the current draft of the 4-K tensile test standard proposed to the ASTM committee E-28 on low-temperature test standards, it is recommended that strain-rates do not exceed $10^{-3} s^{-1}$.

The reduction of ultimate tensile strength in the higher strength Fe-25Cr-14Ni-0.37N alloy is associated with discontinuous yielding. At strain rates below $10^{-4} s^{-1}$ serrated yields were rarely observed; occasionally one serrated yield occurred and initiated specimen failure. Therefore, based on previous studies[3,5,6] we can conclude that at lower strain rates the specimen temperature was maintained at (or very near) 4 K. At higher strain rates discontinuous yielding was always observed, and deviations of flow stress to lower values accompanied them. This distinction between lack of serrations and higher flow stress on the other hand, and serrations and lower flow stress on the other is illustrated by the stress-strain curves of Fig. 4.

In lower-strength austenitic steels, the serrations are smaller (25-150 MPa as opposed to 300-350 MPa for this alloy). In the lower-strength alloys there is some plastic deformation with attendant strain hardening in the interval between elastic reloading (following a serration) and the initiation of a new serration. These strain-hardening regions result in similar stress-strain curves for both high and low strain rates.

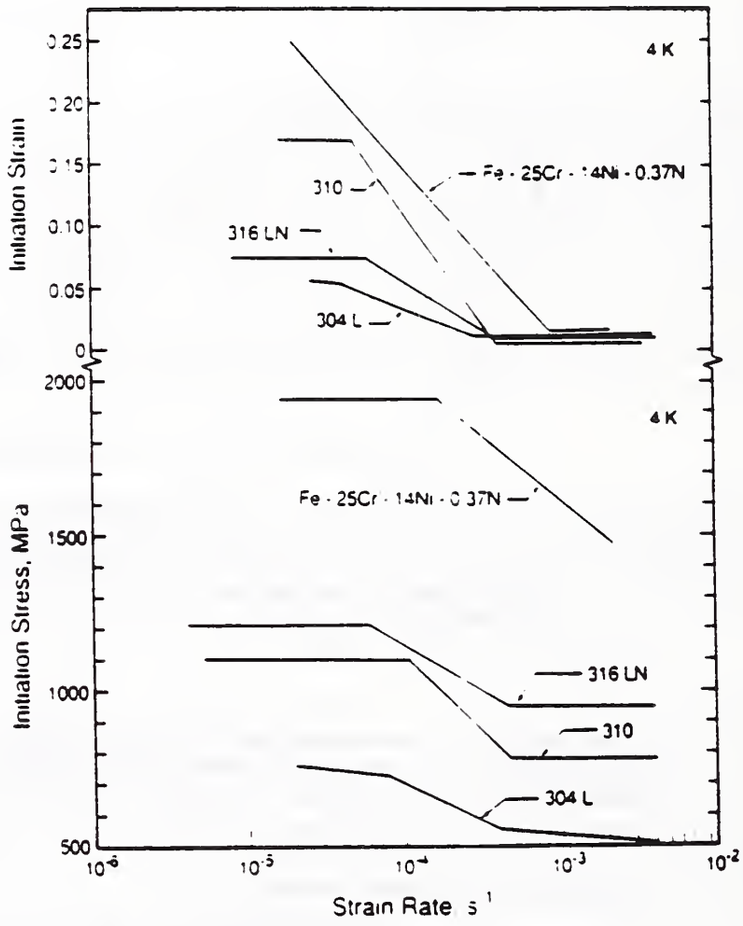

Fig. 6. The stress and strain corresponding to initiation of discontinuous yielding at 4 K as a function of strain rate, comparing alloy Fe-25Cr-14Ni-0.37N to other austenitic alloys (304L, 310, and 316LN).

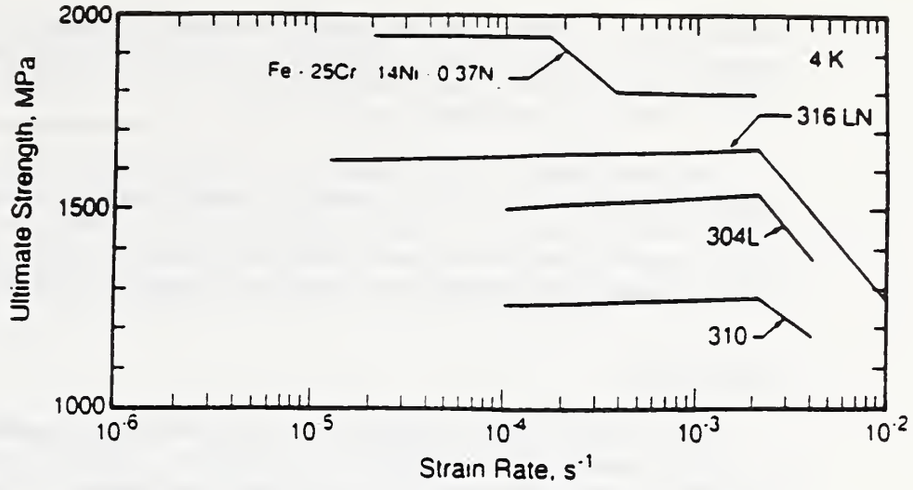

Fig. 7. Ultimate tensile strength at 4 K as a function of strain rate for selected austenitic steels.

The large magnitude of the serrations in the present alloy strongly suggests very high temperature spikes. For alloy 304L[2], load drops of about 50 MPa produced localized temperature spikes of about 50 K; load drops of about 150 MPa produced temperature increases of nearly 100 K. This suggests that local temperature increases of over 150 K may result from discontinuous yielding in the Fe-25Cr-14Ni-0.37N alloy. Therefore, since the ultimate strength of this alloy is approximately 1400 MPa at 76 K, it is not surprising that the failure strength is reduced under discontinuous yielding conditions at 4 K. The increase of tensile elongation with increasing strain rate (Fig. 3) is also expected to originate from the large temperature increases associated with discontinuous yielding.

Effects on Round-Robin Interpretation and Standards

The range of strain rates used by the 16 laboratories participating in the VAMAS round-robin[1] of tensile tests at 4 K was 1.3 to 11.1 x $10^{-4}s^{-1}$. It is evident from Figs. 2-6 that the data from all laboratories should not be expected to coincide, but should be expected to be dependent on the strain rate. For example, the ultimate strengths at 4 K of alloy Fe-25Cr-14Ni-0.37N reported by the 16 laboratories ranged from 1791 to 1960 MPa. Of the 42 data points for this property, only three exceeded 1900 MPa (1920, 1920, and 1962 MPa). In contrast, at low strain rates ($< 10^{-4}s^{-1}$) all of our measured values exceeded 1900 MPa. Therefore, the round-robin test program on the Fe-25Cr-14Ni-0.37N is inconclusive for assessment of the tensile data associated with specimen failure. The reported data are biased toward lower (approximately 10%) values of ultimate strength and toward higher values (approximately 25%) of elongation.

The results reported in this paper indicate that the tensile test procedures at 4 K commonly used in many laboratories need to be revised. Many laboratories begin testing at 4 K at low strain rates, then increase the strain rate by an order of magnitude following measurement of the yield strength. This increase of strain rate is performed to conserve liquid helium and test time. But either the exact opposite of this procedure or continuous maintenance of a single slow strain rate ($<10^{-4}s^{-1}$) is necessary to avoid serious specimen thermal imbalances. The thermal imbalances that occur in specimens during testing of high-strength austenitic steels have

been shown in this study to result in lower ultimate strengths and higher elongations. The currently proposed draft standards for low temperature testing now suggest strain rates below $10^{-3}s^{-1}$; this should be changed to $10^{-4}s^{-1}$ for high strength steels.

Two challenges still remain for future research on low temperature tensile standards: (1) to identify, quantitatively, the conditions under which lower strain rates are necessary during tensile tests at 4 K, and (2) to extend the strain-rate studies to nonferrous materials, particularly high-strength, low-conductivity alloys (such as Ti-based alloys).

CONCLUSIONS

In the very high-strength Fe-25Cr-14Ni-0.37N austenitic alloy used in the VAMAS round-robin tensile test program, reduced strength and increased elongation were measured at strain rates an order of magnitude lower than usual. Two major conclusions result from this study:

1. The variability of the VAMAS round-robin tensile data (other than yield strength) is partially attributable to the different strain rates used by each laboratory. Therefore, these results are inconclusive with respect to analyzing material and interlaboratory test reproducibility.

2. The tensile test standards currently under development worldwide need to be revised to reflect the effects of strain rates above $10^{-4}s^{-1}$ in high-strength, ductile austenitic steels.

ACKNOWLEDGEMENTS

The authors thank K. Ishikawa, K. Nagai, and T. Ogata of Japan's National Research Institute of Metals for supplying tensile specimens and mutual cooperation on this program.

REFERENCES

1. VAMAS Superconducting and Structural Materials, The Third TWP Meeting, National Research Institute for Metals, Science and Technology Agency, Japan (May 30, 1988).

2. R.P. Reed and R.P. Walsh, "Tensile Strain-Rate Effects in Liquid Helium," Adv. Cryo. Eng.-Mater. 34:199-208 (1988).

3. R.P. Reed and N.J. Simon, "Discontinuous Yielding in Austenitic Steels at Low Temperatures," Cryogenic Materials '88, Vol. 2, International Cryogenic Materials Conference, Boulder, CO (1988), pp. 851-863.

4. T. Ogata, K. Ishikawa, O. Umezawa, and T. Yuri, "Effects of Specimen Geometry on Temperature and Discontinuous Deformation during Tensile Tests at Liquid Helium Temperature," Adv. Cryo. Eng. - Mater. 34:209-215 (1988).

5. R.P. Reed and N.J. Simon, "Discontinuous Yielding During Tensile Tests at Low Temperatures," Adv. Cryo. Eng.-Mater. 36: (1990).

6. D.T. Read and R.P. Reed, "Heating Effects during Tensile Tests of AISI 304L Stainless Steels at 4 K," Adv. Cryo. Eng.-Mater. 26:91-101 (1980).

LOAD-CONTROLLED TENSILE TESTS OF AUSTENITIC STEELS AT 4 K

H.M. Lee

Korea Standards Research Institute
Taejon, Korea

R.P. Reed

National Institute of Standards and Technology
Boulder, Colorado

J.K. Han

Research Institute of Industrial Science and Technology
Pohang, Korea

ABSTRACT

Load-controlled tensile tests were conducted at 4 K on high-strength austenitic steels. The rate of loading was varied from 5 to 5000 N/s. This change of loading rate affected the onset of discontinuous yielding and, in turn, the fracture characteristics of the steels. Ultimate strength decreased at higher loading rates. The role of discontinuous yielding in affecting the dependence of these properties on loading rate is discussed. If conventional pressure vessel codes are used for the designation of structural design stresses, these data suggest that the ultimate strength, not the yield strength, controls this assignment.

INTRODUCTION

To simulate the operating conditions in high-field superconducting magnets, load-controlled tensile tests were conducted on selected strong austenitic steels. Most tensile tests at cryogenic temperatures have been carried out under constant displacement rate. In many practical applications such as superconducting magnets and pressure vessels, however, the structural material experiences unrestricted force. It is, therefore, desirable to characterize the load-controlled tensile properties at cryogenic temperatures. Earlier research[1] on lower-strength austenitic stainless steels (304L, 310, 316LN) indicates that, at higher load rates, the ultimate tensile strength and elongation are affected; the ultimate strength is reduced, and the elongation increases. Tensile yield strength and reduction of area are relatively unaffected at 4 K by load rate. The effect of load rate on initiation of discontinuous yielding was documented and associated with the reduction of ultimate strength.

Advances in Cryogenic Engineering (Materials), Vol. 36
Edited by R. P. Reed and F. R. Fickett
Plenum Press, New York, 1990

Table 1. Material Characterization

Alloy	Alloy Content, wt.%										Grain Size (μm)	Hardness (R_B)
	Cr	Ni	Mn	Mo	N	C	S	P	Si	Other		
Fe-18Cr-3Ni-13Mn	18.1	3.3	13.2	0.1	0.37	0.04	0.005	0.028	0.52	0.18 Nb, 0.15 V	48	93
Fe-21Cr-12Ni-5Mn	21.2	12.4	5.0	2.2	0.31	0.04	0.015	0.026	0.49	-	34	98
Fe-20Cr-25Ni-6Mo	20.3	24.7	1.6	6.3	0.19[a]	0.02	0.002	0.021	0.43	0.20 Cu	45	88

a: independent N analyses yielded 0.198, an average of three data sets.

There is concern that, under constant load-rate conditions, the initiation of a discontinuous yield could lead directly to catastrophic fracture at 4 K. A single discontinuous yield originates locally along the reduced section of the specimen, similar to a shear band. The deformed area throughout the specimen cross section had a band width (of the temperature rise) about 10 mm^2. Local temperature rises within this thermal band have been measured to be between 50 and 150 K.[2-4] In higher-strength alloys and at higher stresses in lower yield-strength alloys, the magnitude of the load drops and corresponding temperature spikes are greater. The higher strength of the austenitic alloys is normally achieved by nitrogen addition. Therefore, the flow and ultimate strengths of these alloys are expected to be strongly temperature dependent. Stronger temperature dependence of the flow strengths, coupled with larger load drops and temperature spikes, is expected to produce a greater dependence on strain or load rate during 4 K tensile tests. This paper explores this dependence for higher strength austenitic alloys.

EXPERIMENTAL PROCEDURES

The Fe-20Cr-25Ni-6Mo alloy was supplied in 38-mm-thick plate from a commercial heat. Its chemistry (Table 1) conforms to UNS NO8367. All alloys tested had been annealed condition; details of heat treatments have been previously reported.[5]

Round, tensile specimens were machined to a 6.35-mm diameter along a gage length of 41.9 mm. The entire specimen length was 71.4 mm.

The cryostat equipment has been described elsewhere.[1-3,6] Tests were conducted in boiling liquid helium and liquid nitrogen. Specimen strain was measured with clip-on, strain-gage extensometers: one extensometer with a 2.5-mm span and a gage length of 25.4 mm was used to measure yield strength. The second, high-range extensometer, with a span of 17.5 mm and a gage length of 38 mm, was used to measure specimen strain throughout the tensile test. Elongation was measured over a specimen-gage length of 3.8 cm. Reported strain rates refer to the nominal rate of plastic deformation within the reduced section of the specimens and can be measured directly in load-controlled tests.

A programmable servohydraulic testing machine (maximum load 250 kN) was used. With a high-resolution function generator, loading rates were varied from 0.5 to 5000 N/s. The machine was programmed for a ramp

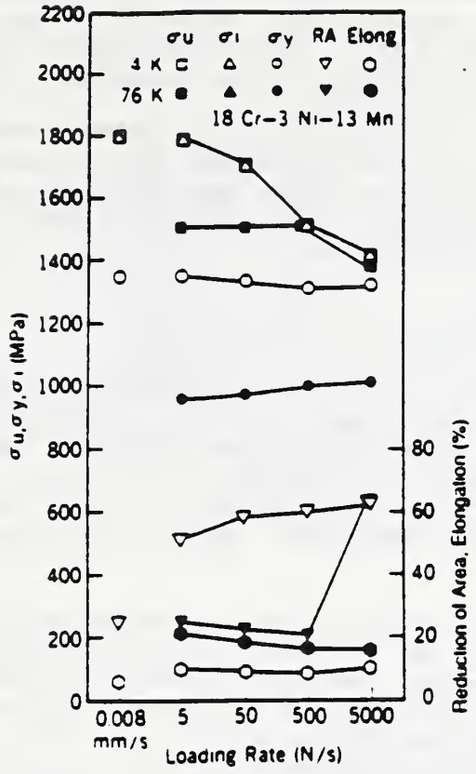

Fig. 1. Tensile properties at 4 and 76 K versus load rate.

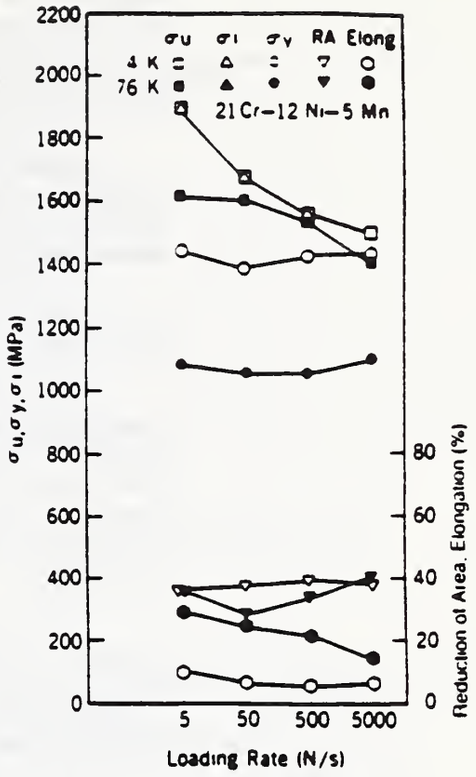

Fig. 2. Tensile properties at 4 and 76 K versus load rate.

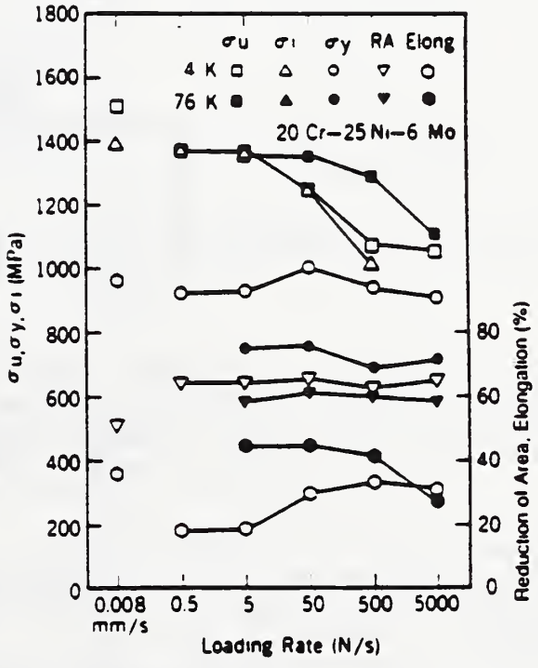

Fig. 3. Tensile properties at 4 and 76 K as a function of load rate.

function in a load-control mode; that is, the machine uniformly increased the load on the specimen until failure. The maximum actuator velocity is esti-mated to be 50 mm/s. The strain rate in the linear-elastic region was 8×10^{-8} s^{-1} to 8×10^{-4} s^{-1}, corresponding to loading rates of 0.5 N/s to 5000 N/s.

Load and strain were recorded with x-y recorders. During load-controlled testing, the strain rate was measured just before discontinuous deformation. A digital oscilloscope or strip-chart recorder was used for measurement of strain rate.

EXPERIMENTAL RESULTS

The effects of load rate on the tensile yield strength, ultimate strength, reduction of area (R.A.), and elongation are summarized in Figs. 1-3. All alloys were tested at both 4 and 76 K. At both temperatures the yield strength is independent of load rate; the ultimate strength decreases with increasing load rate. In one case (alloy 20Cr-5Ni-6Mo, Fig. 3) at higher load rates, the ultimate strength at 76 K is higher than at 4 K.

With increasing load rate the reduction of area tends to increase very slightly, except for the large increase measured for alloy 18Cr-3Ni-13Mn at 76 K and the highest load rate (5000 N/s). Elongation decreases with increasing load rate at 76 K, but remains constant or increases (Figs. 3, 4 with increasing load rate at 4 K.

The tensile data for displacement-controlled tests at 0.008 mm/s are provided in Figs. 1-3. The ultimate tensile strength at this displacement rate for 295, 76, and 4 K are shown in Fig. 4. The more ductile 20Cr-25Ni-6Mo alloy has lower tensile strength at low temperatures, but all alloys have almost equivalent strength at room temperature.

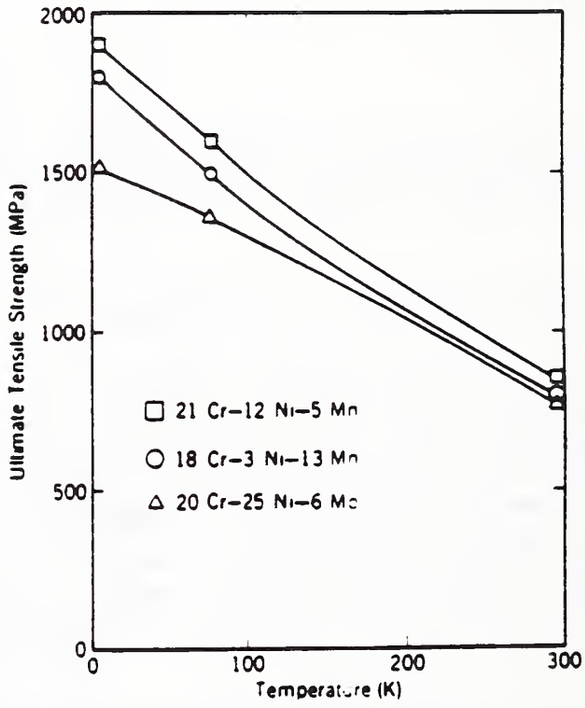

Fig. 4. Ultimate tensile strength (displacement control) vs temperature.

1276

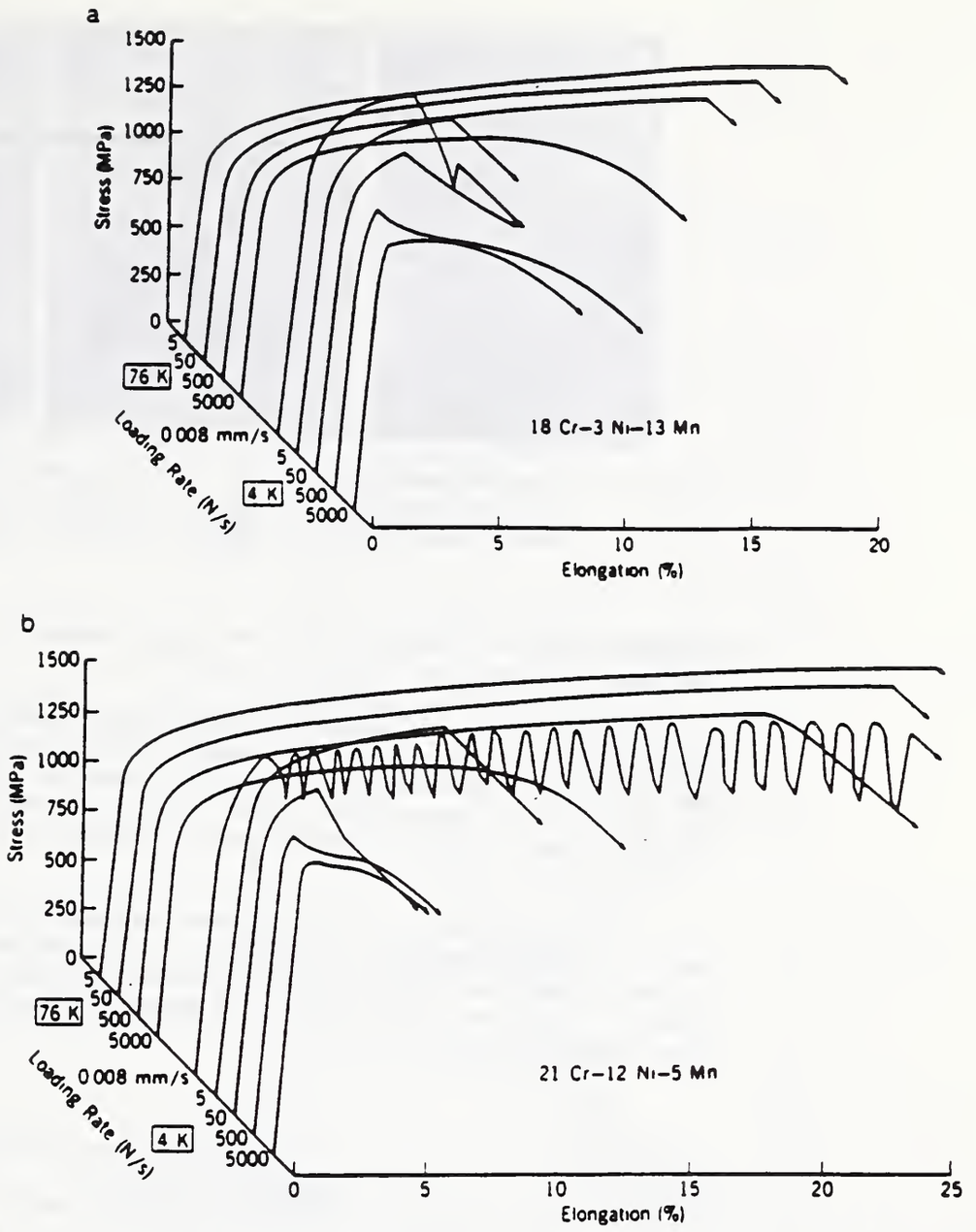

Fig. 5. Engineering stress-strain curves at 4 and 76 K for various rates of loading (a) alloy 18Cr-3Ni-13Mn, (b) alloy 21Cr-12Ni-5Mn.

Stress-strain curves (engineering) are shown for various load rates in Figs. 5a-b. At 4 K, alloys 21Cr-12Ni-5Mn and 18Cr-3Ni-13Mo in displacement control exhibit many discontinuous yields. In load-controlled tests at 4 K, all specimens fractured during the first discontinuous yield. No discontinuous yielding was detected in any alloy at 76 K.

The occurrence of discontinuous yielding was sometimes ambiguous. Therefore, a digital oscilloscope was used to verify discontinuous yielding. Figure 6 shows load and strain signals versus time, obtained from the alloy of Fe-18Cr-3Ni-13Mn. At lower load rates there is a clear discontinuity of both load and strain with time; at the highest rate (5000 N/S) no discontinuity was observed, yet the load decreased. This indicates that the

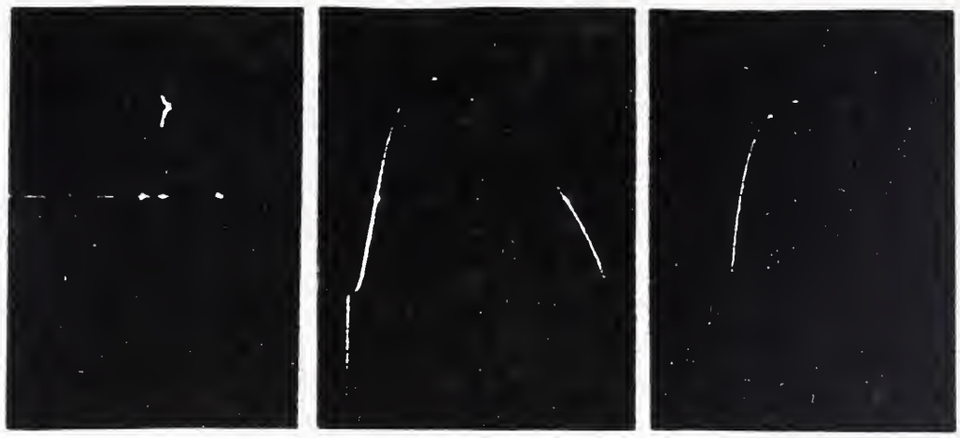

Fig. 6. Load (curves) and strain (lower curves) versus time for alloy 18Cr–3Ni–13Mn during plastic deformation at 4 K for various load rates (left: 5 N/s; center: 500 N/s; right: 5000 N/S).

actuator velocity (50 mm/s) was not large enough to keep pace with the increased strain rate of about $7 \times 10^{-1} s^{-1}$.

Maximum internal specimen temperatures during testing at 4 K for the three alloys were estimated by comparing the magnitude of the load drop with the temperature dependence of the flow strength. The results are shown in Fig. 7. Both the magnitude of the load drops and the estimated internal specimen temperature increase (almost linearly) with increasing loading rate for all alloys.

The initiation of discontinuous yielding is dependent on the strain rate of plastic deformation. In Fig. 8 we plot this dependency for three of the alloys plus alloys that had been previously tested at NIST[1] in load control. All have transitions from higher initiation stress and strain to lower values at about $10^{-4} s^{-1}$.

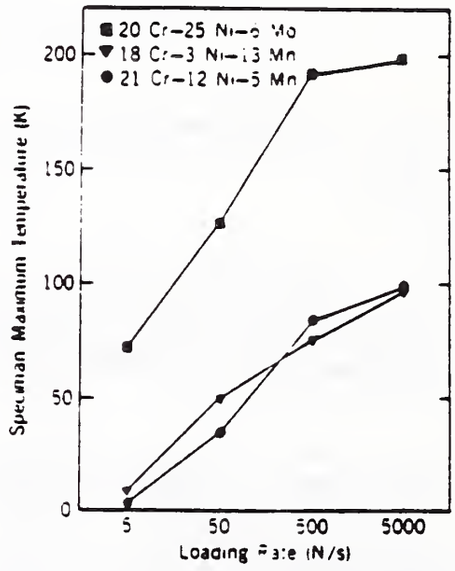

Fig. 7. Estimated maximum temperature of specimens during deformation at 4 K as a function of rate of loading.

1278

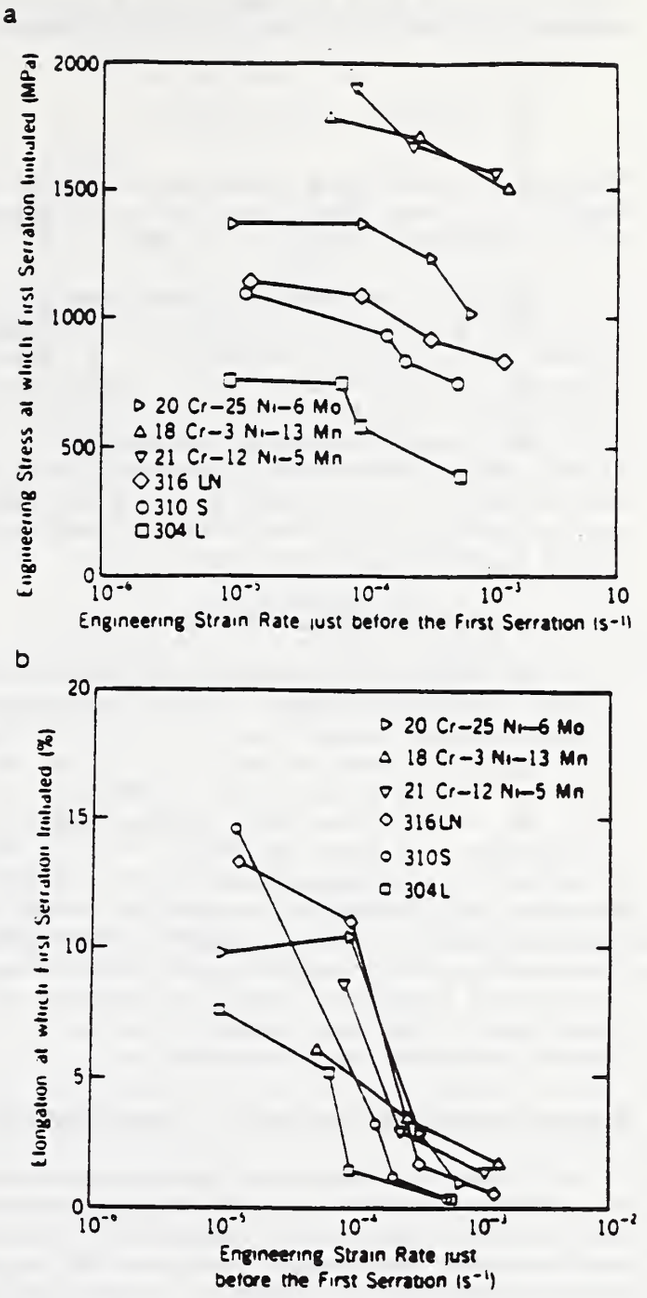

Fig. 8. The stress (a) and strain (b) to initiate discontinuous yielding for selected alloys versus specimen strain rate at initiation.

DISCUSSION

Discontinuous Yielding and Yield Strength

In displacement-control studies, the stress (σ_i) to initiate discontinuous yielding is proportional to the yield strength (σ_y). In particular, we reported[6] that

$$\sigma_i = \sigma_y + 320 \text{ MPa} \qquad (1)$$

for over 80 measurements of austenitic steels using low strain rates.

Generally, the flow strength (σ) is considered a sum of contributions from strain hardening (σ_d) and solution hardening (σ_f)

$$\sigma = \sigma_d + \sigma_f. \qquad (2)$$

The solution-hardening contribution may be equated to the yield strength ($\sigma_f = \sigma_y$). Then, when $\sigma = \sigma_i$ at the initiation of discontinuous yielding, σ_d is a constant, equal to 320 MPa.

The yield strength at lower load rates for the austenitic alloys of this study plus a previous study at our laboratories[1] is plotted in Fig. 9 versus the initiation stress (σ_i). A linear relation is obvious, with the intercept of 350 MPa at $\sigma_y = 0$. Within experimental uncertainty, the results from the previous study[6] and from these data are identical. Therefore, the strain hardening contribution to initiate discontinuous yielding is constant, independent of strength level and of metallurgical variables, such as stacking fault energy and grain size. However, external variables, such as strain rate, heat transfer coefficients, and test temperature do affect σ_i and σ_d.[1-4,6]

Discontinuous Yielding and Strain Rate

At higher load rates, the stress and strain (ϵ_i) to initiate discontinuous yielding declines. This corresponds to the influence of strain rate in displacement control tests.[3,6] Under displacement control, a transition from higher to lower values of σ_i occurs at strain rates of the order of $10^{-4}s^{-1}$. If the strain rate is measured at σ_i and plotted versus σ_i (Fig. 8a) and ϵ_i (Fig. 8b) for load-control the data, a similar transition is apparent. In previous work,[6] we have suggested that the transition may be caused by a change of local heat transfer in boiling liquid helium from nucleate to film boiling conditions at the microscopic level (at slip bands within grains). This was argued because the macroscopic work and heat balance at 4 K (considering work performed, stored energy, and solid and liquid heat conduction) does not produce sufficient heating to account for a transition in the heat transfer process. This process is also discussed in another paper of these proceedings.[7]

Discontinuous Yielding and Ultimate Strength

The major distinction between displacement and load-controlled tests at 4 K is the effect on tensile fracture characteristics. In displacement-controlled tensile tests, the sudden strain associated with a discontinuous yield results in a sudden reduction of the applied load. That is, the load train experiences an effective relaxation, dependent on its effective stiffness. This permits time for the local deformation band within the specimen to achieve thermal and mechanical equilibrium at a higher temperature and lower load level. Equilibrium is realized when the local strength at the higher temperature is balanced by the strain hardening of the deformation band.

In load-controlled tests, following a discontinuous yield, the machine increases its rate of displacement and attempts to maintain constant load. This results in additional strain to the local shear band since its temperature is higher and effective stress level lower than the surrounding material. The additional local strain within the shear band produces additional heating and reduction of effective strength. Thus, the process may be cumulative and will usually result in fracture within the shear band. Our results demonstrate this effect; in load-controlled tests fracture strength was usually associated with the stress necessary to initiate discontinuous yielding.

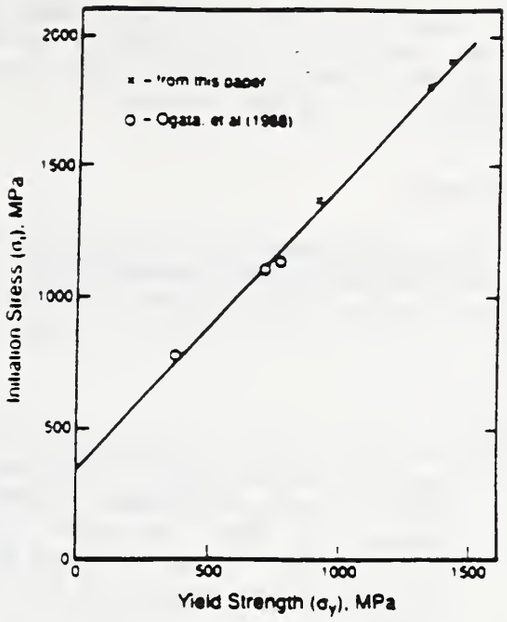

Figure 9. Stress to initiate discontinuous yielding versus yield strength for alloys from this study and from Ogata et al.[1,4]

Applications to Engineering Practice

The severe decline of the ultimate tensile strength (σ_u) under load control raises the issue of the application of ASME Boiler and Pressure Vessel Codes, Section VIII. This code is sometimes used to ensure sound design and material application practice in superconducting magnet construction.

The code usually requires operating stresses of either 1/2 to 2/3 σ_y or 1/3 σ_u. For all load rates, the ultimate strength ratio is lower than the yield-strength ratio, in contrast to displacement-control results. Therefore, if the Boiler and Pressure-Vessel Code is thought applicable for use in low temperature technology development, the ultimate strength controls alloy selection for load-controlled structural applications such as superconducting magnets. We suggest that two directions need to be taken to resolve this dilemma: (1) tests on thicker section components are needed to permit better development of thermal and mechanical scale-up models from laboratory specimen data and (2) development of alternative or amended design codes is necessary for superconducting magnet structures.

SUMMARY

To simulate operational conditions of a structural material in a superconducting magnet, load-controlled tests were conducted at 4 K on three high-strength austenitic steels.

(1) The onset of discontinuous yielding was correlated to the yield strength ($\sigma_i = \sigma_y + 350$ MPa) and to the strain rate; σ_i and ϵ_i undergo a transition to lower values as the strain rate increases above 10^{-4} s^{-1}.

(2) The ultimate strengths in load-controlled tests are associated with the onset of discontinuous yielding. Failure occurs within the deformation band of the original discontinuous yield.

1281

(3) The issue of the application of ASME Boiler and Pressure Vessel Code to low temperature technology is raised by these data: under code rules the ultimate strength, not the yield strength, controls the assignment of design stresses.

ACKNOWLEDGMENTS

We thank John Grubb of Allegheny-Ludlum Steel for sending a plate of the Fe-20Cr-25Ni-6Mo alloy. Robert Walsh assisted and advised in the measurement program. The Office of Fusion Energy partially sponsored this program.

REFERENCES

1. T. Ogata, K. Ishikawa, R.P. Reed, and R.P. Walsh, "Loading Rate Effects on Discontinuous Deformation in Load-Control Tensile Tests," Ad. Cryo. Eng.-Mater. 34:233-240 (1988).
2. D.T. Read and R.P. Reed, "Heating Effects during Tensile Tests of AWI 304L Stainless Steel at 4 K," Adv. Cryo. Eng.-Mater. 26:91-101 (1980).
3. R.P. Reed and R.P. Walsh, "Tensile Strain-Rate Effects in Liquid Helium," Adv. Cryo. Eng.-Mater. 34:199-208 (1988).
4. T. Ogata, K. Ishikawa, O. Umezawa, and T. Yuri, "Effects of Specimen Geometry on Temperature and Discontinuous Deformation during Tensile Tests at Liquid Helium Temperature," Adv. Cryo. Eng.-Mater. 34:209-215 (1988).
5. D.T. Read and R.P. Reed, "Toughness, Fatigue Crack Growth, and Tensile Properties of Three Nitrogen-Strengthened Stainless Steels at Cryogenic Temperatures", The Metal Science of Stainless Steels, Metall. Soc. AIME, New York (1979), pp. 92-121.
6. R.P. Reed and N.J. Simon, "Discontinuous Yielding in Austenitic Steels at Low Temperatures," Cryogenic Materials '88, (Shenyang, China), International Cryogenic Materials Conference, Boulder, CO (1988), pp. 851-863.
7. R.P. Reed and N.J. Simon, "Discontinuous Yielding during Tensile Tests at Low Temperatures," Adv. Cryo. Eng.-Mater. 36:(1990).
8. "Basis for Establishing Allowable Stress Values," ASME Boiler and Pressure Vessel Code, Section VIII, Division 1, Appendix P, American Society of Mechanical Engineers, New York.

EFFECT OF PROCESSING ON 4-K MECHANICAL PROPERTIES OF A MICROALLOYED AUSTENITIC STAINLESS STEEL[+]

P.T. Purtscher
Advanced Steel Processes and Products Research Center
Colorado School of Mines
Golden CO

M.C. Mataya
Rockwell International
Rocky Flats Plant
Golden, CO

L.M. Ma* and R.P. Reed
National Institute of Standards and Technology
Boulder CO

ABSTRACT

Tensile and fracture toughness tests were performed at 4 K as a function of hot-rolling temperature and compared with similar data for the steel in the annealed condition. Results show that the properties in hot-rolled conditions were comparable to annealed steel so there was no advantage to annealing after processing. Microalloy precipitates were effective at controlling grain size during processing at temperatures below 1150 C, and did influence the flow stress at 4 K.

INTRODUCTION

Development of austenitic stainless steels for superconducting magnet cases has concentrated on the effect of alloy composition on mechanical properties in the annealed condition after processing. The familiar NIST trend line for fracture toughness as a function of yield strength at 4 K was generated for a series of annealed austenitic stainless steels, AISI 304-type with different interstitial contents [1].

Limited data on the effect of thermomechanical processing of austenitic steels are available. Ogawa and Morris [2] have studied the influence of processing on the 4-K mechanical properties of a high-manganese, austenitic stainless steel. They found that reducing the hot-rolling temperature from 1250 to 1150°C refined the grain size, producing an increased yield strength. However, fracture toughness decreased rapidly. Room temperature deformation (30%) improved the 4-K strength-toughness relationship.

[+]contribution of NIST, not subject to copyright
*on leave from Institute of Metal Research Academia Sinica, Shenyang, P.R. China

Advances in Cryogenic Engineering (Materials), Vol. 36
Edited by R. P. Reed and F. R. Fickett
Plenum Press, New York, 1990

Table 1. Tensile Properties of As-Received Bar at 4 K

Location	0.2%Y.S. (MPa)	U.T.S. (MPa)	Elong. %	R.A. %
#1 Outer diameter	1540	1877	24.4	33.7
#2 Mid-radius	1212	1810	16.3	30.4
#3 Center	1107	1794	13.3	26.6
#4 Mid-radius	1171	1792	20.8	37.1
#5 Outer diameter	1503	1858	28.4	40.4

This investigation will determine the effect of hot-rolling conditions on the mechanical properties of an austenitic, structural steel for 4-K service. The starting temperatures for rolling (1150 to 950°C) are lower than that used by Ogawa and Morris [2]. If the mechanical properties after hot rolling are comparable to the properties in the annealed condition, then it should be possible to save the time and expense of a final annealing treatment before these types of steels are fabricated into structures.

MATERIALS AND PROCEDURES

Starting Material: The steel, Fe-22Cr-13Ni-5Mn-2.3Mo-0.21Nb-0.18V-0.03C-0.31N, was provided by a commercial, specialty-steel maker in the form of a 76-mm-diameter bar in the mill-annealed condition. The high concentrations of V and Nb control the grain size during processing and contribute slightly to the room temperature yield strength. The as-received microstructure of the bar was 100% austenitic at the outer diameter, but the center of the bar contained 0.1 to 0.2 volume fraction of sigma phase in the austenitic matrix. A hardness profile through the cross section of the as-received material showed a higher hardness, R_A 61, at the outer surface decreasing to R_A 54.5 in the center where the sigma phase was present. Table 1 shows the 4-K tensile properties, measured as a function of location through the diameter of the as-received bar. The large variation in tensile properties for the bar at 4 K could cause a problem when the steel is fabricated for cryogenic service.

Material Processing: In the first step, the round bar was heated to 1200°C and flattened in two hits by a steam hammer to a thickness of 38 mm. Next,

Fig. 1. Microstructure of steel after hot rolling from 1050 C and water quenching. Small remanent of sigma phase (arrow) and transgranular precipitates are visible in austenitic matrix. etch: HNO_3+H_2O @ 8 volts

sections were reheated to 1150, 1050, or 950°C for 30 min before final hot rolling in two passes to the final thickness of 28 mm. Immediately after rolling, the plate was straightened in the steam hammer. The hot rolling and straightening typically took about 2.5 min before the section was quenched into water. The finish temperatures before quenching were 875, 790, and 775°C respectively. One section rolled from 1150°C was annealed after processing for comparison to the hot-rolled material and is designated condition A. The sections rolled from 1150, 1050, and 950°C are called conditions D, B, and C, respectively.

Test Procedures: Two round tensile specimens oriented across the rolling direction and three 12.7-mm-thick compact specimens (C-T) with T-L orientations were taken from the top half of the plate. The #1 and #3 C-Ts were taken from the edges of the plate, and #2 came from the center of the width. Additional C-Ts were machined from edge locations of selected plates. Longitudinal tensile specimens were machined from the different conditions so there are five specimens equally spaced across the width of the bottom half of the plates, #1 and #5 at the edges of the plate and #3 in the center.

The toughness tests were conducted according to ASTM E813-81 with the unloading compliance method for measuring crack growth during the test. The only problem in testing was that the crack resistance curve usually contained only three or four data points between the exclusion limits of 0.15 and 1.5 mm set by the standard. For a valid test, the standard requires at least four data points between the exclusion limits. J_{Ic} was defined as the intersection of straight line drawn through the data within the exclusion limits and the blunting line as defined in the standard. More details of the tensile and fracture toughness testing are described in a separate paper in this volume [3].

RESULTS

Material Characterization: The processed plates had relatively uniform microstructures with little evidence of sigma phase. Figure 1 shows a remanent of sigma after rolling from 1050°C and a random precipitate distribution V and Nb(C,N) in the austenite that was present in all the plates. The grain size of the steel in all four conditions was between 40 and 60 μm. The precipitates were effective at pinning the grain boundaries and preventing grain growth during hot rolling and annealing. Annealing at 1163°C for 8 h was required to grow the grains significantly [4]. The hardness of sections taken through a plate from each test condition showed that the materials were relatively uniform: for plate A -- R_A 59.5 to 62, for plate B -- R_A 61 to 64.5, for plate C -- R_A 64.5 to 66, and for plate D -- R_A 59.5 to 63.

Tensile test: The results are summarized in the left half of Table 2 for both longitudinal and transverse orientations. Hot rolling at lower temperatures has increased the 0.2% FS with little change in ductility or ultimate strength at 4 K. Each of the plates shows better uniformity than the as-received bar. The tensile properties with the most variablity are yield strength (0.2% FS) and percent elongation. Figure 2 shows the variation about the average values in these properties in the longitudinal orientation for each condition. Hot rolling at lower temperatures reduced the variations observed across the width of the plate.

Toughness test: The results are summarized in the right half of Table 2. The data for condition A (annealed) appear to be divided in two distinct groups, one with an average K_{Ic} of 110 MPa/m and a second with an average K_{Ic} of 144 MPa/m. There is no systematic variation in toughness across the

Table 2. Mechanical Properties of Processed Plates at 4 K

Tensile Properties					Fracture Toughness Properties			
Spec.	0.2% FS MPa	UTS MPa	Elong. %	R.A. %	Spec.	J_{Ic} kJ/m²	K_{Ic}* MPa√m	T*
condition A -- annealed								
AL-1	1320	1795	28.8	31.7	A-2	98.6	140.4	22.6
AL-2	1448	1784	22.4	42.5	A-3	102.2	143.0	13.6
AL-3	1425	1799	26.4	46.2	A-4	108.9	108.9	7.3
AL-4	1439	1764	23.0	39.7	A-5	58.4	108.1	6.1
AL-5	1425	1779	23.4	51.6	A-6	62.3	111.6	7.7
AT-2	1264	1764	22.1	45.0	A-7	58.4	107.6	5.3
AT-3	1441	1877	14.3	43.9	A-8	109.5	148.0	18.4
					A-9	111.8	149.5	17.7
conditon B -- hot rolled from 1050°C								
BL-1	1714	1917	19.4	39.5	B-1	48.6	98.6	3.2
BL-2	1704	1919	18.4	38.6	B-2	43.7	93.5	3.6
BL-3	1687	1915	18.2	41.3	B-3	47.0	97.0	3.0
BL-4	1704	1913	12.9	44.4				
BL-5	1707	1912	18.2	42.3				
BT-1	1677	1876	16.4	43.5				
BT-2	1696	1867	16.2	40.3				
condition C -- hot rolled from 950°C								
CL-1	1800	1970	17.5	36.8	C-1	33.9	82.3	1.5
CL-2	1807	1949	17.2	39.2	C-2	34.2	82.7	3.2
CL-3	1759	1904	19.8	35.4	C-3	42.0	91.6	2.6
CL-4	1801	1952	18.0	34.7	C-4	32.5	80.6	2.1
CL-5	1839	1967	17.1	42.7				
CT-1	1740	1968	9.6	39.1				
CT-2	1737	1971	15.3	35.1				
conditon D -- rolled from 1150°C								
DL-1	1629	1914	16.7	47.6	D-1	66.1	115.0	6.5
DL-2	1569	1894	21.0	41.6	D-2	72.5	120.4	9.2
DL-3	1478	1816	19.5	42.6	D-3	88.8	133.3	9.5
DL-4	1534	1888	15.3	45.3	D-4	61.2	110.6	5.0
DL-5	1642	1902	12.1	40.4	D-5	59.8	109.4	5.3
DT-1	1574	1829	21.8	44.3				
DT-2	1558	1889	12.0	42.3				

* $K_{Ic}(J)^2 = JI_c \times E$ where E = 200000 MPa

* $T = (\Delta J/\Delta a) \times (E/sY^2)$ where sY = (0.2% FS + UTS)/2

width of the plates. Figure 3 shows the toughness values plotted as a function of average, transverse 0.2% FS. The results from this study are compared with the original data used in the NIST trend line for AISI 304-type steels corrected for the same J_{Ic}-to-K_{Ic} conversion factor. The data for condition A fit the previous trend for annealed steels, but the data for conditions B, C, and D are above the extrapolation of the lower-strength data.

DISCUSSION

In a hot-rolled condition, austenitic steels should have higher yield strengths than the same steel after annealing. In general, fracture toughness properties are inversely related to material strengths [5]. By quenching directly after rolling, excess dislocations are retained in the room temperature structure and make additional dislocation motion more difficult, that is, raise the flow stress compared to condition A. As the

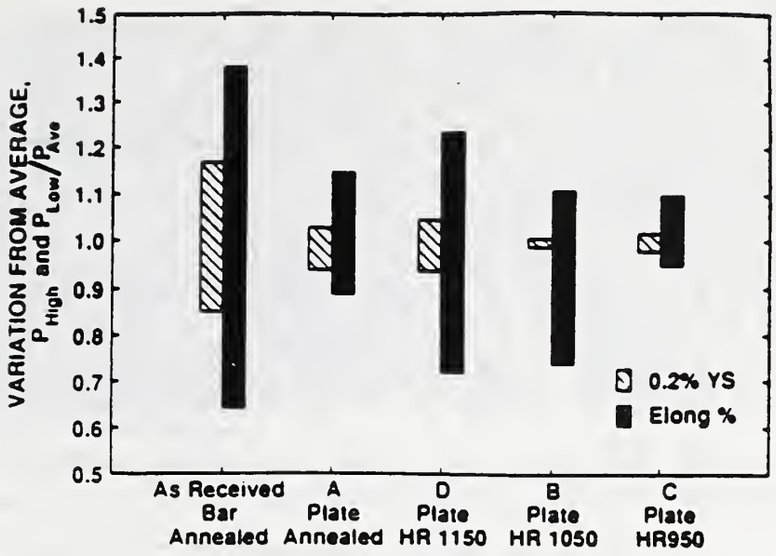

Fig. 2. The effect of processing on the variation in tensile properties, P (0.2% FS and % elongation), is shown as the ratio of the highest and lowest value, P_{high} and P_{low}, divided by P_{ave}.

rolling temperature decreases, more dislocations should be retained in the room temperature structure and, as a result, the flow stress should increase and fracture toughness would be expected to decrease. The annealing treatment should remove all excess dislocations that are produced in hot rolling. The steel used in this study has an additional complication due to the presence of V and Nb in the composition. These alloying element combine with C and N to form precipitates which stabilize the austenite, prevent Cr carbide precipitation, resist grain growth, and strengthen the matrix.

If there were no Nb and V in the Fe-22Cr-13Ni-5Mn-2.3Mo-0.3N steel, the 0.2% FS could be predicted from the results of Simon and Reed [12] to be 1300 MPa with a S.D. of 40 MPa. The 0.2% FS in condition A was measured to

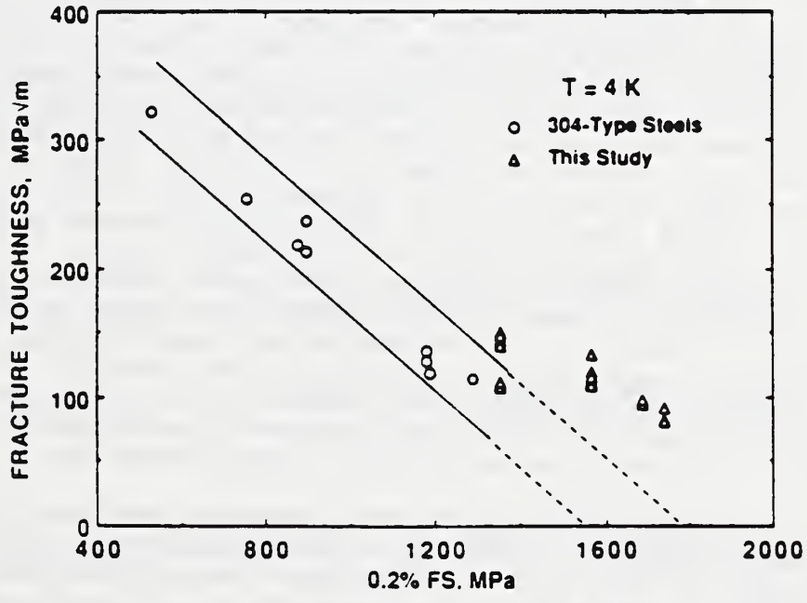

Fig. 3. Fracture toughness plotted against 0.2% FS Data for 304-type steels are from ref. 1.

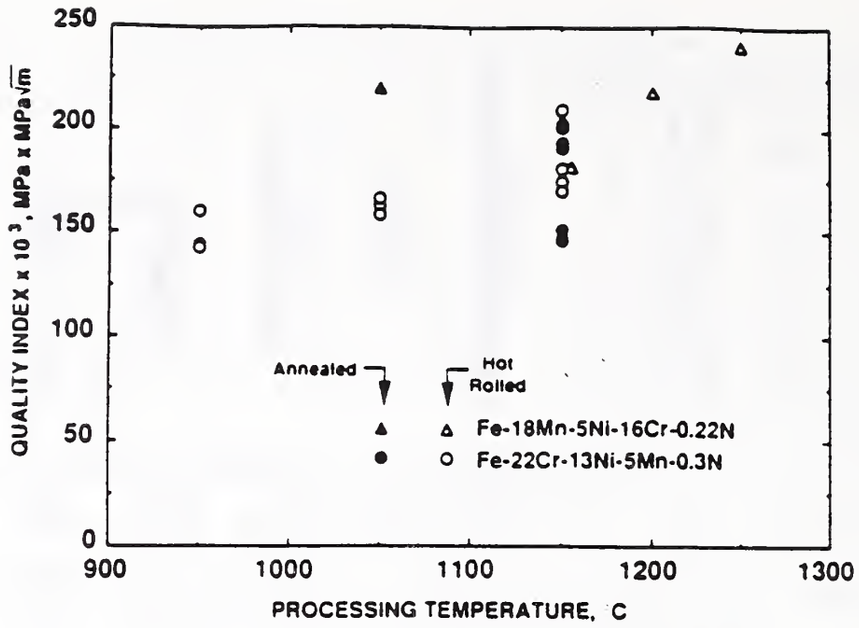

Fig. 4. Quality index plotted against processing temperature for either hot rolling or annealing. Data for high-Mn steel is from ref. 2.

be as high as 1540 and 1448 MPa in the bar and plate, respectively. The difference between the measured and predicted values can be attributed to the Nb and V precipitates.

One effect of hot rolling was to make the tensile properties more uniform (Fig. 2). The increase in uniformity is related to the precipitation behavior of the steel. When the steel is annealed, there are fewer nucleation sites for precipitates and the density of particles is probably more variable. In the hot-rolled conditions, excess dislocations left from processing can nucleate a more uniform distribution of particles.

The higher strength that comes from lowering the rolling temperature for this microalloyed steel does reduce J_{Ic}, but the decrease is not as dramatic as Ogawa and Morris [2] observed. To help illustrate this point, compare the quality index (QI) calculated for each test condition; see Fig. 4. The QI is the product of K_{Ic} and 0.2% FS and has been used to relate the influence that chemical composition and annealing temperature have on the strength-toughness relationship in austenitic steels [3,6,7,8]. The data from Ogawa and Morris [2] is included in Fig. 4 for comparison. Reducing the rolling temperature from 1250 to 1150°C reduced the QI for Fe-18Mn-5Ni-16Cr-0.22N (high-Mn steel) to a level below that of the annealed condition. For the Fe-22Cr-13Ni-5Mn-0.3N steel in this study, the QI decreases slightly as the rolling temperature goes down. Again, the larger variablity of the data for condition A is obvious. There does not appear to be an inherently better strength-toughness combination for annealed steel than for steel processed in the 1150 to 950°C range. The overall higher QI for the high-Mn steel compared to the steel in this study can be attributed to the different chemical composition and different test orientation.

The scatter in J_{Ic} for specimens from condition A appears significant, but is probably a reflection of the variaolity in the flow stress discussed above. To verify this, representative fractographs were taken from the surface of the broken C-Ts. Figure 5 shows a picture that is representative of all of the specimens. The fracture surfaces were similar to other austenitic stainless steels broken at 4 K. No stretch zone was observed

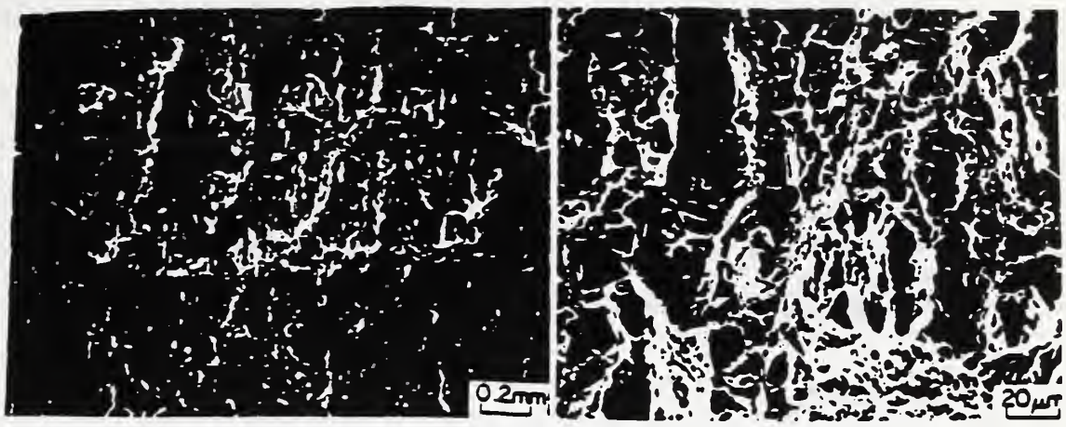

Fig. 5. Typical fracture surface appearance representative of both annealed and hot rolled C-T specimens: (a) low and (b) high magnification.

between the fatigue precracked region and the J-test region [9]. The J-test region is covered with dimples. The smaller dimples have nucleated at Nb and V particles that are uniformly dispersed in the austenite. The long dimples have nucleated from patches of sigma phase that elongated as a result of hot rolling. The SEM observations in this study support the previous observations [10,11] that fracture surface features are not directly related to variations in J_{Ic}.

Simple design considerations can be used to quantify the effect of hot rolling. The design stress is usually limited by the lower of two factors: (1) 2/3 yield stress or (2) 1/2 ultimate stress [13]. Looking at the tensile data in Table 2 for the transverse orientation, the first criterion is always higher or equal to the second. Criterion #2 would set the design stress at about 900 MPa, regardless of which condition is chosen. With similar design stresses, the best choice for the steel's processing is the one with the higher fracture toughness. The data in Table 2 show that condition D has the same lower-bound value for fracture toughness, about 110 MPa$\sqrt{m}$, as condition A. There does not appear to be a good reason for annealing the steel if sufficient control of the hot rolling process is available. In practice, many steel makers are moving in this direction, directly quenching austenitic stainless steels after the final pass in the rolling mill.

CONCLUSIONS

1. Decreasing the hot rolling temperature increases the 0.2% FS, but decreases fracture toughness. The calculated QI decreases slightly as the rolling temperature goes down.

2. An annealing treatment after hot rolling is not necessary to obtain the best combination of design stress and toughness in this microalloyed austenitic steel plate.

3. The addition of Nb and V to the Fe-22Cr-13Ni-5Mn-0.3N composition produced carbonitride precipitates that play two important roles in determining the mechanical properties: first, they helped to maintain a a fine grain size during processing, and second, the precipitates appear to increase the flow stress and the uniformity of mechanical properties in this steel, particularly in the annealed condition.

4. The trend line for fracture toughness as a function of yield strength of annealed austenitic stainless steels at 4 K does not extrapolate to higher strength levels for hot rolled steels.

ACKNOWLEDGMENTS

This work was partially supported by the Office of Fusion Energy, Department of Energy. The authors wish to thank M. Riendeau from Rockwell International and D. Vigliotti from National Institute of Standards and Technology for their help in processing the steel and T. Kosa from Carpenter Technology Corp. for helpful discussions.

REFERENCES

1. R.L. Tobler, D.T. Read and R.P. Reed: in Fracture Mechanics, Thirteenth Conference, ASTM STP 743, R. Roberts ed., American Society for Testing and Materials, Philadelphia, 1981, p.350.
2. R. Ogawa and J.W. Morris, Jr.: in Advances in Cryogenic Engineering-Materials, vol 30, eds. A.F. Clark and R.P. Reed, Plenum Press, New York, 1984, p. 177.
3. P.T. Purtscher, M. Austin, C. McCowan, R.P. Walsh, R.P. Reed, and J. Dunning: this volume
4. C.A. Perkins: M. Sc. Thesis, Colorado School of Mines, Golden CO, 1987.
5. P.K. Liaw and J.D. Landes: Metal. Trans., vol. 17A, 1986, p. 473.
6. P.T. Purtscher, R.P. Walsh, and R.P.Reed: in Advances in Cryogenic Engineering-Materials, vol. 34, eds. A.F. Clark and R.P. Reed, Plenum Press, New York, 1988, p. 191.
7. R.P. Reed, P.T. Purtscher, and K.A. Yushenko: in Advances in Cryogenic Engineering-Materials, vol. 32, eds. R.P. Reed and A.F. Clark, Plenum Press, New York, 1986, p. 43.
8. M.O. Spiedel: in Proceedings of High Nitrogen Steels, HNS--88, eds. J. Foct and A Hendry, Institute of Metals, London, 1989, p. 92.
9. P.T. Purtscher: JTEVA, vol. 15, Sept. 1987, p. 296.
10. P.T. Purtscher, D.T. Read, and R.P. Reed: in Fracture Mechanics: Perspectives and Directions (Twentieth Symposium), ASTM STP 1020, eds., R.P. Wei and R.P. Gangloff, American Society for Testing and Materials, Philadelphia, 1989, p. 433.
11. P.T. Purtscher, R.P. Reed, and D.K. Matlock: accepted for publication in Proceedings of Materials Research Society meeting on Advanced Materials, Fracture Mechanics Symposium, Tokyo Japan, June, 1988.
12. N.J. Simon and R.P. Reed: in Advances in Cryogenic Engineering-Materials, Vol 34, eds. A.F. Clark and R.P. Reed, Plenum Press, New York, 1988, p. 165
13. S. Shimamoto, H. Nakajima, K.Yoshida, and E. Tada: in Advances in Cryogenic Engineering-Materials, Vol. 32, eds. R.P. Reed and A.F. Clark, Plenum Press, New York, 1986, p.23.

AUSTENITIC STEELS WITH 9% Cr FOR STRUCTURES AT CRYOGENIC TEMPERATURES+

P.T. Purtscher*, M. Austin, C. McCowan, R.P. Reed,
R. P. Walsh, and J. Dunning**

Fracture and Deformation Division
National Institute of Standards and Technology
Boulder, CO USA 80303

*Advanced Steel Processing and Products Research Center
Colorado School of Mines
Golden, CO USA 80401

**U.S. Bureau of Mines
Albany, OR USA 97321-2198

ABSTRACT

Tensile and fracture toughness tests at 76 and 4 K are performed on austenitic steels containing 9% Cr. The results are comparable to similar data for AISI 304 and 316-type steels. Weight-loss experiments show that these steels will provide good resistance to rust formation. All of the data indicate that 9% Cr austenitic steels with appropriate alloy additions would be suitable for structural applications at cryogenic temperatures.

INTRODUCTION

Commercial austenitic (fcc) stainless steels (typically AISI 304 and 316 with 10-12% Ni and 16-20% Cr) are the most common materials for structural applications at low temperatures. These steels provide good mechanical properties at the service temperature, a nonmagnetic structure, and excellent corrosion resistance. The mechanical properties and austenitic structure are important for devices such as superconducting magnet cases, but the excellent corrosion resistance afforded by 304 and 316 is not necessary.

Steels with only 9% Cr plus small additions of Ni, Mo, and possibly Cu and V additions have an austenitic microstructure and corrosion resistance comparable to 304 in less severe environments. The lower Cr steel did not present any special problems in melting and hot rolling the material. The room-temperature mechanical properties are comparable to that of 304 stainless steel [1,2]. No information exists regarding the properties of 9% Cr austenitic steels at cryogenic temperatures.

Advances in Cryogenic Engineering (Materials), Vol. 36
Edited by R. P. Reed and F. R. Fickett
Plenum Press, New York, 1990

Table 1. Chemical Composition of Low Cr Steels (wt.%)

Alloy	Cr	Ni	Mn	Si	Mo	C	S	O	P	N
X	9.7	8.6	9.5	0.6	2.2	0.047	0.014	0.019	0.006	0.130
Y	8.8	13.7	4.2	0.5	2.0	0.022	0.007	0.025	0.004	0.082
Z	8.7	4.1	14.1	0.6	2.0	0.024	0.007	0.026	0.004	0.100
A	8.5	8.8	9.0	0.4	4.0	0.036	0.010	0.024	0.042	0.077

The goal of our research is to measure the cryogenic mechanical properties and corrosion resistance of several steels with 9% Cr. If the properties are comparable to the commercial austenitic stainless steels, then 9% Cr austenitic steels could be considered for low-temperature service. Several alloy compositions are studied where the Ni, Mn, and Mo contents are varied while the Cr content is held constant at 9%. Uniaxial tension and fracture toughness tests in liquid nitrogen (76 K) and liquid helium (4 K) are used to characterize the mechanical properties. Weight-loss experiments are also run to verify that these compositions would provide adequate corrosion resistance.

MATERIALS

Four alloys (36 kg heats) were prepared in an induction furnace with electrolytic-grade alloying elements. The heats were poured in cast iron molds, 10x10x27.5 cm_3. The ingots were homogenized for 24 h at 1100°C, upset forged approximately 75% at 1000°C, and then warm-worked at 700°C into 25 mm thick plates. The plates were given a recrystallization anneal at 1000°C for 45 min and water quenched. The chemical compositions of the four heats are shown in Table 1.

Table 2. Summary of Weight-Loss Corrosion Tests

Alloy	Solution	Corrosion Rate (mpy)
A	Glacial acetic acid	0
X	Glacial acetic acid	< 0.1
Y	Glacial acetic acid	< 0.1
Z	Glacial acetic acid	< 0.1
304 S.S.	Glacial acetic acid	< 20.0
A	Phosphoric acid	1.05
X	Phosphoric acid	2.15
Y	Phosphoric acid	524.0
Z	Phosphoric acid	1.4
304 S.S.	Phosphoric acid	< 20.0
A	Distilled water	< 0.01
X	Distilled water	< 0.01
Y	Distilled water	< 0.01
Z	Distilled water	< 0.01
304 S.S.	Distilled water	< 20.0

PROCEDURES

Corrosion testing: Weight-loss immersion tests were conducted on all alloys. Coupons 51 mm x 25 mm x 1.5 mm were cut from annealed plate and polished to a 120-grit finish. Tests were conducted in three different environments: glacial acetic acid at 80°C, 86% H_3PO_4 at 80°C, and distilled water at room temperature. The results can be characterized according to NACE classification: fully satisfactory resistance is < 0.5 mm/y (20 mpy, millinches/year); useful resistance is less than 0.5 to 0.5 mm/y; doubtful utility is 0.5 to less than 2.5 mm/y; severe attack is > 2.5 mm/y.

Mechanical testing: Uniaxial tension tests were performed on specimens oriented transverse to the rolling direction of the plate. The specimens had a 6.4 mm diameter and a 38 mm long gage length. The flow stress at 0.2% plastic strain is defined as the yield strength. The fracture stress is defined as the true stress at failure.

Fracture toughness tests were conducted on 25 mm thick compact specimens in the T-L orientation according to ASTM standard E 813-87. Tests were done in liquid helium (4 K) and in liquid nitrogen (76 K). The specimens were fatigue precracked at 76 K and then side-grooved 10% of the specimen thickness on each side before testing. The details of the exact test techniques are found in an earlier paper [3].

RESULTS AND DISCUSSION

Table 2 shows the corrosion test results. Alloys A, X, and Z were acceptable in all environments evaluated. Alloy Y corroded significantly only in the phosphoric acid solution. All four compositions would provide excellent resistance to rusting during the thermal cycling that cryogenic structures experience.

Table 3 is a summary of the mechanical test results. In general, the tensile properties of alloys X, Y, and A were typical of what would be expected for annealed 316-type steel at cryogenic temperatures. Alloy Z exhibited significantly lower tensile properties, particularly the elongation and fracture stress values at 4 K. Even at the higher test temperature, the fracture stress is still considerably lower than any of the other three alloys.

Material characterization: Metallography and X-ray diffraction showed that the alloys were austenitic after annealing. The microstructure of alloy Z was heavily faulted, see Fig. 1, but no hcp (nonmagnetic) or bcc (magnetic) martensite was observed before testing. Fractography was performed to document the fracture and deformation behavior of the 9% Cr steels. X-ray diffraction identified the second phases that were present after deformation. The x-ray beam contained Cu-Kα radiation with Kα2 stripped away. A Ge crystal detector measured the diffracted intensities. The relative volume fractions of each phase were determined by integrated areas under the peaks found by fitting the data to a Lorentzian profile.

Yield strength is usually the most important mechanical property. A linear relationship between the N content and yield strength indicates solid solution strengthening of the austenite by the interstitial element. Figure 2 shows the yield strengths of the four steels plotted as a function of N content and test temperature. The results for alloy Z do not fit the linear trend drawn through the results from the other three steels. For alloy Z, the yield strength is apparently controlled by transformation of the austenitic structure to martensite. Excluding the data for alloy Z, the slope of the 4-K data for 9% Cr steels is about 3400 MPa/wt.% N. Over the limited

Table 3. Summary of Mechanical Test Results from 9% Cr Steels at Cryogenic Temperatures

Alloy	Test Temp. (K)	Yield Strength (MPa)	Ultimate Strength (MPa)	% Elong., % R.A.	Uniform Strain (%)	Fracture Stress (MPa)	Fracture Toughness (MPa/m)	Quality Index x 10^3 (MPa·MPa/m)
X	4	851	1510	48,55	3.6	3330	175	148.9
X	4	869	1524	45,55	3.8	3380	183	159.0
X	76	668	1302	63,70	45	3284	287	191.7
X	76	672	1334	57,70	45	3518	290	194.9
Y	4	700	1484	48,60	3.1	3690	246	172.2
Y	4	720	1491	44,57	4.2	3504	–	177.1
Y	76	577	1259	55,74	42	3344	394	227.3
Y	76	578	1290	57,70	43	3444	425	245.7
Z	4	587	1210	21,23	2.4	1578	165	96.9
Z	4	608	1161	14,16	2.4	1389	167	101.5
Z	76	436	1310	52,57	41	2694	317	138.2
Z	76	445	1310	52,57	41	2694	333	148.2
A	4	704	1552	45,57	1.9	3608	227	159.8
A	4	658	1542	43,54	2.8	3218	176	115.8
A	76	528	1336	56,69	45	3236	406	214.4
A	76	544	1364	57,69	44	3546	425	231.2

Figure 1. Annealed microstructure of alloy Z prior to testing was austenitic with large areas of faults indicated by arrows.

1268

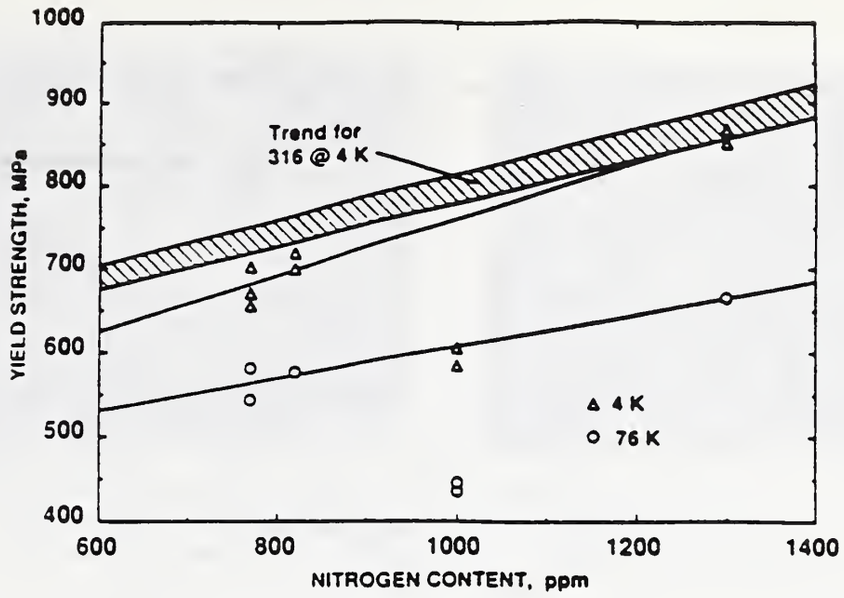

Figure 2. Tensile yield strength of 9% Cr steels as a function of nitrogen content and temperature compared to data from ref. 4.

range of N content tested here, the solid solution strengthening of the lower Cr steels appears to be more effective than for 316-type steels at 4 K [4] (trend shown on Fig. 2). The yield strength increases at a lower rate, about 2370 MPa/wt.% N, but with a higher intercept on the y axis of the plot. Higher yield strengths should be possible in 9% Cr steels if the nitrogen content is increased, but the rate of strengthening may change. Modified alloy contents to increase the N solubility in austenite or special melting practices to create a super-saturated austenite with respect to N [5] may be required to increase the yield strength.

The toughness of alloy Y at 4 K was higher than any of the other 9% Cr steels and alloy Z had the lowest toughness value. Previous research has shown that the Ni content and yield strength are the most important factors that determine the fracture toughness of austenitic stainless steels at 4 K. The simplest way to characterize the overall mechanical performance at 4 K is to calculate a quality index (QI), the product of toughness and yield strength [6]. Spiedel [7] has used the same product to characterize the performance of steels at room temperature. A higher QI value indicates a better combination of strength and toughness. Previous research has shown that increasing the N or Mo content of austenitic stainless steels did not change the QI whereas increasing Ni content did increase QI [6,8]. In Fig. 3, the calculated QI of the 9% Cr steels is compared to a trend of QI vs Ni content for other austenitic steels tested at 4 K. The QI values for each of the 9% Cr steels at 4 K fit the same trend determined for 304LN and 316LN-type steels. At 76 K, the results for the 9% Cr steels are above the trend line for 4 K data, but they still show the effect of Ni on the QI. Limited data for 304-type steels at 76 K are also above the QI-vs-Ni trend for 4-K tests [9]. In general, it appears that test results at 76 K give higher QI values than test results at 4 K.

Plastic strain at low temperatures transformed part of the austenitic matrix to hcp and bcc martensite in all of the steels. X-ray diffraction was performed on samples taken from broken, 4-K tensile specimens, approximately 10 mm away from the fracture surface. The volume fractions of each phase in these steels are shown in Table 4 along with the plastic strain at that point. The high hcp content in alloy Z is the most significant point,

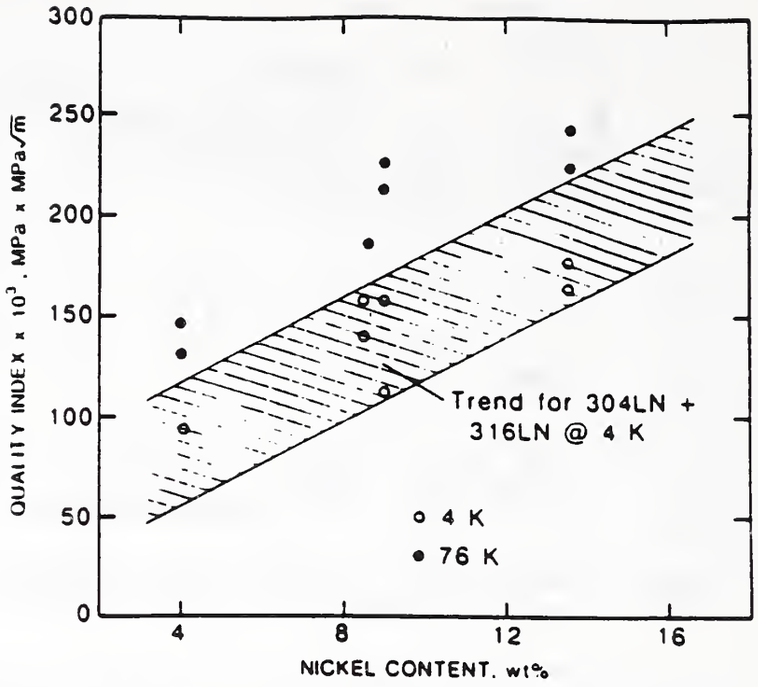

Figure 3. Calculated quality index vs. Ni content for 9% Cr steels compared to data from 304 and 316-type steels tested at 4 K.

apparently reducing the properties of the steel when plastically deformed. Commercial austenitic stainless steels partially transform to martensite, mainly bcc-type, during cryogenic deformation without any degradation of the tensile or fracture properties. Tomota et al. [10] have also shown that a large volume fraction of hcp martensite can reduce ductility in tensile tests.

Fractography on the broken compact tension specimens to documented the micromechanisms of fracture which occur in the 9% Cr steels. No stretch zones were observed between the fatigue precracked region and the J-test region, similar to the appearance of commercial austenitic stainless steels tested at cryogenic temperatures [11]. Figure 4 shows an example of the dimpled rupture morphology that was found on the J-test region of specimens from alloys X and Y tested at 4 K. Similar features were observed for steels X, Y, and A when tested at 76 K. Voids form at non-metallic inclusions in the austenite to start the fracture process.

Table 4. Phases Present after deformation of 9% Cr Steels at 4 K

Alloy	True - Strain	fcc	bcc	hcp
X	0.39	40	34	26
Y	0.48	29	71	0
Z	0.14	27	8	64
A	0.33	36	40	24

1270

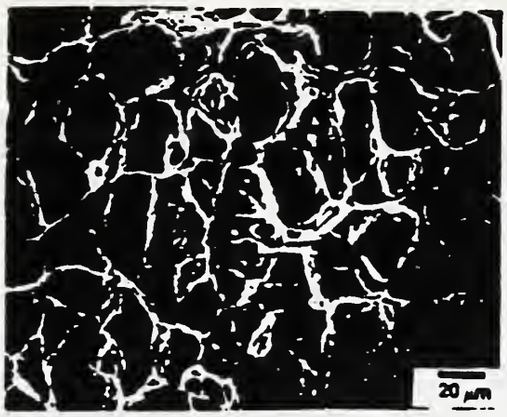

Fig. 4. SEM micrograph of the fracture surface of a compact specimen from alloy X tested at 4 K.

Fig. 5. SEM micrograph of the fracture surface of a compact specimen from alloy Z tested at 4 K.

For alloy Z, the fracture morphology appears crystallographic; see Fig. 5. Cross sections through the fracture plane were examined and compared to the appearance of the fracture. Apparently, the fracture starts at the hcp martensite plates that are present ahead of the crack tip rather than at nonmetallic inclusions. The fracture morphology for alloy A tested at 4 K was also crystallographic, but with some evidence of void nucleation at nonmetallic inclusions.

It has been suggested that martensite formation during mechanical testing is responsible for transformation-induced plasticity (TRIP) where the mechanical properties are greatly enhanced at certain test temperatures [12]. No significant improvement in any of the mechanical properties of these 9% Cr steels has been observed at 4 or 76 K. On the contrary, the poor mechanical properties of alloy Z at cryogenic temperatures are directly related to the presence of hcp martensite. If there is a TRIP effect in our alloys, it must lie at some temperature above 76 K.

CONCLUSIONS

1. With appropriate alloying, 9% Cr steels have mechanical properties which are equivalent to commercial stainless steels at cryogenic temperatures. The Ni content is a key ingredient for low-temperature toughness. The N content is most important for controlling the yield strength.

2. All four of the 9% Cr steels tested here have sufficient corrosion resistance for currently anticipated cryogenic structural applications.

3. The formation of hcp martensite in 9% Cr austenitic steels can reduce tensile and fracture properties at cryogenic temperatures.

ACKNOWLEDGMENTS

The help of Luming Ma, a guest work at NIST on leave from the Chinese Institute of Metals, Shenyang, China in performing many of the tensile tests for this program is gratefully acknowledged. The research was partially supported by DOE Office of Fusion Energy.

REFERENCES

1. S. Floreen, Metal. Trans., 13A:2003 (1982).
2. J.S. Dunning, J.M. Oh, and J.C. Rawers, in: Alternate Alloying for Environmental Resistance, edited by G.R. Smolik and S.K. Banerji, Metallurgical Society of AIME, Warrendale, PA (1987), p. 3.
3. R.L. Tobler, D.T. Read, and R.P. Reed, in: Fracture Mechanics, Thirteenth Conference, ASTM STP 743, R. Roberts, ed., American Society for Testing and Materials, Philadelphia (1981) p. 350.
4. N.J. Simon and R.P. Reed, in: Advances in Cryogenic Engineering, Materials, Vol. 34, eds. A.F. Clark and R.P. Reed, Plenum Press, New York (1988), p. 165.
5. R.P. Reed, Journal of Metals, 41:16 (1989).
6. R.P. Reed, P.T. Purtscher, and K.A. Yushenko, in: Advances in Cryogenic Engineering, Materials, Vol. 32, eds. R.P. Reed and A.F. Clark, Plenum Press, New York (1986), p. 43.
7. M.O. Spiedel, in: High Nitrogen Steels, HNS -88, eds. J. Foct and A. Hendry, Institute of Metals, London (1989), p 92.
8. P.T. Purtscher, R.P. Walsh, and R.P. Reed, in: Advances in Cryogenic Engineering, Materials Vol. 34, eds. A.F. Clark and R.P. Reed, Plenum Press, New York (1988) p. 191.
9. P.T. Purtscher and R.P. Reed, in: High Nitrogen Steels--HNS 88, eds. J. Foct and A. Hendry, Institute of Metals, London (1989), p. 189.
10. Y. Tomoto, M. Strum, and J.W. Morris, Jr., Metal. Trans., 17A:537 (1986).
11. P.T. Purtscher, JTEVA, 15:296 (1987).
12. S.D. Antolovich and B. Singh, Metal. Trans., 2:2135 (1971).

MICROMECHANISMS OF DUCTILE FRACTURE AND FRACTURE TOUGHNESS IN A HIGH-STRENGTH AUSTENITIC STEEL

P.T. Purtscher
Materials Reliability Division
National Institute of Standards and Technology
Boulder, CO USA

The micromechanisms of ductile fracture in a high strength austenitic stainless steel have been studied as a function of test temperature and stress state. Two different micromechanisms are important in this steel: void formation that leads to microvoid coalescence (MVC) and shear fracture. The differences between the two micromechanisms is related to when strain localization occurs. For MVC, strain becomes localized between voids that nucleate when a critical stress is reached during uniform deformation. For shear fracture, strain becomes localized across the deforming section before any significant volume fraction of voids have nucleated, that is, before the stress for nucleation is reached. In uniaxial and biaxial stress states, shear fracture becomes the important micromechanism of failure as the test temperature decreases because the stress for void nucleation increases for lower test temperatures. In the triaxial stress state associated with fracture toughness testing, MVC is the dominant micromechanism observed on the fracture surface of specimens tested between 295 and 4 K. Observations from interrupted fracture toughness tests show that void nucleation from large, scattered particles has little influence on the measured fracture toughness. Void nucleation, growth and coalescence at small, closely spaced microalloy particles occurs at an applied value of J less than J_{Ic}, the critical value that is associated with the measured fracture toughness of the steel. Observations and preliminary calculations suggest that fracture toughness is related to void nucleation ahead of the crack where the hydrostatic stress associated with crack tip blunting is a maximum.

1.0 INTRODUCTION

The effect of temperature on the fracture of iron alloys depends on the crystal structure of the dominant phase. In ferritic steels, body-centered-cubic struct re, the normal fracture behavior at room temperature (295 K) is ductile. As the test temperature is decreased, a brittle, cleavage fracture occurs at a critical temperature, commonly called the ductile-to-brittle transition temperature (DBTT). Fracture of ferritic steels at temperatures near the DBTT has been studied extensively [1] and is not considered here. In contrast, most austenitic stainless steels, face-centered-cubic structure, do not undergo any transition to cleavage fracture as the temperature is decreased to temperatures as low as 4 K [2]. Only ductile fracture is important for ductility and toughness in austenitic stainless steels.

Austenitic stainless steels are commonly used for structural applications in severe environments, for example, superconducting magnet cases, liquefied gas storage vessels, and rotors for turbine generators at elevated temperatures. All of these applications require good mechanical properties such as strength, ductility, and toughness, in addition to excellent corrosion resistance.

Recent alloy development programs have improved the mechanical properties of austenitic stainless steels [3-4]. The strength can be raised by additions of nitrogen and careful control of grain size during processing. The basic mechanisms that control tensile ductility are not well known for austenitic stainless steels. The relationship between ductility and toughness is vague because there are different ways to evaluate toughness. In this study, toughness is discussed in terms of fracture toughness. Fracture toughness is a material property that describes the conditions under which an initially sharp crack begins to grow. The basic framework for defining fracture toughness was proposed in the late 1950's by Irwin [5]. Fracture toughness is more valuable than other measures of toughness because it directly relates to the performance of a material in service. Fracture toughness is the only type of toughness that is considered in this work.

The micromechanisms related to toughness and ductile fracture in an austenitic stainless steel are the subject of

this work. Much has been written on this subject, and several good review articles and books have recently been published [6-10]. These references provide a thorough description of the present state of knowledge regarding ductile fracture, and only background information pertinent to the micromechanisms of ductile fracture in steels are discussed here. The state of the art in toughness testing and modeling is reviewed briefly with respect to how the micromechanisms of ductile fracture relate to toughness. The next section summarizes preliminary work on toughness of austenitic stainless steels at cryogenic temperatures. At the end of the introduction, the hypothesis for this report is presented along with a proposed experimental plan.

1.1 Ductile fracture

There are many definitions of ductile fracture. All agree that ductile fracture requires plastic deformation. For example, Dieter [11] defines ductile fracture as "fracture occurring with appreciable gross plastic deformation." In this work, materials that fail after localized plastic deformation are called "ductile" regardless of the micromechanisms that lead to fracture. A micromechanism is a physical process that operates as a result of plastic deformation. The micromechanisms that cause ductile fracture are those that produce localized deformation.

Ductile fracture under tensile loading can be classified according to three fundamental micromechanisms [11] shown in Fig. 1: (a) necking to a point, (b) shear, and (c) pore formation or void nucleation (referred to as microvoid coalescence or MVC). Neck formation and fracture at a point (Fig. 1a) occur when plastic deformation is localized by neck formation and continues until the macroscopic cross sectional area reduces to a point. Void nucleation is not required for fracture by necking to a point. This first type of ductile fracture is typical of soft, pure materials and/or, materials in high-temperature tests.

Shear fracture (Fig. 1b) occurs when plastic strain is localized into a shear band oriented at 45° to the tensile axis and is characteristic of single crystals in tension. Again, void nucleation is not required for shear fracture. Void nucleation, growth, and coalescence are often observed on the fracture surface of shear fractures, but the MVC features form after strain is localized in the shear band.

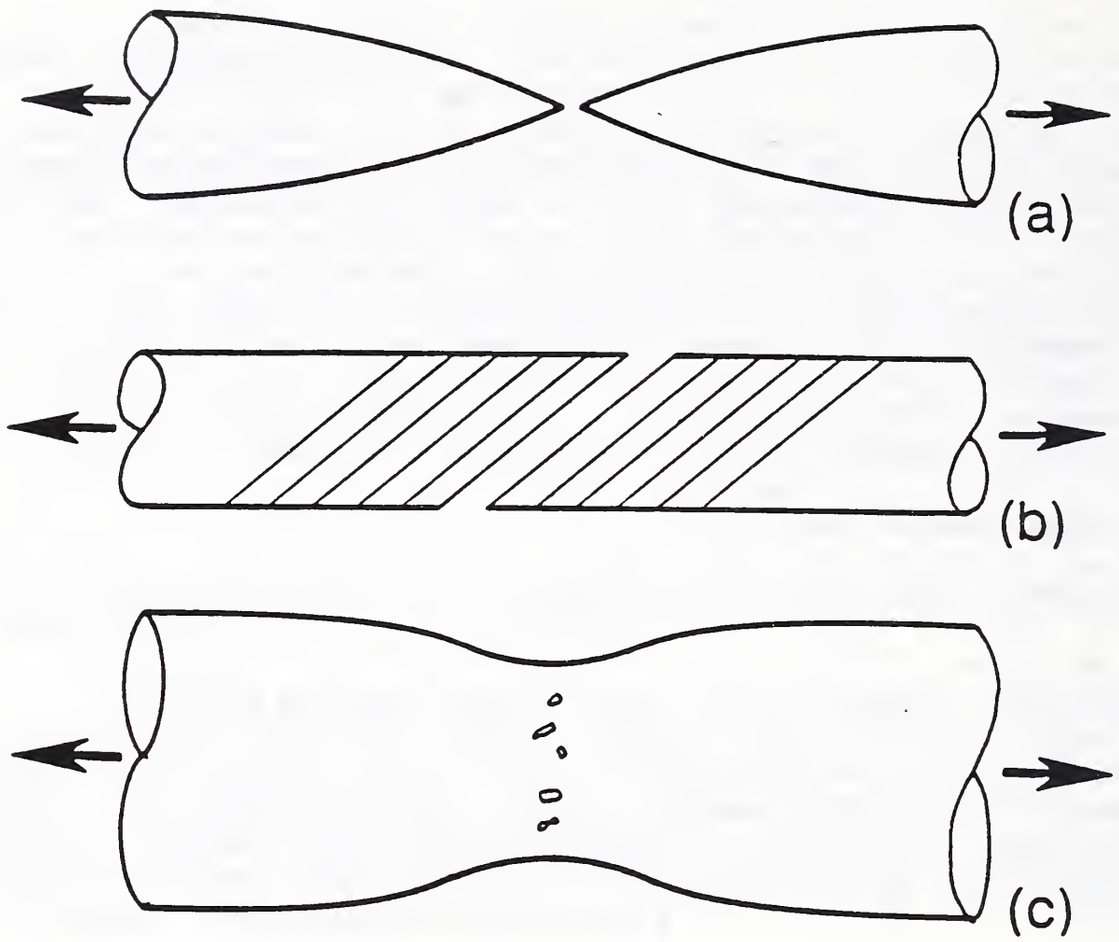

Figure 1. Schematic diagram of micromechanisms of ductile fracture: (a) necking, (b) shear, and (c) void formation.

MVC (Fig. 1c) is a three step process. First, voids nucleate inside the material. After nucleation, void growth starts and continues to a critical point where voids coalesce to form a fracture surface. In steels, nucleation normally occurs at second phase particles in the matrix when a critical stress is reached. The voids can form either by decohesion of the interface between the particle and the matrix or by particle cracking. Void growth is related to plastic deformation in the intervoid regions. The ductile behavior is commonly observed in both ferritic steels, strained at a temperature above the DBTT, and austenitic steels.

To summarize, fracture by necking to a point is the simplest case. No voids are required to form and no shear

bands form. Shear fracture occurs when strain is localized into a shear band before void nucleation. MVC occurs when void nucleation occurs before strain is localized into a shear band. After primary void nucleation, fracture of the ligaments between voids is caused by one of three mechanisms: a neck forms and deforms to a point, strain is localized into a shear band, or a second set of smaller voids form.

Because many engineering materials fail by a ductile, MVC mode in service, MVC has been studied extensively [6-10,12-15]. The most common method used to study MVC has been to measure the area fraction of voids found on the polished cross section of a deformed tensile specimen as a

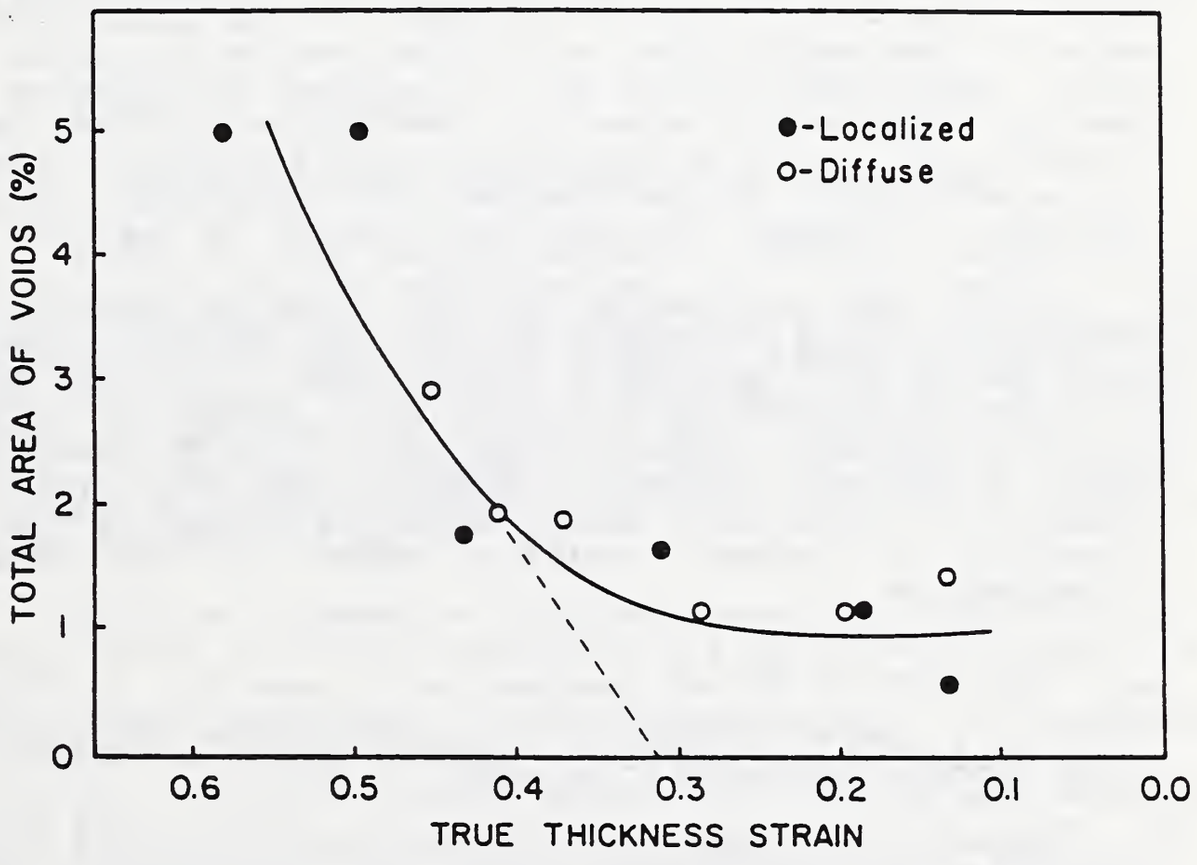

Figure 2. Plot of area fraction of voids vs. true strain for sheet tensile specimens of a dual-phase steel tested at room temperature [12].

function of strain. Figure 2 shows the results of such a study of necking and ductile fracture in a dual-phase steel [12]. The first voids nucleate at a relatively small strain. The area fraction of voids increased only after the specimen was strained past the uniform strain. The void nucleation strain can be defined as the strain where voids were first observed. In this case, the nucleation strain is a small fraction of the fracture strain. The absolute value of nucleation strain will be a strong function of the resolution of the technique used to observe nucleation. Conversely, the strain for void nucleation can be operationally defined by extrapolating the void area fraction to 0, as shown in Fig. 2. In this case the void nucleation strain is a large fraction of the fracture strain.

The increase in void area with strain above the nucleation strain is due to nucleation of new voids as well as growth of existing voids. Individual voids start to coalesce to form macrovoids, which then can be described as a crack. Additional strain may be required to fracture the specimen after void coalescence as observed by Park and Thompson [13]. Growth and coalescence are concentrated in the necked region of the specimen and occur over a small increment of remote, applied displacement in the test.

Models for void nucleation are normally based on void decohesion of the interface between the matrix and second-phase particles. Decohesion occurs when a critical strain or stress is reached at the interface. Argon and Im [14] applied a critical stress criterion to void nucleation; theirs is the most generally accepted approach. They suggest that decohesion occurs when the stress at the interface, σ_i, reaches a critical value, σ_c. The value of σ_i is defined as

$$\sigma_i = \sigma_{eq} + \sigma_T, \qquad (1)$$

where σ_{eq} = the equivalent flow stress of the material and σ_T = the imposed hydrostatic stress.

Beremin [15] applied the Argon model for void nucleation to the formation of voids at MnS stringers in A508 Class 3 steel, a C-Mn steel typically used in construction. Argon's nucleation criterion did not yield a consistent value of σ_c for different test temperatures and test orientations. The following criterion for σ_c fitted all the experimental observations of void nucleation:

$$\sigma_c = \sigma_1 + C(\sigma_{eq} - \sigma_o), \qquad (2)$$

where σ_1 is the maximum principal stress and σ_o is the yield stress. The constant C is a fitting parameter that was equal to 1.6 for longitudinal and 0.6 for short transverse orientation.

Modeling of void growth and coalescence [16-18] usually assumes that nucleation and growth are separate events and that void growth is proportional to plastic strain. The extent of growth depends on the stress state and material properties. As Fig. 2 shows, voids start to grow in the necked region and the specimen fractures when the void area fraction approaches 0.1. Thomason [19,20] has suggested a different approach to model void growth that considers the effect of void nucleation on growth as well as the effects of strain localization in the matrix, which depends on the stress state.

1.2 Fracture toughness

1.2.1 Description and measurement of toughness

There are two basic methods to describe toughness, the local crack opening displacement (δ), or the remote, applied energy required to open the crack [21]. The applied energy methods can be described by a stress intensity factor (K) when the plastic zone size is much smaller than the dimensions of the specimen (linear-elastic, small-scale yielding), and by the J-integral (J) when the plastic zone is comparable to the specimen dimensions (elastic-plastic, or large-scale yielding).

Methods to measure toughness have been developed to the point where standard procedures are well accepted and the external factors, like specimen design and loading rate, that affect toughness are well established. In the United States, the energy methods are often preferred over δ testing. The most common measurement methods are standard ASTM tests, E-813 for large-scale-yielding and E 399 for small-scale-yielding. Both methods use small, fatigue precracked specimens with a gage mounted at a convenient location to monitor the specimen displacement while the load is applied. A load vs. displacement curve (P-u) is recorded to characterize the test. The transition from small-scale yielding to large-scale yielding can occur for a given steel

by decreasing the specimen dimensions or increasing the test temperature.

The critical point for toughness measurement in both large- and small-scale yielding is represented by a significant change in the compliance or stiffness of the specimen. In the case of large-scale yielding, the change is more gradual and the crack grows in a stable manner. For the E-813 procedure, periodic unloadings are performed to monitor the change in compliance. The criterion that defines toughness is a specified decrease in compliance. In small-scale yielding, the compliance drops rapidly and the critical point can be determined by inspection of the load-displacement (P-u) curve. Therefore, a key question is, "How do the micromechanisms of ductile fracture change the compliance of the test specimen?"

A generally accepted correlation between micromechanisms and compliance for a "ductile" material taken from the literature [22] is presented in Fig. 3. The P-u curve, Fig. 3a, is linear over a short range of displacement (elastic behavior), and the curve becomes nonlinear (plastic behavior) when the material yields. The test is stopped briefly at regular intervals and unloaded to check the compliance of the specimen. At point 1 in Fig. 3, the elastic stresses at the crack tip are higher than the flow strength of the bulk material. To relieve the stresses near the tip, the crack blunts (changes shape at the tip), and a plastic zone forms around the tip. The shape change produces a small increment of crack growth, called a stretch zone (SZ), from the original fatigue crack. Voids will nucleate and grow in the material as soon as the plastic zone engulfs a nucleation site, Fig. 3b. A small change in compliance is measured because the crack has grown slightly. A data point is then plotted on the energy vs. change in crack length (J-Δa) curve, Fig. 3c.

After unloading at point 1, the specimen is reloaded and more nonlinear behavior is seen in Fig. 3a and more unloadings are made. As long as the nonlinear behavior is due to plasticity, the crack tip in Fig. 3b will continue to blunt and the size of the plastic zone will increase. Any voids close to the tip can grow while new void-nucleation sites are activated in the plastic zone. The SZ continues to grow relatively slowly and requires considerable energy per unit crack growth. Each unloading produces a data point in Fig. 3c. At applied $J < J_{Ic}$, the points lie along a

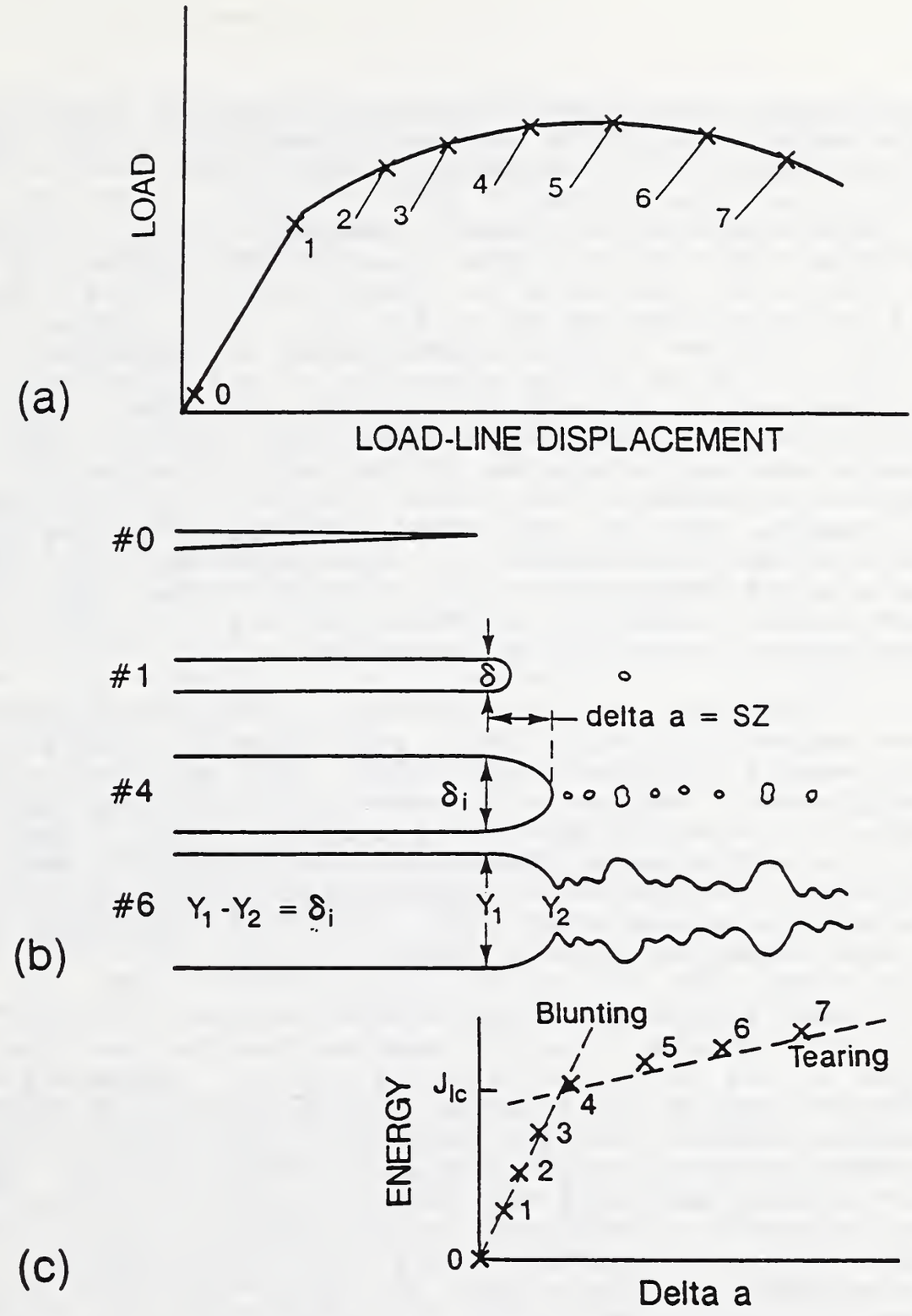

Figure 3. Schematic diagram showing the correlation between micromechanisms of ductile fracture and fracture toughness: (a) load-displacement curve, (b) crack tip profile, and (c) energy vs. crack growth curve [22].

line, referred to as a blunting line with a slope = dJ/da. From experience, dJ/da can be approximated by the properties of the material in a uniaxial tension test.

At some critical point, labeled 4 in Fig. 3 for this example, the growing voids ahead of the blunted tip impinge on each other, so there is a continuous surface connected to the fatigue crack and SZ in Fig. 3b. This change in crack length produces a significant change in compliance. Point 4 in Fig. 3c is below the extension of the blunting line. At each successive unloading along the P-u curve, more of the growing voids link up with the fatigue crack. The crack growth rate at this point in the test is called the tearing line or regression line in E-813 and can be characterized by the tearing modulus (T). The intersection of the blunting and tearing lines defines J_{Ic}, the parameter that characterizes the toughness of the material. The local displacement values, δ and SZ, at this critical point could also be used as characterizing parameters.

If the same ductile material is tested again at the same temperature, but with a sufficiently large specimen, small-scale yielding could exist. The small-scale yielding may promote a different failure mechanism than the observed mechanism under large-scale yielding. If no transition in failure mechanism is observed, the correlation between external loading and micromechanisms should be similar to the events described in Fig. 3, only the processes occur inside a smaller plastic zone.

Small-scale yielding is often called "brittle" or stress-controlled fracture because the specimen can break after little or no measurable yielding. Large-scale yielding is called "ductile" or strain-controlled fracture because there is obvious deformation before the specimen breaks. In both large- and small-scale yielding, the fracture surface can have the same microscopic features (MVC). The macroscopic roughness of the fracture surface and the shape of the P-u curves do not correlate directly to the microscopic fracture mode. The terms "ductile" and "brittle" are misleading in this context because they are relative terms that describe the scale of the plastic zone compared to the specimen dimensions, not the micromechanism of fracture. For the two cases, small-scale yielding and large-scale yielding, the material behavior is different, but both can have the same measured toughness. J_{Ic} and K_{Ic} are related by the elastic properties of the material. This

equality is the major reason to use fracture mechanics. Small specimens can be tested to predict the behavior of much larger structures, provided that the failure mechanism is the same in both the large structure and small test specimen. A more thorough discussion of this subject is given by Banerjee [23].

1.2.2 Modeling of toughness

The stress and strain distributions ahead of the crack tip form the basis for modeling toughness. Many researchers have modeled the stresses and strains around the crack tip of a fracture mechanics specimen as a function of δ with analytical and numerical approaches [24-27]. The finite element method (FEM) results of McMeeking [24], shown in Fig. 4 for a low-strength, nonhardening material, are the most often referenced. The radial stress is highest ahead of the crack with a maximum value of 3 to 4 times the tensile yield strength at a distance of 2δ. The strain is highest at the crack tip and decreases exponentially with the distance from the tip, but is always highest at an angle, θ, of $\pi/4$ with respect to the original crack tip. McMeeking concluded from his results that if the direction of initial crack growth was straight ahead of the crack tip, then the maximum stress controlled the fracture. If the crack grew initially at a $\theta = \pi/4$ to the tip, then the strain was more important. The numerical results are in good agreement with analytical results of Hutchinson [25], and Rice and Rosengren [26] (called the HRR strain and stress fields), and the Rice and Johnson [27] slip-line analysis.

Shoji et al. [28] and Luo et al. [29] measured the strain distribution around a blunted crack tip in ferritic steels at room temperature by different techniques. In both cases, the results agree with the FEM results for the region directly ahead of the crack tip. However, the strain was not a maximum at $\theta = \pi/4$ to the crack plane. The highest strains were found directly ahead of the crack tip. Also, no voids were observed in the matrix ahead of the crack tip.

The simplest approach to modeling [30] assumes that toughness is the product of the average flow stress in the plastic zone (σ_y), the local strain to failure (ϵ_f), and a characteristic distance (L) related to the spacing of weakly bound inclusions where voids can nucleate easily. One form

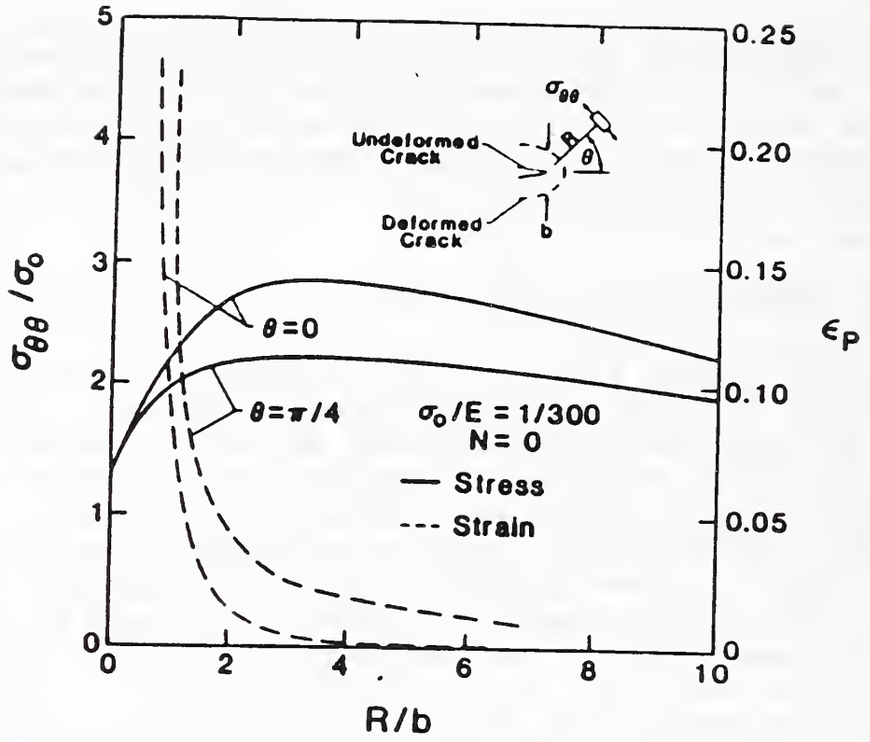

Figure 4. Plot of FEM results showing the distribution of stress and strain ahead of the crack tip in a nonhardening material [24].

of the equation with J_{Ic} as the toughness parameter is,

$$J_{Ic} = \sigma_Y \times \epsilon_f \times L. \quad (3)$$

The main difference between models is the way in which ϵ_f is determined. Some models assume that the fracture strain measured in a plane strain tensile test is the same as ϵ_f in the model for toughness. Another approach is to assume that the fracture surface morphology is a measure of ϵ_f. Ritchie and Thompson [30] assume the microroughness is a measure of ϵ_f while Garrison [31] suggests that the ratio of inclusion size to void size is related to ϵ_f. These types of fracture surface observations assume that the growth of the largest voids are related to toughness and that void nucleation does not contribute.

A recent experimental study of fracture mechanisms [32] measured the mechanical properties of ASTM A533B steel as a

function of the size of pre-existing voids in the matrix. The results showed that the presence of pre-existing voids of any size reduced the tensile and toughness properties significantly compared to the properties with no pre-existing voids. The fracture surface appearance suggests that void coalescence starts almost immediately when voids are present prior to plastic strain. A similar experiment with silver [33] showed the same results. The strain appeared to concentrate in the ligaments between pre-existing voids with little uniform strain. The energy required to nucleate voids was a large fraction of the tensile ductility and contributed significantly to toughness.

Two different research groups [34,35] have tried to incorporate Beremin's criterion for void nucleation into a model for toughness. In both cases, the void-nucleating particles were large, elongated inclusions in a low-strength (< 500 MPa) ferritic steel matrix. The nucleation criterion was easy to achieve in the triaxial stress state at the crack tip, so resistance to void nucleation did not contribute significantly to toughness.

1.2.3 Toughness correlations:

The toughness of many engineering materials has been measured according to the standard test methods described above and correlated to tensile properties. A summary of toughness data at room temperature for different wrought engineering alloys is plotted as a function of tensile yield strength in Fig. 5 [36]. Data for austenitic stainless steel at 4 K [37] have been added to Fig. 5. All the alloys show a similar trend in which toughness decreases as yield strength increases. Scatter within the band for each material is an indication of other factors that influence toughness. The important "other" factors are the melting practice and residual alloy content that determine the volume fraction, size, distribution, and type of inclusions.

Alloy development programs have improved the properties of structural steels over the years by optimizing the factors that influence the mechanical behavior of steel. Some results are summarized in Fig. 6 [38]. The strength and toughness have increased since 1960, moving the curve towards the upper right corner of the plot.
Speidel [38] suggests that the product of yield strength and toughness, defined here as the quality index (QI), appears

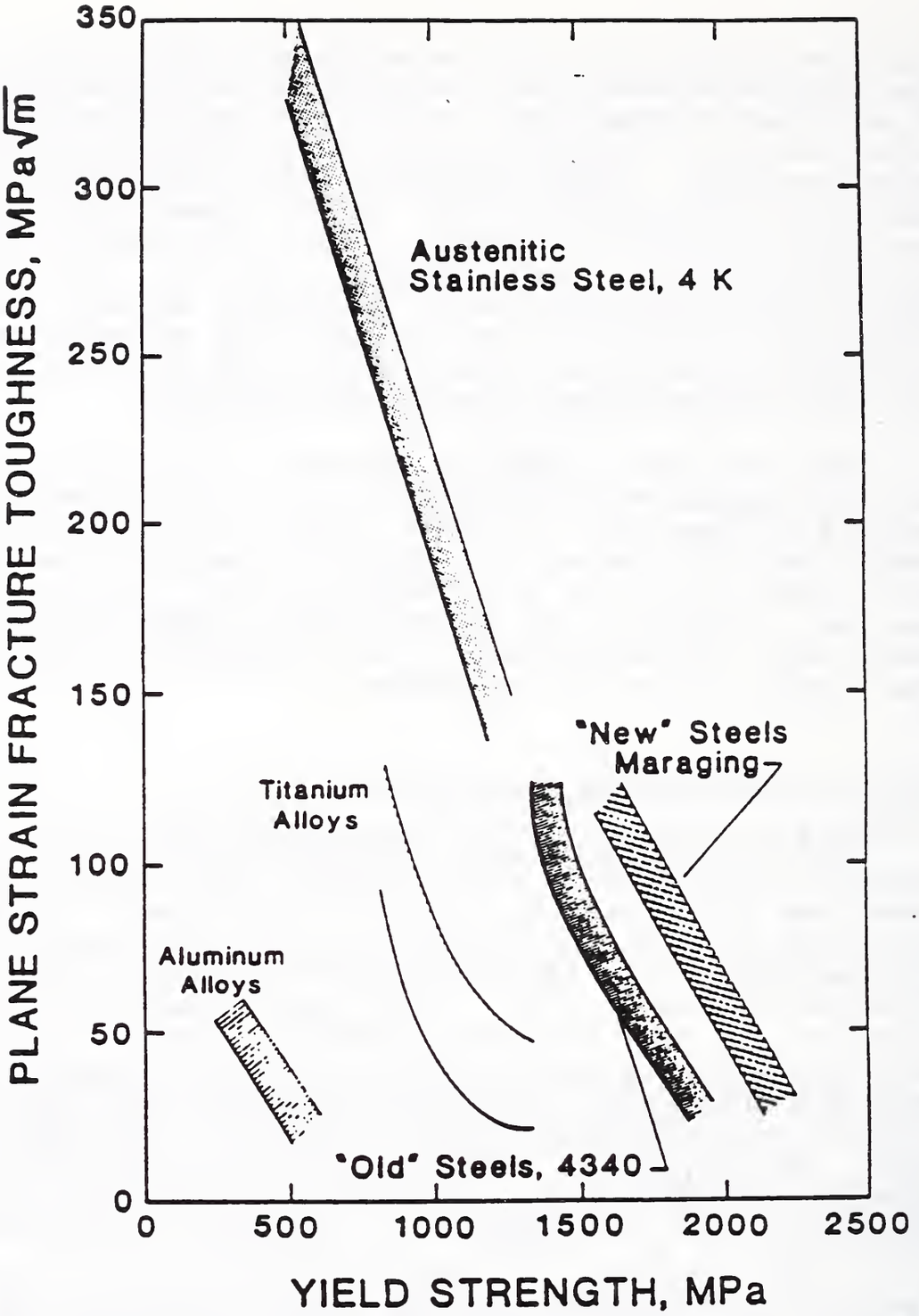

Figure 5. Plot of fracture toughness vs. yield strength for high-strength structural alloys from [36] and similar data for austenitic stainless steels at 4 K [37].

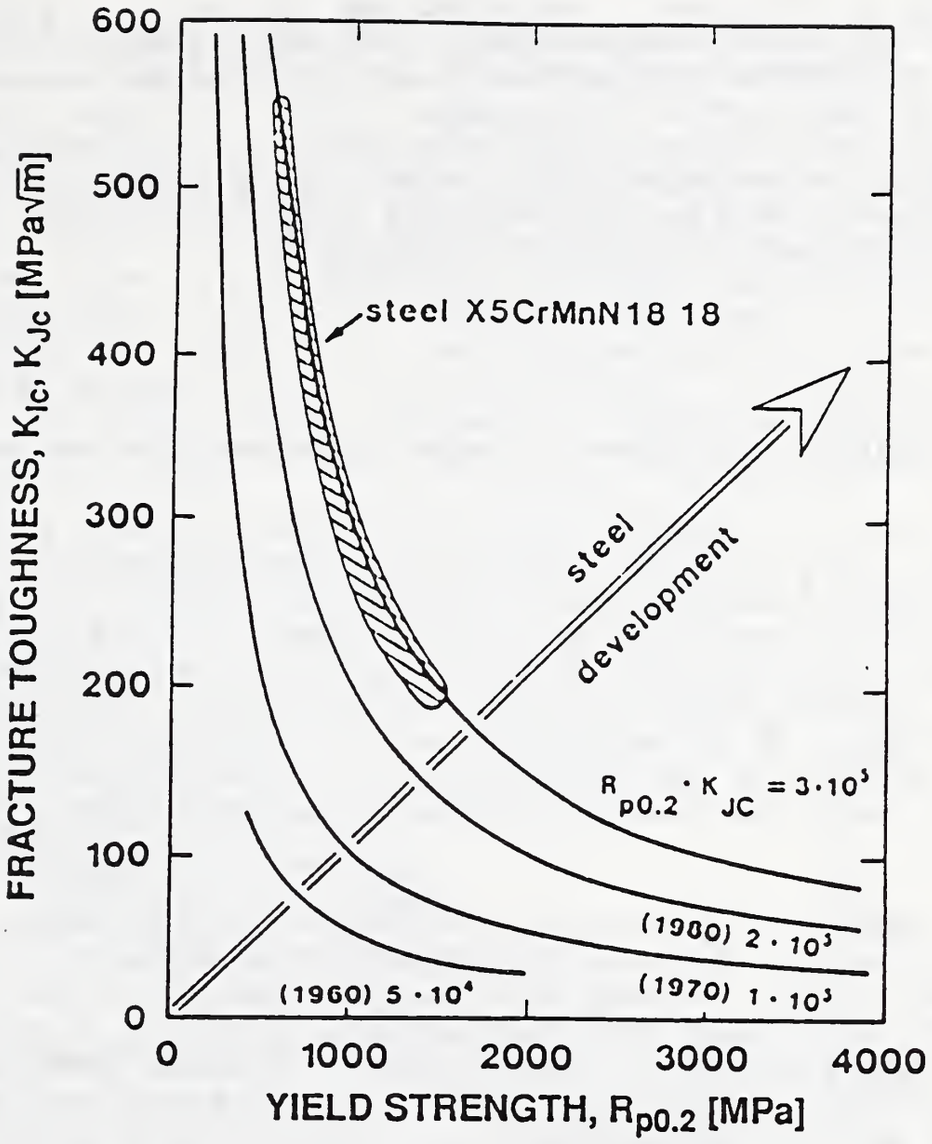

Fig. 6. Plot of toughness vs. yield strength for high-strength structural steels showing how the properties have improved since 1960 [38].

to be a valuable indicator of improved mechanical properties. Speidel found that an austenitic, Cr-Mn-N steel had a higher QI than any other structural steel at room temperature.

The QI can also be used to quantify the effect of thermal-mechanical processing and changes in alloy composition on mechanical properties of austenitic stainless

steels at cryogenic temperatures [39,40]. A summary of the QI at cryogenic temperatures for austenitic stainless steels with different compositions and processing is shown in Fig. 7 as a function of Ni content [41]. A higher temperature results in a lower yield strength, but the increase in toughness produces a larger QI. At a constant temperature, a higher Ni content has little effect on yield strength, but a significant increase in toughness.

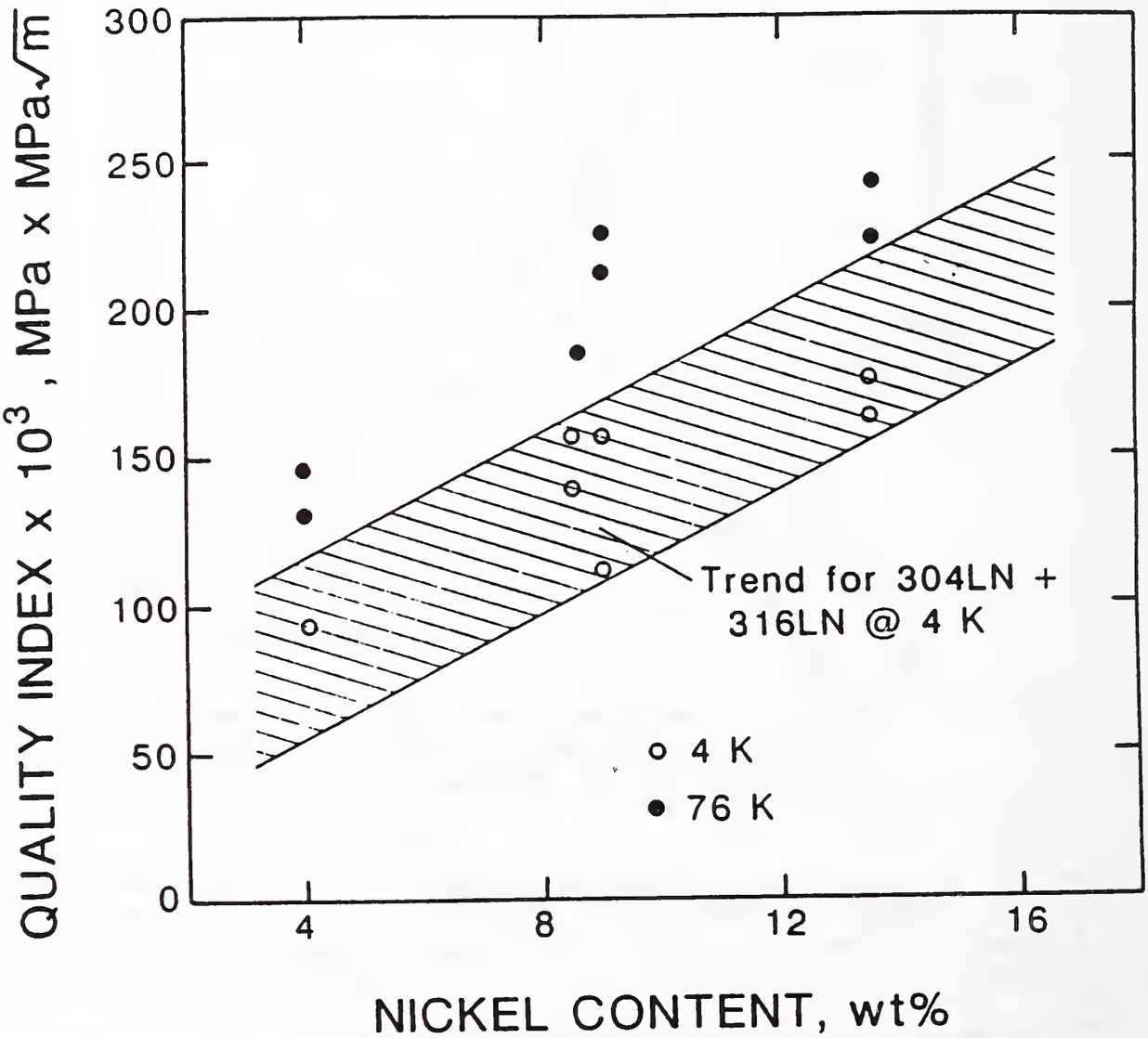

Figure 7. Plot of the quality index of austenitic stainless steels at 4 and 76 K as a function of Ni content [41].

1.3 Preliminary work on toughness of high strength austenitic stainless steel at low temperatures

The most significant observation regarding austenitic stainless steels at cryogenic temperatures is that these steels fracture without an observable SZ on the fracture surface [42]. The fracture surfaces of two austenitic stainless steels and one ferritic steel are shown in Fig. 8. Each has nearly the same measured toughness, yet the surface morphology at the tip of the fatigue crack in the austenitic stainless steels show no sign of a SZ. A separate region, the SZ, is easily seen between the fatigue crack and the MVC features of the toughness test in the ferritic steel.

This apparent anomaly was explained in a paper in terms of the micromechanisms of ductile fracture [43]. In order for a SZ to form, the material directly ahead of the crack tip had to be strained significantly before voids nucleated. The distribution of strain around the crack tip of an austenitic steel (AISI 304) at 76 K is shown in Fig. 9. At the crack tip, the strain is concentrated at $\theta = \pi/4$ to the tip. A crack forms at the crack tip when the applied J is less than J_{Ic}. Separate voids were not observed ahead of the crack tip.

Another key observation was that the initial crack growth in austenitic stainless steels at cryogenic temperatures was straight ahead of the fatigue crack even under large-scale yielding. McMeeking [24] predicted these observations from his FEM analysis when a critical stress criterion controlled fracture. Ferritic steels typically showed more angled crack growth in the direction of the maximum strain. For both the ferritic and austenitic stainless steels, the micromechanisms for ductile fracture were limited to a region approximately 2δ around the crack tip. This region was defined as the process zone (PZ).

A simple model to describe the stress intensity factor required to nucleate voids ahead of a blunt crack was described by Purtscher et al. [44]. This approach assumed that void nucleation occurred when the interfacial stress between the matrix and inclusion reached a critical level, σ_c, that was equal to the maximum applied stress plus the local stress due to dislocations. For austenitic stainless steels at 4 K, the applied stress was related to the yield strength of the steel, and the local stress was controlled by the strain that was related to the Ni content of the

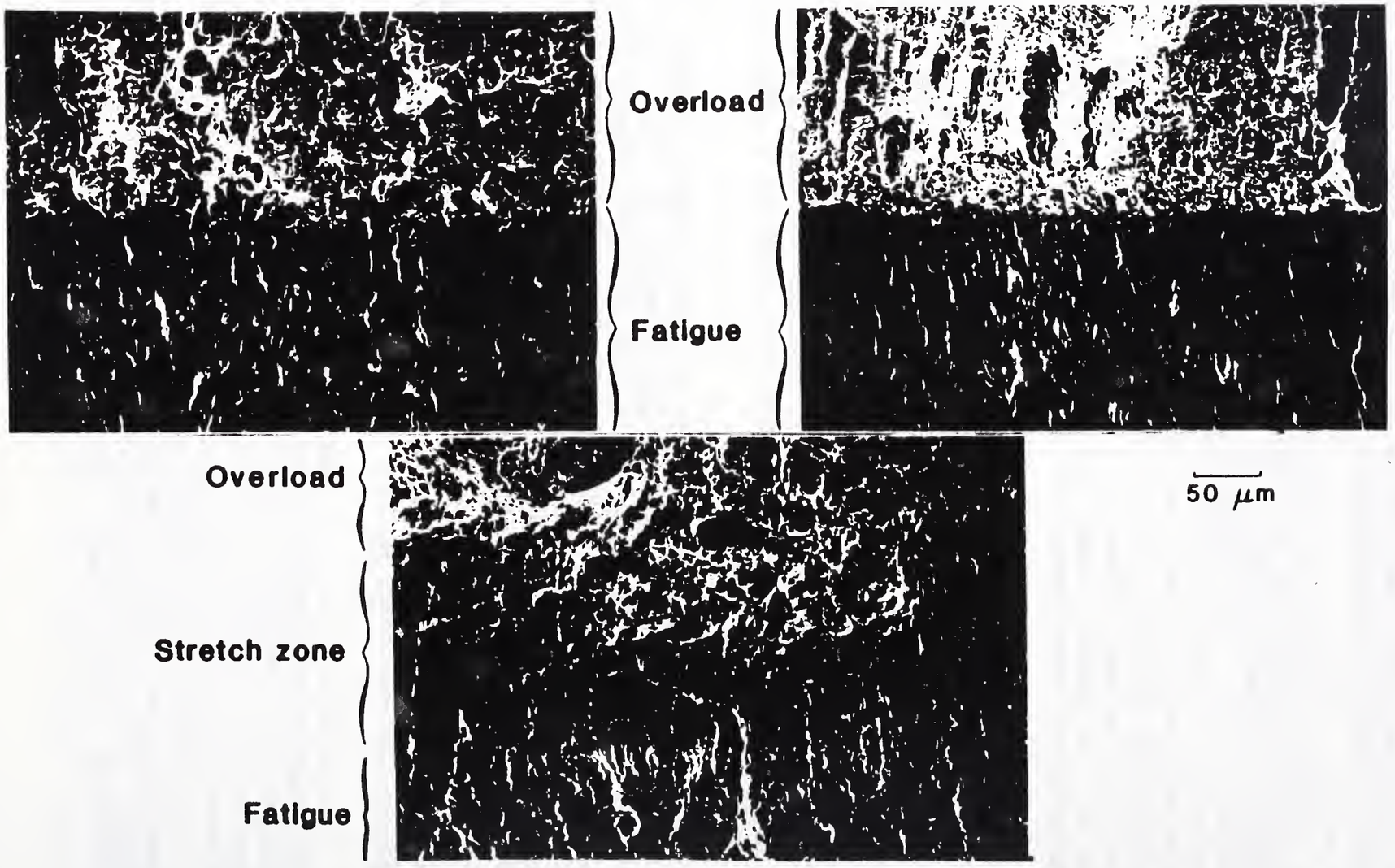

Fig. 8 Comparison of the fracture surface from different steels: (a) AISI 316LN tested at 4 K, (b) AISI 308L tested at 76 K, and (c) HY 80 ferritic steel tested at 295 K.

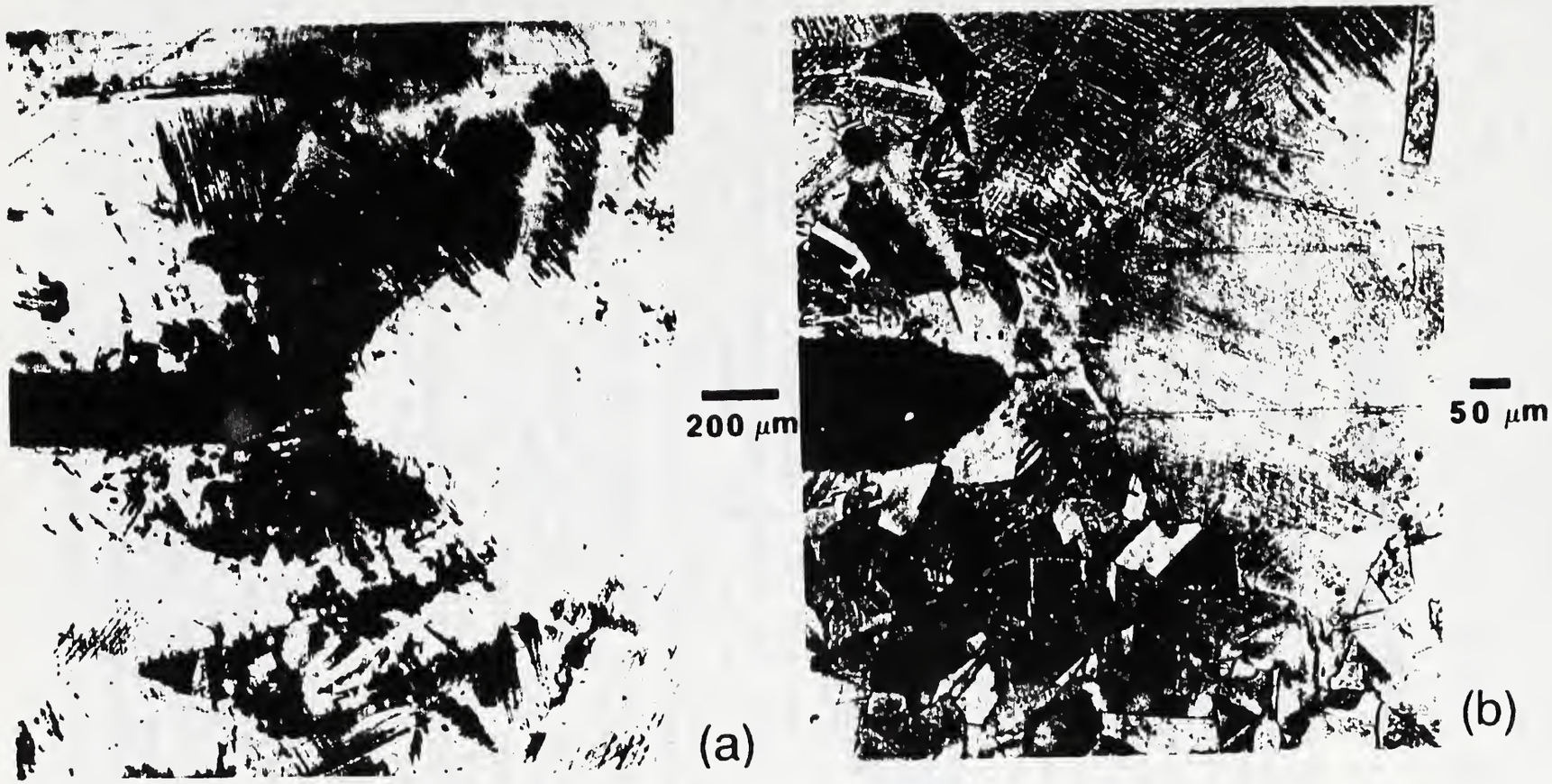

Fig. 9 Metallographic section through the crack tip of toughness specimen of AISI 304 steel tested at 76 K: (a) etched to stain the strain-induced martensite and (b) etched to show austenite grain size.

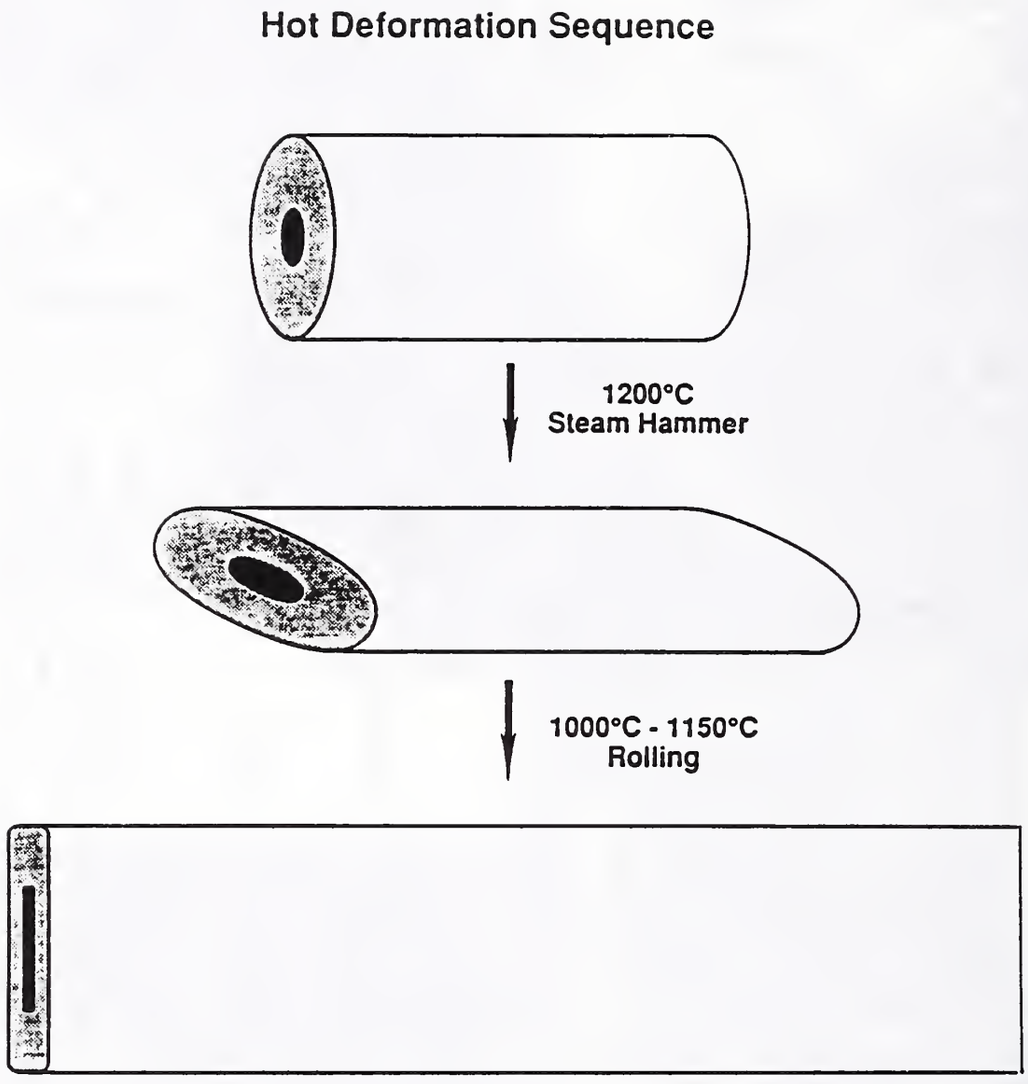

Figure 10. Schematic diagram showing the hot deformation processing used to produce a plate section from the as-received bar. The dark cross-hatched region in the center of the cross section represents the region that contained sigma phase in the starting microstructure.

steel. The model was extremely sensitive to the assumed value of the local and macroscopic stress. Given best estimates of the stress terms, the model predicted that nucleation accounts for the majority of the measured toughness for austenitic steels at strengths above 600 MPa.

1.4 Purpose and Experimental Program

The purpose of this report is to determine the effect of temperature and stress state on the micromechanisms that cause ductile fracture in an austenitic steel. Observations of the micromechanisms of ductile fracture are correlated to the macroscopic stress and strain conditions in terms of two different criteria, Eqs. 1 and 2, as proposed by Argon et al. [14] and Beremin [15] . Critical conditions for ductile fracture in simple stress states is related to ductile fracture in a complex stress state present in the fracture toughness test. The toughness is modeled with a MVC model (void nucleation, growth and coalescence) by the the matrix plastic flow properties and the distribution of second-phase particles in the matrix.

Other researchers [30-32,34,35] have studied the effect of matrix plastic flow properties and second-phase particle distributions on toughness. In the past, the critical event was interpreted to be the growth of voids from the largest second-phase particles. Void nucleation was assumed to contribute little to the total energy absorbed.

The first step to understand ductile fracture and toughness better is to quantify the role of void nucleation. In the past, very little quantitative data have been generated. Clearly, nucleation is the first stage in the overall process and must be accounted for in any generally applicable theory. It is not clear if the same criterion required for void nucleation in a tension test can be applied to different stress states and test temperatures.

Other key questions relate to the role of second-phase particles. How can the critical inclusions involved in nucleation be determined? Is the average inclusion spacing the important parameter, or is the actual distribution important for determining the characteristic distance? Clusters of inclusions have been known to promote cleavage fracture in ferritic steels [1]. The characteristic distance, L, used in most models is always equated with the spacing of void-nucleating inclusions. In practice

[32], the model is assumed to fit the data, and a value of L is calculated from the measured toughness. L is then equal to some multiple of the inclusion spacing, sometimes less than 1 or other times 6 to 7 times the spacing. L is used more as a fitting parameter with no physical significance. A different approach to the idea of a characteristic distance for toughness testing could provide insight.

The final point addressed in the research deals with the material properties of austenitic stainless steels. The influence of different constituents in the microstructure are described in terms of the observations.

2.0 MATERIAL

The steel chosen for this study is a commercially available nitrogen-strengthened austenitic stainless steel with the composition shown in Table 1. The steel, called 22-13-5 in this report, was received in the form of a round bar, 76 mm in diameter. Perkins [45] studied the hot deformation behavior of the same heat of 22-13-5 steel.

Table 1 Composition of 22-13-5 (mass %)

C	0.03
Mn	5.2
Si	0.3
P	0.025
S	0.001
Cr	21.5
Ni	12.4
Mo	2.3
Nb	0.21
V	0.18
N	0.31
Fe	balance

The microstructure of the as-received bar was initially characterized by Perkins [45]. The center of the bar contained a large fraction of second-phase particles distributed in the austenitic matrix. The elongated, second phase was identified as sigma phase. The hardness varied from R_A

61 near the outer surface to R_A 54.5 in the center of the bar. Five tensile specimens were machined from the bar, evenly spaced through the diameter and parallel to the rolling direction, and tested at 4 K to characterize the starting material. The results of these initial tests are shown in Table 2. The 4-K yield strength and elongation are higher around the edge of the bar and decrease in the center of the bar. The tensile properties and hardness reflect the

Table 2 Tensile Test Results at 4 K for 22-13-5 Bar

Location	YS (MPa)	UTS (MPa)	Elongation %	Reduction in Area %
Edge	1540	1877	24	34
Mid-radius	1212	1810	16	30
Center	1107	1794	13	27
Mid-radius	1171	1792	21	37
Edge	1503	1858	28	40

influence of the large volume fraction of sigma phase in the center of the bar.

Sections of the as-received bar were rolled into plates, approximately 28-mm thick, 105-mm wide, and 63-cm long. The hot deformation sequence for processing the as-received bar is shown in a schematic diagram in Fig. 10. The round bar was first deformed into an elliptical shape in a steam hammer and then rolled into a plate with a rectangular cross section. The lighter cross-hatched region of the cross section represents regions free of sigma phase. The darker cross-hatched region in the center of the cross section represents the region that contained large volume fraction of sigma in the starting microstructure. The temperature for final hot rolling was varied between 1150 and 950 C. All the specimens in this research program received a final annealing treatment at 1150 C for 1 to 2 h, followed by a water quench.

In a separate program, specimen blanks were machined from the hot-rolled material to evaluate the effect of the different processing histories on mechanical properties at 4 K. Those results were reported eleswhere [40]. Lower

hot-rolling temperatures resulted in higher 4-K yield strength, but slightly lower tensile ductilities and toughness.

3.0 EXPERIMENTAL PROCEDURES

3.1 Material Characterization

Specimens for light microscopy were taken from both deformed and undeformed regions of the various test specimens. The samples were prepared by standard procedures for mounting and mechanical polishing. The samples were then etched with different etchants to reveal various microstructural constituents [46]. Sigma phase was identified by an electrolytic KOH etch that attacks only sigma and delta ferrite; sigma is differentiated by color (sigma is stained darker than delta ferrite). The grain size and deformation structure were delineated by an electrolytic nitric acid and water etch.

Scanning electron microscopy (SEM) was used for fracture surface observations and inclusion counts on the cross sections. All inclusions with average diameters greater than 0.5 μm were counted by a particle recognition program (PRC). Each analysis took between 2 and 3 h to count individual frames at 500x, and to measure the shape and size parameters associated with each inclusion.

Transmission electron microscopy (TEM) of thin foils was used to observe the distribution of sub-micrometer size particles and to evaluate deformation structures as a function of deformation temperature. An electrolyte (containing 5% perchloric acid, 75% ethyl alcohol, and 20% glycerin) was used at room temperature with a current of about 80 mA. Four different deformed conditions were observed, two at 295 K (strain = 0.02 and 0.05) and two at 76 K (strain = 0.03 and 0.12).

Microhardness measurements at 50- and 200-gram loads were used to characterize the annealed and deformed material on a fine scale. Around the crack tip, microhardness readings were taken in a cylindrical coordinate system centered at the tip of the fatigue precrack. The parameter r is the distance from the center. The angle θ refers to the angular displacement from the plane parallel to the

fatigue crack with $\theta = 0$ directly ahead of the crack and $\theta = \pi/2$ and $-\pi/2$ perpendicular to the crack.

3.2 Mechanical testing

3.2.1 Uniaxial tension (uniaxial stress state)

Blanks, 13-mm square, were removed from the top and bottom of the plates in both transverse (T) and longitudinal (L) orientations with respect to the rolling direction. Specimens with a 6.25-mm-gage diameter were machined with either a 45- or a 28-mm-gage length. The specimens were tested in a screw-driven test machine with a 100-kN load capacity. The displacement was measured by a special extensometer for cryogenic service [47]. The initial cross-head rate was 0.05 cm/min for tests at 295 and 76 K. For tests at 4 K, the initial cross head rate (CHR) was 0.02 cm/min. For most tests, the CHR was increased to 0.1 cm/min after a strain of about 0.05. When the fracture stress and hydrostatic stress concentration factor are reported, the CHR was held constant at 0.05.

The load and displacement data for each tension test was recorded continuously on an AT-compatible data acquisition system. The data were analyzed to determine the yield strength (YS), ultimate strength (UTS), percent elongation (%EL), and reduction in area (RA). YS is defined as the flow stress at a plastic strain of 0.002. UTS is defined as the maximum load divided by the original cross sectional area. %EL is the change in change in length of the uniform gage section divided by the original length. RA is the change in cross-sectional area at the point of fracture divided by the original area. The strain hardening rate was obtained by first smoothing the stress and strain data with a nine-point average, and then calculating a slope at each point on the curve that represents true stress vs. strain. The fracture stress for those specimens tested to failure at a constant CHR is defined as the load at the point of fracture divided by the final cross-sectional area.

Flat tension specimens with a 25-mm-long gage section were machined transverse to the rolling direction according to the design shown in Fig. 11a. These specimens were tested to different strain levels at 295 and 76 K for later evaluation by TEM; these tests were run in the same test machine used for uniaxial tension testing.

3.2.2 Plane-strain tension testing (biaxial stress state)

Tests were conducted at three test temperatures and in two ways: to the point of fracture and interrupted at a given strain. The flat, plane-strain specimens had a gage section that was 2 x 25 x 0.75 mm, see Fig. 11b. The design was used by Corrigan [48] to produce a biaxial stress state and maximum constraint in the gage section. The specimens were machined with a transverse orientation with respect to the rolling direction so that the width of the specimen, the direction of zero strain in the specimen, traversed the thickness of the plate.

The specimens were tested in a servo-hydraulic controlled test machine operated in stroke control. The displacement rate was 0.02 cm/min, which corresponded to an elastic loading rate of 1.44 kN/min. The load and change in thickness of the specimen were monitored during the test with an X-Y recorder. The through-thickness strain, ϵ_t, was calculated according to the equation,

$$\epsilon_t = \ln t_o / t_i, \qquad (4)$$

where t_o = initial thickness and t_i = instantaneous thickness.

3.2.3 Fracture toughness testing (triaxial stress state)

Fracture toughness tests were conducted according to ASTM standard procedure E 813-81 at the three test temperatures. The unloading compliance method was used to monitor crack growth. The 1981 standard analysis calculates J_{Ic} from the intersection of the blunting line, with a slope that is twice the average of the YS and UTS, σ_{fl}, times Δa, and tearing line, with a slope given by a linear fit to the experimentally determined J-Δa data points. The 1981 procedure yields lower J_{Ic} values (closer to the actual start of crack growth) than the newer, 1987 standard method [49]. At 295 K, the J-Δa data points in the blunting region did not correlate to the standard slope for the blunting line. Mills [50] observed similar behavior for austenitic stainless steels tested at room temperature and above. He found that the data fit a blunting line with a steeper slope, $4\sigma_{fl}\Delta a$. The steeper slope was used for analysis of specimens tested at 295 K in this report because the steeper slope fit the data better than the standard slope of $2\sigma_{fl}\Delta a$. At 76 and 4 K, there was little difference in results for the two different slopes, so the standard slope was used for analysis.

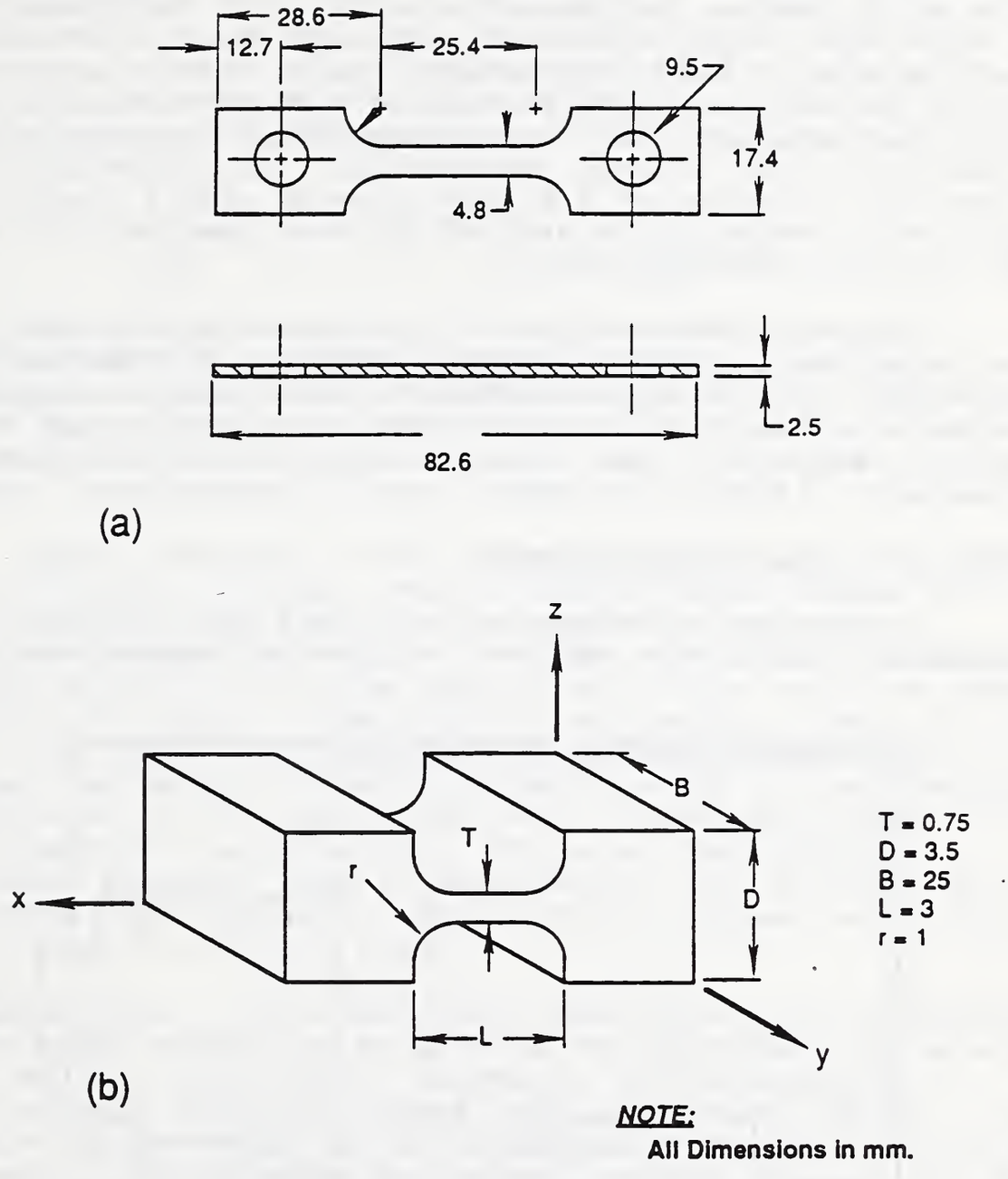

Figure 11. (a) Drawing for flat, uniaxial tension specimen.
(b) Drawing for flat, biaxial tension specimen.

Blanks for toughness testing were either 26- or 13-mm thick, and were taken from the plate with a T-L orientation so that the center of the plate is not tested, Fig. 12. Two 13-mm thick blanks were machined with a L-T orientation. Compact, C(T) specimens were designed according to the ASTM

standard, 12.7-mm thick for 4-K tests and 25-mm thick for the other tests. Fatigue precracking was performed with an R ratio of 0.1 at 20 Hz with a maximum K of 35 MPa m. The fatigue precracking temperature was 76 K for 4- and 76-K tests and 295 K for 295-K tests. Side grooves, 10% of the thickness on each side, were machined in the 295- and 76-K specimens after fatigue precracking. Specimens with T-L orientation tested at 4 K were labeled with a prefix, A. Specimens tested at 76 and 295 K were identified by AAA and AA prefixes respectively.

The tests were conducted in stroke-control with a servo-hydraulic controlled test machine, 100 kN load capacity. The mechanical testing at cryogenic temperatures requires a modified loading frame. The details of the exact configurations for the tests described here are given elsewhere [47,51].

3.3 Post-test observations

The load-displacement curves from the fracture toughness tests were analyzed after the testing to determine

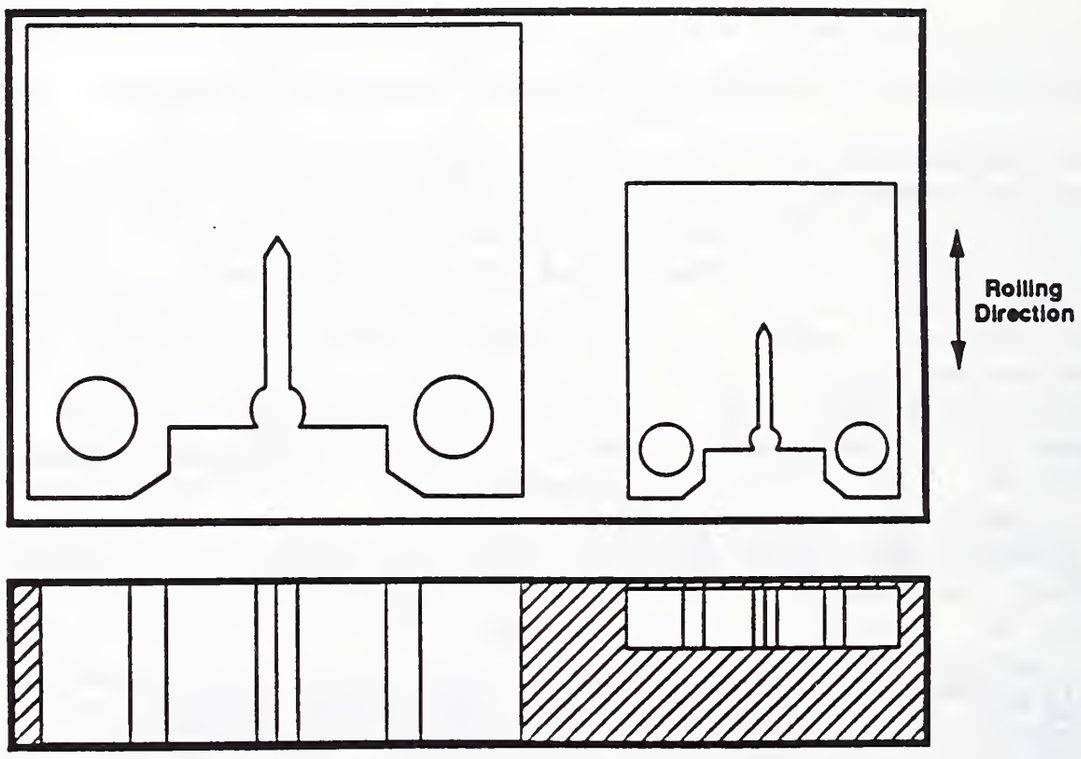

Fig. 12. Relative location of 25 and 12.7-mm thick compact specimens with T-L orientation in processed plate.

the value of δ at J_{Ic} or at the end of the tests that were stopped prior to J_{Ic}. The value of δ up to the point of J_{Ic} can be calculated from the load-displacement curve for a given specimen by the procedure described in BS 5762 [52]. The total δ is the sum of the small-scale yielding (δ_s) and the large-scale-yielding (δ_l) as shown in the equation,

$$\delta = \delta_s + \delta_l \quad (5)$$

$$\text{where} \quad \delta_s = K^2(1-\nu^2)/[2\,YS\,E] \quad (6)$$

$$\text{and} \quad \delta_l = V_{pl} \,/\, 1+k(a\,/W-a_o) \quad (7)$$

The V_{pl} = plastic contribution to the mouth opening displacement, W = specimen width, a_o = original crack length, and k = rotational factor generally assumed to be 2.5. The elastic constants, Young's modulus (E) and poisson's ratio (ν), are taken to be 200 GPa and 0.3 respectively, independent of test temperature [53].

After testing at each temperature, selected specimens from uniaxial, biaxial, and triaxial stress states were sectioned through the deformed region to observe micromechanisms of ductile fracture. For the C(T) specimens tested at 295 K, a wedge was placed in the crack to keep the δ constant during unloading and sectioning. One half of each sectioned C(T) specimen was fatigue post-cracked to reveal the extent of ductile crack growth on the fracture surface while the other half was polished and etched for metallographic examination. Three or four different polished sections (serial sectioning) were observed for each selected C(T) specimen. The distance between each serial section was 1.25 to 1.5 mm.

The goal of the post-test observations is to observe where void nucleation occurs and to characterize the strain that exists at different locations in the specimen, particularly the point where void nucleation starts. The stress at any point can be estimated from the load and the geometry. In uniaxial and biaxial stress states, the strain is known and can be correlated to the change in microhardness (▲DPH). In the triaxial stress state, the strain can be inferred from ▲DPH, compared to ▲DPH of the tension specimens strained to known values. The stress can be estimated from FEM results. The maximum stress ahead of the crack tip in a fracture mechanics specimen is a function of distance from the crack tip and the applied energy. The relationship developed by Anderson and Dodds [54] for small-scale yielding is used in this study.

4.0 RESULTS

4.1 Material Characterization

The grain structure of the austenitic matrix varied depending on the location in the plate and was related to the nonuniform structure found in the as-received bar. Figure 13 shows the cross section of the annealed plate in a schematic diagram that outlines three regions where the microstructure varied. Region I is a fine-grained matrix, austenite grain size between 40 and 50 μm in diameter, with a dispersion of spherical particles. A typical distribution of the spherical particles is shown in a TEM micrograph, Fig. 14. The majority of the particles are < 1 μm in diameter and scattered randomly in the austenite. Based on the chemical composition of the steel, the submicrometer particles are assumed to be V,Nb(C,N) precipitates. The precipitates will be referred to as microalloy particles. Region I corresponds to the hatched region in Fig. 10 that was free of sigma phase in the microstructure of the as-received bar.

Regions II and III of Fig. 13 correspond to the darker cross hatched region in Fig. 10 that contained sigma in the starting microstructure. Figure 15 shows the typical microstructure of Region II. The structure has a duplex grain size with fine-grained areas like Region I plus areas of extensive grain growth due to the hot deformation processing

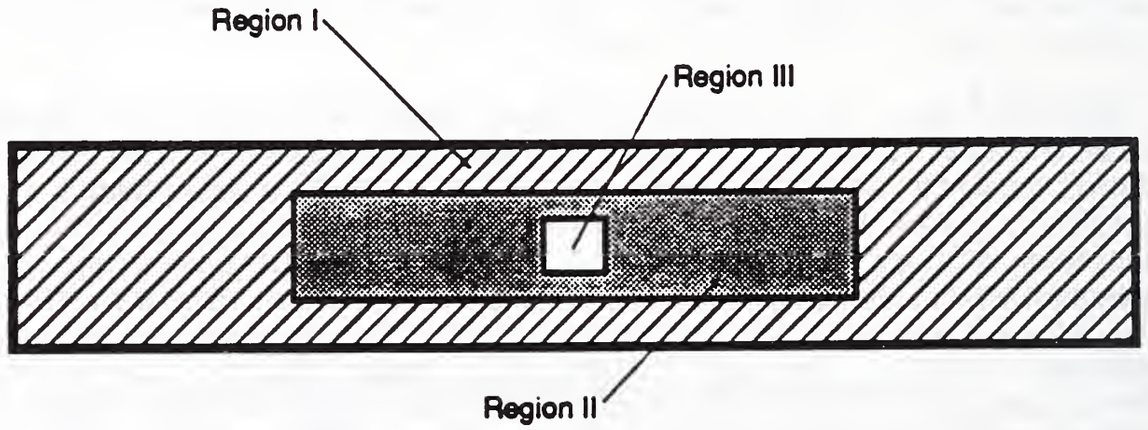

Figure 13. Schematic drawing of the cross section of the processed plate. Region I has a uniform fine grain size. Region II has a duplex grain size while Region III in the center of the plate has a uniform large grain size.

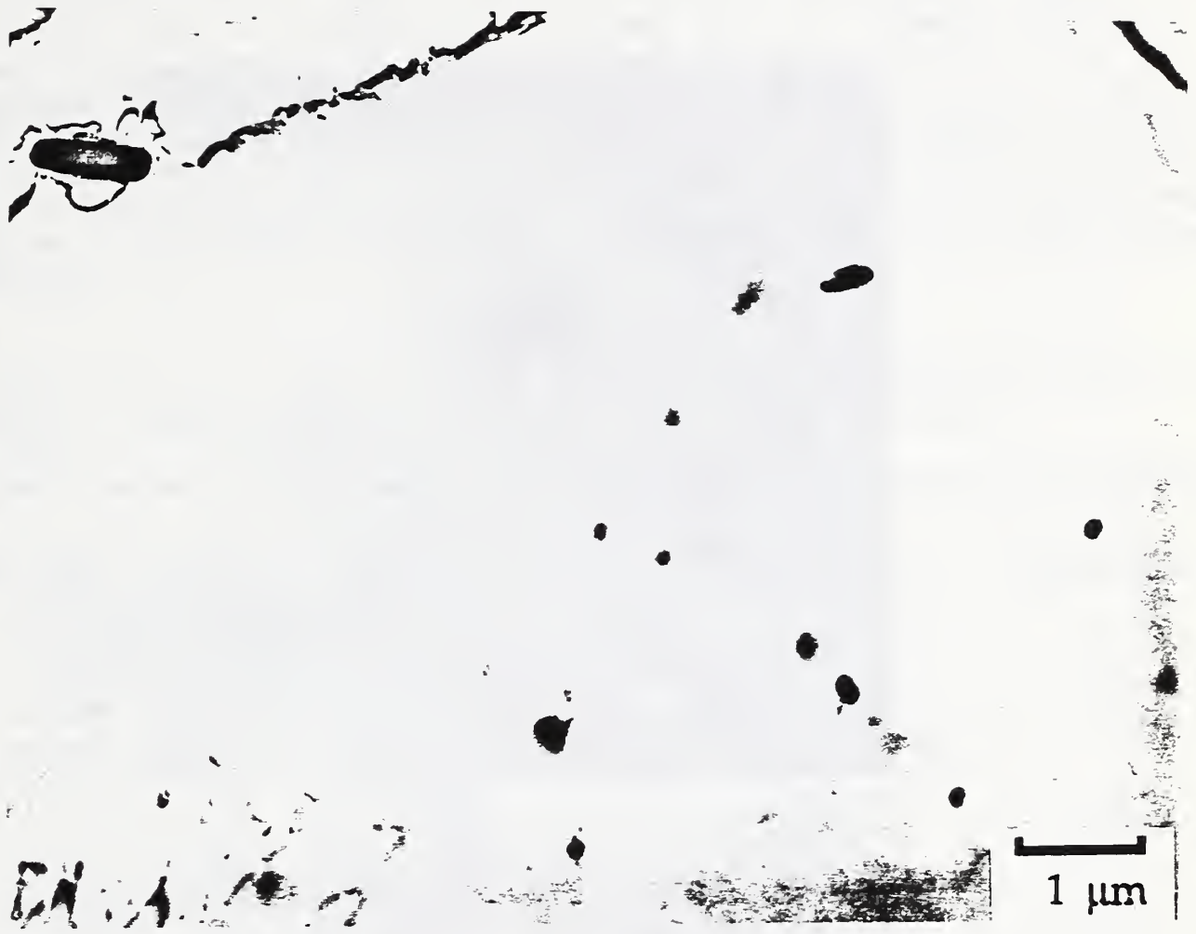

Figure 14. Representative TEM micrograph shows the distribution of submicrometer particles in the processed plate after annealing.history.

The small arrows in Fig. 15a point out the remanent of sigma phase from the starting structure. The large arrow in Fig. 15a highlights an isolated nonmetallic inclusion. The composition of the majority of inclusions included Mn, Si, and S. The higher magnification view, Fig. 15b, shows distinctive lines of the microalloy particles within the coarse-grained regions (200 to 300 μm in diameter). Region III had a uniform, large grain size that was equal to the coarse-grained areas in Region II.

SEM with the PRC program quantified the size and distribution of inclusions. The results for three separate regions of transverse-oriented specimens taken from Region I

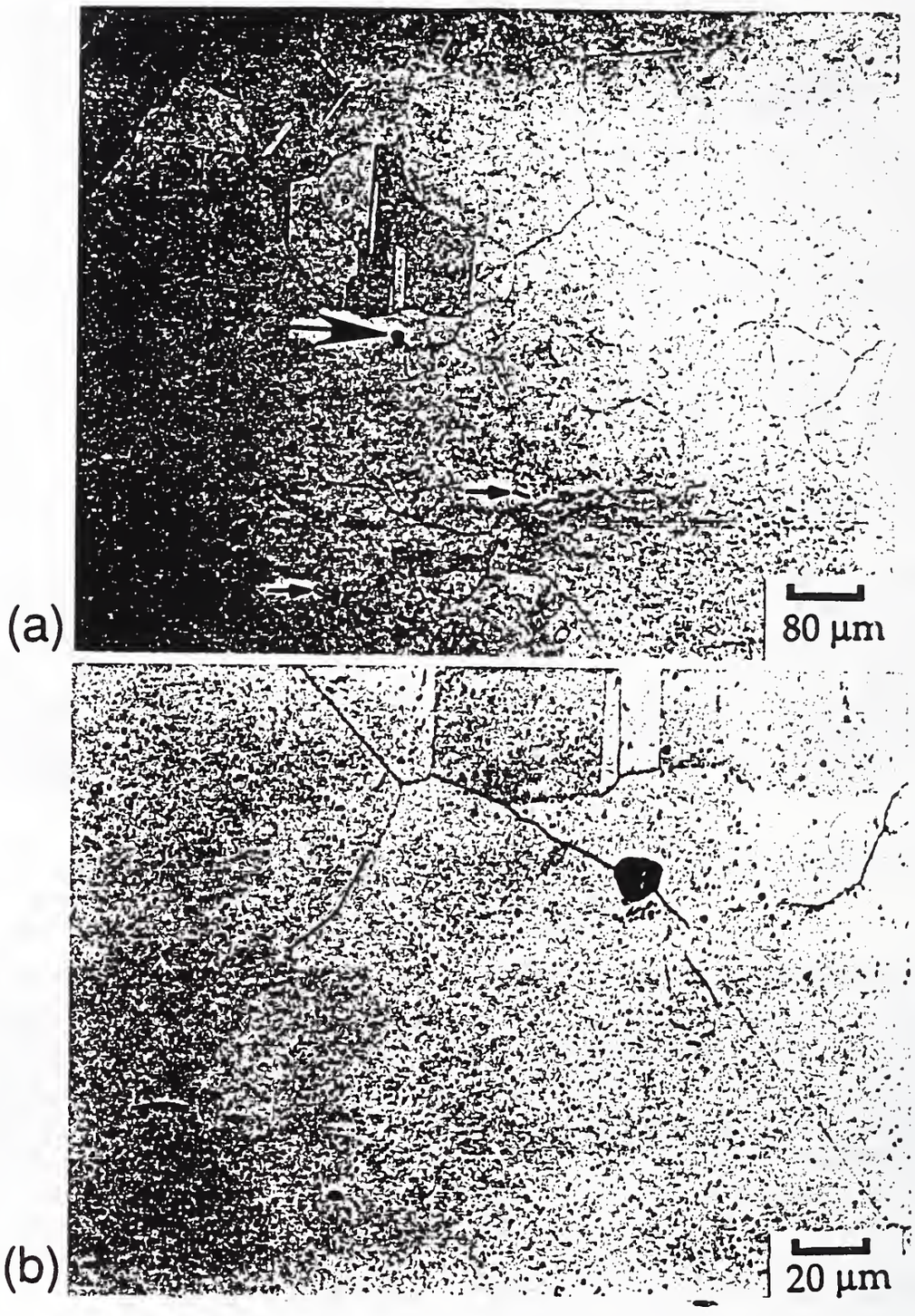

Fig. 15 Microstructure found in Region II of the plate cross section. The large arrow shows a nonmetallic inclusion and the small arrows point out σ phase.

in the plate are shown in Table 3. The area fraction of inclusions varies from 0.01 to 0.05% of the total area observed and is largely determined by the largest inclusions, > 3.8 μm in diameter, found in the distribution. Most of the inclusions were spherical and < 1 μm in diameter. The average inclusion spacing is the parameter that is most representative of the complete inclusion distribution. The spacing was calculated by taking the inverse square root of the total number of inclusions divided by the total area observed.

Table 3. Inclusion distributions in 22-13-5 from PRC program.

max. dia. (μm)	Region 1	Region 2	Region 3
0.6	23	20	10
0.8	25	29	10
1.0	17	15	17
1.2	14	14	7
1.4	15	14	5
1.6	4	9	10
1.8	9	11	4
2.0	6	4	1
2.2	8	8	2
2.4	7	6	7
2.6	4	1	2
2.8	1	5	6
3.0	2	1	4
3.2	3	3	4
3.4	1	4	3
3.6	0	1	2
3.8	3	1	1
4.0	0	1	2
4.2	2	2	2
>4.2	1	1	4
# of inclusions	145	150	103
fields	30	36	28
Area fraction	0.0004	0.0001	0.0005
ave. spacing	95 μm	102 μm	109 μm
ave. diameter	1.4 μm	1.6 μm	1.9 μm

4.2 Mechanical testing

4.2.1 Uniaxial tensile test results

The test temperature has a large effect on the plastic flow properties of 22-13-5. The complete load-vs.-time curves to the point of fracture are shown in Fig. 16. At 295 K, the steel showed extensive nonlinear behavior before the maximum load was reached (the region of uniform deformation) and relatively little between the maximum load and the fracture load (the region of post-uniform deformation). At 76 K, the steel had a higher load capacity (flow stress), approximately twice that at 295 K. The shape of the load vs. time curve at 76 K is essentially the same as at 295 K. At 4 K, the initial flow stress is nearly three times higher than 295 K, but the uniform deformation is interrupted at an early point by load drops. The sawtooth behavior is caused by local heating from plastic deformation. Each load drop in the curve for the 4-K test reflects a local neck forming in the gage section where the specimen was heated and then strain hardened. The last load drop is associated with the fracture of the specimen.

The true stress-vs.-true strain curves for representative specimens are shown in Fig. 17. The curves for 295 and 76 K stop at the point where the extensometer fell off the specimen. The curve for 4 K stops at the point where serrated yielding began. The elastic modulus is nearly independent of test temperature, but the initial flow stress is a strong function of temperature. Figure 18 shows the strain hardening rates for each test shown in Fig. 17. A decrease in test temperature produces a higher hardening rate in these tests. The hardening rate at strains < 0.02 are a strong function of temperature and strain. Above 0.02 strain, the hardening rates become relatively constant with strain, but still depend on temperature.

The summary of tensile properties from all the tests is shown in Table 4. The specimens were taken randomly from Regions I and II in the plate. The scatter in properties may be attributed partially to the variation in the grain size and density of microalloy particles found in Regions I and II. The UTS and % EL values reported for the 4-K specimens are influenced by the heating of the specimen during deformation. The fracture stress and the hydrostatic stress concentration factor, σ_f/σ_o (calculated according to [55]), for the 4-K specimen were calculated based on the smallest diameter present on the gage section away from the fracture.

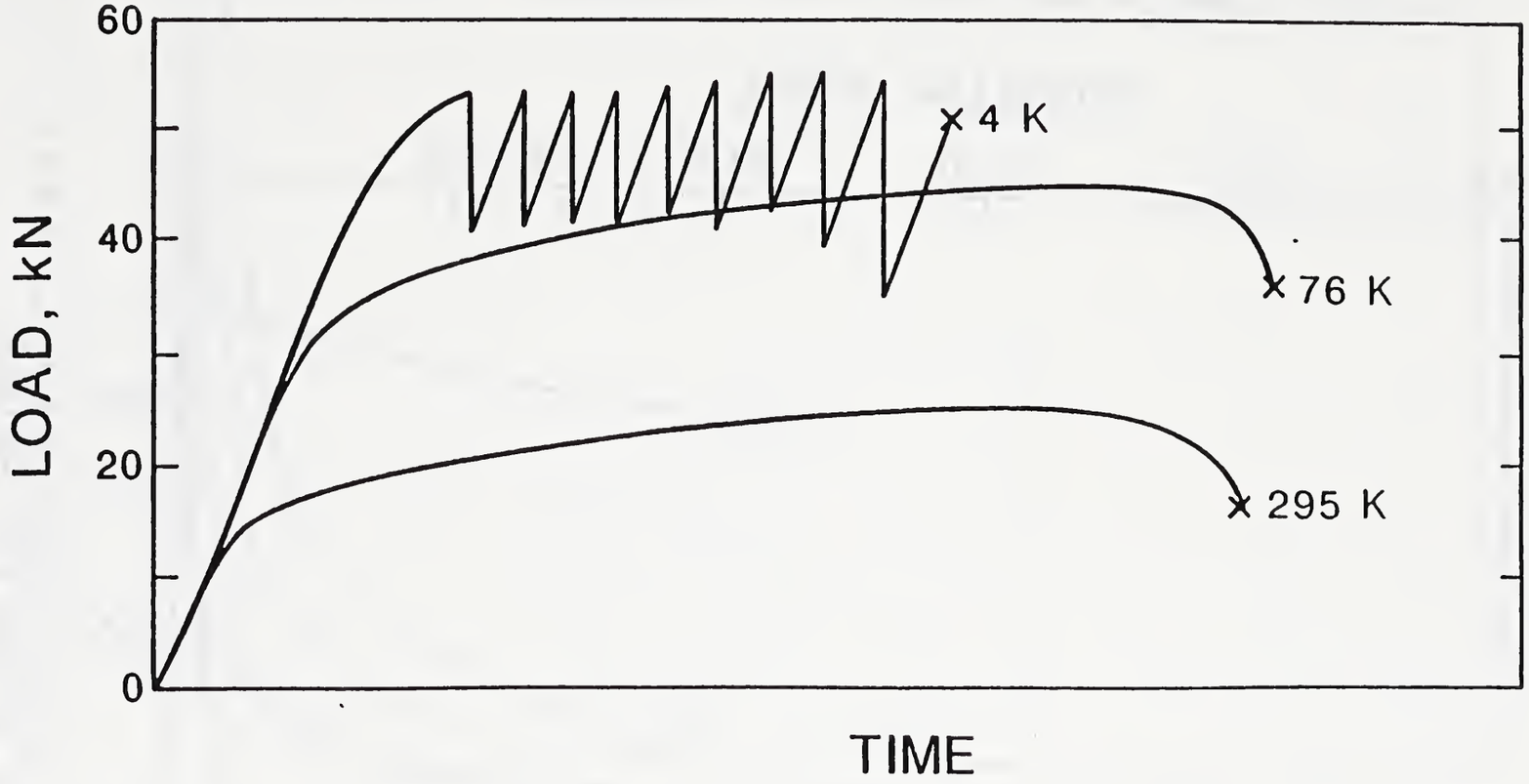

Figure 16. Uniaxial tension test load vs. time curves for 22-13-5 as a function of test temperature showing the complete load history up to failure.

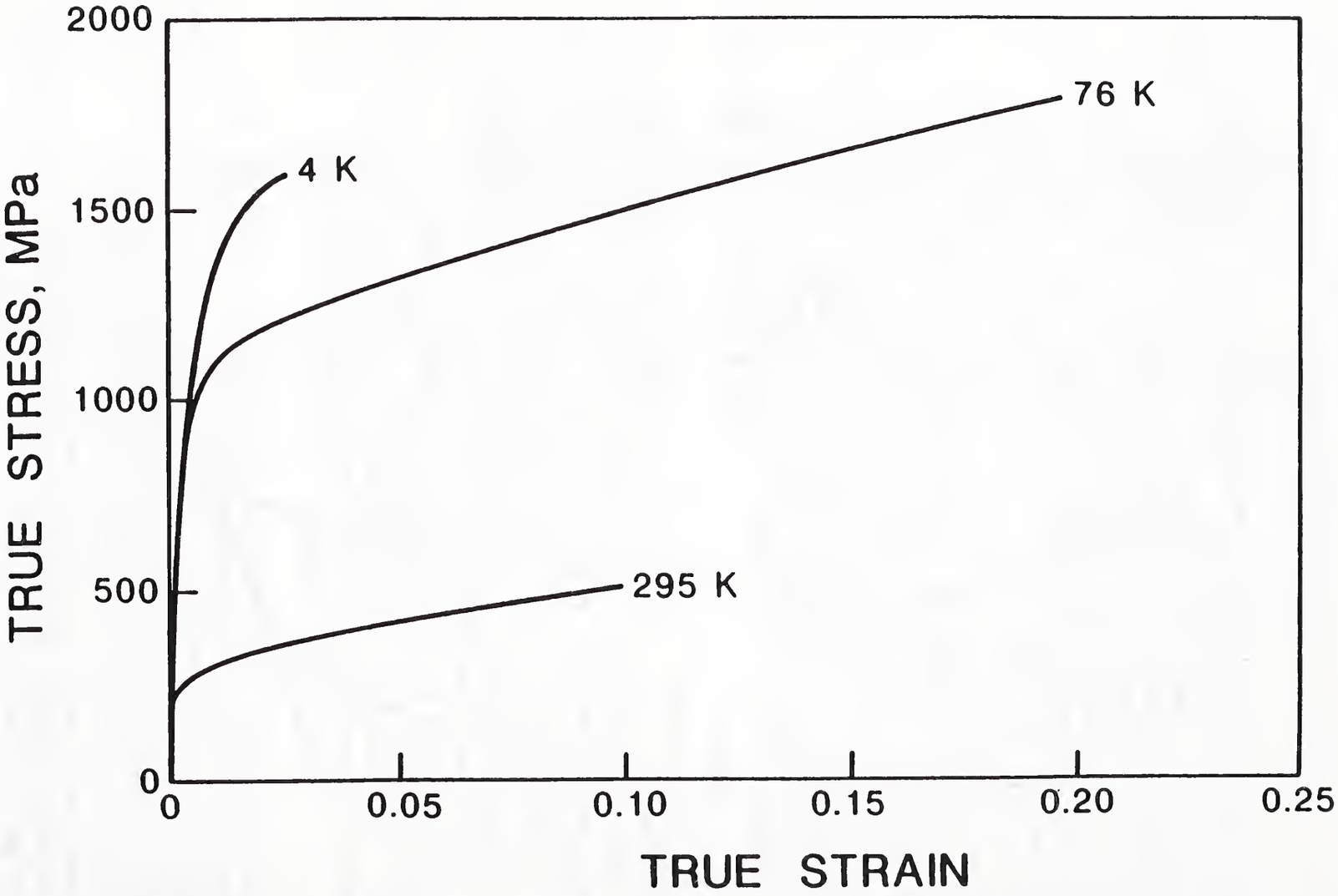

Figure 17. Uniaxial tensile test true stress vs. strain curves for 22-13-5 as a function of test temperature.

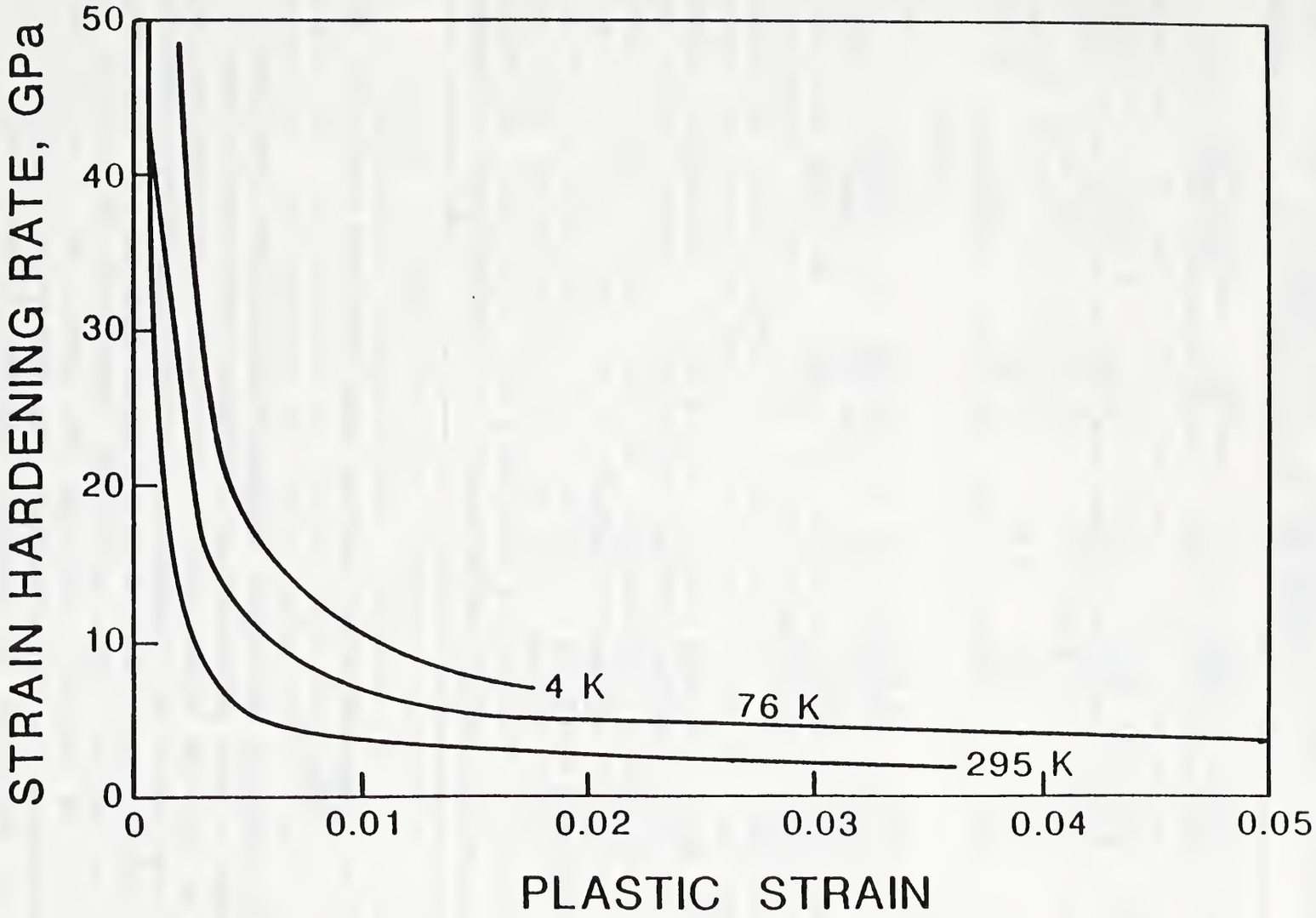

Figure 18. Uniaxial tensile test strain hardening rate vs. plastic strain curves for 22-13=5 as a function of test temperature.

Table 4. Uniaxial tension test results for annealed 22-13-5 plate.

Spec #	YS (MPa)	UTS (MPa)	El (%)	RA (%)	fracture stress	σ_f/σ_o
295 K						
T-10	465	798	41	1.25	2014	0.63
T-11	438	793	44	1.21	1780	0.63
T-1	400	779				
T-3	430	788	41	1.32		
T-4	398	752		1.06	1681	0.52
76 K						
T-8	1067	1430	39	0.97	3026	0.48
T-9	1034	1515	35	0.56	2568	0.37
T-12	1030	1523	27	0.80	2988	0.45
T-5	1097	1545	37	0.88	3726	
T-6	1101	1543				
4 K						
T-7	1272	1765	25	0.65	3117	0.42
L-1	1320	1795	29			
L-2	1448	1784	22			
L-3	1425	1799	26			
L-4	1439	1764	23			
T-2	1264	1764				

T = transverse orientation and L = longitudinal orientation

4.2.2 Plane-strain tension test results (biaxial stress state)

Decreasing the test temperature raised the flow stresses in the plane-strain tension test, analogous to the behavior in the uniaxial tension tests. Curves for representative load vs. change in specimen thickness (displacement) for plane-strain tension specimens at 76 and 295 K are shown in Fig. 19. The specimen tested at 76 did not show a load drop or necking prior to fracture. At a point near the fracture load at 76 K in Fig. 19, the strain hardening rate prior to fracture is greater than the flow stress. The fracture was associated with a shear instability rather than the plastic instability associated with necking. At a point near the maximum load in the curve for the specimen tested

at 295 K, the strain hardening rate was almost equal to the flow stress so that the steel meets the criterion for necking at the maximum load. Fracture is associated with the local neck that forms after maximum load.

Table 5 shows the results of plane strain tension tests at the three temperatures. The yield strengths of these specimens do not correlate well with the uniaxial test results in Table 4. The center of the specimen gage section where the displacement was measured was located in Region III of the plate (see Fig. 13) where the grain growth occurred during processing.

4.2.3 Fracture toughness test results (triaxial stress state)

A typical P-u curve for a toughness test at 76 K is shown in Fig. 20. The point where J_{Ic} is measured is less than the maximum load. For each increment of imposed displacement after J_{Ic} extra displacement and a load drop were measured under fixed-grip conditions. The compliance appears to decrease during the load drops so that the crack grows during the load drops. This behavior indicates that the crack growth at cryogenic temperatures was not stable even though it was ductile in nature. From the P-u curve in Fig. 20, the J vs. Δa is calculated from the area under the curve and the change in compliance at each unloading point. The data points are shown in Fig. 21 and were fit to a blunting line with the standard slope and a tearing line. The intersection of the two dashed lines is J_{Ic}.

Table 6 summarizes the fracture toughness test results as a function of temperature. Figures 22, 23, and 24 show the J-vs.-Δa curves for all the tests at each temperature, while Fig. 25 summarizes the results as a function of temperature. Decreasing the test temperature results in lower toughness. The three complete tests at 295 and 76 K, Figs. 22 and 23, were reproducible within the usual scatter expected in toughness testing. For the 4-K results (Fig. 24), the first three complete tests were run and showed more scatter. To check the first three tests, an additional five specimens were tested. With the eight complete tests together the results sort into two groups, HI-4K and LO-4K. Two interrupted tests were also run at each temperature for subsequent metallographic analysis of ductile fracture micromechanisms. The C(T) specimens tested at 295 and 76 K are physically larger than the 4-K specimens (refer to Fig. 12) and sample more material than the 4-K specimens because

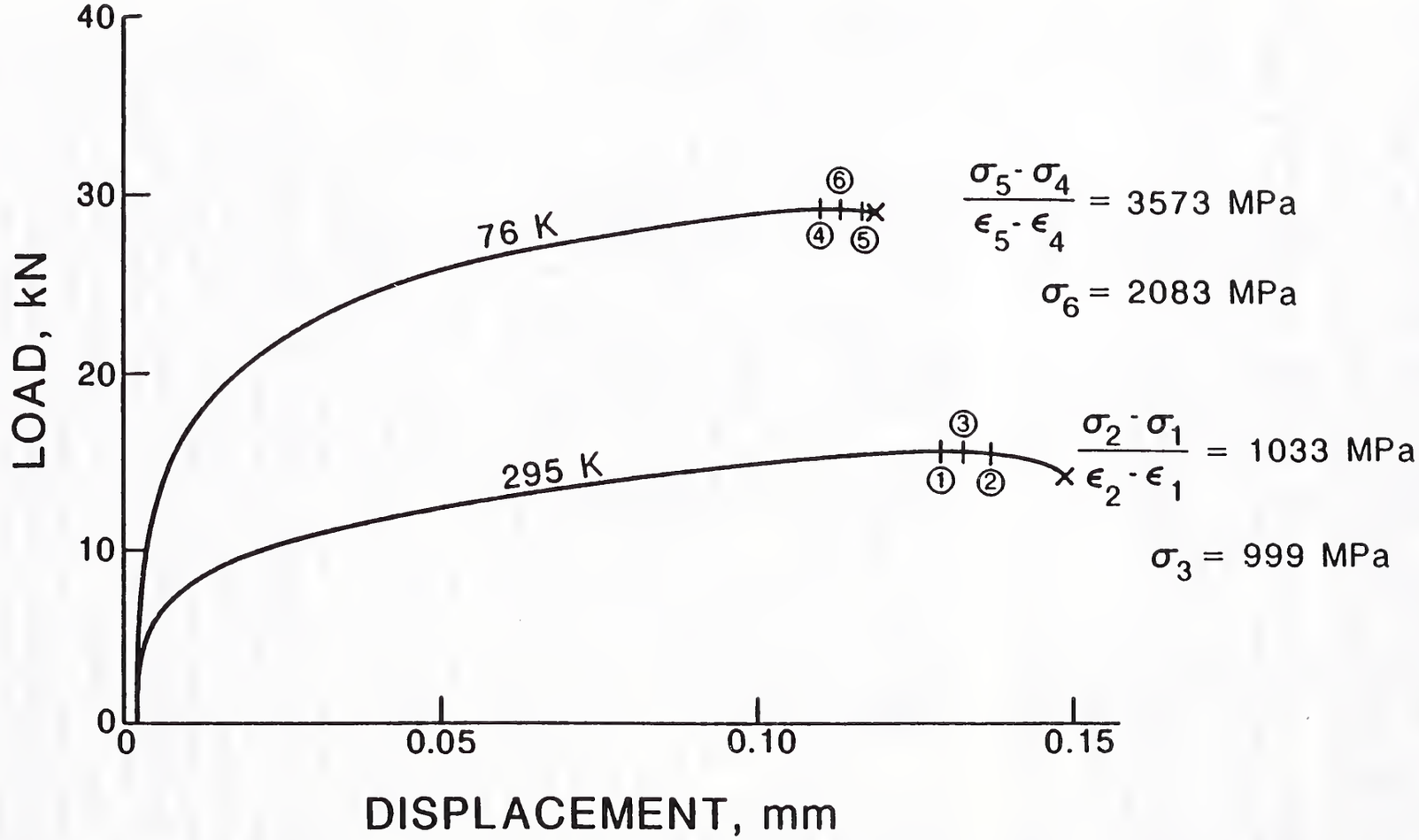

Figure 19. Plane strain tension test load vs. displacement curves for 22-13-5 at 295 and 76 K.

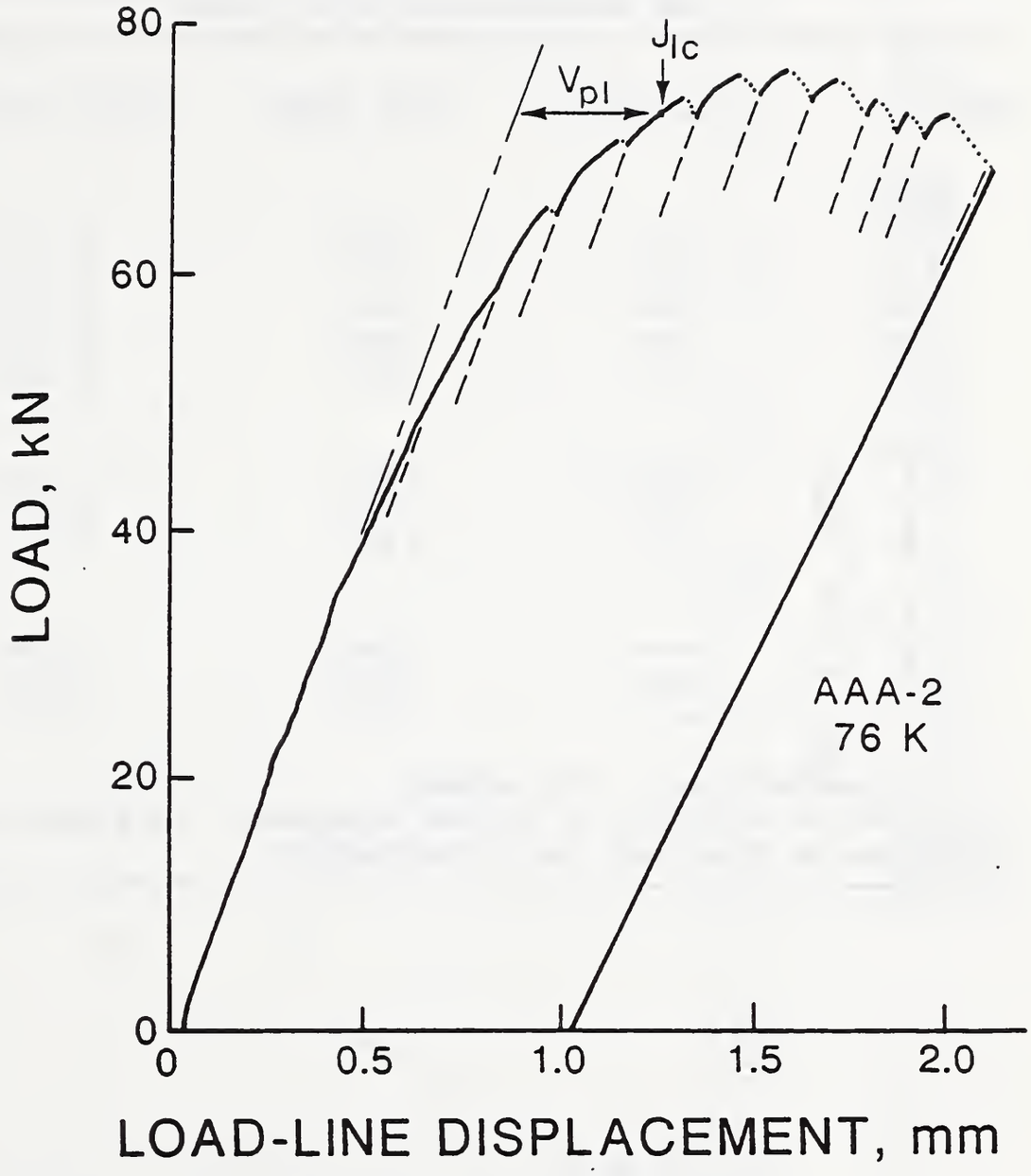

Figure 20. Load vs. displacement curve for AAA-2 tested at 76 K. The solid lines represent the imposed displacement, the dashed lines are for the unloading compliance experiments, and the dotted lines represent load relaxation under fixed-grip conditions.

Table 5 Plane-strain tension test results for annealed 22-13-5 plate

Spec. #	YS (MPa)	UTS (MPa)	Final Strain**
295 K			
3	267	954	0.24
4*	293	967	0.21
8*	265	696	0.10
9*	304	958	0.22
12	307	801	0.12
76 K			
2	1016	1893	0.18
5	720	2082	0.21
6*	952	1800	0.15
4 K			
7	----	2040	0.08
10	1639	2015	0.03
11	----	2187	0.09

* interrupted test, not broken
** fracture strain for failed specimen, or strain at the point where the test was interrupted

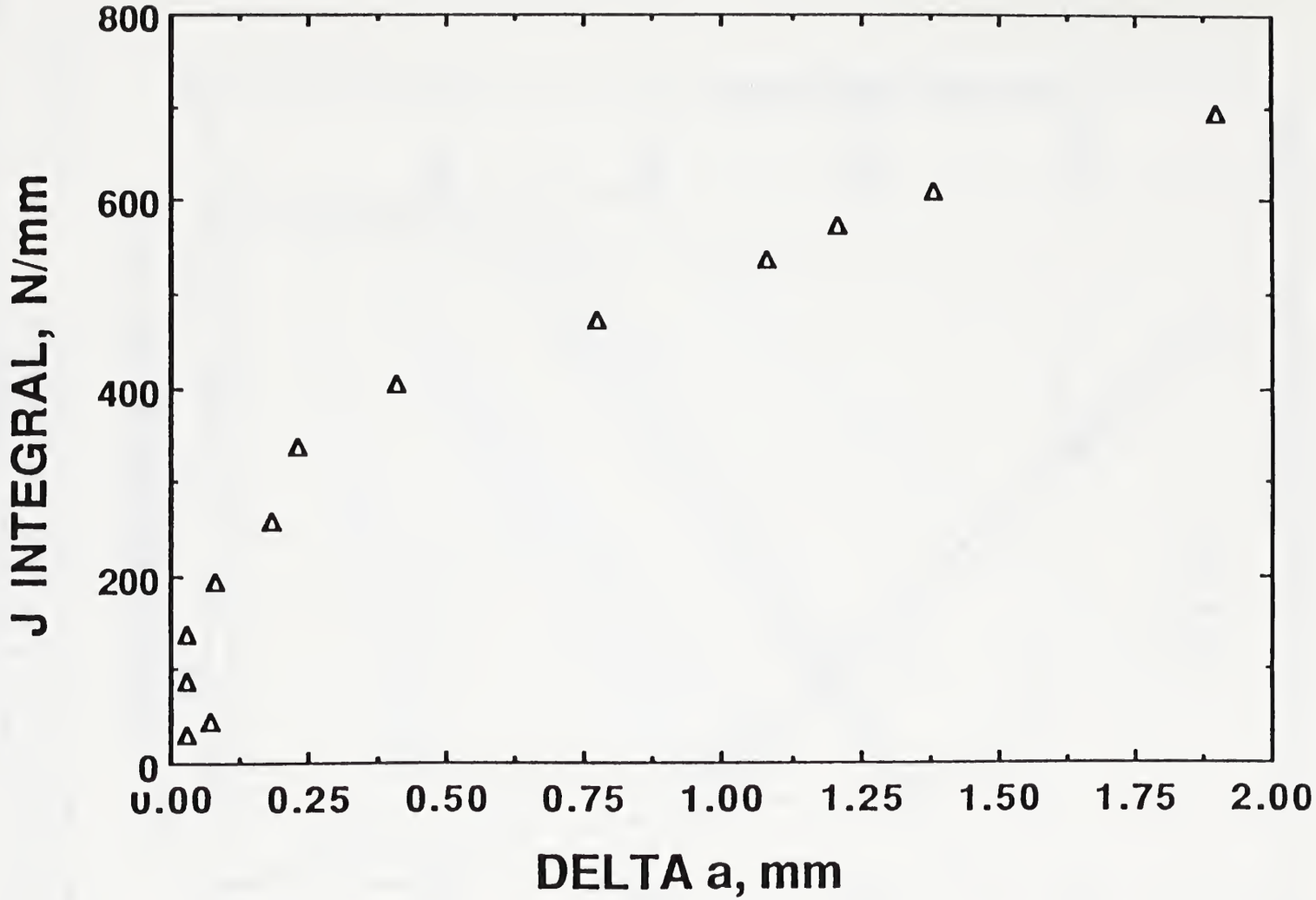

Figure 21. Toughness test J vs. ▲a plot for AAA-2 calculated from the load vs. displacement curve shown in Fig. 20.

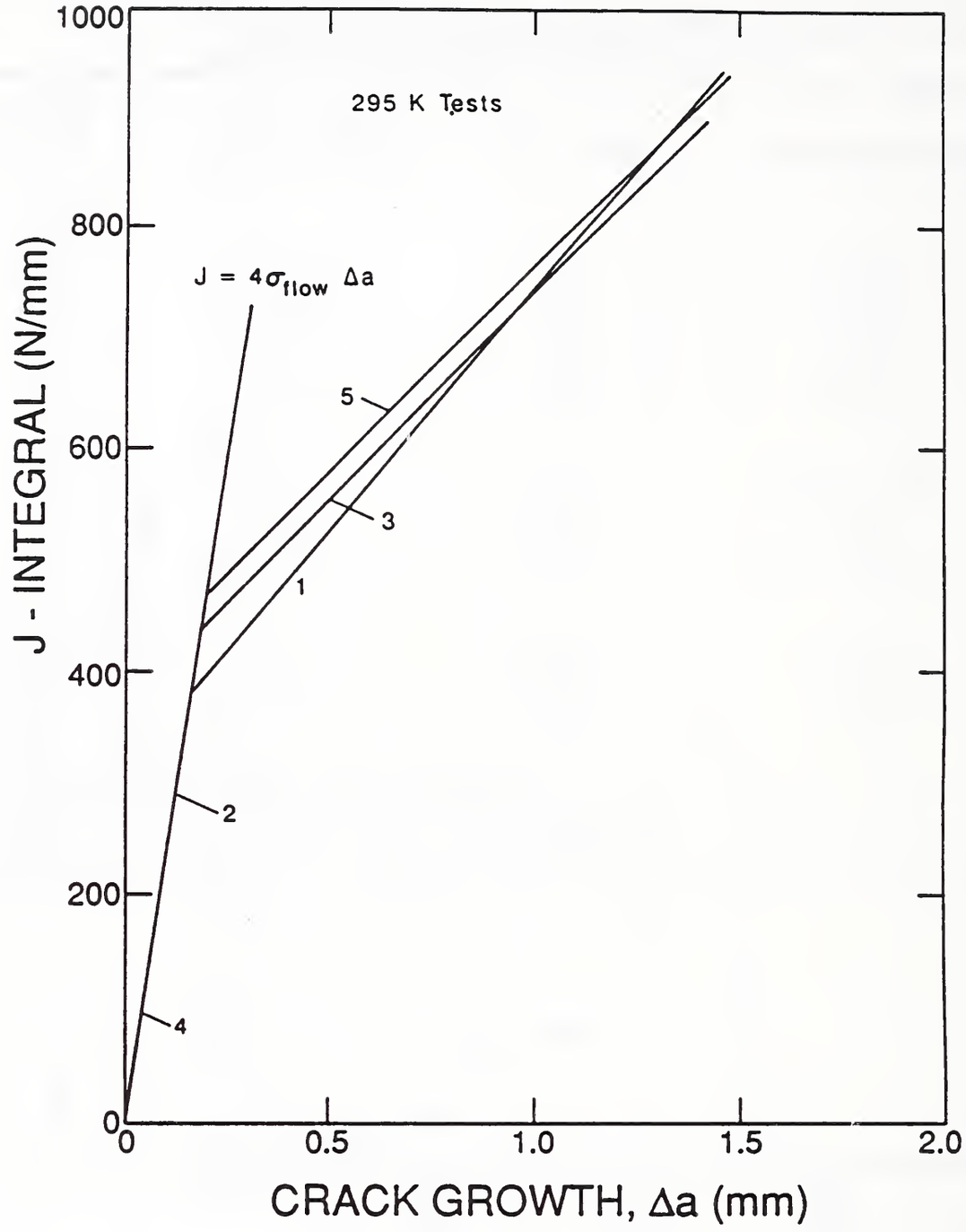

Figure 22. Toughness tests blunting and tearing lines for 22-13-5 at 295 K, T-L orientation. Three complete tests and two interrupted tests are shown.

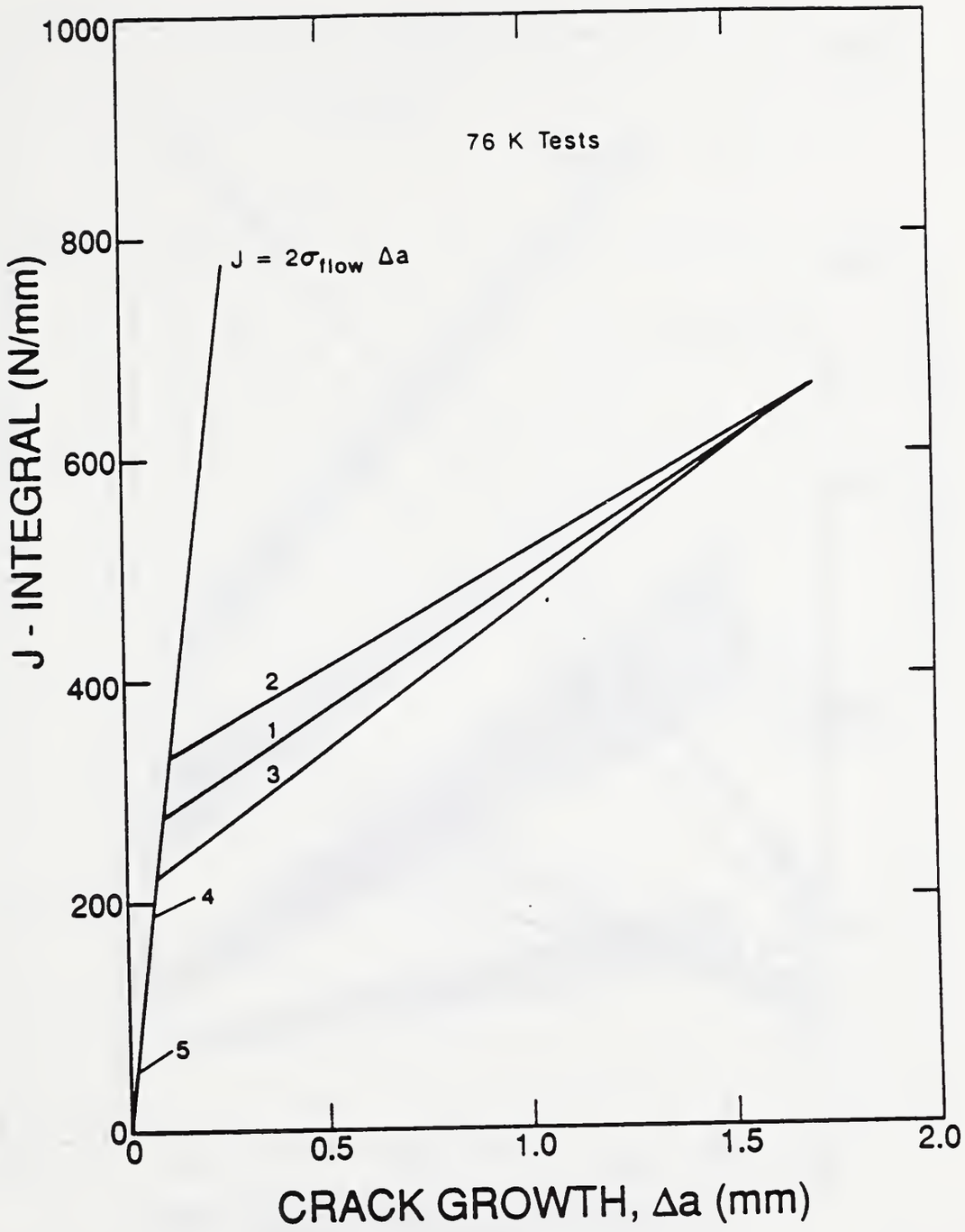

Figure 23. Toughness test blunting and tearing lines for 22-13-5 at 76 K, T-L orientation. Three complete tests and two interrupted tests are shown.

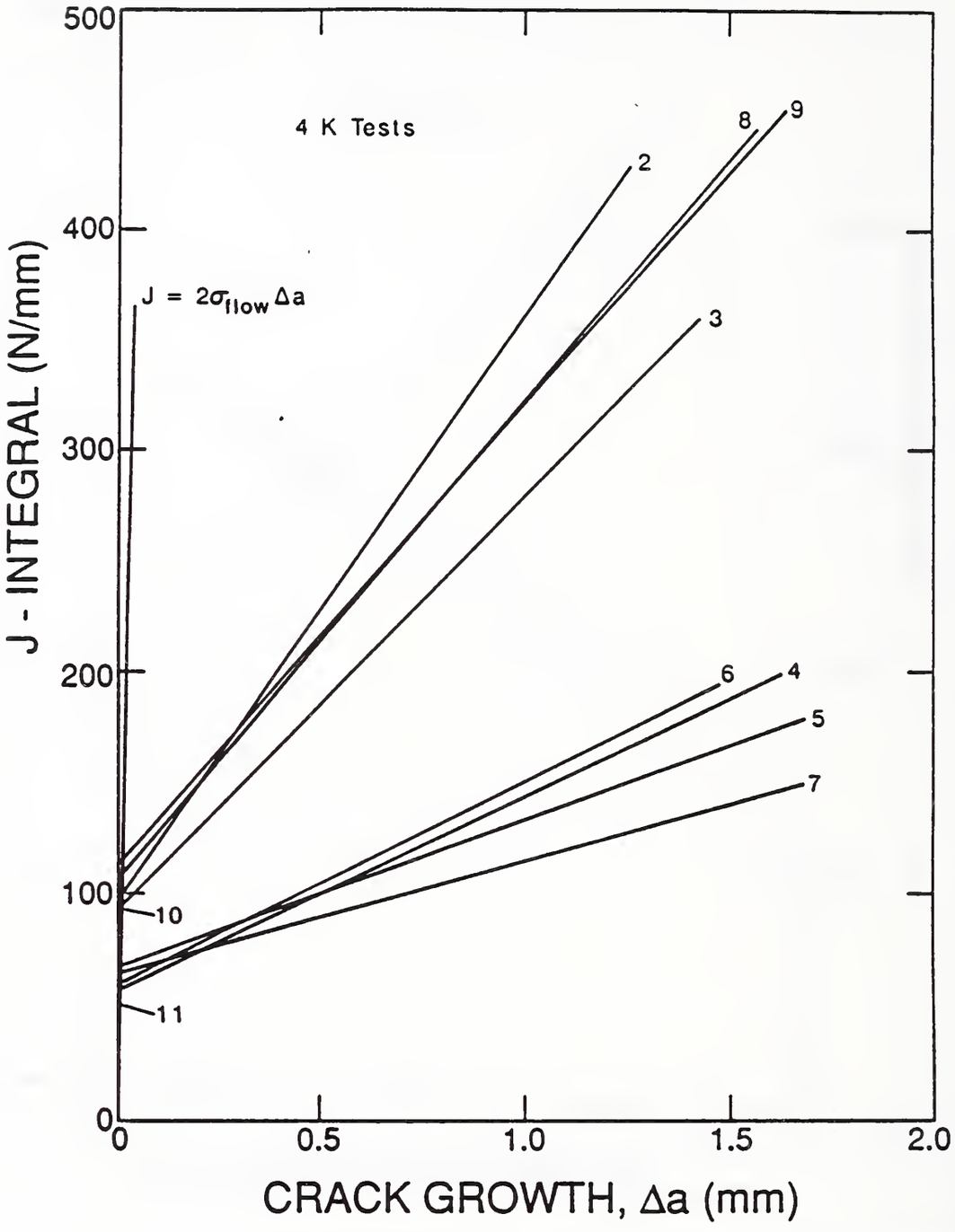

Figure 24. Toughness test blunting and tearing lines for 22-13-5 at 4 K, T-L orientation. Eight complete tests and two interrupted tests are shown.

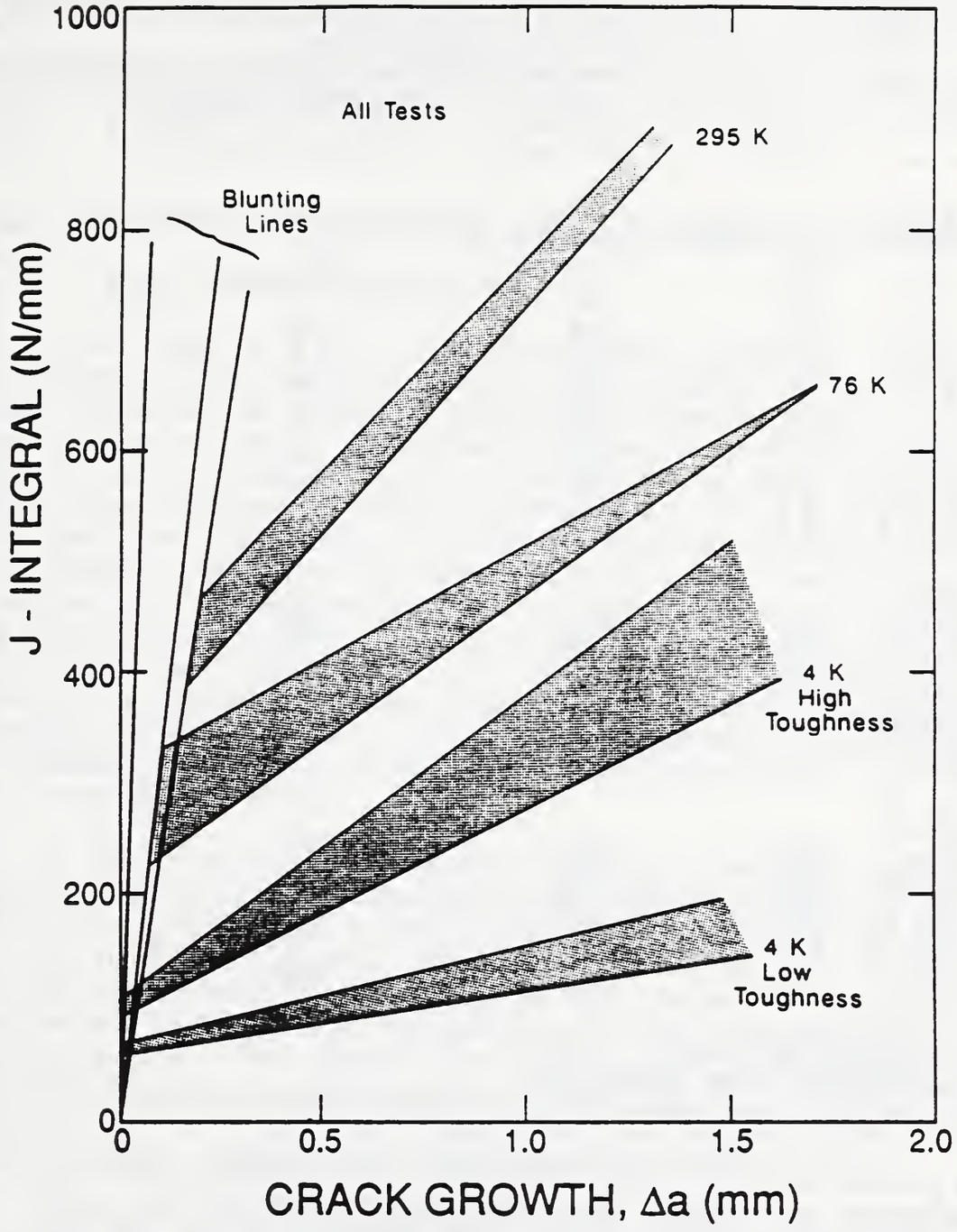

Figure 25. Summary of all complete toughness tests for 22-13-5, T-L orientation.

Table 6 Fracture toughness results for 22-13-5 in T-L orientation

Specimen	J_{Ic}	$K_{Id}(J)$	Tearing Modulus	δ_i
4 K				
A-2	99 N/mm	141 MPa m	23	46 μm
A-3	122	143	14	44
A-4	59	109	7	28
A-5	58	108	6	28
A-6	62	111	8	26
A-7	58	108	5	28
A-8	110	148	18	46
A-9	112	150	18	49
A-10*	94	137	--	36
A-11*	51	101	--	2
76 K				
AAA-1	267	231	28	156
AAA-2	330	257	26	156
AAA-3	220	210	30	131
AAA-4*	187	193	--	97
AAA-5*	54	104	--	33
295 K				
AA-1	524	324	222	280**
AA-2*	228	213	--	220**
AA-3	540	329	197	385
AA-4*	100	100	--	79**
AA-5	576	339	198	387

* interrupted test
** measured from specimen

the plastic zone size is larger at higher temperatures. The toughness specimens were machined so that the crack path in the specimens would avoid the center region of the plate, Region III of Fig. 13, where extensive grain growth occurred.

Two toughness tests were run at 4 K on specimens with L-T rather than T-L orientation. The J vs. Δa curves for the two L-T tests and one of the HI-4K and one of the LO-4K tests are shown in Fig. 26. The data points for the L-T specimens fall in between the HI-4K and LO-4K results. The

toughness is not a strong function of specimen orientation because the matrix material is relatively isotropic (little difference in tensile properties in the two orientations) and the second-phase particles in the matrix are small, widely spaced, and mostly spherical (Table 3).

4.3 Post-test observations from uniaxial stress state

4.3.1 Room temperature tests

Fracture at 295 K was a cup-cone type of failure where there is a flat central region surrounded by a ring of shear lips, typical of ductile fracture caused by MVC. The fracture surface from a transverse tension specimen shown in Fig. 27 is typical. The low magnification view, Fig. 27a, shows the dimpled rupture features of MVC in the center of the specimen contained within an annular ring of shear lips. The biggest features in the central region are elongated troughs with rough surfaces characteristic of extensive plastic deformation. The troughs form at isolated nucleation sites and grow together by plastic deformation. The elongated troughs are surrounded by smaller, equiaxed dimples with a smooth surface. The dimples form from closely spaced nucleation sites that coalesce with little associated plasticity.

A cross section through a failed specimen oriented across the rolling direction and tested at 295 K is shown in Fig. 28. The profile of the fracture surface is shown at the top of the figure. The dark features in the unetched matrix represent voids. The first voids to nucleate are scattered through the necked region of the specimen, indicating that the strain for nucleation is greater than the uniform strain. The largest voids are elongated along the tensile axis, which is transverse to the rolling direction of the plate from which this specimen was taken.

The primary void nucleation sites in the uniaxial stress state at 295 K are the sigma phase left from the as-received structure. The etched microstructure below the fracture surface of the specimen from Figs. 27 and 28 is shown in Fig. 29. Sigma is the light etching phase elongated across the figure. The dark patches within the sigma phase are voids that have nucleated by particle cracking. Void nucleation was limited to the elongated sigma. The troughs observed on the fracture surface correspond to the spacing of sigma in the microstructure.

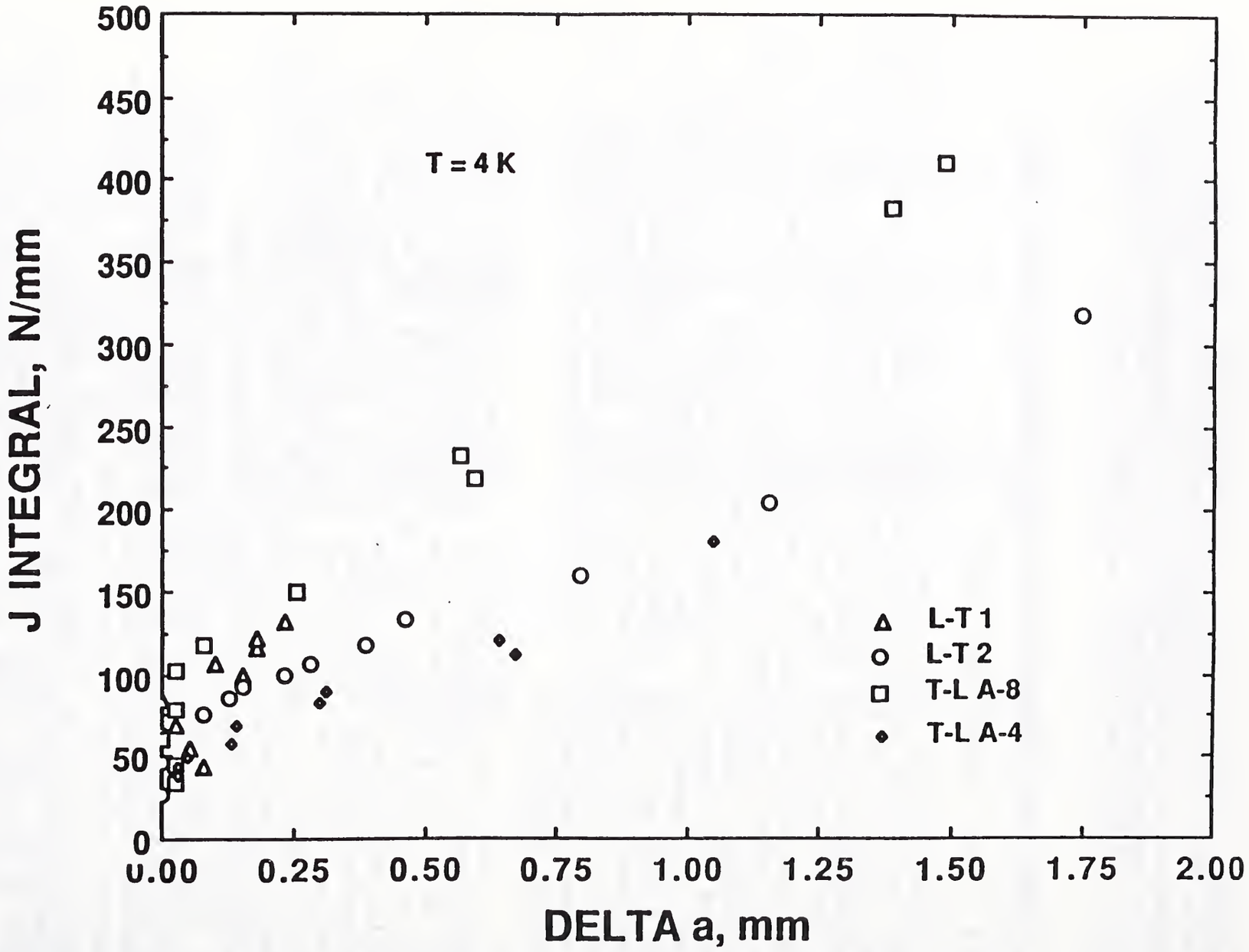

Figure 26. Toughness test J vs. Δa data points for the two L-T specimens at 4 K compared with a T-L HI-4K specimen (A-8) and a T-L LO-40K specimen (A-4).

toughness is not a strong function of specimen orientation because the matrix material is relatively isotropic (little difference in tensile properties in the two orientations) and the second-phase particles in the matrix are small, widely spaced, and mostly spherical (Table 3).

4.3 Post-test observations from uniaxial stress state

4.3.1 Room temperature tests

Fracture at 295 K was a cup-cone type of failure where there is a flat central region surrounded by a ring of shear lips, typical of ductile fracture caused by MVC. The fracture surface from a transverse tension specimen shown in Fig. 27 is typical. The low magnification view, Fig. 27a, shows the dimpled rupture features of MVC in the center of the specimen contained within an annular ring of shear lips. The biggest features in the central region are elongated troughs with rough surfaces characteristic of extensive plastic deformation. The troughs form at isolated nucleation sites and grow together by plastic deformation. The elongated troughs are surrounded by smaller, equiaxed dimples with a smooth surface. The dimples form from closely spaced nucleation sites that coalesce with little associated plasticity.

A cross section through a failed specimen oriented across the rolling direction and tested at 295 K is shown in Fig. 28. The profile of the fracture surface is shown at the top of the figure. The dark features in the unetched matrix represent voids. The first voids to nucleate are scattered through the necked region of the specimen, indicating that the strain for nucleation is greater than the uniform strain. The largest voids are elongated along the tensile axis, which is transverse to the rolling direction of the plate from which this specimen was taken.

The primary void nucleation sites in the uniaxial stress state at 295 K are the sigma phase left from the as-received structure. The etched microstructure below the fracture surface of the specimen from Figs. 27 and 28 is shown in Fig. 29. Sigma is the light etching phase elongated across the figure. The dark patches within the sigma phase are voids that have nucleated by particle cracking. Void nucleation was limited to the elongated sigma. The troughs observed on the fracture surface correspond to the spacing of sigma in the microstructure.

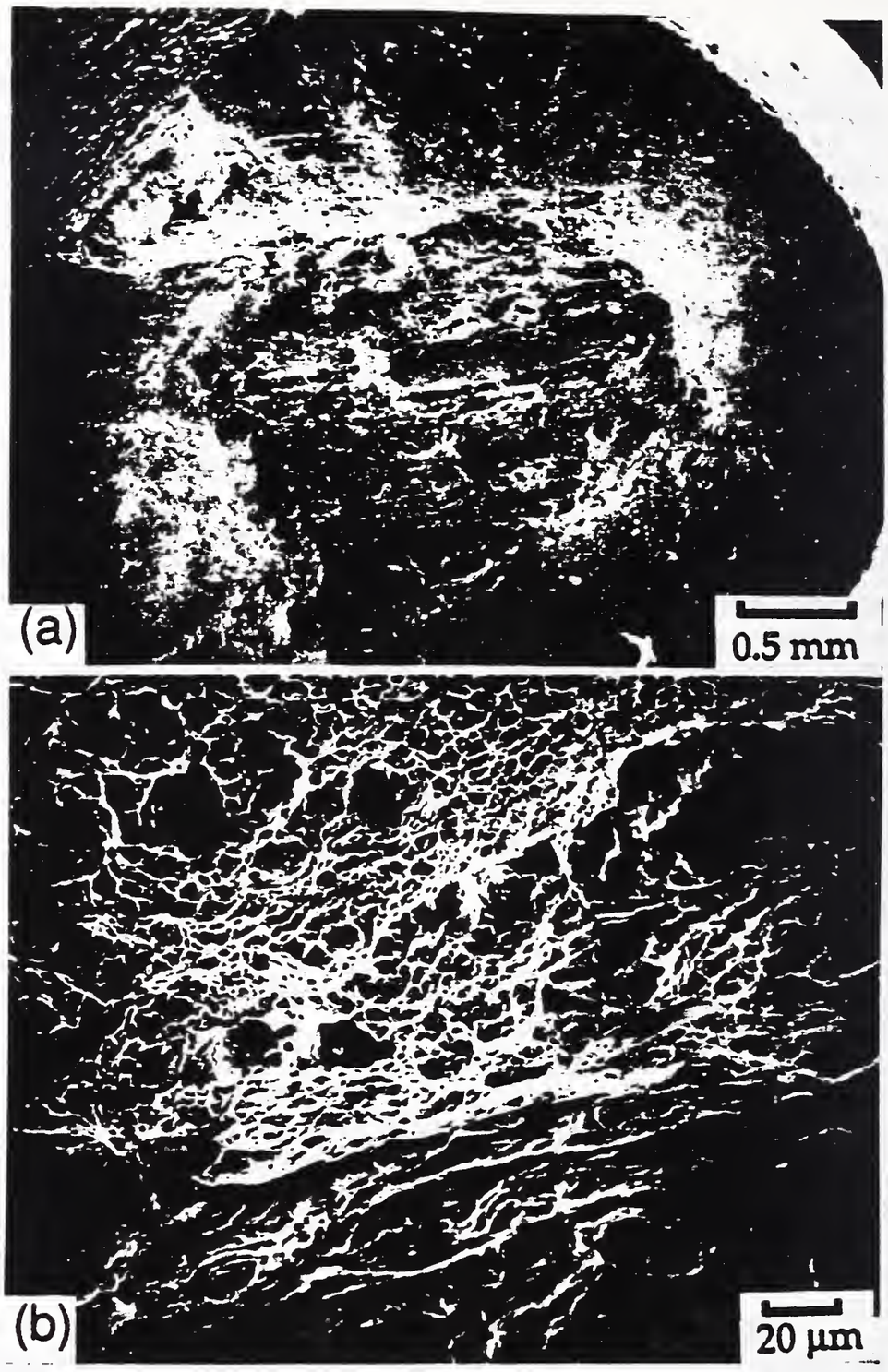

Figure 27. The fracture surface appearance of tension specimen with transverse orientation with respect to the rolling direction, tested at 295 K.

Figure 28. Cross section, unetched, through transverse uniaxial tension specimen broken at 295 K.

Figure 29. Microstructure below the fracture surface of tensile specimen cross section shown in Fig. 28. The darker patches across the center of the picture are voids.

The micromechanisms of ductile fracture at 295 K are interpreted from the observations as follows. Voids form at sigma phase after large strains at a stress near the UTS. Voids grow in the ligaments between cracked particles to form the elongated voids observed in the cross section below the fracture surface. At the fracture stress, the equiaxed dimples nucleate from microalloy particles in the matrix between the elongated voids. The equiaxed dimples are assumed to be associated with the submicrometer size microalloy particles even though the particles are not observed on the fracture surface. Fracture surfaces of martensitic steel [56,57] display submicrometer, equiaxed features like those found on the fracture surfaces of 22-13-5. For the martensitic steels, carbon extraction replicas proved unambiguously that the equiaxed dimples nucleate at undissolved carbides in the steel.

4.3.2 Liquid nitrogen tests

When the test temperature was reduced from 295 to 76 K, the macroscopic fracture changed from a cup-cone fracture associated with MVC in the center of the specimen to a mixture of MVC and shear. A low magnification view of a failed 76-K specimen is shown in Fig. 30. The specimen broke into three pieces where the necked region separated

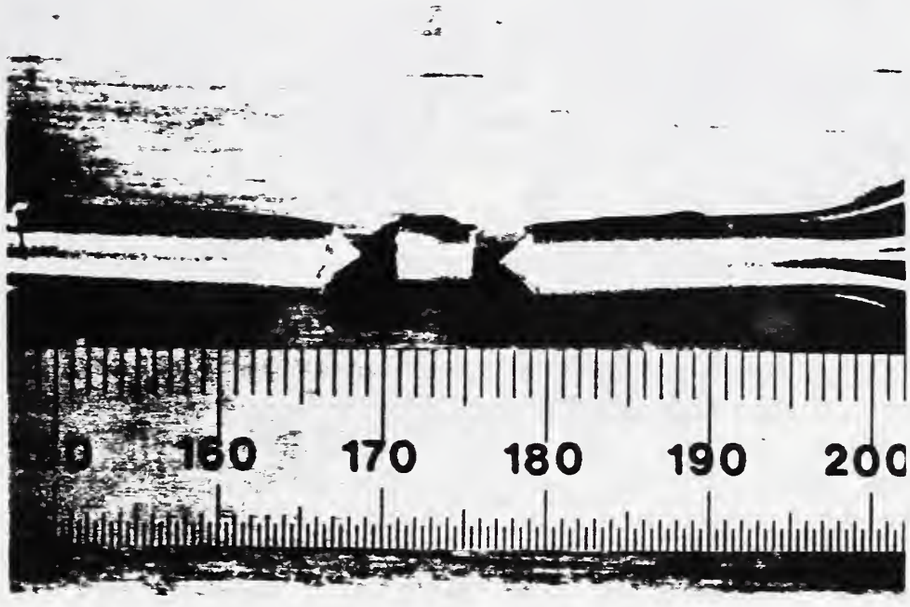

Figure 30. Macrograph of uniaxial tension specimen broken at 76 K where the necked region has separated intact from the ends of the tension specimen.

cleanly from the ends of the specimen, leaving a hole in the center of the necked piece. The fracture surface is all shear lip.

The fracture surface of a second tension specimen tested at 76 K is shown in Fig. 31. Most of the surface consists of shear lips. At higher magnification (Fig. 31b), the center of the fracture surface shows large facets, 20-50 μm in diameter, surrounded by smaller dimples, 1-2 μm in diameter, that lie on planes inclined to the tensile axis.

A polished section taken from the tension specimen tested at 76 K is shown in Fig. 32. The profile of the fracture surface is made up of a series of intersecting shear planes with a small, 150 μm long, flat section in the center. Voids are observed below the fracture surface, but less elongated than observed in the cross section of the 295-K specimen (Fig. 28).

At 76 K, the micromechanisms of ductile fracture are different than those at 295 K. Shear fractures cover a larger percent of the surface. The primary void nucleation sites are still the patches of sigma left in the microstructure after thermomechanical processing. After void nucleation, strain is localized into shear bands between voids. Within the bands, a smaller set of voids are nucleated as a type of void sheet coalescence. In an extreme case like that observed in Fig. 30, the fracture surface was all shear lip because strain became localized into shear bands between a single void near the center of the specimen and the outer surface of the specimen.

4.3.3 Liquid helium tests

The appearance of the fracture surfaces of specimens tested at 4 K is similar to the observations made at 76 K. Away from the fracture surface of 4-K specimens, several diffuse necks are observed along the gage length of the specimen, as well as at the point of fracture. The specimen heating occurs locally along the gage section causing extensive plastic deformation, producing neck formation, and strain hardening the matrix. Subsequent strain occurs away from the neck because the matrix is softer. The temperature can rise as much as 100 K in the neck during testing [47]. Given the local heating of the 4-K specimens, it is not surprising that the fracture surfaces of 4-K specimens resemble those at 76 K.

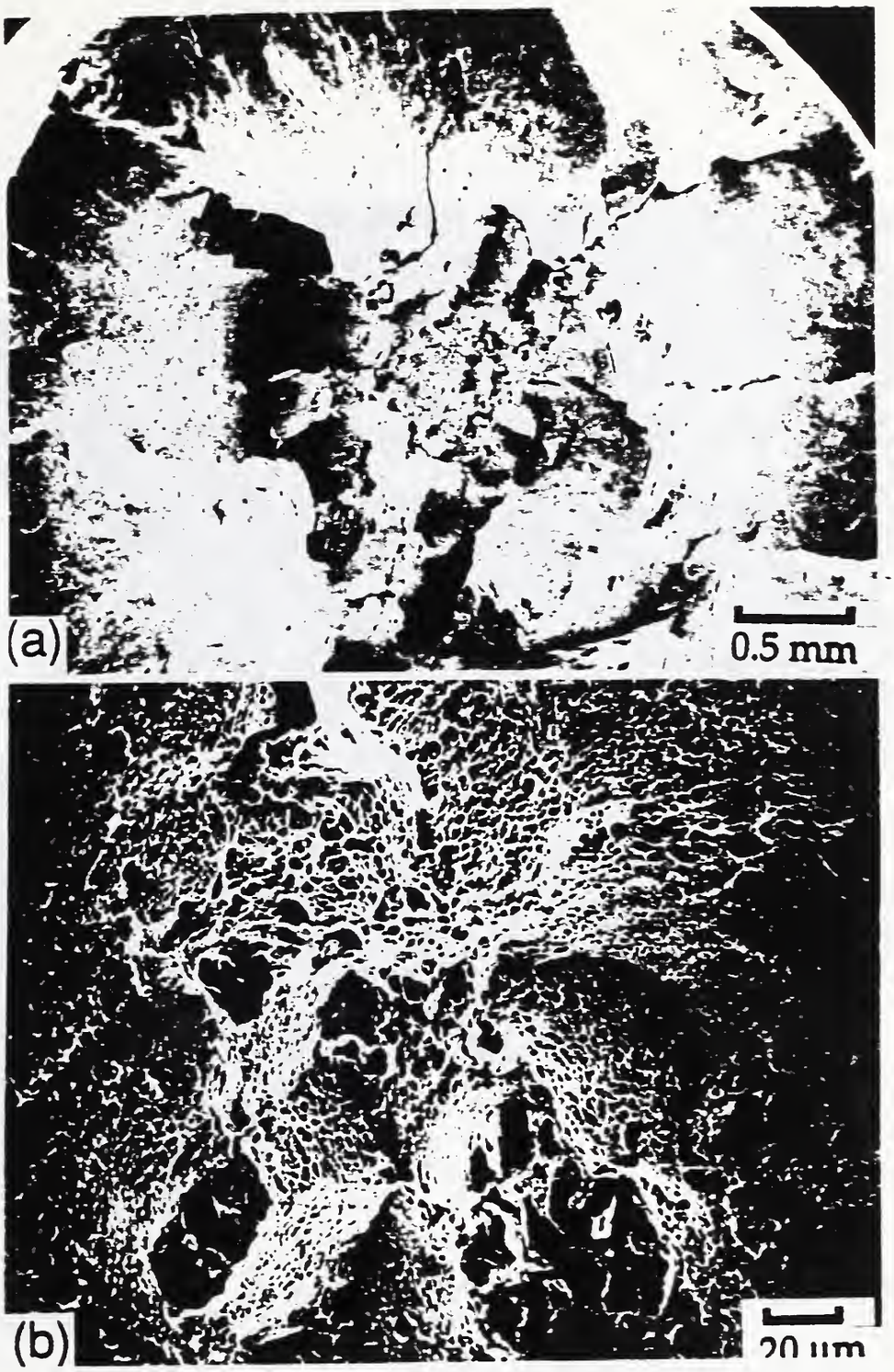

Figure 31. The fracture surface appearance of transverse tension specimen broken at 76 K.

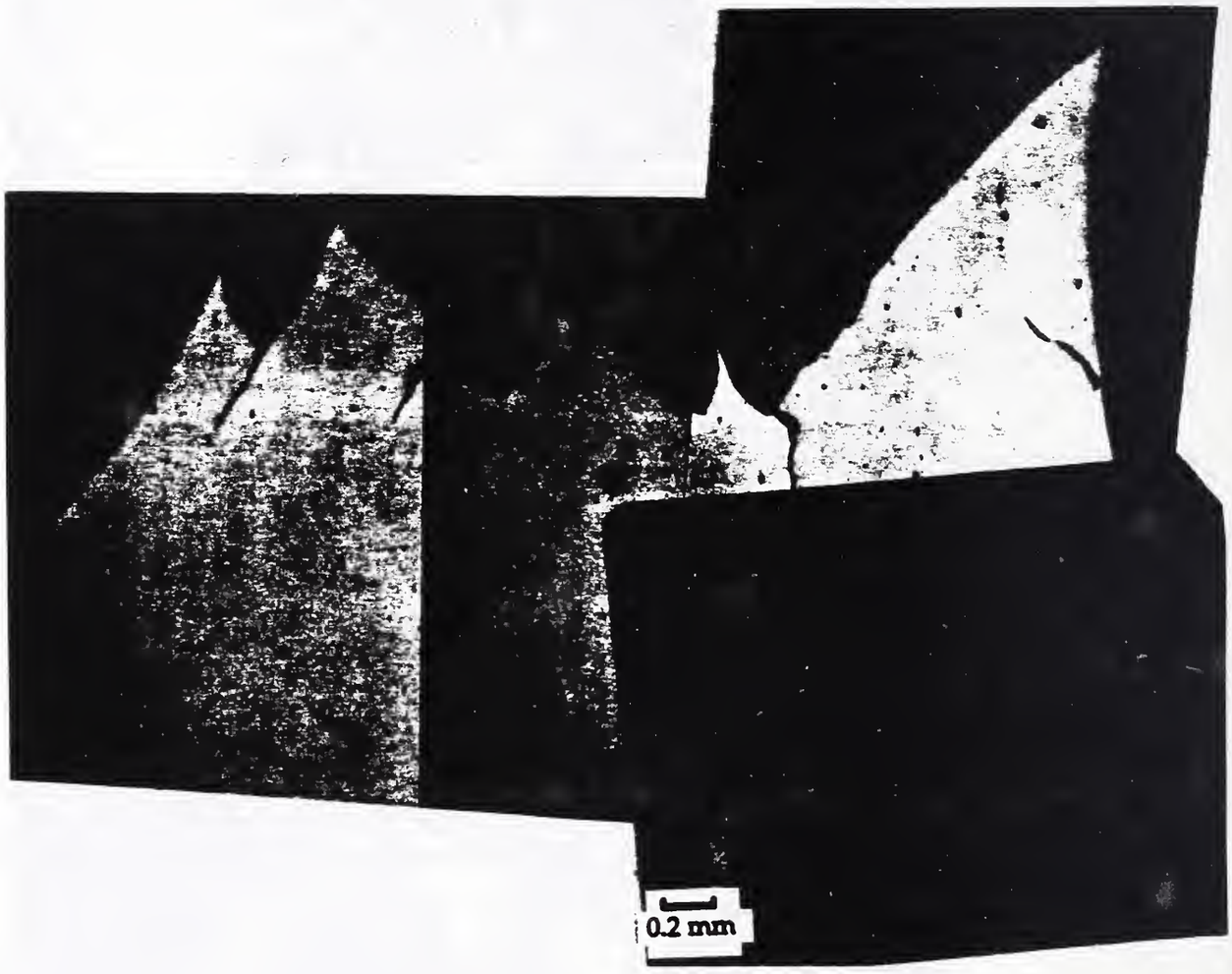

Figure 32. The cross section, unetched, through transverse uniaxial tension specimen, broken at 76 K.

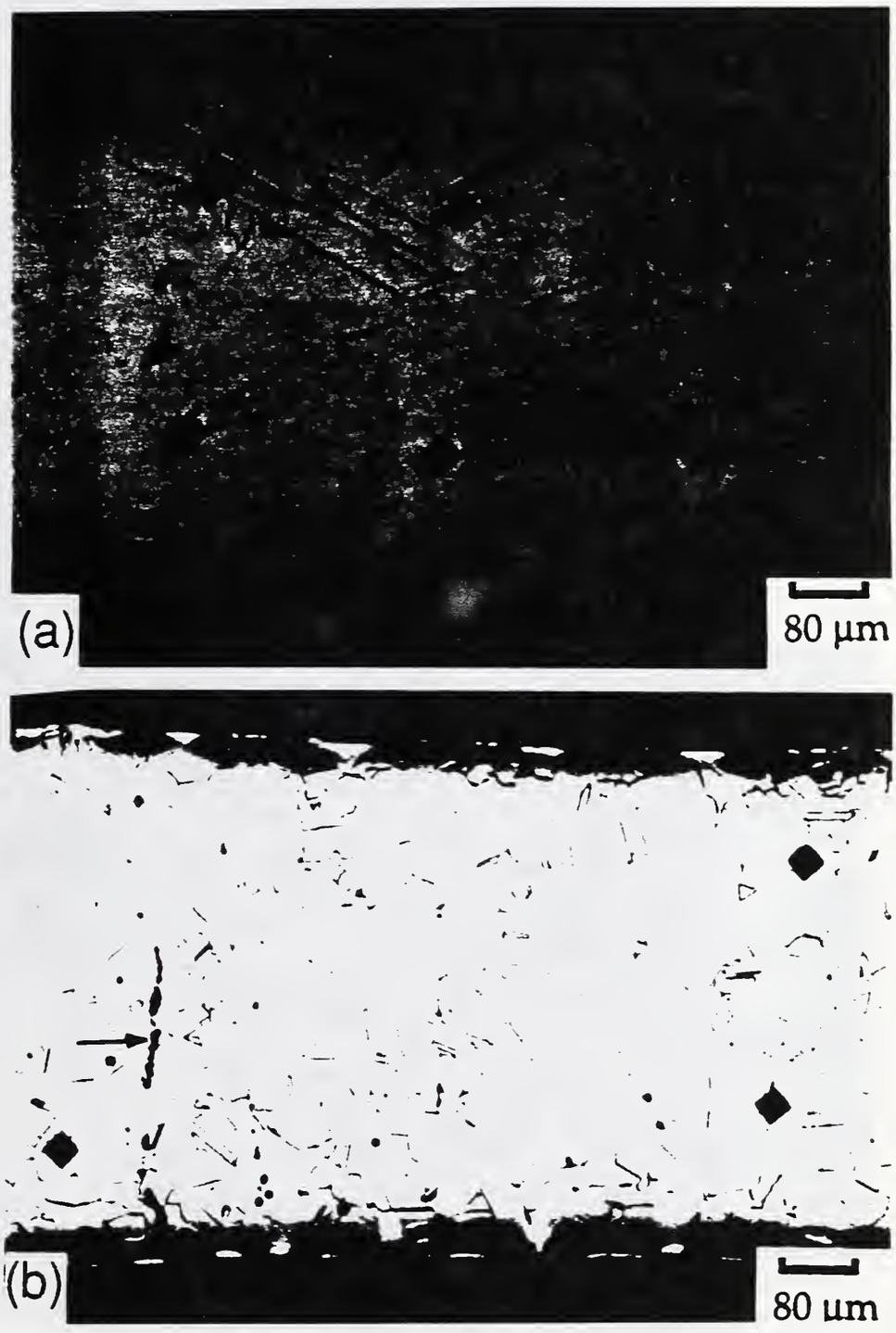

Figure 33. The cross section through biaxial tension specimen strained at 295 K, but not broken: (a) center of gauge section and (b) edge of gage section. Arrow shows elongated second phase stringer.

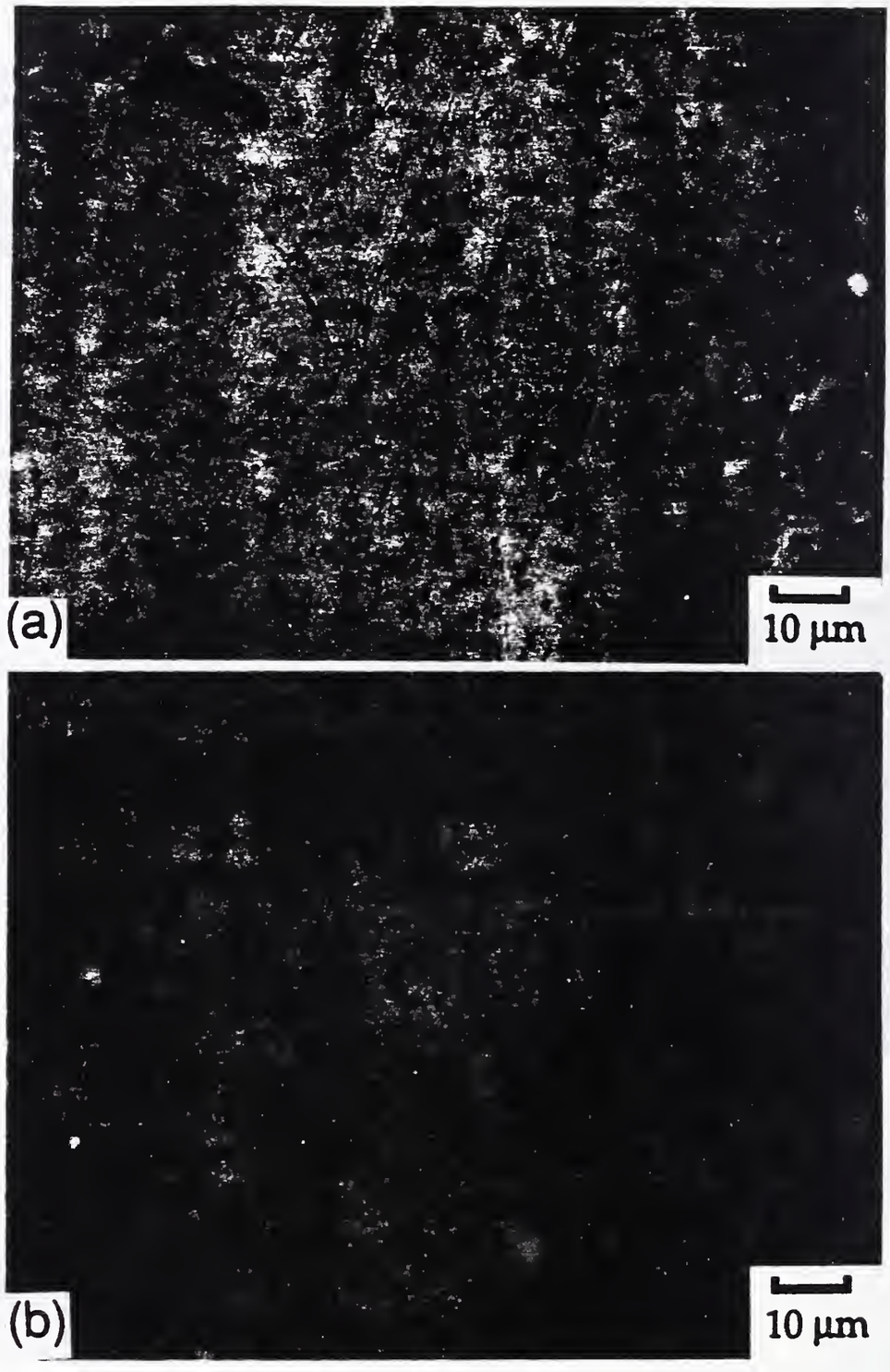

Figure 34. Microstructure found in specimen shown in Fig. 33: (a) center of gage section where a patch of σ phase is cracked, and (b) edge of gage section.

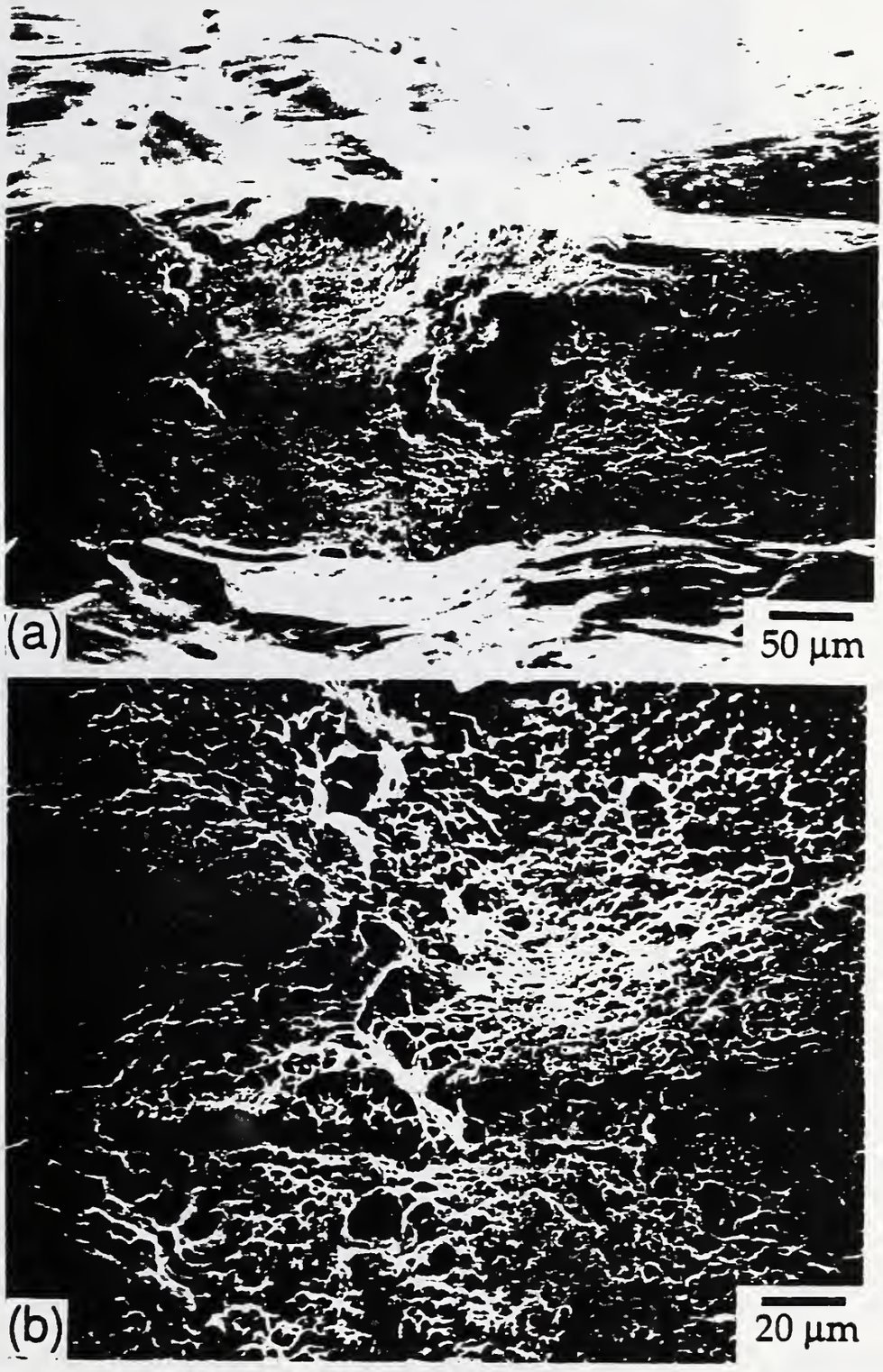

Figure 35. The fracture surface appearance of biaxial tension specimen broken at 295 K.

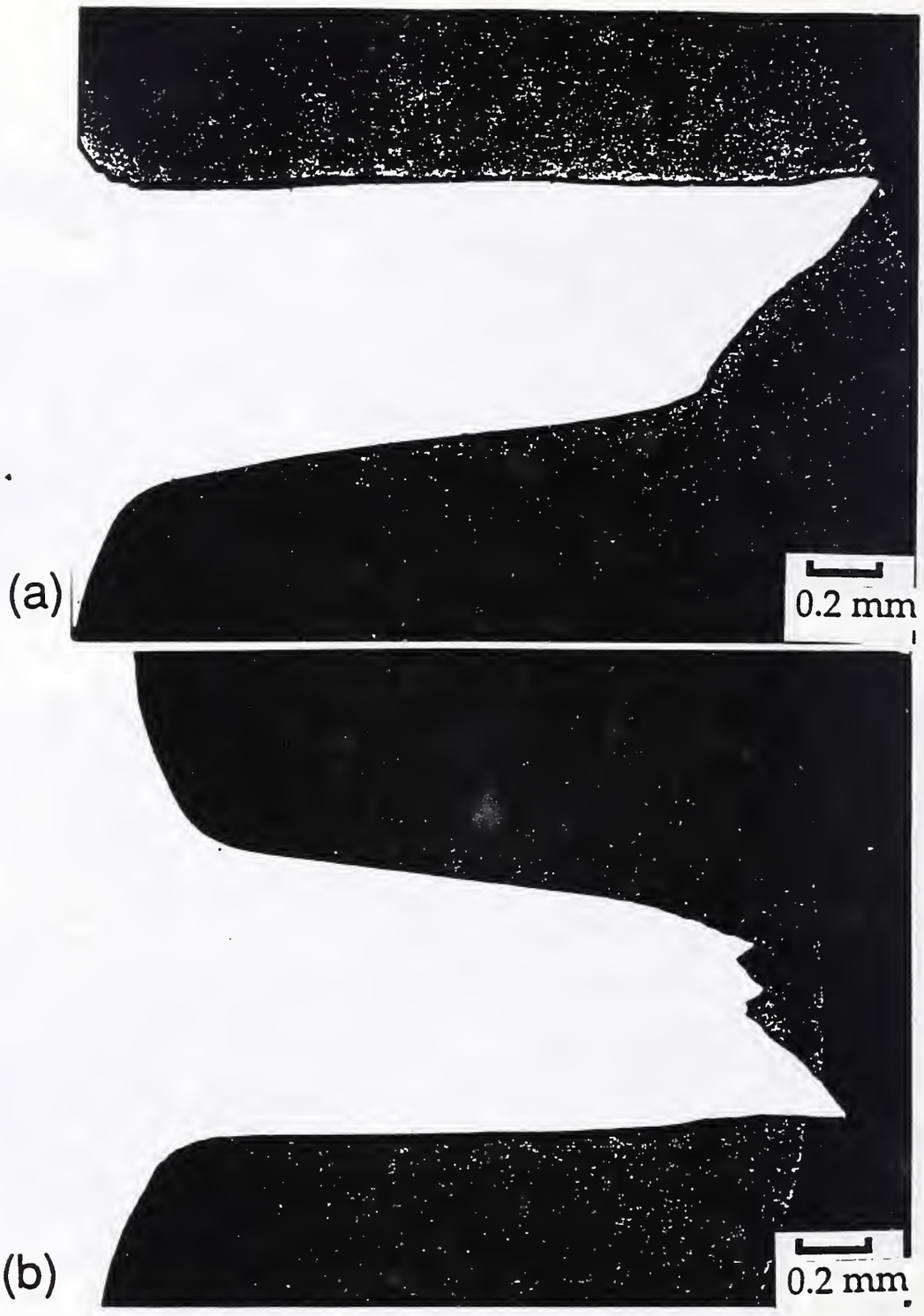

Figure 36. The cross section, unetched, through biaxial tension specimen broken at 4 K: (a) center of gage section, and (b) edge of gage section.

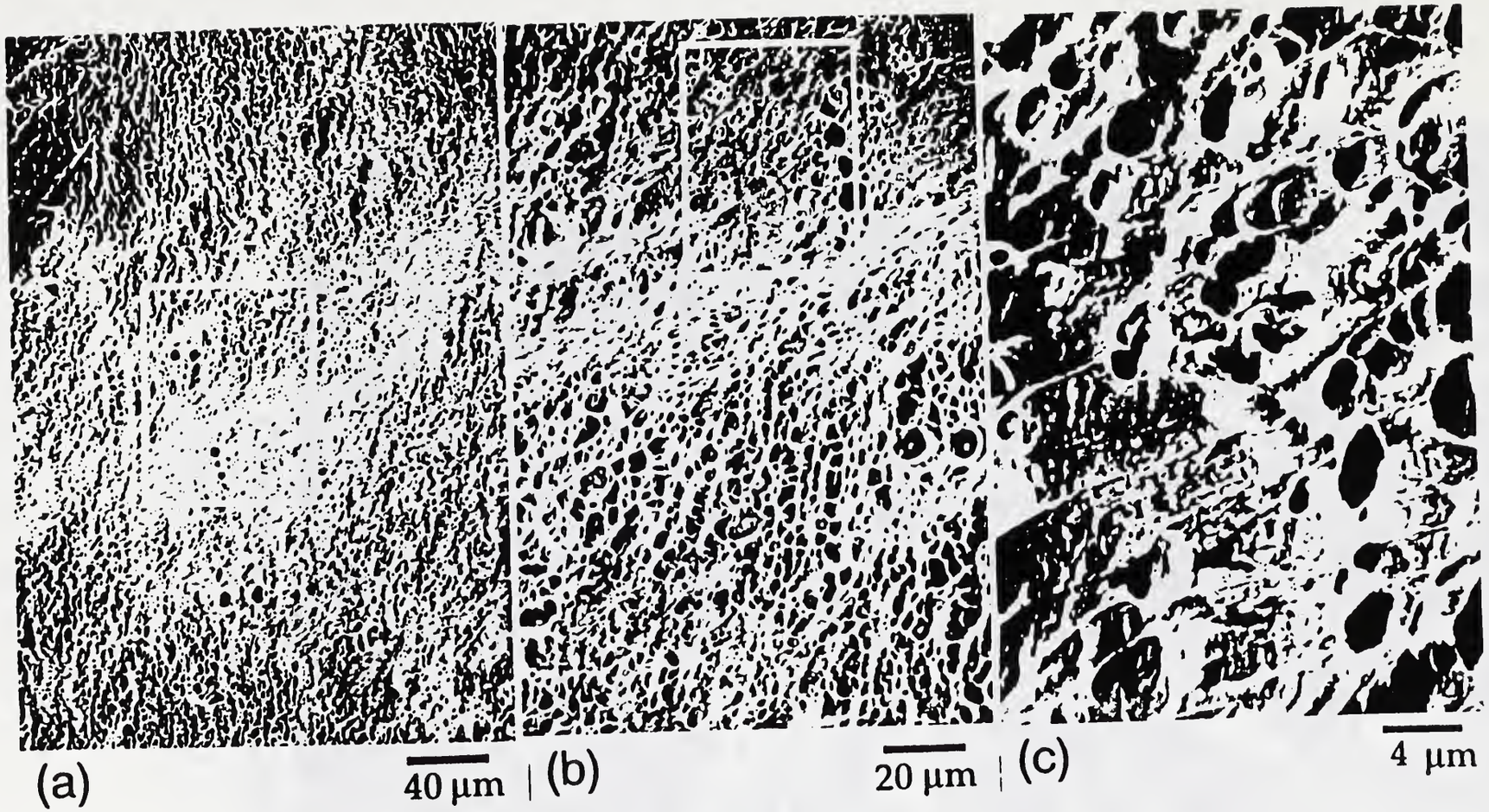

Figure 37. The fracture surface appearance of specimen tested at 4 K showing MVC features on the shear fracture surface.

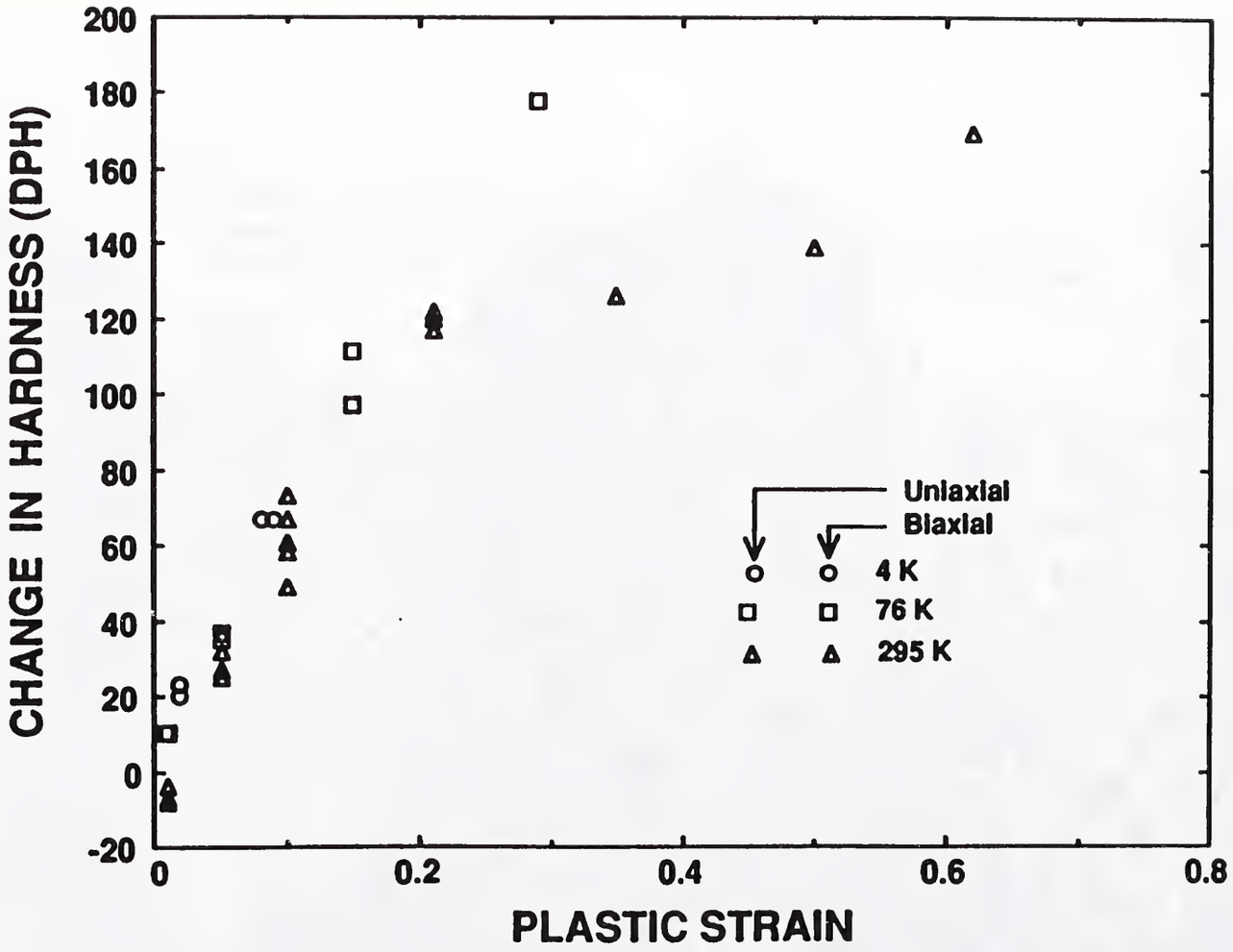

Figure 38. The change in microhardness (▲DPH) as a function of strain in uniaxial and biaxial tensile tests at 4, 76, and 298 K.

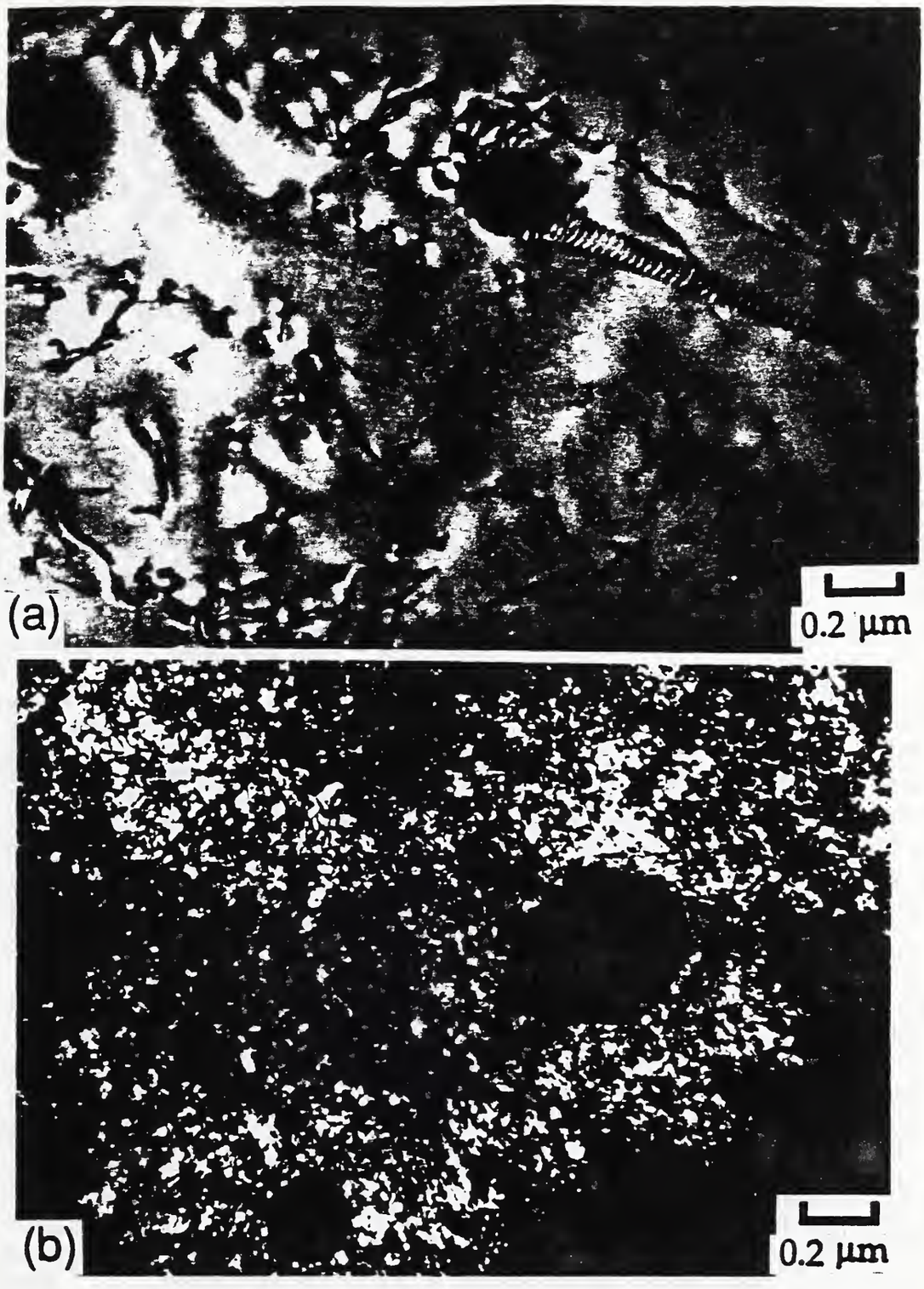

Figure 39. Deformation substructure found in specimen deformed at 295 K: (a) after 0.02 strain, and (b) after 0.05 strain.

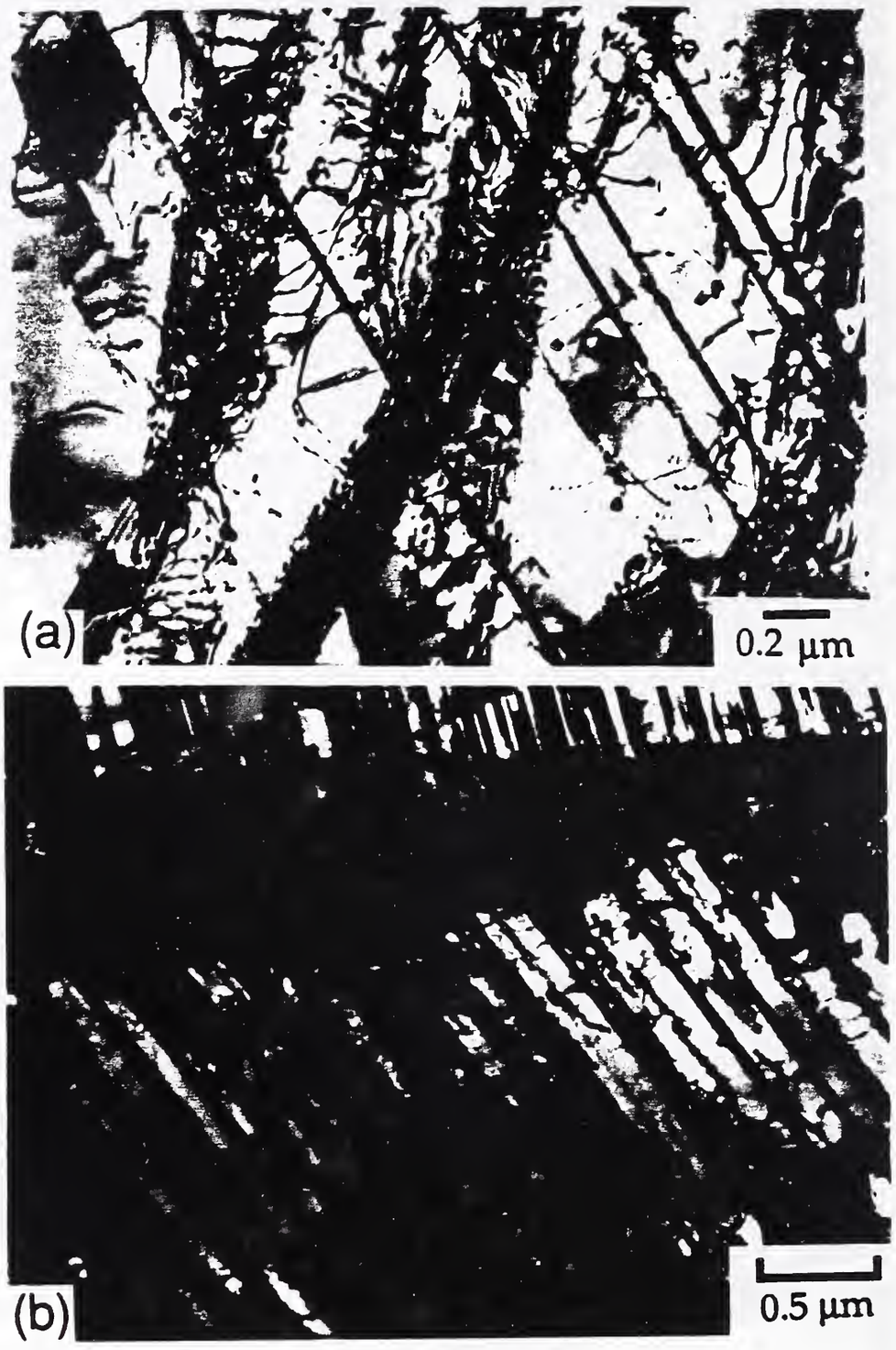

Figure 40. Deformation substructure found in specimen deformed at 76 K; (a) after 0.03 strain, and (b) after 0.12 strain.

associated fracture surface will be examined first. Finally, the ▲DPH around the crack tip of each specimen is shown.

4.7.1 Room temperature tests:

The test of specimen AA-4 was stopped at a point where the section was just starting to yield (transition from small-scale yielding to large-scale yielding); see Fig. 22. A representative section through the blunted fatigue crack is shown in Fig. 41. δ at this point is about 0.08 mm. The grain size next to the crack tip in this section is larger than the bulk material. The crack at this point was located in Region II of the plate microstructure; see Fig. 13. Along the crack front, the grain size varies between 0.04 and 0.2 mm. There is a cluster of second-phase particles, probably sigma phase, ahead of the crack tip, but the distance from the tip is greater than 2δ, the process zone size.

The next set of observations come from specimen AA-2, interrupted at a point just below J_{Ic} (Fig. 22). The profile of the blunted crack tip is shown in Fig. 42. δ at this point is 0.22 mm. The blunted tip has a rough, irregular shape and a crack has grown about 0.05 mm ahead of the blunted tip. A void is observed at an angle below the crack path, 0.25 mm or about a distance δ away from the crack present at the blunted tip.

The fracture surface from the second half of specimen AA-2 is shown in Fig. 43. The region created during the interrupted test is a narrow ribbon of material across the figure, similar to the SZ discussed in the introduction. At the higher magnification (Fig. 43b), the SZ appears as a lip sticking up above the fatigue features that formed during precracking and post-cracking. The surface of the SZ looks like a series of slip steps. The fatigue features above (post-cracking) and below (pre-cracking) the SZ are the same.

Specimen AA-1 was tested to a crack growth of about 1.8 mm. A cross section through the crack is shown in Fig. 44. δ for initiation was estimated from this picture to be about 0.28 mm by subtracting the δ at the tip of the original fatigue crack from the δ at the left edge of the figure. The actual crack tip after 1.8 mm of growth remains sharp. Voids have nucleated and grown above and below the crack at elongated, second-phase particles in the matrix. The

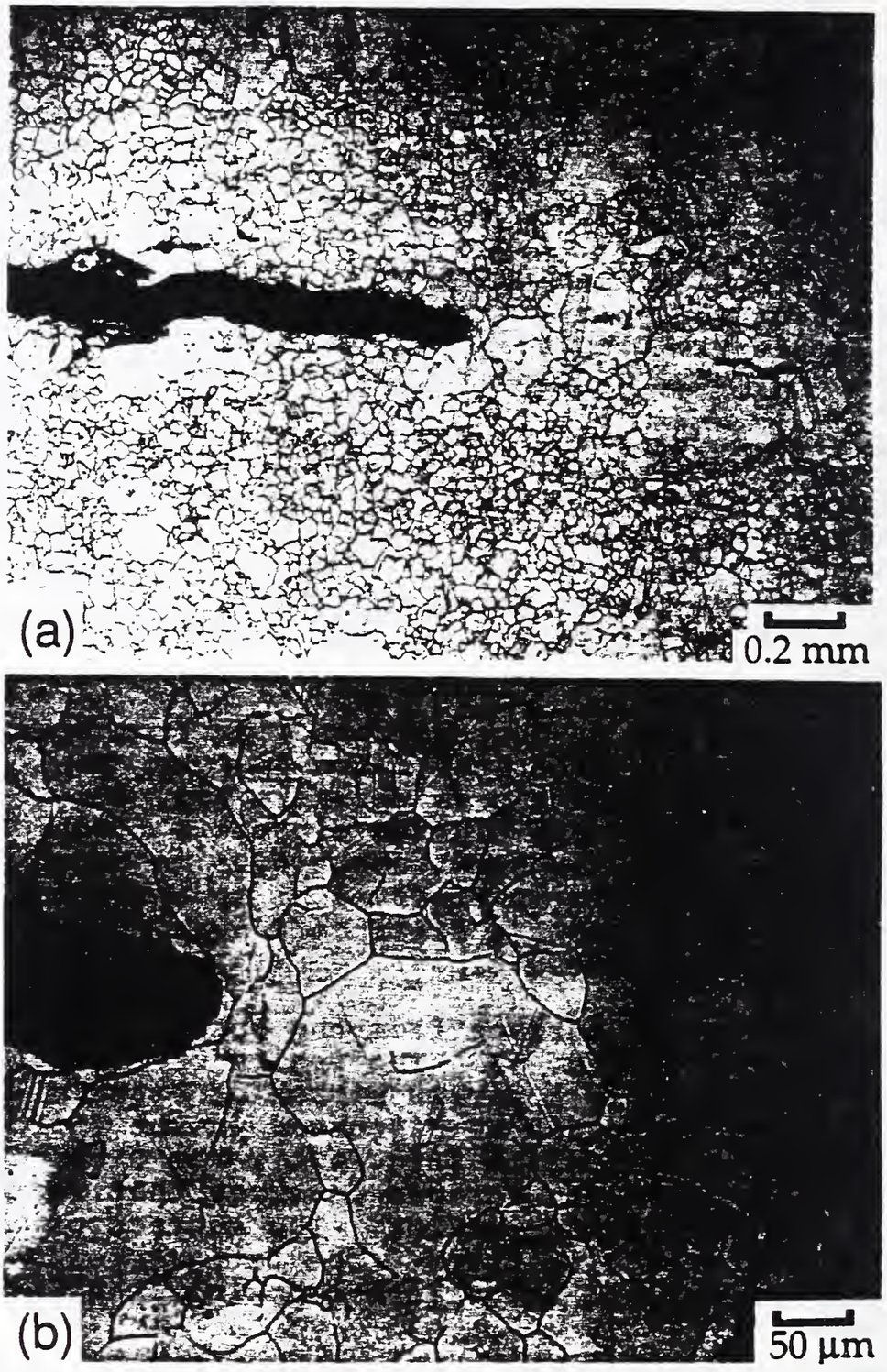

Figure 41. The cross section through compact specimen AA-4 tested at 295 K. Crack growth direction is left to right.

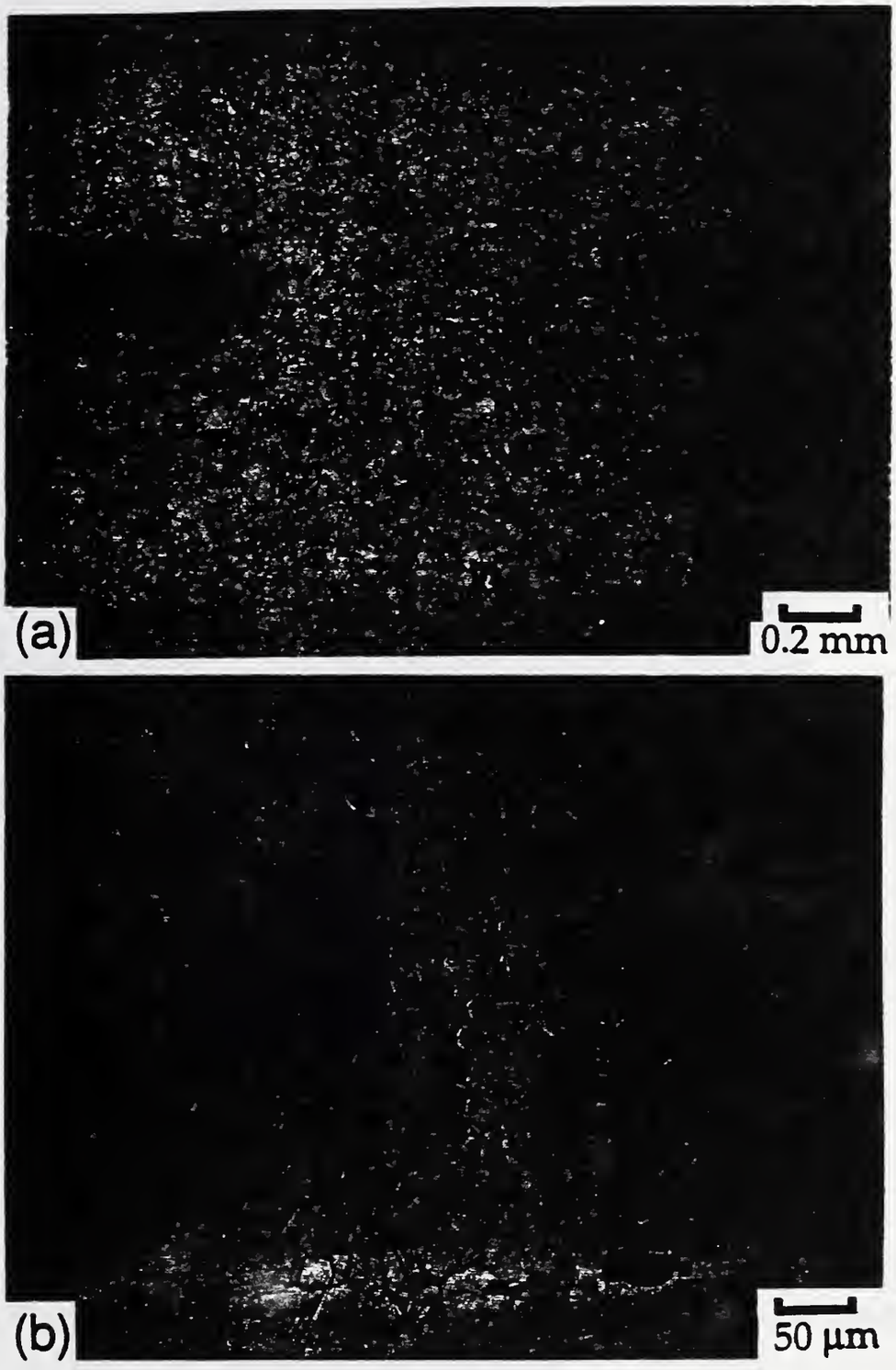

Figure 42. The cross section through compact specimen AA-2 tested at 295 K. Crack growth direction is left to right.

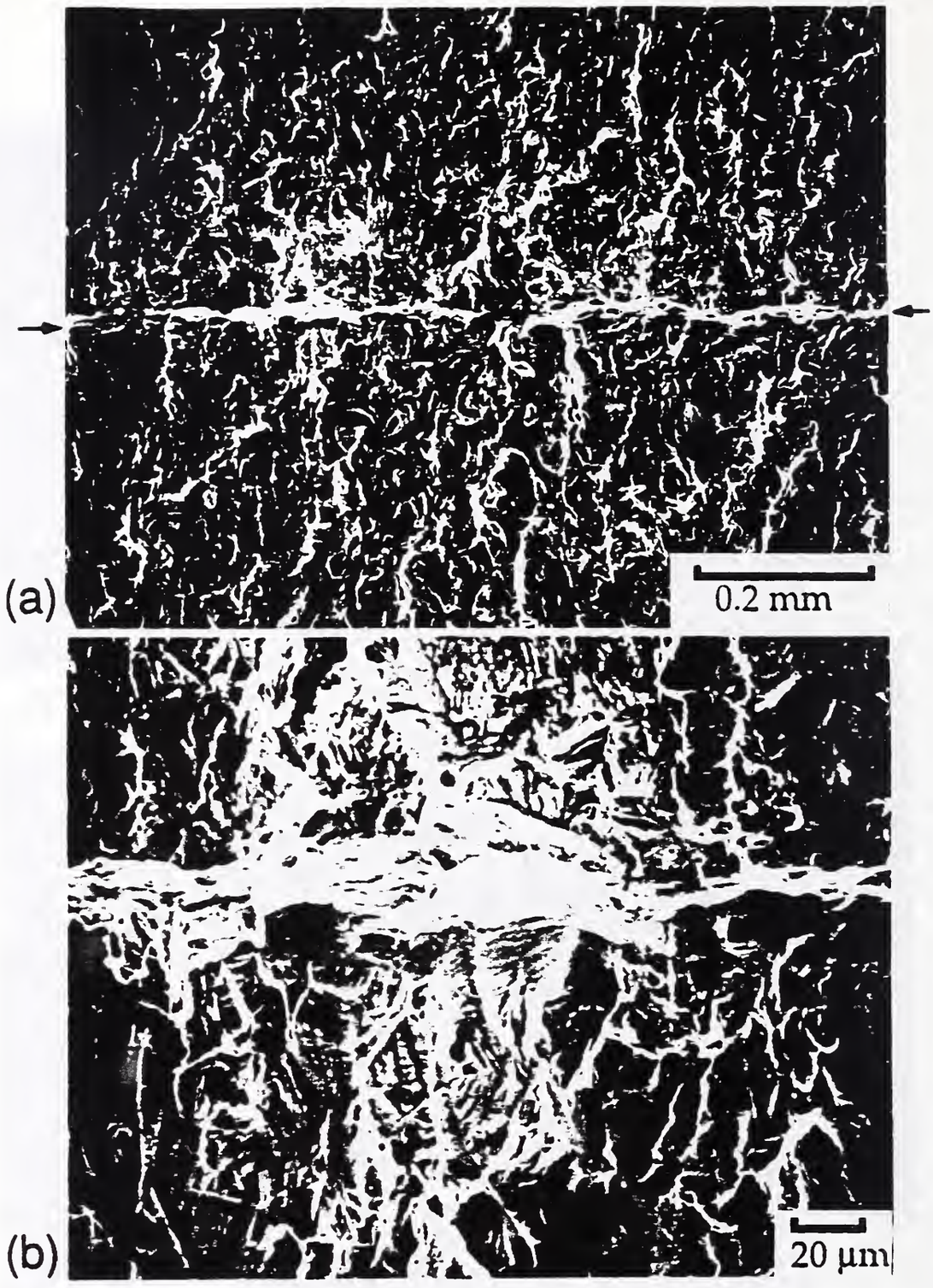

Figure 43. The fracture surface appearance of specimen AA-2 tested at 295 K. The SZ formed during the toughness test is marked with arrows.

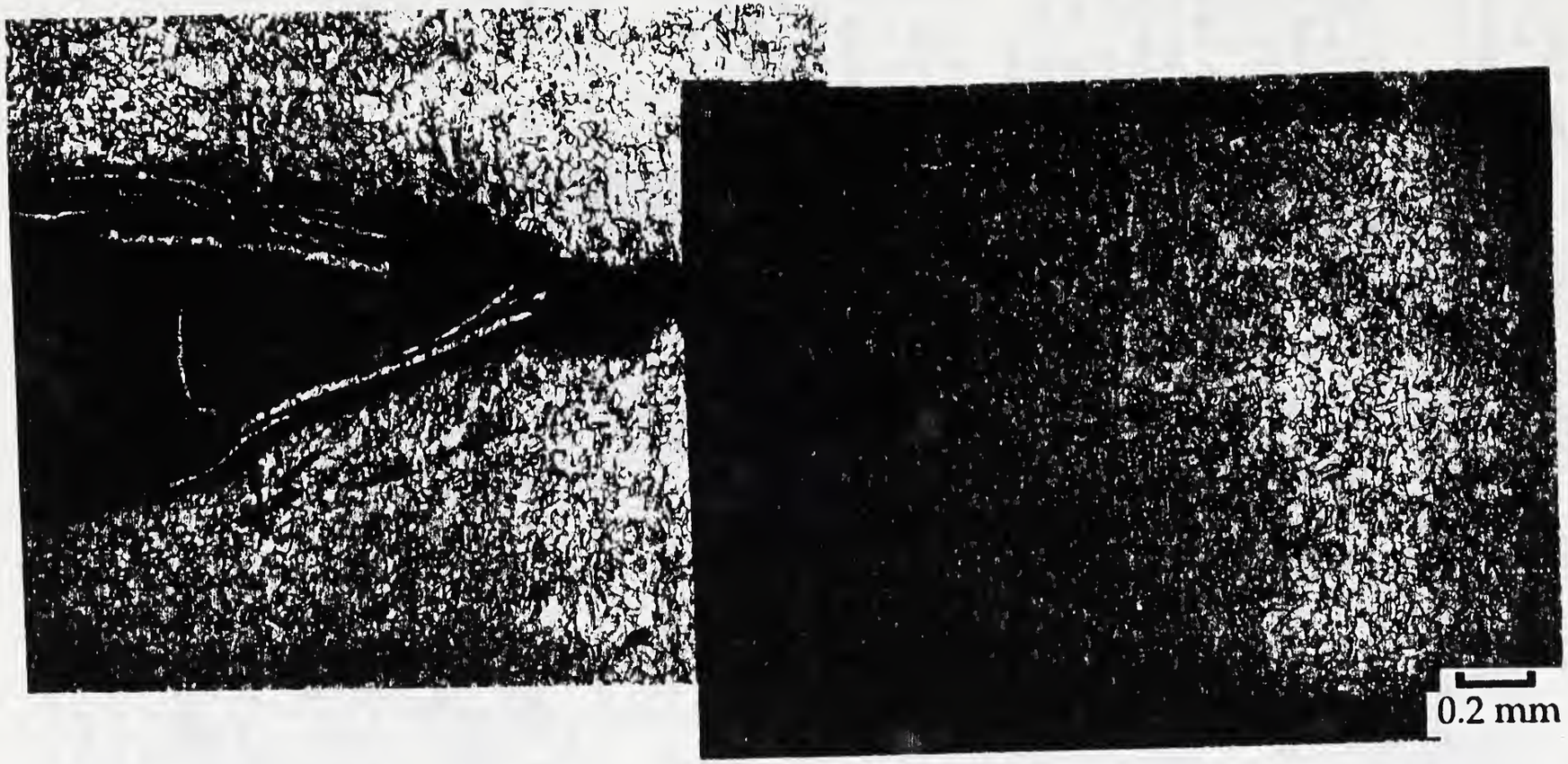

Figure 44. The cross section through compact specimen AA-1 tested at 295 K. Crack growth direction is left to right. Arrow denoted location of original fatigue precrack.

initial crack growth was directly ahead of the fatigue crack where the stress is a maximum. After about 1 mm of crack growth, the crack moved out of the plane of maximum stress, apparently to link up with neighboring voids that had formed ahead of the continuous crack tip.

The fracture surface from the second half of specimen AA-1 is shown in Fig. 45. The fatigue precrack features (the bottom of Fig. 47a) lead into the SZ, followed by the dimpled rupture features characteristic of MVC (at the top of Fig. 47a). At a higher magnification in Fig. 47b, the dimples show a variety of sizes and shapes. The larger, elongated dimples resemble the troughs observed on the fracture surface of uniaxial tension specimens tested at 295 K, see Fig. 27, which formed from the sigma phase. Between the elongated dimples, equiaxed dimples with varying size cover the rest of the surface. The equiaxed dimples nucleate at the submicrometer-size microalloy particles.

The ▲DPH around the crack tip of the three 295-K C(T) specimens examined above are shown in Fig. 46. The maximum value of ▲DPH is normally found next to the crack tip in each specimen and the maximum value does not change appreciably with orientation around the crack. The gradient in ▲DPH is sharper ahead of the crack than perpendicular to the crack plane. The ▲DPH decreases to a value between 20 and 40 at a distance of 2 to 3 times δ ahead of the crack tip. Perpendicular to the crack, the comparable ▲DPH are at a distance of 10 to 20 times δ.

The C(T) specimens from the interrupted tests at 295 K were wedged open so that the actual values of δ could be measured from the serial sectioning experiments. The measured values of δ for the interrupted tests were used to derive a rotation factor that would give the same values of δ calculated from Eq. 5. Table 7 shows the results of these calculations. For specimen AA-2 (interrupted near J_{Ic}), the calculate factor was 2.6, nearly equal to the standard value of 2.5. However, for the specimen interrupted at the lowest applied energy, AA-4, the calculated factor was 4.2.

The dominant micromechanism of crack growth in the triaxial stress state at 295 K is MVC. The plastic strains defined by DPH measurements associated with the ductile crack growth are distributed over large distances around the crack tip, 10 to 20 times δ, but the micromechanisms of crack growth are limited to a region directly ahead of and close to the crack tip, 1 to 3 times δ. The observa-

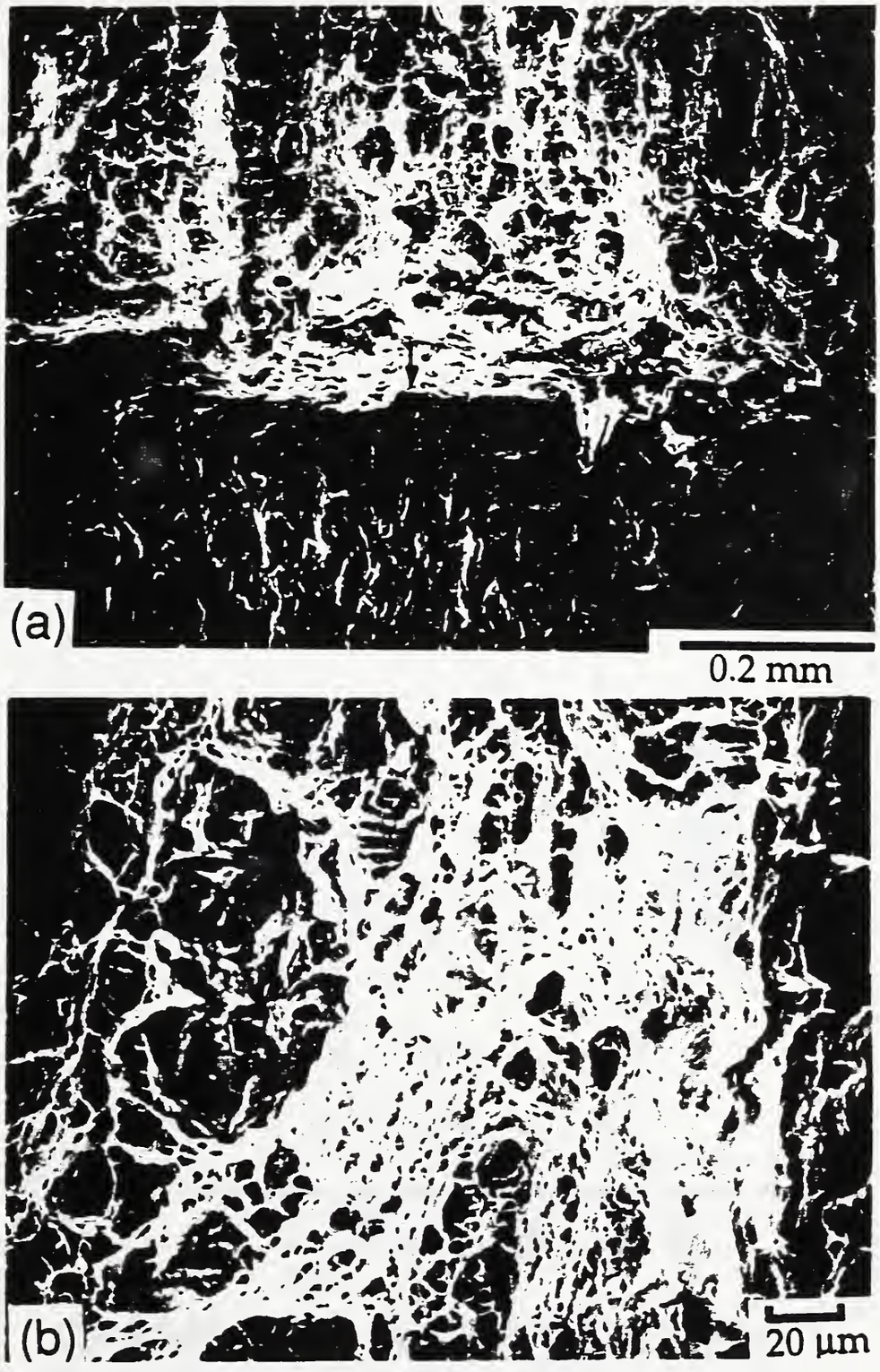

Figure 45. The fracture surface of compact specimen AA-1 tested at 295 K. The SZ is marked with arrows in the center of the part (a).

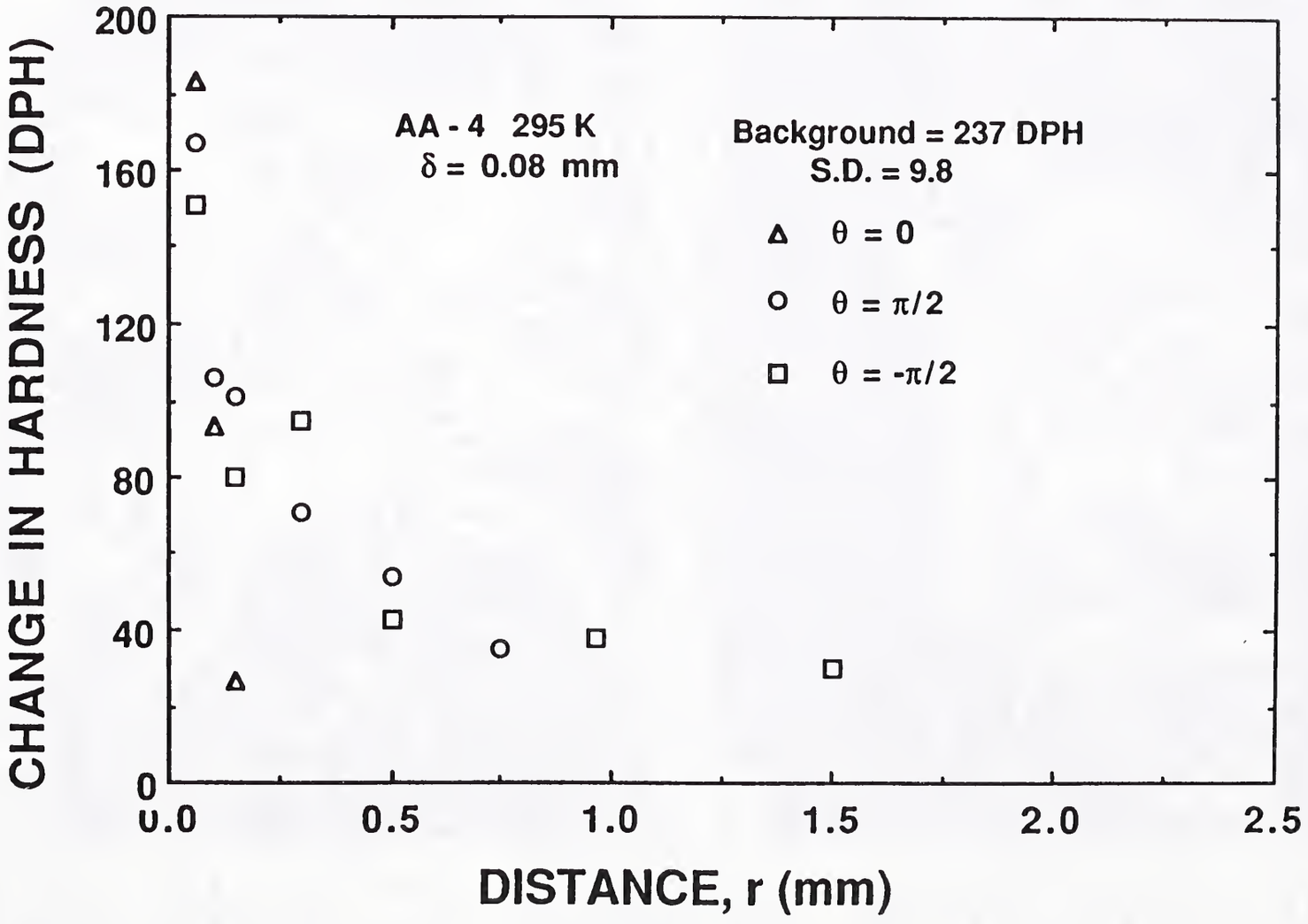

Figure 46a. The ▲DPH around the crack tip of specimen AA-4 tested at 295 K.

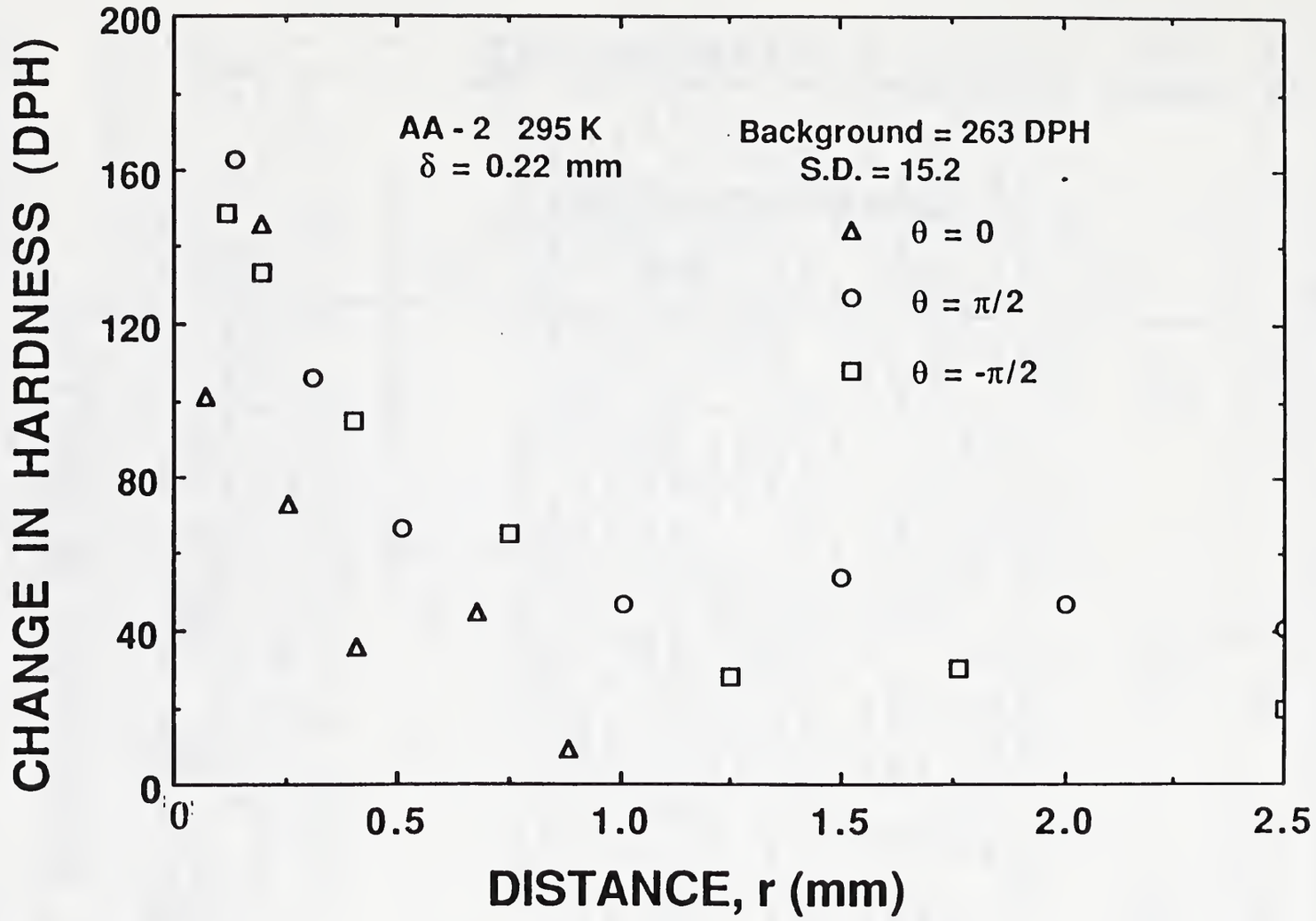

Figure 46b. The ▲DPH around the crack tip of specimen AA-2 tested at 295 K.

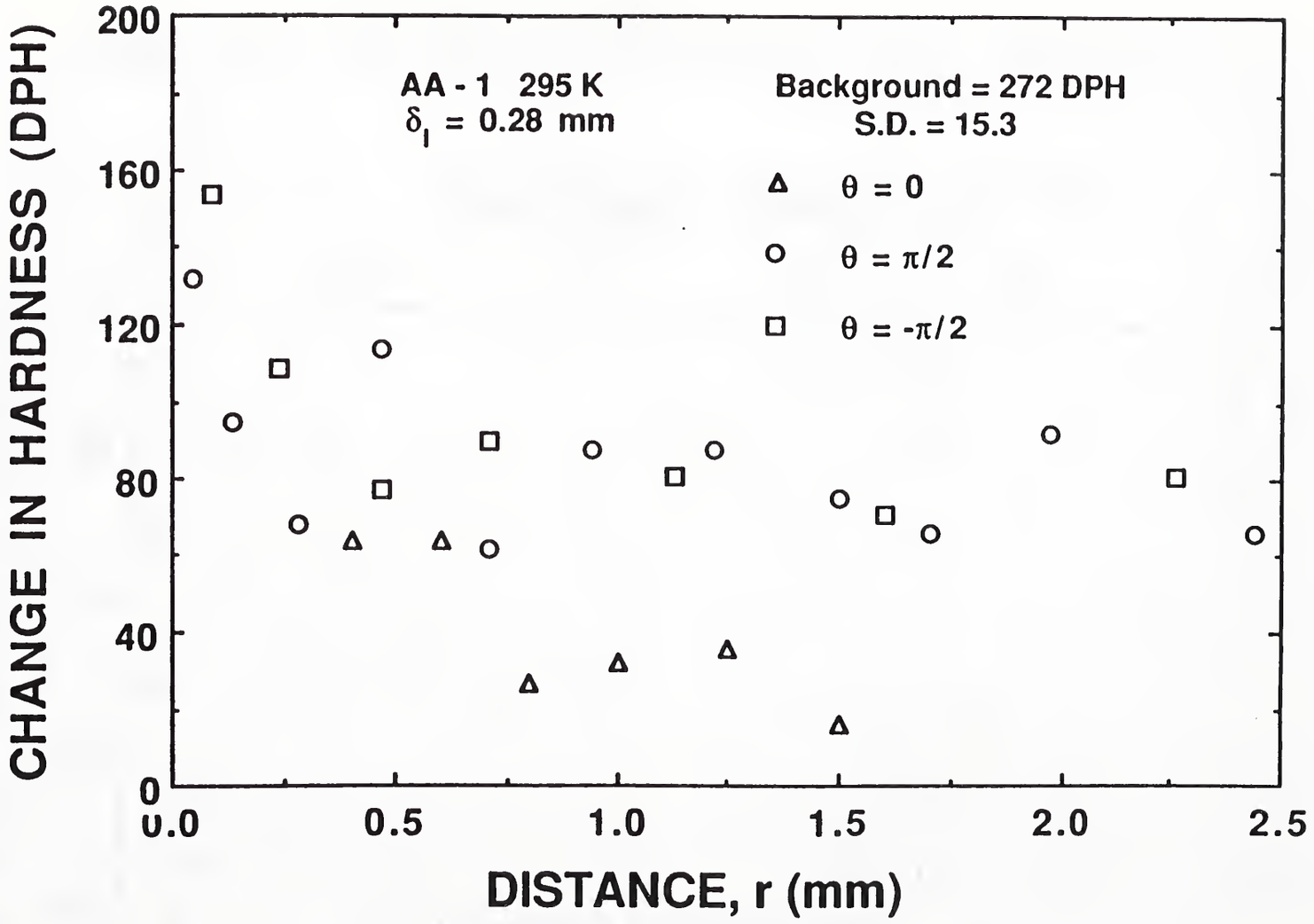

Figure 46c. The ▲DPH around the crack tip of specimen AA-1 tested at 295 K.

Table 7 The δ calculations for compact specimens tested at 295 K

Spec. #	δ (mm)	δ_s (mm)	δ_i (mm)	R_p(adj)
AA-2	0.22	0.06	0.16	2.6
AA-4	0.08	0.027	0.054	4.2

tions on the fracture surface (Fig. 45b) show that the first crack to grow from the fatigue precrack is associated with slip steps and not with MVC. The slip steps are characteristic of shear localization on the scale of the deformation bands observed in TEM (Fig. 39a). The microalloy particles are scattered randomly throughout the matrix with a spacing of 1 to 5 μm so there are numerous potential nucleation sites inside the PZ at 295 K, PZ = 80 μm for AA-4 and 440 μm for AA-2. The stress required to nucleate voids from the microalloy particles is higher than the local stress in the two interrupted tests, AA-4 and AA-2. At a higher applied energy and δ that must be approximately equal to the average J_{Ic} value for the room temperature tests, the local stress exceeds the value of σ_c for the microalloy particles. The value of σ_c for nucleation from sigma phase is lower than that for nucleation at the microalloy particles, but the distribution of the weaker sigma particles is such that the probability of finding a particle of sigma in the PZ is small.

4.7.2 Liquid nitrogen tests

For the C(T) specimens tested at cryogenic temperature, a wedge could not be used to keep the crack tip open after unloading and sample preparation. The elastic component of δ is lost on unloading and the observed δ is less than the actual value of δ during the test. The value of δ for all low-temperature C(T) specimens was calculated from Eq. 7 with a rotational factor of 3.0, a compromise value in-between the two values calculated from the 295-K results.

At the next lower temperature (76 K), specimen AAA-5 was interrupted at the transition from small-scale yielding to large-scale yielding; see Fig. 23. The polished and etched profile of the crack-tip region is shown in Fig. 47.

The calculated value of δ was 20 μm and compared favorably to the measured value of δ from Fig. 47. The fatigue precracked surface profile shows slight undulations and occasional branching, suggesting a crystallographic nature to fatigue crack growth. The crack tip does not appear rounded, but blunted to a sharp corner.

At a higher applied energy, specimen AAA-4 was interrupted near J_{Ic}. One profile through the blunted, crack-tip region is shown in Fig. 48. The calculated value of δ has increased to 74 μm. A short crack is present at this point in the toughness test. The new crack that has formed ahead of the blunted fatigue crack is sharp with a value of δ of about 5 μm. Another section from AAA 4 is shown in Fig. 49. Voids, 10 to 20 μm in diameter, are associated with the short crack in this section. Higher ▲DPH values were associated with regions of cracking and void growth like Fig. 49 compared to the ▲DPH found in Fig. 48.

The fracture surface appearance of the other half of AAA-4 is shown in Fig. 50. At the lower magnification (Fig. 50a), a SZ is difficult to distinguish from the fatigue pre- and post-cracking features. In an isolated region along the crack front, a large, 20 μm, void has opened up with smaller, 2 to 5 μm, dimples surrounding the cavity. Presumably, this is a result of the nonuniform distribution of sigma phase in the matrix.

The profile from a completed test, AAA-2, in which the average crack growth was 2.0 mm, is shown in Fig. 51. The location of the original fatigue precrack is shown by the arrow. The apparent δ_i from this picture is 0.12 mm. The δi calculated from equation 7 is 156 μm. The crack growth direction is predominantly straight ahead of the crack tip, but does take discrete jumps out of the plane of maximum stress. The crack tip remains relatively sharp at the end of crack growth with a δ of about 15 μm.

The fracture surface from the second half of C(T) AAA-2 is shown in Fig. 52. The dimples are more or less spherical in shape, but the size varies from submicrometer to 25-30 μm in diameter. The large, elongated dimples are present, but are not as prominent as those found in Fig. 45 for the fracture surface of the C(T) tested at 295 K.

The deformed zones measured around the crack tip in the 76-K specimens are shown in Fig. 53. Again, the maximum ▲DPH directly ahead of the crack tip is similar to the

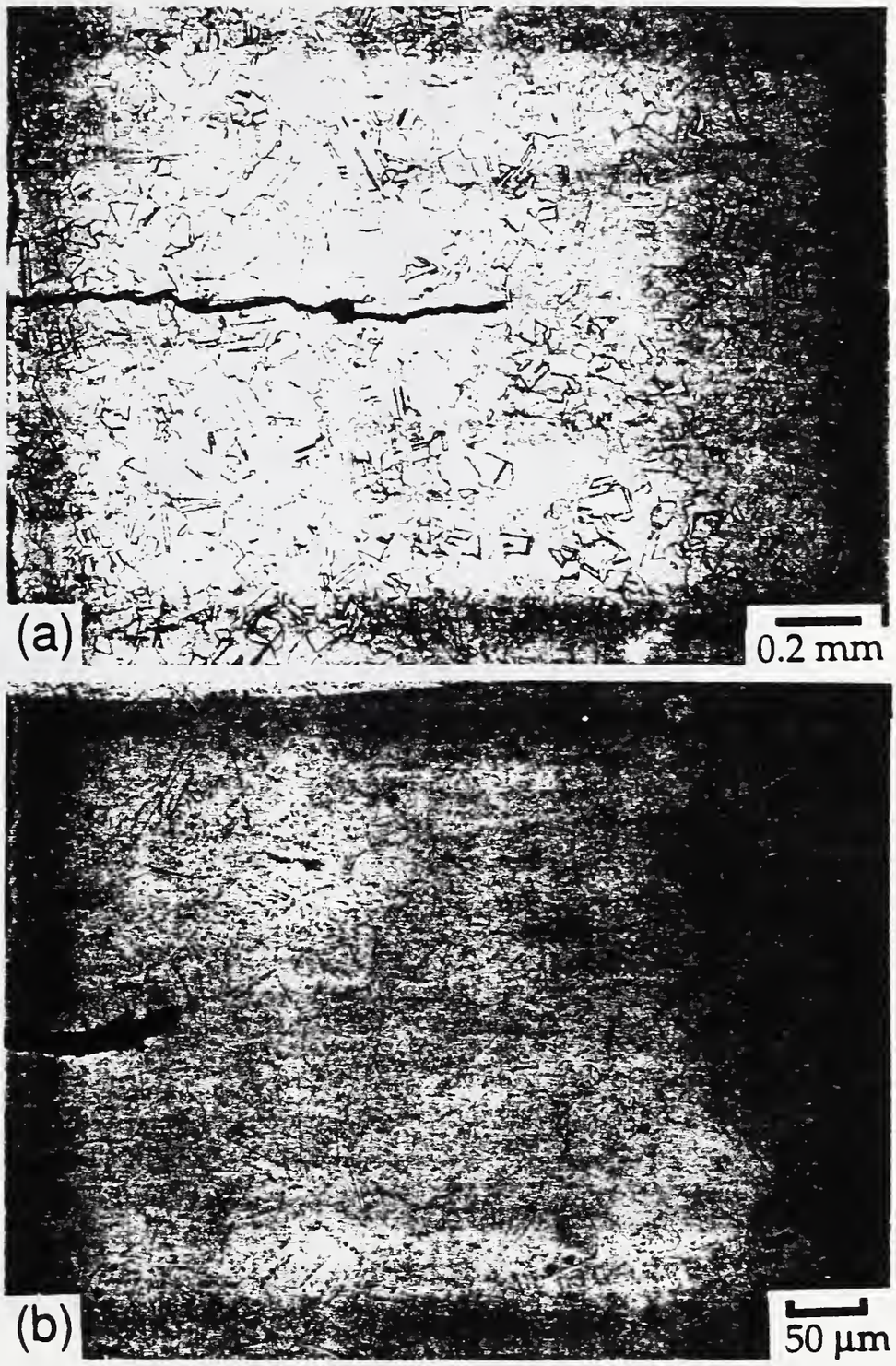

Figure 47. The cross section through compact specimen AAA-5 tested at 76 K. Crack growth direction is left to right.

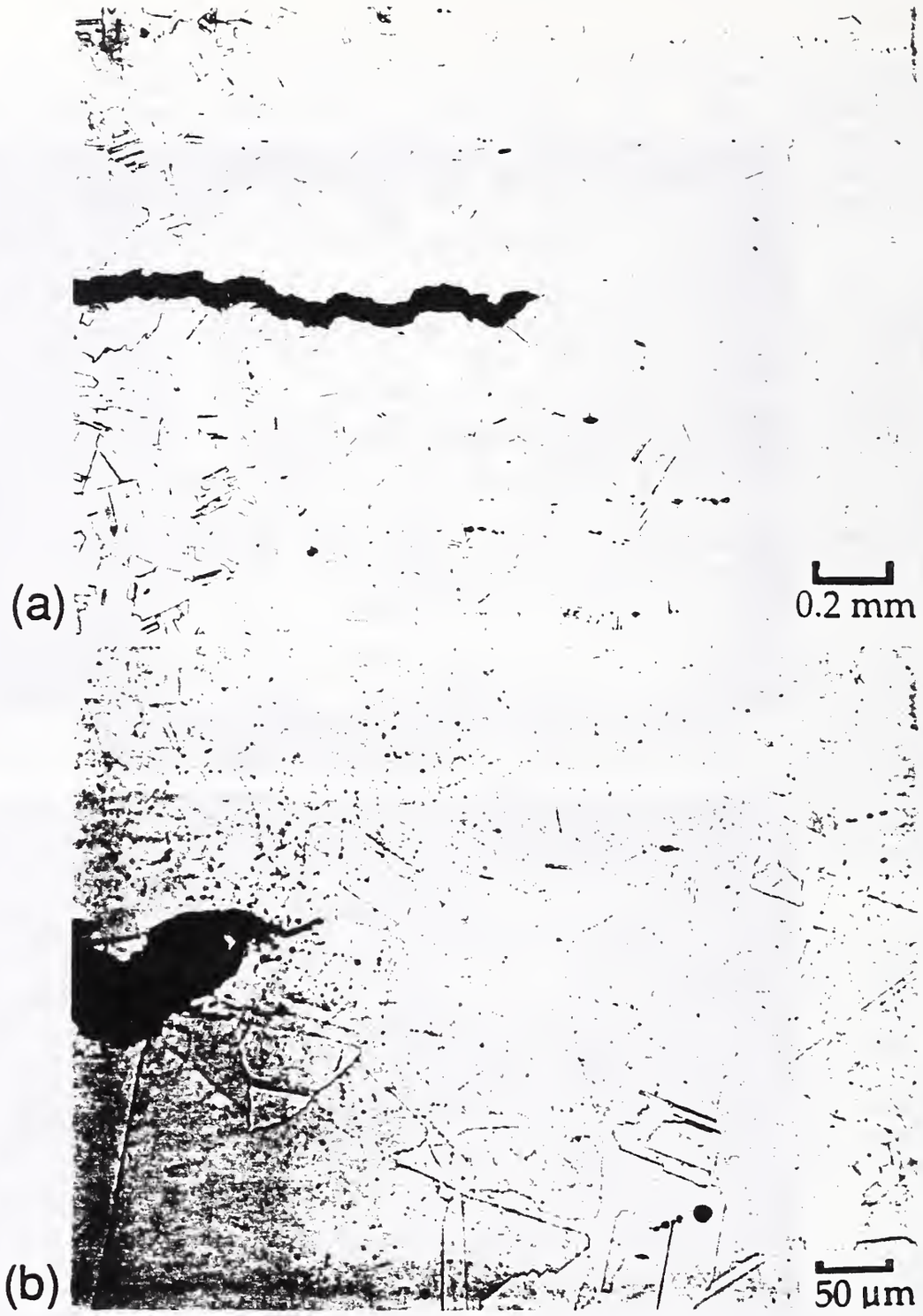

Figure 48. The cross section through compact specimen AAA-4 tested at 76 K. Crack growth direction is left to right.

Figure 49. A second cross section through compact specimen AAA-4 tested at 76 K.

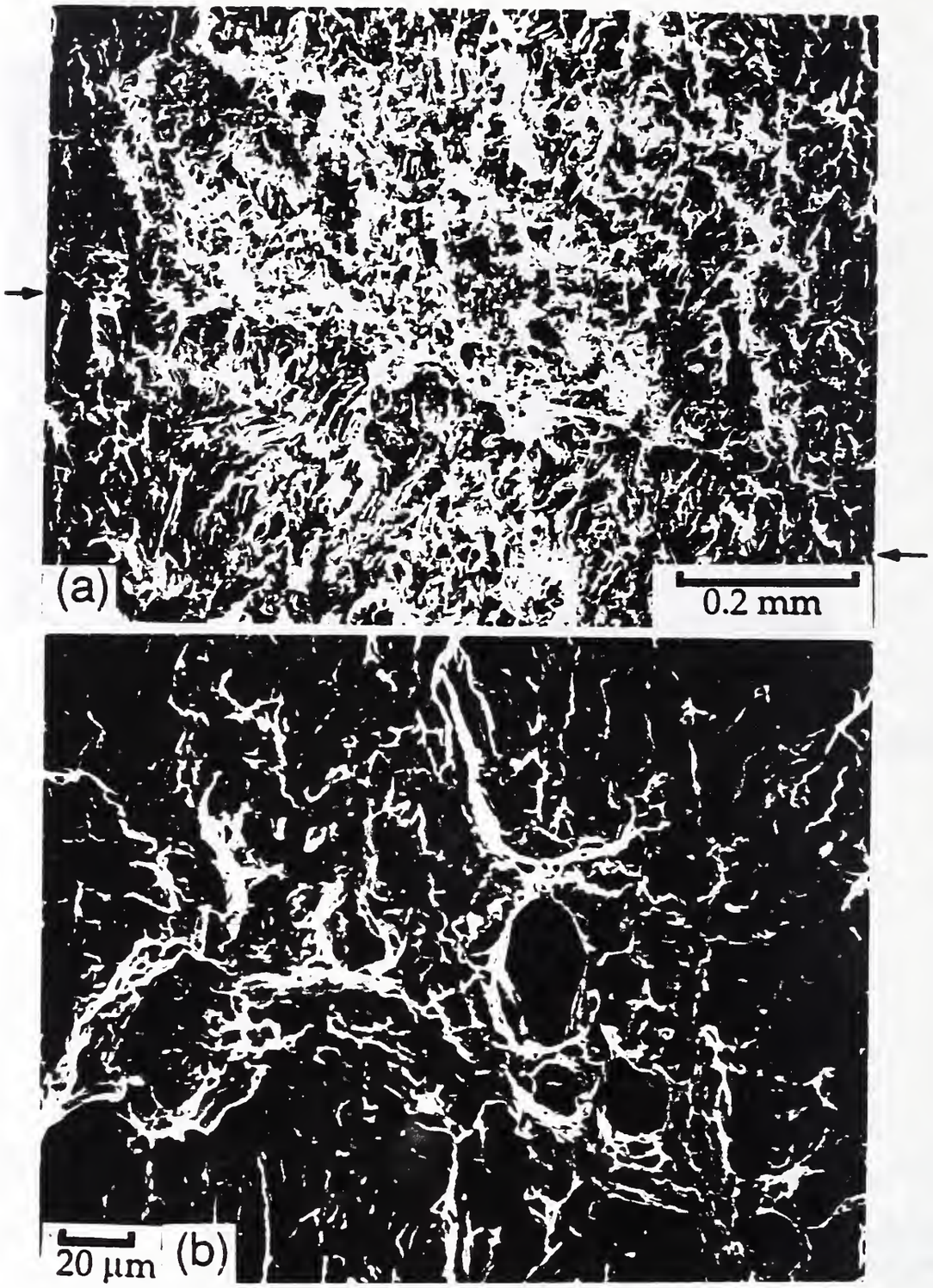

Figure 50. The fracture surface appearance of compact specimen AAA-4 tested at 76 K. Crack growth direction is bottom to top.

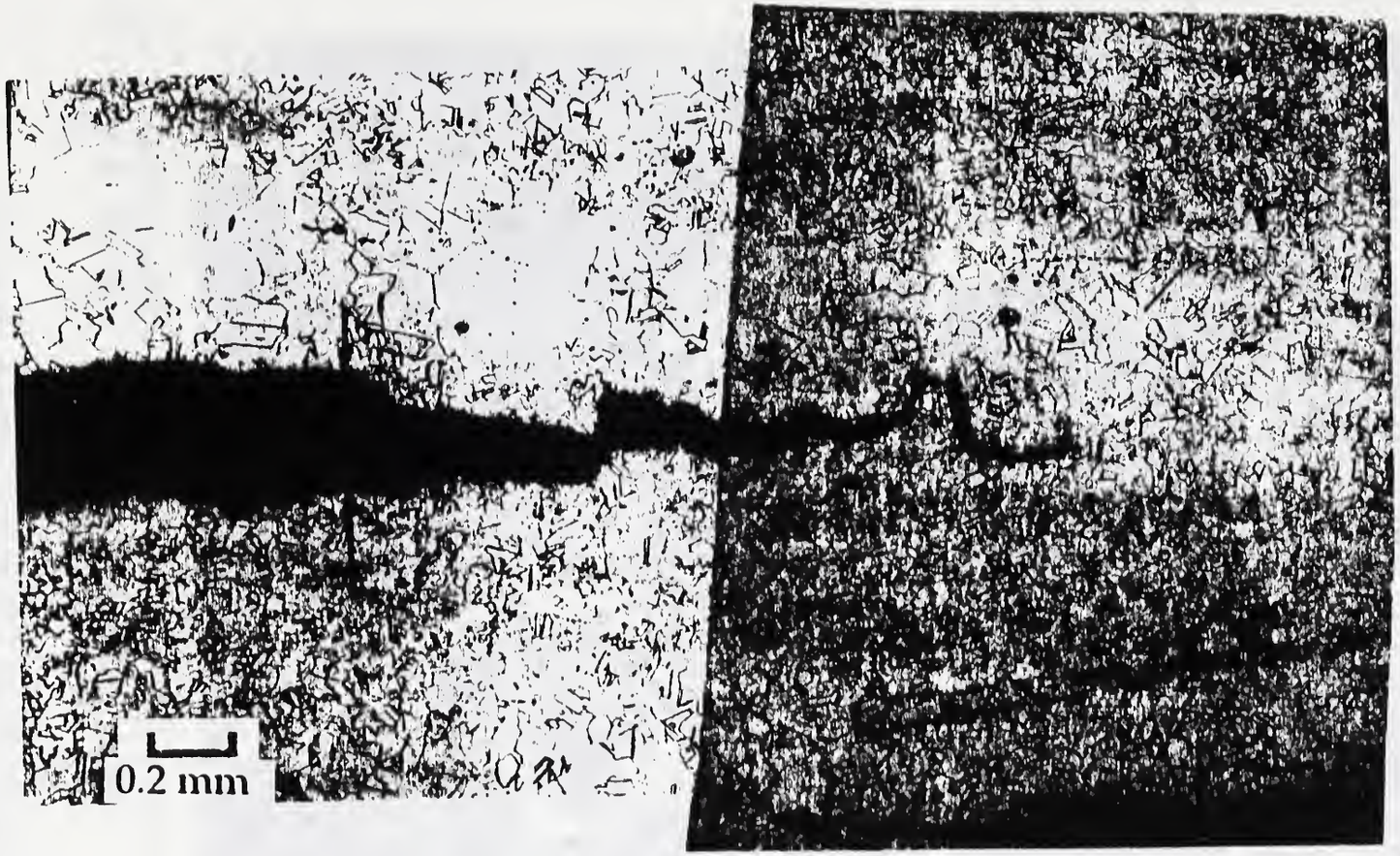

Figure 51. The cross section through compact specimen AAA-2 tested at 76 K. Arrow denoted location of original crack tip.

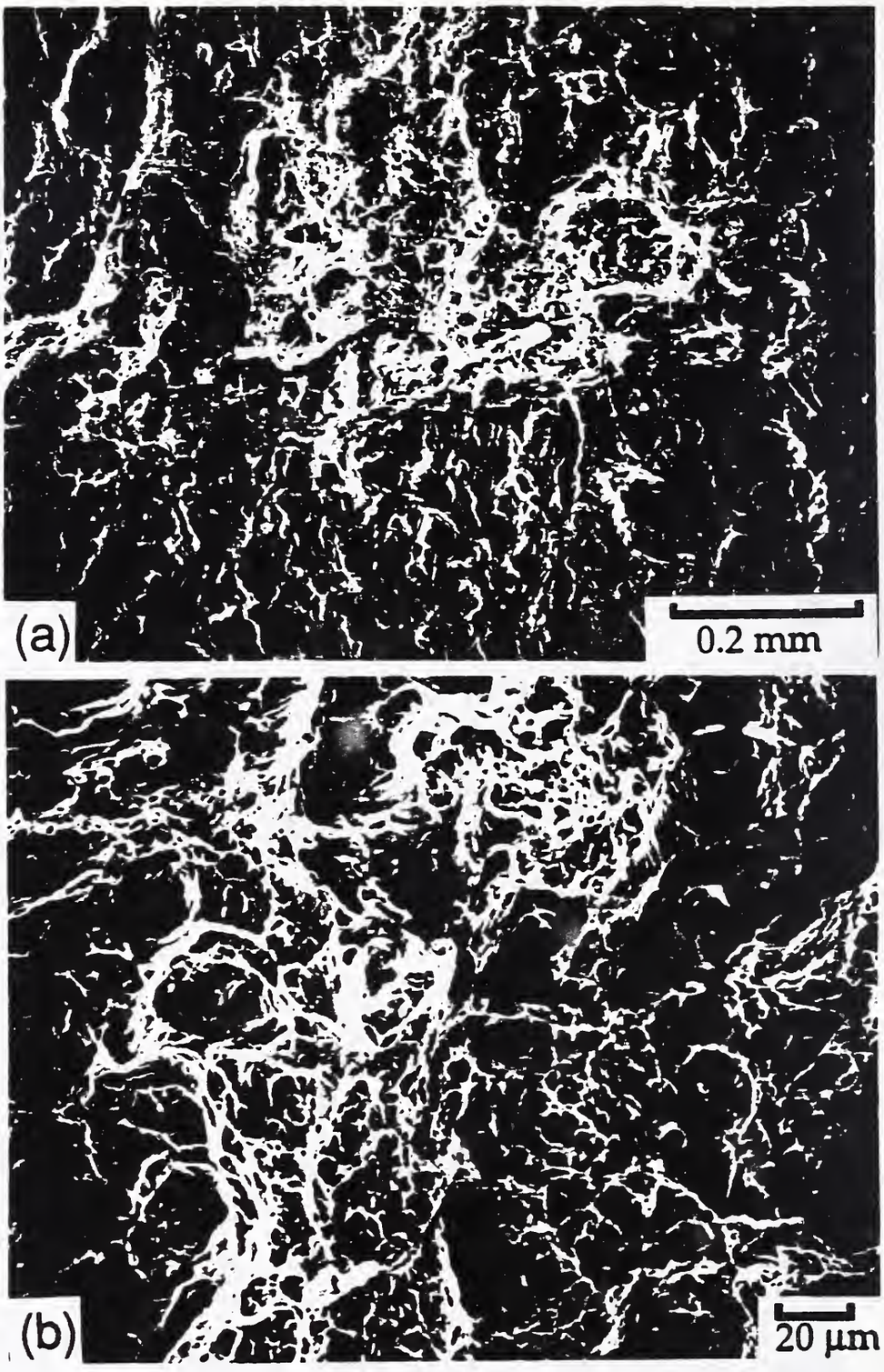

Figure 52. The fracture surface appearance of specimen AAA-2 tested at 76 K. Crack growth direction is bottom to top.

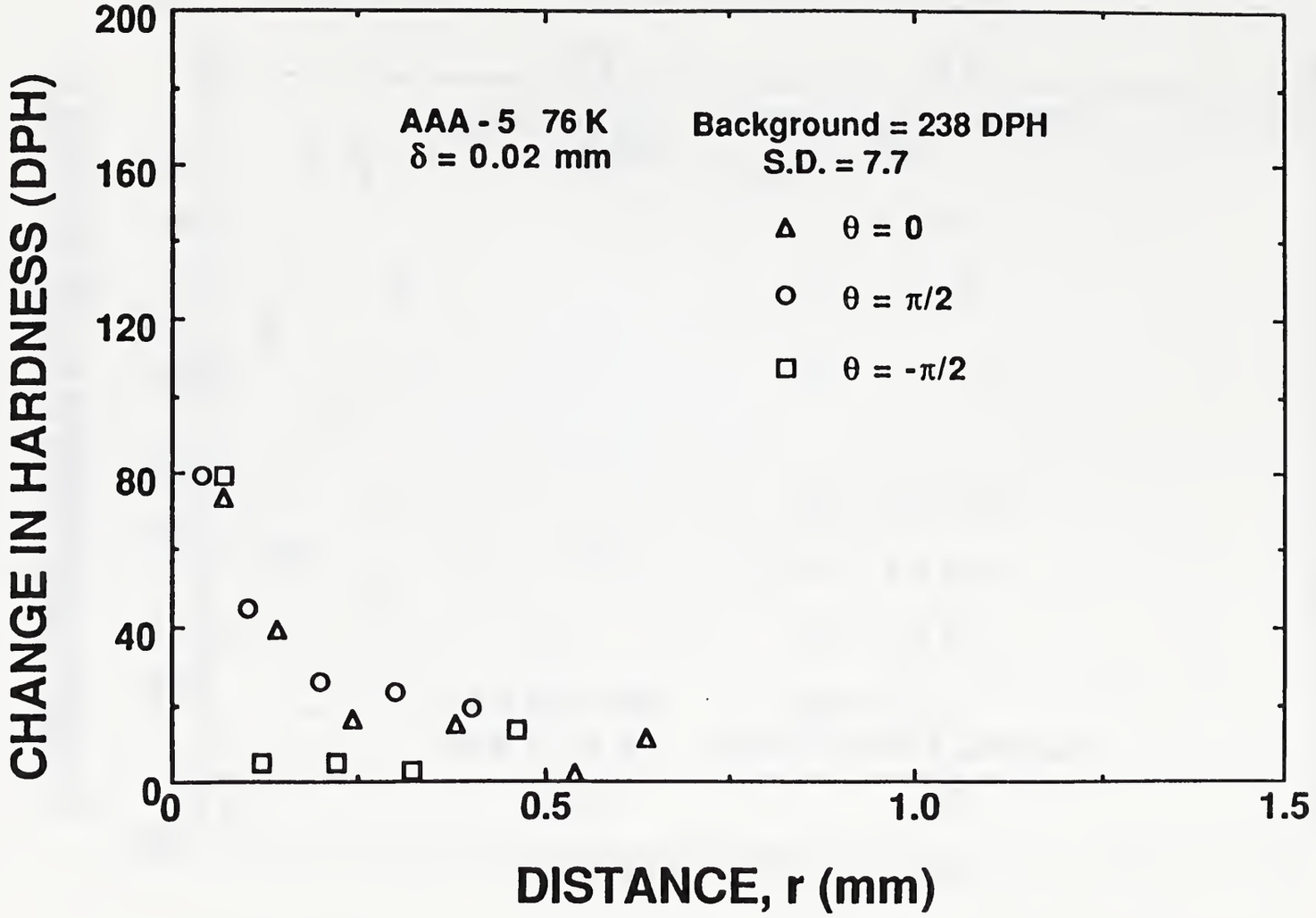

Figure 53a. The ▲DPH around the crack tip of specimen AAA-5 tested at 76 K.

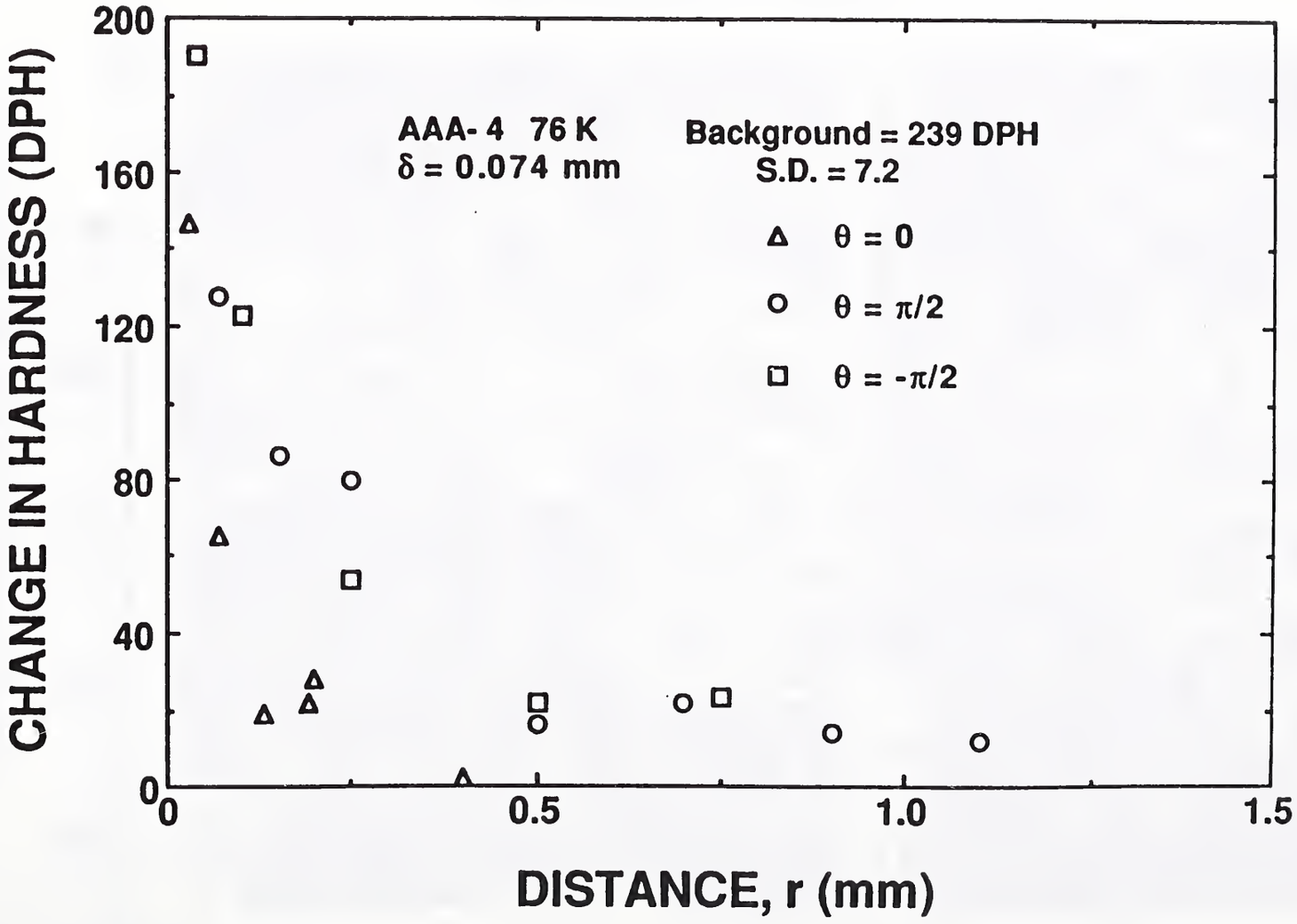

Figure 53b. The ▲DPH around the crack tip of specimen AAA-4 tested at 76 K.

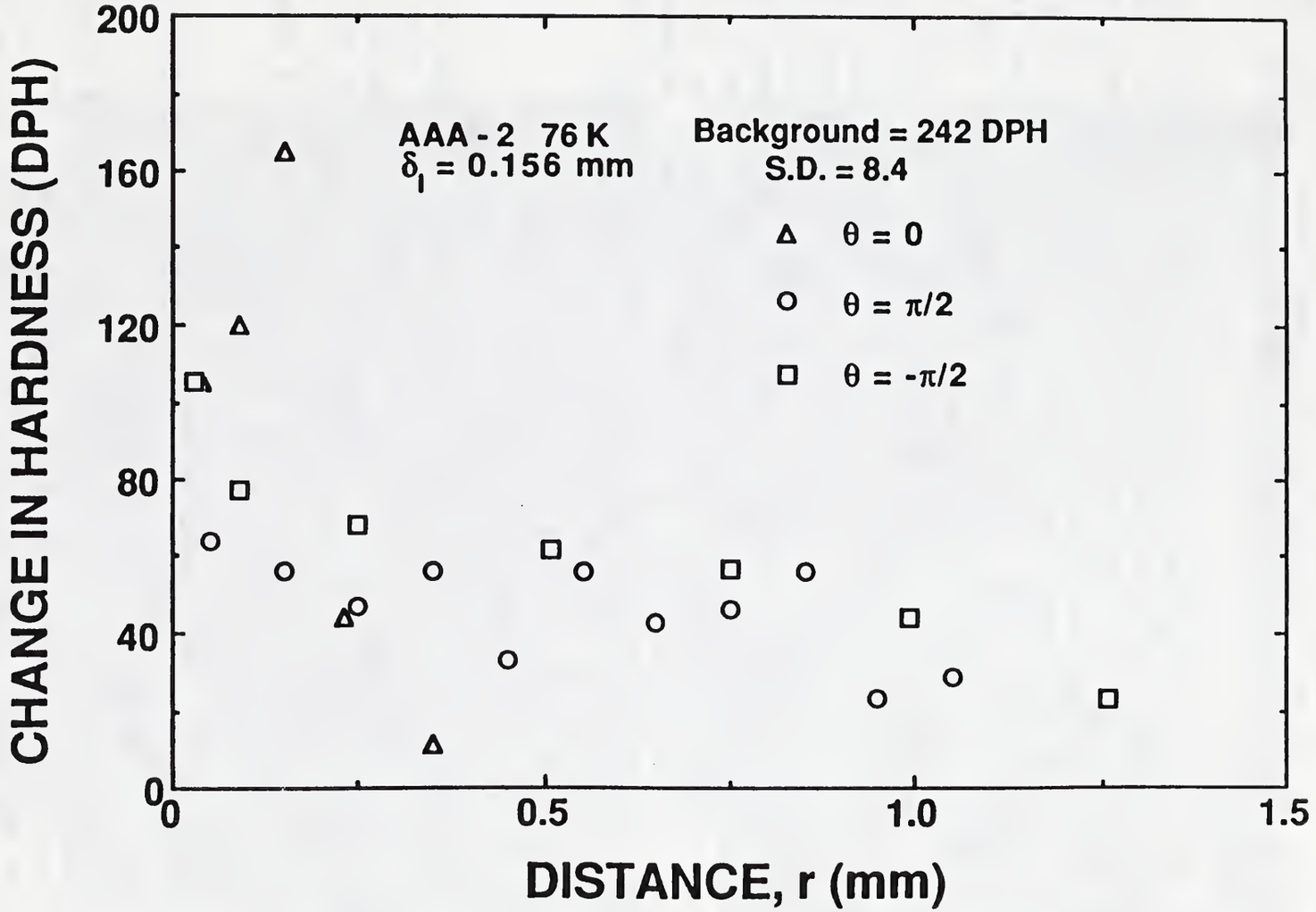

Figure 53c. The ▲DPH around the crack tip of specimen AAA-2 tested at 76 K.

maximum value perpendicular to the tip, but the deformed zone is larger perpendicular to the crack. Directly ahead of the crack, the deformed zone is approximately twice the value of δ for each respective specimen. The deformed zone directly ahead of the tip in specimen AAA-2 (Fig. 53c) does not show the smooth exponential decrease observed in other specimens.

The micromechanisms of fracture in toughness testing at 76 K are different than those observed at 295 K. No SZ was observed between the fatigue precracked and post-cracked regions. The dominant features associated with the toughness test on the fracture surface are small, 2 to 5 μm dimples nucleated from microalloy particles. The local stress due to the applied energy for AAA-5 was less than σ_c for void nucleation from microalloy particles. With the higher applied energy for specimen AAA-4, the local stresses were high enough to form a crack close to the tip in the PZ. Isolated voids from microalloy particles are not visible ahead of the crack tip. Once the critical stress for void nucleation was reached, the voids formed a crack without additional applied energy. However, the stresses at the edge of the PZ were not high enough to nucleate voids. With higher applied energy, taken to be equal to the average J_{Ic} value for AAA-1, AAA-2, and AAA-3, the local stresses ahead of the PZ exceeded σ_c for nucleation from the microalloy particles and the crack advanced through the PZ.

4.3.10 C(T) specimens at 4 K

The specimen interrupted at the lowest load is specimen A-11, see Fig. 24. The applied energy at this point is less than J_{Ic} for any of the completed tests. The crack-tip profile is shown in Fig. 54. The crack tip has a very small value of δ, about 7 μm measured from the picture. The calculated value of δ was 2 μm. No evidence of damage was observed at magnifications at high as 1000x.

Specimen A-10 was tested to an applied energy above J_{Ic} for LO-4K specimens, but less than J_{Ic} for the HI-4K specimens; see Fig. 24. The profile from the blunted crack tip of A-11 is shown in Fig. 55. The crack has blunted to a square shape. The calculated δ was 36 μm. The δ observed in the picture is similar to that observed for A-11 in Fig. 54. A maximum of 0.11 mm crack growth was observed ahead of the crack tip. The crack growth is directly ahead of the fatigue precrack.

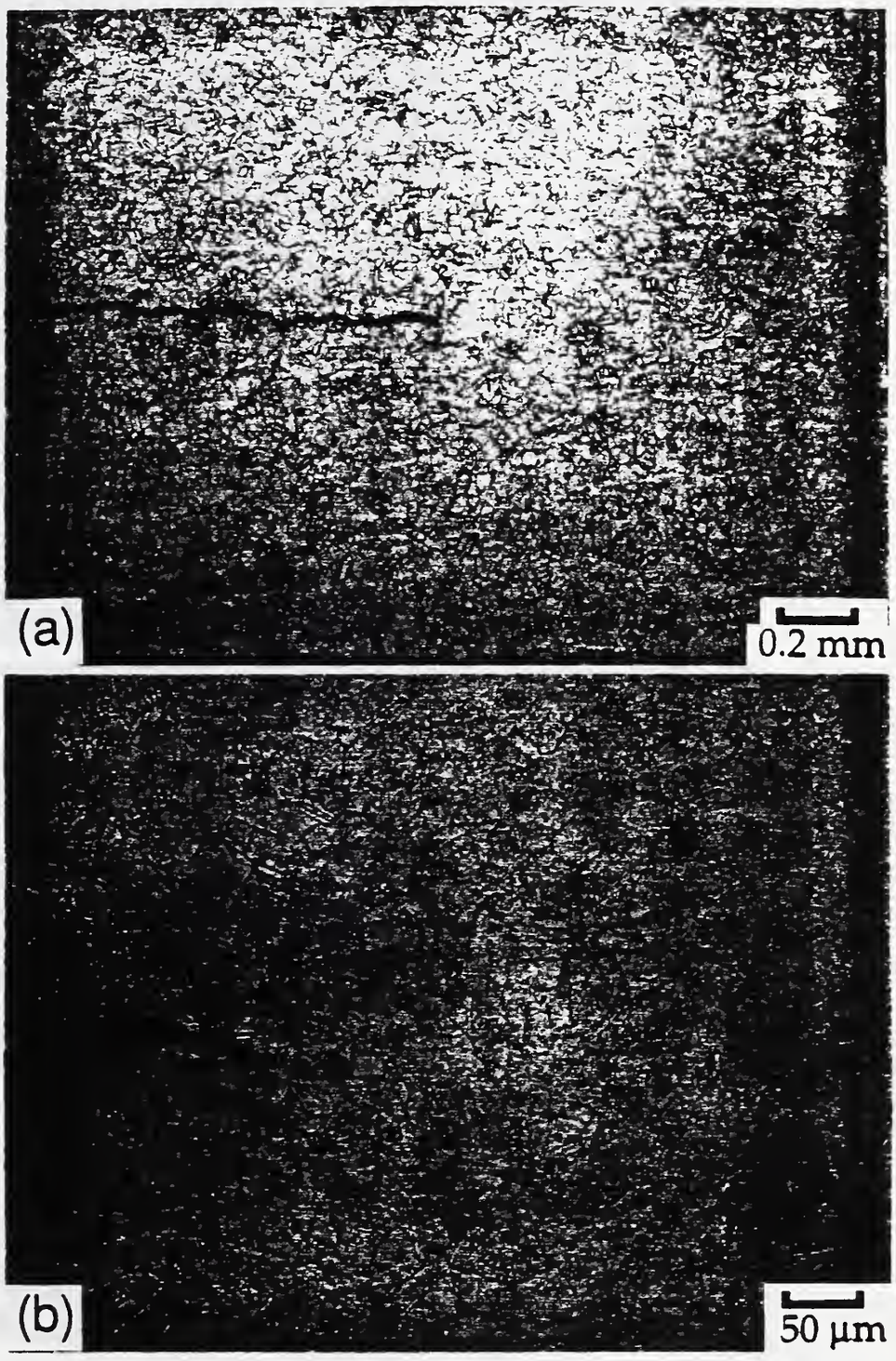

Figure 55. The cross section through compact specimen A-10 tested at 4 K with T-L orientation.

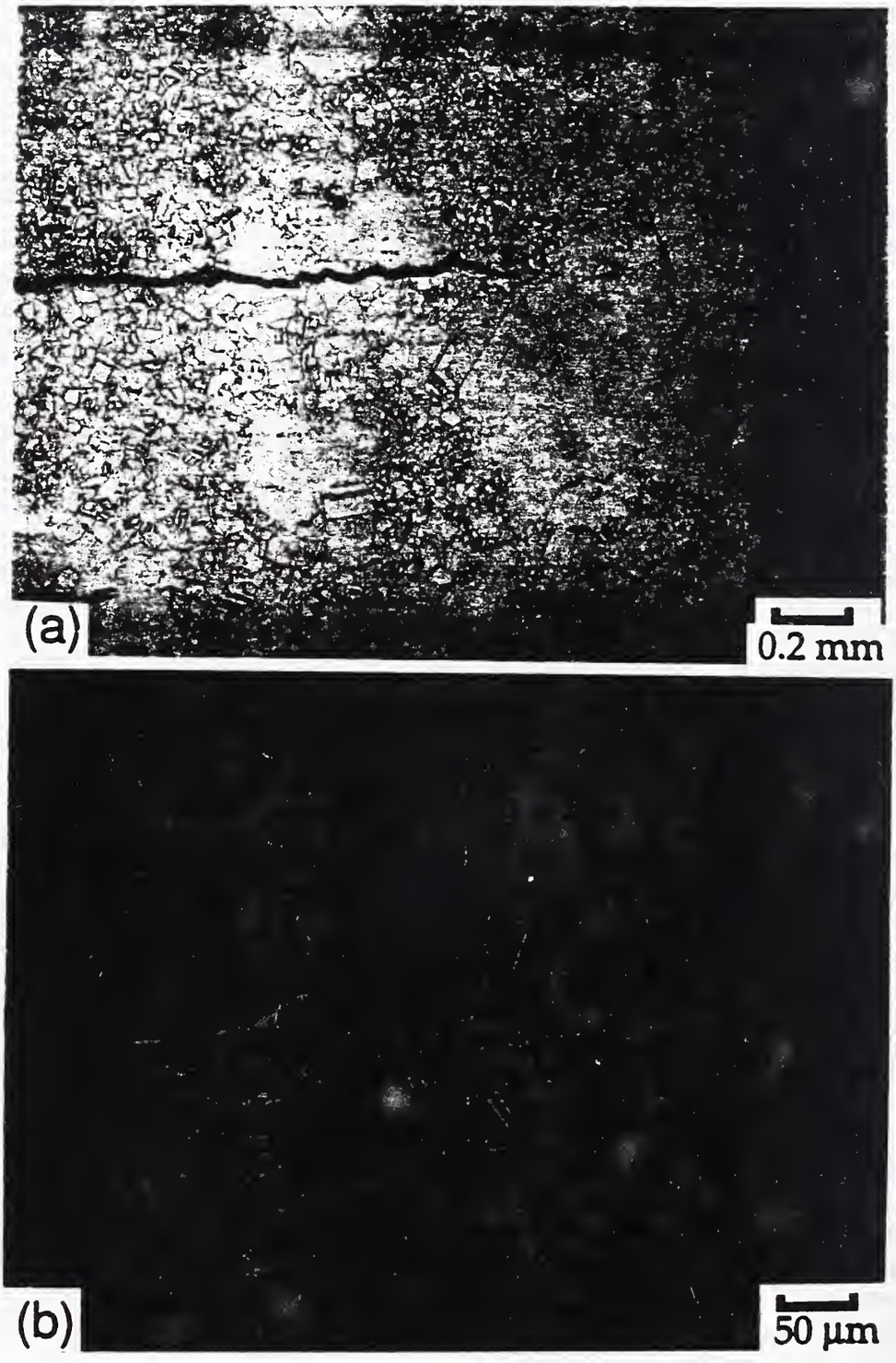

Figure 54. The cross section through compact specimen A-11 tested at 4 K with T-L orientation.

The fracture surface from the second half of A-10 is shown in Fig. 56. A thin, discontinuous ribbon of material created during the test is visible between the fatigue precrack on the bottom and the post-crack on the top. At higher magnification (Fig. 56b), the fracture surface created during toughness testing is made up of small dimples, 2 to 5 μm diameter. The fatigue precrack just below the MVC features exhibits a dispersion of small particles on the fatigue features.

A specimen tested to a crack growth of about 2 mm from the LO-4K test group was sectioned for observation. The crack-tip region from specimen A-4 is shown in Fig. 57. The approximate position of the original crack-tip is indicated by the arrow. The profile of the growing crack is similar to the appearance of fatigue crack growth profile.

The scatter measured in the 4-K specimens during testing was not attributable to differences on the fracture surface of the specimens. A representative area from the fracture surface of a LO-4K specimen is shown in Fig. 58. The typical appearance of the fracture surface of a HI-4K specimen is shown in Fig. 59. A SZ is not visible in either Figs. 58 or 59 between the fatigue precrack and dimpled rupture features of MVC. The dimpled rupture features for Figs. 58 and 59 are similar. The larger, 20 to 30 μm dimples are elongated in the crack growth direction and are surrounded by smaller, 1 to 2 μm, equiaxed dimples. There were no systematic differences in fracture appearance between T-L specimens that could be related to J_{Ic} at 4 K.

The fracture surface of the L-T specimens tested at 4 K were significantly different from the surfaces of the T-L specimens. Figure 60 shows the fracture surface appearance of specimen L-T 2. Dimples as large as 50 μm in diameter are observed surrounded by smaller, 2 to 20 μm diameter dimples. The overall features have a more equiaxed appearance than those found in Figs. 58 and 59 for the T-L specimens. The difference in fracture appearance between T-L and L-T specimens at 4 K was not reflected by the toughness; see Fig. 26.

The deformed zones around the crack tip of specimens A-10, A-11, and A-4 are shown in Fig. 61. The maximum value of ▲DPH around the crack tip is about 80, smaller than the maximum value of 160 to 200 measured at 76 K (Fig. 53). At 4 K, the deformed zone ahead of the crack tip is spread over

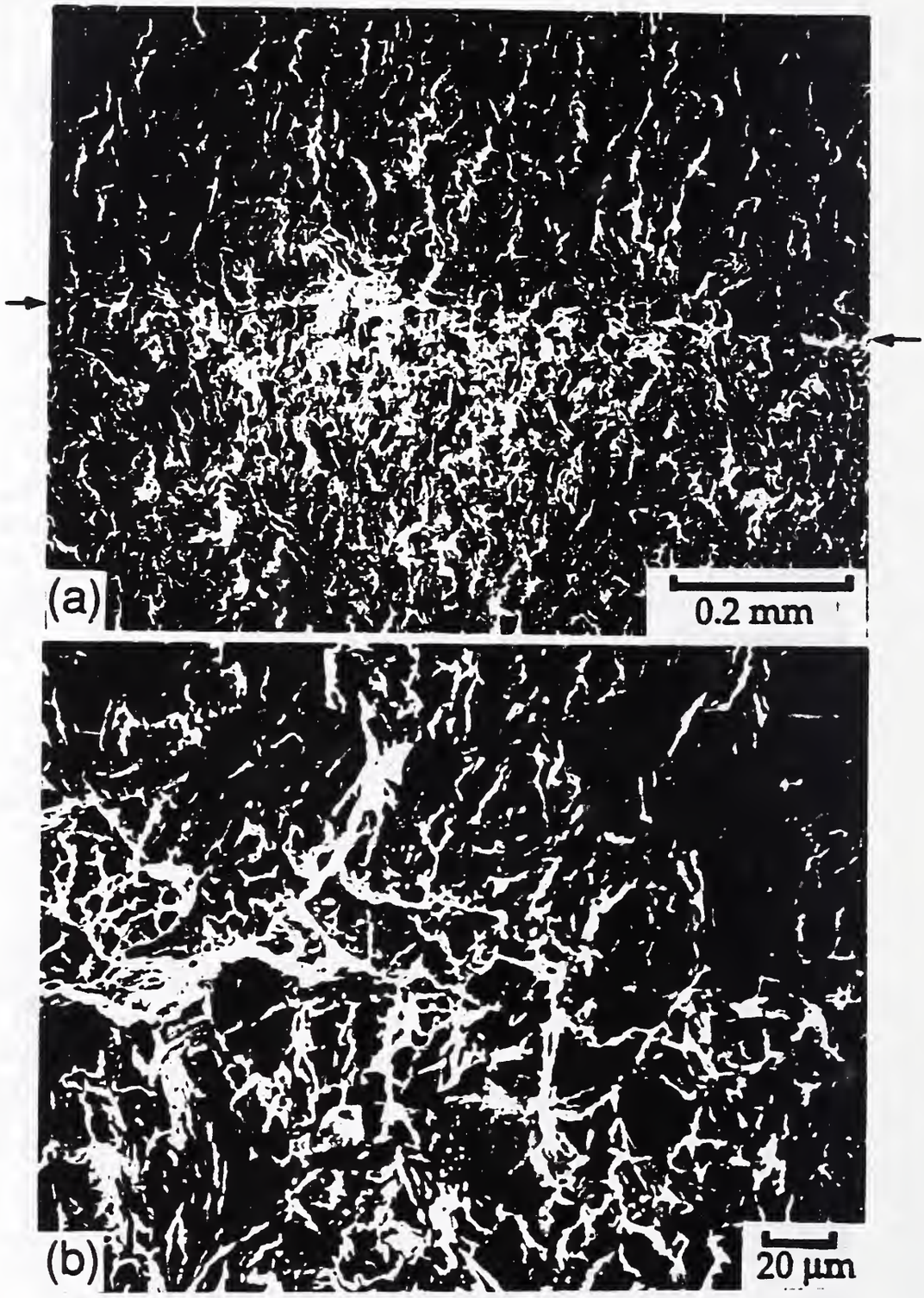

Figure 56. The fracture surface of compact specimen A-10 tested at 4 K with T-L orientation. Arrows mark the original fatigue crack tip.

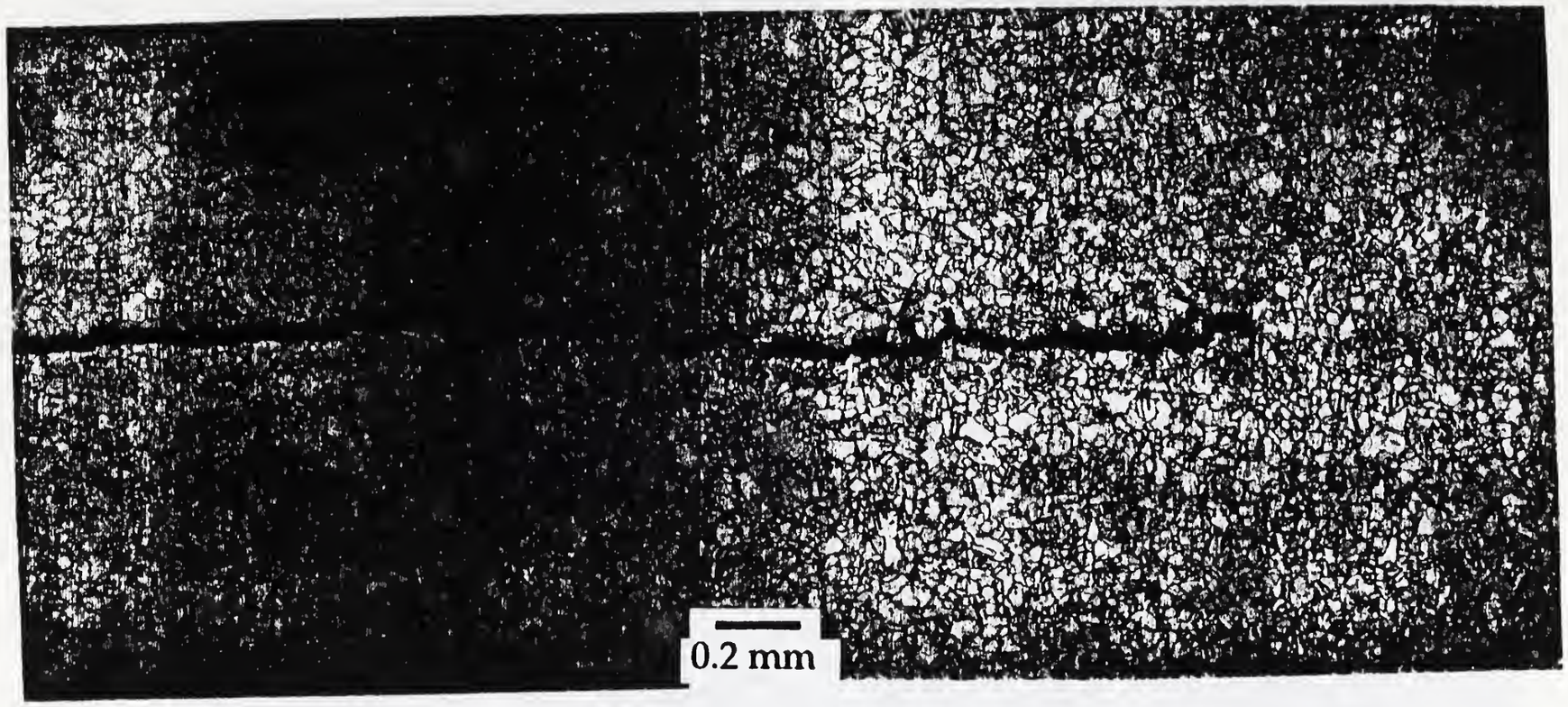

Figure 57. The cross section through compact specimen A-4 (LO-4K) tested at 4 K with T-L orientation. Arrow shows approximate location of original fatigue precrack.

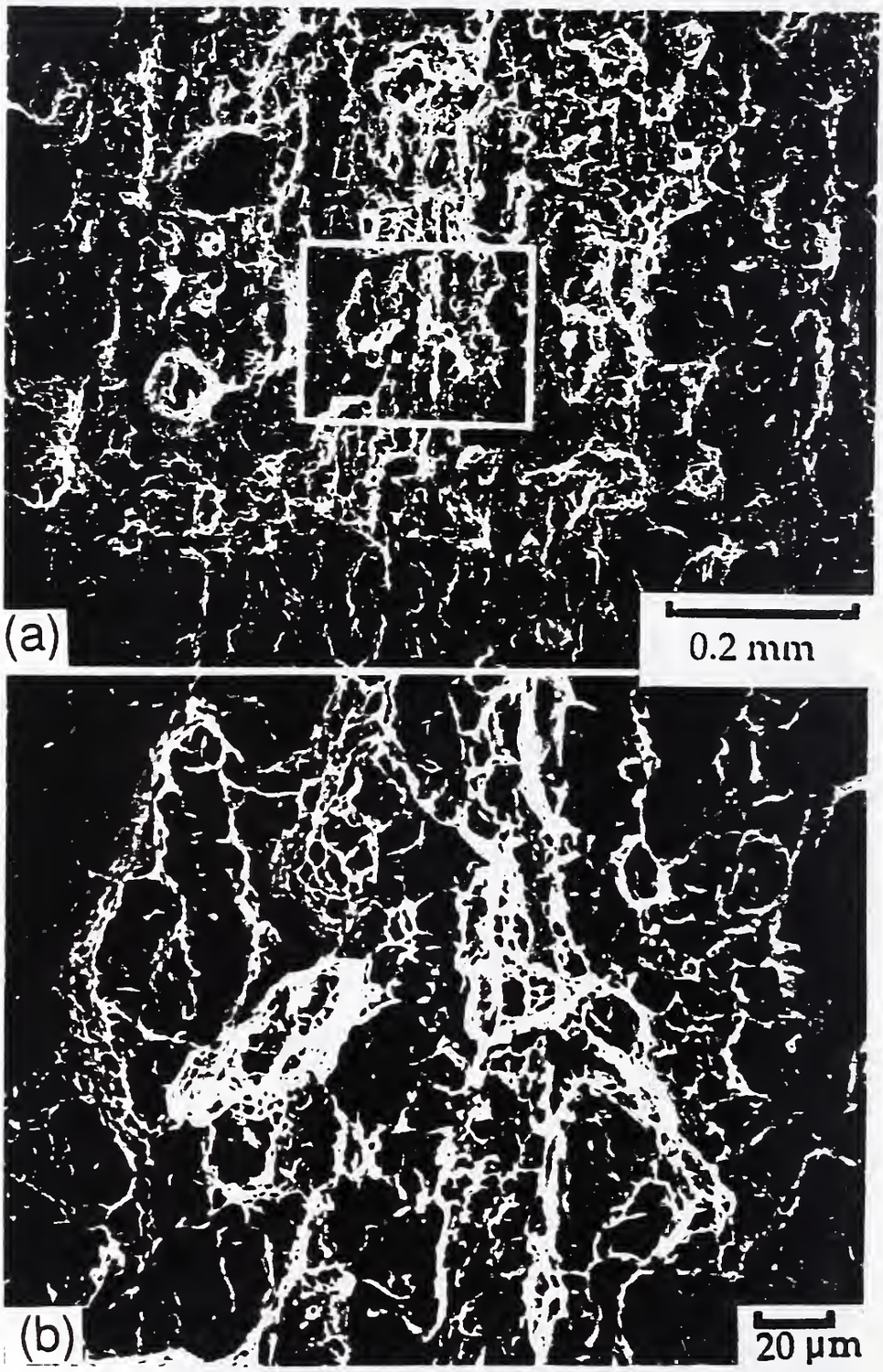

Figure 58. The fracture surface appearance of a LO-4K compact specimen with T-L orientation. Crack growth direction is bottom to top.

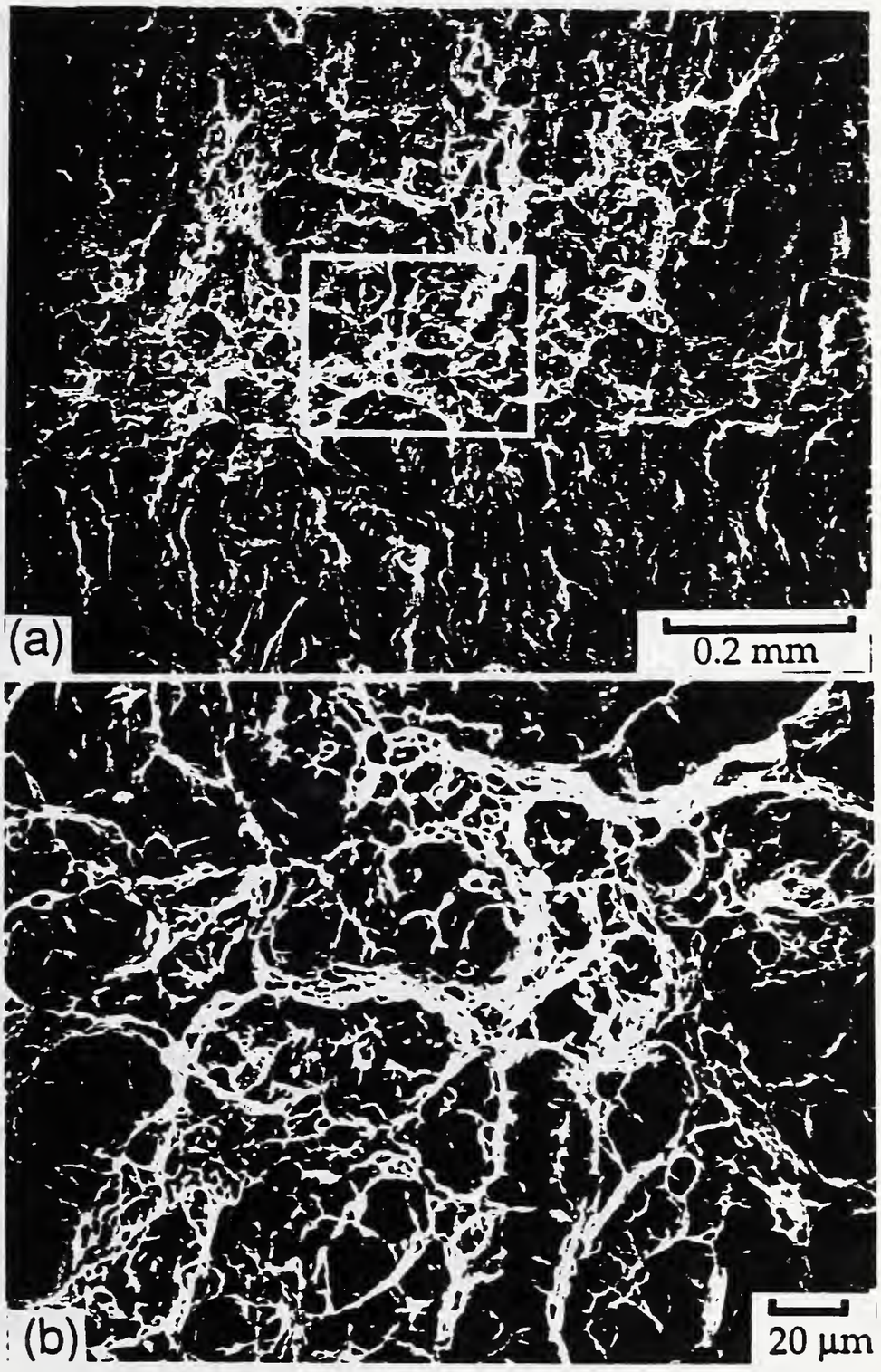

Figure 59. The fracture surface appearance of a HI-4K compact specimen with T-L orientation. Crack growth direction is bottom to top.

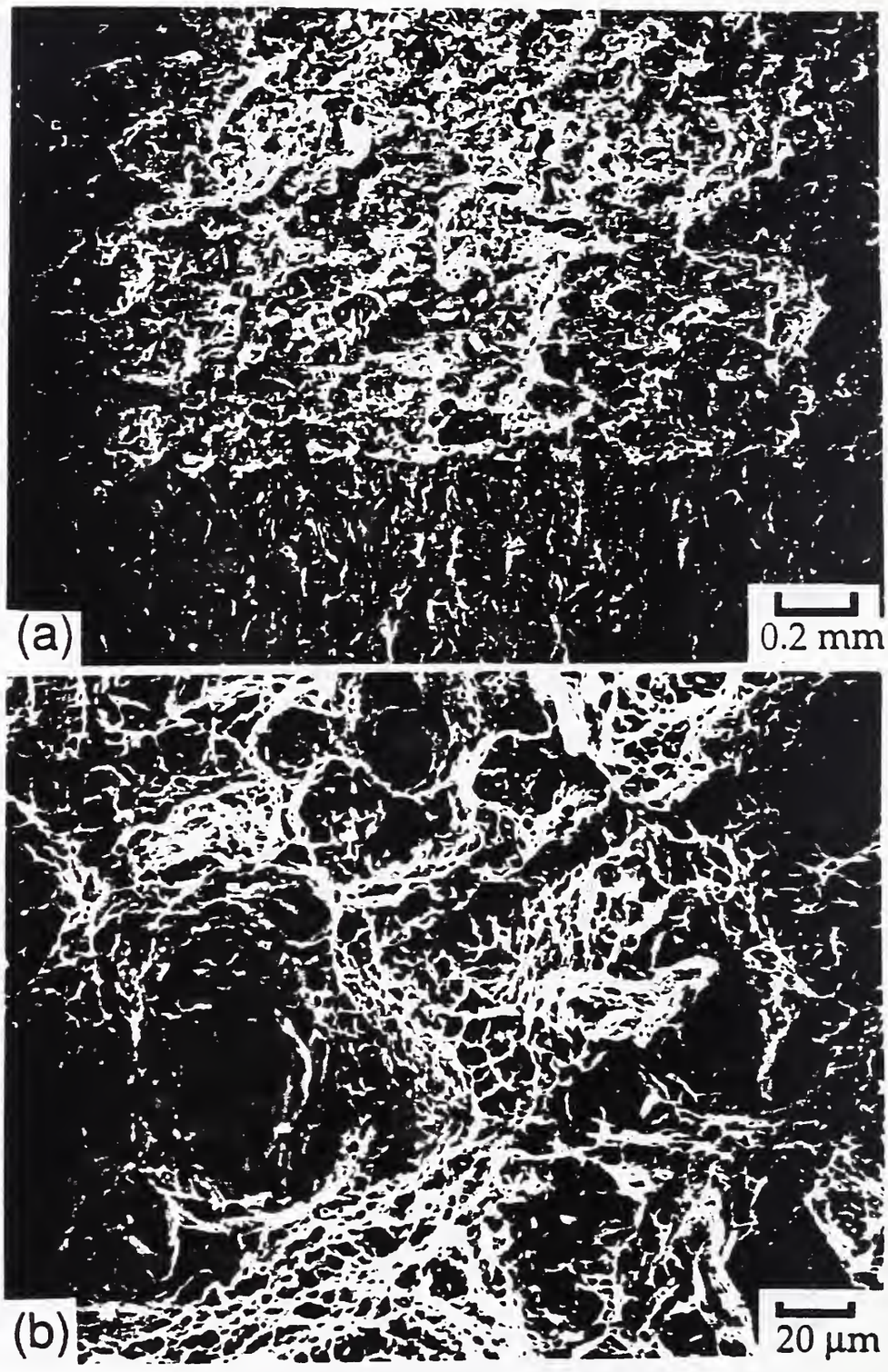

Figure 60. The fracture surface appearance of a compact specimen tested at 4 K in the L-T orientation.

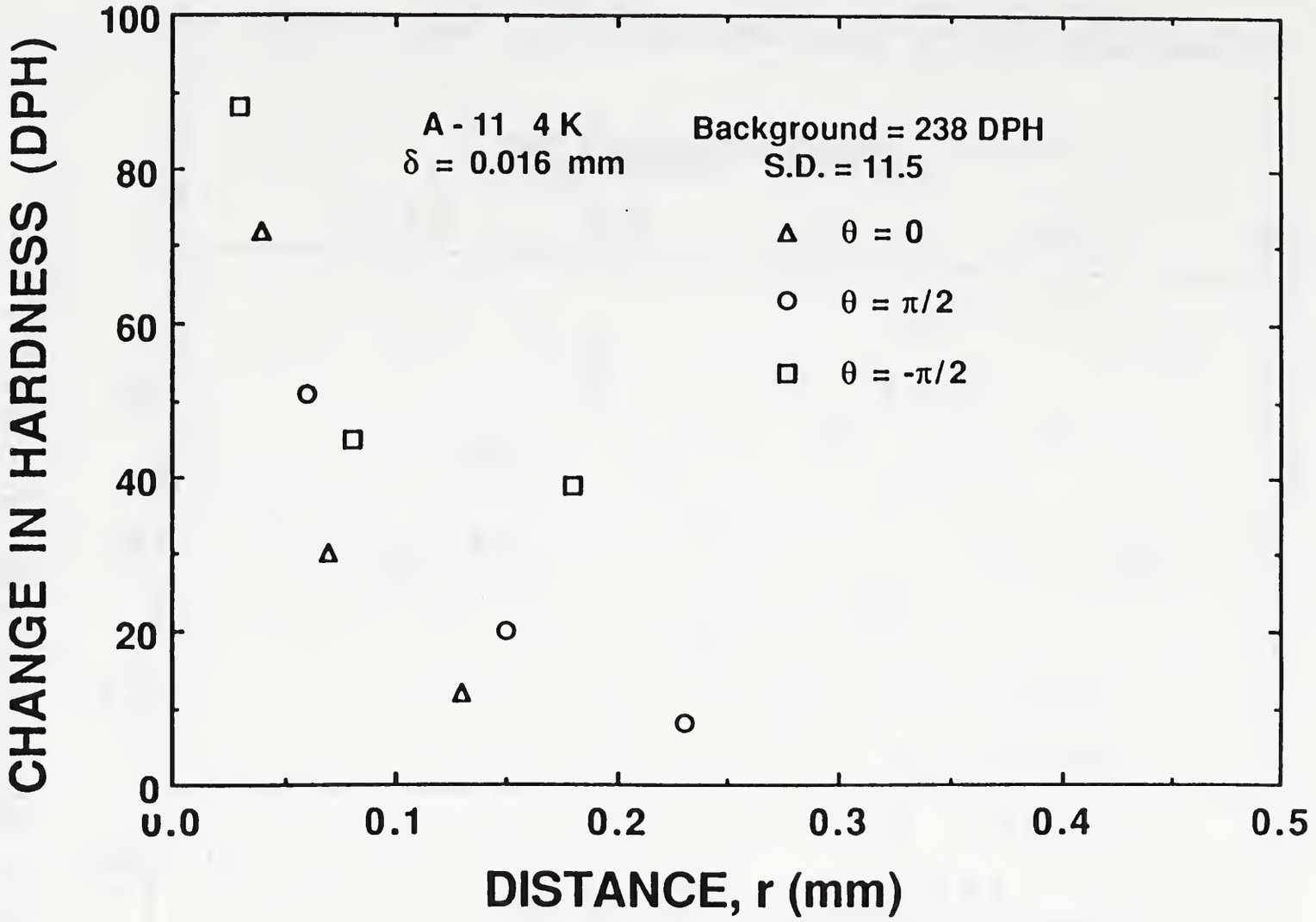

Figure 61a. The ▲DPH around the crack tip for specimen A-11 tested at 4 K with T-L orientation.

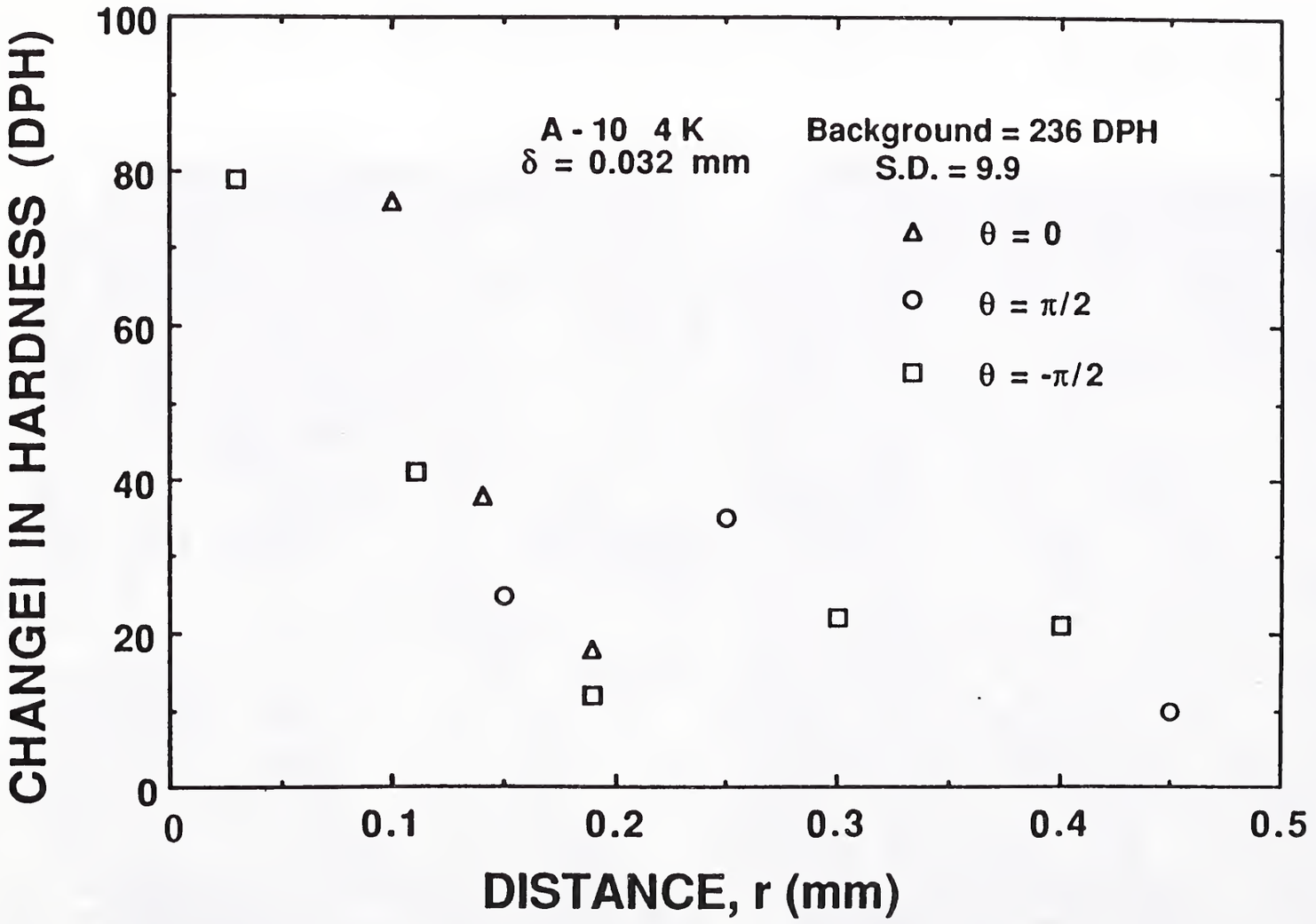

Figure 61b. The ▲DPH around the crack tip for specimen A-10 tested at 4 K with T-L orientation.

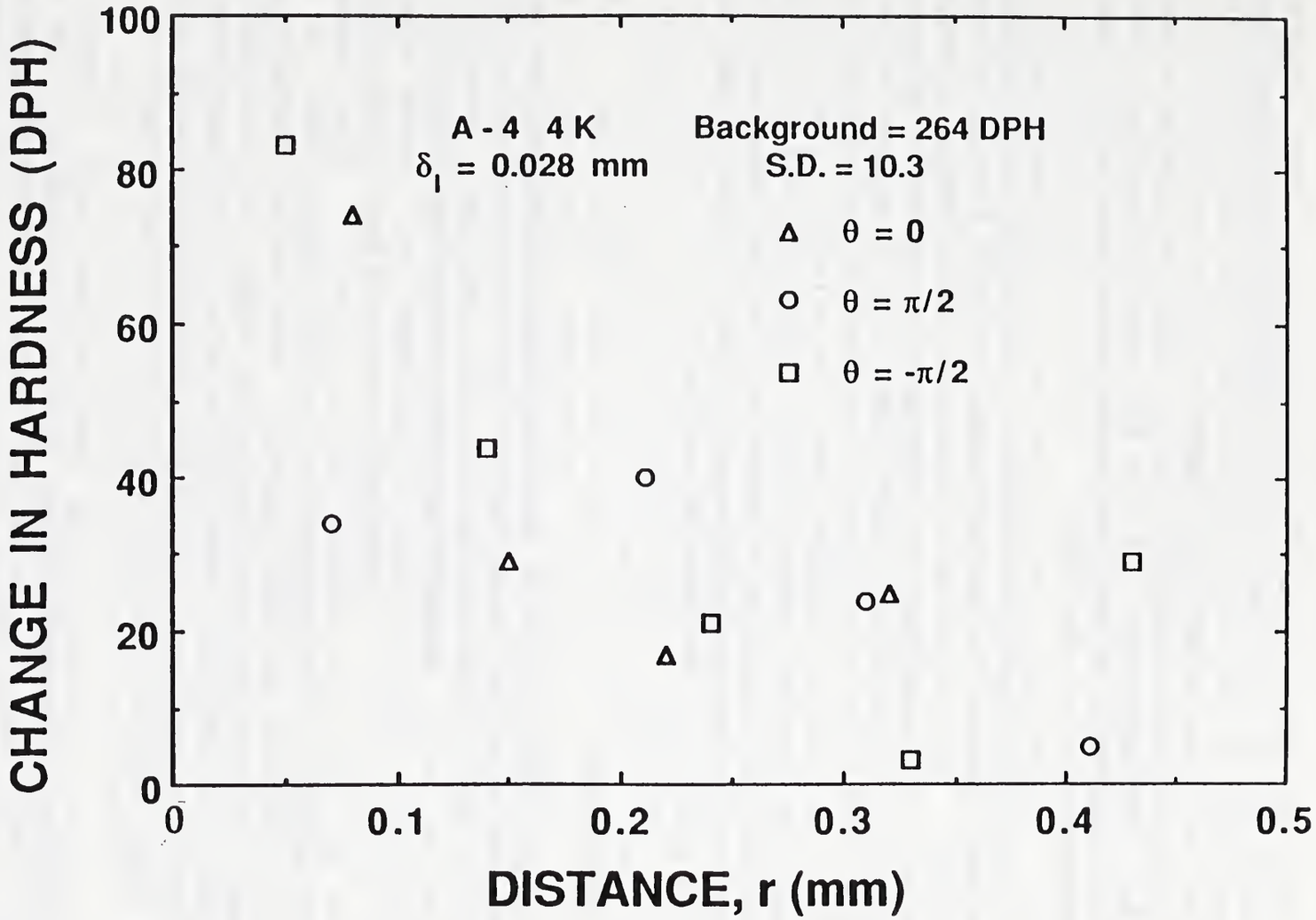

Figure 61c. The ▲DPH around the crack tip for specimen A-4 tested at 4 K with T-L orientation.

a distance larger than 2δ. At any given distance away from the crack, the ΔDPH is greater at $\theta = \pm \pi/2$ than at $\theta = 0$.

The micromechanisms of fracture at 4 K are similar to those found at 76 K. The local stresses in specimen A-11 were less than σ_c for void nucleation from the microalloy particles. With a slightly higher applied energy, A-10, the local stresses were greater than σ_c close to the crack tip in the PZ, but not ahead of the PZ. At the applied energy equal to J_{Ic} for the HI-4K specimens, the local stresses are equal to σ_c ahead of the PZ.

For the 4-K specimens tested with a L-T orientation, the process appears to be the same as that found for the T-L orientation. The orientation has no influence on the matrix flow properties and does not change the relative shape of the spherical, microalloy particles with respect to the loading direction. The sigma phase particles are not spherical, but are pancake-shaped and the relative shape will be different for the L-T orientation. The lack of elongated features on the fracture surface of the L-T specimens suggest that the interface between the matrix and sigma particles is stronger in that direction.

5.0 DISCUSSION

The variations in YS and toughness as functions of temperature reported here for 22-13-5 are typical of other austenitic stainless steels [37-41]. The main question is, what are the basic mechanisms that control toughness? The metallographic observations of deformed and broken specimens are not particularly different from what was previously observed in ferritic steels [12-15, 30-32]. What makes this work different is the emphasis on void nucleation, or more correctly, a lack of void growth. No special techniques have been used to measure the point where voids first separate from the matrix. Instead, this work concentrates on the global conditions required to nucleate and grow voids to a size that can be observed with light microscopy.

In this discussion, the observations with respect to the different micromechanisms of ductile fracture are reviewed. The second part of the discussion concentrates on quantifying the conditions required for significant void nucleation as a function of test temperature and stress state. Models for toughness are discussed in light of the observations of micromechanisms in 22-13-5. The effect of

test temperature and stress state on the behavior of the material are considered last.

5.1 Micromechanisms

The results of this study are summarized in terms of the micromechanisms of ductile fracture in Table 8. When two micromechanisms are listed, the first is dominant. At the highest test temperature (295 K), MVC was the dominant micromechanism observed. Void nucleation occurred at the sigma phase particles before void nucleation occurred at microalloy particles. At lower test temperatures in the uniaxial and biaxial stress states, shear fracture due to strain localization became more important. Strain localization interrupted the uniform deformation in the matrix that leads to MVC. For shear fracture to be the dominant micromechanism, no significant void nucleation can be present.

In the triaxial stress state, void nucleation from microalloy particles is the most important micromechanism related to toughness. Shear fracture manifested by the SZ was visible only at room temperature. Strain localization without prior void nucleation is an important metallurgical phenomenon, particularly in metal forming operations [6, 57]. The conditions existing in the tests where shear fracture occurs represent a subcritical point for the nucleation of a significant volume fraction of voids. Because shear fracture is not significant in toughness testing of 22-13-5, the discussion concentrates on MVC, the micromechanism observed in toughness testing.

5.2 Void nucleation conditions

The data presented in the results section emphasize the relationship between void nucleation and crack formation in 22-13-5. Two different approaches to quantify the stress required to nucleate voids were discussed in Section 1.0. The data for uniaxial and biaxial stress states were analyzed by these two criteria, and the results are summarized in Table 9 for the micromechanisms that lead to failure.

The specimen at 4 K in uniaxial stress state does not actually fracture at 4 K because the specimen heats locally during fracture [47], so the value of σ_c here refers to the maximum stress on the minimum cross section that stayed at 4 K. The critical stress for void nucleation from the large

Table 8. Summary of types of ductile fracture in 22-13-5.

	Micro-mechanisms	Comments
at 295 K		
Uniaxial stress state	MVC	voids nucleate from sigma phase at UTS, smaller voids nucleate at microalloy particles at fracture stress
Biaxial stress state	MVC + shear	splits form from sigma phase at UTS, remaining ligament fails by shear
Triaxial stress state	MVC + shear	SZ forms by shear, voids form at microalloy particles
at 76 K		
Uniaxial stress state	shear + MVC	strain localization in neck after UTS, voids nucleate from sigma phase
Biaxial stress state	shear	strain localization before UTS
Triaxial stress	MVC	voids form at microalloy particles
at 4 K		
Uniaxial stress state	shear + MVC	strain localization in neck before UTS, voids nucleate from sigma phase
Biaxial stress state	shear	strain localization before UTS

Table 8. Summary of types of ductile fracture in 22-13-5 (continued).

	Micro-mechanisms	Comments
Triaxial stress state	MVC	voids form at micro-alloy particles

second-phase particles at 4 K in a uniaxial stress state must be greater than the value shown in Table 9.

For the biaxial stress state, the σ_c calculated for void nucleation from sigma at 295 K is approximately the same as the σ_c for nucleation from sigma at 295 K in uniaxial stress state. The value of σ_c calculated for the biaxial stress state at cryogenic temperatures (shear fracture) in Table 9 is less than the value required to nucleate a significant volume fraction of voids necessary for MVC.

Criterion 2 generally predicts a higher value than criterion 1; the difference is larger for uniaxial than the biaxial stress state. The most striking point is that the values are higher at cryogenic temperatures than at 295 K. The analysis shows that void nucleation requires higher stresses at cryogenic temperatures than at room temperature.

For the triaxial stress state, an analysis similar to that shown in Table 9 for the critical stress required to nucleate voids is difficult. To develop a basis for discussion, look at the stress-strain history of a second-phase particle outside of the process zone, PZ. The critical location outside the PZ should be where the maximum normal stress is found. McMeeking [24] found that the maximum normal stress was at a distance of 2 or 3 times the value of δ. His results also show that the peak stress coincides with a relatively low strain, approximately 0.01 (see Fig. 4). For this discussion, the peak in maximum stress is taken as the position ahead of the crack where the strain is 0.02 because 0.02 strain is the smallest strain that can be estimated from the ΔDPH gradients. The stress-strain

Table 9. Data Used for Calculation of σ_c (MPa) Required for Void Nucleation in 22-13-5.

Critical point	σ_1	σ_T	σ_{eq}	σ_o	$\sigma_c(1)$	$\sigma_c(2)$
uniaxial						
voids nucleate from sigma at 295 K	1060	350	1060	425	1410	2075
voids nucleate from microalloy particles at 295 K	1820	1080	1630	425	2710	4065
voids nucleate from sigma at 76 K	2860	1240	2810	1065	4050	5650
neck formation due to local heating at 4 K	2065	865	2025	1360	>2890	>3130
Biaxial						
voids nucleate from sigma at 295 K	880	440	690	290	1130	1520
shear fracture at 76 K	1990	990	1720	895	>2710	>3310
shear fracture at 4 K	2080	1040	1800	1640	>2840	>2340

is interpreted in terms of a void-nucleation criteria and called the interfacial stress, σ_I. The next two paragraphs outline a method of estimating σ_1, σ_{eq} and σ_T for a distance ahead of the crack where the strain is 0.02.

As the applied energy, J_a, increases, the size of the deformed zone around the crack increases. The location ahead of the crack tip where the strain is 0.02 can be estimated from the results of the ▲DPH gradient. The hard-

ness gradient ahead of the crack tip has been measured at each test temperature as a function of applied energy, Figs. 46, 53, and 61. The results of Fig. 38, where the strain in unaxial and biaxial stress states was related to measured ▲DPH, indicate that 0.02 strain is about 20 ▲DPH. For example, in Fig. 46b for specimen AA-2, a smooth curve fit through the ▲DPH data for $\theta = 0$ reaches 20 ▲DPH about 0.78 mm from the zero point, the tip of the original fatigue precrack. The critical distance for AA-2 is 0.78 mm. The next step is to draw a new modulus line, slope = 200 GPa, on Fig. 17 at an offset of 0.02 strain. The value of σ_{eq} at each temperature is given by the intersection of the new modulus and the flow curves for the different temperatures.

Given the J_a at any point in the test, the maximum stress, σ_1, in the elastic region ahead of the crack tip can be estimated from the results of the analysis of small-scale yielding. The FEM results shown in Fig. 62 were used for the calculation of σ_1. For any point inside the PZ, the small-scale-yielding results are invalid. Given a value of σ_{eq} and σ_1, then the value of σ_T can then be calculated according to the equation,

$$\sigma_T = \sigma_1 - \{1/3\}\,\sigma_{eq} \qquad (8)$$

of Anderson [58]. The purpose of calculating the σ_1 is to compare the local values of σ_1 in the toughness test to the comparable values of σ_c for void nucleation calculated in the biaxial and uniaxial stress states.

The results of the calculation of σ_1 at 4 K are shown first because the 4-K tests show the least amount of plasticity. The critical distance ahead of the crack tip in the interrupted C(T) specimens, A-10 and A-11, is 0.18 and 0.10 respectively. A third value of J_a in the calculations is taken to be equal to J_{Ic} for specimen A-4 for which the hardness gradient was taken; see Fig. 61c. The critical distance r = 0.18 mm for A-4.

The data used in the procedure are shown in Table 10 and the results of these calculations in terms of criteria 1 and 2 are shown. The results for criterion 1 are plotted in Fig. 63 as a function of J_a. The values of σ_c calculated for shear fracture in the uniaxial and biaxial stress states are shown for comparison. The value of σ_1 must start at 0 because it is the sum of two parameters related to the applied force. The value rises rapidly to 4.2 GPa,

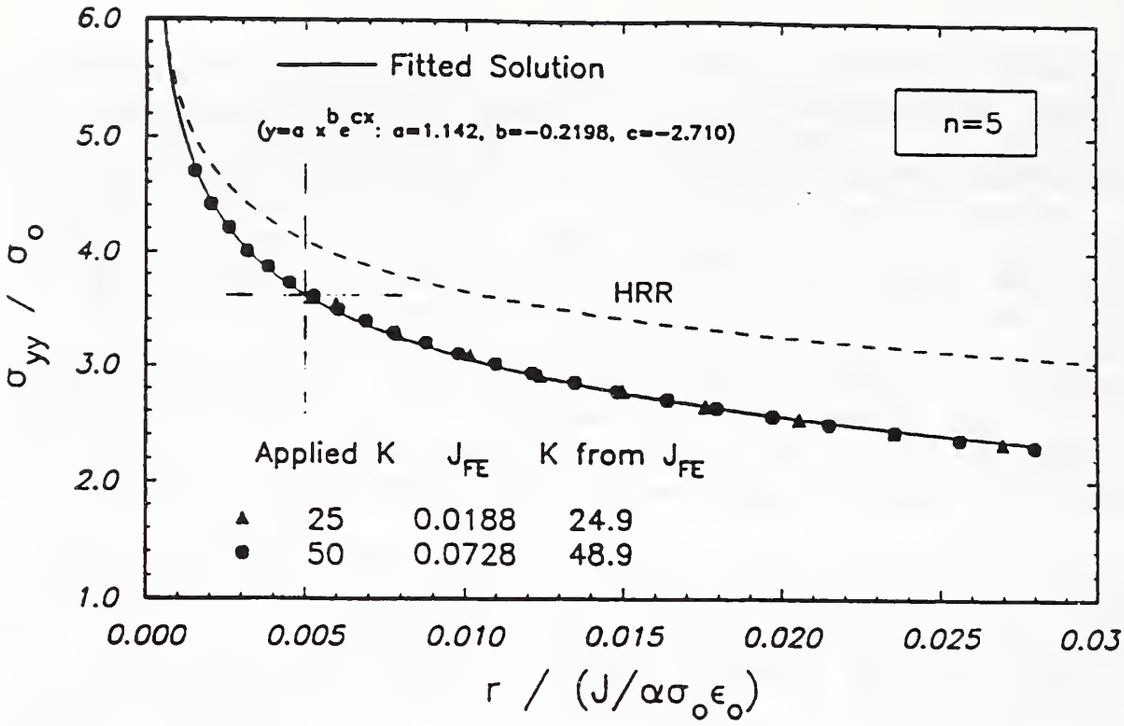

Figure 62. Plot of the maximum normal stress ahead of the crack tip in a strain hardening material calculated as a function of applied J [54].

Table 10. Summary of data for calculation of σ_I at 4 K from results of toughness testing

Distance ahead of crack	σ_{eq} (MPa)	σ_1 (MPa)	σ_T (MPa)	Crit. 1 (MPa)	Crit. 2 (MPa)
@ J_a = 51 N/mm					
r = 0.10 mm	1600	3540	2620	4220	3980
@ J_a = 94 N/mm					
r = 0.18 mm	1600	3540	2620	4220	3980
@ J_a = 59 N/mm					
r = 0.18 mm	1600	3110	2180	3780	3550

assuming YS = 1325 MPa.

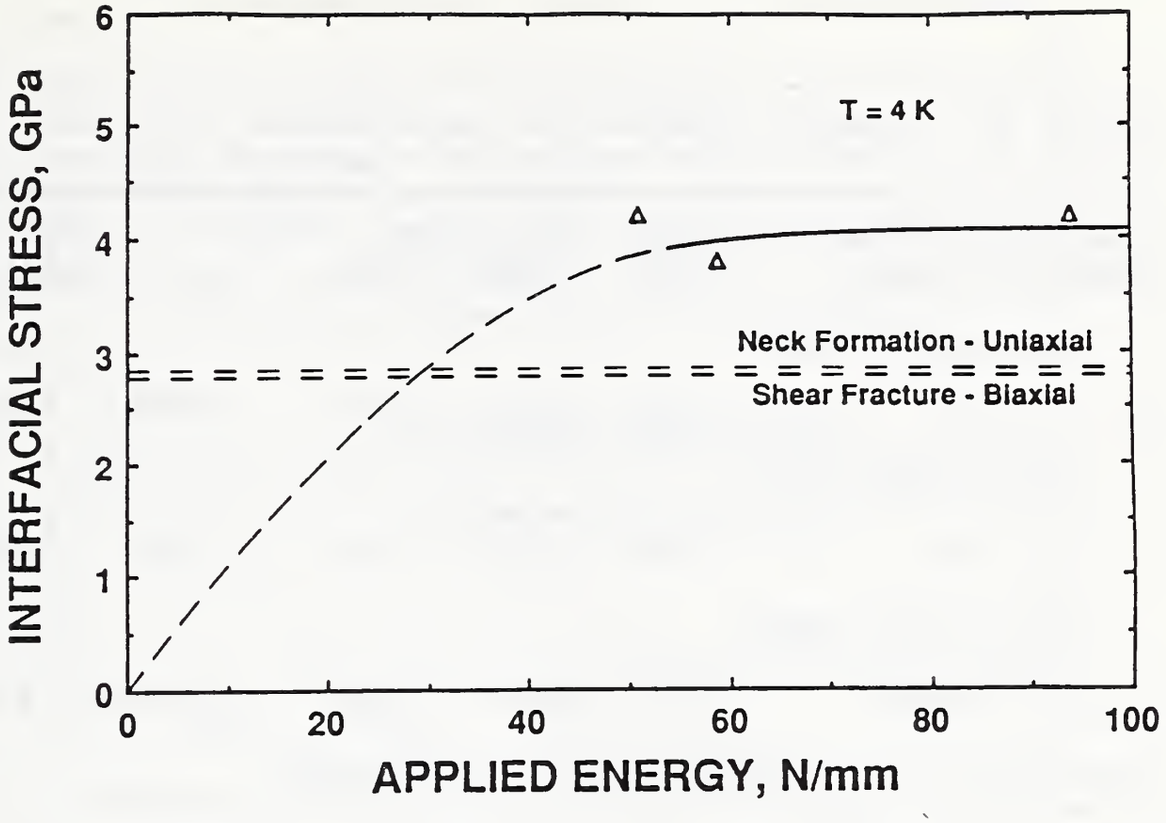

Figure 63. Plot of the interfacial stress (σ_I), calculated according to Argon and Im [14], ahead of the crack tip in compact specimens at 4 K of 22-13-5 as a function of applied J. Values of σ_c for uniaxial and biaxial stress states are shown for comparison.

decreases slightly to 3.8, and then increases back to 4.2 GPa. The maximum value of σ_I at each of the three given J_a is greater than the value of σ_c from uniaxial and biaxial stress states where no significant void nucleation occurred, see Table 9. These results appear to be reasonable.

At 295 and 76 K, the load-displacement curves for the complete tests are as shown in Fig. 3. Large-scale yielding conditions exist at the point where J_{Ic} is measured (refer to Fig. 20 for an example of a test at 76 K). Despite the plasticity observed in the P-u curves, the deformed zones ahead of the blunted crack tip are approximately 2 times δ. Calculations similar to those in Table 10 for the 4-K data were performed on the comparable specimens (AA-4, AA-2, and AA-1 at 295 K and AAA-5, AAA-4, and AAA-2 at 76 K) and the results are shown in Tables 11 and 12. Again, the σ_I calculated by criterion 1 are plotted as a function of J_a in Figs. 64 and 65.

Table 11. Summary of data for calculation of σ_I at 295 K from results of toughness testing.

Distance ahead ahead of crack	σ_{eq} (MPa)	σ_1 (MPa)	σ_T (MPa)	Crit. 1	Crit. 2 (MPa)
@ J_a = 100 N/mm					
r = 0.15 mm	520	2070	1770	2290	2220
@ J_a = 228 n/mm					
r = 0.78 mm	520	1710	1410	1930	1860
@ J_a = 524 N/mm					
r = 1.38 mm	520	1820	1520	2040	1970

assuming YS = 425 MPa

Table 12. Summary of data for calculation of σ_I at 76 K from results of toughness testing.

Distance ahead ahead of crack	σ_{eq} (MPa)	σ_1 (MPa)	σ_T (MPa)	Crit. 1	Crit. 2 (MPa)
@ J_a = 54 N/mm					
r = 0.21 mm	1200	2650	1960	3160	2870
@ J_a = 187 N/mm					
r = 0.21 mm	1200	3690	3000	4200	3910
@ J_a = 330 N/mm					
r = 0.31 mm	1200	3780	3090	4290	4000

assuming YS = 1066 MPa

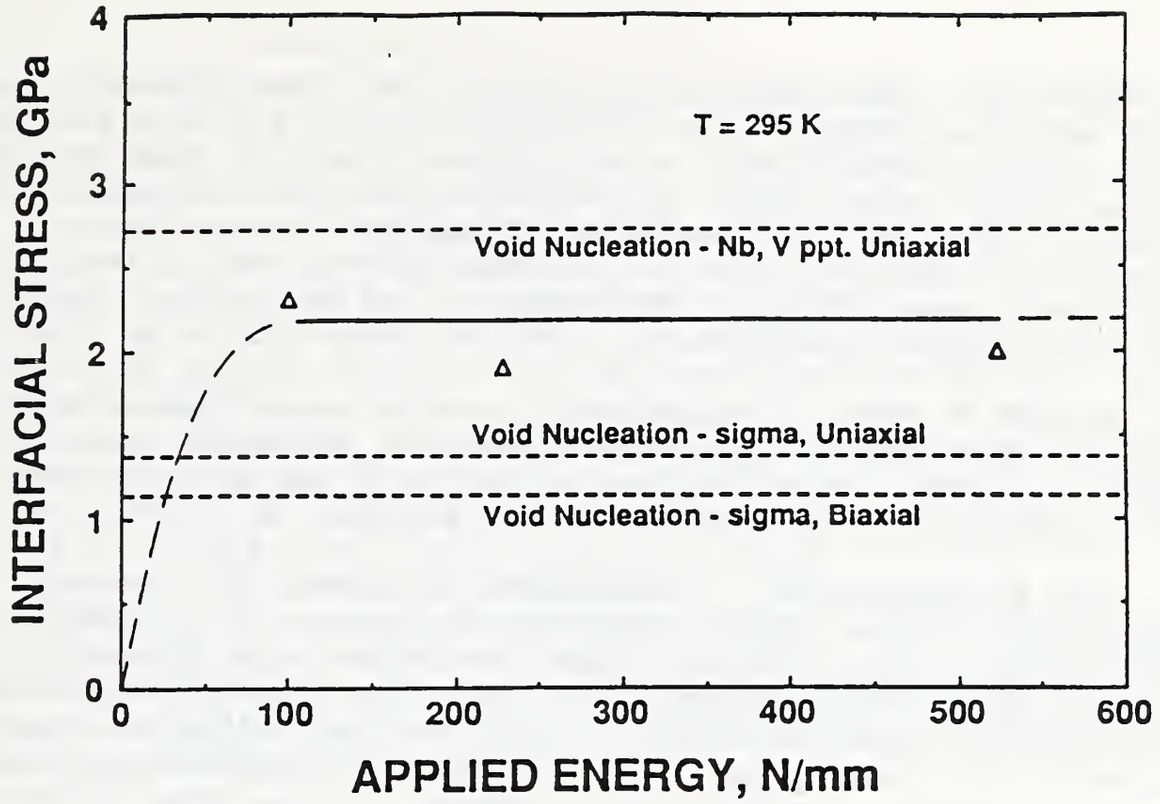

Fig. 64 Plot of σ_I ahead of the crack tip in C(T) specimens tested at 295 K.

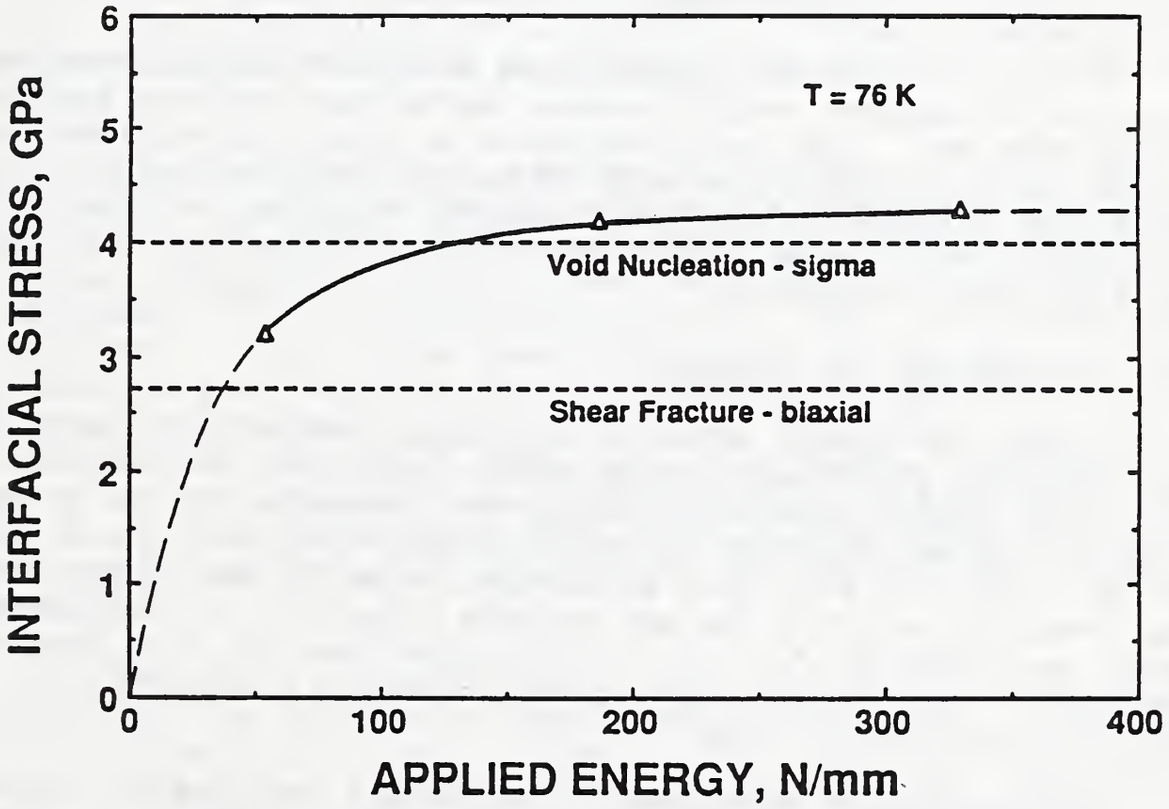

Fig. 65 Plot of σ_I ahead of the crack tip in C(T) specimens tested at 76 K.

At 76 K, the values of σ_I calculated from the toughness tests increase steadily to 4.2 GPa at a J_a of 187 N/mm. The value increases slightly to 4.3 GPa at JIc for specimen AAA-2. The σ_I for the lowest J_a is below the value required to nucleate voids from sigma in the uniaxial stress state. At a slightly higher J_a, the σ_I is large enough to nucleate voids from sigma phase. The value of σ_c for void nucleation from microalloy particles is greater than 4.05 GPa.

At 295 K, the σ_I values at J_a are greater than the σ_c for void nucleation from sigma phase in uniaxial stress state (1.4 GPa). The maximum value of σ_I is below σ_c for void nucleation from microalloy particles (2.7 GPa).

The procedure for calculating σ_I allows for useful comparison of the different micromechanisms of fracture for 22-13-5. The values of σ_I reach a plateau and do not increase significantly after a point. The plateau value is a by-product of the procedure, which is limited by the small-scale-yielding analysis. The small-scale-yielding assumption does not hold after the ligament is yielding in the P-u curve. A three-dimensional, large-scale-yielding analysis of the peak stress would probably that show the value of σ_I increases continually with J_a.

The procedure described here does not relate to the value of σ_I between second-phase particles and the matrix inside the PZ. The local value of σ_c for void nucleation at microalloy particles appears to be met inside the PZ soon after the specimen shows macroscopic yielding. Observations of subcritical crack growth below J_{Ic} in Figs. 42, 51, and 55 support this conclusion.

5.3 Discussion of models

Existing models attempt to characterize MVC in toughness testing by observations after the test is complete [30-31]. The local strain to failure is assumed to be a function of the morphology of the fracture surface, SZ or dimple shape. For 22-13-5, the formation of a SZ and dimples on the fracture surface do not relate directly to toughness. A crack can form at $J_a < J_{Ic}$. A key question is, Why does the crack grow at a low rate, (dJ/da), for $J_a < J_{Ic}$ and at a higher rate for $J_a > J_{Ic}$?

The measured toughness is directly related to a given decrease in compliance of the specimen (a global parameter), which is a function of the sensitivity of the experimental

procedure, and not necessarily to the local parameters at the crack tip. The distribution of plastic strain around the crack tip could explain why the formation of a crack inside the PZ does not directly lead to detectable increase in compliance. The best example to illustrate this point is Fig. 9 in the introduction. AISI 304 austenitic stainless steel tested at 76 K transforms to martensite when plastically strained. The etch has clearly defined the regions of high strain because the martensite is attacked heavily. With a different etch, a crack can be seen at the crack tip for $J_a = 0.33\ J_{Ic}$. When the specimen is unloaded to measure its compliance, the plastically deformed regions around the crack tip can exert a closure stress on the sharp crack. The hardness profiles around the crack tips for 22-13-5 (see Figs. 46, 53, and 61) show that a large plastic zone is concentrated around the tip in a wake. This wake moves along with the crack and could serve to close the crack when the specimen is unloaded. This wake effect can be thought of as similar to plasticity-induced crack closure in fatigue crack growth experiments [60].

The analysis of σ_I for different micromechanisms leads to a model for toughness based on nucleating voids in the highly stressed, elastically constrained region outside the PZ. The critical point is defined at the J_a where the σ_I for void nucleation equals σ_c for void nucleation outside the PZ.

If the value of σ_I reaches σ_c inside the PZ, voids can form, grow, and coalesce to form a subcritical crack. The plastic zone will exert a compressive stress on the crack tip so that on unloading, the true crack length is not recorded. If $\sigma_I = \sigma_c$ outside the PZ, then the voids can nucleate. Once voids have nucleated, it is easy for the voids to grow and coalesce with no additional J_a. The increment of crack growth is relatively large and measureable by the unloading compliance technique. Fracture toughness is then defined as the point where the σ_I (a function of J_a and the material's strain hardening characteristics), equals the material's resistance, σ_c, at a point outside of the PZ.

The value of σ_c depends upon many factors and would be difficult to calculate from first principles. Argon and Im [14] found that σ_c was a function of the local spacing of void-nucleating particles and correlated with the material's elastic modulus. In addition, the strain hardening characteristics should also be important in determining σ_c. The

value of σ_c is relatively independent of stress state so that it can be experimentally measured in a uniaxial tensile test and used as a failure criterion in the toughness test.

Observations from this test program support the idea that void nucleation is the most important micromechanism affecting toughness and that void growth is not directly related to toughness. If void growth were important in the determination of toughness, then the fracture surface appearance of the specimens at different test temperatures should reflect the measured toughness. In fact, the fracture surfaces of toughness specimens tested in the T-L orientation at different temperatures (Figs. 45, 52, 58, and 59) are remarkably similar despite the difference in toughness. With L-T test orientation at 4 K, the fracture surface appears more equiaxed, even though the toughness is approximately the same as for the T-L specimens at 4 K.

The revised model for toughness described above is based on the applied stresses for void nucleation from microalloy particles. The initial model [44] was based on the resistance of the material to void nucleation at widely spaced inclusions. The definition of the critical point that characterizes toughness in the revised model depends on the applied stresses outside the PZ. In the initial model, the critical point depended on the local stresses that exist near an inclusion.

In order to predict the test results, a distance parameter is needed. The characteristic distance, L, is a key feature of most models for toughness by either ductile or brittle fracture mechanisms. Typically, the value of L for ductile fracture is taken as the average spacing of void-nucleating particles. In brittle fracture, the value of L is related to the value of δ at which a suitable nucleation site for cleavage enters the PZ [2]. The average inclusion spacing, like the distribution of cleavage nucleation sites, is related to the resistance of the material to void nucleation and does not change as J_* increases.

If a steel is tested at a high test temperature, the flow strength is low, the PZ is relatively large, and may includes many inclusions. A correlation between inclusion spacing and toughness may be appropriate. For the 22-13-5 steel at 295 K, the PZ extends about 0.6 mm ahead of the crack tip. Since the average inclusion spacing is about 0.1 mm, the larger particles (inclusions) could play an important role in determining σ_c and toughness.

If the same steel is tested at a lower temperature, the flow strength is higher, the PZ is smaller, and may not include significant numbers of inclusions. In this case, the average spacing of inclusions can not be fundamentally related to toughness. For 22-13-5 steel at 4 K (HI-4K), the PZ is about 0.1 mm, or equal to the average inclusion spacing. Because there are few inclusions found in the PZ, it is difficult to imagine the same relationship between average inclusion spacing and toughness that is found at higher test temperatures.

The values of J_i and δ relate directly to the distance ahead of the crack for which the stress and strain are raised over the values in the bulk. The micromechanisms for fracture can only operate within the PZ (2 to 3δ). The value of L is then defined in terms of the applied stresses for void nucleation rather than in terms of the resistance of the material. L could be related to the inclusion spacing for some test materials and limited test conditions, but not in general. A similar conclusion was reached by others [34].

The σ_{fl} and ϵ^* terms from equation 3 are not needed in this analysis of void nucleation. The failure criterion is defined only at the edge of the PZ where the plastic strain is low. This fact simplifies the analysis, but technically restricts the model to small-scale yielding or K_{Ic} testing. A better analysis for the location of the peak stress would improve the method. The limiting case would be if σ_1 never reached σ_c outside the PZ. This would represent the situation where a different micromechanism interrupts the process, like in cleavage fracture. This frequently occurs in toughness testing of ferritic steels [57,60], particularly at high strain rates.

5.4 Material properties of 22-13-5

A key question in this work is, What effect do metallurgical variables like yield strength, second-phase-particle distribution, and alloy content have on ductile fracture? The observations reported here form a basis to evaluate these factors.

The best example is the role of the large, scattered second-phase particles like sigma and nonmetallic inclusions. They are most important when the deformed zone is largest, that is when the test temperature is highest and

the stress state is uniaxial. Then, a large volume of material is deformed and many particles are sampled. The particles do change the stresses locally in the matrix (Fig. 39b), and the location of final fracture is probably associated with the largest particles. However, the global effect of large, scattered particles on the fracture stress is minimal so the resistance of the steel to void nucleation is not altered.

The results of the calculations of σ_I for the triaxial stress state are consistent with the idea that the inclusions and sigma do not affect toughness. The value of σ_I reaches σ_c for void nucleation from the sigma particles at low J_a. If void nucleation from sigma influenced toughness, then J_{Ic} would be lower than the values measured here.

The calculation of σ_I is not affected by the presence of the large particles because σ_I is a function of the yield strength and macroscopic strain hardening, factors the particles do not influence. In theory, a given distribution could change the stress state locally from triaxial to biaxial and reduce the constraint ahead of the crack tip. This would lower the applied stresses.

Test temperature has a large effect on the yield strength of 22-13-5. Decreasing the temperature from 295 to 4 K increased the yield strength by a factor of three. This directly raises the applied stresses by an equal amount. A similar effect could be ascribed to any strengthening mechanisms, like grain refinement or precipitation strengthening. Any local variation in yield strength would cause a similar local variation in σ_I. As the volume of material that is strained decreases, the likelihood of yield strength variations increases. These two factors imply that larger scatter in toughness can be expected at 4 K compared to test results at higher temperatures.

Decreasing the test temperature from 295 to 76 K for 22-13-5 raised the resistance of the steel to void nucleation, σ_c, in uniaxial stress state. At 4 K, local heating and shear fracture interrupt the fracture process in uniaxial and biaxial stress states so that it is not clear if σ_c at 4 K increases or not. The product of strength and toughness, QI, does peak at 76 K so that qualitatively, the mechanical performance also peaks at 76 K. It could be that specimen heating at 4 K is affecting the material properties rather than a direct consequence of the resistance of the steel to void nucleation.

The microalloy particles do not affect the yield strength of 22-13-5 directly. Indirectly, the presence of microalloy particles influences the grain coarsening resistance of the steel and the interstitial content of the matrix. Both factors relate to the yield strength and therefore influence the driving force for void nucleation.

The substitutional alloying elements like Cr, Ni, and Mn were constant in this research program, so there are no direct observations on alloying effects can be discussed.

6.0 CONCLUSIONS

1. Both shear fracture and MVC are important micromechanisms of ductile fracture in 22-13-5. Where MVC is observed, void nucleation absorbs considerable energy and contributes significantly to the total energy absorbed in ductile fracture. When shear fracture occurs, it can be assumed that the energy required to nucleate a significant volume fraction of voids is greater than the energy required to cause shear fracture.

2. In fracture toughness testing, the first observation of MVC on the fracture surface does not correspond to the measured fracture toughness. The calculations of the applied stresses related to void nucleation ahead of the crack tip suggest that fracture toughness may be described by the point where a critical stress for void nucleation is reached at a characteristic distance ahead of the crack tip instead of at the crack tip.

3. The characteristic distance related to toughness is a function of the applied stresses for void nucleation in this steel. This is in direct contrast to the generally accepted approach which is to relate the characteristic distance to the inclusion spacing, the resistance of the steel to fracture.

4. The applied stress for void nucleation in fracture toughness testing (σ_1) is a strong function of the yield strength, which for 22-13-5 depends mainly on test temperature and interstitial nitrogen content. Variations in nitrogen content will produce scatter in the measured yield strength and fracture toughness for different locations in the plate.

5. The critical stress, σ_c, for void nucleation can be measured in a simple, uniaxial tensile test and can be related to the critical value of fracture toughness (K_{Ic} or J_{Ic}).

6. The small microalloy particles in the austenitic matrix influence the properties of the steel indirectly in two ways. First, the particles help resist grain coarsening during thermal processing. A fine grain size will increase the yield strength of the steel and its resistance to strain localization. Second, the particles contain nitrogen, which decreases the nitrogen content in solution and lowers the yield strength.

7.0 REFERENCES

1. G.T. Hahn, "The influence of microstructure on brittle fracture toughness," Met. Trans., vol. 15A, 1984, pp. 947- 959.

2. J. Heerens and D.T. Read, Fracture behavior of pressure vessel steel in the ductile to brittle transition region," NISTIR 88-3099, Nat. Inst. of Stand. Tech., Boulder, Colorado, 1987.

3. J.W. Morris Jr. and E.N.C. Dalder, "Cryogenic structural materials for superconducting magnets," JOM, Oct., 1985, pp. 24-33.

4. R.P. Reed, "Nitrogen in austenitic steel," JOM, vol. 41, Mar., 1989, pp. 16-21.

5. G. R. Irwin, "Analysis of stresses and strains near the end of a crack traversing a plate," J. Appl. Mech., vol. 24, 1957, pp. 361-364.

6. B. Dodd and Y. Bai, Ductile Fracture and Ductility, Academic Press, London, 1987.

7. J. W. Martin, Micromechanisms in Particle-Hardened Alloys, Cambridge University Press, New York, 1980.

8. H.G.F. Wilsdorf, "The ductile fracture of metals: a microstructural viewpoint," Mat. Sci. Engrg., vol. 59, 1983, pp. 1-19.

9. W.M. Garrison, Jr. and N.R. Moody, "Ductile fracture," J. Phys. Chem. Solids, vol. 48, no. 11, 1987, pp. 1035-1074.

10. R.H. Van Stone, T.B. Cox, J.R. Low, Jr, and P.A. Psioda, "Microstructural aspects of fracture by dimpled rupture," Int. Met. Rev., vol. 30, 1985, pp. 157-179.

11. G. Dieter, in Mechanical Metallurgy, 3rd edition, McGraw-Hill, New York, 1976.

12. D. L. Steinbrunner, D. K. Matlock, and G. Krauss, "Void formation during tensile testing of dual phase steels," Metall. Trans., vol. 19A, 1988, pp. 579-589.

13. I. Park and A. W. Thompson, "Ductile fracture in spheroidized 1520 steel," Acta Met., vol. 36, 1988, pp. 1653-1664.

14. A. S. Argon, J. Im, and R. Safoglu "Cavity formation from inclusions in ductile fracture," Met. Trans., vol. 6A, 1975, pp. 825-837.

15. F.M. Beremin, "Cavity formation from inclusions in ductile fracture of A508 steel," Met. Trans., vol. 12A, 1981, pp. 723-731.

16. A. L. Gurson, "Continuum theory of ductile rupture by void nucleation and growth: Part 1 -- yield criteria and flow rules for porous ductile media," J. Engrg. Matls. Tech., vol. 99, 1977, pp. 2-15.

17. M. Saje, J. Pan, and A. Needleman, "Void nucelation effects on shear localization in porous plastic solids," Int. J. Fract., vol. 19, 1982, pp. 163-182.

18. V. Tvergaard, "On localization in ductile materials containing spherical voids," Int. J. Fract., vol. 18, 1982, pp. 237-252.

19. P. F. Thomason, "Three-dimensional model for ductile fracture by the growth and coalescence of microvoids," Acta Metall., vol. 33, 1985, pp. 1087-1095.

20. P. F. Thomason, "A theoretical relation between K_{IC} and basic material properties in ductile metals," Int. J. Fract., vol. 7, 1971, pp. 409-418.

21. J.F. Knott, Fundamentals of Fracture Mechanics, Wiley, New York, 1973.

22. C. M. Gilmore, V. Provensano, F. A. Smidt, Jr., and J. R. Hawthorne, "Infulence of thicknes and temperature on stretched zone size in J_{Ic} tests," Met. Sci., vol. 17, 1983, pp. 177-185.

23. S. Banerjee, "Influence of specimen size and configuration on the plastic zone size, toughness and crack growth," Engrg. Fract. Mech., vol. 15, 1981, pp. 343-390.

24. R. M. McMeeking, "Finite deformation analysis of crack tip opening in elastic-plastic materials and implication for fracture," J. Mech. Phys. Sol., vol. 25, 1977, pp. 357-381.

25. J.W. Hutchinson, "Singular behaviour at the end of a tensile crack in a hardening material," J. Mech. Phys. Solids., vol. 16, 1968, pp. 13-31.

26. J. R. Rice and G.F. Rosengren, "Plane strain deformation near a crack tip in a power-law hardening material," J. Mech. Phys. Solids, vol. 16, 1968, pp. 1-12.

27. J. R. Rice and M. A. Johnson, "The role of large crack tip geometry changes in plane strain fracture," in Inelastic Behavior of Solids, edited by M. F. Kanninen et al., McGraw-Hill, New York, 1968, pp. 641-672.

28. T. Shoji, H. Takahashi, and M. Suzuki, "Significance of crack opening displacement and crack tip plastic strain energy in fracture initiation," Met. Sci., vol. 12, 1978, pp. 579-586.

29. L.G. Luo, A. Rykd, and, J.D. Embury, "On the development of a metallographic method to determine the strain distribution ahead of a crack tip," Metallography, vol 23, 1989, pp. 101-117. 1989

30. R.O. Ritchie and A. W. Thompson, "On macroscopic and microscopic analyses for crack initiation and crack growth toughness in ductile alloys," Met. Trans., vol. 16A, 1985, pp. 233-248.

31. W. M. Garrison Jr., "The effect of silicon and nickel additions on the sulfide spacing and fracture toughness," Met. Trans., vol. 17A, 1986, pp. 669-678.

32. R. H. Dauskardt, R. D. Pendse, and R. O. Ritchie, "Effect of pre-existing grain boundary microvoid distributions on fracture toughness and fatigue crack growth in low alloy steel," Acta Met., vol. 35, 1987, pp. 2227-2242.

33. J. C. Gibeling, "The effect of pre-existing voids on the ductile fracture of silver," Scr. Met., vol. 23, 1989, pp. 167-172.

34. J.C. Lautridou and A. Pineau, "Crack initiation and stable crack growth resistance in A508 Steels in relation to inclusion distribution," Engrg. Fract. Mech., vol. 15, no. 1-2, 1981, pp. 55-71.

35. D.-Z. Sum, D. Siegele, B. Voss and W. Schmitt, "Application of local damage models to the numerical analysis of ductile rupture," Fat. Fract. Engrg. Mater. Struct., vol. 12, no. 3, 1989, pp. 201-212.

36. R.J.H. Wanhill, "Microstructural influences on fatigue and fracture resistance in high strength structural materials," Engrg. Fract. Mech., vol. 10, 1978, pp. 337-357.

37. R. L. Tobler, D. T. Read, and R. P. Reed, "Strength-toughness relationship for interstitially strengthened AISI 304 stainless steels at 4 K temperature," in Fracture Mechanics: Thirteenth Conference, ASTM STP 743, R. Roberts, ed., American Society for Testing and Materials, Philadelphia, 1981, pp. 250-268.

38. M. Spiedel, "Properties and applications of high nitrogen steels," in High Nitrogen Steels 88, eds. J. Foct and A. Hendry, Institute of Metals, London, 1989, pp. 92-96.

39. R.P. Reed, P.T. Purtscher, K. Yushchenko, "Nickel and nitrogen alloying effects on the strength and toughness of austenitic stainless steels at 4 K," in Advances in Cryogenic Engineering-Materials, Vol. 32, eds. R.P. Reed and A.F. Clark, Plenum Press, New York, 1986, pp. 43-50.

40. P.T. Purtscher, M.C. Mataya, L. Ma, and R. P. Reed, "Effect of processing on 4-K mechanical properties of microalloyed austenitic stainless steels" to be published in Advances in Cryogenic Engineering-Materials, Vol. 36, Plenum Press.

41. P.T. Purtscher, M. Austin, C.N. McCowan, J. Dunning, R.P. Walsh, and R.P. Reed, "Austenitic steels with 9% Cr for structures at cryogenic temperatures" to be published in Advances in Cryogenic Engineering-Materials, Vol. 36, Plenum Press.

42. P. T. Purtscher, "Stretch zone formation in austenitic steels fractured at cryogenic temperatures," JTEVA, vol. 15, 1987, pp. 266-268.

43. P. T. Purtscher, R. P. Reed, and D. K. Matlock, "Metallographic study of the crack-tip region from fracture mechanics specimens of austenitic and ferritic steels," in IMAM-5 Structural Ceramics/Fracture Mechanics, Materials Research Society, Pittsburgh, 1989.

44. P. T. Purtscher, D. T. Read, and R. P. Reed, "Effect of void nucleation on the fracture toughness of high strength austenitic steels," in Fracture Mechanics, Twentith Symposium, ASTM STP 1020, American Society for Testing and Materials, Philadelphia, 1989, pp. 433-446.

45. C.A. Perkins, "Hot deformation behavior of a high nitrogen austenitic stainless steel," M.S. thesis, Colorado School of Mines, April, 1987.

46. G.F. Vanderoot, "The metallography of stainless steels," JOM, 41, Mar., 1989, pp. 6-11.

47. R.P. Reed and R.P. Walsh, "Tensile strain rate effects in liquid helium," in Advances in Cryogenic Engineering--Materials, vol. 34, R.P. Reed and A.F. Clark, eds., Plenum Press, New York, 1988, pp. 199-208.

48. D.A. Corrigan, R.E. Travis, V.P. Ardito and C.M. Adams, Jr. "Bi-axial strength of welds in heat-treated sheet steel," Weld. J., vol. , 1962, pp.123s-128-s.

49. Y.A. Rosenthal, R.L. Tobler, and P.T. Purtscher, "J_{Ic} data analysis with a 'negative' crack growth correction procedure," submitted to JTEVA.

50. W.J. Mills, "On the relationship between stretch zone formation and the J integral for high strain-hardening materials," JTEVA, vol. 9, 1981, pp. 56-62.

51. C.W. Fowlkes and R.L. Tobler, "Fracture testing and results for a Ti-6Al-4V alloy at liquid helium temperature," Eng. Fract. Mech., vol. 8, 1976, pp. 487-500.

52. D. Hellmann and K.-H. Schwalbe, "On the experimental Determination of CTOD based on R-curves," in The Crack Tip Opening Displacement in Elastic-Plastic Fracture Mechanics, ed. K.-H. Schwalbe, Springer-Verlag, New York, 1986, pp. 115-132.

53. H.L. Ledbetter, "Austenitic steel elastic constants," in Austenitic Steels at Low Temperature, R.P. Reed and T. Horiuchi, eds., Plenum Press, New York, 1983, pp. 83-104.

54. T.L. Anderson and R.H. Dodds, Jr., "Specimen size requirements for fracture toughness testing in the transition region," submitted to JTEVA.

55. A.S. Argon, J. Im, and A. Needleman, "Distribution of plastic strain and negative pressure in necked steel and copper bars," Met. Trans., vol. 6A, 1975, pp. 815-824.

56. P.T. Purtscher, "Effect of austenitizing temperature on fracture toughness of AISI 4485 roll steel," M.S. thesis, Colorado School of Mines, 1983.

57. F. Zia-Ebrahimi, "A study of mechanisms of tempered martensite embrittlement in low-alloy, medium carbon steels" PhD thesis, Colorado School of Mines, 1982.

58. I.C. Howard and A.A. Willoughby, "Mechanics and Mechanisms of ductile fracture," in Developments in Fracture Mechanics-2, edited by G.G. Chell, Applied Science Publishers, London, 1981, pp.39-100.

59. T.L. Anderson, "Crack tip parameters for large scale yielding and low constraint configurations," Int. J. Fract., vol. 41, 1989, pp. 79-104.

60. W. Elber, "Fatigue crack closure under cyclic tension," Eng. Fract. Mech., vol. 2, 1970, pp. 37-45.

61. M. Leap, "The effects of forging on the microstructural development, strength, and dynamic fracture behavior of microalloyed ferrite-pearlite steels," M.S. thesis, Colorado School of Mines, 1987.

WELDING

WELDING PROGRAM

LEADER: T.A. Siewert
CONTRIBUTOR: C.N. McCowan

OBJECTIVES:

- Investigation of the metallurgical factors that affect the mechanical properties of stainless-steel weldments at cryogenic temperatures.
- Contribution to the development of improved filler metals for welding stainless steels for use at 4 K.
- Evaluation of the mechanical properties of weldments at 4 K.
- Development of methods for detecting defects and evaluation of their significance in stainless steel weldments.

RESEARCH HIGHLIGHTS:

- We evaluated a series of welds produced with a type 904L electrode (20Cr-25Ni-4.5Mo). They had the highest toughness values which we have measured for high strength welds (near 1000 MPa) at 4 K.

- A series of shielded metal arc compositions based on a type 308 stainless steel were unable to match the toughness of type 316LN and 21Cr-6Ni-9Mn base materials, even at 76 K.

- A study of a type 316L gas metal arc weld revealed a low energy interdendritic fracture mode as nitrogen was added to reduce the ferrite content and increase the strength.

SUMMARY OF MECHANICAL PROPERTY MEASUREMENTS OF WELDS

Weld Alloy [designation]	Welding Process	Tensile	Charpy Impact	Fracture Toughness	Fatigue Crack Growth Rate	Report Volume* (page)
AUSTENITIC STAINLESS STEELS						
Fe-13Cr-13Ni-20Mn-0.2C	SMAW	XI		XI		XI (171)
Fe-13Cr-20Ni-9Mn-2Nb	SMAW	I,II	I,II, VIII			I (159,169) II (299) VIII (29)
Fe-15Cr-12Ni-10Mn	SMAW	IV	IV,VIII			IV (453) VIII (29)
Fe-16Cr-15Ni-4Mo	SMAW	IV		IV		IV (275)
Fe-16Cr-16Ni-2Mo	FCAW	II		III	III,VI	III (155) VI (199)
Fe-16Cr-16Ni-4Mo	FCAW	IV	IV,VIII	IV		IV (275) VIII (29)
Fe-16Cr-35Ni-4Mn [330 modified]	SMAW	I	I,VIII	II		I (159) II (299) VIII (29)
Fe-17Cr-9Ni-Mn-N	SMAW	IX	IX			IX (217)
Fe-17Cr-16Ni-4Mo	SMAW	IV		IV		IV (275)
Fe-18Cr-11Ni-2Mo-N	EBW LBW	X X	X X	X X		X (299)
Fe-18Cr-16Ni-6.5Mn-2Mo	SMAW	IX	IX			IX (257)
Fe-18Cr-16Ni-9Mn-N	GMAW	III,IV	IV	III,IV	III,VI	III (155) IV (275,453) V (199)
Fe-18Cr-18Ni-2Mo-5Mn-N	SMAW	IV	IV			IV (453)
Fe-18Cr-20Ni-5Mn-N	GMAW	IX,XI		IX,XI		IX (247) XI (247)
Fe-18Cr-20Ni-6Mn-0.3Nb	GMAW	IV	IV	IV		IV (275)
Fe-18Cr-20Ni-6Mn-0.2Ti	GMAW	IV	IV	IV		IV (275)
Fe-19Cr-12Ni-2Mo [316]	SMAW	II	II,VIII	II		II (315) VIII (29)
Fe-19Cr-12Ni-2Mo [316L]	EBW	IV		IV	IV,VI	IV (275,415) VI (199)
	GMAW	III,IV, XII	III,IV, VIII	IV, XII		III (155,195) IV (303) VIII (29) XII (199)

*MATERIALS STUDIES FOR MAGNETIC FUSION ENERGY APPLICATIONS AT LOW TEMPERATURES: NBSIR 78-884 (I); NBSIR 79-1609 (II); NBSIR 80-1627 (III); NBSIR 81-1645 (IV); NBSIR 82-1667 (V); NBSIR 83-1690 (VI); NBSIR 84-3000 (VII); NBSIR 85-3025 (VIII); NBSIR 86-3050 (IX); NBSIR 87-3067 (X); NBSIR 88-3082 (XI); NISTIR 89-3931 (XII)

SUMMARY OF MECHANICAL PROPERTY MEASUREMENTS OF WELDS, continued

Weld Alloy [designation]	Welding Process	Tensile	Charpy Impact	Fracture Toughness	Fatigue Crack Growth Rate	Report Volume* (page)
Fe-19Cr-12Ni-2Mo [316L], continued	GTAW	III,IV, XI	III,IV, VIII	IV	XI	III (155,195) IV (303) VIII (29) XI (215)
	SAW	III,IV, V	III,IV, V	III,IV	III,VI	III (155,195 IV (275,415) V (233) VI (199)
	SMAW	II,III, IV	II,VIII	II,III, IV	III,IV,VI	II (299,315) III (155,167) VI (199) VIII (29)
Fe-19Cr-12Ni-2Mo-N [316LN]	SMAW	II	II,VIII	II		II (299) VIII (29)
Fe-19Cr-16Ni-7Mn	GMAW	IV	IV			IV (453)
Fe-20Cr-10Ni [308]	SMAW	I	I,VIII			I (169) VIII (29)
Fe-20Cr-10Ni [308L]	FCAW	III		III	III,VI	III (155) VI (199)
	GMAW	III		III	III,VI	III (155) VI (199)
	GTAW	XI			XI	XI (215)
	SMAW	II,III	II,VIII	II,III	III,VI	II (299) III (155) VI (199) VIII (29)
Fe-20Cr-10Ni-N [308LN]	FCAW	IV		IV	IV,VI	IV (275,415) V (199)
Fe-20Cr-10Ni-9Mn-N	SMAW	I	I			I (159,169)
Fe-20Cr-16Ni-7Mo-2W	SAW	IV		IV		IV (275)
Fe-20Cr-34Ni-2Mo-Nb	SMAW	VII		VII		VII (253)
Fe-21Cr-6Ni-9Mn-N	GTAW	XI			XI	XI (215)
	SMAW	I,II	I,II			I (159,169) II (299)
Fe-25Cr-22Ni-4Mn-2Mo	GMAW	XII		XII		XII (167)

*MATERIALS STUDIES FOR MAGNETIC FUSION ENERGY APPLICTIONS AT LOW TEMPERATURES: NBSIR 78-884 (I); NBSIR 79-1609 (II); NBSIR 80-1627 (III); NBSIR 81-1645 (IV); NBSIR 82-1667 (V); NBSIR 83-1690 (VI); NBSIR 84-3000 (VII); NBSIR 85-3025 (VIII); NBSIR 86-3050 (IX); NBSIR 87-3067 (X); NBSIR 88-3082 (XI); NISTIR 89-3931 (XII)

SUMMARY OF MECHANICAL PROPERTY MEASUREMENTS OF WELDS, continued

Weld Alloy [designation]	Welding Process	Tensile	Charpy Impact	Fracture Toughness	Fatigue Crack Growth Rate	Report Volume* (page)
AUSTENITIC STEELS						
Fe-15Mn-8Ni-1Mo-0.7C	SAW	VIII		VIII		VIII (15)
Fe-5Cr-25Mn-1Ni		V		V,VII	V,VI	V (233) VI (199) VII (245)
Fe-6.5Cr-25Mn-3Ni-1Mo	SMAW	V		V	V,VI	V (233,245) VI (199)
ALUMINUM ALLOYS						
Al-5Mg [5183]	GMAW	III		IV	IV	III (155,217) IV (323)
Al-5Mg-0.12Ti [5556]	GMAW	III		IV	IV	III (155, 217) IV (323)
Copper Alloys						
Cu-0.08Ag [C10700]		XI				XI (201)
Cu-0.4Be-1.8Ni [C17510]		XI				XI (201)

*MATERIALS STUDIES FOR MAGNETIC FUSION ENERGY APPLICTIONS AT LOW TEMPERATURES: NBSIR 78-884 (I); NBSIR 79-1609 (II); NBSIR 80-1627 (III); NBSIR 81-1645 (IV); NBSIR 82-1667 (V); NBSIR 83-1690 (VI); NBSIR 84-3000 (VII); NBSIR 85-3025 (VIII); NBSIR 86-3050 (IX); NBSIR 87-3067 (X); NBSIR 88-3082 (XI)

DEVELOPMENT OF AN SMA ELECTRODE TO MATCH TYPE 316LN BASE METAL CRYOGENIC PROPERTIES

T.A. Siewert and C.N. McCowan
Materials Reliability Division
National Institute of Standards and Technology
Boulder, Colorado

A series of shielded metal arc electrodes was fabricated and the mechanical properties of the resultant welds were measured. The compositions are based on a high-Mn, high-N version of a type 308 electrode, to which additional Mn, N, Ni, and Mo were added. The strength was measured at 4, 76, and 298 K, and the Charpy V-notch absorbed energy was measured at 76 K. The strengths of the welds met or exceeded the values for the base metal, but the Charpy V-notch absorbed energies fell short.

BACKGROUND

The trend toward more efficient designs for structures continues, with designers seeking more strength and toughness from the structural materials. This general observation is true even for the special category of cryogenic structures. The Compact Ignition Tokamak being designed by Princeton Plasma Physics Laboratory requires property data on such high strength materials for the service range of 76 K to 298 K. Designs for other cryogenic structures are also expected to require a combination of high strength and toughness, to temperatures as low as 4 K when used with conventional superconducting magnets. Thus, it is useful to collect information on high strength candidate materials, in an attempt to understand how the properties can be improved further.

Whereas several stainless steel plate materials, such as 21Cr-6Ni-9Mn and type 316LN, demonstrate properties that might be suitable for cryogenic structures, the welding electrodes necessary to join these compositions into a fabricated structure remain poorly characterized. Early studies developed screening data on high strength weld compositions, but the volume of such data is limited.

Espy compared the properties of the matching composition electrode for 21Cr-6Ni-9Mn with various experimental compositions, at both room temperature and cryogenic temperatures.[1] Although the yield strength increases sharply as the temperature drops, his data in Table 1 also show that the toughness of these welds at liquid nitrogen temperature is marginal when compared to a common design requirement, such as 20 J of absorbed energy in Charpy V-notch (CVN) testing. Such a toughness requirement becomes more important as the thickness of the structure increases.

Table 1. Mechanical Properties of Variations on a 21Cr-6Ni-9Mn Weld.

Composition	Mechanical Properties at Room Temperature		Mechanical Properties at 76 K	
	Yield Strength (MPa)	CVN absorbed Energy (J)	Yield Strength (MPa)	CVN Absorbed Energy (J)
21Cr-6Ni-9Mn-0.2N	570	54	1120	14
13Cr-20Ni-9Mn-0.18N	525	36	820	16
20Cr-10Ni-9Mn-0.19N	560	66	945	13
18Cr-16Ni-9Mn-0.15N	-	-	880	24

Espy attributed the poor toughness shown in Table 1 to the high strength (due to nitrogen additions). This causes a problem for structural designers since the high strength is precisely what makes the 21Cr-6Ni-9Mn composition attractive, and produces benefits such as reducing the required section thickness. The Espy study also contained data for welds having the same combinations of Cr, Ni, and Mn but with lower concentrations of N. These compositions had better toughness (up to 38 J) at 76 K, but the strength dropped (as low as 640 MPa).

The 21Cr-6Ni-9Mn base metal has much better properties than the welds (similar strength to the 21Cr-6Ni-9Mn weld metal at the two temperatures with CVN absorbed energies of 280 J at room temperature and 88 J at 76 K). This good combination of strength and toughness in the base metal could lead a designer to make incorrect assumptions about the weld properties. Unless the structural designers are aware of the lower toughness of the welds, they might assume similar properties for the welds and base metal, and jeopardize the integrity of the structure. Perhaps the most important unanswered question is: if the various weld compositions have toughness values that are inferior to the base metal, how can a high toughness structure be constructed?

Other austenitic stainless steels and matching weld compositions, such as AISI type 304 (19Cr-9Ni) and type 316 (18Cr-12Ni-2Mo), have received a more thorough evaluation at cryogenic temperatures.[2-4] One study of the welds (Ref. 2) shows a linear increase in strength (measured at 4 K) as the nitrogen is increased from 0.04 to 0.28 wt.%. The study presented the CVN absorbed energy for the same alloys at 76 K and showed a reduction in the absorbed energy (one measure of toughness) from 41 to 20 J as the strength increased. These data indicate that the strength and toughness are inversely related for these austenitic stainless steels, as they were for the 21Cr-6Ni-9Mn. Another study (Ref. 3) reports such an inverse relationship between strength and toughness in both type 304 base metal and types 308L (20Cr-10Ni) and 316L weld metal, as the alloys are alloyed with N. The 4 K yield strength versus 4 K fracture toughness is shown in Figure 1. This relationship implies that a designer can modify the strength and the toughness by varying the nitrogen content, but that a choice of higher strength implies lower toughness and vice versa.

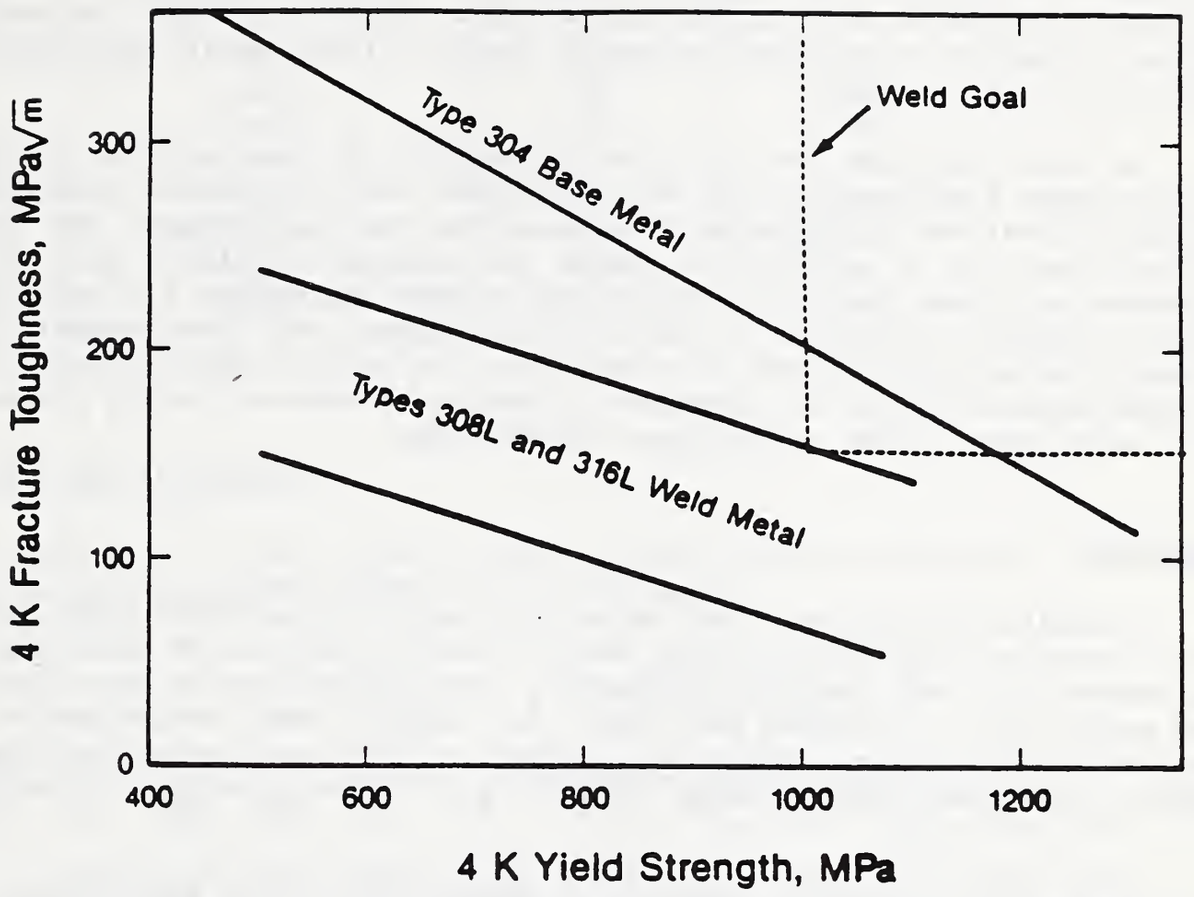

Figure 1. Fracture toughness versus yield strength for welds and base metal at 4 K.

The strength-toughness trend has been used to define a higher strength stainless steel base metal, type 316LN. This alloy has a similar composition to type 316 (18Cr-12Ni-2Mo), but has the carbon restricted below 0.03 wt.% and a nitrogen range of 0.10 to 0.16 wt.%. This nitrogen level strengthens this alloy over that of type 316 or 316L, and reduces the toughness. However, the retained toughness is quite adequate for the intended applications. The trend line for type 304 base metal in Figure 1 is also representative of type 316LN. For a strength of 1000 MPa, the trend line indicates a toughness near 200 $MPa \cdot m^{-1/2}$ at 4 K. Notice that the welds that match this alloy in strength have much lower toughnesses. When evaluated at 76 K, the type 316LN base metal strength drops to near 730 MPa, but the toughness increases, perhaps as much as 50 % over the 4 K value. Therefore type 316LN base metal is also a good candidate for use at liquid nitrogen temperature. Again, the most important question is, what electrode can be used to match both the strength and the toughness of this base metal at cryogenic temperatures, whether at 4 or 76 K?

One solution for applications requiring high toughness and strength is presented in Ref. 4. This study shows that the 76 K CVN absorbed energy is influenced strongly by the Ferrite Number (FN) and nickel content. The toughness increases with nickel and decreases with FN. Since increasing the nickel content is also known to reduce the FN, nickel additions improve the toughness by both means.

An alloy designer can use this information to construct new alloys. Of course other factors must also be considered, but in simplest terms the nitrogen level can be adjusted to achieve the desired strength and the nickel level can be adjusted to change the toughness. Alloys with desirable balances of properties do not exist yet because the market for welds in thick cryogenic structures is still in its infancy and these composition-property relationships have been determined in detail only recently. The program reported here was designed to develop electrodes having properties that match type 316LN, or perhaps 21Cr-6Ni-9Mn.

PROCEDURE

A series of eight shielded metal arc welding electrodes were produced by an outside contractor. Using each electrode, welds were produced in accordance with AWS Specification A5.4. This specification also describes the production of standard weld pads, for compositional determination. From each weld, five CVN specimens (all tested at 76 K) and three 6-mm-diameter tensile specimens were prepared (one for each temperature 4, 76, and 298 K).

The eight electrodes comprised a composition matrix with a base composition near type 308. The matrix included significant variations in the contents of Mn, Mo, N, and Ni to determine the optimum level for these elements. In other words, should we chose a standard weld composition that nearly matched the type 316LN base plate (near 18Cr-10Ni-2Mo-0.14N), or would a significantly different composition provide some substantial property benefits? The matrix consisted of two levels of molybdenum (0 and 3 wt.% to compare a type 308 to the upper limit of a type 316 composition), two levels of nickel (to measure how much this addition increased the toughness), two levels of nitrogen (0.16 and 0.24 wt.% to evaluate the toughness at two strength levels), and two levels of manganese (3 and 6 wt.% for the low nitrogen level and 6 and 9 wt.% to provide a higher solubility level for the higher nitrogen level).

The base nitrogen level of 0.16 wt.% was chosen to match the strength of the type 316LN base metal. Since little data is available at these temperatures and for higher nitrogen alloys, the other elements were varied to evaluate the effects of their interactions on toughness. Our composition range is shown in Table 2. The identification system is based on which elements in the matrix are at higher levels for a given composition.

Table 2. Shielded Metal Arc Composition Design Matrix.

Weld Identification	Content in Weight Percent Mn	Ni	Mo	N
Ni	3	14	-	0.16
NiMo	3	14	3	0.16
Mn	6	9	-	0.16
MnMo	6	9	3	0.16
NiN	6	14	-	0.24
NiNMo	6	14	3	0.24
MnN	9	9	-	0.24
MnNMo	9	9	3	0.24

RESULTS and DISCUSSION

Table 3 lists the actual compositions from the weld pads, including both the major elements and the trace elements.

Table 3. Weld Compositions.

Weld ID	Content in Weight Percent C	Mn	Si	P	S	Cr	Ni	Mo	Cu	N	O	FN
Ni	0.027	2.76	0.29	0.018	0.008	17.94	14.15	0.07	0.11	0.147	0.070	0
NiMo	0.029	2.67	0.31	0.019	0.006	18.06	13.66	2.66	0.09	0.147	0.066	0
Mn	0.034	5.82	0.31	0.019	0.009	19.58	9.17	0.07	0.11	0.177	0.052	1.5
MnMo	0.034	5.52	0.30	0.021	0.011	16.80	9.21	2.95	0.09	0.162	0.054	2.4
NiN	0.027	5.58	0.32	0.017	0.010	18.33	14.24	0.07	0.10	0.216	0.054	0
NiNMo	0.028	5.08	0.34	0.019	0.009	18.36	13.90	2.57	0.09	0.206	0.054	0
MnN	0.033	8.51	0.27	0.018	0.012	20.59	9.29	0.07	0.10	0.241	0.063	1.6
MnNMo	0.030	8.79	0.33	0.021	0.016	17.94	9.29	3.03	0.09	0.221	0.053	2.4

In most cases, the actual compositions in Table 3 are very close to the desired values in Table 2. An exception was that the nitrogen content was limited by reaching saturation in several of the weld pools. We concluded that saturation had been reached because reformulation of the electrode coating with a higher nitrogen level (to bring the nitrogen content closer to the desired value) had no effect, other than to produce microporosity in the weld pool. This microporosity did not appear on the tensile or CVN fracture surfaces and so is not thought to have had a significant effect on the properties. Notice that the chromium level fluctuates more among the four welds with the lower nitrogen contents. This is because these alloys were formulated to a ferrite value near 2 FN, which reduces the cracking sensitivity for these alloys in the FA solidification mode (primary austenite, then ferrite also).

comfortable margin over the strength of type 316LN base metal (76 K yield strength near 735 MPa), showing that we reached this goal. Unfortunately, the CVN values are far below the 88 J absorbed energy value for the 21Cr-6Ni-9Mn base metal. (The absorbed energy value for the type 316LN base metal is expected to be even higher.) The welds with the higher nickel level are tougher, on the average, than those with the lower nickel levels, but none of the compositions have a toughness high enough above the desired lower bound value of 20 J to allow for the inevitable lot-to-lot and procedural fluctuations that occur in the fabrication of large and complex structures. The inferior toughness compared to what was desired is attributed both to not increasing the nickel above the 14 wt.% level, and to the higher inclusion contents inherent in welds produced with the shielded metal arc process. In retrospect, we might have been able to fit several more percent nickel into the coating formulation of the higher nickel compositions, but even that may have been insufficient since the required range may be as high as 20 to 25 wt.% Ni.

Table 6. Mechanical Properties of Shielded Metal Arc Welds at 4 K.

Weld ID	Yield Strength (MPa)	Tensile Strength (MPa)	Elongation (%)
Ni	980	1200	12
NiMo	1070	1400	30
Mn	1040	1470	31
MnMo	1160	1390	11
NiN	1200	1410	12
NiNMo	1180	1315	5
MnN	1275	1540	17
MnNMo	1295	1455	2

The 4 K data confirm the trends seen at 298 and 76 K. The strengths continue to increase as the temperature is lowered to 4 K, and the specific alloy compositions that were strongest at 298 and 76 K tend to be the strongest at 4 K also.

Figure 2 summarizes the strength data for the three temperatures. This figure clearly shows the increasing effect of nitrogen strengthening at lower temperatures. This figure is also useful in identifying the nitrogen level that is necessary to achieve a specified strength at a given temperature.

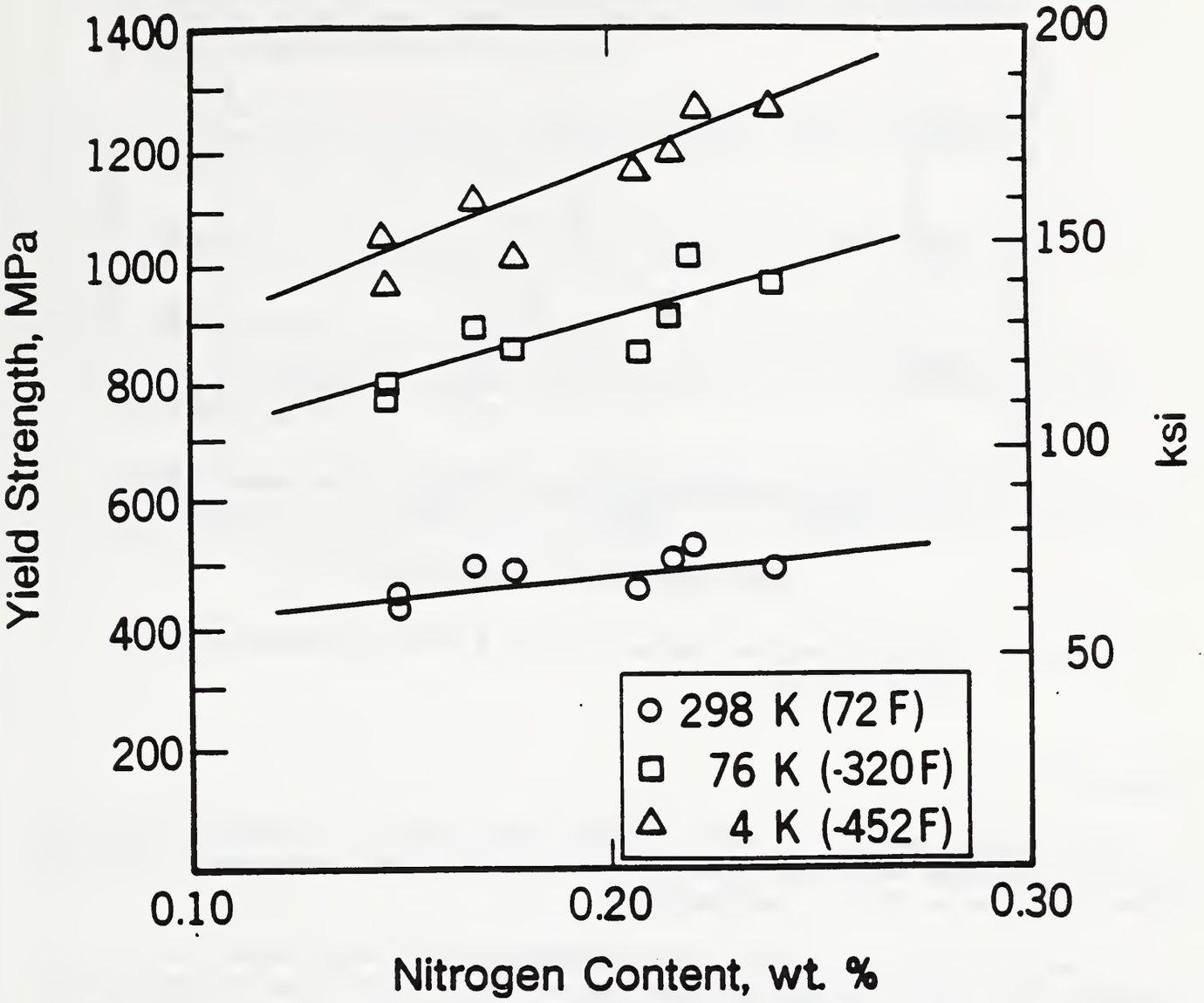

Figure 2. Yield Strengths versus Nitrogen Contents at Three Temperatures

Figure 3 compares the 76 K strength and the 76 K absorbed energy. All the data fall within the same trend band. Although the higher nickel content is along the upper side of the band, this is much less of an improvement in toughness that what we had expected from previous studies.[4] Therefore, it is difficult to predict what nickel level is necessary for the desired absorbed energy level, but it is expected to be near the levels in Ref. 4 (25 wt.% Ni).

The trend band has the expected shape. The highest strength compositions have the lowest toughness.

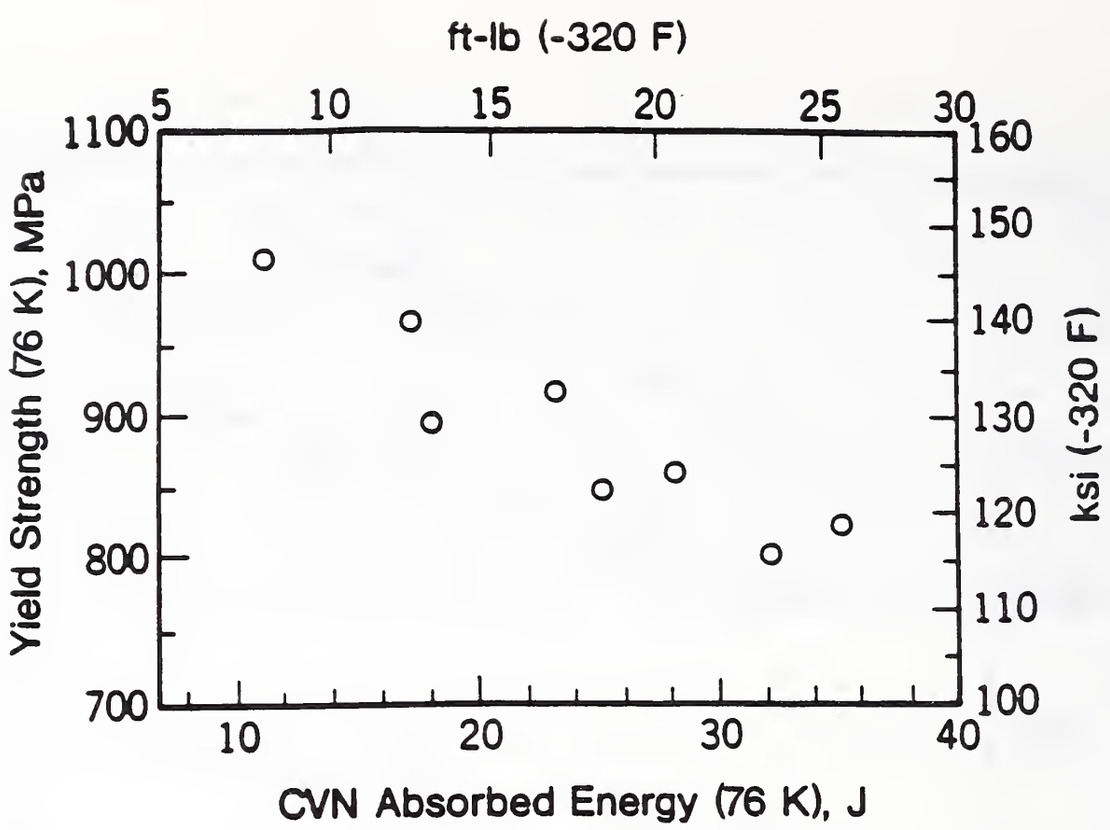

Figure 3. Yield Strengths versus Charpy V-notch Absorbed Energy, both at 76 K.

CONCLUSIONS

1. The shielded metal arc welds, formulated to match the properties of the type 21Cr-6Ni-9Mn and 316LN base metals, matched their strengths, but fell short of matching their toughnesses.

2. To match both the strength and toughness of the base metal, a substantially higher nickel content is necessary. This demonstrates that the standard rule of choosing a welding electrode composition that nearly matches the base plate is not appropriate for cryogenic applications of stainless steels with stringent mechanical property requirements.

ACKNOWLEDGMENTS

Support for the 298 and 76 K part of the program was furnished by Princeton Plasma Physics Laboratory. Support for the 4 K part of the program was furnished by the Department of Energy. The electrodes were formulated and welded by Alloy Rods.

REFERENCES

1. R.H. Espy, Weldability of 21-6-9 Stainless Steel, Materials Studies for Magnetic Fusion Energy Applications at Low Temperatures - I, NBSIR 78-884, National Institute for Standards and Technology, Boulder, Colorado, 1978, p. 169.

2. C.N. McCowan, T.A. Siewert, R.P. Reed, and F.B. Lake, Manganese and Nitrogen in Stainless Steel SMA Welds for Cryogenic Service, Welding Journal, 66, 1987, p. 84-s.

3. R.L. Tobler, T.A. Siewert, and H.I. McHenry, Strength-Toughness Relationship for Austenitic Stainless Steel Welds at 4 K, Cryogenics, 26, July 1986, p. 392.

4. T.A. Siewert, Predicting the Toughness of SMA Austenitic Stainless Welds at 77 K, Welding Journal, 65, 1986, p. 23.

5. C.N. McCowan and T.A. Siewert, The Effect of Inclusions on the Fracture Toughness of 316L Stainless Steel Welds at 4 K, Materials Studies for Magnetic Fusion Energy Applications at Low Temperatures - XII, NISTIR 89-3931, 1989, p. 199.

6. C.N. McCowan and T.A. Siewert, The Fracture Toughness of 25Cr-22Ni-4Mn-2Mo Stainless Steel Welds at 4 K, submitted to Advances in Cryogenic Engineering, Vol. 36, 1989.

CRYOGENIC MECHANICAL PROPERTY DATA FOR 20Cr-25Ni-4.5Mo GAS METAL ARC WELDS

T.A. Siewert and C.N. McCowan
Materials Reliability Division
National Institute of Standards and Technology
Boulder, Colorado

A 20Cr-25Ni-4.5Mo gas metal arc electrode was welded with Ar-N shielding gas mixtures to evaluate their effect on the cryogenic mechanical properties. The welds were found to follow the expected trend of increasing strength with increasing nitrogen content at temperatures between 4 and 298 K. At 76 K and the solubility limit of N in the weld (0.18 wt.%), the welds were found to have the best combination of strength (830 MPa) and Charpy V-notch absorbed energy (104 J) which we have ever measured for a weld.

BACKGROUND

Welds with properties that match those of the base plate are necessary if designers are to have maximum latitude in planning the fabrication of a structure. This general statement is also quite applicable to structures for high-strength cryogenic applications. Various plate materials have been developed and evaluated in some detail for high-strength cryogenic structures, but few welding electrodes have been developed to join these plates into a fabricated structure. Also, the existing stainless steel electrodes (primarily designed for high-temperature applications) have been poorly characterized for cryogenic service.

Recent studies reveal some of the relationships that determine the strength and toughness for these stainless steels when evaluated for cryogenic service. One study [1] shows a linear increase in strength (measured at 4 K) as the nitrogen content of type 308 and 316 welds is increased from 0.04 to 0.28 wt.%. The study determined the Charpy V-notch (CVN) absorbed energy for the same welds at 76 K and found a reduction in absorbed energy, from 40 to 20 J, as the 4 K strength increased from 400 to 1200 MPa. Of course only the low-nitrogen end of the range contains compositions that satisfy the nitrogen limits for these grades, but these data do show (1) how to increase the strength and (2) that the strength and toughness are inversely related for these austenitic stainless steels. Another study [2] reports such an inverse relationship for 4-K strength and 4-K toughness (fracture toughness) in both type 304 base metal and types 308L and 316L weld metal. These studies both imply that a designer can choose either higher strength or higher toughness by varying the nitrogen content, but that a choice of higher strength implies lower toughness and vice versa.

Advanced designs for superconducting coils supports require high-strength materials. Some early studies developed screening data specifically for high-strength weld compositions, but the volume of such data is very limited. Espy [3] compared the properties of the matching composition electrode for 21Cr-6Ni-9Mn-0.2N with various experimental compositions, at cryogenic temperatures. He found that the toughness values at liquid nitrogen temperature for these high-strength welds are marginal when compared to a common design requirement, such as 20 J of absorbed energy in Charpy V-notch (CVN) testing. Espy attributed the poor toughness to the high strength of these electrodes (due to nitrogen additions).

This causes a problem for structural designers since the high strength that justifies a reduction of wall thickness is precisely what makes the 21Cr-6Ni-9Mn composition particularly attractive for cryogenic applications. The 21Cr-6Ni-9Mn base metal (unwelded) has much better toughness (CVN absorbed energies of 88 J at 76 K) than the welds of similar strength.

One solution for applications requiring welds with both high strength and high toughness is presented in Ref. 4. This study shows that the 76 K CVN absorbed energy is determined primarily by the Ferrite Number and the nickel content. Since increasing the nickel content is known to also reduce the Ferrite Number, nickel additions can be used to improve the toughness.

The present study evaluates such a high-nickel composition, when alloyed with nitrogen to produce high strength.

PROCEDURE

Since we did not have sufficient resources or time to melt a series of alloys in a suitable test matrix, we used a welding technique to modify the nitrogen content of a GMA electrode with a composition near the desired value.

We obtained a gas metal arc welding (GMAW) electrode with a high nickel content and low levels of the impurity elements that might promote hot cracking. The electrode had a 1.2 mm diameter, with an American Welding Society designation of E904L and a nominal composition of 20Cr-25Ni-4.5Mo-1.5Mn. The strength of this composition was increased by adding N to the weld pool through the shielding gas. We produced a reference weld with a pure argon gas shield and then added nitrogen at increasing levels until porosity occurred in the weld. Such an approach is not recommended in production because arc length changes affect the nitrogen recovery, but the approach does provide a rapid method of surveying the mechanical properties over a range in strength. We chose gas mixtures with 10, 15, and 20% nitrogen by weight. Previous research has shown that these shielding gas mixtures cause a large increase in the strength, as N content increases to the solubility limit of the weld pool [5]. This procedure had some limitations, such as not allowing us to add Mn to increase the N solubility, but did allow us to develop screening data for a weld of the modified composition.

We produced welds using a 60 degree included angle single-V-groove joint in 25-mm-thick stainless steel plate. We made the welds in the flat

position using 220 A and 30 V, current and voltage levels that produced the best bead shape and droplet transfer. After radiography, we machined 6-mm-diameter tensile specimens and 10-mm-square CVN specimens, both with their test areas centered in the weld metal. The tensile specimens had a 25-mm gage length, so the elongation values were computed on this basis. The room temperature and cryogenic tensile specimens were evaluated by the standard procedure of ASTM E 6; however the cryogenic specimens required a special load frame to keep them at the test temperature [3]. The CVN specimens were immersed in a liquid nitrogen bath (76 K), then tested according to the requirements of ASTM E 23.

RESULTS and DISCUSSION

Weld Nitrogen Contents

Table 2 lists the amount of nitrogen that was measured in the welds, as a function of the shielding gas mixture. The poor correlation between the mixture ratio and the amount of nitrogen reinforces the statement that this is not a suitable technique for production welds. The irregularity is attributed to variations in the arc length from one weld test plate to another, which changes the amount of nitrogen dissolved in the weld. However, for each weld plate, we noted less than a 5% variation in the two or three individual measurements that were averaged to give these values. This consistency within a weld indicates that the values are representative of each weld. The weld with 0.27 wt.% nitrogen had some pores, indicating that this weld exceeded the solubility limit for nitrogen.

Table 2. Nitrogen Contents (wt.%) for the Shielding Gas Mixtures.

Shielding Gas	Nitrogen Content
pure Ar	0.06
Ar/10% N	0.16
Ar/15% N	0.27
Ar/20% N	0.18

Mechanical Properties

Table 3 lists the mechanical properties for the gas metal arc electrode. The strength values compare favorably with those reported by Espy, but the toughness values are substantially higher. Therefore, the plan to improve the toughness by higher nickel contents was successful.

The measured nitrogen contents for each weld are included for comparison. Notice the lack of an increase in strength as nitrogen is increased above 0.18 wt.%. This indicates that nitrogen above this level is not distributed in the matrix in a form that promotes strengthening, but is probably in the form of pores. The data in Ref. 1 suggest that higher

strength would have been achieved if the composition had a higher solubility for nitrogen (such as an electrode formulated with a higher manganese level). The optimum manganese level would be the level sufficient to dissolve the nitrogen content that provides the desired strength.

Table 3. Mechanical Properties of 904L (20Cr-25Ni-4.5Mo-1.5Cu).

Temperature (K)	Nitrogen Content	Yield Strength (MPa)	Tensile Strength (MPa)	Elongation (%)	Reduction of Area (%)	CVN Energy* (J)
298	0.16	385	640	40	63	-
"	0.18	420	675	47	70	-
"	0.27	415	665	48	67	-
76	0.16	750	1160	55	48	139
"	0.18	830	1240	57	36	104
"	0.27	780	1170	50	48	147
4	0.06	800	1110	35	-	-
"	0.16	940	1310	52	35	-

* Average of results from two or three specimens.

These CVN absorbed energy values are the highest we have ever measured for a weld. (The slightly lower values at 76 K for the 0.27 wt.% N weld are attributed to the porosity that was revealed on the fracture surface.) These excellent values are attributed to the combination of a very tough and stable austenitic structure, and the use of a shielding gas that is very low in oxygen content. Our recent research has shown a strong correlation between high toughness and low oxide inclusion contents [5]. Since most austenitic stainless steel GMAW electrodes are welded with an Ar/2% O shielding gas, it is reasonable that replacement of the oxygen with nitrogen will reduce the weld oxygen content, and so the inclusion content. An Ar/N shielding gas mixture produces a transfer mode and weld puddle fluidity different and less desirable than an Ar/O mixture, but the importance of good properties dominates for this application.

Microstructural Evaluation

In addition to measuring the mechanical properties, we investigated the microstructure of the 904L welds. Figure 1 shows the structure of a tensile specimen at a 20X magnification for the weld produced with the Ar/10% N mix. The microstructure has the large grain size typical of a fully austenitic structure, each grain containing many dendrites of the same orientation (dendrite packets). The interdendritic regions and grain boundaries are free of the large second phase regions and precipitates seen in fully austenitic welds of lower toughness [6]. The inclusion content, distribution, and diameters are typical of austenitic welds produced with a low-oxygen welding procedure.

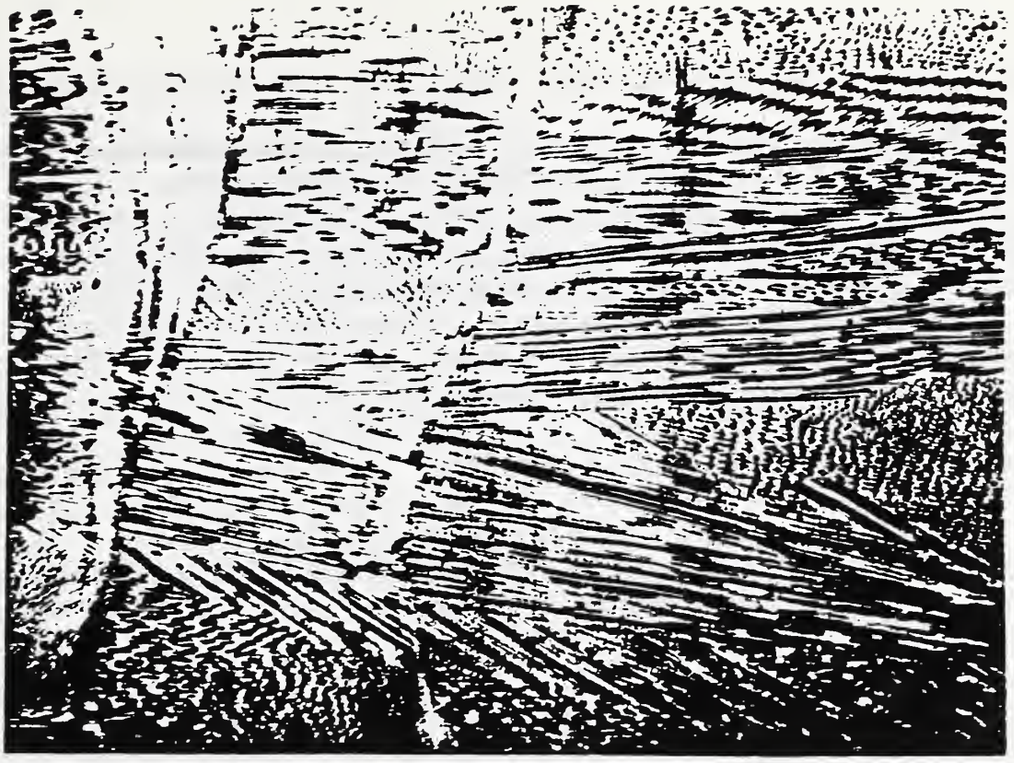

Figure 1. Microstructure of weld produced using a Ar/10% N shielding gas. (20X)

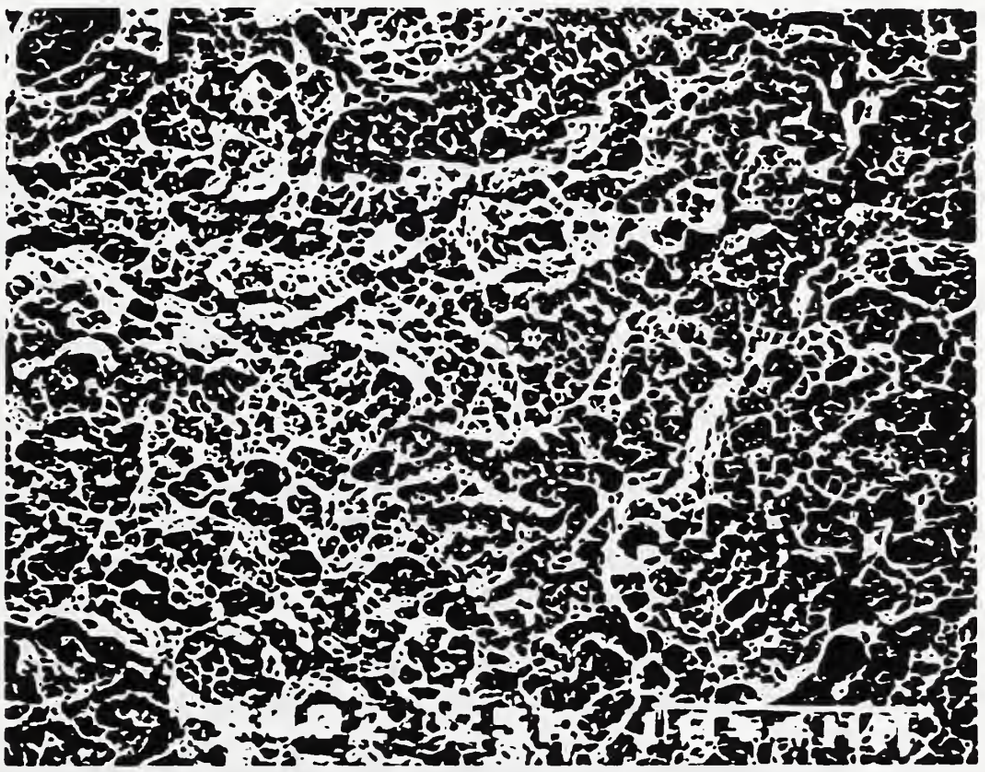

Figure 2. Fracture surface of a tensile specimen from a weld produced using an Ar/15% N shielding gas. (300X)

Fracture Surface Appearance

The fracture surfaces of the tensile specimens had macroscopic fracture features associated with high toughness, and could be best described as consisting of ductile dimples and shear zones. There was no evidence of

brittle fracture, and only several indications of fracture along the dendrite cell boundaries (also known as ribbed or corduroy fracture). This behavior is quite consistent with other welds that exhibited good toughness. Previous studies of compositions with poorer toughness exhibited very large percentages of brittle fracture or rupture along austenite grain boundaries. Figure 2 shows the ductile dimple appearance of the fracture surface at 300X, in this case the fracture surface of a specimen tested at 4 K. This specimen shows several examples of the corduroy fracture.

CONCLUSION

(1) This 904L weld exhibited excellent CVN absorbed energy values, the highest values which we have ever developed for welds at 76 K.

(2) The combination of good toughness and strength make 904L a good candidate material for cryogenic structures.

ACKNOWLEDGMENTS

This program was supported by Princeton Plasma Physics Laboratory. The electrode was furnished by the Wire Division of Sandvik Steel.

REFERENCES

1. C.N. McCowan, T.A. Siewert, R.P. Reed, and F.B. Lake, Manganese and Nitrogen in Stainless Steel SMA Welds for Cryogenic Service, Welding Journal, 66, 1987, p. 84-s.

2. R.L. Tobler, T.A. Siewert, and H.I. McHenry, Strength-Toughness Relationship for Austenitic Stainless Steel Welds at 4 K, Cryogenics, 26, July 1986, p. 392.

3. R.H. Espy, Weldability of 21-6-9 Stainless Steel, Materials Studies for Magnetic Fusion Energy Applications at Low Temperatures - I, NBSIR 78-884, National Institute for Standards and Technology, Boulder, Colorado, 1978, p. 169.

4. T.A. Siewert, Predicting the Toughness of SMA Austenitic Stainless Welds at 77 K, Welding Journal, 65, 1986, p. 23.

5. C.N. McCowan and T.A. Siewert, The Effect of Inclusions on the Fracture Toughness of 316L Stainless Steel Welds at 4 K, Materials Studies for Magnetic Fusion Energy Applications at Low Temperatures - XII, NISTIR 89-3931, 1989, p. 199.

6. C.N. McCowan and T.A. Siewert, The Fracture Toughness of 25Cr-22Ni-4Mn-2Mo Stainless Steel Welds at 4 K, submitted to Advances in Cryogenic Engineering, Vol. 36, 1989.

FRACTURE CHARACTERIZATION OF 316LN WELDS WITH INTERCELLULAR FERRITE at 4 K

C.N. McCowan and T.A. Siewert
Materials Reliability Division
National Institute of Standards and Technology
Boulder, CO 80303

The cryogenic strength and toughness of type 316LN stainless steel welds were evaluated. The weld composition was produced by adding nitrogen to an argon based shielding gas during welding with a type 316L stainless steel gas metal arc welding (GMAW) electrode. The solidification mode of the welds was primary austenitic: intercellular ferrite contents are approximately 4 percent. The average yield strength (950 MPa), ultimate strength (1400 MPa) and fracture toughness (135 $MPa \cdot m^{\frac{1}{2}}$) of the welds at 4 K are typical of values found for austenitic stainless steel welds at cryogenic temperatures. This report focuses principally on the fracture paths observed in tensile and compact tension specimens, and the role of ferrite in the fracture. The ferrite phase in these welds deformed in a ductile manner during failure.

INTRODUCTION

The good strength and toughness of type 300 series stainless steels at 4 K makes them attractive for use as structural materials in superconducting magnet designs using Nb_3Sn superconductors [1]. In particular, type 316LN plate material is currently considered a prime candidate for the fabrication of superconducting magnet cases, and welds of matching composition to join this plate material are an obvious choice [2]. Having identical compositions for the weld and plate materials, however, does not necessarily result in identical mechanical, physical, and corrosion properties.

The grain morphology, compositional homogeneity, and microstructural phase constituents in the welds and plate material differ significantly due to differences in their thermal and deformation histories. Type 316 plate microstructures are fully austenitic, typically have equiaxed grain sizes of around 50 μm, and have a homogeneous composition [3-4]. In type 316LN welds, the microstructures are often two-phase (austenite + ferrite) [5]. Also, differences between primary ferritic and primary austenitic solidification modes affect the morphologies and location of the respective phases in the microstructure, and modify the solute segregation [6-7]. Finally, the grain size and inclusion content of the welds are much greater than those typical of stainless steel plate materials.

Past studies show type 300 stainless steel welds have a broad range of strength and toughness at 4 K [8]. In Fig. 1, the range in these properties

is indicated by a scatter band that is based on data from type 308L and 316L welds. The individual data points identified in the figure are from stainless steel GMA welds made to evaluate the effect of inclusion content on toughness. For these welds, the inclusion contents varied over a range similar to the inclusion contents of the welds used to construct the scatter band (55 000 to 10 000 inclusions per mm^2) and they show that much of the scatter in properties for the 308L and 316L welds is attributable to differences in the inclusion contents [9]. The data for the fully austenitic welds (18Cr-20Ni-5Mn-0.15N) in Fig. 1 also show the increased toughness, due to the higher Ni content, and the increased strength, due to the higher N content of these welds compared with the type 316L stainless steel weld composition [10].

This study evaluates the mechanical properties of a low-ferrite-content 316LN weld composition that solidified in a primary austenitic mode. Some ferrite was desired in the welds to increase their resistance to solidification cracking [7]. The welds in this study were expected to be tougher than 316L welds previously tested (Fig. 1) due to slightly higher Ni content, lower ferrite content, and austenitic grain morphology. Increasing inclusion content was expected to decrease the toughness of the welds.

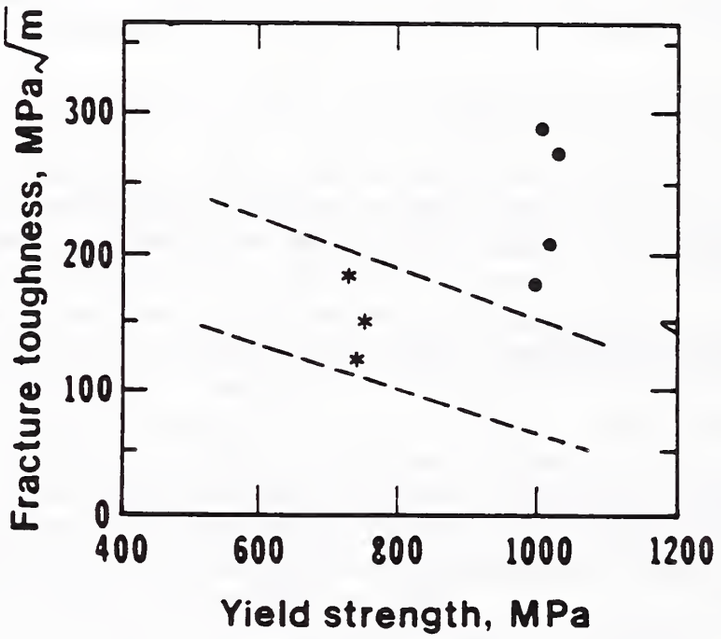

Figure 1: The trend of decreasing toughness with increasing strength at 4 K is indicated by the scatter band (dotted lines) developed using type 308L and 316L stainless weld data (data not shown) [8]. The data points included in the figure are from: (1) fully austenitic (18Cr-20Ni-5Mn-3Mo-0.15N) GMAW welds (dots) in which inclusion contents range from 9 000 to 23 000 inclusions per mm^2, and (2) 316L stainless steel GMAW welds (18Cr-11Ni-2Mn-3Mo, FN=7) that solidified in an FA mode and have inclusion contents ranging from 19 000 to 55 000 inclusions per mm^2 [9].

MATERIALS AND PROCEDURE

The composition of the 316L GMA electrode used in this study is given in Table 1. This composition was chosen because it has a sufficiently high ferrite content (predicted to be 8 FN (approximately 8% ferrite) by the WRC diagram [11], so that N could be added during welding, to increase the strength of the weld, and some ferrite would still be present in the microstructure. Ideally, we wanted to produce welds that solidified in a primary austenitic mode, had ferrite contents near 4 or 5 FN, and had yield strengths of 1000 MPa at 4 K.

Table 1. The GMA electrode composition.

C	Mn	P	S	Si	Cr	Ni	Mo	Co	Cu	Nb	Ti
.014	1.63	0.014	0.010	0.38	18.6	12.2	2.58	0.03	0.08	0.01	0.01

To make the welds, a type 304L stainless steel base material was beveled to provide a 60° single V-groove weld configuration. The plates were approximately 300 mm long and 20 mm thick: 12 weld passes were needed to fill the joint. Welding was done at 27 V and 230 A with an electrode extension of 16 mm. A shielding gas of 10% N and 90% Ar was used. The weld identified as SN was made using a conventional GMA shielding nozzle and a Ar-10%N shielding gas. The DN weld was made using double Ar-N shielding: a second, larger shielding nozzle was fitted around the usual shielding nozzle to provide improved shielding of the arc. This reduces the amount of oxidation that occurs during welding and thereby lowers the inclusion content of austenitic stainless steel GMA welds [9].

From each weld, one all-weld-metal tensile specimen and two compact specimens, notched in the direction of welding, were machined for testing at 4 K. Testing procedures and equipment are described elsewhere [12].

One compact tension specimen from each weld was postcracked and fractured following the determination of the $K_{Ic}(J)$ values, to examine their fracture surfaces. The second specimen from each set was left intact following testing, so that metallographic cross sections of the crack tips could be ground and polished for evaluation.

RESULTS

Microstructure

The microstructure of the welds had cellular-dendritic features indicative of primary austenitic solidification. Eutectic ferrite was

present at intercellular regions in the structure: magnetic measurements showed ferrite content to be approximately 4 FN. The inclusion contents of the welds were estimated at 17 000 and 11 000 inclusions per squared millimeter for the SN and DN welds respectively. Inclusion counts were made at 2000X using an image analysis system on a light microscope (10 fields per weld were evaluated).

Mechanical Properties

The mechanical properties measured for the welds are given in Table 2. The yield strengths of the SN (962 MPa) and DN (936 MPa) welds differ only slightly. Although both welds had strengths of less than 1000 MPa, the strengths are high enough to give a good indication of the toughness that can be anticipated at 1000 MPa.

The fracture toughness values of the DN (132 $MPa \cdot m^{\frac{1}{2}}$) and SN (141 $MPa \cdot m^{\frac{1}{2}}$) welds are typical of type 300 series stainless steel welds. However, these 316LN welds were expected to increase in toughness with decreasing inclusion content and this did not occur. The results show that the SN weld, which has a higher inclusion than the DN weld, also has the higher toughness of the two welds. To explore reasons for this anomalous behavior, we examined the fracture surfaces of the weld specimens.

Table 2. Mechanical Properties of the Type 316L Welds.

Specimen	Strength (MPa)		Elongation	Fracture Toughness ($MPa \cdot m^{\frac{1}{2}}$)
	Yield	Ultimate	%El	K_{Ic}(J)
DN-1	936	1458	52	135
DN-2				129
SN-1	962	1352	24	140
SN-2				142

Fractography

The fracture surfaces of the tensile and compact tension specimens have rib-like features formed by ductile failure at intercellular regions of the microstructure. Figure 2 shows a portion of the fracture surface on the SN compact tension specimen that is dominated by these rib-like features. This fracture surface morphology, sometimes called corduroy fracture, has been reported previously for type 316 [13], and for type 310 [14] stainless steel welds. To gain a better understanding of how these features relate to the weld microstructure, the fracture surface of this specimen was partially

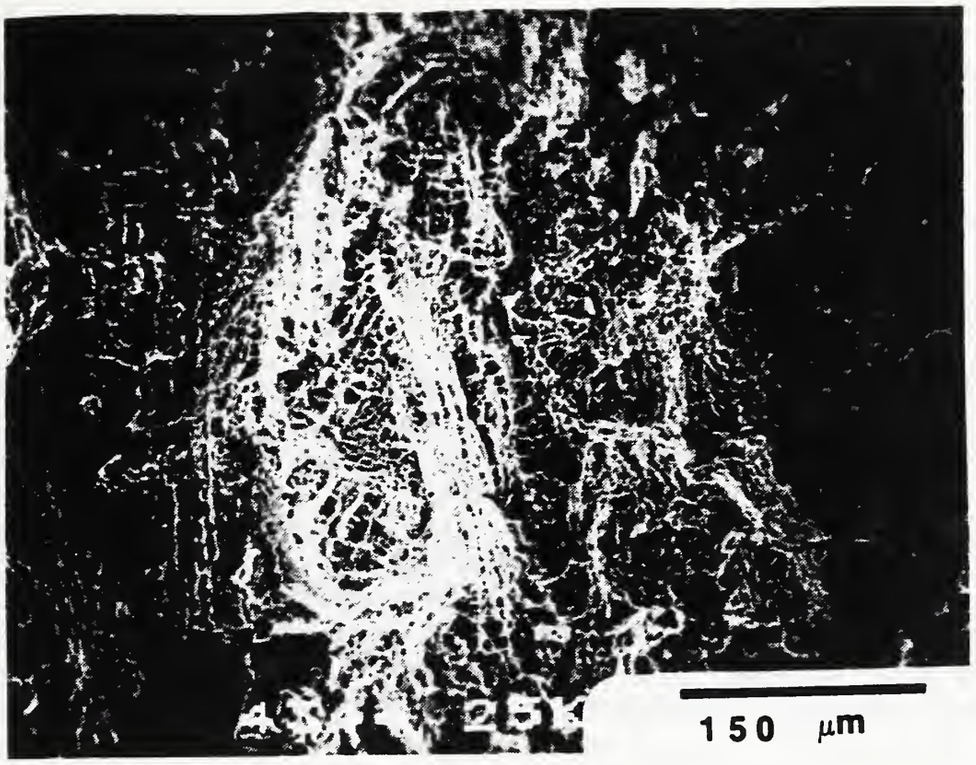

Figure 2: The fracture surface of the SN compact tension specimen has rib-like features formed during ductile failure of intercellular regions in the weld microstructure.

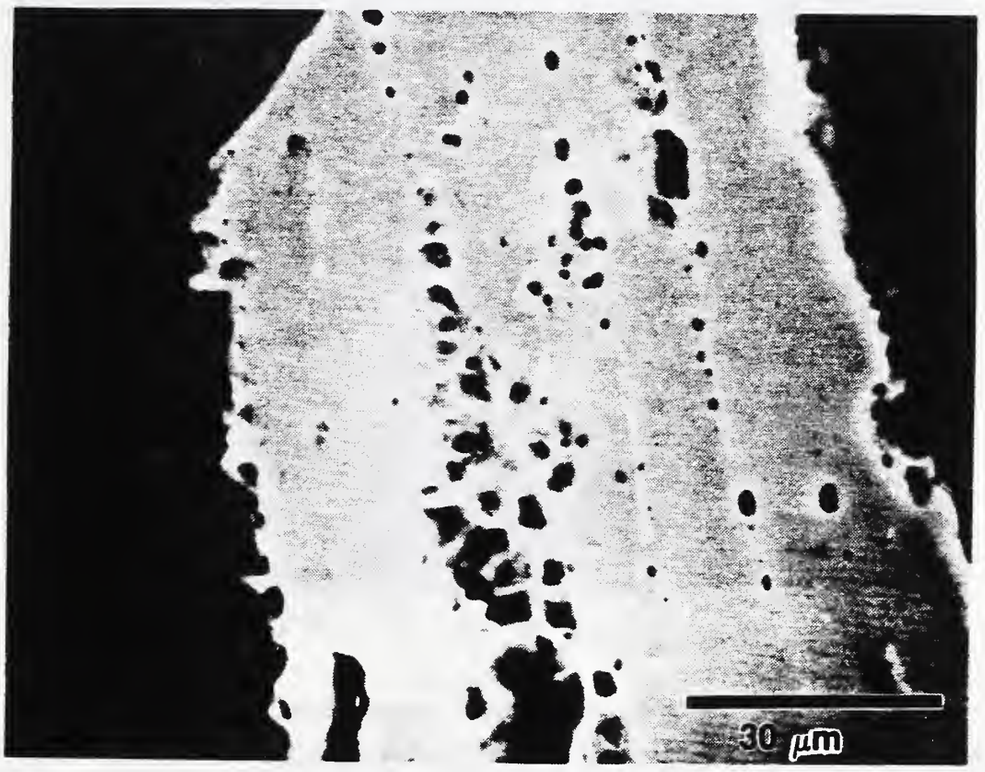

Figure 3: A plane polished parallel to the fracture surface of the SN compact tensile specimen shows void formation associated with the ferrite phase (light contrast, linear features).

ground and polished for light microscopy. In Fig. 3, areas of weld microstructure and regions of the fracture surface below the polished plane are shown. We see that the ribbed fracture features (dark band of ductile dimple rupture) run along the intercellular regions of the microstructure. Ferrite (light phase) is present in these regions, and failure appears to originate near the ferrite-austenite interface. Voids preferentially nucleate at inclusions or precipitates near the ferrite-austenite interface, and coalescence of these voids results in the ribbed features present on the fracture surface.

A similar failure scenario was developed from observations made on cross sections of the SN compact tension specimen as shown in Figure 4. This specimen was sectioned perpendicular to the crack growth plane, parallel to the crack growth direction. The regions near the crack tip, where cracks are not fully linked, show the crack path generally follows intercellular regions in the microstructure, identified by the presence of the ferritic phase. Again voids are observed near the ferrite-austenite interface and they appear to be nucleated at inclusions. The ferrite phase dig not crack or behave in a brittle manner in these specimens, nor in cross sections of the tensile specimens which had extensive plastic flow prior to failure.

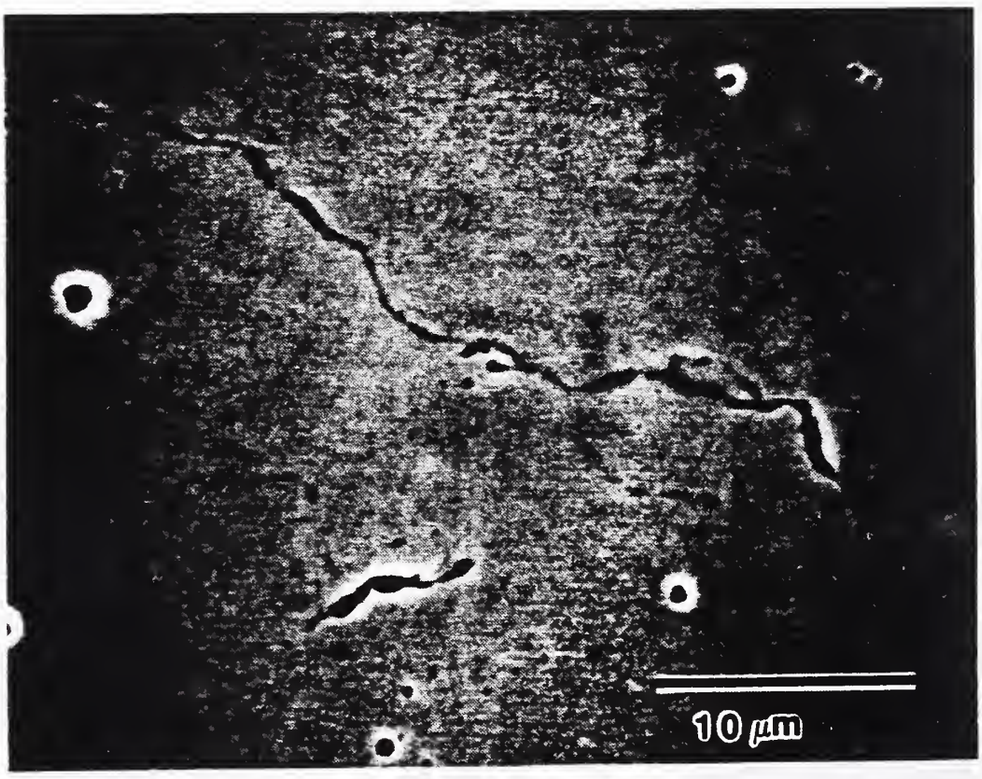

Figure 4: On cross sections polished perpendicular to the fracture plane in the compact tension specimens, the crack path was found to be associated with the ferrite phase. The ferrite is visible here (not etched) as a skeletal network that is only slightly darker than the austenite matrix.

DISCUSSION

We suspect that the toughness of the intercellular regions is what has been measured in these tests and that the importance of average inclusion content and strength play a diminished role in determining fracture toughness when failure occurs at intercellular regions. In the 18Cr-20Ni (FN=0) and 316L (11Ni, FN=7) welds that were tested previously (Fig. 1), for example, inclusion content was shown to be a principal factor in limiting the toughness of stainless steel welds whether the primary phase in solidification is ferrite or austenite. In these cases, where inclusions affect toughness, fracture surfaces have a more transgranular appearance than those of the 316LN (12Ni, FN=4) welds tested in this study. The intercellular fracture of the 316LN and the lack of a significant effect of inclusion content on toughness may be due to the weld solidification mode.

As shown in Fig. 5, the liquidus surface of the Fe-Cr-Ni equilibrium diagram, the type 316 stainless steel weld compositions cross over the eutectic trough. Therefore, large regions of these weld structures can have eutectic phase morphologies (austenite + ferrite) and compositions. The 316LN welds made in this study contain appreciable amounts of eutectic structure. The 316L welds previously tested showed little evidence of eutectic ferrite and welds with similar Cr content to these welds, but higher Ni solidify in a fully austenitic mode. Comparing the 316 data, we find significant gain in the strength-toughness relationship due to a change in the solidification mode from FA (316L welds, FN=7) to AF (316LN, FN=4). There are significant changes in the structures of these two types of welds (austenite morphology, ferrite morphology, ferrite composition, segregation), but the effect of these differences on the strength and

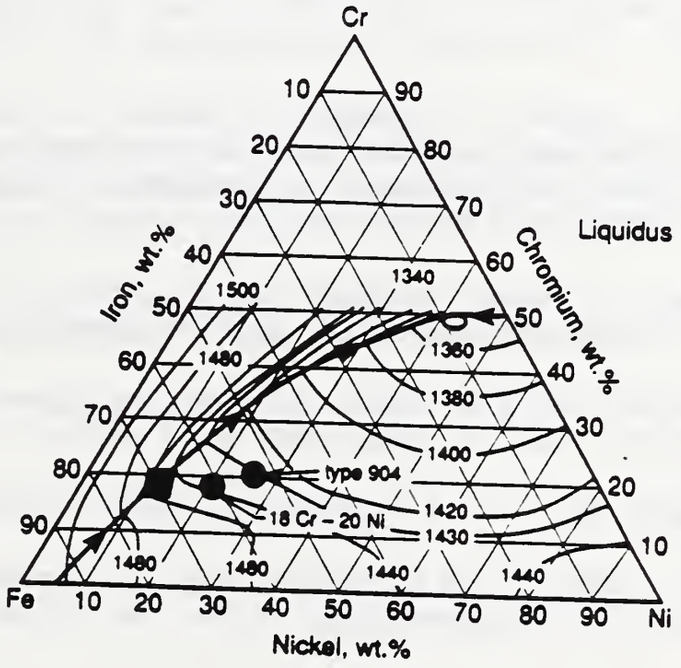

Figure 5: The liquidus surface of the Fe-Cr-Ni system. The specification limits for type 316 stainless steel welding compositions are indicated by the parallelogram at the liquidus trough. Also, the positions of 18Cr-20Ni alloys and type 904 stainless steel alloys are shown.

toughness of the welds is not resolvable in our data. Quite possibly, beneficial effects on toughness, such as slightly higher Ni and lower ferrite content for the 316LN weld, are offset by the compositional inhomogeneities inherent in its more eutectic-like solidification. Although the toughness of the 316LN welds might be improved by optimizing Cr-Ni contents, increases in toughness are expected to be small.

To improve toughness significantly, it appears that major increases in Ni content are needed, increases beyond the specification limit for type 316 stainless steel weld compositions. Such increases in Ni move the alloy composition away from the liquidus trough, so the benefits of Ni on toughness can realized [2]. Therefore, to weld type 316LN base materials, it seems that welds of matching composition cannot be used if the strength and toughness of the base material must also be matched. The 18Cr-20Ni and the type 904L weld compositions shown on the Fe-Cr-Ni ternary diagram, have proved to have mechanical properties more similar to the type 316LN base metal.

CONCLUSIONS

(1) A lower toughness intercellular region in the welds inhibited improvements in toughness through reduction of the inclusion content.

(2) The type 316LN weld compositions tested in this study do not have high enough toughness at 4 K to match the properties of type 316LN base materials.

REFERENCES

1. J.L. Young, C.J. Heyna, P. Komarek, H. Krauth, G. Vecsey, and C. Marinucci, The Forced Flow Cooled Coils For the International Energy Agency Large Coil Task, Advances in Cryogenic Engineering, Vol. 27, Plenum Press, 1981, pp 11-19.

2. N.J. Simon and R.P. Reed, Strength and Toughness of AISI 304 and 316 at 4 K, Journal of Nuclear Materials, 141-143 (1986), pp 44-48.

3. G.F. Vander Voort and H.M. James, Wrought Stainless Steels, Metals Handbook, 9th Ed., Vol. 9, ASM, 1985, pp 279-304.

4. Metals Handbook, Ed. 9, Vol 9, American Society for Metals, pp 279-296.

5. N. Suutala, T. Takalo, and T. Moisio, Ferrite-Austenitic Solidification Mode in Austenitic Stainless Steel Welds, Met Trans. A., Vol 11A, 1980, pp 717-725.

6. J.A. Brooks, J.L. Williams, and A.W. Thompson, STEM, Analysis of Primary Austenitic Solidified Stainless Steel Welds, Met. Trans. A., Vol. 14A, 1983, pp 23-31.

7. Y. Arata, F. Matsuda, and S. Katayama, Solidification Crack Susceptibility in Weld Metals of Fully Austenitic Stainless Steels (Report II) - Effect of Ferrite, P, S, C, Si and Mn on Ductility Properties of Solidification Brittleness, Transactions of JWRI, Vol. 6, No. 1, Welding Research Institute, Osaka, Japan, 1977, pp 105-116.

8. R.L. Tobler, H.I. McHenry, and T.A. Siewert, Strength-Toughness Relationship for Austenitic Stainless Steel Welds at 4 K, Cryogenics, Vol. 26, 1986, pp 392-396.

9. C.N. McCowan and T.A. Siewert, Fracture Toughness of 316L Stainless Steel Welds With Varying Inclusion Contents at 4 K, Advances in Cryogenic Engineering (Materials), Vol. 136, Plenum Press, 1989, pp 1331-1338.

10. C.N. McCowan et. al, Inclusions and Fracture Toughness in Stainless Steel Welds at 4 K, Advances in Cryogenic Engineering - Materials, Vol. 32, 1986, Plenum Press, pp 335-342.

11. C.N. McCowan and T.A. Siewert, Stainless Steel Weld Metal: Prediction of Ferrite Content, Welding Research Council Bulletin 342, 1989, pp 1-36.

12. R.L. Tobler, D.T. Read and R.P. Reed, Strength/Toughness Relationship for Interstitially Strengthened AISI 304 Stainless Steels at 4 K, Fracture Mechanics: 13th Conference, ASTM STP 743, ASTM, 1981, pp 250-268.

13. J.C. Lippold, M.C. Judas, and E.N.C. Dalder, The Relationship between Microstructure and Fracture Behavior of Fully Austenitic Type 316L Weldments at 4.2 K, Metallurgical Transaction A, Vol. 16A, 1985, pp 1835-1848.

14. C.N. McCowan and T.A. Siewert, The Fracture Toughness of 25Cr-22Ni-4Mn-2Mo Stainless Steel Welds at 4 K, NISTIR 89-3931, Material Studies for Magnetic Fusion Energy Applications at Low Temperature XII, 1989, pp 187-198.

15. Metals Handbook, Ed. 8, Vol. 8, American Society for Metals, pp 424.

TEST STANDARDS

UNITED STATES-JAPAN DEVELOPMENT OF TEST STANDARDS PROGRAM

LEADER: R.L. Tobler
CONTRIBUTORS: P.T. Purtscher, R.P. Reed, D.P. Vigliotti, and R.P. Walsh

OBJECTIVES:

- Draft mechanical property test standards for structural alloys and composites at 4 K.
- Participate in other standards organizations including the American Society for Testing and Materials (ASTM) and its task group activities for the purpose of establishing the documents as voluntary concensus standards.
- Conduct experimental research to evaluate technical questions relating to standard test procedures at 4 K.
- Administer interlaboratory test programs to support standards developments.

PROGRAM HIGHLIGHTS:

Structural Alloys

- Nine drafts of a proposed standard 4-K tensile test procedure were written and submitted for review at domestic and international workshops. The ninth draft has been formally submitted to ASTM, and is two-thirds of the way through the balloting process required to establish a new standard.

- At ASTM's request the sixth draft of a proposed standard for 4-K fracture toughness testing was rewritten in the form of an annex for ASTM Method E 813-89; the annex was submitted to ASTM to begin due process for standardization.

- Interlaboratory tension and fracture toughness tests were conducted on a Japanese Fe-24Cr-15Ni alloy. A summary of results was published in the proceedings of the International Cryogenic Materials Conference held July 24-28, 1989 in Los Angeles.

- Research on the problems of Charpy impact testing at 4 K was conducted. NIST, the Massachusetts Institute of Technology, and the Japan Atomic Energy Research Institute cooperated to produce three research papers on this subject. On the basis of this work, balloting has begun at ASTM on a revision of the notched bar impact test standard, Method E 23-88.

- Standards development work for structural metals is now sufficiently advanced at ASTM and prestandards research for composites has begun.

Composites

- Various national and international meetings were attended to establish liaison with task groups involved in standards development. These included:

    1. ASTM's biannual D-30 technical committee meetings,
    2. SACMA's Interface '89 conference on implementing composite standardization,
    3. the National Planning Committee's meeting to achieve industry-wide standardization for composite materials, and
    4. VAMAS' Technical Working Group meeting on Cryogenic Structural Materials.

- Composite materials scientists were interviewed to obtain information necessary to identify the status of activities in standards development for shear and compression tests of composites.

- An international symposium on composites testing was organized by NIST as part of the International Cryogenic Materials Conference in Los Angeles, CA, July 24-28, 1989. Special sessions were devoted to shear, compression, and irradiation testing. The 16 papers presented were published along with a summary paper to establish a point of departure for initiating research in support of cryogenic standards.

- Improved experimental apparatus was constructed at NIST to evaluate optimum test procedures at temperatures as low as 4 K. Interchangeable fixtures allow various specimen types to be tested in the same cryostat. Initial evaluation of shear testing has begun with comparison of torsion, short beam, Iosipescu, and double-notched compact specimen shear tests of glass-epoxy composites.

VAMAS Technical Working Party
Business Meeting, March 1990

CRYOGENIC STRUCTURAL MATERIALS

VAMAS (the Versailles Project on Advanced Materials and Standards) is an international organization that conducts prestandards research to promote and accelerate the development of standards for advanced materials. On March 5 and 6, representatives from Austria, England, Germany, Italy, Japan, Switzerland, and the U.S. met to discuss the VAMAS projects on cryogenic structural materials and test standards. Kernforschungzentrum, Karlsruhe, West Germany was the location. The first day (March 5) was devoted to planning current programs up to the end of 1991. The second day explored possible work beyond 1991.

First Day

Host Dr. A. Nyilas delivered the opening remarks and welcome. Dr. T. Ogata then presented the goals of the technical working party and outlined the current status of round robin tests for alloys. Specific technical presentations followed by Drs. Reed (standardization issues), Nyilas (fatigue crack growth), and Ferrero (strain gage research). Presentations were mixed with questions and discussion. The following is a summary of information related to ongoing cooperative works.

The subject receiving most attention was the forthcoming round robin on stainless steel. Seven labs in Japan and four in Europe and the U.S. have agreed to participate. The test material is modified A-286 (Fe base, 26 Ni, 14Cr, 2Mo, 2Ti, and 0.1Al), a potential candidate for superconducting conduit sheaths with Nb_3Sn conductors. Five tension and five toughness specimens will be distributed to each laboratory in May. Several points of protocol were resolved at this meeting:

(1) tension and toughness tests will be carried out using the draft documents that NIST has written for ASTM,
(2) selected interpretive tests will be carried out at certain institutes to supplement the basic program, and
(3) the test material will be properly screened beforehand, by tests at NRIM.

The supplementary tests will be performed at various institutes and are intended to answer remaining questions such as load cell calibration and specimen size effects.

The 4-K strain gage calibration program was discussed by C. Ferrero. In the past few weeks, materials and strain gages from major European, U.S., and Japanese manufacturers were distributed to all participants. This round robin program is expected to take about six months to complete. Ferrero informed us about the thermal expansion and Kondo resistivity effects expected to be present in the calibration of Cu–Ni alloy strain gage outputs on this program.

Second Day

This was an informal meeting (with lower attendance) to explore work beyond 1991. Considerable time was spent discussing a possible 5-year effort devoted to composites. With draft standards for metals and alloys being processed in several countries, it appears that composites pose the next crucial problems in structural materials. A VAMAS program is desirable because no single laboratory has the resources to tackle this subject alone.

The testing of composites is not a new idea; it was proposed at previous VAMAS working meetings, and a special session was held in July 1989 at ICMC to define the state of the art in this area. Many different tests are used for structural insulating composites in different countries, and results for bulk materials are not in agreement, even at room temperature. For example, shear testing at 76 and 4 K yields ultimate strengths that range from 8 to 160 MPa for similar materials. This wide disparity is frustrating and clearly unacceptable for designers. It is unclear how the results for different test methods might be related to each other, and it is impossible to specify the appropriate values for design calculations.

Specifically, a program to promote standard cryogenic shear test methods for filamentary polymer-based composites was strongly advocated by R.P. Reed. After initial discussions, the attendees at this meeting focussed on the possibility of initiating a program with Dave Evans (Rutherford National Laboratory) as the likely leader for such work. The material of primary interest would be a glass-reinforced epoxy, perhaps G10CR. First, a large batch of commercial material would be obtained and characterized thoroughly with respect to composition and microstructure. Then a double round robin would be executed in three steps:

I. Conduct the first round robin, showing the spread of results for various shear test methodologies,
II. Draft the proposed shear test standard, and
III. Conduct a second round of tests to refine the draft.

While this plan progresses, volunteer labs would conduct selected supportive research. The results would be assembled and analyzed to find correlations between different techniques. A large reserve of material would be available for supplemental or future use so that a large database would continuously build for at least one material. The results could lead to the development of miniature specimens for cryogenic irradiation studies.

In the past, this task had been tabled due to lack of a lead laboratory with composites expertise, insufficient number of qualified labs (at least six are required for round robins), and the priority of establishing metals standards. At this time, Dave Evans can provide the necessary leadership, and Rutherford has already provided his initial support for material procurement and characterization expenses. The number of participating laboratories would be increased to a sufficient level by inviting new participation from organizations known to be interested in composites at cryogenic temperatures. (A list of prospective organizations was readily assembled at this meeting from the attendee's recommendations.)

SIDE GROOVES AND K_{Ic} CALCULATIONS*

R.L. Tobler
Materials Reliability Division
National Institute of Standards and Technology
Boulder, Colorado

This note discusses the method of stress intensity factor (K) calculations for side grooved specimens of a high strength austenitic steel. Two specimens with grooves and two without grooves were tested. The K_{Ic} measurements are equivalent if calculations for grooved specimens use the net thickness instead of the gross or effective thicknesses.

INTRODUCTION

Side grooves are sometimes advocated for ductile fracture tests according to ASTM Methods E 813-87 [1], and yet no provision is made for their use in linear elastic tests according to ASTM Methods E 399-83 [2]. Given a material of unknown toughness, it may be desirable to side groove a specimen, test it, and then (depending on the loading response) evaluate the toughness using either the K_{Ic} or the J_{Ic} test methodologies. Permitting side grooves in tests of linear elastic materials would facilitate the development of a common specimen geometry and test procedure for K_{Ic} and J_{Ic} tests.

For standard compact specimens without side grooves,

$$K = \{P/(BW^{1/2})\} \cdot f(a/W), \qquad (1)$$

where:

P = applied load,
B = gross thickness,
W = specimen width,
a = average crack length, and
f(a/W) = a function of relative crack length [2].

With side grooves, the thickness in the fracture plane is reduced and Eq. (1) must be modified. Two substitutions for B in Eq. (1) are plausible. Methods E 813-87 Section A2.5.3 [1] substitutes an effective thickness, $(B \cdot B_n)^{\frac{1}{2}}$, where B_n is the net thickness. Freed [3], however, simply substituted B_n in his study of the effects of side grooves on single-edge-notched specimens of various alloys at room temperature. The more accurate procedure can be determined experimentally. Here, we compare measurements for plane (ungrooved) and side grooved compact specimens of an austenitic steel tested in liquid helium at 4 K. The plane specimens were tested previously by Read and Reed [4]. Two additional specimens remaining from their study were fatigue cracked, then side grooved and tested.

PROCEDURE

The test material was a 5 cm thick steel plate in the as-received condition: annealed at 1120°C for 2 h and water-quenched. The mill chemical composition in mass per cent is Fe-21.15Cr-12.37Ni-4.96Mn-0.31N-0.041C-2.17Mo-0.49Si-0.015S-0.026P-0.18Nb-0.15V. The alloy in this condition has an austenitic microstructure, an average grain diameter of 34 μm, and some grain boundary precipitation [4]. Tension test results for this alloy are listed in Table 1.

Fracture toughness tests followed Methods E 399-83 and used compact specimens 38.1 mm thick and 76.2 mm wide. The crack orientation was T-L. The specimens were not tested at room temperature, but at liquid helium temperature (4 K) where linear elastic behavior prevails. Essentially, the K_{Ic} test at 4 K does not differ much from that at 295 K, except for the provision of cryogenic apparatus.

The specimen geometry used in these tests [4] deviates from Method E 399-83 only in that the crack starter notch was modified to enable the clip gage to be positioned at the loadline. However, a finite element analysis [5] indicated that such modifications have negligible effect on K calculations for relative crack lengths (a/W) greater than 0.4.

There was a slight difference in specimen preparation procedures in that the specimens of the original study were precracked at 76 K using constant minimum and maximum fatigue loads; the maximum fatigue stress intensity factor steadily increased with crack length, reaching 35 $MPa \cdot m^{\frac{1}{2}}$ at the end of

Table 1. Mechanical properties of an Fe-21Cr-12Ni-5Mn-0.31N steel (two tests per temperature, averaged).

Temperature K	Yield Strength MPa	Ultimate Strength MPa	Elongation %	Reduction of area %
295	528	842	35	61
4	1446	1893	9	33

precracking. In the present study, the test specimens were fatigue cracked in liquid nitrogen at 76 K, side grooved, and then fractured at 4 K at a crosshead rate of 0.03 mm/s. The fatigue cycling was computer-controlled with a sinusoidal wave in load control at 30 Hz. The minimum-to-maximum load ratio during fatigue was 0.1. The stress intensity factor range ΔK in fatigue was held constant at 35 MPa·m$^{\frac{1}{2}}$ by load reductions as a function of crack growth. The side grooves were 3.8 mm (10% of B) deep on each side, B_n was 30.50 mm, and $(B \cdot B_n)^{\frac{1}{2}}$ was 33.3 mm. The groove radii and included angles were 0.25 mm and 60°, respectively.

RESULTS

A 4-K test record for a Fe-21Cr-12Ni-5Mn-0.31N specimen with side grooves is shown in Fig. 1. Type 1 load-displacement behavior is observed, with slight nonlinearity before fast fracture. The critical loads P_Q used for calculating K_{Ic} from Eq. (1) were determined by the secant offset procedure in the usual manner [2].

Table 2 lists the K_{Ic} values and validity criteria for the side grooved specimens. The net specimen thickness is more than twice that is required for valid tests. If B_n is used instead of B in Eq. (1), the toughness calculations for side grooved specimens agree with the results for plane specimens tested by Read and Reed [4]. If $(B \cdot B_n)^{\frac{1}{2}}$ is used, the calculated fracture toughness values for side grooved specimens are 10% lower than those for the plane specimens.

A representative 4-K fracture surface is shown in Fig. 2. Whether side grooved or not, the Fe-21Cr-12Ni-5Mn-0.31N steel specimens after testing show essentially zero slant fracture along the edges. The fatigue crack curvature is pronounced, but not drastic enough to disqualify the test results. The edge cracks a_e are 12–4% shorter than the 3-point average crack lengths a_a, but up to 15% is tolerable [2]. In this regard, note that Read and Reed's datum [4] for one ungrooved specimen was reported as invalid (K_Q) in 1979, because the crack front curvature was excessive according to the standard of those days (Method E 399-74). Today, that K_Q value qualifies as a valid K_{Ic} measurement because the curvature tolerances were relaxed in the updated standard [2]. The degree of crack curvature was further alleviated by side grooving after fatigue cracking because that removes material from the specimen edges and tends to reduce the difference between a_e and a_a.

DISCUSSION

At 4 K, the Fe-21Cr-12Ni-5Mn-0.31N steel is linear elastic because of its high nitrogen content and less than optimum metallurgical condition. The precipitates in the microstructure are conducive to linear elastic fracture and are not usually desired for cryogenic service. The specimen thickness, whether side grooved or not, is more than sufficient to establish plane strain in this study.

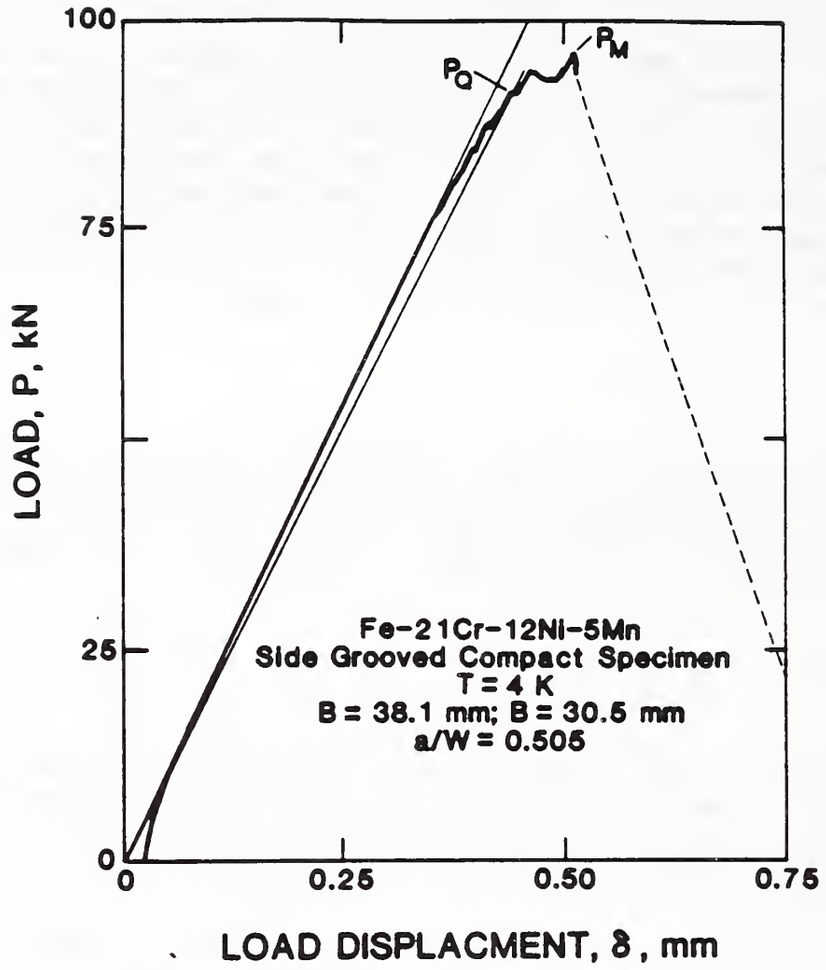

Figure 1. Load–displacement record for a side grooved specimen tested at 4 K.

Table 2. Toughness results at 4 K for side grooved compact specimens, with toughness calculated using different corrections for thickness. The values for ungrooved specimens were 104 and 108 MPa·m$^{1/2}$ [4].

Specimen number	P_M/P_Q	$\frac{a_a - a_e}{a_a}$ mm	Required Thickness[a] mm	K_{Ic} (using $B \cdot B_n)^{1/2}$ MPa·m$^{1/2}$	K_{Ic} (using B_n) MPa·m$^{1/2}$
2	1.05	12	13.7	95	107
12	1.03	14	13.4	94	106

[a]calculated from $B = 2.5(K_{Ic}/YS)^2$, as specified by E 399-83, Section 9.1.3.

Figure 2. Appearance of a 38 mm thick compact specimen with side grooves after fracture at 4 K.

Side grooves are sometimes used in ductile fracture tests for increased constraint, but they cost more to machine and are not needed if a high degree of plane strain constraint is already achieved in the gross thickness. For ductile alloys, several benefits may derive from side grooves: they suppress the formation of shear lips at the specimen surfaces in plane stress, improve the uniformity of the stress state through the thickness, improve compliance predictions of the crack length, and tend to alleviate tunnelling of the crack front. Side grooves may also help to define the point at which slow-stable crack extension begins in J-tests [6]. Side grooves are of little practical value for linear elastic specimens but there is no reason to exclude the use of side grooves in K_{Ic} tests if that serves a purpose such as the development of a common test method.

CONCLUSION

If side grooves are used in linear elastic tests the most accurate method of calculation is desired. For compact specimens of a high strength austenitic steel in this study we obtained best results by substituting B_n for B in the conventional K-calibration, Eq. (1). Use of the effective thickness $(B \cdot B_n)^{\frac{1}{2}}$ appears to be less accurate, giving toughness values that are 10% lower than K_{Ic}. The experimental results favor the procedure of Freed: B_n replaces B in Eq. (1). The implication is that the elastic strain energy works uniformly across the net thickness, and that any perturbation of the elastic strain energy at the specimen edges caused by the presence of side grooves is negligible for thick specimens. Our experiments, however, are limited to only a few tests of a material that exhibits a fairly high degree of crack front curvature. More tests of other alloys having straighter crack fronts are necessary to confirm this study.

REFERENCES

1. Standard Test Method for J_{Ic}, A Measure of Fracture Toughness, ASTM Designation E 813-87, 1988 Annual Book of ASTM Standards, Section 3, Metals Test Methods and Analytical Procedures (Amer. Soc. Test. Maters., Philadelphia, 1988) 686-700.

2. Standard Test Method for Plane-Strain Fracture Toughness of Metallic Materials, ASTM Designation E 399-83, 1988 Annual Book of ASTM Standards, Section 3, Metals Test Methods and Analytical Procedures (Amer. Soc. Test. Maters., Philadelphia, 1988) 480-504.

3. C.N. Freed, Application of side grooves in the determination of K_{Ic} for high-strength metals, in: Fracture Mechanics of High Strength Materials: Theory and Practice, ISI Pub 120 (Iron and Steel Institute, London, 1970) 29-34.

4. D.T. Read and R.P. Reed, Toughness, fatigue crack growth, and tensile properties of three nitrogen-strengthened stainless steels at cryogenic temperatures, in: The Metal Science of Stainless Steels, E.W. Collings and H.W. King, eds. (TMS-AIME, New York, 1979) 92-121.

5. R.L. Tobler and W.C. Carpenter, A numerical and experimental verification of compliance functions for compact specimens, Eng. Fract. Mechs., 21: 547-556 (1985).

6. P.K. Poulose, Determination of fracture toughness from thin side-grooved specimens, Eng. Fract. Mechs., 26: 203-211 (1987).

INTERLABORATORY TENSION AND FRACTURE TOUGHNESS TEST RESULTS FOR CSUS-JN1 (Fe-25Cr-15Ni-0.35N) AUSTENITIC STAINLESS STEEL AT 4 K*

H. Nakajima, K. Yoshida, and S. Shimamoto

Japan Atomic Energy Research Institute
Naka-machi, Ibaraki, Japan

R.L. Tobler, R.P. Reed, R.P. Walsh, and P.T. Purtscher[1]

National Institute of Standards and Technology
Boulder, Colorado, U.S.A.

ABSTRACT

Interlaboratory tests are part of the U.S.–Japan cooperative program in fusion energy to establish cryogenic test standards for structural alloys. The second round of 4-K tension and fracture toughness tests for CSUS-JN1 (Fe-25Cr-15Ni-0.35N) austenitic stainless steel are described in this paper. The scatter of interlaboratory measurements is acceptable if some fracture toughness data are excluded as outliers.

INTRODUCTION

A data base and a mechanical design standard are required to build superconducting coils for fusion reactors. The Japan Atomic Energy Research Institute (JAERI) in collaboration with Japanese steel industries[1] successfully developed Japanese Cryogenic Steels (JCS) that have 4-K yield strengths over 1,200 MPa, and fracture toughnesses over 200 MPa$\sqrt{m}$. Still, the design data base is insufficient and there is no design standard yet because the collaboration of many organizations is necessary to establish them.

The U.S.–Japan Workshop on Low Temperature Structural Materials and Standards was held in December, 1984. The ultimate goals of this work are to establish the data base and design standard. The first collaborative program was initiated to evaluate existing material test procedures and standardize them. For this purpose, the first interlaboratory tension and fracture tests for CSUS-JK2 (Fe-22Mn-13Cr-5Ni-0.2N) austenitic stainless steel were conducted at 4 K in 1987.[2] Drafts of the cryogenic test standards were written based on those results. This paper presents the second interlaboratory test results for CSUS-JN1 (Fe-25Cr-13Ni-0.35N) austenitic stainless steel that was tested according to the drafted standards.

---

[1]Present affiliation: Advanced Steel Processing and Products Research Center, Colorado School of Mines, Golden, Colorado.

Advances in Cryogenic Engineering (Materials), Vol. 36
Edited by R. P. Reed and F. R. Fickett
Plenum Press, New York, 1990

Table 1. Participating Laboratories and Personnel

Institute	Supervisor	Researcher	Staff
@ Hitachi Research Laboratory (HRL)	T. Matsumoto	Y. Wadayama	H. Sato
@ Japan Atomic Energy Research Institute (JAERI)	S. Shimamoto	H. Nakajima	M. Oshikiri K. Yoshida
@ Kawasaki Steel Corp. (KSC)	K. Nohara	N. Matsuno	T. Katoh
@ Kobe Steel, Ltd. (KSL)	T. Horiuchi	M. Shimada	S. Nakayasu
@ Lawrence Berkeley Laboratory (LBL)	J.W. Morris, Jr.	J.W. Chan J. Glazer P.A. Kramer	
@ Lawrence Livermore National Laboratory (LLNL)	J.R. Miller	L.T. Summers	D.A. Freeman R.A. Riddle
@ Massachusetts Institute of Technology (MIT)	R.G. Ballinger	I.S. Hwang M.M. Morra	
@ National Institute of Standards and Technology (NIST)	R.P. Reed	R.L. Tobler P.T. Purtscher	R.P. Walsh
@ NKK Corp. (NKK)		Y. Kohsaka	N. Yamagami
@ National Research Institute of Metals (NRIM)	K. Ishikawa	T. Ogata K. Nagai O. Umezawa	T. Yuri
@ Nippon Steel Corp. (NSC)	H. Abo	T. Nakazawa T. Takeshita	K. Oki
@ Tohoku University, Research Institute for Strength and Fracture of Materials (RISFM)	H. Takahaski	T. Shoji	K. Nakano
@ Toshiba Research and Development Center (TRDC)	H. Ogiwara	E. Fukushima	S. Kobatake M. Tanaka

PURPOSE AND PARTICIPANTS OF THE SECOND INTERLABORATORY TESTS

The tests described here were conducted according to the proposed draft cryogenic standards that were based on room temperature standards (ASTM E 8, E 8M, JIS Z 2241) and the first interlaboratory test results. Several aspects of testing at 4 K, such as test rate, specimen size, and serrations, are considered in those drafts. The purpose of the second round tests is to confirm the procedures defined by the draft cryogenic standards and to check some items which must be resolved before the draft standards are ratified.

The participants are volunteers from government, academic, and industrial organizations with recognized experience in materials testing. Table 1 lists the laboratories and personnel. Thirteen laboratories participated, including nine from Japan and four from the U.S.

MATERIAL AND SPECIMENS

The test material is CSUS-JN1, one of the new JCS austenitic stainless steels. It was supplied from a commercial steel manufacturer as 100 mm thick plate from a 50 metric ton industrial heat. Table 2 lists the chemical composition.

Table 2. Chemical Composition of CSUS-JN1

C	Si	Mn	P	S	Ni	Cr	N
0.018	0.33	4.1	0.019	0.002	15.26	25.2	0.37

Samples were cut at one laboratory from 1/4 thickness locations of the original plate stock. This was done to minimize variables such as machining and specimen location as factors influencing the results. We selected 18-mm diameter bars for tension tests, and 25-mm thick compact tension (CT) specimens for fracture toughness tests, and distributed them to each participant. The tension specimens were machined to their final dimensions by each laboratory to suit individual preferences.

Tensile Specimens

The tension specimens were machined in the T orientation (load axis is perpendicular to the hot-rolled direction) and in a cylindrical bar configuration. Table 3 lists the final specimen dimensions for each laboratory.

Fracture Specimens

Most specimens used in this study were proportional CT specimens (defined by Method E 813-81) with a 25 mm thickness, a 26.5 mm notch length, and a 50 mm width. The CT specimens used for multiple-specimen tests were proportional but were 20 mm wide. The notch orientation was T-L, and displacement was measured at the loadline. Fatigue precracking varied for each laboratory. Maximum stress intensity factors ranged from 22 to 43 MPa/m, and initial crack-length-to-width ratios were 0.55 to 0.70. Most specimens were precracked at room temperature (RT), but specimens F8, 9, 14, 15, and 16 were precracked at liquid nitrogen temperature (LNT), and F14, 15, and 16 were side-grooved after precracking to a net thickness reduction of 20%. Except for side grooving, these variations in specimen preparation did not lead to any resolvable effects on the fracture toughness measurements.

Table 3. Nominal Specimen Dimensions (mm)

Specimen	D	G	A	R	L
T1,T2	6.0	30.0	36.0	15.0	85.3
T3,T4	7.0	35.0	42.0	20.0	105.0
T5,T6	7.0	35.0	42.0	20.0	105.0
T7,T8	5.0[a]	25.0	30.0	15.0	100.0
T9,T10	7.0	--	42.0	20.0	105.0
T11,T12	6.3	25.4	34.3	4.75	77.7
T13	6.3	25.4	33.3	4.75	77.7
T14,T15	6.3	25.4	31.8	4.76	63.5
T16,T17,T18	6.3	25.4	44.0	9.52	71.8
T19,T20	7.0	35.0	50.0	20.0	105.0
T21,T22	6.25	32.0	35.0	10.0	83.0
T23,T24	7.0	--	43.0	20.0	105.0

D: Diameter
G: Gage length
A: Length of reduced section
R: Radius of fillet
L: Total length of specimen
(See ASTM E 8 or 8M, Fig. 8)

a: Classified as a sub-size according to the 4-K draft standard

TEST PROCEDURE

Tension Test

The tensile properties of interest are the yield strength (YS), the ultimate tensile strength (UTS), the elongation (EL), and the reduction of area (RA). YS is defined by the 0.2% plastic strain offset method applied to load-strain gage, load-extensometer, or load-time chart recordings. UTS is the maximum load divided by the original area. EL is computed by three methods: dividing the change in gage length by the original gage length (ELG), dividing the change of total length by the original length of reduced section (ELL), and dividing the change in length of the reduced section by the original length of reduced section (ELA). RA is the change in cross-section area divided by the original area. Most tests were conducted using screw-driven machines with crosshead displacement control and nominal strain rates less than 1×10^{-3} s^{-1}, where the nominal strain rate is the crosshead speed divided by the initial length of the reduced section. Young's modulus (E) measurements were optional.

Fracture Properties

The fracture properties of interest are J_{Ic} and $K_{Ic}(J)$, as estimated from $K_{Ic}(J)^2 = J_{Ic} \cdot E$. J_{Ic} is defined by the intersection of the blunting and linear regression lines as per ASTM Method E 813-81. Ten laboratories used the single-specimen unloading compliance (ULC) technique, but the multiple-specimen (MS) method and a special single-specimen Key-Curve technique[2] were also used. Seven labs used servohydraulic machines (four used clip gage control, three used stroke control). Five labs used screw-driven machines (crosshead speed control). Four labs used specimen rotation and/or crack growth corrections to J-Δa data.

RESULTS

Tensile Properties

Figure 1 shows the YS and UTS data plotted versus nominal strain rate. There are no measurable effects for the strain rates covered in this study: 0.23 to 8.3 x 10^{-4} for YS, and 0.79 to 12 x 10^{-4} for UTS. The time chart YS data are nearly equivalent or slightly higher than results from strain or extensometer plots, with differences ranging from -3.4 to 13.1%. Three laboratories discovered an unusual serration phenomenon: at low strain rates, as shown in Fig. 2, only one serration occurred before failure.

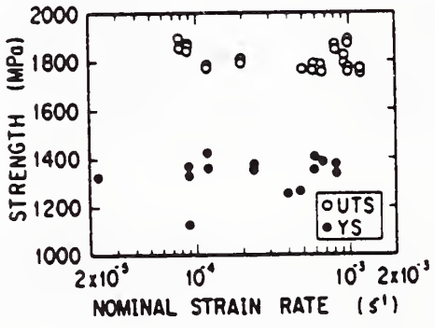

Fig. 1 Yield and ultimate strength measurements at 4 K

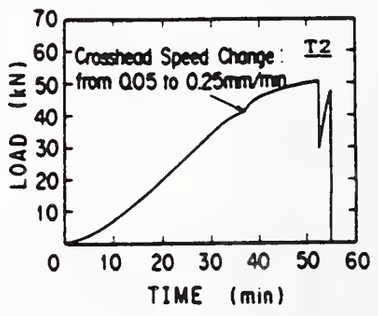

Fig. 2 Load-time chart for a test at low strain rate

Table 4. Tensile Properties of CSUS-JN1

Spec.	YS[a] S-S (MPa)	YS[b] L-T (%)	UTS (MPa)	EL ELG (%)	EL ELL (%)	EL ELA (%)	RA (%)	E (GPa)	Strain Rate (10^{-4} s^{-1})
T1	--	--	1778	20	21	21	39	--	0.23, 1.2[c]
T2	1328	-0.3	1789	23	23	21	42	195	0.23, 1.2[c]
T3	1356	1.0	1740	--	31	--	45	189	2.4, 12.0[c]
T4	1371	2.1	1768	--	35	--	47	208	2.4, 12.0[c]
T5	1426	1.8	1851	24	21	--	39	210	1.2, 0.79[c]
T6	1375	2.8	1893	25	24	--	44	194	1.2, 0.79[c]
T7	1384	-3.4	1876	37	37	35	43	240	6.7, 10.0[c]
T8	--	--	1893	33	37	32	45	--	6.7, 10.0[c]
T9	1254	2.1	1770	--	33	--	45	191	4.0, 10.0[c]
T10	--	--	1757	--	34	--	46	--	4.0, 10.0[c]
T11	1352	-0.5	1760	32	38	37	46	196	5.9
T12	1407	-1.8	1794	28	32	28	46	194	5.9
T13	1333	--	1872	39	--	--	45	208	8.3
T14	1379	--	1848	35	--	--	48	209	8.3
T15	--	--	1768	--	34	37	50	--	5.0
T16	1125	13.1	1855	24	22	17	38	195	0.9
T17	1330	5.5	1873	21	20	16	42	202	0.9
T18	1361	4.2	1845	24	20	15	37	202	0.9
T19	--	--	1787	38	42	38	46	--	6.7
T20	--	--	1754	38	43	33	52	--	6.7
T21	--	--	1822	31	32	--	42	210	4.8, 9.5[c]
T22	1263	8.7	1792	37	35	--	34	208	4.8, 9.5[c]
T23	--	--	1817	--	29	29[d]	47	--	2.0
T24	--	--	1797	--	27	27[d]	49	--	2.0
Max. (%)	6.7		4.5	9	13	10	8		
Min. (%)	-15.8		-4.0	-10	-10	-13	-10		
Avg.	1336		1812	30	30	28	44		

a: S-S -- Measured from stress-strain curve.
b: L-T -- Measured from load-time curve and reported as % of YS[a].
c: A rate change was used; cited first is the rate before the YS measurement; second is the rate after YS measurement until failure.
d: Measured from length of fillet.

A summary of tension test results is given in Table 4. The variation in EL values obtained by the three different measurement methods is within 9% (see specimen T18), but the scatter of measurements among laboratories is about 20%. The relations between ELL, RA, and nominal strain rate are given in Fig. 3. At low strain rates, ELL increases with increasing nominal strain rate and becomes constant at rates higher than 5×10^{-4} s^{-1}. The effect of strain rate on RA is weaker compared to its effect on ELL.

Fracture Toughness

The fracture toughness data are listed in Table 5. Except for the data of specimens F8 and 9 which indicate low toughness, and F10 and 11 which indicate high toughness, the bulk of the results are consistent as explained in the Discussion.

Table 5. Fracture Properties of CSUS-JN1

Spec.	J_{Ic} (kJ/m^2)	$K_{Ic}(J)$ (MPa$\sqrt{m}$)	C1[a] (MPa)	C2[a] (kJ/m^2)	a_o[b] (%)	Δa_p[b] (%)	Method	Precrack Temp.
F1	254	226	235	234	0.2	-17.8	ULC	RT
F2	243	221	199	227	-1.7	-0.6	ULC	RT
F3	240	220	187	226	-3.0	-11.3	ULC	RT
F4	224	213	173	211	-2.7	-15.3	ULC	RT
F5	228	214	188	214	0.01	-4.1	ULC	RT
F6	238	219	140	227	--	--	ULC	RT
F7	208	205	270	190	-3.4	-10.0	ULC	RT
F8	134	164	206	123	-4	-22	ULC	LNT
F9	49	100	206	46	-8	0.7	ULC	LNT
F10	466	305	195	439	--	--	ULC	RT
F11	411	286	174	390	--	--	ULC	RT
F12	216	219	132	207	0.3	24.0	ULC	RT
F13	239	230	193	225	-0.5	12.0	ULC	RT
F14[c]	149	173	230	138	-0.03	-2.4	ULC	LNT
F15[c]	234	217	197	220	1.0	-10.9	ULC	LNT
F16[c]	163	182	178	153	-2	-8.9	ULC	LNT
F17	207	204	269	189	-0.5	-36.1	ULC	RT
F18	237	219	281	216	-0.6	-8.6	ULC	RT
F19	231	216	--	--	--	--	Key-Curve	RT
F20-24[d]	254	226	270	232	--	--	MS	LNT
Max.(%)	102	43						
Min.(%)	-79	-53						
Avg.	231	213						

a: C1 and C2 are constants of the R-curve [$J = C1 \cdot \Delta a + C2$].
b: Calculated from (prediction - measurement)/measurement.
c: Specimens were side-grooved after precracking.
d: Crack extension is the average of center three points.

DISCUSSION

Tension Test

The YS and UTS measurement consistency in this study is similar to the first interlaboratory test results. It appears that limiting the nominal strain rate to 1 x 10^{-3} s^{-1} or less, as in the current draft standards, is reasonable. This study indicates that a small bias may be introduced in YS

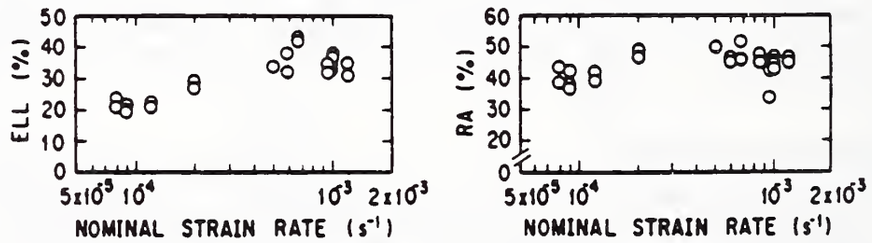

Fig. 3 Elongation and reduction of area measurements at 4 K

measurements when the 0.2% offset procedure is applied to time chart plots, rather than strain gage or extensometer plots. This bias depends not only on the test apparatus but also the technician's skill. For convenience, however, the load-time chart method is quite useful in alloy screening or commercial production control where maximum precision is not required.

ELL and ELA measurements are specified in the draft tension test standards based on the assumption that plastic elongation of the gripped part is negligible compared with that of the specimen's reduced section. ELL and ELA are easy to measure, and are potentially useful since they eliminate the need for gage length marks which sometimes cause failure. As there are only small differences between ELG, ELL, and ELA in this study we can employ ELL and ELA in addition to ELG at 4 K.

Unusual serration behavior explains the observed dependence of EL on strain rate. When tested at low strain rates, specimens of JN1 showed lower ductility and fewer serrations. This slow strain rate effect increases the scatter of interlaboratory elongation measurements, and if it is taken into account the overall data scatter may be reduced to half that shown in Table 4. This effect depends on the material tested, and further experiments will be needed to fully evaluate it. Revised draft standards should note this effect, and a lower limit of strain rate should perhaps be selected to establish the data base for such materials.

Fracture Toughness

The scatter of reported J_{Ic} values, as shown in Table 5, is very large in this study. However, if the F8, 9, 10, and 11 data are eliminated, the pooled average values of toughness for specimens without side-grooves are

$$J_{Ic} = 232 \text{ kJ/m}^2 \quad +9.5\%, \quad -10.8\%,$$

and

$$K_{Ic}(J) = 216 \text{ MPa}\sqrt{\text{m}} \quad +4.6\%, \quad -5.6\%.$$

Then, as before,[2] there is little scatter. The pooled data include a datum obtained from five specimens tested by the MS method (F20-24, Table 5). In the MS method, thinner specimens were used, but the data are comparable as there is no size effect for 12.5 to 75 mm thicknesses in this alloy.[3]

Evidently, side grooving reduces J_{Ic} for this material. In a separate study of CSUS-JN1, side-grooved specimens gave about 20% lower values than those without grooves.[4] If the data from specimens F14, 15, and 16 are increased by 20%, those results, too, agree with the pooled average value.

The data of F8, 9, 10, and 11 clearly fall outside the range of pooled data. The resistance curves for these specimens contained no data in the blunting line region, and only three to five points in the regression line region, which contributes to scatter in determination of J_{Ic}. For example, resistance curves at the onset of testing often show negative Δa. In the cryogenic standard, we treat this by shifting the blunting line to the left on the Δa axis until there is a best fit to experimental data. If there are too few data in the blunting region, the blunting line is not shifted to the best position. We conclude that more data in the blunting region as well as in the regression line region should be taken when the unloading compliance technique is used.

As shown in Table 5, the Δa_p agreement is not good in this study. In most cases the ULC-predicted values are smaller than those measured from fracture surface. The measured and calculated values must agree to within 15% according to ASTM Method E 813-81. Our J_{Ic} data, however, are not sensitive to the Δa_p disagreement, as also indicated previously.[2] Although

the Δa_p agreement affects the slope of the resistance curve, apparently it has a negligible effect on J_{Ic}.

SUMMARY

Eleven laboratories measured tensile properties and twelve measured J_{Ic} for CSUS-JN1 (Fe-25Cr-15Ni-0.35N) austenitic stainless steel according to the proposed cryogenic test standards. Aside from the slow strain rate effect on elongation which is peculiar to this material, there are few systematic effects for tensile properties as long as tension tests are conducted according to the proposed standards. Therefore standardization of the drafts is being pursued through JIS in Japan and ASTM in the U.S.

The unloading compliance method appears to be reliable for J_{Ic} measurements at 4 K, but some technical details remain to be clarified. Modifications of the current draft standard and further experiments may be required to achieve a consensus standard. The results suggest that the current Δa_p agreement requirement may be relaxed, and that more than the minimum of 4 J–Δa data points should be obtained when using the resistance curve method.

ACKNOWLEDGMENTS

The authors would like to thank Drs. S. Mori, M. Yoshikawa, and M. Tanaka for their continuous encouragement of this work. The organizers of this activity wish to express appreciation to all participants for their contributions. Without such collaboration, the development of consensus standards is impossible. Finally, special appreciation is due to Nippon Steel Corporation for providing the test material.

REFERENCES

1. H. Nakajima, K. Yoshida, M. Oshikiri, Y. Takahashi, K. Koizumi, S. Shimamoto, M. Shimada, S. Tone, S. Sakamoto, K. Suemune, and K. Nohara, Tensile properties of new cryogenic steels as conduit materials for forced flow superconductors at 4 K, in: "Advances in Cryogenic Engineering– Materials", Vol. 34, A.F. Clark and R.P. Reed, eds., Plenum, New York (1988).
2. H. Nakajima, K. Yoshida, S. Shimamoto, R.L. Tobler, P.T. Purtscher, and R.P. Reed, Round robin tensile and fracture test results for an Fe-22Mn-13Cr-5Ni austenitic stainless steel at 4 K, in: "Advances in Cryogenic Engineering–Materials", Vol. 34, A.F. Clark and R.P. Reed, eds., Plenum, New York (1988).
3. K. Yoshida, H. Nakajima, M. Oshikiri, R.L. Tobler, S. Shimamoto, R. Miura, and J. Ishizaka, Mechanical tests of large specimens at 4 K: facilities and results, in: "Advances in Cryogenic Enineering–Materials", Vol. 34, A.F. Clark and R.P. Reed, eds., Plenum, New York (1988).
4. H. Nakajima, K. Yoshida, and S. Shimamoto, Effects of specimen size, side grooves, and control on fracture toughness in the JCS, presented at The Third U.S.–Japan Workshop on Low Temperature Structural Materials and Standards, Tokai-mura, Japan, 1988.

TECHNICAL NOTE

Y. A. Rosenthal,[1] *R. L. Tobler,*[2] *and P. T. Purtscher*[3]

J_{Ic} Data Analysis Methods with a "Negative Crack Growth" Correction Procedure

REFERENCE: Rosenthal, Y. A., Tobler, R. L., and Purtscher, P. T., "**J_{Ic} Data Analysis Methods with a 'Negative Crack Growth' Correction Procedure,**" *Journal of Testing and Evaluation*, JTEVA, Vol. 18, No. 4, July 1990, pp. 301–304.

ABSTRACT: It often occurs in *J-R* testing that some of the initial crack extension (Δa) data points have anomalous negative values. ASTM Methods E 813-87 and E 813-81, however, do not specify any procedures for treating such data. We propose a procedure for data analysis which utilizes the negative Δa values and is consistent with ASTM E 813-87. The proposed correction procedure is illustrated using a data set for austenitic steel; also, J_{Ic} values obtained using ASTM E 813-87 are compared to those obtained from its predecessor E 813-81.

KEY WORDS: ASTM Method E 813-87, fracture toughness, *J*-integral, *J-R* testing, negative crack growth, *R*-curve

ASTM Method E 813-87 covers the experimental determination of J_{Ic}, which can be used as an engineering estimate of fracture toughness near the initiation of slow stable crack growth for metallic materials. The single-specimen elastic compliance technique (as described in Section 8.4 of that standard) is commonly used. According to that procedure, crack extension (Δa) measurements, inferred by partial unloading, are performed frequently throughout the loading of the specimen. It often occurs, due to friction [*1*], to misalignment in the loading train [*2*], to the electronic equipment balancing and zeroing, or perhaps to physical blunting behavior effects [*3*], that some of the initial inferred Δa data points have anomalous negative values. ASTM E 813-87, however, does not discuss the problem of "negative crack growth" or specify any procedure for treating such data.

In a recent interlaboratory program, most of the participants observed some negative crack growth in tests of a tough austenitic steel [*4*]. It is not possible to repeat each test which resulted in negative Δa data (especially when environmental effects are also involved), because of the cost. In many laboratories dealing with *J-R* testing, this problem is treated by eliminating the negative Δa values, or by shifting the resistance curve to a new zero, such as the most negative Δa point. Such treatment is arbitrary and undesirable, since it depends on the operator's decision. Obviously it can also be a source of scatter when comparing interlaboratory toughness data for the same material tested under the same conditions.

The purpose of this Technical Note is to propose a data analysis procedure for J_{Ic} determination which explicitly recognizes and utilizes the negative Δa values and is otherwise consistent with ASTM E 813-87.

Data Analysis Procedure

The data analysis procedure is carried out using a personal computer with an interactive computer program especially developed for this purpose. A typical *J*-versus-Δa data set may include some initial negative Δa values that cannot be analyzed according to the existing standard, because it demands the use of a method of least squares to determine the linear regression line:

$$\ln(J) = \ln(C_1) + C_2 \ln(\Delta a) \qquad (1)$$

where C_1 and C_2 are constants. According to ASTM E 813-87, one is asked to fit only the data which fall within the exclusion interval (Section 9.2.5). In extreme cases it is possible that some negative Δa values will be included in the acceptable data points, but Eq 1 cannot accept negative values for Δa. In any case, the exclusion interval is defined in relation to the blunting line, the true zero of which is questionable in the case of negative Δa values. Therefore the operator usually resorts to shifting the Δa values arbitrarily.

The details of a better procedure, proposed by the authors, are shown in Fig. 1. The first step is to fit all data to a nonlinear (power) function having an inverse form of Eq 1:

$$\Delta a = K_1 (J)^{K_2} + K_3 \qquad (2)$$

Manuscript received 7/20/89; accepted for publication 1/11/90.

[1]On a sabbatical from the Nuclear Research Center—Negev, PO Box 9001, Beer Sheva 84190, Israel.

[2]National Institute of Standards and Technology, Materials Reliability Division, Boulder, CO 80303-3328.

[3]Advanced Steel Processing and Products Research Center, Colorado School of Mines, Golden, CO 80401.

0090-3973/90/0007-0301$00.00

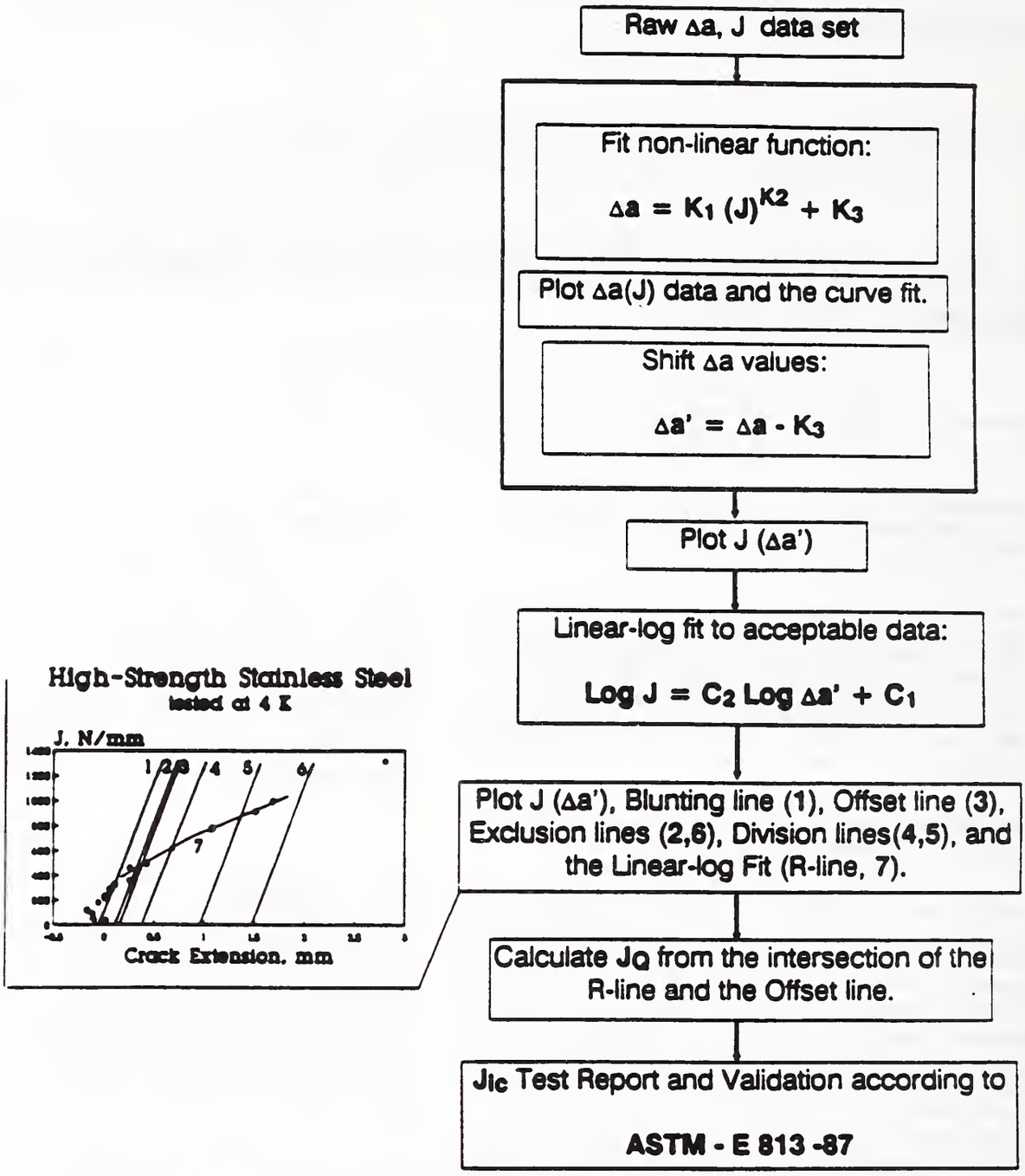

FIG. 1—*Schematic description of the proposed* J-R *testing data analysis procedure for* J_{Ic} *determination.*

where K_1, K_2, and K_3 are constants. This function is fitted to all the data, including negative Δa. In the next step, K_3 is identified and used as the amount needed for shifting the data to a new zero. Then, the entire J-versus-Δa plot (including the blunting line, the exclusion lines, the division lines, and the offset line) is shifted along the abscissa by an amount, K_3, thus creating new $\Delta a'$ crack extension values. The data points for the final curve fit are defined in the third step. According to Section 9.2.5 of ASTM E 813-87, a regression line having the form of Eq 1 is fitted to the acceptable data, and J_Q is determined at the intersection point between the nonlinear regression line and the 0.2 mm offset line (Fig. 2). The J_Q values, as calculated from the regression line and from the offset line at the point of intersection, converge to within less than 0.1%, whereas 2% or less is required in ASTM E 813-87, Section 9.2.6.4.

For the sake of comparison, we analyzed one set of data three ways. Figure 2 shows the original data analyzed with the proposed procedure. Figure 3 shows the same data set, analyzed after shifting the Δa values to the most-negative value. The analysis was also repeated for this data set after eliminating all the

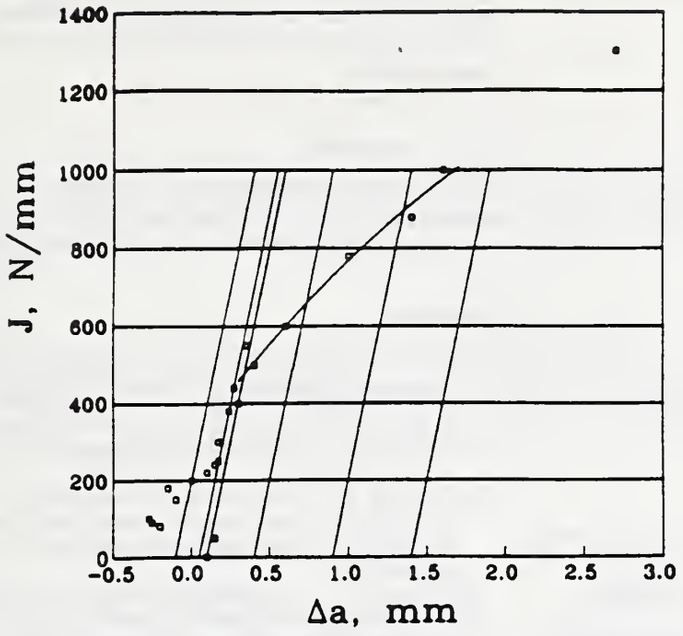

FIG. 2—J-Δa *curve for a tough austenitic stainless steel at 4 K (obtained using a standard 25.4 mm thick compact specimen in a liquid helium environment), which includes negative Δa values, as analyzed using the proposed procedure.*

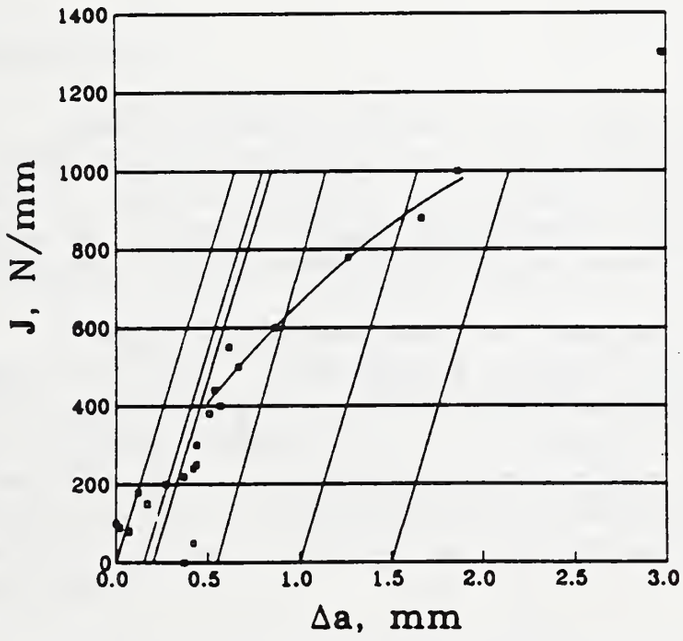

FIG. 3—*Same data set as shown in Fig. 2 analyzed after shifting the zero to the most negative Δa value.*

negative Δa values (Fig. 4). J_{Ic} values, calculated in these three different ways, are shown in Table 1. The results vary from 385 to 480 N/mm, depending on the data reduction procedure, but the proposed procedure generally gives higher values.

In addition to the problem of negative crack growth, we wanted to assess the significance of the revised standard test

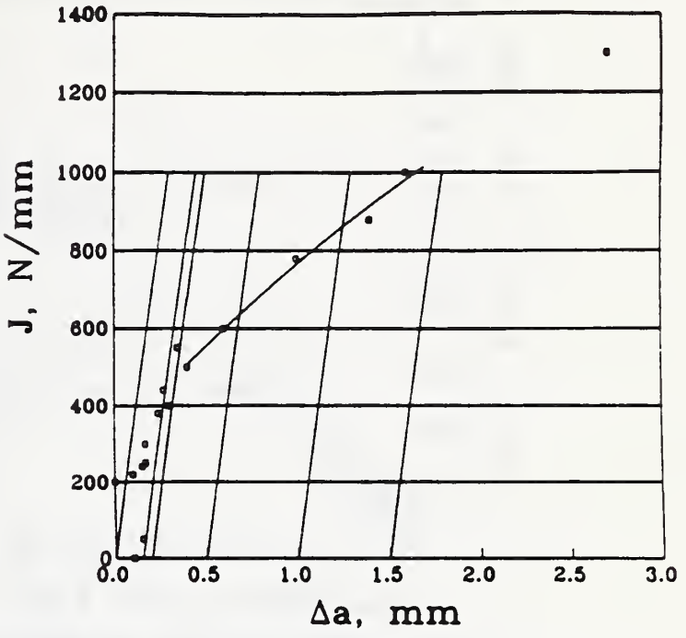

FIG. 4—*Same data set as shown in Fig. 2 analyzed after eliminating the negative Δa values.*

TABLE 1—*Comparison of J_{Ic} obtained after different treatments to negative Δa values.*

Procedure	J_{Ic}, N/mm
(1) Using all the data and the proposed procedure (Fig. 2)	480
(2) Zero shifted to the most negative Δa value (Fig. 3)	385
(3) Eliminating the negative Δa values (Fig. 4)	475

methodology on J_{Ic} measurements. We analyzed a data base of results based on 42 *J-R* tests (mostly at 4 K) with austenitic stainless steel specimens (with yield strengths ranging from 400 to 1700 MPa) using ASTM E 813-87 and its predecessor E 813-81. K_J determined from the proposed correction procedure (Fig. 1) was used as the amount of crack extension for shifting the Δa values in both cases. The J_{Ic} values obtained using the new method are plotted versus J_{Ic} values obtained from the previous method's analysis (Fig. 5).

For most cases, J_{Ic} obtained using the new method is higher than J_{Ic} obtained using the old method, and the difference between the two J_{Ic} values tends to increase as the toughness increases. This trend is not influenced strongly by our negative crack growth correction, but results primarily from the different definitions of J_{Ic} used in the two methods.

Conclusions

1. The data analysis procedure proposed here enables J_{Ic} determination even when minor testing problems produce negative values of crack extension. This proposed data analysis procedure eliminates arbitrary treatment with respect to negative crack extension values and therefore enables a more meaningful comparison of *J-R* curve results, as obtained by different laboratories, by excluding operator bias.

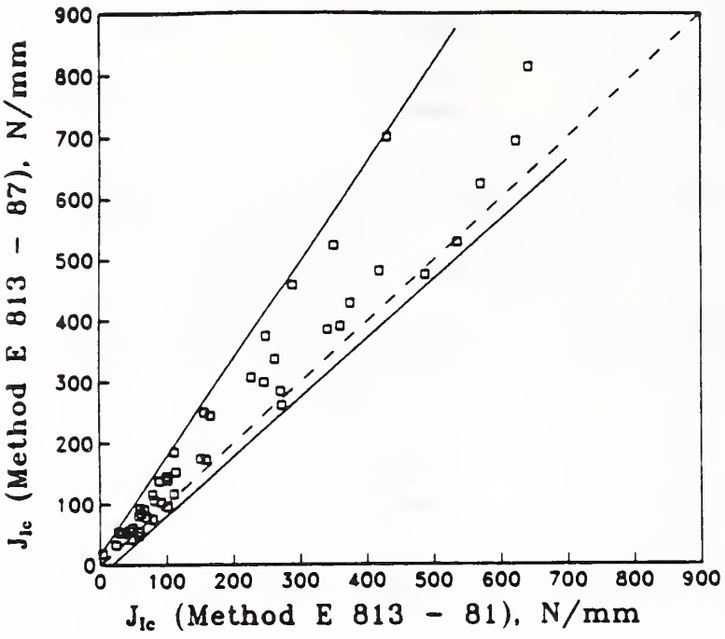

FIG. 5—J_{Ic} *obtained using ASTM E 813-87 (with the proposed correction procedure) plotted versus* J_{Ic} *from ASTM E 813-81 analysis. The dashed line represents equal* J_{Ic} *values.*

2. J_{Ic} data obtained using ASTM E 813-87 may be considerably higher than those obtained using its predecessor ASTM E 813-81. The difference may be substantial, especially for high toughness materials.

Acknowledgments

The authors would like to acknowledge Dr. D. T. Read, National Institute of Standards and Technology, for discussions during the development of the data analysis procedure.

References

[1] Voss, B., "On the Problem of Negative Crack Growth and Load Relaxation in Single Specimen Partial Unloading Compliance Tests," in *Ductile Fracture Test Methods* (Proceedings of a CSNI Workshop Paris, 1–3 Dec. 1982), Organization For Economic Cooperation and Development, Nuclear Energy Development, Paris, 1983, pp. 210–219.

[2] Bowman, R., Antolovich, S. D., and Brown, R. C., "A Demonstration of Problems Associated with Crack Closure Measurement Techniques," *Engineering Fracture Mechanics*, Vol. 31, No. 4, 1988, pp. 703–712.

[3] Purtscher, P. T., "Absence of Stretch Zones in Austenitic Stainless Steels Fractured at Cryogenic Temperatures," *Journal of Testing and Evaluation*, Vol. 15, No. 5, 1987, pp. 296–298.

[4] Nakajima, H., Yoshida, K., Shimamoto, S., Tobler, R. L., Purtscher, P. T., and Reed, R. P., "Round Robin Tensile and Fracture Test Results for an Fe-22Mn-13Cr-5Ni Austenitic Stainless Steel at 4 K," in *Advances in Cryogenic Engineering*, Vol. 34, A. F. Clark and R. P. Reed, Eds., Plenum, New York, 1988, pp. 241–249.

CHARPY IMPACT TESTS OF SUPERCONDUCTOR CONDUIT ALLOY WELDS NEAR ABSOLUTE ZERO

R.L. Tobler and D.P. Vigliotti
Materials Reliability Division
National Institute of Standards and Technology
Boulder, CO 80303

This note describes a technique used at the Japan Atomic Energy Research Institute (JAERI) and now at the National Institute of Standards and Technology (NIST) for conducting Charpy impact tests in flowing helium at an initial test temperature near 5 K.

INTRODUCTION

Impact tests at temperatures near absolute zero are controversial at present because there is no standard method for conducting the tests. Certain regulatory agencies require impact tests on structural materials for service at liquid helium temperature, even though there is no scientific consensus on the meaning of impact measurements near absolute zero.

We previously reviewed the problems of impact testing at temperatures as low as 4 K [1]. ASTM Method E 23-88 [2], the existing standard for notched bar impact tests, specifies that the specimen must be transferred from the cooling bath through air to the machine and tested within 5 s. That procedure does not work at temperatures below 77 K. To attain more extreme cryogenic test temperatures it is necessary to insulate the specimen from contact with air, but Method E 23-88 does not specify an appropriate procedure.

Incoloy 908 is a newly developed alloy for superconducting conduit applications in fusion energy magnets at 4 K. Research at the Massachusetts Institute of Technology (MIT) shows that this material resists degradation during thermal aging treatments and has desirable thermal expansion behavior for superconductor sheath applications. The 4-K tensile, fatigue, and fracture toughness properties of this conduit alloy were measured and reported previously [3]. The alloy was selected for use in the United States Demonstration Poloidal Coil (USDPC) which will be installed and tested at JAERI according to international agreements. Before the coil could be installed, nonstandard impact tests for the conduit alloy were required by Japanese law. We tested the conduit alloy welds and two austenitic stainless steel base metals for comparison as described in this report.

PROCEDURE

MIT provided the test material, fabricated the Charpy test specimens, and sent them to NIST to be tested. The test material was a gas-tungsten-arc (GTA) welded plate of 2.35 mm thickness identical to that of the outer conduit of the USDPC. Conduit walls are typically 2 mm thick, whereas the conventional Charpy specimen has a 10 x 10 mm cross section. A 10 x 10 mm cross section was achieved in this study by welding a stack of 2 mm thick laminates. These specimens were tested in the manner described to satisfy Japanese law.

Laminates were cut from solution annealed plate and wet-ground to 2 mm thickness; 5 such specimens were electron beam welded to create each composite Charpy test specimen. The GTA welded central region of the composite specimen, a length of 10 mm, was not bonded by electron beam welding in order to avoid any heating effect. The composite was then machined to the standard Charpy size: 10 x 10 x 55 mm. Each specimen was notched in the weld at the center of specimen length. The specimens were then heat treated in vacuum for 200 h at 650°C to precipitation harden the alloy. The notch location was checked after heat treatment by etching each specimen to be sure that it was centered in the weld metal.

The service environment for the conduit is liquid helium at 4 K. Method E 23-88 is invalid for tests at 4 K because moisture condensation on the specimen quickly warms it up to about 60 K as it is being transferred through air to the test machine. Therefore we used a variant of the "flow" method to obtain an initial test temperature near 4 K.

Originally, the flow method was introduced by Jin, Horwood, Morris, and Zackay [4]. It was later modified, greatly simplified, and used in Japan [5]. The system used recently at JAERI is adopted here. The specimen is wrapped in a thin sheet of plastic, a tubular container, that is attached to a liquid helium transfer line. The container is placed on the test machine anvil, and liquid helium is pumped through the tube. After cooling at least two minutes, and while helium is still flowing through the tube, the specimen and container are fractured by release of the pendulum.

The plastic wrapping used in our tests was transparent overhead projection sheets, 0.1 mm thick. The sheets are cut to 220 x 55 mm and marked with inklines for specimen positioning as shown in Fig. 1A. Double-sided adhesive tape is applied to the sheet at symmetrical locations to secure the specimen as it is positioned on the sheet. The plastic is then folded and wrapped around the specimen, and the seam is sealed with cellophane tape (Fig. 1B). Finally, the specimen container is taped to the helium transfer line and carefully positioned with the notch centered on the test machine anvil.

The 360 J test machine used in this study is a conventional swinging pendulum machine with a C-shaped pendulum. The angle of pendulum swing is read from the machine's dial indicator and the reading in degrees is converted to absorbed energy using conversion tables.

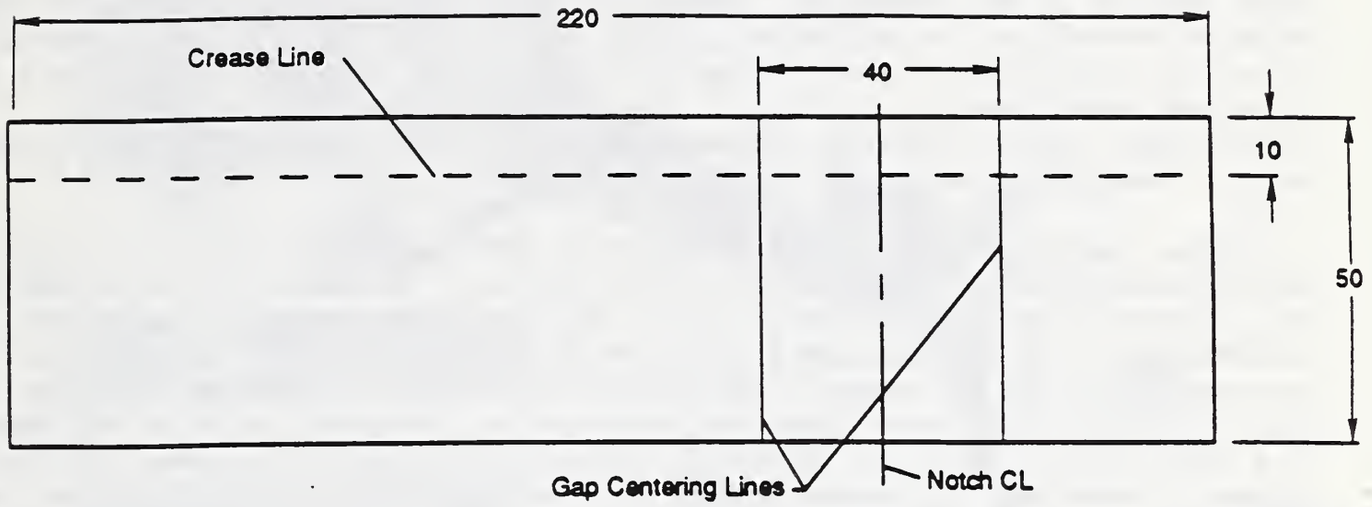

Plastic Film

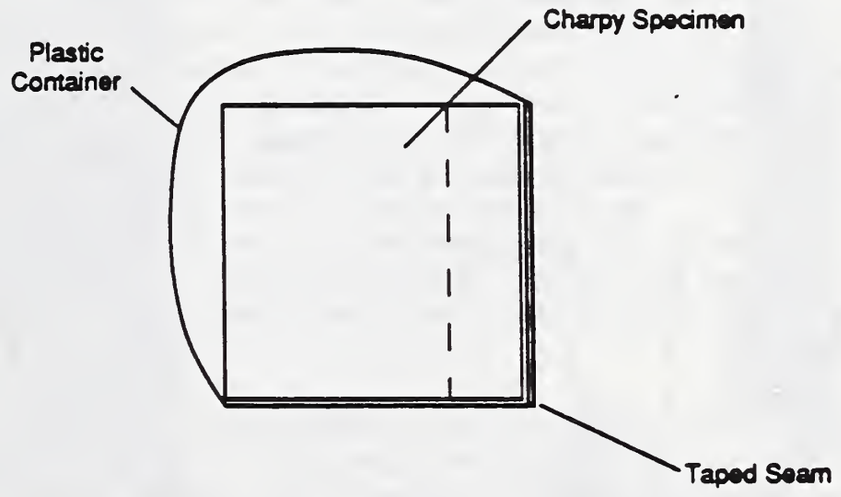

Wrapped Specimen

Figure 1. Plastic film wrapper (A), cross sectional view of wrapped specimen (B). The dimensions are mm.

During a test, liquid helium is transferred from a 100 l storage Dewar. In these tests, helium gas was used to pressure the storage Dewar, and the flow of pressurizing gas was consistently maintained at a value of 30 standard cubic feet per hour. For this rate of transfer, it takes 2 min to cool the specimen. The minimum temperature that can be reached depends on some details of the apparatus, especially the length of the metal tube that extends beyond the vacuum-jacketed portion of the transfer line. With our existing transfer line about 25 mm of tube was exposed (that is, wrapped with foam and tape, inserted in the the specimen wrapper, but not vacuum insulated), and the minimum temperature that could be reached at the center of the Charpy specimens was 5.5 K.

The specimen cooling time and initial test temperature were verified by calibrations using a conduit alloy weld specimen containing a thermocouple. We selected a Chromel versus gold + 0.03% iron thermocouple for maximum sensitivity at 4 K. Our thermocouple wire diameters were 0.305 and 0.127 mm, respectively, and we bonded them using a thermocouple welder at low power. We drilled a 1.6 mm hole along the calibration specimen's axis to the base of the notch, and then inserted the thermocouple. After adding some fine copper powder to ensure good thermal contact between the thermocouple bead and the specimen, we filled and sealed the hole with thermally nonconducting varnish.

We calibrated the thermocouple following a procedure suggested by Sparks and Powell [6]. They published detailed calibrations for various chromel versus gold + 0.02% iron thermocouples and proposed that their reference data could be used for similar thermocouples if adjusted satisfactorily with data from spot calibrations. For spot calibrations, we immersed our thermocouple in liquid nitrogen and liquid helium baths. The difference between our output and that reported by Sparks and Powell at 4 K was only 210 μV (a variation of 4.5%). We shifted their reference curves by that much. Based on calibrations with the instrumented specimen in a container on the machine anvil, we achieved an initial test temperature of 5.5 K in flowing helium. Temperature-versus-time curves confirmed that this temperature is completely stable after 2 min.

The impact test apparatus is illustrated in Figs. 2–5. Shown is the impact machine with the pendulum raised (Fig. 2), a container on the anvil with the specimen centered in the gap (Fig. 3), helium flowing through the line (Fig. 4), and a close-up depicting the moment of impact (Fig. 5).

RESULTS

The Charpy test results are listed in Table 1. Four weld specimens were tested, and the average absorbed energy is 32.9 J. The individual values range from 30.5 to 34.3 J. One plastic container with no specimen inside was tested to confirm that very little energy is absorbed in fracturing the insulation at 5.5 K. The extra energy added by the container is negligible at not more than a few tenths of one joule. Accordingly, no calibration correction was made to the data listed in Table 1.

Figure 2. Overall view of the impact test machine.

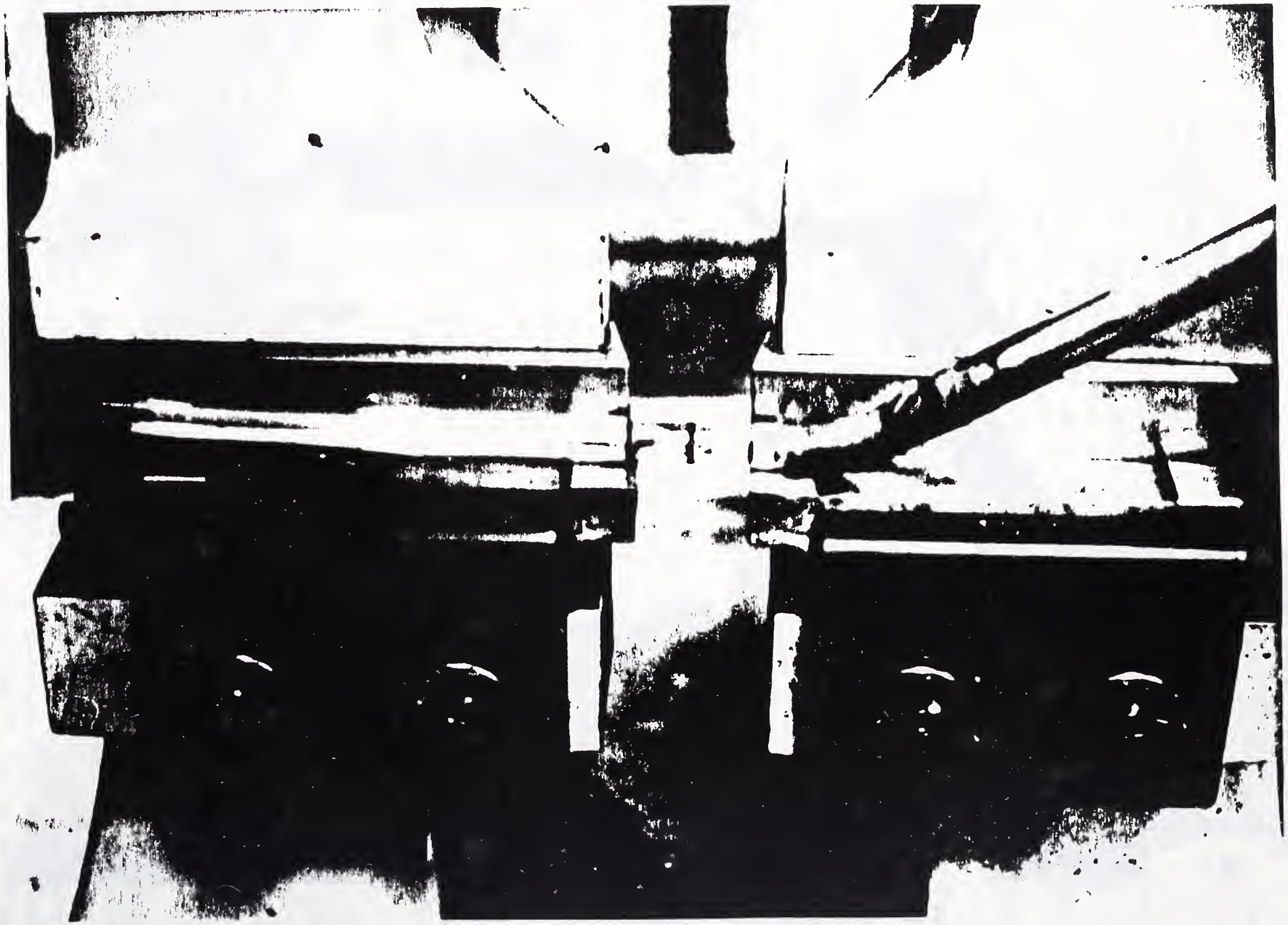

Figure 3. Encapsulated specimen on the anvil at the beginning of a test. Inked lines on the plastic container are used to center the specimen.

Figure 4. Helium transfer through the specimen container.

Figure 5. The pendulum as it collides with the specimen container at 5.5 K.

Table 1. Charpy test results for specimens initially at 5.5 K

Material	Specimen No.	Charpy absorbed energy J[a]	Charpy absorbed energy ft-lbf[b]	JAERI's result J
908 Weld (laminated)	1A	33.5	24.7246	
	1B	34.3	25.2799	
	1C	30.5	22.5072	
	2G	33.2	24.7246	
		Avg = 32.9		—
Fe-19Cr-8Ni-4Mn	1	101.8	75.0591	
	2	97.1	71.6403	
		Avg = 99.4		93.7[c]
AISI 316LN	1	240.0	176.9678	
	2	221.4	163.3087	
		Avg = 230.7		230.6[c]

a: J = 1.356 times reading in ft-lbf.
b: Value in ft-lbf is read from table after noting angle of pendulum swing.
c: Average value for three specimens tested using the flow method, and same alloy heat.

In addition, we conducted Charpy tests in duplicate for two austenitic stainless steel base metals: an Fe-19Cr-8Ni-4Mn-0.21N alloy and AISI 316LN. Standard specimens (10 x 10 x 55 mm) were machined from commercially annealed 25 mm thick plates. The average absorbed energies for these steels were 99.4 and 230.7 J, respectively, as shown in Table 1. The same two steels were tested in triplicate at JAERI. Using their virtually identical flow method, they reported average absorbed energies of 93.7 and 230.6 J, respectively. The NIST and JAERI data are in fair agreement, which gives some assurance about the reproducibility of measurements obtained using the flow method.

ACKNOWLEDGMENTS

The flow test method is being used in an ongoing cooperative study by JAERI, MIT, and NIST. Special acknowledgments are due to H. Nakajima (JAERI) for sharing the details of this test technique with us, and to M.M. Steeves and I.S. Hwang (MIT) for test specimens and helpful discussions.

REFERENCES

1. R.L. Tobler, R.P. Reed, I.S. Hwang, M.M. Morra, R.G. Ballinger, H. Nakajima, and S. Shimamoto, S., Charpy Impact Tests Near Absolute Zero, ASTM Journal of Testing and Evaluation, accepted for publication in Jan, 1991.

2. Standard Test Methods for Notched Bar Impact Testing of Metallic Materials, Designation E 23-88, 1989 Annual Book of ASTM Standards, Vol. 03.01, Amer. Soc. Test. Maters., Philadelphia, 1989, p. 198-213.

3. M.M. Morra, I.S. Hwang, R.G. Ballinger, M.M. Steeves, and M.M. Hoenig, Effect of Cold Work and Heat Treatment on the 4 K Tensile Fatigue and Fracture Toughness Properties of Incoloy 908, Proceedings of the Eleventh International Conference on Magnet Technology, MT-11, Aug 28, 1989, Tsukuba, Japan.

4. S. Jin, W.A. Horwood, J.W. Morris, Jr., and V.F. Zackay, A Simplified Method for Charpy Impact Testing Below 6 K, in: Adv. Cryo. Eng., Vol. 19, Plenum Press, New York, 1974, pp. 373-378.

5. T. Ogata, K. Hiraga, K. Nagai, and K. Ishikawa, A Simplified Method for Charpy Impact Testing Near Liquid Helium Temperature, Cryogenics, Vol. 22, 1982, pp. 481-482.

6. L.L. Sparks and R.L. Powell, Low Temperature Thermocouples: KP, "Normal" Silver, and Copper versus Au-0.02 at% Fe and Au-0.07 at% Fe, Journal of Research of the National Bureau of Standards A. Physics and Chemistry, Vol. 76A, No.3, May–June, 1972, pp. 263-283.

COMPARISONS BETWEEN J_{Ic} AND CHARPY ABSORBED ENERGY AS MEASURES OF CRYOGENIC FRACTURE TOUGHNESS

I.S. Hwang, M.M. Morra, and R.G. Ballinger
Departments of Materials Science and Engineering and Nuclear Engineering
Massachusetts Institute of Technology
Cambridge, Massachusetts 02139, U.S.A.

H. Nakajima and S. Shimamoto
Naka Nuclear Fusion Establishment
Japan Atomic Energy Research Institute
Naka-machi, Ibaraki-ken, 311-02, Japan

R.L. Tobler
Materials Reliability Division
National Institute of Standards and Technology
Boulder, Colorado 80303, U.S.A.

The Charpy impact test has been used in cryogenics as a simplified method to determine the fracture toughness of structural alloys at low temperatures. A major problem in Charpy testing near absolute zero is that adiabatic heating during high strain rate deformation increases the fracture temperature [1]. In this paper, we establish experimental correlations between the critical energy line integral (J_{Ic}) and Charpy absorbed energy (C_v) at both 4 and 77 K for materials ranging from fully austenitic alloys to ferritic steels. Fracture mechanics tests are used for J_{Ic} determinations and the liquid cryogen flow method is used for C_v measurements. At 77 K, a good correlation is found between J_{Ic} and C_v. At 4 K the correlation is poor, indicating that C_v is a poor indicator of static fracture toughness at this temperature. Interestingly, a good correlation is observed between J_{Ic} at 77 K and C_v at 4 K. The results are explained by the temperature rise of Charpy specimens from 4 K to near 200 K during impact, as predicted earlier from energy balance calculations.

For annealed austenitic stainless steels between 77 and 4 K, C_v changed little although J_{Ic} decreased significantly. For ferritic steels, both C_v and J_{Ic} decreased strongly between 77 and 4 K. For a precipitation-hardened superalloy, both C_v and J_{Ic} were insensitive to temperature in this range. This demonstrated wide variability of material response depends on the relative magnitude of thermal softening. The use of C_v may lead to a serious overestimation of fracture resistance near absolute zero, especially for alloys having large thermal-softening effects. Therefore, the Charpy test near absolute zero is regarded as an invalid measure of the static fracture resistance. A C_v-based acceptance criterion developed for one group of alloys will not be validity for another group.

INTRODUCTION

Both linear elastic (K_{Ic}) and elastic-plastic (J_{Ic}) fracture mechanics tests and Charpy impact tests have been used in cryogenics to characterize the cryogenic fracture behavior of structural alloys. Both methods relate to the energy absorbed during fracture. Temperatures of interest vary from 4.2 K for nuclear fusion devices and 20 K for aerospace applications to 77 K and higher for more general cryogenic applications. Since alloys with plastic fracture behavior are selected for these applications, the J_{Ic} test is routinely used. The J_{Ic} test established as ASTM Method E 813-88 can be performed in cryogenic environments with special modifications to testing machines. Recently, a proposed standard cryogenic test procedure was developed that employs slow loading to minimize the crack tip temperature rise [2]. The procedure can be used to determine the critical energy line integral, J_{Ic}, for crack growth, using a compact specimen. The single specimen technique using unloading compliance for crack size measurement has been successfully used for a wide variety of structural alloys including tough austenitic alloys. Often the plane strain fracture toughness is estimated from

$$(K_{Ic})^2 = \frac{J_{Ic} E}{1-\grave{a}^2}, \qquad (1)$$

where E is the elastic modulus and à is Poisson's ratio. For cleavage fractures, Method E 813-88 is not appropriate; then, the plane strain fracture toughness test specified by ASTM Method E 399 may be used and J_{Ic} can be estimated from K_{Ic} using Eq. (1).

The impact test, ASTM Methods E 23-88, was originally developed as a simple measure of toughness for ferritic steels exhibiting ductile-to-brittle transition behavior. It is especially meaningful if the Charpy absorbed energy (C_v) and the plane strain fracture toughness can be correlated. Charpy tests require significantly less complicated apparatus and a much smaller specimen size (10 x 10 x 55 mm) than fracture mechanics tests. However, the Charpy specimen's temperature will rise during transfer from a helium Dewar to the anvil and during impact loading, which is a serious drawback. We showed recently [1] that although the temperature rise during specimen transfer can be minimized by various cooling techniques, the unavoidable adiabatic heating effect at impact is too significant to be ignored, especially at start temperatures below 77 K. The effect of the temperature rise on C_v measurements can be two-fold: at least large data scatter, and more seriously a lack of correlation with K_{Ic} or J_{Ic}.

In this paper we present Charpy impact and fracture mechanics test results at 77 and 4 K for various structural alloys ranging from ferritic steels to fully austenitic alloys. Correlations are developed between J_{Ic} and C_v for alloys representing a broad range of toughness. The results demonstrate the limitations of C_v as a measure of cryogenic toughness below 77 K.

MATERIALS

Eight structural materials, including 4 fully austenitic alloys, two metastable austenitic stainless steels, and two ferritic steels, were tested. The material designations and compositions are listed in Table 1 in the order of decreasing nickel content.

Incoloy 908 [4] was supplied in the form of 27 mm plate in the solution annealed condition; the material was then aged for 200 h at 650°C in vacuum. Stainless steel SUS 310 was a commercial heat of 25 mm plate in the solution annealed condition [5]. JN1 was supplied in the form of 30 mm plate taken from the surface of a 100 mm hot-rolled plate [3].

AISI 316LN was part of the forged cylindrical vessel of Alcator C-MOD [6] being constructed at the Plasma Fusion Center of Massachusetts Institute of Technology (MIT). The vessel was forged at 1400 K and solution annealed at 1330 K for 14 h and water-quenched. Then a 12% cold work was applied and the alloy was stress-relieved at 873 K for 20 h and furnace cooled. Material for test specimens was taken from one of the pin holes drilled in the radial direction of the machined vessel which had a 190 mm thick wall.

Metastable austenitic stainless steel 304LN, from an earlier experimental program at the National Institute of Standards and Technology (NIST) [7], was a modified heat containing 3.85% Mn; it was produced from a 25 mm plate that was hot-rolled at 1450 K and solution annealed at 1340 K for ½ h.

Ferritic 5Ni steel was obtained as a 32 mm plate in the austenitized, temperized, and reversion annealed condition according to ASTM specification A 645-74 [8]. Fe-18Cr-3Ni-13Mn steel was supplied as 25 mm plate in the hot-rolled condition. This alloy is of interest because although it is austenitic, it fails in static tests at 4 K by slip-band cracking which is a form of cleavage. Ultra-low carbon steel was supplied in the form of 25 mm plate in the hot-rolled condition [9]. The tensile and elastic properties for the eight alloys at selected temperatures are summarized in Table 2.

EXPERIMENTAL PROCEDURES

Tension and fracture toughness properties for some of the alloys were available from previous tests at NIST; additional tests were performed using a cryogenic facility at MIT. The MIT test facility consists of a servohydraulic fatigue machine equipped with a specially designed load frame. The loading system, with a maximum capacity of 90 kN, operates with a commercial Dewar. A schematic of the cryostat is shown in Fig. 1. Total load train compliance is estimated to be 2.6×10^{-5} mm/N. The load cell was calibrated to an accuracy of 0.25% of full scale (90 kN). Specimen strain or crack opening displacements were measured using ring-shaped extensometers designed for use down to 4 K. The extensometers were calibrated on a weekly basis to a precision of 2.5 μm using a dial gage.

Compact specimens and Charpy specimens with notches in the T-L orientation were machined from the same blocks of materials. Two specimens of each type were tested. The 25 mm thick compact specimen is a standard design recommended in Method E 813-88. Most specimens were precracked at room temperature with a final ΔK of 33 MPa·m^{½} and stress ratio of 0.1. The ultra-low carbon steel specimens were precracked with a final ΔK of 20 MPa·m^{½} to minimize any warm prestress effect on the fracture toughness at low temperatures [9]; they were also stress relieved at 550°C for 1 h in vacuum. The stress relief can remove up to 80% of residual stress [10].

For all materials the initial crack lengths were 64 to 70% of specimen width. A clip gage extensometer was mounted at the load-line for measurement of

Table 1. Chemical compositions of test materials (mass %).

Material	Fe	Ni	Cr	C	Mn	Al	Nb	Ti	Mo	N	P	Si
Incoloy 908	40.6	49.7	3.83	0.01	0.04	1.04	2.99	1.58	-	-	-	0.14
SUS 310	bal.	19.64	24.58	0.06	1.52	-	-	-	-	-	0.013	0.37
JN1	bal.	15.26	25.2	0.018	4.1	-	-	-	-	0.37	0.019	0.33
AISI 316LN	bal.	13.10	16.70	0.02	1.52	-	-	-	2.58	0.19	0.02	0.41
304LN (+Mn)	bal.	7.84	19.25	0.024	3.85	-	-	-	0.31	0.21	0.022	0.65
5Ni steel	bal.	5.03	-	0.08	0.60	0.08	-	-	0.30	0.01	0.01	0.25
Fe-18Cr-3Ni-13Mn	bal.	3.26	18.09	0.038	13.32	-	-	-	0.12	0.37	0.028	0.52
Ultra-low carbon steel	bal.	-	-	0.00	0.021	0.052	-	-	-	0.003	0.012	0.00

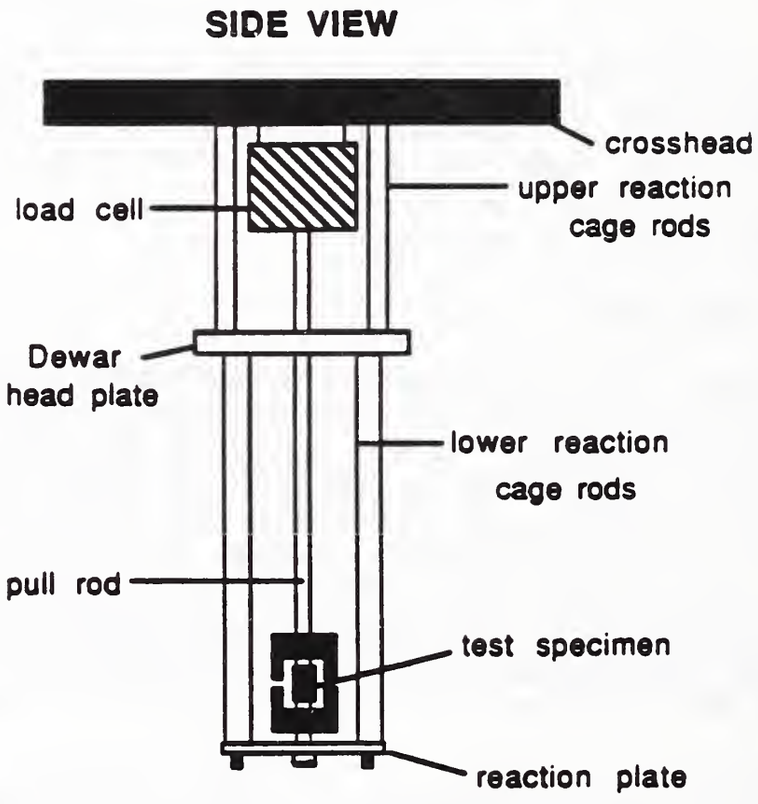

Figure 1. The MIT cryostat for tension and fracture tests.

Table 2. Tensile and elastic properties of test materials.

Material	Temperature (K)	YS (MPa)	UTS (MPa)	Elongation (%)	Elastic Modulus (GPa)
Incoloy 908	295	961	1354	13	179
	77				182
	4	1070	1780	20	182
SUS 310	295	225	558	52	190[c]
	4	796	1322	80	200[c]
JN1[a]	295	420	813	52	190[c]
	77	1031	1599	46	200[c]
	4	1336	1812	30	203
AISI 316LN	295	303	664	56	187
	77	684	1304	58	174
	4	889	1369[b]	56[b]	207
304LN (+Mn)	295	329	645	56	190[c]
	76	781	1474	28	200[c]
	4	986	1668	38	200[c]
5Ni steel	295	534	675	34	198
	76	738	1124	22	208
	4	1103	1103	~1	209
Fe-18Cr-3Ni-13Mn	295	440	796	56	195
	76	1144	1519	18	196
	4	1540	1811	4	196
Ultra-low carbon steel	295	137	268	49	207
	76	758	793	1.6	211
	4	705	744	1.2	211

[a] Data are measured at 4 K and estimated from Ref. [3] at 295 and 77 K.
[b] Liquid helium level was low during plastic deformation.
[c] Estimated values.

displacement. Crack length was determined from the unloading compliance using the equations of Saxena and Hudak [11]. Specimen rotation and moving crack effects were taken into account in the crack length determinations. Tests were performed with a fully automated procedure at a constant gage displacement rate, typically 0.1 mm/min. All testing was in accordance with Method E 813-88. Data analysis was in accordance with ASTM 1152-87. The J_{Ic} test system was verified by interlaboratory tests using two austenitic stainless steels with known fracture toughness [12].

To complete the database, tension tests were performed where necessary using specimens 6.35 mm in diameter and 25.4 mm in gage length. Tests were according to the proposed ASTM standard for tension tests at liquid helium temperature. The specimens were axially oriented in the same direction as the loading axis of the fracture toughness specimens. All tests were strain-controlled at 2×10^{-4} s^{-1} by using an extensometer with 25.4 mm gage length.

The Charpy test specimens were full size (10 x 10 x 55 mm) with a 2 mm deep notch in strict accordance with ASTM Method E 23-88. Most tests were performed with a standard C-type pendulum machine at the Superconducting Magnet Laboratory of the Japan Atomic Energy Research Institute (JAERI). Some tests at 4 K used a C-type pendulum machine at NIST, and some at 77 K used a U-shaped pendulum machine at MIT. There was an overlap in the testing program at the three institutions so that a cross check of data can be made. The impact test machines meet the requirements of Method E 23-88 with a full scale of 300 J, except for the MIT machine which was not firmly attached to the floor. This influenced the MIT data slightly, as discussed later.

The 77 K Charpy tests at JAERI and MIT followed the standard Method E 23-88 procedure: conventional cooling of specimens in a Dewar for about 10 min, and subsequent transfer to the anvil within 5 s. As pointed out previously [1], there is no standard test procedure for Charpy testing at 4 K. Therefore, two test techniques at 4 K were considered: the glass Dewar method [1,13] and the flow method [1,14]. The advantages and disadvantages of each technique were studied and will be reported elsewhere in detail. In this paper, Charpy data from the flow method were preferred because that method applies equally well to both low and high toughness materials, and no calibration correction of C_v data is required. In the flow method, the specimen is loosely wrapped with polyethylene sheet of 0.5 mm thickness. The specimen is secured in the wrap using double-sided adhesive tape; then the assembly is connected to the cryogenic transfer line. The specimen in a continuous flow of helium cools to within 2 K of the intended start temperature in approximately 2 min. The specimen cooling time and start temperature (5 K $\pm$ 1 K) were monitored and confirmed by calibrations using a gold-iron thermocouple. In this paper we call absorbed energy measurements made by this method "Cv at 4 K."

RESULTS AND DISCUSSION

The J_{Ic} and C_v measurements at 77 and 4 K are listed in Table 3. Some J_{Ic} values were estimated from K_{Ic} data reported earlier. SUS 310 stainless steel was tested at 4 K only due to shortage of stock material. Type 316 LN stainless steel in J_{Ic} tests at 77 K did not exhibit the required crack growth and a valid J_{Ic} was not obtained at this temperature. The 4 K Charpy test results at JAERI and NIST agree within 5% as shown in Table 3. The 77 K Charpy test results at JAERI and MIT agree within 15%. The larger deviation in the latter case is

Table 3. Results of fracture toughness and Charpy impact tests.

	J_{Ic} (kJ/m^2)		Charpy Absorbed Energy (J)	
Material	77 K	4 K	77 K	4 K
Incoloy 908	243 ± 6	235 ± 5	63 ± 2(a)	70 ± 1
SUS 310	-	391(c)	-	166 ± 2
JN1	600	225 ± 22	274(b)	235 ± 3
AISI 316LN	(d)	576 ± 22	255 ± 5 279 ± 5(b)	231 ± 7 231 ± 9(e)
304LN (+Mn)	332 ± 7	101(c)	102 ± 6	94 ± 3 99 ± 3
5Ni steel	93 ± 1(f)	15.2 ± 2.7(c)	39 ± 4(b)	17 ± 1
Fe-18Cr-3Ni-13Mn	227 ± 2	31.2(c)	80 69 ± 4(a) 80 ± 4(b)	45 ± 2
Ultra-low carbon steel	3.3 ± 0.5(c)	0.9(f)	2.7(b)	8 ± 1

Note: (a) Method E 23-88 tests conducted at JAERI.
(b) Method E 23-88 tests conducted at MIT.
(c) Estimated from KIc using Eq. (1).
(d) Required crack extension for valid test was not obtained.
(e) Flow method tests conducted at NIST.

significant for high C_v; presumably, it is due to less firm attachment of the testing machine to the floor at MIT. Although the difference is small, JAERI's data are used in the correlations with J_{Ic}.

The $J_{Ic} - C_v$ correlations at 77 and 4 K are presented in Figs. 2 and 3, respectively. Each figure shows a solid parabolic trend line drawn by least squares fitting. At 77 K,

$$C_v = 10.4 + 0.136(J_{Ic}) + 0.04996(J_{Ic})^2 \quad \text{with } r^2 = 0.988, \tag{2}$$

and at 4 K,

$$C_v = 18.0 + 0.6708(J_{Ic}) - 0.05562(J_{Ic})^2 \quad \text{with } r^2 = 0.727, \tag{3}$$

where r^2 is the correlation coefficient. Based on the correlation coefficients and data scatter shown in our figures, the correlation between J_{Ic} and C_v at 77 K is good, but the correlation at 4 K is poor.

The poor correlation at 4 K cannot be attributed to property measurement errors (they change little between 77 and 4 K), but is attributable to large temperature rises in the Charpy test specimens. Below 77 K, the specific heats of structural alloys are extremely low. Because the specimens heat during high strain rate deformation, we expect fracture temperatures much higher than the start temperature. As shown in Fig. 4 from previous work [1], temperature increases as high as 180 K are predicted and measured for Charpy specimens initially at 4 K. The predicted maximum temperature rises for alloys are nearly the same for different starting temperatures ranging from 77 to 4 K.

Assuming adiabatic heating is the main reason for the poor correlation between C_v and J_{Ic} at 4 K, and that the behavior predicted in Fig. 4 is accurate, it follows that:

(1) Impact tests at 4 K actually involve fractures near 180 K, and a fair correlation is expected between C_v at 4 K and J_{Ic} at 77 K.

(2) Regardless of the Charpy test start temperature (77 or 4 K), the maximum specimen temperature reached during fracture and the measured C_v values will be similar for a given alloy, even if J_{Ic} at these temperatures is quite different.

(3) For alloys exhibiting transitional fracture behavior, scatter should increase if there is a difference in failure mechanisms between Charpy and compact specimens. Charpy specimens of certain alloys may exhibit ductile tearing rather than cleavage if they heat during impact to temperatures above the ductile-to-brittle transition temperature.

The first hypothesis is examined by Fig. 5 where C_v at 4 K is plotted versus J_{Ic} at 77 K. A least-squares fit gives

$$(C_v)4\text{ K} = 5.43 + 0.1158(J_{Ic})77\text{ K} + 0.000446[(J_{Ic})77\text{K}]^2, \tag{4}$$

with $r^2 = 0.994$.

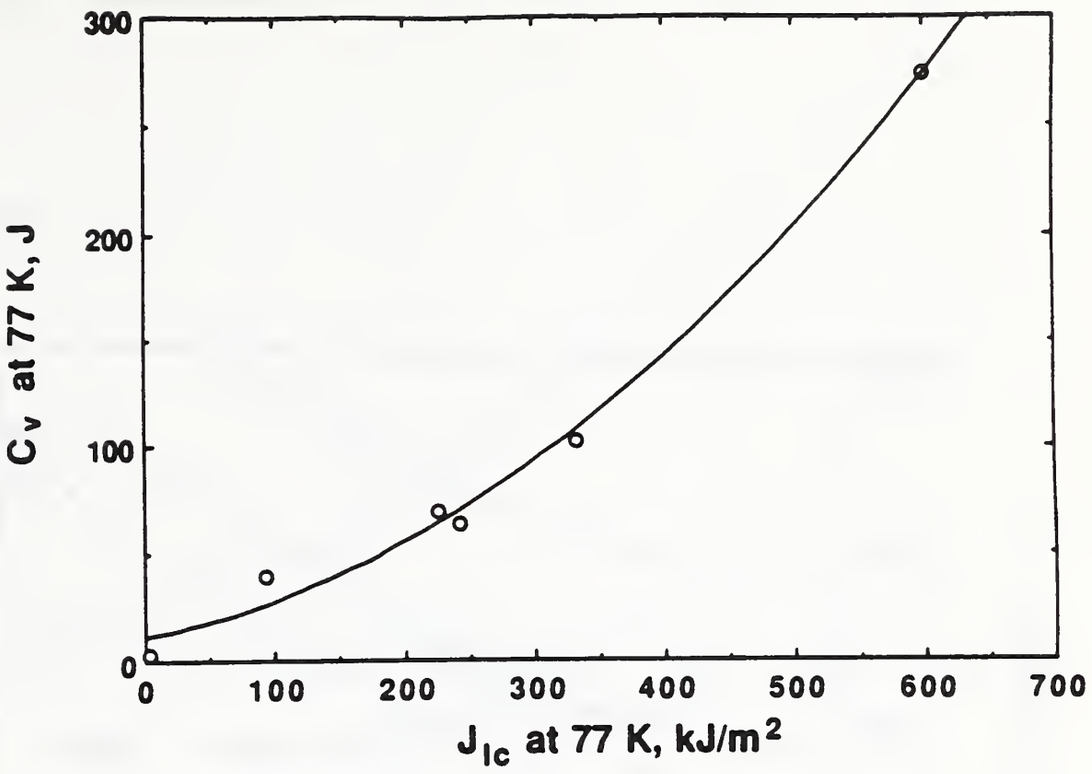

Figure 2. Relationship between J_{Ic} and Charpy absorbed energy at 77 K.

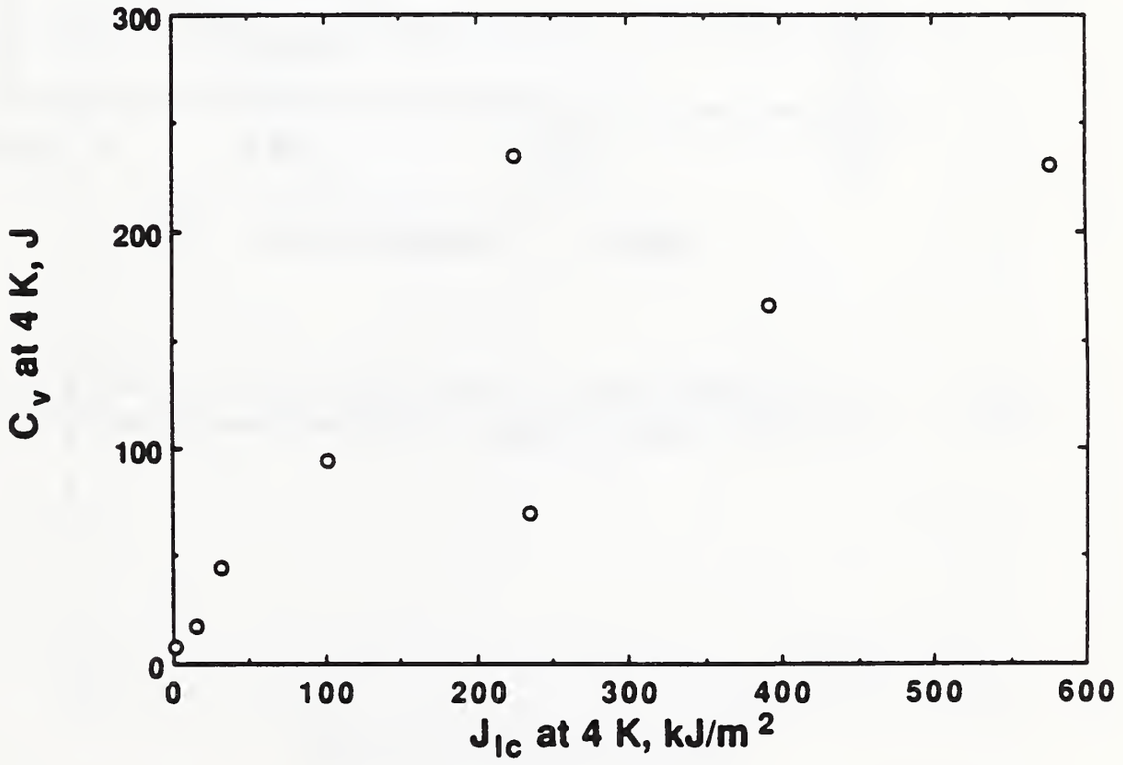

Figure 3. Relationship between J_{Ic} and Charpy absorbed energy at 4 K.

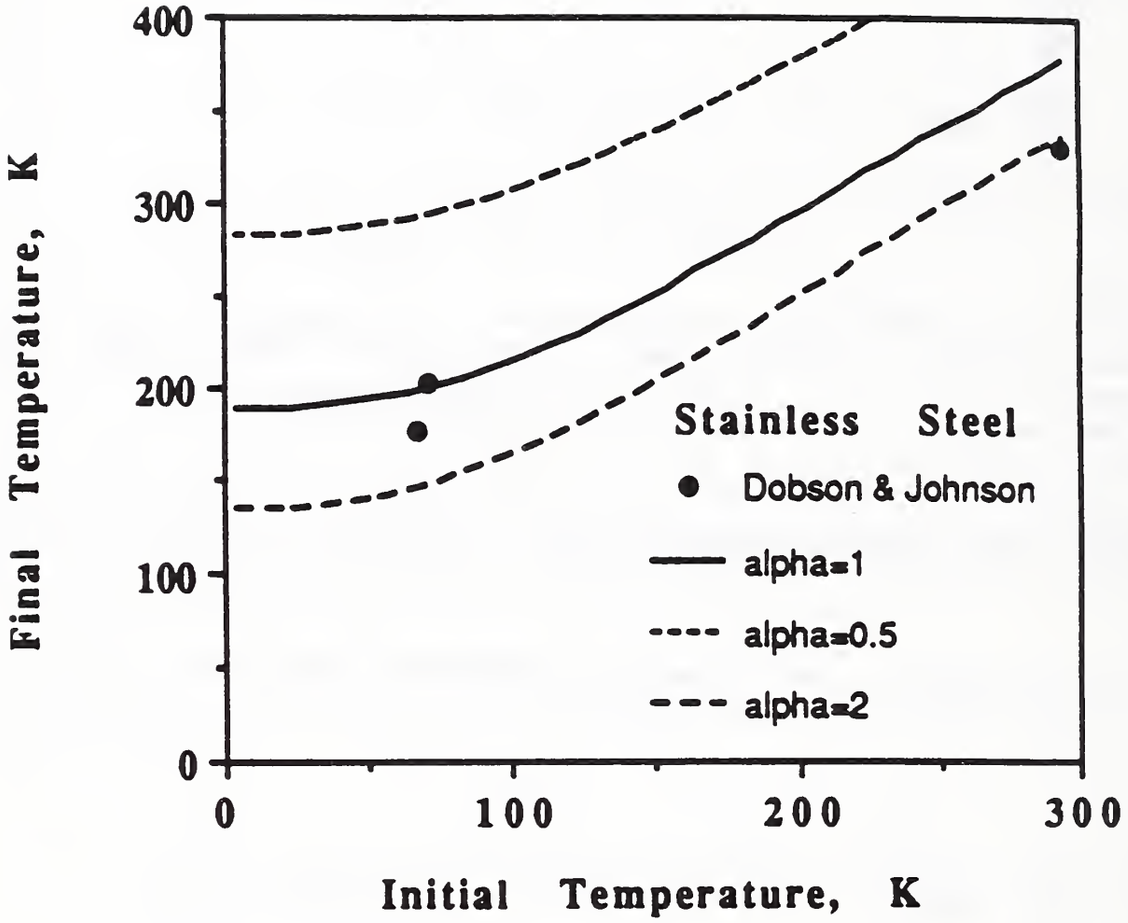

Figure 4. Predicted maximum temperature rise for Charpy specimens as a function of initial temperature (from Ref. [1]).

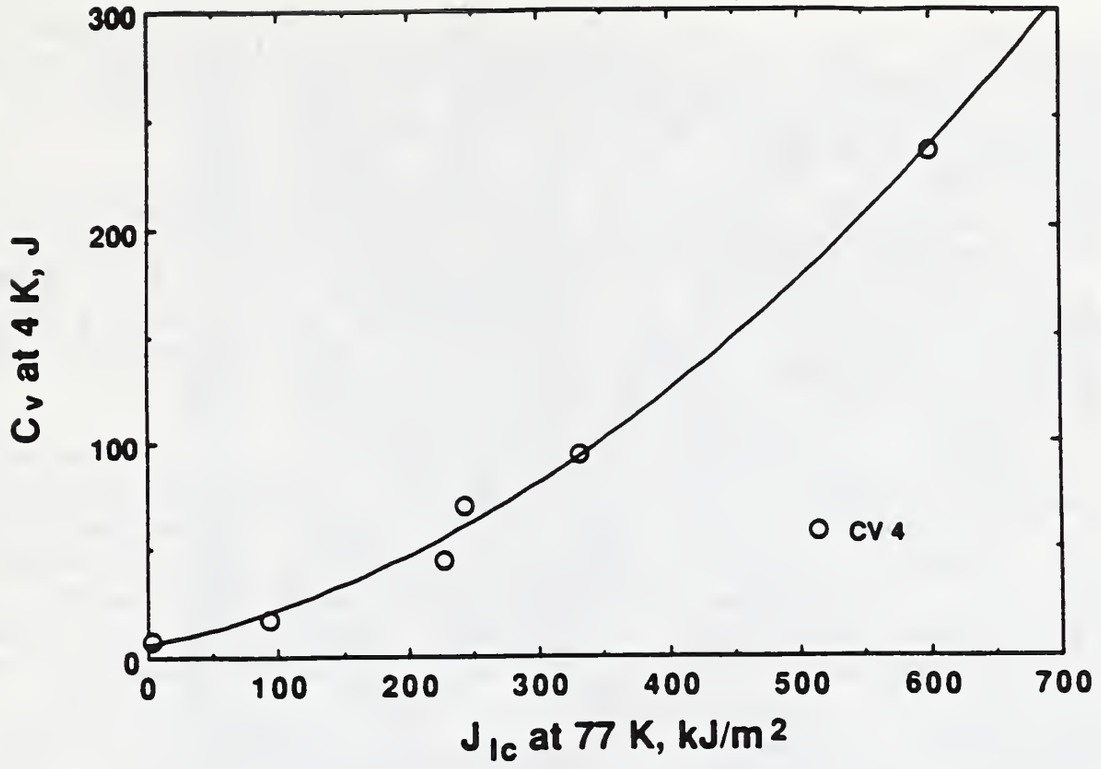

Figure 5. Relationship between J_{Ic} at 77 K and Charpy absorbed energy at 4 K.

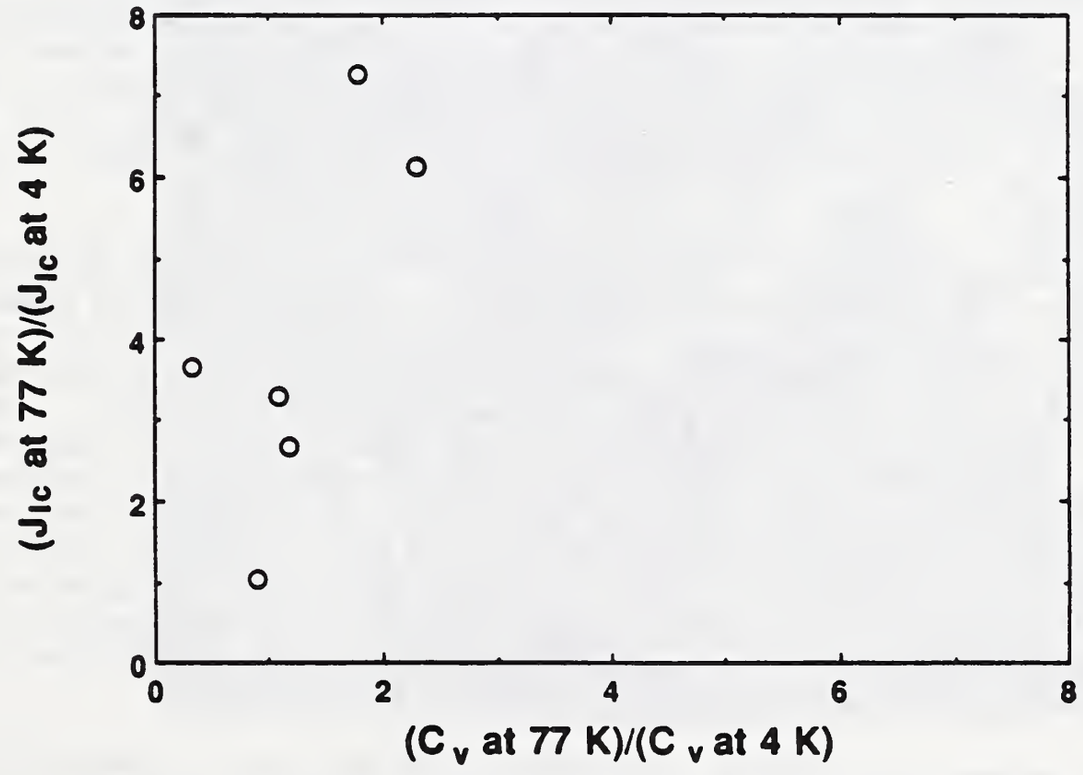

Figure 6. Comparison of J_{Ic} and C_v after normalization to 4 K values.

This correlation is much better than that for C_v and J_{Ic} at 4 K given in Eq. (3). The improvement in the correlation from Fig. 3 and Eq. (3) to Fig. 5 and Eq. (4) suggests that the 4 K Charpy specimens fractured at a higher temperature than JIc specimens.

The correlations in Figs. 2 and 5 are quite similar because there is little difference in C_v at 77 and 4 K. To show this point clearly, in Fig. 6 the ratio of C_v at 77 K to that at 4 K is plotted vs. the ratio of J_{Ic} at 77 K to that at 4 K. For alloys at 77 and 4 K, C_v does not change by more than a factor of 2, whereas J_{Ic} increases by factors up to 7. The results support our second hypothesis.

Two steels that cleave at 4 K and show large changes in J_{Ic} between 77 and 4 K were examined under the scanning electron microscope. The ferritic 5Ni and austenitic Fe-18Cr-3Ni-13Mn steels show changes in fracture morphology depending on the type of test performed. For 5Ni steel, Figs. 7 and 8 show representative fracture surfaces of Charpy and compact specimens tested at 77 and 4 K. Cleavage predominates in both the Charpy impact and fracture toughness test specimens at 77 and 4 K, as shown in Fig. 7. Unlike the fracture toughness specimens, however, the Charpy specimens include narrow regions at the notch tip where microvoid coalescence occurs. Figures 9 and 10 show fracture surfaces for Fe-18Cr-3Ni-13Mn stainless steel. In this case, the fractographic features of Charpy specimens tested at high strain rates are quite unlike those for compact specimens at low strain rates. Figure 9 shows that the Charpy specimen fracture surfaces are entirely microvoid coalescence type ductile tearing at both test temperatures. In contrast, Fig. 10 shows that the J_{Ic} specimens exhibit a substantial portion of cleavage, although the percentage is higher at 4 K than at 77 K at 77 K. Fibrous fracture also occurs as an intermediate fracture mode between cleavage and microvoid coalescence modes. Thus, fractographic evidence for Fe-18Cr-3Ni-13Mn indicates that the Charpy specimens, initially at 4 K, heated above 77 K to temperatures at which the fracture mechanism is microvoid coalescence. The point is that a good correlation between J_{Ic} and C_v cannot be expected if different test specimens of the same alloy fail by different mechanisms.

For annealed austenitic stainless steels JN1 and AISI 304 LN between 77 and 4 K, J_{Ic} changed by factors of 2 to 3, while C_v changed little as shown in Table 3. In contrast, the aged superalloy shows almost no change in J_{Ic} or C_v between 77 and 4 K. This temperature insensitivity is expected because the tensile properties of the alloy are also temperature insensitive [14]. Indeed, the mechanical properties of precipitation-hardened alloys are generally less temperature dependent than solution treated or annealed alloys, and the relative magnitude of the thermal softening increases from the precipitation-hardened superalloys, to austenitic stainless steels, and finally to ferritic steels. This variation in thermal-softening among the studied alloys is shown in Fig. 6 by the ratio of J_{Ic} measurements at two temperatures. Variations in thermal softening of alloys is the primary reason why a general correlation between J_{Ic} and C_v below 77 K can not be obtained.

It appears that Charpy tests are of little value for characterizing the static fracture toughness at 4 K. At best, we might attempt to use the 4 K Charpy test for screening of brittle materials, as in regulatory protocols. The attempt can be seriously faulted due to the wide variation in the thermal softening of alloys. If an acceptance criterion were to be derived from data for

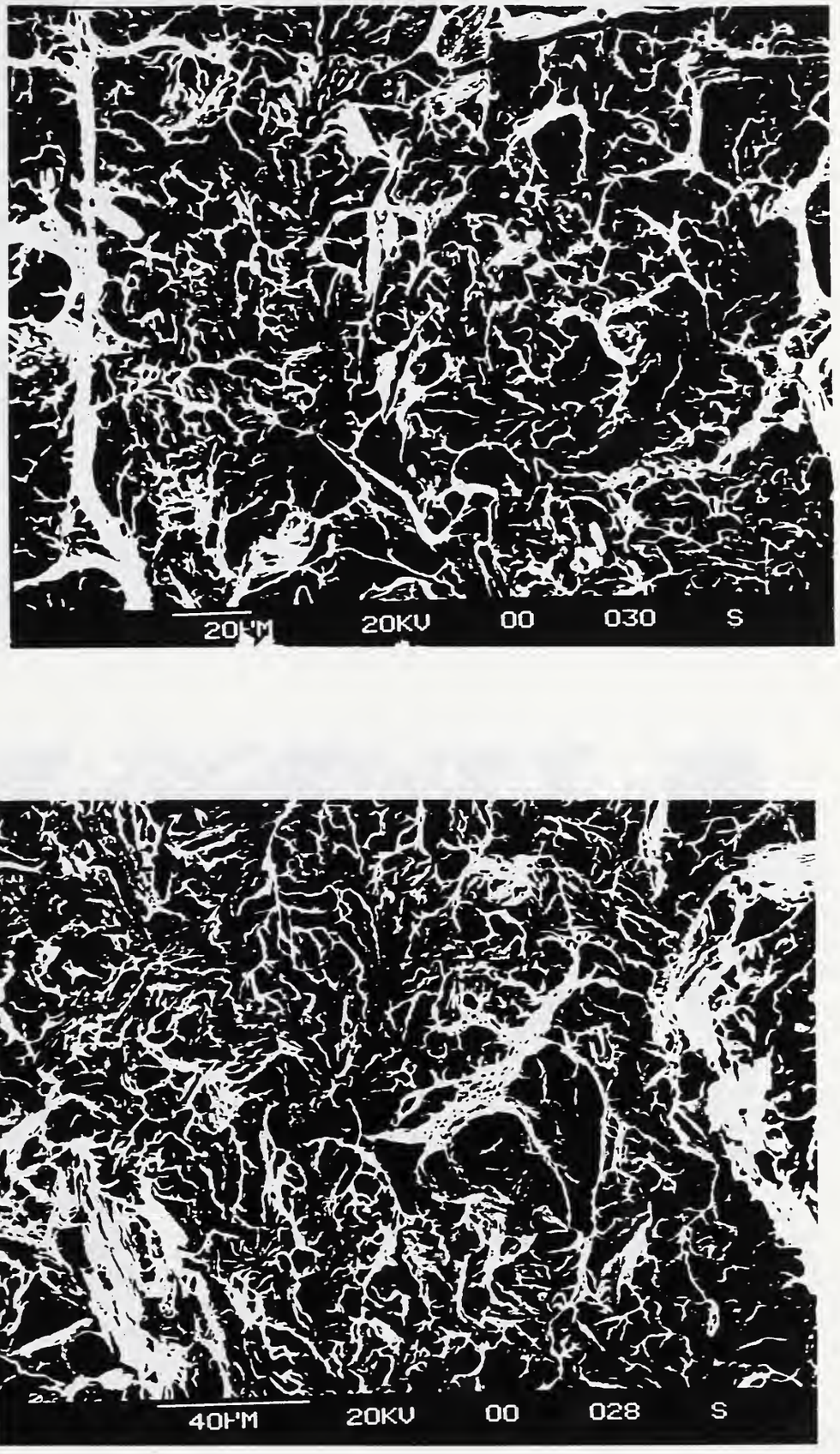

Figure 7. SEM fractographs of Charpy specimens: 5Ni steel tested at 4 K (upper, 500X) and at 77 K (lower, 500X).

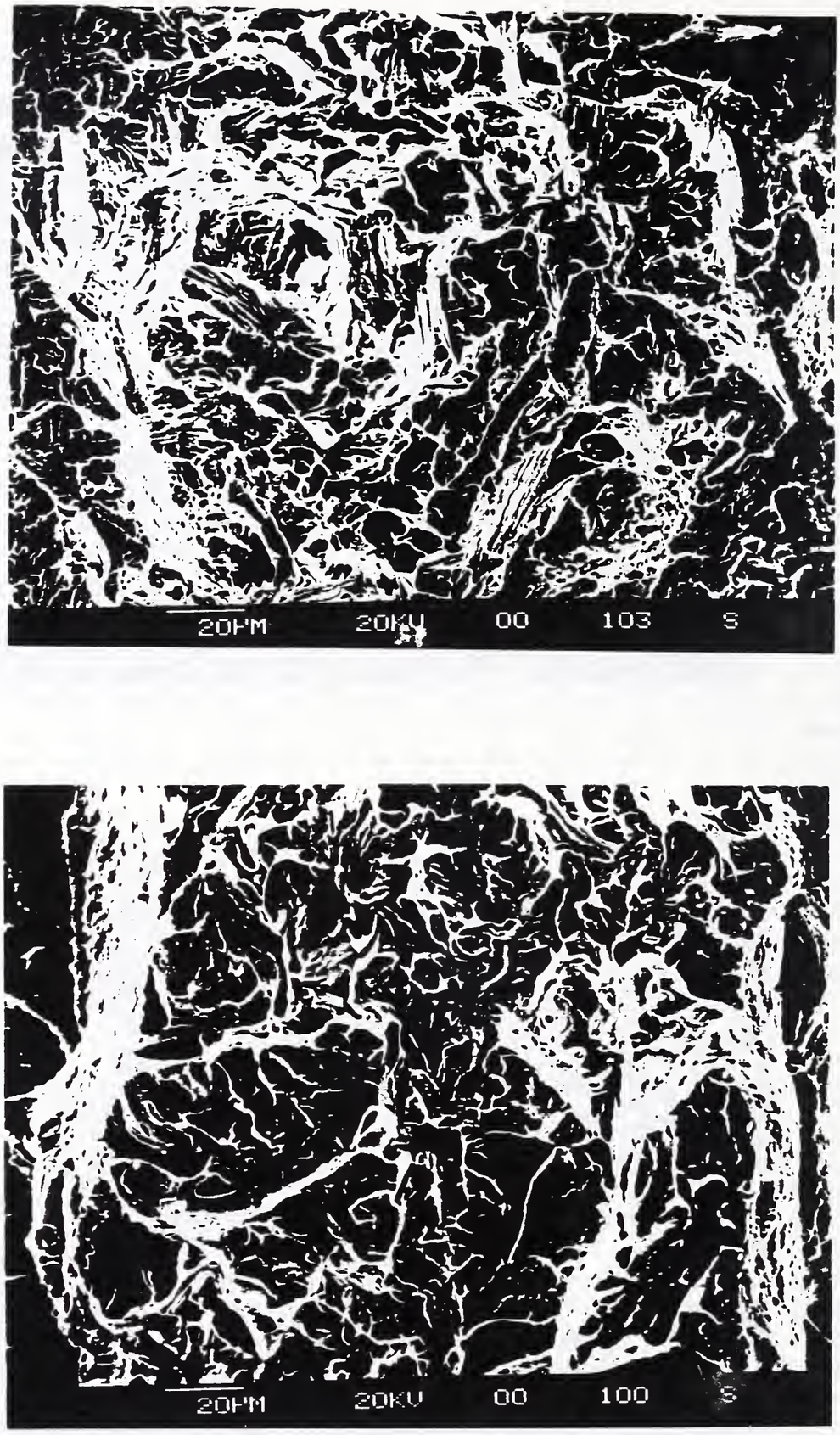

Figure 8. SEM fractographs of fracture toughness specimens: 5Ni steel tested at 4 K (upper, 500X) and at 77 K (lower, 500X).

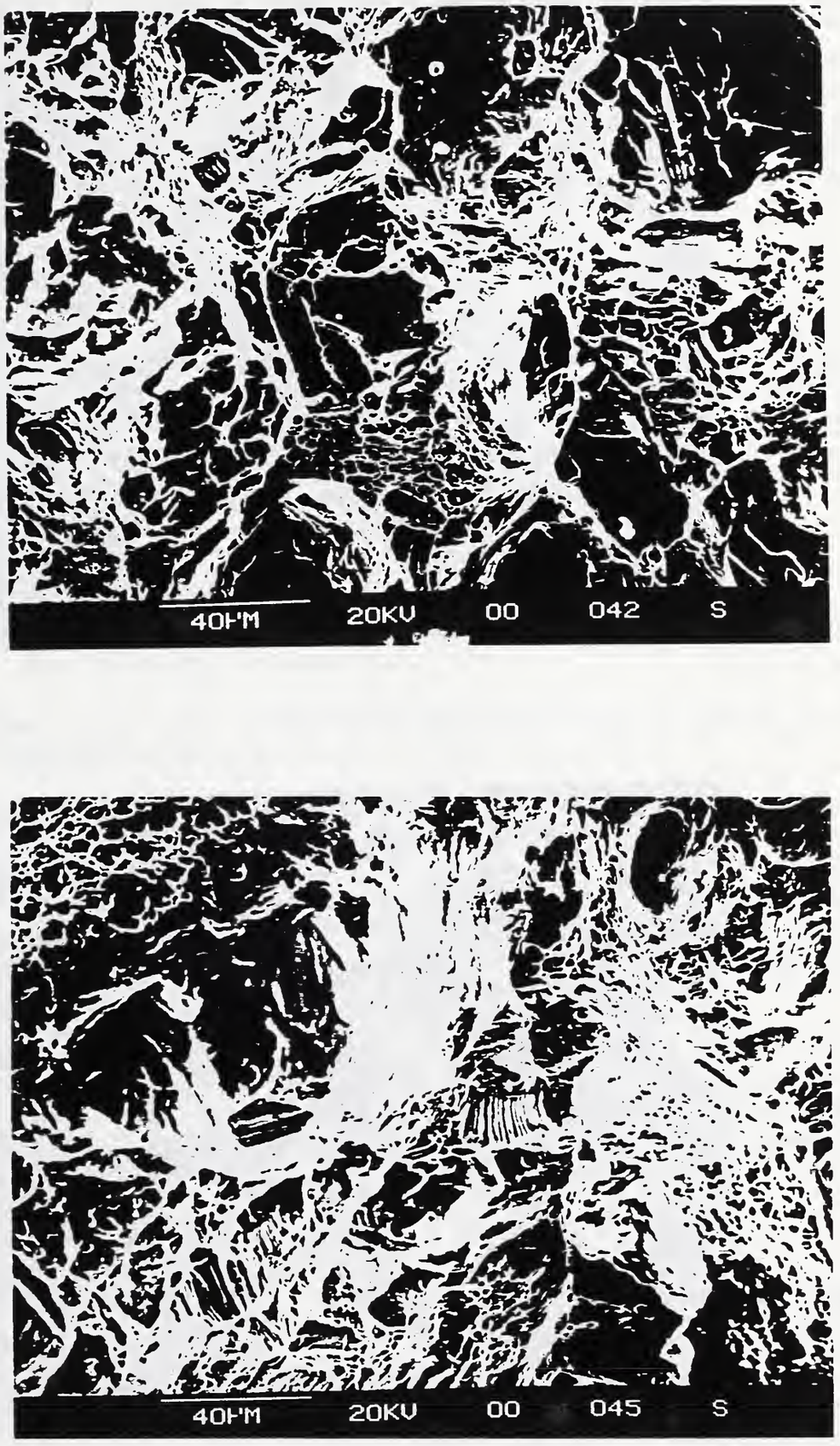

Figure 9. SEM fractographs of Charpy specimens: Fe-18Cr-3Ni-13Mn steel tested at 4 K (upper, 500X) and at 77 K (lower, 500X).

Figure 10. SEM fractographs of fracture toughness specimens of Fe-18Cr-3Ni-13Mn steel specimens: tested at 4 K (upper, 500X) and at 77 K (lower, 500X).

a particular group of alloys, it would be quite inappropriate for screening other alloys. Depending on circumstances, the criterion would be either overconservative or underconservative. Suppose that a 4 K C_v-based acceptance criterion were to be established for annealed austenitic stainless steels in accordance with a J_{Ic}-based acceptance criterion. Since annealed austenitic stainless steels have significant thermal softening, the same criterion would be unduly restrictive for precipitation-hardened steels or nickel-based superalloys that have negligible thermal softening.

In using C_v as a measure of energy absorption at extreme cryogenic temperatures, a dangerous overestimation is possible due to the thermal softening. Certain alloys in Charpy tests at 4 K may fail by ductile fracture mechanisms even though the normal fracture mechanism at slow loading rates below 77 K is cleavage. The risk of overestimation, the poor correlation with J_{Ic}, and the lack of quantitative data for use in design makes the Charpy impact test unacceptable as a measure of fracture toughness near absolute zero.

CONCLUSIONS

(1) Charpy test specimens with an initial temperature at or near 4 K actually fracture at temperatures well above 77 K due to adiabatic heating. We observe the following consequences:

   (a) There is a poor correlation between C_v and J_{Ic} at 4 K, and a good correlation between C_v at 4 K and J_{Ic} at 77 K.

   (b) There is little difference in C_v measurements for alloys at 77 and 4 K, even if J_{Ic} changes by several factors.

   (c) For some alloys such as Fe-18Cr-3Ni-13Mn stainless steel, Charpy specimens tested at an initial temperature near 4 K show different fractographic features than slowly loaded compact specimens tested at 4 K.

(2) High strain rate tests including the Charpy impact test are of limited value for predicting the static toughness below 77 K. Even for screening, an acceptance criterion for one group of alloys would significantly overestimate or underestimate the fracture toughness for another group due to wide variations in thermal softening among alloys.

REFERENCES

[1] Tobler, R.L., Reed, R.P., Hwang, I.S., Morra, M.M., Ballinger, R.G., Nakajima, H., and Shimamoto, S., "Charpy Impact Tests Near Absolute Zero," Journal of Testing and Evaluation, in press.

[2] Tobler, R.L., "A3. Test Procedures for Austenitic Alloys in Liquid Helium at 4 K," annex proposed for ASTM method E 813-88, presented to subcommittee E 24.04 at ASTM Technical Committee Week Meeting, San Francisco, April 24, 1990.

[3] Nakajima, H., Yoshida, K., Shimamoto, S., Tobler, R.L., and Reed, R.P., "Round Robin Tensile and Fracture Toughness Test Results for CSUS-JN1(Fe-

25Cr-15Ni-0.35N) Austenitic Stainless Steel at 4 K," in Adv. Cryo. Eng., Vol. 36, to be published.

[4] Morra, M.M., M.S. Thesis, submitted to Massachusetts Institute of Technology, 1990.

[5] Tobler, R.L., Shoji, T., Takahashi, H., and Ohnishi, K., "Fracture, Acoustic Emission and Adiabatic Heating of Austenitic Stainless Steels at Liquid Helium Temperature," in Acoustic Emission III, The Japanese Society of NDI, Tokyo, 1986, pp. 453-461.

[6] Ballinger, R.G., Becker, H.D., Hwang, I.S., and Morra, M.M., "Superstructure for Super Tokamak," 13th IEEE Symposium on Fusion Engineering, Knoxville, TN, 1989.

[7] Tobler, R.L., and Reed, R.P., "Tensile and Fracture Properties of Manganese-Modified AISI 304 Type Stainless Steel," in Adv. Cryo. Eng., Vol. 28, Plenum, New York, 1982, pp. 83-92.

[8] Tobler, R.L., Mikesell, R.P., Durcholz, R.L., and Reed, R.P., "Low Temperature Fracture Behavior of Iron-Nickel Alloy Steels" in Properties of Materials for LNG Tankage, ASTM STP 579, American Society for Testing and Materials, Philadelphia, 1975, pp. 261-287.

[9] Tobler, R.L., Ma, L.M., and Reed, R.P., "Mechanical Properties and Warm Prestress of Ultra-Low Carbon Steel at 4 K," presented in 12th Cryogenic Structural Materials Workshop, Vail, CO, October 11-12, 1989.

[10] Salkin, R.V., "The Stress Relaxation Heat Treatments after Welding," Proc. Int. Conf. on Stress Relieving Heat Treatments of Welded Steel Constructions, Sofia, Bulgaria, July 6-7, 1987.

[11] Saxena, A., and Hudak, S.J., Jr., "Review and Extension of Compliance Information for Common Crack Growth Specimens," Int. J. Fracture, Vol. 14, No. 5, 1978, pp. 453-468.

[12] Morra, M.M., Hwang, I.S., Ballinger, R.G., Steeves, M.M., Hoenig, M.O., "Effect of Cold Work and Heat Treatment on the 4 K Tensile, Fatigue, and Fracture Toughness Properties of Incoloy 908," presented at 11th Interntional Conference on Magnet Technology, August 28-September 1, 1989.

[13] Mori, K., and Kuroda, T., "Prediction of Energy Absorbed in Impact for Austenitic Weld Metals at 4 K," Cryogenics, Vol. 25, 1985, pp. 243-248.

[14] Ogata, T., Nagai, K., Hiraga, K., Ishikawa, K., and Irie, H., "Effect of EB-Weld and Cold Rolling on Low Temperature Strength and Toughness of Austenitic Stainless Steels," in Austenitic Steels at Low Temperatures," R.P. Reed and T. Horiuchi, Eds., Plenum, New York, 1983, pp. 211-220.

JAPAN—U.S. COOPERATIVE PROGRAM COMMITTEE ON TEST METHODOLOGY

NINTH DRAFT
NOVEMBER 1989

NOTE: This is a working document of a standard being developed by ASTM subcommittee E 28.10; it is intended for committee review, but not for general distribution at this time.

Proposed Standard Test Method for TENSION TESTING OF STRUCTURAL ALLOYS IN LIQUID HELIUM

1. Scope

1.1 This standard describes procedures for the tension testing of structural alloys immersed in liquid helium. The format is similar to that of other ASTM tension test standards, but the contents include modifications for cryogenic testing, which requires special apparatus, smaller specimens, and concern for serrated yielding, adiabatic heating, and strain-rate effects.

1.2 To conduct a tension test by this standard, the specimen in a cryostat is fully submerged in normal liquid helium (He I) and tested using crosshead displacement control at a nominal strain rate of 10^{-3} s^{-1} or less. Tests using load control or high strain rates are not considered.

1.3 This standard specifies methods for the measurement of yield strength, tensile strength, elongation, and reduction of area. The determination of the elastic modulus is treated in Method E 111.

1.4 Values stated in SI units are treated as primary; values stated in U.S. customary units are treated as secondary.

1.5 This standard may involve hazardous materials, operations, and equipment. This standard does not purport to address all of the safety problems associated with its use. It is the responsibility of the user of this standard to establish the appropriate safety and health practices and determine the applicability of regulatory limitations before use.

NOTE 1—The boiling point of normal liquid helium (He I) at sea level is 4.2 K (−452.1°F or 7.6°R). It decreases with geographic elevation and is 4.0 K (−452.5°F or 7.2°R) at the National Institute of Standards and Technology in Colorado, 1677 m (5500 ft) above sea level. In this standard the temperature is designated 4 K.

2. Applicable Documents

2.1 *ASTM Standards*:

A 370 Methods and Definitions for Mechanical Testing of Steel Products (*Annual Book of ASTM Standards*, Vol. 01.04)

E 4 Practices for Load Verification of Testing Machines (*Annual Book of ASTM Standards*, Vols. 03.01, 04.02, 07.01, and 08.03)

E 6 Definition of Terms Relating to Methods of Mechanical Testing (*Annual Book of ASTM Standards*, Vols. 03.01 and 08.03)

E 8 Methods for Tension Testing of Metallic Materials (*Annual Book of ASTM Standards*, Vols. 01.02, 02.01, 02.02, 02.03, and 03.01)

E 8M Methods for Tension Testing of Metallic Materials, Metric (*Annual Book of ASTM Standards*, Vol. 03.01)

E 29 Recommended Practice for Indicating Which Places of Figures Are to Be Considered Significant in Specified Limiting Values (*Annual Book of ASTM Standards*, Vols. 02.03, 03.01, 03.03, 03.05, and 14.02)

E 74 Standard Practice of Calibration of Force-Measuring Instruments for Verifying the Load Indication of Testing Machines (*Annual Book of ASTM Standards*, Vol. 03.01)

E 83 Practice for Verification and Classification of Extensometers (*Annual Book of ASTM Standards*, Vol. 03.01)

E 111 Method for Young's Modulus, Tangent Modulus, and Chord Modulus (*Annual Book of ASTM Standards*, Vol. 03.01)

E 1012 Standard Practice for Verification of Specimen Alignment Under Tensile Loading (*Annual Book of ASTM Standards*, Vol. 03.01)

2.2 *Japanese Industrial Standards (JIS)*:

B 7721 Tensile Testing Machines

B 7728 Load Calibration Devices for Verifying Material Testing Machines

G 0567 Method of High Temperature Tensile Test for Steels and Heat-Resisting Alloys

Z 2201 Test Pieces for Tensile Test for Metallic Materials

Z 2241 Method of Tensile Test for Metallic Materials

Z 8103 Glossary of Terms Used in Instrumentation

Z 8401 Rules for Rounding Off of Numerical Values

NOTE 2—Japanese and English versions of these standards are published by the Japanese Standards Association, 1-24, Akasaka 4, Minato-ku, Tokyo, 107 Japan.

3. Definitions

3.1 The definitions of terms relating to tension testing that appear in ASTM Standard E 6 shall apply here. The following definitions also apply:

3.1.1 *tensile cryostat*—a test apparatus for applying tensile forces to test specimens in cryogenic environments. A schematic illustration is shown in Fig. 1.

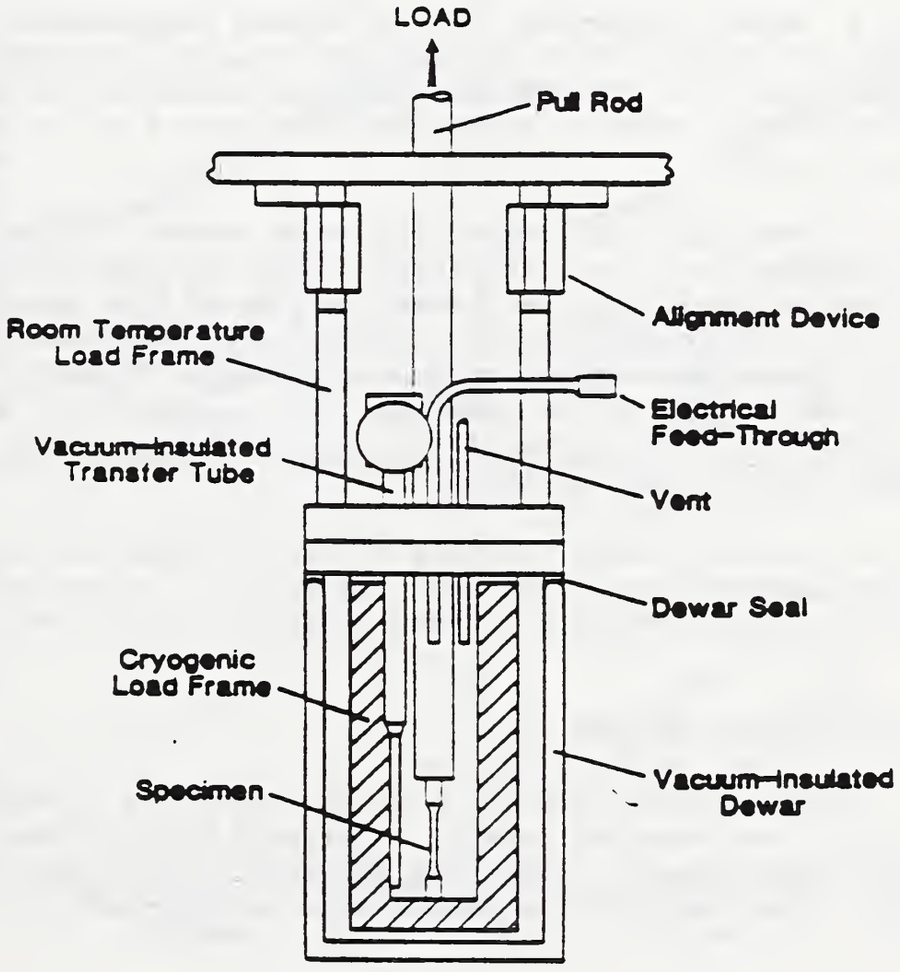

FIG. 1 Typical Cryostat for Tension Testing at 4 K.

3.1.2 *Dewar*—a vacuum-insulated container for cryogenic fluids.

3.1.3 *adiabatic heating*—the internal heating of a specimen resulting from tension testing under conditions such that the heat generated by plastic work cannot be quickly dissipated to the surrounding cryogen.

3.1.4 *reduced section*—section in the central portion of the specimen, which has a cross section smaller than the gripped ends.

3.1.5 *length of the reduced section*—the distance between the tangent points of the fillets that bound the reduced section.

3.1.6 *adjusted length of the reduced section*—the length of the reduced section plus an amount calculated to compensate for strain in the fillet region.

3.1.7 *gage length*—the original distance between gage marks made on the specimen for determining elongation after fracture.

3.1.8 *axial strain*—the average of the longitudinal strains measured at opposite or equally spaced surface locations on the sides of the longitudinal axis of symmetry of the specimen. The longitudinal strains are measured using two or more strain-sensing devices located at the mid-length of the reduced section.

3.1.9 *bending strain*—the difference between the strain at the surface of the specimen and the axial strain. The bending strain varies around the circumference and along the reduced section of the specimen.

3.1.10 *maximum bending strain*—the largest value of bending strain in the reduced section of the specimen. It is calculated from strains measured at two, three, or more circumferential positions, and at each of two different longitudinal positions.

3.1.11 *discontinuous yielding stress*, σ_i—the stress at the initiation of the first measurable serration on the curve of stress-versus-strain. The parameter σ_i is a function of test variables and is not a material constant.

4. Significance and Use

4.1 Tension tests provide information on the strength and ductility of materials under uniaxial tensile stresses. This information may be useful for alloy development, comparison and selection of materials, and quality control. Under certain circumstances, the information may also be useful for design.

4.2 The load–time and load–deflection records for alloys tested in liquid helium using displacement control are serrated (1). Serrations are formed by repeated bursts of unstable plastic flow and arrests. The unstable plastic flow (discontinuous yielding) is a free-running process occurring in

localized regions of the reduced section at higher than nominal rates of strain with internal specimen heating. Examples of serrated stress–strain curves for a typical austenitic stainless steel with discontinuous yielding are shown in Fig. 2.

4.3 A constant specimen temperature cannot be maintained at all times during tests in liquid helium. The specimen temperature at local regions in the reduced section rises temporarily above 4 K during each discontinuous yielding event (see Fig. 2), owing to adiabatic heat. The number of events and the magnitude of the associated load drops are a function of the material composition and other factors such as specimen size and test speed. Typically, altering the mechanical test variables can modify but not eliminate the discontinuous yielding (2-4). Therefore, tensile property measurements of alloys in liquid helium (especially tensile strength, elongation, and reduction of area) lack the usual significance of property measurements at room temperature where deformation is more nearly isothermal and discontinuous yielding typically does not occur.

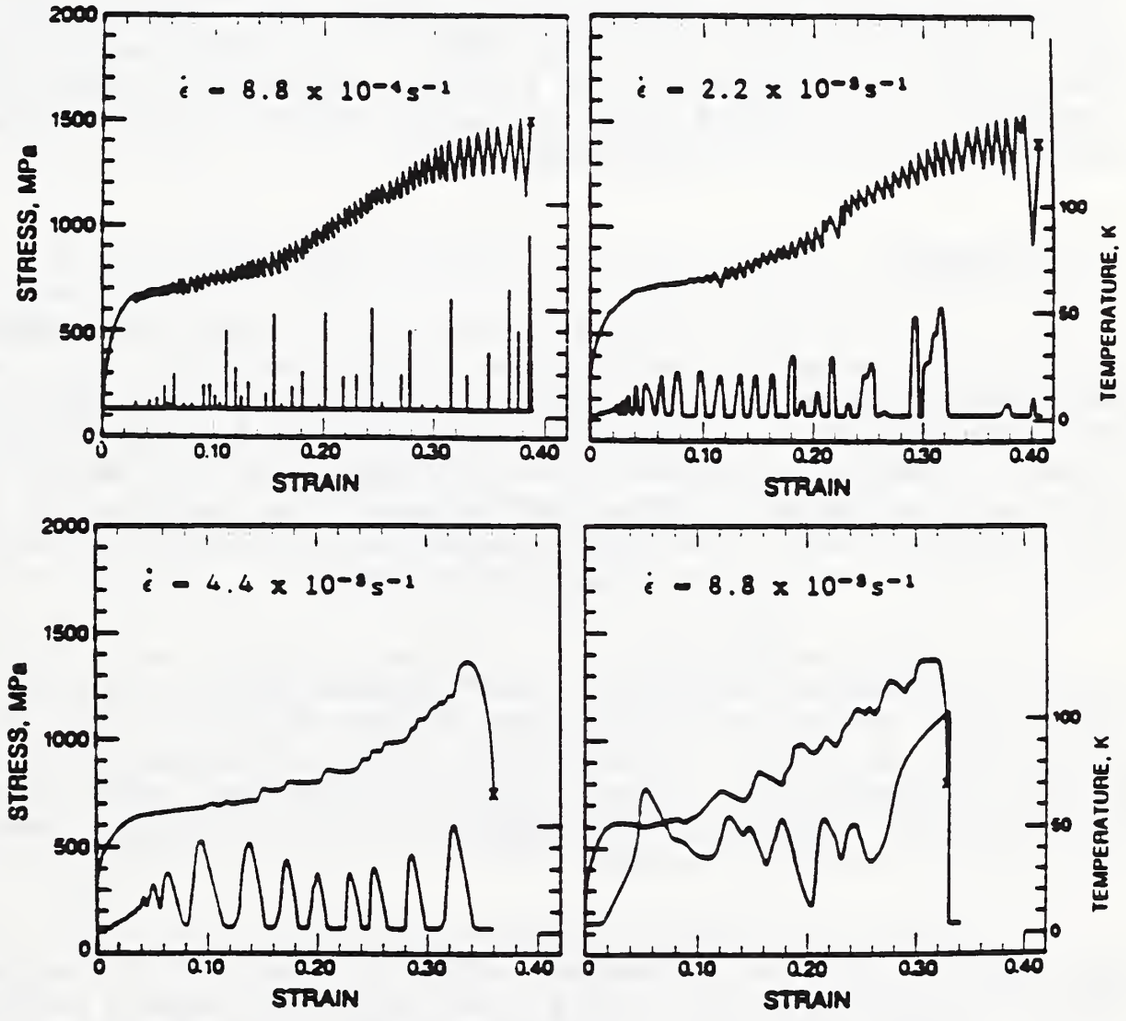

FIG. 2 Typical Engineering Stress–Strain Curves and Specimen Temperature Histories, at Four Different Nominal Strain Rates, for AISI 304L Stainless Steel Tested in Liquid Helium (Ref. 4).

4.4 The stress–strain response of a material tested in liquid helium depends on whether load control or displacement control is used (3). Crosshead displacement control is specified in this standard since the goal is material characterization by conventional methods. The possibility of a different and less favorable material response must be taken into account when data are used for design in actual applications subject to load-controlled conditions.

5. Hazards

Several precautions must be observed in the use of cryogenic fluids and equipment. Skin or eye contact with cryogens will produce burns. The appropriate protection may require goggles, clothing without pockets or cuffs, gloves, and tongs for handling cold specimens. Cryogenic containers that are internally pressurized or evacuated are potentially hazardous in that damage or leaks can produce explosions or implosions. Also, when liquids evaporate to gases, there is a huge volume increase; therefore asphyxiation is a potential threat where liquid nitrogen or liquid helium evaporates in rooms that are not properly ventilated. Safety guidelines pertaining to the use of liquid helium and other cryogenic fluids are considered elsewhere in more detail (5).

6. Apparatus

6.1 *Test Machines*—Use a test machine that meets the requirements of Practices E 4 regarding verification of force accuracy. The test machine compliance (displacement per unit of applied force of the apparatus itself) should be known. The compliance can be measured by coupling the load train without including a specimen, by replacing the specimen with a rigid block, or by using a special calibration specimen. The compliance is then measured at a low force and at the highest force used to qualify the machine, as directed in section 6.4.1 of this standard.

6.2 *System Design*—Typically, alloys in liquid helium exhibit double or triple their ambient strengths. For the same specimen geometry, higher forces must be applied to the cryostat, test specimen, load train members, and grips at cryogenic temperatures. Since many conventional test machines have a maximum force of 100 kN (22 480 lbf) or less, it is recommended that the apparatus be designed to accommodate one of the small specimens cited in section 8.2.2 of this standard.

6.3 *Construction Materials*—Many construction materials, including the vast majority of ferritic steels, are brittle at 4 K. To resist failure in service, fabricate the grips and other load-train members using strong, tough, cryogenic alloys. Materials that have low thermal conductivity are desirable to reduce heat flow. Austenitic stainless steels (AISI 304LN), maraging steels (200, 250, or 300 grades, with nickel plating to prevent rust), and extra-low-interstitial (ELI) grade titanium alloys (Ti–6Al–4V and Ti–5Al–2.5Sn) have been used with proper design, for grips, pull rods, and

cryostat frames. Nonmetallic materials (for example, glass–epoxy composites) are excellent insulators and are sometimes used for compression members.

6.4 *Alignment*:

6.4.1 *Single-Specimen Apparatus*—Proper system alignment is essential to avoid bending strains in tension tests. For a conventional single-specimen cryostat, the machine and grips should be capable of applying force to a precisely machined calibration specimen so that the maximum bending strain does not exceed 10% of the axial strain. Reduce bending strain to an acceptable level by making proportional adjustments to a cryostat having alignment capability, or by using spacing shims to compensate an unadjustable fixture. Calculation the strain based on readings taken while the calibration specimen is subjected to a low force, as well as at the highest force for which the machine and load train are being qualified. Procedures for measuring specimen alignment are given in Standard Practice E 1012.

NOTE 3—This requirement will minimize contributions from the test apparatus to the bending strain. Tests performed with a qualified apparatus may still vary in amount of bending strain owing to small variations in the proposed test specimen configurations, or differences in machining.

6.4.2 *Multiple-Specimen Apparatus*—For this type of cryostat the alignment depends on the type of fixtures used. Measure and reort the maximum bending strain.

6.4.3 Qualify the apparatus by making axiality measurements at room temperature and at 4 K. To perform axiality tests of the apparatus, the specimen form should be the same as that used during cryogenic tests, and the specimen concentricity should be as nearly perfect as possible. To the limit of strength for the alignment specimen, no plastic strains should occur in the reduced section. In some cases this may necessitate the use of a relatively stiff, high-strength calibration specimen.

6.4.3.1 For cylindrical specimens, calculate the maximum bending strain defined in 3.1.10 from the strains measured at three circumferential positions, at each of two different longitudinal positions. Measure the strains with three electrical-resistance strain gages, extensometers, or clip gages equally spaced around the reduced section of the specimen. The two longitudinal positions should be as far apart as possible, but not closer than one diameter to a fillet.

6.4.3.2 For specimens of square or rectangular cross section, measure strain at the center of each of the four sides or, in the case of thin cross sections, near the outer edges of each of the two broad sides.

6.4.3.3 To eliminate the effect of specimen bias, repeat the axiality measurements with the specimen rotated 180°, but with the grips and pull rods retained in their original positions. Then calculate the maximum bending

strain and the strain at the specimen axis as the average of the two readings at the same position relative to the machine.

6.4.4 *Strain-Averaging Technique*—Nonaxiality of loading (which may be introduced due to the machining of the test specimens) is usually sufficient to introduce errors in tension tests at small strains when strain is measured at only one position on the specimen. Therefore measure strains at three equally spaced (or, if good alignment has been achieved, at least two opposing) positions within the reduced section. Report the average of the strains from the two or three positions centered on the reduced section.

6.5 *Gripping Mechanisms*—The choice of gripping mechanism to be used is influenced by specimen type. The mechanisms described in Methods E 8 and E 8M are satisfactory at 4 K, but cryogenic materials must be used in the construction of components to avoid failure in service.

6.6 *Dimension-Measuring Devices*—For measuring the dimensions of specimens, use a micrometer or other device that is accurate and precise to at least one-half of the smallest unit to which a given dimension must be measured.

6.7 *Cryostats and Support Apparatus*

6.7.1 *Cryostats*—A cryostat capable of retaining liquid helium is required. In general, cryostat load frames for existing test machines must be custom-built, but they may accommodate commercially available Dewars. The cryostat may employ adjustable load columns to facilitate alignment. Several practical designs, including turret-disc designs for multiple-specimen testing with a single cooling, are discussed in the literature (6–10).

6.7.2 *Dewars*—Stainless steel Dewars are safer (that is, more fracture resistant) than glass Dewars and less expensive than fiberglass Dewars. Generally, a single helium Dewar (see Fig. 1) is sufficient for short-term tensile tests. Also possible is a double-Dewar arrangement in which an outer Dewar of liquid nitrogen surrounds the inner Dewar of liquid helium.

6.7.3 *Ancillary Equipment*—Dewars and transfer lines for liquid helium must be vacuum insulated. Vacuum pumps, pressurized gas, and liquid nitrogen facilities are therefore required. After testing, the helium may be released to the atmosphere, recycled as a gas, or reliquefied. Recycling or reliquefaction requires large investments in purification and support systems.

6.8 *Temperature Maintenance and Liquid-Level Indicators*—The intended test condition is ensured by maintaining a liquid helium environment. With the specimen completely immersed, a thermocouple to measure its temperature is not required for routine tests. Instead, a simple indicator or meter is required to ensure that the specimen remains fully submerged throughout the test. An on–off indicator of the carbon-resistor type located at some reference point in the cryostat may be used to verify that the liquid level always remains above the specimen. Alternatively, the liquid level may be

continuously monitored using a superconducting wire sensor of appropriate length positioned vertically inside the cryostat.

NOTE 4—One indication of the system nearing and reaching a steady state condition is the amount of condensation flare. As liquid helium is transferred into the cryostat, the flare becomes visible when boiled-off helium contacts room temperature air at the vent of the cryostat (Fig. 1). As cool-down proceeds, the flare decreases to a slowly issuing cloud due to less active boiling as the internal temperature of the cryostat reaches operating temperature.

6.9 *Strain Gages*:

6.9.1 *Precautions*—Strain-gage films bonded directly to the specimen surface may be used to measure strain at 4 K (11). The use of bonded strain gages at 4 K, however, requires precautions not customarily required at room temperature. There are two major complications: the gage factor varies with temperature, and thermal output (apparent strain) is introduced as the specimen–gage combination is cooled from room temperature to 4 K. Thermal output is caused by two concurrent and algebraically additive effects in the strain gage installation: (1) the electrical resistivity of the gage grid element and (2) the differential thermal expansion between the gage grid element and the test specimen to which the gage is bonded. These effects must be accounted for, or considerable error in strain measurements may be introduced.

Gage manufacturers generally do not supply thermal output data at 4 K; neither do they state gage factors at 4 K. For high accuracy the user may need to perform gage factor and thermal output calibrations for his system to establish a stable reference gage output at 4 K before beginning tension tests. For this reason, strain gage calibrations may be more difficult than extensometer calibrations (see Section 6.10.3).

6.9.2 *Selection and Characteristics*—Not every type of strain gage is usable at cryogenic temperatures. Select a satisfactory combination of gage active element, backing material, and bonding agent based on experience and manufacturer's recommendations. A common choice for extreme cryogenic service is a Ni–Cr-Al–Fe alloy gage with a temperature-compensated active element (8). Typically the gage resistance is 120 or 350 Ω, and a low excitation voltage is used to reduce Joule heating at 4 K. The full-scale operating range is typically 1% at room temperature and 2% at 4 K.

6.9.3 *Wiring*—Various circuits may be used for wiring strain gages. The choice depends on purpose and accuracy desired. One circuit that is satisfactory for tension tests according to this standard is the three-wire temperature-compensating hookup and Wheatstone bridge arrangement shown, for example, in Fig. 3. The three-wire circuit nullifies or eliminates thermally induced resistance changes in the leadwires if the wires R_{ℓ_1} and R_{ℓ_3} in Fig. 3 have the same resistance and experience the same temperature

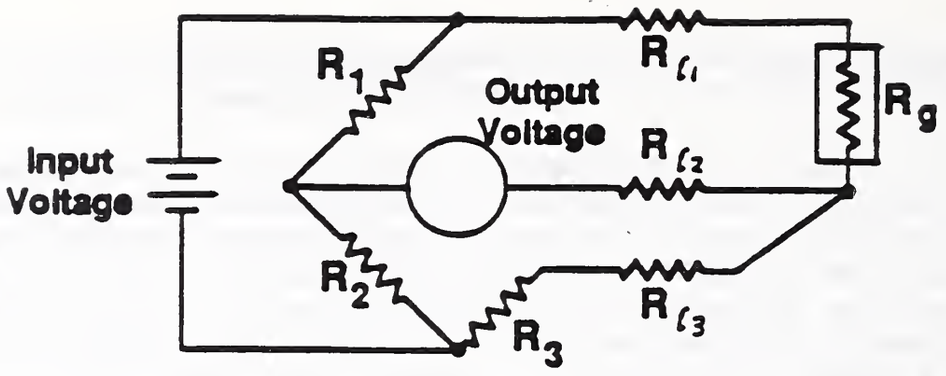

FIG. 3 A Method of Strain-Gage Wiring for Cryogenic Tests

changes along their lengths. This circuit may be used with commercial strain indicators. First, balance the Wheatstone bridge at room temperature. Then, to compensate for any apparent strain induced on cooling the specimen and gage to the test temperature, cancel the change in electrical signal after cooling before the force is applied and testing begins. Other circuits and instruments are possible, and some techniques may offer higher accuracy than the illustrated example.

NOTE 5—Some gage manufacturers provide estimated values of the gage factors for the use of their products at low temperatures. Their estimated values do not necessarily agree with published research, and calibration by controlled experimental determinations are preferred. Gage factors at temperatures as low as 4 K for some common materials have been published in a few studies. For example, findings for Ni–Cr alloy gages show that the gage factor increases nonlinearly by 2.5 or 5% as the temperature is reduced from 295 to 4 K (12-14).

6.10 *Clip-Gage Extensometers:*

6.10.1 *Types*—Reliable clip-gage extensometers for use at 4 K may be purchased or built. An example is the beam gage, which uses four strain-gage films bonded in a full Wheatstone bridge. Extension within the specimen gage length is sensed by the detachable extensometer, which is clipped to retaining pins that are fixed to the specimen reduced section.

6.10.2 *Characteristics*—To measure the 0.2% offset yield strength, one or more Class B–2 or better extensometers, as identified in Method E 83, may be used. Each extensometer must meet the sensitivity and accuracy requirements of Method E 83 and must be tested to ensure accuracy at 4 K. Whenever possible, mount the extensometer(s) directly to the specimen reduced section.

NOTE 6—It may be desirable to use several extensometers to detect the amount of bending, especially for brittle

specimens. One method for obtaining multi-planar strains is to fasten a pair of collars to the specimen reduced section, using sharpened radial thumbscrews. The collars are made with detents (located on the inboard faces) to accept spring-loaded clip gages. This arrangement also serves to define a fixed gage length within the specimen reduced cross section.

6.10.3 *Calibration*—Calibrate extensometers at room temperature and at 4 K. For calibrations at 4 K, a device such as a micrometer with vertical extension tubes can be used with the extensometer(s) mounted at the lower end and immersed in liquid helium. If the calibration is known and proved to be accurate, linear, and reproducible, then room-temperature checks may be performed before each series of tests to indirectly verify the 4-K calibration. However, direct calibration at 4 K must be performed periodically, especially if damage is suspected or repairs have been made.

6.11 *Capacitance Extensometers*—Extensometers that use capacitance measurement to monitor strain may be used (11). The type with overlapping concentric cylinders has an extended strain range, an output that is linear with displacement, and an adjustable sensitivity. The type with parallel plates has high sensitivity, but its output is nonlinear, and it must be compensated for the hyperbolic dependence of capacitance on displacement.

7. Sampling

7.1 Take samples for tension testing from the material in its final condition to ensure that the properties measured are representative of the product. Allow for any superficial effects introduced by the cutting operations.

7.2 Cut specimens from locations thought to be most representative of the stock material, realizing that data for specimens taken from selected locations of a structure or material may not be representative of the whole. The conventional locations should normally be used:

7.2.1 For products 40 mm (1.6 in) or less in thickness or diameter, the location should be at the center.

7.2.2 For products over 40 mm (1.6 in) in thickness or diameter, the location should be midway from the surface to the center.

7.3 Choose a specimen size and shape based on the requirements necessary to obtain representative samples of the material, and on the test machine's force capacity (section 6.2).

7.4 Using the notation in section 4 of Method A 370, specify the orientation of the specimen's axis relative to the most predominant of either the grain flow or the principal working direction of the final form of the stock.

8. Test Specimens

8.1 *General*:

8.1.1 *Types and Specifications*—Any specimen configuration cited in Methods E 8 or E 8M may be used. Specifications for dimensions, tolerances, and surface finish are stated in sections 6.1 through 6.17 of those standards.

8.1.2 *Size*—Specimens from sheet or wire products having relatively small cross-sectional areas can be tested within the force capacities of conventional apparatus. Specimens from thick plate or bar products, however, must be machined to a reduced cross-sectional area so the force capacity of the machine is not exceeded. Preferably, the specimen in this case should have the same configuration as the standard specimen but with an appropriately reduced cross section.

8.2 *Round Bar Specimens*:

8.2.1 *Standard Room-Temperature Specimens*—A 12.5 mm (0.5 in) diameter round bar is the standard configuration for room-temperature tests according to Methods E 8 and E 8M. Specimens of that size, however, require high test forces to fracture strong alloys at 4 K. For example, 210 kN (47 208 lbf) is required to test typical AISI 304LN steel at 4 K, whereas 100 kN (22 480 lbf) is the limit for most test machines.

8.2.2 *Standard 4-K Specimens*—To meet the load limitations of conventional test machines, the round bar specimens in sections 7.2.2.1 and 7.2.2.2 are defined as standard for 4-K tests. The required dimensions and tolerances for these specimens are given in Table 1. Threaded or shouldered ends are common for gripping these specimens, and the requirement of section 6.4.1 can be met by precise machining.

8.2.2.1 *Standard, small metric specimens*. These specimens have a 7-mm (0.275-in) diameter and a G-to-D ratio of 5:1.

8.2.2.2 *Standard, small U.S. customary specimens*. These specimens have a 6.25-mm (0.250-in) diameter and a G-to-D ratio of 4:1.

8.2.3 *Alternatives*—If the 4-K standard specimens described above are inappropriate for some reason, other sizes may be selected following the guidelines of Methods E 8 and E 8M. The proportions of such specimens should be similar to those of the standard specimens (see Fig. 4 of this Method and Fig. 8 of Methods E 8 or E 8M).

8.2.4 *Subsize specimens*—Special care in fabrication and testing is required for specimens with diameters less than 6 mm (0.236 in). As the specimen size is reduced, factors such as machining, surface finish, and alignment show increasing importance. Also, to ensure polycrystalline deformation, some experimenters insist on the need for a minimum of ten grains per cross section; if the number of grains per cross section is approximately ten or less, note this in the report.

TABLE 1 Standard Specimens for Room-Temperature Tests and Recommended Proportionally Reduced, Standard Small Specimens for 4-K Tests[1]

(a)

Metric Versions G/D ratio = 5 (dimensions, mm)	Standard Specimen	Standard Small Specimen
Nominal Diameter	12.5	7
G, gage length	62.5 ± 0.1	35 ± 0.1
D, diameter	12.5 ± 0.1	7 ± 0.1
R, fillet radius	10	7
A, reduced section	75	42

(b)

U.S. Customary Versions G/D ratio = 4 (dimensions, in)	Standard Specimen	Standard Small Specimen
Nominal Diameter	0.5	0.25
G, gage length	2.000 ± 0.005	1.000 ± 0.005
D, diameter	0.500 ± 0.010	0.250 ± 0.005
R, fillet radius	0.375	0.1875
A, reduced section	2.25	1.25

[1]See also the notes to Fig. 8 in Methods E 8 and E 8M.

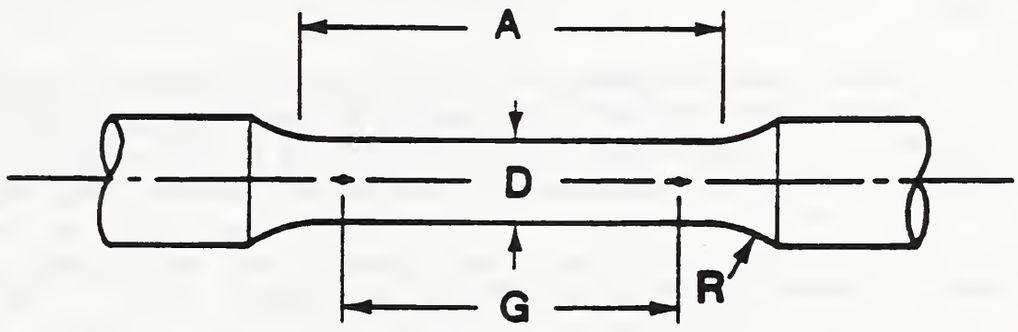

FIG. 4 Round Bar Specimen Configuration (see Table 1)

9. Procedures

9.1 *Marking and Measuring the Test Specimen:*

9.1.1 *Gage Length*—Gage marks may be lightly punched, scribed, or inked at appropriate locations on the reduced section of the specimen. This is the preferred method. After marking the gage length, measure it to the nearest 0.05 mm (0.002 in). The conventional gage length is five times the diameter for metric specimens or four times the diameter for U.S. customary specimens. If another gage length is used for elongation measurements, describe it in the report.

> NOTE 7—For metals of low ductility, gage marks punched or scribed on the reduced section may induce failure at those locations due to stress concentrations. To avoid this, coat the reduced section with layout ink, and mark the gage length by rotating the specimen in a jig with knife edges scraping off the ink at the appropriate intervals. Otherwise, gage marks may be placed on the specimen shoulders, or the overall length of the specimen may be used to determine elongations (see section 9.6.5); in that case some error is introduced from measurement across section changes and the results should be qualified.

9.1.2 *Reduced Section* and Overall Length—Measure the length of the reduced section (A) and the adjusted length of the reduced section, if applicable, to the nearest 0.05 mm (0.002 in). If overall specimen length (L) is used as a basis for determining elongations, measure the initial overall length of the specimen to the nearest 0.05 mm (0.002 in).

9.1.3 *Cross Section*—Determine the cross-sectional area of the reduced section by measurements according to section 7 of Methods E 8 and E 8M.

9.2 *Specimen Installation*—Leaving sufficient slack for instrumentation wires so they will not be stretched or crimped during positioning of the Dewar or subsequent motions during testing, install the specimen in the cryostat.

9.3 *Seating and Alignment*—If the gripping fixture involves loosely fitting components, such as spherically seated bearings, prevent friction or mismatch of the bearing surfaces at 4 K by first checking the seating and alignment at room temperature. During alignment, keep the applied tensile force below one-third of the proportional limit of the material being tested. Subsequently maintain a small but sufficient load to ensure that the alignment is retained during cool-down.

9.4 *Cooling Procedure*—Ice can block cryogenic transfer lines or cause erratic loading behavior if it forms between various parts of the specimen, clip gage, and load train. To prevent icing, remove any condensate from the apparatus before cooling by drying it thoroughly with an air jet or heat gun. If a clip gage with a protective casing is used, position the gage so that cryogenic fluid can enter freely to surround the gage's active elements to prevent the entrapment of gas bubbles and the associated clip gage noise.

Next, position the Dewar and precool the apparatus by transferring liquid nitrogen into the cryostat. After boiling subsides and thermal equilibrium is reached, remove all the liquid nitrogen from the cryostat, and transfer liquid helium into the cryostat until the specimen and grips are fully submerged. Testing may begin after the system has reached thermal equilibrium at 4 K. The specimen must remain fully submerged at all times during the test.

NOTE 8—The heat-transfer characteristics of gaseous helium are inferior to those of liquid helium; therefore it is imperative that the specimen remain submerged in liquid helium to minimize the influence of generated heat on the mechanical property measurements.

9.5 *Testing Speed:*

9.5.1 *Rate Control*—Since tensile property measurements in liquid helium are affected by testing speed, the test must include a means of measuring and controlling the rate of crosshead motion. A nominal strain rate must be specified, since the actual rate cannot be precisely controlled or maintained in view of discontinuous yielding. The nominal strain rate is calculated by dividing the crosshead rate by the length of the reduced section. Alternatively, a pacing or indicating device may be used to monitor the strain rate, or an average strain rate may be determined by observing the time required to effect a known increment of strain.

9.5.2 *Rate Limit*—Any convenient crosshead speed may be used to reach an applied stress of one-half the yield strength; after that, the crosshead speed must be chosen so that the nominal strain rate never exceeds 1×10^{-3} s^{-1}. Higher rates may cause excessive specimen heating and therefore are not acceptable for basic mechanical property measurements of materials.

9.5.3 *Rate Selection*—Strain rates ranging from 10^{-5} to 10^{-3} s^{-1} are generally recommended for tension tests at 4 K, but some alloys are moderately sensitive to strain rate variations in this range. Some high strength austenitic steels show mild transitions in tensile properties at strain rates in the range 10^{-4} to 10^{-3} s^{-1}, and other alloys with high ratios of strength to thermal conductivity (perhaps titanium alloys) may show similar trends (15). Consequently, it may be desirable in some tests to use strain rates much lower than the 1×10^{-3} s^{-1} maximum allowed by this Method.

9.5.4 *Rate Change*—It may be desirable to change the strain rate during a test. For example, the strain required to initiate discontinuous yielding typically increases with decreasing strain rate. If the first serration occurs near 0.2% plastic strain, it may be possible to reduce the speed of the test to postpone the first serration, and to prevent interference in the measurement of the yield strength (see Fig. 5). This may be accomplished by first using a relatively low strain rate to determine the yield strength, and then using a higher strain rate to complete the test.

9.6 *Measurement of Mechanical Properties:*

9.6.1 *Force–Extension (Load–Extension) Method*—To measure the yield strength, a record of force versus extension must be obtained up to at least 0.2% plastic strain. The use of a strain measurement device for autographic recording is recommended.

Measure the yield strength by applying the 0.2% offset method, following Methods E 8 or E 8M. If the 0.2% offset line intersects the curve at a decrease in force associated with discontinuous yielding, then the highest stress before that force decrease is reported as the yield strength.

9.6.2 *Force–Time Method*—Yield strength measurements based on a 0.2% offset procedure applied to force-versus-time (or force-versus-crosshead) curves at 4 K are generally not recommended, but may be used for commercial test purposes with the agreement of all parties involved. If this method or some other technique is used, state it clearly in the report.

> NOTE 9—Force–time curves for tests at 4 K are typically nonlinear at the start and less regular than force–extension curves. The effective modulus of a thermally efficient load train may be low and dependent on the liquid helium level. Also the time to achieve a steady state condition may be affected by changes in heat path efficiency through the increase of force upon nesting of pull rod interfaces. As a consequence, yield strength data from force–time curves may be less accurate than those of the recommended method. For this reason, check any calculations using time-based deformation against system stiffness calibrations at the same temperature. In addition, compare the total system deflection with total specimen strain using post-test gage mark extension (with allowance for specimen elastic spring-back, especially if the material is relatively brittle).

9.6.3 *Discontinuous Yielding Stress*—Calculate the stress corresponding to the point of initiation of the first discontinuous-yielding event by dividing the maximum force sustained at the beginning of the first measurable serration by the cross-sectional area of the specimen.

9.6.4 *Tensile Strength*—Calculate the tensile strength by dividing the maximum force sustained by the specimen during the tension test by the original cross-sectional area of the specimen.

9.6.5 *Elongation*—If possible, calculate the percent elongation from the change in gage length according to Methods E 8 or E 8M. Otherwise, calculate the percent elongation from the initial (A_0) and final (A_f) values of the reduced section length: $100 \cdot (A_f - A_0)/A_0$, or from the percent elongation based on the initial (L_0) and final (L_f) values of the overall length, and the initial length (A_0) of reduced section: $100 \cdot (L_f - L_0)/A_0$.

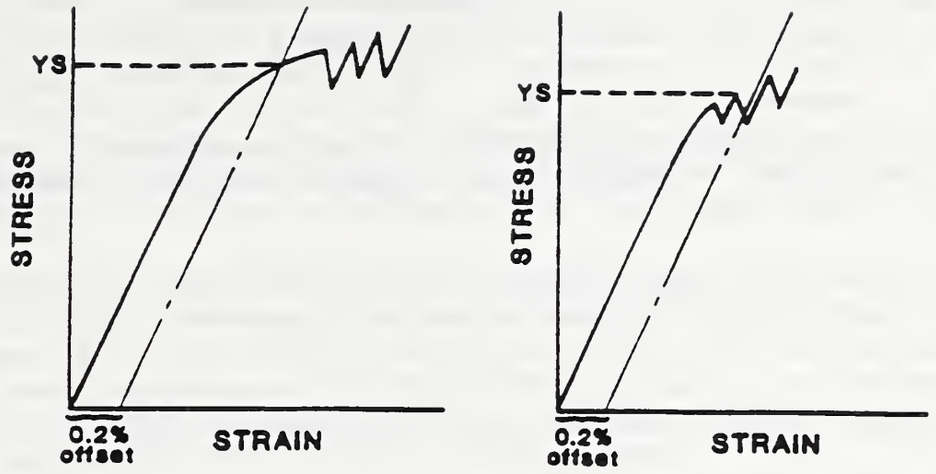

A – Serrations after 0.2% strain B – Serrations before 0.2% strain

FIG. 5 Stress–Strain Diagram for Determination of Yield Strength by the Offset Method

9.6.6 *Reduction of Area*—Calculate the percent reduction of area according to Methods E 8 or E 8M.

9.6.7 *Rounding Reported Test Data*—Round off the calculated numerical test results according to Methods E 8 or E 8M.

9.6.8 *Replacement Specimens*—If necessary, discard any invalid data and test replacement specimens as per Methods E 8 or E 8M.

10. Report

10.1 *General:*

10.1.1 *Material Characterization*—Describe the test material, including manufacturing, processing, and metallurgical information.

10.1.2 *Specimen Characterization*—Describe the specimen location and its orientation relative to the principal working directions or grain flow of the stock. Also report the specimen dimensions, including the cross-section dimensions, the fillet radius, the reduced section length, and the adjusted length of the reduced section (if used).

10.1.3 *Strain Rate*—Report the crosshead speed and nominal strain rate for the entire test. If the rate was changed during the test, report the effective nominal strain rates before and after the rate was changed. If direct strain measurements were made from the fractured specimen, report the calculated rates from these data.

10.1.4 *Mechanical Property Measurements*—Report the yield strength, the tensile strength, the method of offset yield strength measurement, and the method of extension measurement. Report the region of attachment and the span of extensometer(s), if used. Also report the discontinuous yielding stress and the strain rate at which it was measured, the tensile elongation and the method of its calculation, the gage-length-to-diameter ratio for cylindrical specimens, and the reduction of area.

10.2 *Optional Data*—Report any optional data of importance or interest, such as measurements of Young's modulus (requires a Class A or Class B1 extensometer) at 4 K, the average grain size of the test material, or the room temperature mechanical properties, if measured or known. Report the compliance of the test machine including the cryostat.

10.3 *Replicate Tests*—If replicate specimens are tested, report the number of tests, the average values of all mechanical property measurements, and a measure of the scatter of the data.

10.4 *Subsize Specimens*—If subsize specimens are tested, state any precautions taken with respect to specimen machining, surface condition, or alignment, and report the grain size of the test material.

10.5 *Anomalies*—Report any anomalies in material behavior, test records, mode of failure, and type and location of fracture.

11. Precision and Bias

11.1 *Precision*—An overall measure of variability in tensile property measurements covered in this Method is being established by a series of interlaboratory tests.

11.2 *Bias*—There are no accepted standard values for the tensile properties of materials. In the absence of any true value, no meaningful statement can be made concerning the bias of data.

12. Keywords

Keywords for this standard are: adiabatic heating, cryogenic properties (of materials), cryostats, discontinuous yielding, liquid helium, low temperature tests, mechanical properties (of materials), tensile properties, tension test.

REFERENCES

(1) Basinski, Z. S., "The Instability of Plastic Flow of Metals at Very Low Temperatures," *Proceedings of the Royal Society*, Vol. A240, 1957, pp. 229–242.

(2) Ogata, T., Ishikawa, K., and Nagai, K., "Effects of Strain Rate on the Tensile Behavior of Stainless Steels, Copper, and an Aluminum Alloy at Cryogenic Temperatures," *Tetsu-to-Hagane*, Vol. 71, No. 10, 1985, pp. 1390-1397.

(3) Ogata, T. and Ishikawa, K. "Time-dependent Deformation of Austenitic Stainless Steels at Cryogenic Temperatures," *Cryogenics*, Vol. 26, 1986, pp. 365–369.

(4) Reed, R. P., and Walsh, R. P., "Tensile Strain Rate Effects In Liquid Helium", in: *Advances in Cryogenic Engineering*, Vol. 34, Plenum Press, 1988, pp. 199-208.

(5) *Cryogenics Safety Manual*—A Guide to Good Practice, 2nd Ed., Mechanical Engineering Publications, London, 1982.

(6) Schwartzberg, F. R., "Mechanical Property Testing Techniques for the Cryogenic Temperature Range," in: *Advances in Cryogenic Engineering*, Vol. 8, Plenum Press, New York, 1963, pp. 608–623.

(7) Evans, D., Simmonds, G. E., and Stapleton, G. B., "Improved Facility for Determining Mechanical Properties of Materials in Liquid Helium," in: *Proceedings, Fourth International Cryogenic Engineering Conference*, IPC Science and Technology Press, Guildford, Surrey, England, 1972, pp. 331–337.

(8) Hartwig, G. and Wuchner, F., "Low Temperature Mechanical Testing Machine," *Review of Scientific Instruments*, Vol. 46, 1975, pp. 481–485.

(9) Novikov, N. V. "Mechanical Property Measurement Techniques of Structural Materials at Cryogenic Temperatures," in: *Advances in Cryogenic Engineering*, Vol. 22, Plenum Press, New York, 1977, pp. 113–118.

(10) Horiuchi, T., Shimada, M., Fukutsuka, T., and Tokuda, S., "Design and Construction of an Apparatus for Testing Materials at Cryogenic Temperatures," in: *Proceedings, Fifth International Cryogenic Engineering Conference*, IPC Science and Technology Press, Guildford, Surrey, England, 1977, pp. 465–468.

(11) Sparks, L. L., "Temperature, Strain, and Magnetic Field Measurements," in: *Materials at Low Temperatures*, R. P. Reed and A. F. Clark, eds., American Society for Metals, Metals Park, Ohio, 1983.

(12) Telinde, T. C., "Strain Gages in Cryogenic Environments," *Experimental Mechanics*, Vol. 10, No. 9, 1970, pp. 394-400.

(13) Greenough, R. D., and Underhill, C., "Strain Gauges for the Measurement of Magnetostriction in the Range 4 K to 300 K," *Journal of Physics E*, Vol. 9, 1976, pp. 451-454.

(14) Freynik, H. S., Jr., Roach, D. R., Deis, D. W., and Hirzel, D. G., "Evaluation of Metal-Foil Strain Gages for Cryogenic Applications in Magnetic Fields," in: *Advances in Cryogenic Engineering*, Vol. 24, Plenum Press, New York, 1978, pp. 473-479.

(15) Reed, R.P., Walsh, R.P., and Tobler, R.L., "Strain-Rate Effects on Tensile Properties at 4K of a VAMAS Round Robin Austenitic Steel," in: *Advances in Cryogenic Engineering*, Vol. 36, Plenum Press, New York, to be published.

Designation: E 23 – 88

Standard Test Methods for Notched Bar Impact Testing of Metallic Materials[1]

This standard is issued under the fixed designation E 23; the number immediately following the designation indicates the year of original adoption or, in the case of revision, the year of last revision. A number in parentheses indicates the year of last reapproval. A superscript epsilon (ε) indicates an editorial change since the last revision or reapproval.

This standard has been approved for use by agencies of the Department of Defense to replace method 221.1 of Federal Test Method Standard No. 151b. Consult the DoD Index of Specifications and Standards for the specific year of issue which has been adopted by the Department of Defense.

1. Scope

1.1 These test methods describe notched-bar impact testing of metallic materials by the Charpy (simple-beam) apparatus and the Izod (cantilever-beam) apparatus. They give: (*a*) a description of apparatus, (*b*) requirements for inspection and calibration, (*c*) safety precautions, (*d*) sampling, (*e*) dimensions and preparation of specimens, (*f*) testing procedures, (*g*) precision and bias, and (*h*) appended notes on the significance of notched-bar impact testing. These test methods will in most cases also apply to tests on unnotched specimens.

1.2 The values stated in SI units are to be regarded as the standard. Inch-pound units are provided for information only.

1.3 *This standard may involve hazardous materials, operations, and equipment. This standard does not purport to address all of the safety problems associated with its use. It is the responsibility of the user of this standard to establish appropriate safety and health practices and determine the applicability of regulatory limitations prior to use.*

1.2 These methods pertain to tests at temperatures as low as the boiling point of liquid nitrogen and higher. The boiling point of liquid nitrogen is -196 C (-321 F) at sea level and is slightly lower at higher elevations. Tests below liquid nitrogen temperature are more complicated and are not covered in this standard.

1.3

1.4

2. Summary of Test Methods

2.1 The essential features of an impact test are: (*a*) a suitable specimen (specimens of several different types are recognized), (*b*) an anvil or support on which the test specimen is placed to receive the blow of the moving mass, (*c*) a moving mass of known kinetic energy which must be great enough to break the test specimen placed in its path, and (*d*) a device for measuring the energy absorbed by the broken specimen.

3. Significance and Use

3.1 These test methods of impact testing relate specifically to the behavior of metal when subjected to a single application of a load resulting in multiaxial stresses associated with a notch, coupled with high rates of loading and in some cases with high or low temperatures. For some materials and temperatures, impact tests on notched specimens have been found to predict the likelihood of brittle fracture better than tension tests or other tests used in material specifications. Further information on significance appears in Appendix X1.

For other material-temperature regimes impact tests of notched specimens may have less significance.

from its cooling (or heating) medium, if used, and positioned on the specimen supports; the pendulum is released without vibration, and the specimen is broken within 5 s after removal from the medium. Information is obtained from the machine and from the broken specimen. The details are described as follows:

11.2.1 *Temperature of Testing*—In most materials, impact values vary with temperature. Unless otherwise specified, tests shall be made at 15 to 32°C (60 to 90°F). Accuracy of results when testing at other temperatures requires the following procedure: For liquid cooling or heating fill a suitable container, which has a grid raised at least 25 mm (1 in.) from the bottom, with liquid so that the specimen when immersed will be covered with at least 25 mm (1 in.) of the liquid. Bring the liquid to the desired temperature by any convenient method. The device used to measure the temperature of the bath should be placed in the center of a group of the specimens. Verify all temperature-measuring equipment at least twice annually. When using a liquid medium, hold the specimens in an agitated bath at the desired temperature within ±1°C (±2°F) for at least 5 min. When using a gas medium, position the specimens so that the gas circulates around them and hold the gas at the desired temperature within ±1°C (±2°F) for at least 30 min. Leave the mechanism used to remove the specimen from the medium in the medium except when handling the specimens.

NOTE 8—Temperatures up to +260°C (+500°F) may be obtained with certain oils, but "flash-point" temperatures must be carefully observed.

Tests at elevated temperatures or low temperatures down to liquid nitrogen temperature may also be performed according to this standard.

APPENDIX

(Nonmandatory Information)

X1. NOTES ON SIGNIFICANCE OF NOTCHED-BAR IMPACT TESTING

X1.1 Notch Behavior

X1.1.1 The Charpy V-notch (CVN) impact test has been extensively in mechanical testing of steel products, in ...ch, and in procurement specifications for over three ...des. Where correlations with fracture mechanics param... are available, it is possible to specify CVN toughness ... that would ensure elastic-plastic or plastic behavior ...acture of fatigue cracked specimens subjected to minimum operating temperatures and maximum in service rates of loading.

X1.1.2 The notch behavior of the face-centered cubic metals and alloys, a large group of nonferrous materials and the austenitic steels can be judged from their common tensile properties. If they are brittle in tension they will be brittle when notched, while if they are ductile in tension they will be ductile when notched, except for unusually sharp or deep notches (much more severe than the standard Charpy or Izod specimens). Even low temperatures do not alter this characteristic of these materials. In contrast, the behavior of the ferritic steels under notch conditions cannot be predicted from their properties as revealed by the tension test. For the study of these materials the Charpy and Izod type tests are accordingly very useful. Some metals that display normal ductility in the tension test may nevertheless break in brittle fashion when tested or when used in the notched condition. Notched conditions include restraints to deformation in directions perpendicular to the major stress, or multiaxial stresses, and stress concentrations. It is in this field that the Charpy and Izod tests prove useful for determining the susceptibility of a steel to notch-brittle behavior though they cannot be directly used to appraise the serviceability of a structure.

211

Exceptions are known for some of the face-centered cubic metals and alloys at extreme cryogenic temperatures, and

some chosen notch will in most instances place the methods in their proper order.

X1.4 Temperature Effect

X1.4.1 The testing conditions also affect the notch behavior. So pronounced is the effect of temperature on the behavior of steel when notched that comparisons are frequently made by examining specimen fractures and by plotting energy value and fracture appearance versus temperature from tests of notched bars at a series of temperatures. When the test temperature has been carried low enough to start cleavage fracture, there may be an extremely sharp drop in impact value or there may be a relatively gradual falling off toward the lower temperatures. This drop in energy value starts when a specimen begins to exhibit some crystalline appearance in the fracture. The transition temperature at which this embrittling effect takes place varies considerably with the size of the part or test specimen and with the notch geometry.

ferritic

Add a new section X1.4.2:

"Section 1.2 restricts the test temperature to no lower than the boiling point of liquid nitrogen. For conventional tests at this temperature and higher, temperature is simply a parameter which affects the material performance. At more extreme cryogenic temperatures, the test temperature affects the test dynamics as well as the material performance. For example, at liquid hydrogen temperature, −253 °C (−423°F), or liquid helium temperature, −269°C (−452°F), tests cannot be performed using the procedure outlined in section 11. Metals at these temperatures have very low specific heats, and any surface condensation of gases, conductive or convective heat transfer, or plastic deformation quickly produces an extraordinary specimen temperature rise. As a result, (1) specimens cannot be transferred from the coolant through air to the anvil in the routine way, and (2) fracture at impact strain rates creates problems of adiabatic heating and temperature control. Various nonstandard methods for Charpy impact testing below liquid nitrogen temperature are described in the literature. They incorporate insulating devices and modified calibration procedures. Initial test temperature as low as −269 °C (−452 °F) may be achieved using some of those techniques, but extreme adiabatic heating on impact is unavoidable and complicates the data interpretation. At present there is no standard method for impact tests below liquid nitrogen temperature, and consensus has not yet been reached on the meaning or usefulness of impact data obtained at such extreme cryogenic temperatures."

U.S.—JAPAN COOPERATIVE PROGRAM COMMITTEE ON TEST METHODOLOGY
FIRST DRAFT
DECEMBER 1989

NOTE: This is a working document being developed by ASTM subcommittee E 24.08; it is intended for committee review, but not for general distribution at this time.

A3. TEST PROCEDURES FOR AUSTENITIC ALLOYS IN LIQUID HELIUM AT 4 K

A3.1 Scope

A3.1.1 This annex describes the equipment, procedures, and data analysis used for J_{Ic} tests of austenitic alloys in liquid helium. Ductile fracture at this temperature involves fast, unstable crack growth. The procedures set forth in the body of the Standard Method are modified in this annex to address the specific needs and concerns of cryogenic testing.

NOTE 1—The boiling point of normal liquid helium (He I) at sea level is 4.2 K (−452.1°F or 7.6°R). It decreases slightly with geographic elevation and is 4.0 K (−452.5°F or 7.2°R) at the National Institute of Standards and Technology in Colorado, 1677 m (5500 ft) above sea level. In this standard the test temperature is designated 4 K.

A3.1.2 For alloys in liquid helium, J_{Ic} is determined from a pseudo-resistance curve plot of J versus Δa_p. A fatigue-cracked specimen is cooled in a cryostat to 4 K and tensile force is slowly applied while it is fully submerged in normal liquid helium (He I). The recommended specimen is a pin-loaded compact specimen, 25.4 mm (1 in) thick and 50.8 mm (2 in) wide. The pseudo-resistance-curve slope, $\Delta J/\Delta a_p$, and the material's apparent tearing modulus lack their customary significance at this temperature, and are not measured.

A3.2 Definitions

In addition to the information in Section 3, the following definitions apply:

A3.2.1 *fracture cryostat*—an apparatus consisting of a reaction frame and Dewar for testing specimens in cryogenic environments. A schematic illustration is shown in Fig. A3.1.

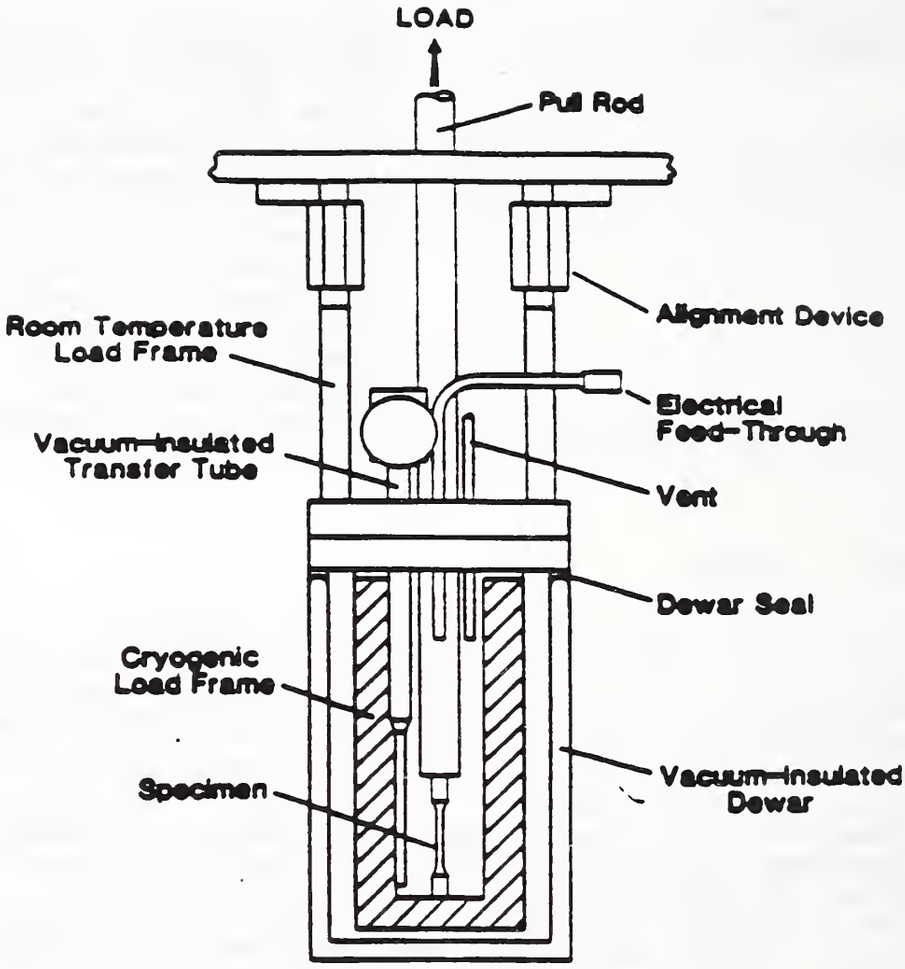

Figure A3.1. Fracture cryostat for tests in liquid helium.

A3.2.2 *Dewar*—a vacuum-insulated container for cryogenic fluids.

A3.2.3 *adiabatic heating*—the internal heating of a specimen caused b testing under conditions such that the heat generated by plastic work cannot be quickly dissipated from the specimen to the cryogen.

A3.3 Summary of Method

A3.3.1 The object is to estimate the critical value of J near the initiation of crack growth for austenitic alloys in liquid helium, despite the occurrence of mechanical and thermal instabilities during the crack growth stage.

A3.3.2 To measure J_{Ic} according to this annex, a fatigue-cracked specimen is cooled to 4 K in a cryostat containing liquid helium. Using crosshead, actuator, or clip-gage displacement control, the specimen is slowly loaded while the load versus load-line displacement curve is autographically recorded and a plot of J versus Δa is prepared. Data interpretation and reduction are identical to that specified in the body of this standard, except that the blunting line approximation for austenitic alloys at 4 K is $J = 4\sigma_Y \Delta a$ rather than $J = 2\sigma_Y \Delta a$.

A3.3.3 The compact specimen is preferred for tests in liquid helium because it offers a large fracture-toughness-measurement capacity for its size. A relatively low force applied to this specimen produces a large stress intensity factor; this enables the mass of the cryostat, grips, and load train to be minimized, lowering the liquid helium consumption and cost per test.

A.3.3.4. The single-specimen unloading-compliance procedure (1–3) is preferred for this environment because, compared to the multiple-specimen technique, it reduces the required number of specimens, conserves helium, and lowers the cost of measurements.

A3.4 Significance and Use

A3.4.1 Austenitic alloys undergo a change in ductile fracture behavior at extreme cryogenic temperatures. The mechanism at room temperature is slow stable tearing, whereas the mechanism at liquid helium temperature consists of unstable plastic deformation (discontinuous flow) events with incremental crack extensions. Typically, the load versus displacement record in liquid helium is composed of continuous and discontinuous deformation stages, as shown in Fig. A3.2. At first the deformation is stable with smoothly rising loads. As testing continues, alternating periods of stable and unstable loading form a series of serrations on the load versus displacement curves. At each serration, plastic deformation and tearing occurs abruptly at fast, uncontrolled rates, and load reduction ensues until the instability is arrested. The serrations are faint at first but steadily increase in magnitude. The frequency of serrations and the magnitude of load reductions is influenced by material and test variables among which are specimen size, machine stiffness, control mode, and testing rate.

A3.4.2 A constant specimen temperature cannot be maintained at all times during tests in liquid helium. Due to adiabatic heating, the temperature in the plastic zone near the crack tip rises above 4 K whenever the rate of plastic work exceeds the cooling capacity of the cryogen. Heating during continuous stable loading can be prevented by testing at a slow rate but heating during periods of mechanical instability is inevitable (4). At slow test speeds, the temperature increase during each instability is transient and quickly falls back to normal when the instability is arrested. Typically, altering the test variables can modify but not eliminate the mechanical instabilities and associated thermal spikes.

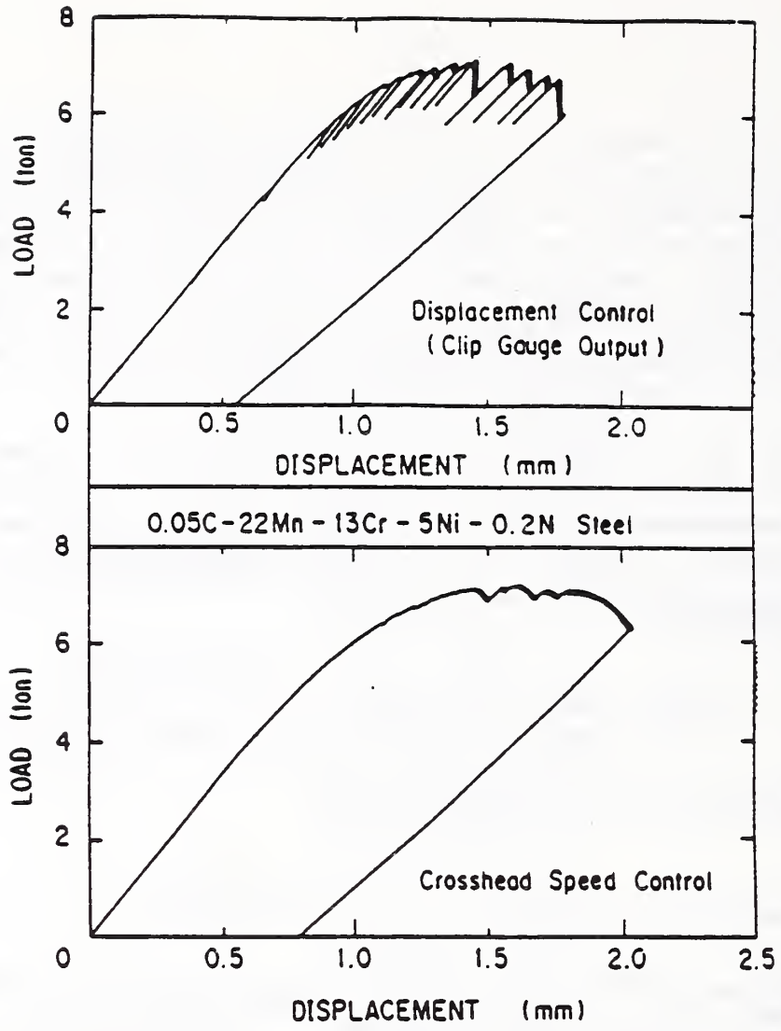

Figure A3.2. Typical loading behavior at 4 K, showing serrations.

A3.4.3 In principle, the J-integral applies to metals only if they fracture by slow-stable ductile tearing. Therefore justification for the us of J_{Ic} as a fracture parameter at 4 K rests primarily on the basis of experimental results. Interlaboratory data for Fe-22Mn-13Cr-5Ni steel show acceptable agreement of J_{Ic} measurements (5), and intralaboratory data available for three alloys show little or no variation of J_{Ic} with size for specimens 12.5 mm (0.5 in) thick or more (6,7). The available data indicat that J_{Ic} retains its usefulness as an estimate of fracture toughness near t onset of ductile fracture in liquid helium, despite discontinuous yielding events and temporary specimen heating.

A3.4.4 By definition, a J-R curve is a plot of resistance to stable crack extension. The J-versus-Δa_p plots at 4 K are pseudo-resistance curve since unstable tearing is involved. The J-versus-Δa_p plots at 4 K are used to estimate J_{Ic} by extrapolation, but they lack the physical significance o resistance curves at ambient temperatures where deformation is more nearly isothermal and crack growth occurs by slow-stable tearing.

A3.4.5 The parameter J_{Ic}, as operationally defined in this Annex, is intended primarily for material characterization and may not be directly applicable to structural designs. Ductile fracture in liquid helium may be significantly affected by high loading rates, and by the mode of machine control during testing. Slow loading rates using crosshead, displacement, clip-gage control are specified in this standard for conventional material characterization. The effects of severe adiabatic heating at high loading

rates must be considered if impact loading is anticipated in service. Also, the possibility and adverse consequences of unarrested ductile tearing must be anticipated in the design of structures subjected to load control at 4 K.

A3.5 Hazards

Several precautions must be observed when handling cryogenic fluids and equipment. Skin or eye contact with cryogens will freeze and destroy tissue (frostbite). The appropriate protection may include goggles, clothing without pockets or cuffs, gloves, and tongs for handling cold specimens. Cryogenic containers that are internally pressurized or evacuated are potentially hazardous in that damage or leaks can produce explosions or implosions. Also, there is a huge volume expansion when cryogenic liquids evaporate; therefore asphyxiation is a potential threat if liquid nitrogen or liquid helium leaks, spills, or is discarded into rooms that are not properly ventilated. Safety information pertaining to cryogens is available elsewhere (8). It is the user's responsibility to learn and implement the appropriate safety practices.

A3.6 Apparatus

A3.6.1 *Test Machines*—Use a servohydraulic or screw-driven tension test machine that meets the requirements of Practices E 4 regarding the verification of force accuracy. The equipment must include a means to autographically record the applied forces and specimen displacements. Since the compliance of the test machine influences its response to mechanical instabilities, it is recommended that the compliance of the test machine and cryostat at 4 K be measured by replacing the specimen with a rigid block, or by linking the upper and lower grips without a specimen. The compliance can then be measured from a plot of force versus crosshead or actuator displacement up to the highest force used to qualify the machine.

A3.6.2 *Cryogenic System Design*—Since most conventional test machines have a maximum force of 10 tons (22 480 lbf), it is recommended that the apparatus be designed to accommodate a standard, 25.4 mm (1 in) thick compact specimen (see Section 8.1.3). A servohydraulic test machine with an inverted stage (actuator mounted above the test chamber) and a reaction frame that is free at the lower end is recommended. These features are desirable for operating convenience and cost effectiveness for testing at 4 K (9).

A3.6.3 *Cryogenic Construction Materials*—Many structural materials, including the vast majority of ferritic steels, are brittle at 4 K. Therefore cryostats must be well designed and fabricated using cryogenic materials of adequate strength and toughness. Materials that have low thermal conductivity are favored to reduce heat conduction. Austenitic stainless steels are widely used, especially those strengthened by the addition of 0.05 to 0.4 weight percent nitrogen. Maraging steels plated with nickel to prevent rusting have been used for specimen clevises. High purity alpha-titanium alloys are especially appropriate for some applications requiring high strength-to-thermal conductivity ratios, such as pull rods.

Nonmetallic materials (for example, fiber-reinforced composites) are excellent insulators and have been used for compression members in some cryostats.

A3.6.4 *Cryostats and Support Apparatus*:

A3.6.4.1 *Cryostats*—A cryostat capable of retaining liquid helium for the duration of testing is required. Cryostats are usually custom-built, but they may be designed to accommodate commercially available Dewars. Efficient designs consider thermal and mechanical trade-offs (9). Several designs are possible, including turret-disc devices for sequential testing of several specimens with a single cooling (3,7,9–11).

A3.6.4.2 *Dewars*—Stainless steel Dewars are recommended for low maintenance, durability, and safety. Glass Dewars are fragile and hazardous if broken, whereas fiberglass Dewars are relatively expensive and may require maintenance. A single Dewar is sufficient for tests of short duration. The alternative is a double-Dewar arrangement using an outer Dewar containing liquid nitrogen to surround the helium Dewar for greater thermal efficiency.

A3.6.4.3 *Ancillary Equipment*—Dewars and transfer lines for handling liquid helium must be vacuum insulated. Pressurized gases, vacuum pumps, and liquid nitrogen apparatus are therefore necessary. After testing, the helium may be recycled as a gas or liquid, or it may be discarded to the atmosphere. Recycling as gas or reliquefaction requires a substantial investment in purification and cryogenic systems.

A3.6.5 *Grips and Pins*—Conventional grips conforming to the design in Fig. A2.2 may be used, but alloys with adequate 4-K mechanical properties are required for construction. Pins and grips require adequate 4-K strength, fracture toughness, and fatigue resistance. Pins should be manufactured from high-strength materials to resist bending. Maraging steels can be used for grips of the conventional design. Lower strength materials such as AISI 304LN may be satisfactory for grips if the clevis arm thickness is enlarged.

A3.6.6 *Extensometer*:

A3.6.6.1 *Requirements*—In addition to rendering accurate displacement measurements at 4 K, cryogenic extensometers must sustain thermal shock and moisture condensation associated with thermal cycling between room and liquid helium temperature. Conventional clip gages that operate in liquid helium may be purchased or built using cryogenic materials and fabrication techniques. Ring-shaped clip gages were originally designed for cryogenic tests, and they offer some practical advantages for tests in liquid helium (12).

A3.6.6.2 *Construction*—Select a satisfactory combination of active strain gage elements, backing materials, and bonding agents for cryogenic extensometers. One common choice is a Ni–Cr-alloy gage with a temperature-compensated active element. Typically, four 350-Ω gages are wired in a full Wheatstone bridge. Leadwires covered with polytetrafluoroethylene insulation and soft solders having low tin contents are recommended to resist mechanical

failures and electrical shorts induced by thermal cycling between room temperature and 4 K.

A3.6.6.3 *Calibration*—Calibrate the clip gage or other displacement measuring device at room temperature and in liquid helium. This may be done with a barrel-micrometer fitted with vertical extension tubes, with the gage mounted at the lower end and immersed in liquid helium for calibration at 4 K (12). Once the calibration is known and proven linear, accurate, and reproducible, then room-temperature checks will suffice to verify the 4-K calibration indirectly. Nevertheless, the calibration should be repeated periodically at 4 K, especially when damage is suspected or repair is performed.

A3.6.6.4 *Temperature Maintenance and Liquid-Level Indicators*—The intended cryogenic bath temperature of 4 K is maintained by the fixed boiling point of liquid helium. It is therefore unnecessary to monitor the specimen temperature directly. Instead, a suitable meter or indicator is required to ensure the proper liquid level. Use an on–off carbon-resistor meter, a continuous-level meter with superconducting wires, or a thermocouple (Chromel versus gold + 0.07% iron which offers maximum sensitivity at temperatures near absolute zero). Position the indicator in the cryostat above the specimen and monitor the liquid level to ensure that the specimen remains submerged throughout the test.

A3.7 Sampling

Remove samples for specimen preparation from the material in its final metallurgical condition. Perform any heat treatments before sampling and specimen machining. Choose the sample location to be representative of the stock material, realizing that samples from one portion of the stock may not be representative of the whole, and allow for areas affected by the cutting process. The usual two-letter specimen orientation code of Methods E 399-83 Section 5.1.3 applies.

A3.8 Specimens

A3.8.1 *Specimen Configuration:*

A3.8.1.1 *Specimen Types*—Various specimen configurations might be used, but the compact specimen offers strong advantages and is preferable to other specimens for routine tests in liquid helium. Bend specimens, for example, require greater mass for an equivalent ligament size, and the long span of the bend specimen transverse to the load axis requires fixtures that are inconvenient for some cryostats.

A3.8.1.2 *Standard 4-K Test Specimen*—A standard compact specimen geometry and size is specified for material evaluations at 4 K. The standard specimen has a thickness, B, of 25.4 mm (1.0 in) and a width, W, of 50.8 mm (2.0 in). The W/B ratio is 2.0, the planar dimensions are proportional to W, and the starter notch is according to the guidelines of Section 7.3. This

specimen is large enough to satisfy the size requirements for most austenitic alloys tested at 4 K.

A3.8.1.3 *Alternative Specimens*—If the standard specimen geometry or size is not practical for any reason, select an alternative. Factors toconsider are: the technical purpose, the load limit of the test machine, the stock dimensions, and the need for representative samples of the test material.

A3.8.2 *Fatigue-Precracking*:

Fatigue-precracking should normally be conducted with the specimen in liquid helium or liquid nitrogen. However, some test materials may be precracked in air at room temperature if it can be demonstrated that room temperature precracking does not affect the toughness subsequently measured at 4 K. For the precracking to be valid, the criteria of Section 7.6 must be satisfied for the temperature selected. If precracking is performed at liquid helium temperature, use 4-K values of σ_Y in 7.6.1 and E in 7.6.2. If precracking is performed in liquid nitrogen or at room temperature, use the appropriate σ_Y and E values for these temperatures.

NOTE 2—The purpose of precracking at liquid nitrogen or room temperature is to conserve liquid helium. The boiling point of nitrogen at sea level is 77 K (−321°F, or 138.7°R). For most alloys, precracking at this temperature is virtually equivalent to precracking in liquid helium, and it is convenient since 4-K test specimens are routinely precooled in liquid nitrogen anyway. On the other hand, precracking at room temperature toughens some (not all) alloys at 4 K. Therefore the precracking of 4-K test specimens at room temperature is acceptable only if it can be demonstrated for the specific alloy being tested that the J_{Ic} value at 4 K is not affected.

A3.8.3 *Side Grooves*—Side grooves might hinder or enhance valid measurements at 4 K, and their use is an option to be considered case by case. At room temperature, side grooves are sometimes employed to alleviate fatigue crack-front curvature and crack-front tunneling, or to improve the agreement between the optically measured and compliance-calculated end-of-test Δa values. Side grooves may serve the same purpose at liquid helium temperature; however, side grooves can lower the J_{Ic} measurements for some materials, and they always promote larger serrations at 4 K. The latter effect can be conducive to invalid results for some materials by making it more difficult to satisfy the Δa_p distribution requirements.

A3.9 General Procedures

A3.9.1 *Specimen Installation*—Install the specimen in the cryostat, leaving sufficient slack for the instrumentation wires so that they will be

neither stretched nor crimped during positioning of the Dewar and subsequent testing. Before cooling, check the seating of the specimen and grips at room temperature. The specimen may be preloaded slightly for this purpose.

A3.9.2 *Cooling*—Ice that forms within the cryostat during cool-down can block cryogenic transfer lines or cause erratic loading behavior. Prevent icing by thoroughly drying the clip gage, specimen, grips, loading pins, and load train members thoroughly before cool-down with a pressurized air jet or heating gun. Also, purge any condensate from the transfer lines. Position the Dewar and precool the apparatus by transferring liquid nitrogen into the cryostat. After the specimen reaches thermal equilibrium, remove all of the liquid nitrogen and add liquid helium to the cryostat. Add extra liquid helium to compensate for evaporation that will occur during the time required to complete the test. Before testing, hold each specimen of standard size in the liquid helium bath for a minimum of 15 min.

NOTE 3—The heat-transfer characteristics of gaseous helium are inferior to those of liquid helium; therefore full submersion in the liquid is required to minimize specimen heating from plastic work during the test.

A3.9.3 *Loading*:

A3.9.3.1 *Control Mode*—Load the specimen using crosshead, actuator, or clip-gage control. The mode of control determines the machine's response during instabilities and influences the frequency and shape of serrations formed on the force–displacement records.

NOTE 4—For screw-driven machines where crosshead speed is controlled, and for servohydraulic machines where actuator position is controlled, the clip gage opens as the load drops with each serration. For servohydraulic machines in clip gage displacement control, the gage displacement is maintained constant by the machine as the load drops with each serration. Clip gage displacement control arrests the instability events sooner than crosshead or actuator control. Thus clip gage control produces smaller, more numerous serrations which benefits some tests by affording more opportunities to locate J–Δa_p data in the exclusion interval.

A3.9.3.2 *Testing Rate*—Tests in liquid helium must be performed slowly to minimize specimen heating. Load the specimen at a rate such that the time to reach the load $0.4P_L$ is between 1 and 10 min. Higher rates may cause excessive heating and obscure the material property characterization.

NOTE 5—The testing rate should be slow enough to prevent a temperature rise of more than 1 kelvin during the initial period of smoothly rising loads; it should

also be slow enough to allow the specimen temperature to return to 4 K after the arrest of each instability. Heating is unlikely to present a practical problem in single specimen tests that are periodically interrupted for unloading compliance measurements. Of greater potential concern are multiple specimen tests where specimens are loaded without interruption to significant plastic displacements. The heating that occurs in those tests is a function of material and test variables; it increases with testing rate, specimen ligament size, and the plastic component of J associated with fracture, J_p, and is favored by the low specific heats and thermal properties of materials at extreme cryogenic temperatures. Few quantitative measurements of specimen temperature rise have been made, but observations for AISI 310 S steel (J_{Ic} = 333 kJ/m^2, or 1900 in·lb·in^{-2}) may be taken for a guideline: for a standard specimen (B = 25.4 mm, W = 50.8 mm, and a/W = 0.7) tested in liquid helium, the internal heating during the initial continuous loading and the periods of stable loading between serrations is virtually eliminated using crosshead speeds of 0.2 mm/min (0.008 in/min) or less.

A3.9.4 *Data Collection*—During periods of instability it is impossible to predict or control the extent of incremental crack growth. Opportunities for unloading and Δa_p determination exist only during the intervals of stable loading. Thus, the number and size of serrations influences the J–Δa_p data distribution that can be obtained in the exclusion interval, and there is no guarrantee that the data distribution requirements of Section 9.2.2 can be satisfied for a given alloy and specimen size.

NOTE 6—Large serrations are problemmatic for some material–test conditions. In some cases, if it is difficult to obtain the required number or spacing of J–Δa_p points, it may be possible to meet the requirements of Section 9.2.2 by: (1) lowering the machine compliance by stiffening the load train, (2) switching to a smaller or thinner specimen, (3) switching from side-grooved to ungrooved specimens, or (4) switching from crosshead to clip-gage displacement control.

A3.9.4.1 *Single Specimen Tests*—Unloadings for Δa_p determination may be chosen randomly or at regular intervals at the experimenter's discretion. Unloadings performed just before load point discontinuities tend to produce J–Δa_p pairs at the upper bound of pseudo-resistance curve scatter, whereas those at arrest points just after load point discontinuities tend to produce J–Δa_p pairs at the lower bound of scatter. This effect becomes significant if the serrations are very pronounced. In that case, the following approach might be used to reduce the data scatter: during the initial stage of testing, while the load is smoothly rising, unloadings might be performed anytime; once serrations begin, the apparent scatter of J–Δa_p might be

reduced by performing the unloadings preferentially at the natural arrest points after serrations.

A3.9.4.2 *Multiple Specimen Tests*—Similarly, in multiple specimen tests, the scatter of $J-\Delta a_p$ plots might be reduced if each specimen loaded into the regime where serrations are formed is unloaded at a natural arrest point just after a serration.

A3.10 Interpretation and Calculation of Results

A3.10.1 Calculate the area under the load-versus-displacement curve, including any area increase associated with serrations.

> NOTE 7—For tests in clip-gage displacement control, the area does not increase during the period of discontinuous flow. Tests in crosshead displacement control give higher values of J for a given crack extension, owing to the fact that the area does increase with serrations. In either case, the data are acceptable: the intent is not to determine a physically meaningful J–Δap curve, but merely to obtain a systematic data distribution permitting extrapolation to J_{Ic}.

A3.10.2 Construct the blunting line (assuming $J = 4\sigma_Y\Delta a$). Then plot the regression line, and qualify the $J-\Delta a_p$ calculations following Section 9.2.

A3.11 Report

A3.11.1 *Material Characterization*—Describe the material tested and report its yield strength, tensile strength, and Young's elastic modulus at room temperature and at 4 K. Supplementary information would include a desription of the material product form, processing, heat treatment, and any other relevant metallurgical information.

A3.11.2 *Fracture Toughness Measurements*—Report each J_{Ic} determination in units of kJ/m^2 ($in\cdot lb\cdot in^{-2}$) and assess the validity according to Section 9.2. State the number of replicate tests performed, the individual and average J_{Ic} values, and a measure of scatter.

A3.11.3 *Specimen Characterization*—Report the crack-plane orientation and the specimen dimensions, including thickness B, width W, and initial ligament size b_0. For side-grooved specimens, report B_N and any other supplemental information about the side-groove geometry.

A3.11.4 *Fatigue-Precracking Conditions*—Report the temperature of fatigue-precracking, the maximum fatigue load, and the maximum stress intensity factor or the stress intensity factor range. Supplemental information would include the final fatigue crack length obtained using the nine point average, the measured surface crack lengths, and the maximum deviation of any single measurement from the average.

A3.11.5 *Test Conditions*—Report the testing rate in mm/min (in/mm) and specify whether crosshead, actuator, or clip-gage opening displacement was controlled. Supplementary information may include the compliance of the test apparatus.

A3.11.6 *Fracture Surface Appearance and Anomalies*—Describe the fracture-surface appearance and report any anomalies in material behavior, test records, or failure mechanisms.

A3.12 *Accuracy and Precision*

A3.12.1 *Accuracy*—There is no accepted standard fracture toughness value for any material. In the absence of such a true value, any statements about accuracy are meaningless.

A3.12.2 *Precision*—Information on the precision of 4-K fracture tests is being obtained from interlaboratory test programs currently in progress.

A3.13 Keywords

Keywords for this annex are: adiabatic heating, cryogenic properties (of materials), cryogenic tests, fracture toughness, liquid helium, and low temperature tests.

REFERENCES

(1) Tobler, R. L., "Ductile Fracture with Serrations in AISI 310S Stainless Steel at Liquid Helium Temperature," in: *Elastic–Plastic Fracture: Second Symposium*, Vol. II—Fracture Resistance Curves and Engineering Applications, ASTM STP 803, C. F. Shih and J. P. Gudas, eds., American Society for Testing and Materials, Philadelphia, 1983, pp. 763–776.

(2) Shimamoto, S., Nakajima, H., Yoshida, K., and Tada, E., "Requirements for Cryogenic Structural Alloys for Superconducting Magnet Cases," in: *Advances in Cryogenic Engineering—Materials*, Vol. 32, Plenum Press, New York, 1986, pp. 23–32.

(3) Shimada, M., Ogawa, R., Moriyama, T., and Horiuchi, T., "Development of a Cryogenic Fracture Toughness Test System," *Cryogenic Technology*, Vol. 21, No. 5, 1986, pp. 269–274.

(4) Tobler, R. L., Shoji, T., Takahashi, H., and Ohnishi, K., "Fracture, Acoustic Emission, and Adiabatic Heating of Austenitic Stainless Steels at Liquid Helium Temperature," in: *Progress in Acoustic Emission III*, The Japanese Society of NDI, Tokyo, 1986, pp. 453-461.

(5) Nakajima, H., Yoshida, K., Shimamoto, S., Tobler, R. L., Purtscher, P. T., and Reed, R. P., "Round Robin Tensile and Fracture Test Results for an Fe–22Mn–13Cr–5Ni Austenitic Stainless Steel at 4 K," in: *Advances in Cryogenic Engineering—Materials*, Vol. 34, Plenum Press, New York, 1988, pp. 241–249.

(6) Shimada, M., Tobler, R. L., Shoji, T., and Takahashi, H., "Size, Side-Grooving, and Precracking Effects on J_{Ic} Data for an SUS 304 Stainless Steel at 4 K," in: *Advances in Cryogenic Engineering—Materials*, Vol. 34, Plenum Press, New York, 1988, pp. 251–258.

(7) Yoshida, K., Nakajima, H., Oshikiri, M., Tobler, R. L., Shimamoto, S., Miura, R., and Ishizaka, J., "Mechanical Tests of Large Specimens at 4 K: Facilities and Results," in: *Advances in Cryogenic Engineering—Materials*, Vol. 34, Plenum Press, New York, 1988, pp. 225–232.

(8) *Cryogenics Safety Manual—A Guide to Good Practice*, 2nd Ed., Mechanical Engineering Publications, London, 1982.

(9) Fowlkes, C. F. and Tobler, R. L., "Fracture Testing and Results for a Ti–6Al–4V Alloy at Liquid Helium Temperature," *Engineering Fracture Mechanics*, Vol. 8, 1976, pp. 487–500.

(10) Read, D. T. and Tobler, R. L., "Mechanical Property Measurements at Low Temperatures," in: *Advances in Cryogenic Engineering—Materials*, Vol. 28, Plenum Press, New York, 1982, pp. 17–28.

(11) Juhas, M. C., Duncan, D. B., and Streit, R. D., "Development of a Facility for Fatigue and Fracture Testing of Stainless Steels at Liquid Helium Temperature," *Cryogenics*, Vol. 23, 1983, pp. 603-607.

(12) Tobler, R. L. and Shepic, J. A., "Design and Performance of a Ring-shaped Clip Gage for Fracture Mechanics Testing," *Journal of Testing and Evaluation*, Vol. 13, 1985, pp. 299–302.

TECHNOLOGY TRANSFER

TECHNOLOGY TRANSFER PROGRAM

LEADER: N.J. Simon
CONTRIBUTORS: E.S. Drexler, R.P. Reed

OBJECTIVES:

- Organization of and participation in workshops to promote interaction between designers and material specialists, to discuss issues related to low-temperature material needs of the fusion energy program, and to present new low-temperature data for structural alloys, composites, and weldments.
- Preparation of an annual report to the Office of Fusion Energy, U.S. Department of Energy.
- Evaluation of low-temperature mechanical and physical properties of insulator, conductor, and structural materials for cryogenic copper and superconducting magnets; preparation of handbook pages and supporting documentation; distribution of handbook pages to participants in the fusion energy program and to the Materials Handbook for Fusion Energy Systems.

RESEARCH HIGHLIGHTS:

- The Twelfth Annual Cryogenic Structural Materials Workshop was organized; it was held October 11-12, 1989 in Vail, Colorado.

- "Materials Studies for Magnetic Fusion Energy Applications — XII," (NISTIR 89-3931, 277 pages, 1989, editors R.P. Reed and R.L. Tobler) was prepared, published, and distributed.

- Handbook pages on the cryogenic tensile, elastic, electromagnetic, fatigue, and thermal properties of C17000—C17510 beryllium-copper were prepared and distributed.

- Handbook pages on C50500—C52400 phosphor-bronze tensile, elastic, fatigue, electromagnetic, and thermal properties are in preparation. Documents (over 250) have been acquired, and preliminary data sets extracted and analyzed. Equations relating yield strength, tensile strength, and elongation to cold work, temperature, Sn content, and grain size between 4 K and room temperature have been developed from the data base. Further analysis of other properties is in progress. These alloys are used as stabilizers for Nb_3Sn superconducting cable.

- The cryogenic data base for AISI 316LN has been updated with data acquired since the AISI 316 handbook pages were prepared in 1982. A preliminary report on this data base was presented at the ITER Specialists Meeting on Magnet Materials in Garching in February, 1990. Alloy 316LN is a prime candidate for use in thick sections in the toroidal field coils in the ITER design.

TWELFTH CRYOGENIC STRUCTURAL MATERIALS WORKSHOP

Vail, Colorado
October 11-12, 1989

The 12th in this series of workshops was attended by about 40 participants. NIST-Boulder staff made the program arrangements, presented nine invited talks, and led three discussion sessions. Other participants were from DOE fusion energy and accelerator projects, national laboratories, universities, and industry. The workshop provided an opportunity for discussion of research accomplishments, problems, and goals in the development of materials for cryogenic and superconducting magnet systems for fusion reactors and high-energy accelerators. The following topics were highlights:

- Materials issues for ITER (International Thermonuclear Experimental Reactor) and CIT (Compact Ignition Tokamak) including short crack fatigue and fracture toughness.
- Manufacture and design of radiation-resistant 3-D composite insulators.
- Development of 4-K mechanical test standards for structural alloys and composites.
- International Collaborative Programs (with USSR, Japan, and Europe)
- Development of new structural design codes for cryogenic temperatures.

A copy of the program and a summary of the technical presentations follow. In a few cases, there were changes in the program as noted in the summary of the workshop.

12th CRYOGENIC STRUCTURAL MATERIALS WORKSHOP
PROGRAM

WEDNESDAY, OCTOBER 11

INTRODUCTIONS

8:30A	Welcome	R. Reed, NIST
	Office of Fusion Energy Overview	D. Beard, OFE

NORMAL-METAL CONDUCTOR MAGNETS

CIT Magnet Design - Structural Alloy Requirements	J. Citrolo, PPPL
CIT Materials, Issues, and Results from Conductor Research Program	C. Bushnell, PPPL
Type 718 Draw Bar Structure Problems for C-MOD	H. Becker, R. Ballinger, I. Hwang, MIT
Creep of Copper: 4 to 295 K	N. Simon, NIST

COLLABORATIVE PROGRAMS

Discussion: US/Japan and (possible) US/USSR Joint Programs on Low Temperature Structural Materials	R. Reed, NIST (Leader)

LUNCH BREAK

STRUCTURAL INSULATORS

1:30P	CIT Insulation Issues and Research Program Results	T. McManamy, ORNL
	Proton Irradiation Study of Insulating Materials: Preliminary Results	N. Munshi, CTD
	Applications of Composite Materials in Superconducting Particle Accelerator Magnets	T. Nicol, Fermilab
	Manufacture of New 3D Composite Insulators	N. Munshi, CTD
	Development of 3D Composites	J. Benzinger, Spaulding
	Current Status of Interlaminar Shear Testing of Composite Materials at Cryogenic Temperatures	M. Kasen, CTD

DESIGN CODES

Discussion: Structural Design Codes for Superconducting Magnets (Leader)	H. Becker, MIT

5:30P RECEPTION (Altitude Club)

THURSDAY, OCTOBER 12

SC MAGNET STRUCTURAL ALLOYS

8:30A ITER Material Issues	L. Summers, LLLN
Fatigue Problems of ITER Central Solenoid Coils and Other Topics	R. Reed, NIST
Properties of Austenitic Stainless Steels in High Magnetic Fields	J. Chan, U. Cal
Progress Report: Handbook of Structural Materials for Superconducting Magnets	N. Simon, NIST
Fatigue of Metastable Austenitic Stainless Steels	M. Xequn and J. Morris, U. of Cal
Cryogenic Properties of Incoloy 908	I. Hwang, M. Morra, R. Ballinger, MIT
Research on Cryogenic Properties of Al-Li Alloys	J. Morris, U.Cal
Large Scale Cryogenic Test Facility at NIST	D. McColskey, NIST

LUNCH BREAK

STRUCTURAL ALLOY WELDING

1:30P Mechanical Properties of Low-Ferrite Welds at 4 K	C. McCowan, NIST
Weld Alloy Design	T. Siewert, NIST
Welding Problems, Panel Discussion	T. Siewert, NIST (Leader)

METAL AND COMPOSITE TEST STANDARDS

Discussion: Low Temperature Mechanical Property Test Standards: Structural Alloys and Composites	R. Tobler, NIST (Leader)
The Effect of Strain Rate on Low-Temperature, Round-Robin Tensile Tests	R. Walsh, NIST
Warm Prestress Effects in Cryogenic Structural Steels	R. Tobler, NIST
J-Integral Test Analysis Procedures and Interpretation	P. Purtscher, NIST

SUMMARY OF TECHNICAL PRESENTATIONS

INTRODUCTION

Office of Fusion Energy Overview: D. Beard, Office of Fusion Energy, Department of Energy, Germantown, MD

The importance of cryogenic properties of structural materials and electrical insulators to the design of high field superconducting magnets design was emphasized. The next generation of high field magnets for plasma confinement may require Nb_3Sn rather than the currently used NbTi as superconductors. Model or prototype coil test facilities are necessary to develop magnets with this new conductor. Conductor test facilities such as FENIX at Lawrence Livermore National Laboratory (LLNL) are also needed. Fusion energy systems being developed in Japan, Europe, and the Soviet Union were reviewed. International and U.S. task-sharing must be worked out so that progress can be made with available funding.

NORMAL-METAL CONDUCTOR MAGNETS

CIT Magnet Design-Structured Alloy Requirements: J. Citrolo, Princeton Plasma Physics Laboratory, Princeton, NJ

An all-welded structure has been chosen for the toroidal field (TF) coils of the Ignition Tokamak (CIT). The choice of welding was made because the inner legs of the TF coil cases must be joined to a complex bucking cylinder to resist strong overturning moments. The presentation generated discussion about the use of 21-6-9 as the baseline alloy for the structure, because of poor reports of weld properties and low cryogenic fracture toughness. This alloy does have very high strength compared to 316LN. Further studies on weldability are planned.

CIT Materials, Issues, and Results From Conductor Research Program: C. Bushnell, Princeton Plasma Physics Laboratory, Princeton, NJ

With the change from a wedged to a bucked design for the TF coil systems, conductor requirements have also changed somewhat. Currently, three systems are undergoing investigation.

(1) A copper-Inconel alloy laminate with less Inconel than in previous designs

(2) Copper C17510 that has been overaged to provide a high conductivity combined with yield strengths in the range of 550-620 MPa.

(3) Copper C15715, with lower yield strength but higher conductivity.

Alloy 718 Drawbar Structure Problems for Alcator C-Mod: R. Balllinger, H. Becker, I. Hwang, and M. Morro, Massachusetts Institute of Technology, Cambridge, MA

In the TF magnet of the C-Mod fusion energy system, the critical parameter for the drawbars that withstand the 110 MN separating force is fatigue life. Crack growth and fracture toughness control the permissible initial crack size. Low fracture toughness was observed after aging of the forged and machined bar to increase yield strength. Therefore, the bars were given an annealing treatment, which lowered the yield strength, but improved the predicted life.

Creep of Copper: 4 to 295 K: N.J. Simon, R.P. Walsh, E.S. Drexler, and R.P. Reed, National Institute of Standards and Technology, Boulder, CO

Creep of copper is of interest both for the CIT machine and for superconductoring magnets, where copper is used as a stabilizer. Measurements of creep were made at 4, 76, and 295 K for periods of several months. Results were compared with logarithmic and steady state creep models.

COLLABORATIVE PROGRAMS

Discussion: U.S./Japan and (possible) U.S./USSR Joint Programs on Low Temperature Structural Materials: R.P. Reed (Leader), National Institute of Standards and Technology, Boulder, CO

Cooperative programs to support the design issues of ITER (International Thermonuclear Experimental Reactor) were the chief topics of discussion. Development of a short-crack fatigue database on the candidate alloys for the conductor jacket of TF coils was one issue identified. Another issue was the writing of specifications for ITER materials such as the structural alloys to be used in very thick (~100-mm) sections in the TF magnet case. Development and adequate cryogenic testing of radiation-resistant insulators was another topic of discussion. A Japanese company has developed a 3-dimensional (3-D) fiberglass weave that is under consideration for use in the magnet insulation. This or another material would be wound around the conductor assembly and vacuum-impregnated with a resin. Creep of such a composite insulator as well as radiation damage to it are possible failure modes for the magnets.

STRUCTURAL INSULATORS

CIT Insulation Issues and Research Program Results: T.J. McManamy, Oak Ridge National Laboratory, Oak Ridge, TN

The change in the CIT design described above also modified the requirements for the insulation. Stresses were considerably reduced, but an additional requirement of a shear strength of 21 MPa with no compression was

generated. In the research program, irradiation and testing at room temperature were carried out on two bismaleimide systems and one epoxy resin system. Two of the systems used a Japanese 3-D weave. Cryogenic thermal cycling of insulation systems was also investigated.

Proton Irradiation Study of Insulating Materials: Preliminary Results, N.A. Munshi, CTD, Inc., Boulder, CO

A linear accelerator at Brookhaven National Laboratory was used to study the effect of proton irradiation on nine prototype magnet insulating materials. Considerable thermal damage was sustained by the specimens, which made it difficult to draw clear conclusions. However, one of the epoxy resin systems with a long pot life showed promise in the tests. A resin system with a long pot life is very desirable for the lengthy process of vacuum impregnation of a large superconducting magnet.

Applications of Composite Materials in Superconducting Particle Accelerator Magnets: T.H. Nicol, Fermi National Accelerator Laboratory, Batavia, IL

Use of composite materials for electrical insulation and as thermal standoffs in structural applications was reviewed. The Tevatron accelerator at the Fermi National Accelerator Laboratory has provided experience with the operation of many superconducting magnets over an extended time period. A sizeable fraction of the magnets have had to be repaired or replaced, sometimes due to inadequate composite properties under extended periods of use. The low shear modulus of structural composites is also a potential problem when transporting a large structure such as a superconducting magnet.

Manufacture of New 3-D Composite Insulators: N.A. Munshi, CTD, Inc., Boulder, CO

Procedures for vacuum-impregnation fabrication of specimens were presented. The methods developed permit production of void-free laminate specimens reinforced with glass. Tests on specimens produced with these methods will be used to model conditions encountered with superconductor magnet insulation.

Development of 3-D Composites: J.R. Benzinger, Spaulding Composites Company, Inc., Tonawanda, NY

The extent of commercial development and availability of 3-D fabrics for composites was reviewed. Recent developments of these materials in Japan were described. No off-the-shelf 3-D materials are currently available in the U.S. It is hoped that the use of such designs will lead to improvements in interlaminar shear strength of composites.

Current Status of Interlaminar Shear Testing of Composite Materials at Cryogenic Temperatures: M.B. Kasen, CTD, Inc., Boulder, CO

Methods of interlaminar shear measurement were illustrated. All such test methods have the objective of producing pure shear over a plane. However, all methods introduce some tensile or compressive components in the stress state. Tensile stresses reduce the measured shear strength below its true value, while compressive stresses increase it. A further difficulty is the requirement to miniaturize the tests for cryogenic use. A variant of a V-notch shear test may prove adaptable for tests at cryogenic temperatures.

Discussion: Materials Questions for the Superconducting Super Collider (SSC) and Continuous Electron Beam Accelerator Facility (CEBAF):
J. O'Meara, CEBAF, Newport News, VA; W.A. Smith, SSC Laboratory, Dallas, TX; T.H. Nicol, Fermi National Accelerator Laboratory, Batavia, IL

An informal discussion summarized materials research needs of accelerator projects using superconducting magnets. Needs identified were: (1) radiation resistance of composites, (2) creep of conductors and composites, (3) fatigue of composite support materials during transport, and of thin-wall stainless steel bellows, (4) methods of weld inspection, (5) thermal conductivity data on structural composites, (6) development of "standard" composites.

DESIGN CODES

Discussion: Structural Design Codes for Superconducting Magnets:
H. Becker, (Leader), Massachusetts Institute of Technology, Cambridge, MA

It was pointed out that previously developed structural design codes relied on failure data, but such data do not exist for superconducting magnets in fusion reactors. Consequently, codes such as the ASME Boiler Pressure Vessel Code (BPVC) have been used as starting points. The BPVC specifies design allowable stresses such as the lesser of 1/3 of ultimate strength or 2/3 of yield strength. This code was also based on periodic inspection of the pressure vessel structure, but inspection during operation will usually be impossible for the magnets in a fusion reactor.

SUPERCONDUCTING MAGNET STRUCTURAL ALLOYS

ITER Materials Issues: L.T. Summers, Lawrence Livermore National Laboratory, Livermore, CA

The design of ITER magnets will place challenging requirements on materials. A reaction heat treatment at temperatures up to about 725°C will be applied after the forced flow conductor system is fabricated. Consequently, alloys for the conductor sheath have to be evaluated after this type of heat treatment. A major issue is the fatigue crack growth rate of short cracks (~150 μm) in these alloys. The external magnet cases require thick section plate that poses development and procurement problems as well as potential problems in welding. The radiation dose that the magnet insulation must sustain is estimated to be 1–2 x 10^7 Gy.

Fatigue Problems of ITER Central Solenoid Coils and Other Topics: R.P. Reed, National Institute of Standards and Technology, Boulder, CO

There is a lack of measurements of fatigue crack growth rate in the short crack (~100 μm) region. A new measurement technique using a variable ratio of minimum to maximum stress intensity factor can be used to supply data in this domain. The number of cycles of fatigue to which the central solenoid will be subjected, ~ 200,000, is close to the expected lifetime of proposed conductor sheath alloys such as Incoloy 908 and JBK-75.

Fracture of Metastable Austenitic Stainless Steels in a High Magnetic Field Environment: J.W. Chan and J.W. Morris, Jr., Center for Advanced Materials, Lawrence Berkeley Laboratory, Berkeley, CA

Metastable austenitic stainless steels are potential structural alloys for high-field superconducting magnets. Previous work showed an increase in fracture toughness of AISI 304 in an 8-T magnetic field. The tests on AISI 304 were repeated and additional tests were run on AISI 310S, stable with respect to transformation at 4 K, and AISI 304L, less stable than the AISI 304 tested. An increase in fracture toughness in an 8-T field was found for the stable AISI 310S, and a decrease was observed for the relatively unstable 304L. These results were contrary to what was expected from previous work and will be investigated further.

Progress Report: Handbook of Structural Materials for Superconducting Magnets: N.J. Simon, E.S. Drexler, R.P. Reed, National Institute of Standards and Technology, Boulder, CO

This handbook differs from earlier handbooks in that much more documentation of design curves and test measurements is presented. The materials covered are those to be used in fusion applications and priorities are set by guidance from fusion materials workshops. To date, materials covered have included AISI 316 and 316LN, 21-6-9, AISI 304LN, 304HN, and 304LHN, C10100-C10700 coppers, and C17000-C17510 beryllium coppers. Work on Cu-Sn alloys, stabilizers for Nb_3Sn superconductors, is currently in progress. Future plans are to update the AISI 316LN database with recently acquired NIST and European data, and to acquire data on the alloys proposed for the cable-in-conduit conductor (CICC) configuration.

Fatigue Crack Growth in Metastable Austenitic Stainless Steels: M. Xequn and J.W. Morris, Jr., Center for Advanced Materials, Lawrence Berkeley Laboratory, Berkeley, CA

AISI 304L, a metastable austenitic stainless steel, has a lower fatigue crack growth rate at 77 K than the more stable AISI 304LN. The hypothesis was advanced that transformation during fatigue induces crack closure, although the volume expansion of the transformation could tend to prop the crack open. Near the threshold of fatigue crack growth, closure dominates. Transformation effects on the fatigue crack growth rate are very complicated, because 21-6-9, with considerable strain-induced martensite, has a relatively high fatigue crack growth rate.

Ballinger, M.M. Steeves, and M.O. Hoenig, Massachusetts Institute of Technology, Department of Materials Science and Engineering, Plasma Fusion Center, Cambridge, MA.

The alloy Incoloy 908 was developed specifically for use with Nb_3Sn superconductors in the CICC configuration. Weldability, maintenance of good mechanical properties through a high-temperature heat treatment of the Nb_3Sn, and low thermal expansion are required attributes of an alloy for CICC use. Alloy composition has been adjusted to improve properties. Fracture toughness, $K_{Ic}(J)$, is very high, 240 $MPa \cdot m^{\frac{1}{2}}$ at 4 K after aging. Material that has been cold-worked, then aged can have yield strengths from 1489 to 1320 MPa, depending upon heat treatment. As noted above in the discussion of the presentation by R.P. Reed on ITER fatigue problems, fatigue crack growth rate in the short-crack region is an important parameter for a CICC alloy. Fatigue crack growth rate tests reported here were for constant ΔK (stress intensity range), and did not cover the short-crack region.

Cryogenic Properties of Al-Li Alloys: J.W. Morris, Jr., Center for Advanced Materials, Lawrence Berkeley Laboratory, Berkeley, CA.

For many structural alloys, such as the austenitic stainless steels, the increased yield strength at cryogenic temperatures is correlated with some decrease in ductility and fracture toughness. However, because of a change in fracture mode at lower temperatures, this effect does not occur for the Al-Li alloy 2091, and fracture toughness at 4 K is higher than it is at room temperature. Problems in welding Al-Li alloys and their use in superplastic forming were also discussed.

Large Scale Cryogenic Test Facility at NIST: J.D. McColskey, R.P. Walsh, W. Fehringer, National Institute of Standards and Technology, Boulder, CO.

Large scale cryogenic testing is required for the development of large superconducting magnetic energy storage (SMES) systems. NIST has recently acquired the capability to test materials under compressive fatigue loads up to 4.4 MN (1 million lb) at temperatures from 4 to 300 K. Thermal isolation members in a SMES system will experience such loading conditions and will be tested by NIST. This is the only facility in the U.S. with this capability. Details of the system were described.

STRUCTURAL ALLOY WELDING

Mechanical Properties of Low Ferrite Welds at 4 K: C.N. McCowan and T.A. Siewert, National Institute of Standards and Technology, Boulder, CO.

The strength and fracture toughness of welds made with three commercially available stainless steel electrodes (types 330, 316L, and 904) were evaluated at 4 K. Nitrogen additions to the shielding gas were varied to change the N content in the gas metal arc (GMA) welds. The type 904 welds were found to have the best combination of yield strength and toughness at 4 K: 942 MPa and 390 and 269 $MPa \cdot m^{\frac{1}{2}}$ (2 tests).

Weld Alloy Design: T.A. Siewert, National Institute of Standards and Technology, Boulder, CO.

A summary of progress at NIST during the past five years in understanding the parameters that govern weld properties for cryogenic applications was given. Critical parameters, such as N, Ni, and O content in weldments, have been identified and quantified for some electrode-base metal systems. Welds of AISI 304L and 21-6-9 failed in a brittle mode at cryogenic temperatures. A transformation-stable electrode material, designated 904, looks promising for cryogenic applications and may have properties in the so-called JAERI-box region where yield strength >1200 MPa and $K_{Ic} > 200$ MPa·m$^{\frac{1}{2}}$. (JAERI is the acronym of the Japan Atomic Energy Research Institute and the JAERI box refers to a region of desired properties on a K_{Ic} vs. yield strength graph.) It was emphasized that no single property can provide adequate characterization of a welded alloy. A welded structure must be considered as a combination of the base metal, weld metal, and the heat affected zone (HAZ). Since these three zones are interrelated, the study of a welded structure is complex.

Welding Problems, Panel Discussion: T.A. Siewert (Leader), National Institute of Standards and Technology, Boulder, CO.

The possibility of using welded 21-6-9 stainless steel alloy in cryogenic applications such as the CIT was discussed. Improved control of metallurgical variables in the current production of this alloy may lead to better properties than were reported in the past. Because of its very high strength, 21-6-9 keeps resurfacing in new projects as a candidate alloy for cryogenic applications. However, a considerable history of past measurements indicates that cryogenic toughness, especially of welds, is poor.

The problem of weld inspection was discussed. Designs of many fusion systems will not permit much inspection of welds after construction is complete. If AISI 316LN is used in thick-section welds for TF coils for ITER, this will be a potential problem.

The composition (in wt.%) of the promising new electrode material for cryogenic applications, 904, is Fe-25Ni-20Cr-5Mo. The compatibility of this material with various base metals must be examined so that it can be used in cryogenic applications.

METAL AND COMPOSITE TEST STANDARDS

Discussion: Low Temperature Mechanical Property Test Standards: Structural Alloys and Composites: R.L. Tobler (Leader), National Institute of Standards and Technology, Boulder, CO.

Standards for cryogenic measurement of both tensile properties and fracture toughness have been progressing steadily through ASTM in recent years. However, standards for composite testing, even at room temperature, are not yet developed. Some new tests, such as the shear test based on the

Iosipescu configuration, are now under consideration for use at cryogenic temperatures. Miniaturization and scaled down apparatus may be a practical necessity for tests carried out in cryostats. The applicability of such scaled-down measurements to actual design conditions then needs to be considered.

The Effect of Strain Rate on Low Temperature, Round Robin Tensile Tests: R.P. Reed, R.P. Walsh, and R.L. Tobler, National Institute of Standards and Technology, Boulder, CO.

The transition to discontinuous yielding in 4 K tensile testing occurs at a lower strain rate for very high strength alloys (yield strength ~ 1400 MPa). Since the measured ultimate tensile strength is a function of strain rate during the test, lack of standards for the strain rate may explain the different results found in recent round-robin testing.

Warm Prestress Effects in Cryogenic Structural Steels: R.L. Tobler, L.M. Ma, and R.P. Reed, National Institute of Standards and Technology, Boulder, CO

Preloads applied to steel specimens at a relatively high temperature, T_1, can influence fracture toughness at a lower temperature, T_2. The effect has been best known in ferritic steels, where T_1 is above the ductile-to-brittle transition temperature, and T_2 is below it. However, this presentation showed that the effect also occurred in some austenitic steels when precracking at room temperature (T_1) preceded fracture toughness testing at 4 K (T_2). The effect increased the toughness measured at 4 K, and was more important for steels of low toughness. It is apparently associated with a change in the fracture mode between T_1 and T_2. To standardize test methods, the effect must be avoided in order to measure the inherent toughness at 4 K. Japanese fracture toughness testing is not comparable with U.S. testing in some cases because the Japanese generally precrack specimens at room temperature.

J-Integral Test Analysis Procedures and Interpretation: P.T. Purtscher, National Institute of Standards and Technology, Boulder, CO

A series of J-integral fracture tests were performed at 76 K on an Fe-22Cr-13Ni-5Mn-2Mo-0.3N steel. The data were analyzed in two ways: first, with the initial ASTM standard (E 813-81) in which J_{Ic} is derived from the intersection of the blunting line and the tearing line; and second, with the new standard (E 813-87) in which J_{Ic} is determined from the crack growth resistance at an offset of 0.2 mm. The new method was shown to produce consistently higher values of J_{Ic} with less scatter.

Negative crack growth was also discussed. Since the plastic zone is not always ahead of the crack, but also at the sides of the crack, compression may cause negative crack growth. The impracticality of Charpy toughness tests below 77 K, and the lack of correlation of 77 K Charpy results with 4-K J_{Ic} toughness were also noted. Specimen warming at 4 K, partly due to low specific heats, results in invalid Charpy tests.

INTERNATIONAL THERMONUCLEAR EXPERIMENTAL REACTOR
SPECIALISTS MEETING ON MAGNET MATERIALS, February 26-28, 1990

Introduction

ITER is a large international fusion energy project. Resident European, American, Soviet, and Japanese specialists occupy two buildings of the Max Planck Institute in Garching, near Munich, West Germany. On February 26-28, resident and visiting representatives from participating countries met in Garching to discuss cryogenic material requirements. The goal was to formalize R&D plans for ITER magnets. The workshop was organized and chaired by John Miller of Lawrence Livermore National Laboratory. NIST representatives (R.P. Reed, N.J. Simon, and R.L. Tobler) contributed technical presentations and drafted 5-year plans for future research. The format was presentations by the participants followed by preparation, and discussion of research plans. Three sessions (each lasting one day) were devoted to the material categories described below.

Structural Alloys and Welds

The structural alloys session focussed primarily on short crack fatigue problems in the jacket of the superconductor cable-in-conduit configuration for the toroidal field coils and on the production and properties of austenitic steels in 400-mm thick sections of the toroidal field coil case.

Simon presented extensive work on parametric optimization of 316 LN alloys and an evaluation of the 316 LN database at 4 K. In general, 316LN has adequate properties for ITER applications, and the properties can be tailored by control of grain size, purity, and composition. As a result, it is clear that much multinational testing will be needed for the various developmental alloys being advocated by Japan and the USSR if databases for these alloys are to become as large as that for AISI 316 LN.

Simon also presented a brief summary of the alloy activation results obtained at the TRIGA reactor of the Atominstitut in Vienna, through Professor Weber. Samples of four steels were activated: (1) 316LN, (2) 310, (3) 18Cr-18Mn, and (4) 25Mn-5Cr. A fast neutron fluence ($E > 0.1$ MeV) of 2×10^{22} m^{-2} was used. This corresponds approximately to the fluence expected at the magnet location from previous studies (MARS and STARFIRE). The lowest activity was obtained for sample (4), next lowest was sample (3), then sample (2), and finally sample (1) 316LN had the highest activation. Low Cr and Co contents were important in determining this ranking. The TRIGA spectrum does not contain 14 Mev neutrons. When a theoretical calculation was carried out for activation of samples (1) and (4), under a neutron fluence of 1×10^{22} m^{-2} at 14 MeV, Mn and Fe contents dominated and the activation position of samples (1) and (4) reversed at a time immediately after irradiation.

Tobler reported mechanical property measurements for a candidate ITER conduit steel. These data for JK1 (a niobium-modified 316 LN steel) were obtained thanks to assistance from J. Berger, R.P. Walsh, R. Santoya, and C. McCowan. NIST provided ITER designers with the first short-crack simulation fatigue data ever measured at 4 K. These fatigue data are essential to safe life predictions. However, we also reported low toughness for this material; the toughness values in terms of $K_{Ic}(J)$ were about half of that reported in developmental studies by the steel manufacturers. This large disparity showed the importance of material specifications, test standards, and verification testing, since fracture toughness minimums were not specified in the steel procurement. Although the tests for JK1 gave the impression that the hoped-for improvement in properties of the conductor jacket might be delayed, or more difficult to realize, alternative alloys will be evaluated at NIST.

Reed contributed a talk on structural alloys and later was asked to write the 5-year plan for structural alloys. These plans include recommendations on screening of candidate alloys for case and conduit applications, welding, design allowables, and development of appropriate low temperature data bases. Considerable research is required in view of the plan to use very thick (400 mm) austenitic steels for the magnet case structures. Both Reed and Summers (LLNL) articulated the importance of production problems for the very thick sections required. The total tonnage required by ITER (50 000) is insufficient to warrant special considerations from mill facilities. A possible alternative, however, is to consider construction of thick sections from thinner sections.

Other items:

-- Muster and coworkers (EMPA, Zurich) report that in 316 LN type alloys only carbides form during sensitization, not nitrides. We can eliminate sensitization effects in nitrogen-strengthened austenitic alloys (if EMPA is correct) by reducing the carbon content to about 0.01. This would constitute a metallurgical breakthrough for austenitic steels.

-- Nyilas (KfK, Karlsruhe) presented data for low-temperature serrated yielding in austenitic steels and his results are identical to those reported by NIST last year.

-- The Efemov Institute (Leningrad) is now collaborating with Yushchenko (Paton Institute, Kiev) in structural alloy development. Alekseev of Efemov also encouraged collaboration between cryogenic structural material groups in the US and USSR. (Yushchenko first broached this subject at the International Cryogenic Materials Conference in 1989.)

Superconductors

Nb_3Sn superconductor cable development was discussed during the second day's session. Nb_3Sn is needed because the ITER magnets must produce fields of

about 12 T with high current density. Compared to NbTi, the Nb_3Sn conductor is in its infancy. As Gregory of IGC explained, there is little or no market at present. Nevertheless, IGC appears to have developed a product that has very favorable J_c and T_c properties. Miller asked participants to respond to questions regarding the size of billets required for development of previous superconductor stabilizer composites, the length of conductor that could be produced, and so forth, to estimate the amount of additional development that would be required to realize Nb_3Sn conductors.

Magnet Insulation

The third session concerned needs for magnet insulation (composites). The Soviets described their cryogenic irradiation facility. Reed reported NIST's plans to develop cryogenic shear tests for bulk and miniaturized specimens. One proposed use of nonmetallics is in very thin layers (about 2 mm) between ITER magnet windings; bulk material tests are inappropriate for this application, and the thin layer shear measurement methods (lap shear) developed by the Europeans have not yet received adequate international validation. The method of construction for ITER magnets is expected to involve vacuum impregnation with an epoxy resin of very long pot life (at least 24 h at room temperature). Other parts of the proposed magnet structure require 12- to 25-mm plates of glass-reinforced epoxy. Previously, NIST contributed to the development of G-10CR, a standard cryogenic grade material that may be applicable for these thicker section structural parts. Bulk test methods are useful for such applications, and they may provide a scaled-up method for validating the lap shear tests needed to evaluate the impregnated insulation after irradiation.

Reed was asked to write a 5-year plan for ITER research on insulators. This plan emphasizes development of radiation resistant insulation. Filament configuration and polymer matrix should be optimized for resistance to shear forces at 4 K, after irradiation at 4 K.

ITER R&D STRUCTURAL MATERIALS PROGRAM

I. ALLOYS

The current design requirements of ITER for structural alloys for the magnet case and cable conduit exceed the existing technology base of use at cryogenic temperatures. Very thick sections (~400 mm) of high-strength (>1000 MPa yield strength) austenitic steels need to be welded and inspected to use as the magnet coil case. The cable conduit requires high strength, excellent fatigue crack growth resistance at 4 K, and the ability to withstand, without metallurgical deterioration, the superconducting processing schedule of a long aging period at about 700°C. These requirements, for structural alloys usage at 4 K, are new and necessitate a sizeable R&D effort. This R&D effort is outlined here.

Phase I: (~1 year): Down select to 2 alloys for case structure and 1 or 2 alloys for conduit. Principal criteria for case alloy selection are strength and toughness; for conduit alloy, strength and fatigue-crack growth rate. Screening tests on these properties for candidate alloys should be run at several national labs.

Phase II: Case Materials

Two classes of alloys should be tentatively included for Phase II study: (1) 316LN, an alloy class that has been extensively studied for the strengthening effects of nitrogen, grain size, and temperature and for which high speed weld techniques are being developed. This alloy should be selected if yield strengths of about 1000 MPa, coupled with a fracture toughness of about 250 $MPa \cdot m^{\frac{1}{2}}$, are required at 4 K; (2) an alloy class that has yield strengths of about 1200 MPa and fracture toughness of about 200 $MPa \cdot m^{\frac{1}{2}}$. Candidate alloys include JN1 (Japan); 20Cr-6Ni-6Mn (USSR); 13Cr-9Ni-10Mn (USSR).

Special considerations for case alloys are the requirements of very thick sections (~400 mm). This thickness has never been used before in a critical structure at cryogenic temperatures. Research studies (Phase II) include:

- Development of thick-section processing techniques (rolling and/or forging).
- Development of thick-section welding techniques and filler rod for high-strength austenitic steels.
- Development of inspection capabilities (NDE).
- Scale-up studies from specimen coupons to nearly full-size thickness and geometry. Measurements include effects of thickness (reflecting variability from grain size and orientation) on strength, toughness and fatigue. Large test facilities (≥ 500 tons) at 4 K are required.
- Compilation, critical review, and measurement of those physical and mechanical properties required in design.
- Development of specifications for chemistry and control, allowable grain size and thermal/mechanical processing.
- Establishment of allowable flaw sizes of weldments.
- Establishment of allowable stresses.

Phase II: Conduit Materials

The structural alloy for the conduit must have low fatigue-crack growth rates with high yield strength at 4 K. A number of candidate alloys exist, but some have not fulfilled expectations. These alloys include JBK-75 and Incoloy 908 (U.S.), JK1 (Japan), and 316LN with very low carbon (A410, Europe).

Research studies (Phase II) include:

- Measurements of fatigue crack growth rate, including long and short-crack simulations, on base alloys and welds.
- Development of welding techniques.
- Development of inspection technique.
- Establishment of allowable flaw sizes.
- Establishment of property variability leading to establishment of allowable operating stress and maximum fatigue cycles.
- Study of effects of spectrum loading on fatigue crack growth rates at 4 K.
- Full-size simulation test of conduit, in fatigue and tensile load.
- Compilation, critical review, and measurement of those physical and mechanical properties required in design.

II. INSULATORS

In current ITER design, only thin layers of potted epoxy base, with tape reinforcement, will be used. Projected layer widths are 0.03-0.05 mm. Thus, for this design that has an absence of bulk insulators, only research to optimize thin-sheet, reinforced epoxy insulation should be supported. This includes the following items:

- Development of irradiation-resistant (5×10^7 Gy) epoxy with a long (~24 h) pot life and low viscosity at room temperature. (Most epoxies that are currently used do not have a long pot life at room temperature.)
- Development and correlation of shear/compression test techniques for comparing thin-sheet materials and the effects of irradiation at low temperatures. (Appropriate test techniques are recommended in the section under Test Techniques for Structural Insulators.)
- Irradiation studies with a higher ratio of neutron to gamma radiation and including more high-energy neutrons are suggested. Parallel irradiation of specimens with gamma radiation only is necessary to separate out the damage from neutrons and gamma rays. Irradiation at 4 K, coupled with <u>in situ</u> tests at 4 K, are needed. Irradiation at 4 K, followed by warming to 295 K and subsequent testing at 4 K are also needed to study Wigner (defect accumulation) and gas accumulation effects.

- Dielectric breakdown tests as a function of compression/shear loading should be conducted at 4 K.

Compression:

Specimen width-to-height ratios must be large enough to prevent column or shell buckling. Constraint (support) at specimen ends eliminates brooming effects and leads to increased strengths. Otherwise, compression testing is relatively simple.

Shear:

There is a wide diversity of shear test methods and test results at cryogenic temperatures. For continuous, filamentary-reinforced composites in bulk form (plate, rod), these include:

torsion
tension ($\pm$ 45°, 10° off axis)
rail shear
short-beam shear
4-point flexure
notched (Guillotine) shear
double-lap shear
Iosipescu test
AFPB*

For thin sheet composites, the following test techniques are used: single-lap shear and double-lap shear

A miniaturization of the single-lap shear test has been developed and used for NET irradiation studies by Fardi, Mitchell, and Poehlchen. Finite element analysis and preliminary test results indicate that the test techniques may be an acceptable alternative for small specimens.

Of special interest is the new technique developed by Okada's group that permits the simultaneous application of both shear and compressive loads. Results from these tests suggest that the shear strength is strongly dependent on simultaneously applied compression loads, increasing with higher load.

For ITER insulation, only very thin sheets of filament-reinforced composites are projected at present. Thus, only single or double lap shear, or the shear/compression type tests developed by Okada will be useful for the selection of a long pot-life epoxy and to measure the shear strength of the selected insulator.

For testing of unirradiated materials, it is recommended that a new test be developed for use as a "standardized ITER shear test." For testing of irradiated insulators, Fardi et al.'s miniaturized lap shear test should be developed and correlated with the newly developed test.

APPENDIX

MECHANICAL PROPERTIES OF ULTRA-LOW CARBON STEEL AND EFFECTS OF WARM PRESTRESS AT 4 K+

R.L. Tobler, L.M. Ma*, and R.P. Reed
Materials Reliability Division
National Institute of Standards and Technology
Boulder CO 80303

The yield strength of ultra-low carbon steel increases from 137 MPa at 295 K to 705 MPa at 4 K. In liquid helium at 4 K the material is brittle and cleaves in tension. Consequently it is difficult or impossible to properly fatigue-precrack toughness specimens for tests at 4 K. In this study, we precracked a series of compact specimens at room temperature (295 K) and then fractured them at 4 K. The toughness measurements at 4 K are affected by precracking at 295 K, and they provide only an estimate of K_{Ic} for this steel which is 15 MPa·m$^{\frac{1}{2}}$. The tensile properties of the steel at 295 and 4 K are reported, and the effects of prestress on the tensile and fracture properties at 4 K are discussed.

INTRODUCTION

Owing to their ferritic microstructures and lack of nickel content, carbon steels undergo ductile-to-brittle transitions at temperatures ranging from 250 to 375 K [1-5]. The transition temperature marks an abrupt change in fracture resistance and it determines the minimum service temperature. On the upper shelf, ductile fracture occurs by microvoid growth and coalescence; on the lower shelf, cleavage fracture occurs with little or no ductility.

Normally, this transitional behavior of carbon steels disqualifies their use as primary load carrying members in cryogenic structures subjected to tensile stress. In an exceptional circumstance, ultra-low carbon steel at a subtransition temperature of 4 K is being considered for magnet yokes in the Superconducting Super Collider. No other steel has the desired ferromagnetic properties for this application. The proposed application prompts serious questions about the maximum load carrying capability of the carbon steel at 4 K, and to what extent it might be affected by prestressing (preloading, or prestraining) at room temperature. The measurements described here provide clarification.

---

* Guest worker at NIST, on leave from Institute of Metal Research, Academia Sinica, Shenyang, P. R. China.

Discussions [6, 7] and reviews [8, 9] of warm prestress (WPS) described how preloads applied to steel specimens or structures at a relatively high temperature T_1 can increase the toughness subsequently measured at a lower temperature, T_2. Toughening from WPS is common in carbon steels when T_1 is above the transition temperature and T_2 is below the transition temperature. Toughening was reported in notched or fatigue precracked specimens of high-C spheroidized steel [6], medium strength steels [10], C–Mn steels [11], 0.36% C steel [12], A 533 B–1 steel [13], and free machining steel [14]. In this paper, we describe the effects of WPS for an ultra-low carbon steel where T_1 is room temperature and T_2 is liquid helium temperature (4 K).

MATERIAL AND SPECIMENS

The test material was a commercial ultra-low carbon steel plate, 89 mm thick, with the following composition (mass percent): Fe-0.007C-0.021Mn-0.012P-0.014S-0.006Si-0.052Al-0.003N. Compared to conventional mild carbon steels, this steel has a lower C and Mn content which confers the desired ferromagnetic behavior at cryogenic temperatures.

Six tension test specimens in the short-transverse orientation were machined from the as-received plate and tested following ASTM Methods E 8-89 [15]. Five compact specimens in the S-L orientation were also machined and tested (after WPS) following ASTM Methods E 399-83 [16].

Figure 1 shows the test specimen orientations with respect to the 89 mm thick plate. Tension specimens were cylindrical with a diameter of 6.35 mm, a length of reduced section of 38.1 mm, and a gage length of 25.4 mm. Displacement was measured using clip-on extensometers. The specimen reduced section was tapered slightly to ensure fracture at the center of the gage length. Fracture toughness specimens were 25.4 mm thick (W) and 50.8 mm wide (W), with the planar proportions recommended by Methods E 399-83.

PROCEDURE

The apparatus for conducting cryogenic tension and toughness tests were described before [17-19]. The test procedures for measuring the tensile properties and stress intensity factors for compact specimens are specified in ASTM Standard Test Methods E 8-89 and E 399-83, respectively.

Tension tests

The crosshead velocity during tension tests was 0.5 $mm \cdot min^{-1}$ which corresponds to a nominal strain rate of 0.013 min^{-1}. Two tests were performed at 295 K, and two at 4 K. Two more tests were conducted to observe the effect of prestrain at 295 K on tensile properties at 4 K; in these tests the specimens were prestrained 5% at 295 K, then unloaded, cooled in liquid helium, and fractured at 4 K.

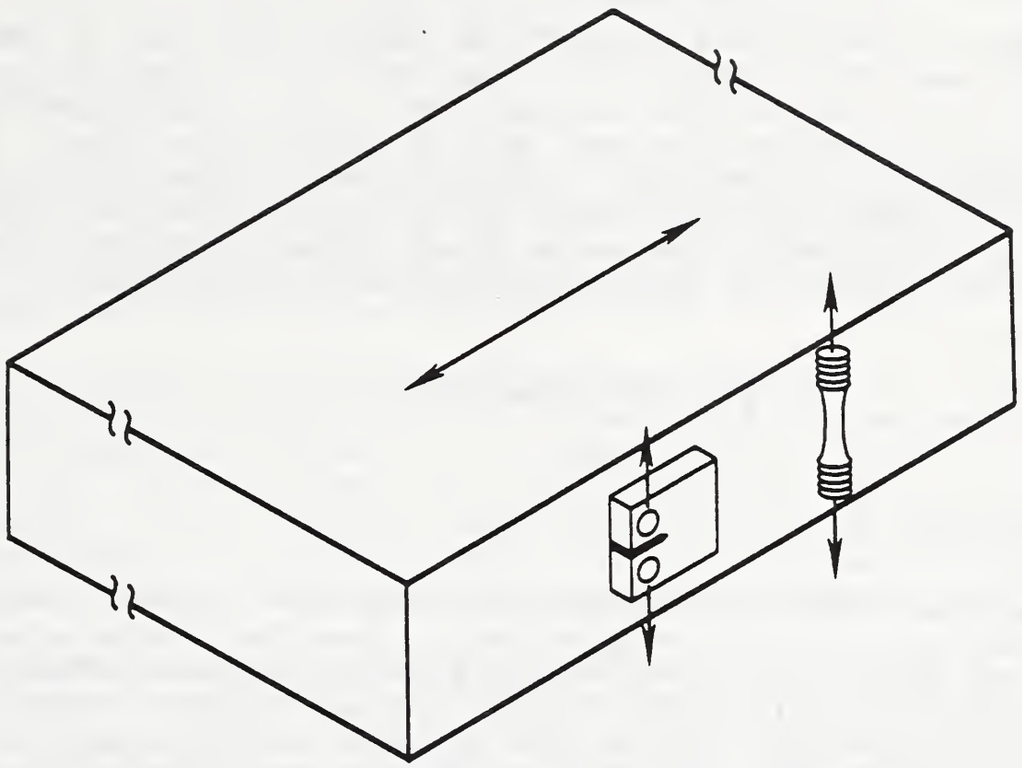

Figure 1. Test specimen geometries and orientations.

Fracture Toughness

Valid K_{Ic} data could not be measured due to difficulties encountered in fatigue-precracking. Usually, test specimens are fatigued in tension and K_{Ic} is then measured at the same temperature. Precracking in tension is routine at temperatures where the material retains ductility (see paragraph A2.1.1 of Method E 399-83), but it is difficult or impossible to fatigue brittle metals in tension at extreme cryogenic temperatures [20, 21]. We therefore precracked the specimens at 295 K where the steel is ductile, although this affects the toughness at 4 K.

Five specimens were fatigued at 295 K, using a minimum-to-maximum load ratio of 0.1. The waveform was sinusoidal in load control at 25 Hz, and crack length was monitored by compliance [19]. The final maximum fatigue stress intensity factor, K_{max}, varied from 11 to 50 MPa·m$^{\frac{1}{2}}$, as Table 2 shows.

The two lowest K_{max}, 11.7 and 16.5 MPa·m$^{\frac{1}{2}}$, were achieved by long-term cycling with periodic load reductions as a function of crack growth. After reaching a crack-length-to-width ratio of ~0.5, the specimens were fractured at 4 K at a displacement rate of approximately 0.03 mm·s^{-1}.

The above procedure is a fatigue-load, unload, cool, and re-load-to-fracture sequence which toughens the steel due to WPS. Since the apparent toughness at 4 K increases with the magnitude of room-temperature fatigue loads, we applied progressively lower K_{max} to diminish the effect. We plotted the apparent 4-K toughness versus the plastic zone size associated with the final maximum fatigue load at 295 K, then extrapolated the trend to estimate K_{Ic}. The plastic zone radius R_p was estimated from the yield strength YS and K_{max} at the appropriate temperature using Irwin's approximation [22]:

$$R_p = (1/6\pi)\cdot(K_{max}/YS)^2 \qquad (1)$$

RESULTS

Tensile properties

The tensile mechanical property measurements are listed in Table 1. The data for specimens numbered 1–4 establish the baseline tensile properties for the ultra-low carbon steel. The average strength increases substantially at 4 K while ductility falls nearly to zero. Between 295 and 4 K the yield strength shows a fivefold increase, the ultimate strength nearly triples, the elongation drops from 48.7 to 1.2%, and the reduction of area drops from 89.4 to 0.5%.

Table 1. Tensile properties of ultra-low carbon steel at 295 and 4 K.

Specimen No.	Temperature (K)	Yield Strength (MPa)	Ultimate Strength (MPa)	Elongation (%)	Red. of Area (%)
1	295	137	267	49.4	89.4
2	295	137	269	47.9	89.4
Average		137	268	48.7	89.4
3	4	700	753	1.4	0.5
4	4	709	735	1.9	0.5
Average		705	744	1.2	0.5
5	295, then 4[a]	NA	679	5.3[b]	4.0[b]
6	295, then 4[a]	NA	702	5.0[b]	4.8[b]
Average		NA	690	5.2[b]	4.4[b]

[a]prestrained approximately 5% at 295 K, unloaded, cooled to 4 K, and then re-loaded to fracture at 4 K.
[b]these values reflect ductility during the initial loading at 295 K.

Table 1 also lists data for specimens (numbers 5 and 6) that were warm prestrained at 295 K before testing at 4 K. The 295-K prestrain slightly lowers the fracture stress of unnotched specimens at 4 K. The prestrained specimens failed at an average stress of 690 MPa; this is nearly equal to the yield strength of specimens that were not warm prestrained, and is about 7% lower than the ultimate strength of specimens that were not prestrained.

Fracture toughness

Load-displacement records for compact specimens are shown in Fig. 2. Most tests satisfy Method E 399-83, except the fatigue load restrictions (Section A2.4.4) were violated by cycling at 295 K to create WPS. Also, the P_m/P_Q ratio for specimen MS-6 slightly exceeded 1.10 which is the allowable limit specified by the standard (Section 9.1.2).

Table 2 lists the toughness calculations as K_Q, not K_{Ic}, because they are invalidated by warm precracking. K_Q decreases systematically from 36 to 23 MPa·m^{½} as K_{max} is lowered, but, as shown in Fig. 3, no plateau is reached at lower K_{max}. In other words, the effect of WPS was reduced but not eliminated by at the low fatigue loads used in this study. We conclude that the lowest measured K_Q value, 23 MPa·m^{½}, is still affected to a degree by WPS, and therefore it represents only an upper bound for K_{Ic} at 4 K.

With some assumptions these data can be used to estimate K_{Ic}. A plot of K_Q (at 4 K) versus plastic zone size approximations corresponding to K_{max} (at 295 K) is shown in Fig. 4. The 4-K toughness varies semilogarithmically with the estimated plastic zone size at the crack tip. The estimated plastic zones after fatigue at 295 K are large (6.9 to 0.39 mm), because the steel's yield strength is relatively low at 295 K. A much smaller deformed zone would form if precracking could be accomplished at low temperatures where the resistance to deformation is higher. Using the upper bound value of toughness (23 MPa·m^{½}) and the 4-K yield strength (705 MPa) in Eq. (1), we estimate the plastic zone size for a valid 4 K test to be 0.05 mm. An extrapolation of the trendline in Fig. 4 to 0.05 mm then gives a K_{Ic} estimate of 15 MPa·m^{½} for this steel with no WPS at 4 K.

Table 2. Precracking conditions and 4-K fracture toughness results.

Specimen No.	Maximum Stress Intensity Factor Used In Fatigue at 295 K, K_{max} (MPa·m^{½})	Fracture Toughness Measured at 4 K, K_Q (MPa·m^{½})
MS-3	49.4	35.6
MS-5	32.9	32.6
MS-2	22.0	28.3
MS-4	16.5	26.5
MS-6	11.7	23.2[a]

[a]Invalid: the ratio P_m/P_Q is 1.12; a ratio of 1.10 or less is permissible (Method E 399-83, Section 9.1.2).

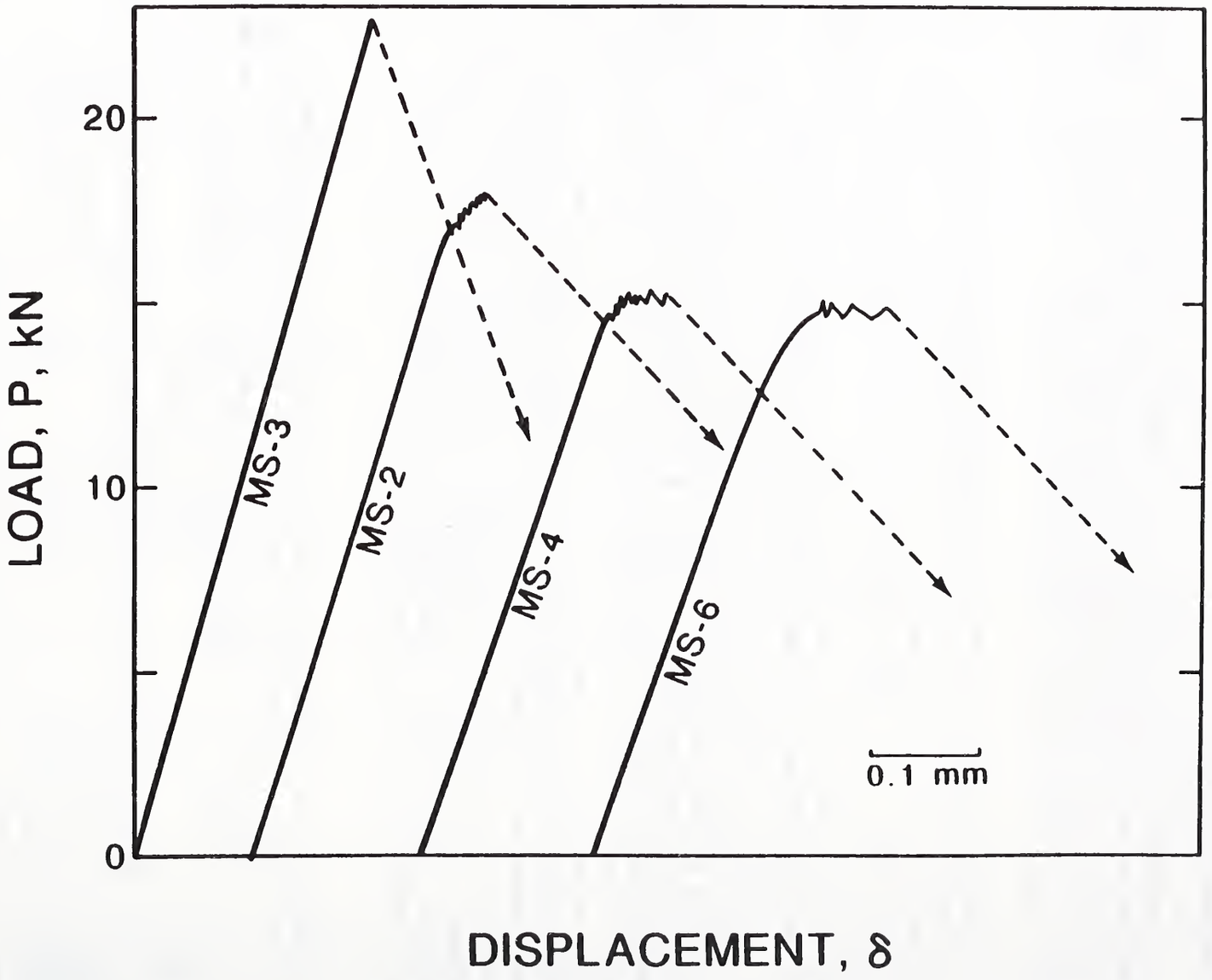

Figure 2. Load-displacement curves for mild steel compact specimens at 4 K.

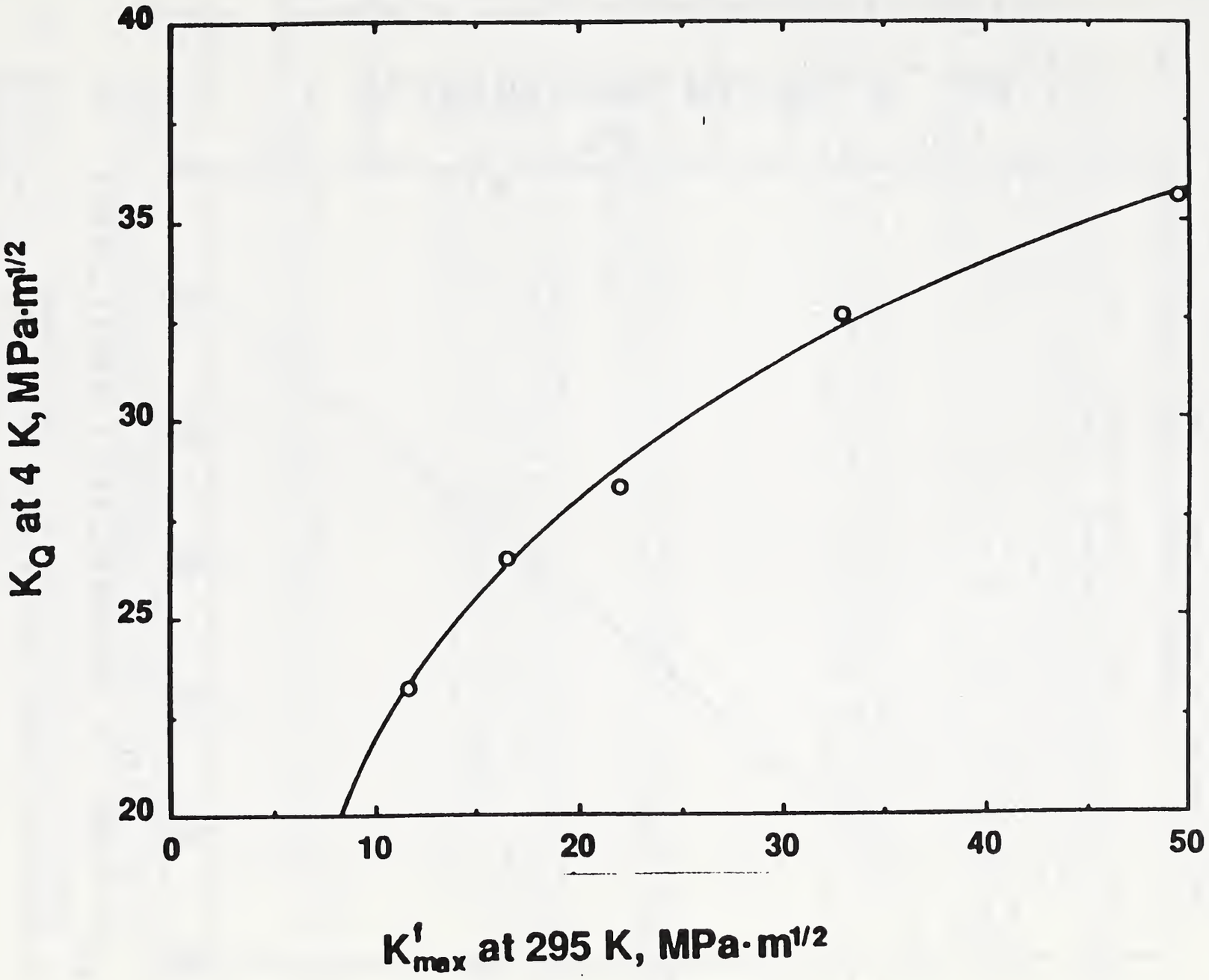

Figure 3. Fracture toughness K_Q, at 4 K, as a function of K^f_{max} applied previously at 295 K.

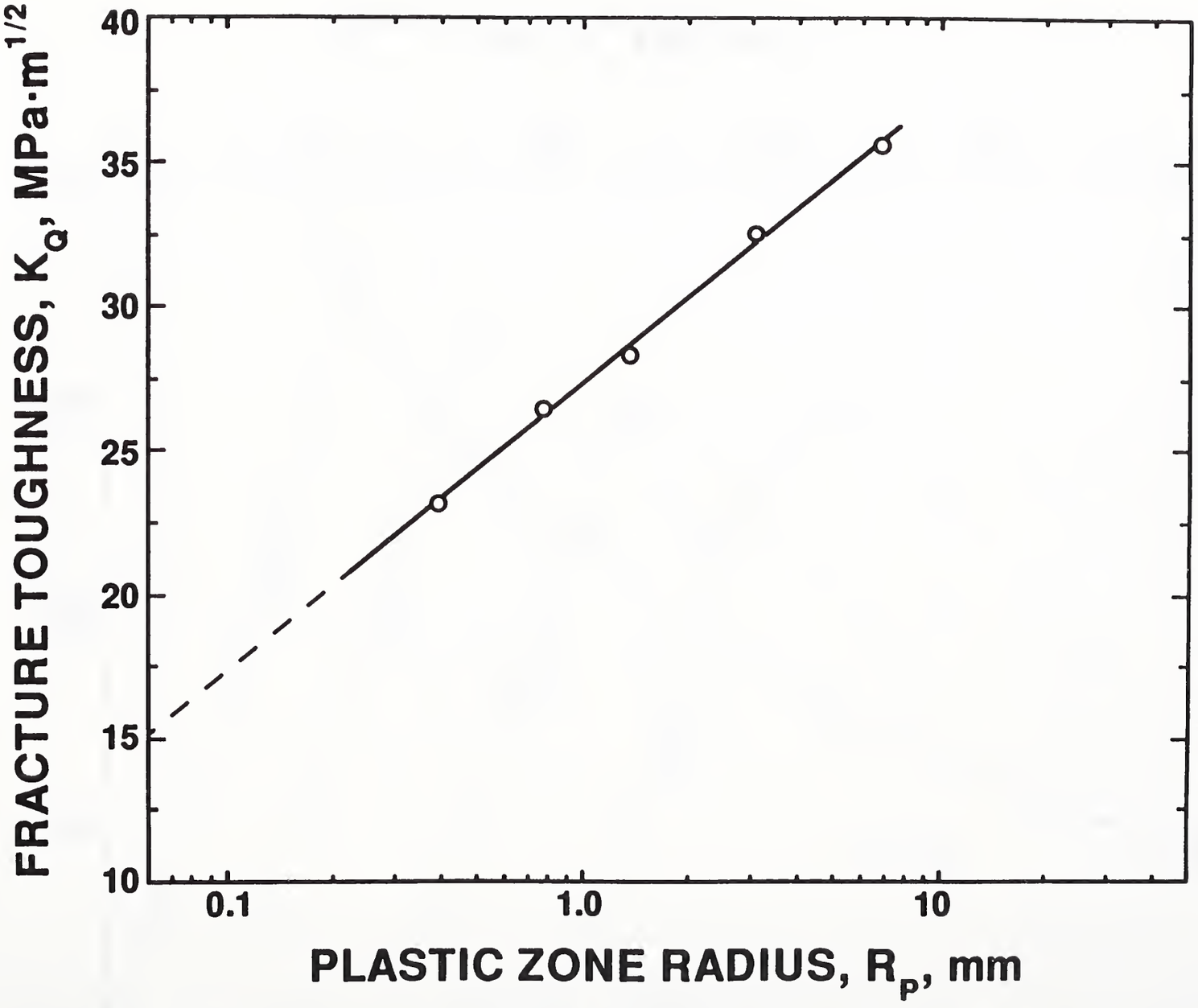

Figure 4. Procedure for fracture toughness estimation based on a back extrapolation of a plot of K_Q vs plastic zone radius.

DISCUSSION

The effect of warm prestrain on unnotched specimens is to lower the fracture stress slightly at 4 K. Prestrain at room temperature further compromises the steel's ability to deform on reloading at 4 K. So, unlike the as-received steel, the 295-K prestrained material could not sustain a 0.2% plastic strain at 4 K (see Fig. 5) and failure in the prestrained specimens occurred at slightly lower tensile stresses.

Contrary to the effect on smooth tensile specimens, WPS is beneficial for deeply cracked compact specimens. Reasons for the toughening of notched or cracked specimens are discussed in the literature [6–9]. In some practical structural applications with linear-elastic materials, the beneficial effect of WPS is used in a strategy of intentional overstressing at T_1 to reduce the probability of fracture at T_2 [8]. In proposed magnet applications, however, it is not clear how WPS could be practically used.

Precracking at low loads is time consuming. In principle, a valid K_{Ic} measurement at 4 K is approached as the precracking loads at 295 K are lowered. However, the time required for precracking this steel is prohibitive at the required low loads. We therefore resorted to estimating the toughness.

CONCLUSIONS

1. The ultimate strength of ultra-low carbon steel at 4 K is 744 MPa. Room temperature prestraining in tension by 5% lowers the ultimate strength at 4 K to 690 MPa.

2. The fracture toughness (K_{Ic}) of this ultra-low carbon steel at 4 K is estimated at 15 $MPa \cdot m^{\frac{1}{2}}$. Valid K_{Ic} measurements could not be obtained by fatigue precracking in tension at a stress ratio of 0.1. Fatigue precracking at 295 K inflated the toughness measurements at 4 K, whereas fatigue precracking at 4 K was impossible because of brittleness.

ACKNOWLEDGMENT

The test material and funds for conducting this work were provided by Brookhaven National Laboratory, with M. Rehak as project monitor.

REFERENCES

[1] Lubahn, J.D., Effect of Temperature on the Fracturing Behavior of Mild Steel, **Welding Journal Research Supplement**, Vol. 35, 1956, pp. 557S-568S.

[2] Wessel, E.T., A Tensile Study of the Brittle Behavior of a Rimmed Structural Steel, **Proceedings of the American Society for Testing and Materials**, Vol. 56, 1956, pp. 540-554.

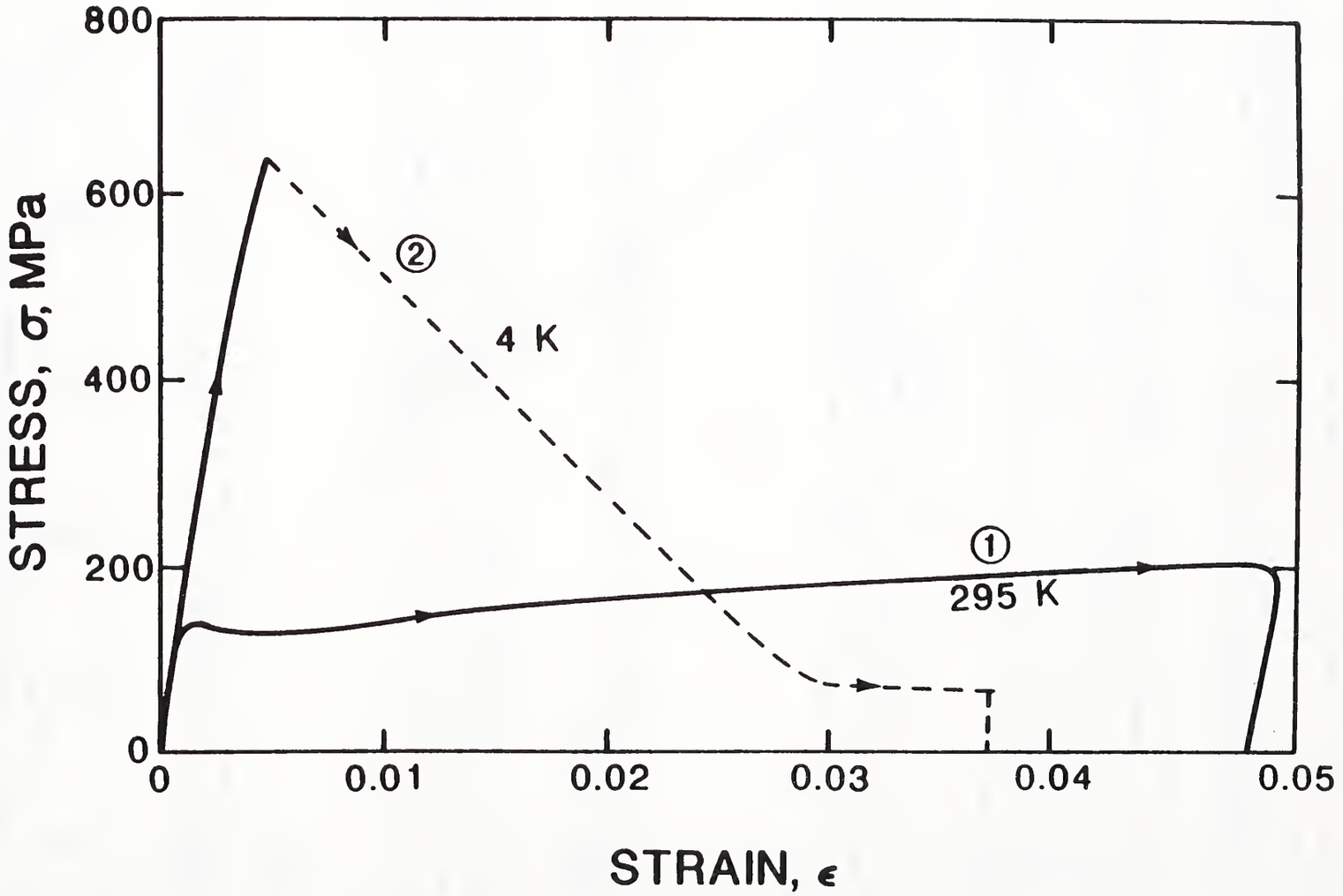

Figure 5. Stress versus strain curve for a mild steel specimen (A) prestrained 5% at 295 K, then (B) reloaded to failure at 4 K.

[3] Hahn, G.T., Averback, B.L., Owen, W.S., and Cohen, M., Initiation of Cleavage Microcracks in Polycrystalline Iron and Steel, in: **Fracture**, Wiley, New York, 1959, pp. 91-116.

[4] Clausing, P., Tensile Properties of Eight Constructional Steels Between 70 and -320° F, **Journal of Materials**, Vol. 4, No. 2, 1969, pp. 473-492.

[5] Shoemaker, A.K. and Rolfe, S.T., The Static and Dynamic Low Temperature Crack Toughness Performance of Seven Structural Steels, **Engineering Fracture Mechanics**, Vol. 3, 1971, pp. 319-339.

[6] Chell, G.G., Haigh, J.R., and Vitek, V., A Theory of Warm Pre-stressing, Experimental Validation and the Implications for Elastic-Plastic Failure Criteria, **CERL Laboratory Note No. RD/L/N63/79**, 1979.

[7] Curry, D.A., A Model for Predicting the Influence of Warm Prestress and Strain Ageing on the Cleavage Fracture Toughness of Ferritic Steels, **International Journal of Fracture**, Vol. 22, 1983, pp. 145-159.

[8] Nichols, R.W., The Use of Overstressing Techniques to Reduce the Risk of Subsequent Brittle Fracture, Parts 1 and 2, **British Welding Journal**, Jan.- Feb., 1968.

[9] Pickles, B.W., and Cowan, A., A Review of Warm Prestressing Studies, **International Journal of Pressure Vessels and Piping**, Vol. 14, 1983, pp. 95-131.

[10] Brothers, A.J., and Yukawa, S., The Effects of Warm Pre-stressing on Notch Fracture Strength, **Journal of Basic Engineering**, Vol. 85, 1963, pp. 97-101.

[11] Harrison, T.C., and Fearnehough, G.D., The Influence of Warm Prestressing on the Brittle Fracture of Structures Containing Sharp Defects, **Journal of Basic Engineering**, Vol. 94, 1972, pp. 373-376.

[12] Nichols, R.W., Levine, W.H., Quirk, A., and Bevitt, E.A., A Limit Approach to the Prevention of Pressure Vessel Failure, **Proceedings of the First International Conference on Fracture**, Sendai, Japan, 1966, pp. 1673-1678.

[13] Nakamura, H., Kobayashi, H., Kodaira, T., and Nakazawa, H., On the Effects of Pre-loading on the Fracture Toughness of A533 B-1 steel, in: **Advances in Fracture Research, Proc. ICF 5**, Vol. 2, Pergamon, New York, 1981, pp. 817-824.

[14] Curry, D.A., A Micromechanistic Approach to the Warm Prestressing of Ferritic Steels, **International Journal of Fracture**, Vol. 17, 1981, pp. 335-343.

[15] Standard Test Methods of Tension Testing of Metallic Materials, ASTM Designation: E 8-89, in: **1989 Annual Book of ASTM Standards, Section 3, Metals Test Methods and Analytical Procedures**, Vol. 03.01, Amer. Soc. Test. Maters., Philadelphia, 1989, pp. 131-146.

[16] Standard Test Method for Plane Strain Fracture Toughness of Metallic materials, ASTM Designation: E 399-83, in: **1989 Annual Book of ASTM Standards, Section 3, Metals Test Methods and Analytical Procedures**, Vol. 03.01, Amer. Soc. Test. Maters., Philadelphia, 1989, pp. 487-511.

[17] Tobler, R.L., and Shepic, J.A., Design and Performance of a Ring-Shaped Clip Gage for Fracture Mechanics Testing, **Journal of Testing and Evaluation**, JTEVA, Vol. 13, No. 4, 1985, pp. 299-302.

[18] Reed, R.P., A Cryostat For Tensile Tests in the Temperature Range 300 to 4 K, in: **Advances in Cryogenic Engineering**, Vol. 7, Plenum, New York, 1961, pp. 448-454.

[19] Read, D.T., and Tobler, R.L., Mechanical Property Measurements at Low Temperatures, in: **Advances in Cryogenic Engineering**, Vol. 28, Reed, R.P. and Clark, A.F., Eds., Plenum, New York, 1982, pp. 17-28.

[20] McCammon, R.D., and Rosenberg, H.M., The Fatigue and Ultimate Tensile Strengths of Metals Between 4.2 and 293 K, **Proceedings of the Royal Society of London**, Vol. A 242, 1957, pp. 203-211.

[21] Stonesifer, F.R., Effect of Grain Size and Temperature on Fatigue Crack Propagation In A 533 B Steel, **Engineering Fracture Mechanics**, Vol. 10, 1978, pp. 305-314.

[22] Irwin, G.R., Plastic Zone Near a Crack and Fracture Toughness, in: **Mechanical and Metallurgical Behavior of Sheet Materials, Proc. 7th Sagamore Ordnance Materials Research Conference**, U.S. Army Office of Ordnance Research, 1960, pp. 63-77.

CRYOGENIC FATIGUE OF HIGH-STRENGTH ALUMINUM ALLOYS AND CORRELATIONS WITH TENSILE PROPERTIES[+]

L.M. Ma*, J.K. Han**, R.L. Tobler, R.P. Walsh, and R.P. Reed

Fracture and Deformation Division
National Institute of Standards and Technology
Boulder, Colorado 80303

ABSTRACT

Notched and unnotched sheet specimens of four aluminum alloys were fatigue tested to evaluate potential use in the Superconducting Super Collider. Alloys 7075-T6, 7475-T761, 2219-T87, and 2090-T8E41 were tested in axial fatigue at a stress ratio of 0.1. The unnotched specimens were tested at 295, 76, and 4 K, whereas notched specimens were tested at 76 K only. We compare the fatigue strengths of these alloys with a practical interest in a life of 10^5 cycles. We also correlate fatigue strengths with static tensile strengths for notched and unnotched specimens.

INTRODUCTION

High-strength aluminum alloys have acquired considerable importance because of their current and potential uses in aerospace structures and superconductor projects.[1] Superconducting Super Collider (SSC) dipole magnets, for example, will probably require an aluminum alloy with high fatigue resistance at low temperatures.[2] Since conventional fatigue data are not readily available in the open literature, we report smooth and notched specimen data in this paper to aid material selection. Strong temperature effects on the fatigue lives of these aluminum alloys are demonstrated, and the possibility of predicting the fatigue resistances of these alloys on the basis of simple correlations with tensile properties is examined.

MATERIALS AND PROCEDURE

Four commercial aluminum alloys were tested in their as-received tempers: 7075-T6, 7475-T761, 2090-T8E41, and 2219-T87. Specimens were taken from sheets in the recrystallized condition that were about 1.6 mm thick. The nominal alloy compositions are:

[+] Contribution of NIST, but not subject to copyright in the United States.
* Guest Researcher at NIST, on leave from the Institute of Metal Research, Academia Sinica, Shenyang, P. R. China.
**Research Institute of Science and Technology, Pohang, South Korea.

7075: Al–5.6Zn–2.5Mg–1.6Cu–0.23Cr
7475: Al–5.7Zn–2.3Mg–1.5Cu–0.22Cr
2090: Al–2.86Cu–2.05Li–0.12Zr
2219: Al–6.3Cu–0.3Mn–0.18Zr–0.10V–0.06Ti.

Figure 1 shows the specimen geometries used. All specimens were fabricated in the transverse orientation relative to the principal rolling direction of the sheets. The square notch, shown in Fig. 1, essentially duplicates the notched condition of an SSC key collar component[2] and has a stress concentration factor K_t of about 3.9. The specimens were ground on each side to remove surface marks from the as-received sheets. Unnotched fatigue specimens were ground to number 1000 grit. Notched specimens were ground and then electropolished in a solution of 30% nitric acid and 70% methanol. The specimen dimensions and notch root radii were measured using a micrometer and a shadowgraph. The radii measurements at both corners and on both sides of each specimen were averaged. The minimum and mean values of the four readings for each specimen were 0.555 mm ± 7% and 0.600 ± 10%, respectively, for all alloys.

The specimens were mounted in a cryostat[3] filled with liquid nitrogen or liquid helium for cryogenic testing. Tension tests were performed at a crosshead rate of 0.5 mm/min. The gage length for elongation measurements was 25.4 mm. Tension-tension fatigue tests were conducted using a servo-hydraulic machine in the load-control mode. The minimum-to-maximum fatigue stress ratio (R) was 0.1. To begin a fatigue test, the mean load was applied at once, and the load amplitude was adjusted while the frequency was gradually increased from 1 to 9, 10, or 15 Hz (notched specimens), or to 15 or 20 Hz (smooth specimens).

RESULTS AND DISCUSSION

Smooth and Notched Specimen Tensile Properties

The conventional tensile properties and notched specimen tensile strength (NTS) measurements are listed in Table 1. For all four alloys, the yield strengths at 0.2% plastic strain (YS) and the ultimate tensile strengths (UTS) increase with decreasing temperature between 295 and 4 K while tensile elongations decrease moderately. Alloy 7075–T6 has the highest strengths and 2219–T87 the lowest strengths at temperatures in this range. The elongations are slightly temperature dependent, ranging from 9.9 to 17.1% (7475–T761 has the highest values).

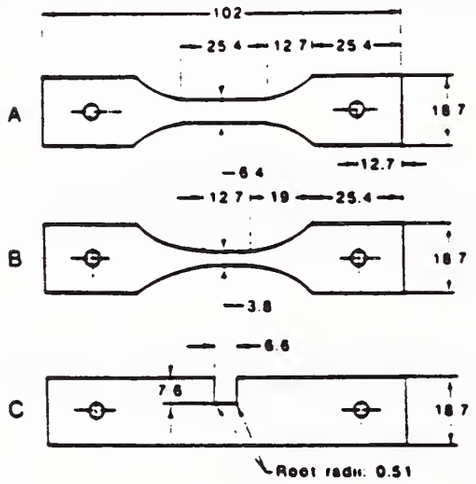

Figure 1. Specimen geometries.
A. Smooth tensile specimen
B. Smooth fatigue specimen
C. Notched tensile or notched fatigue specimen

Note: All dimensions in mm.

Table 1. Static Tensile Properties for Smooth and Notched Specimens data are mean values from two tests)

Alloy	Temp. K	YS MPa	UTS MPa	El %	E GPa	NTS MPa	NSR NTS/UTS	NYR NTS/YS
7075	295	502	589	16.9	63.2			
-T6	76	589	714	15.8	73.2	450	0.63	0.76
	4	648	810	10.1	74.4			
7475	295	460	515	17.1	66.3			
-T761	76	549	636	17.3	75.3	472	0.74	0.86
	4	572	739	15.1	76.4			
2219	295	397	475	12.6	67.8			
-T87	76	484	597	13.5	76.5	435	0.73	0.90
	4	539	711	12.4	77.9			
2090	295	488	528	12.1	74.0			
-T8E41	76	551	640	10.8	76.9	443	0.69	0.80
	4	614	727	9.9	84.1			

Despite moderate ductility in the unnotched tension tests, the notch-strength ratios (NSR = NTS/UTS) and notch-yield ratios (NYR = NTS/YS) for the alloys at 76 K range from 0.63 to 0.90, and are less than one, indicating notch sensitivity in each case. The NSR and NYR ratios are qualitative indicators of notch sensitivity and fracture toughness. In particular, the NYR for round bar specimens correlates well with the plane-strain fracture toughness, K_{Ic}.[4] As previously illustrated by plotting YS versus NYR for these alloys, the cryogenic toughness of our recrystallized 1.6 mm 2090-T8E41 sheet alloy is not at all exceptional compared to the other alloys.[5]

Fatigue Life

The fatigue life data are plotted in Fig. 2 where S_m is the maximum fatigue stress applied in each test, and N_f is the number of cycles to failure. The studied range of N_f is between 10^4 and 10^7. For all alloys, N_f increases with decreasing Sm, and the fatigue life curves improve by substantial margins at cryogenic temperatures. Figure 3 compares the alloys at 295, 76, and 4 K. Alloy 7075–T6 has superior fatigue resistance at all three temperatures, and the ranking of the other alloys varies for specific conditions as shown in Fig. 3.

Temperature Dependence of Fatigue Strength

Fatigue strength (FS), defined here as the maximum fatigue stress corresponding to a specified life, is plotted in Fig. 4 for a life of 10^5 cycles (unnotched specimens). With decreasing temperature, FS increases strongly, but the effect diminishes as N_f increases. At any temperature, alloy 7075–T6 has the highest FS for $N_f = 10^5$; the other three alloys show little difference for $N_f = 10^5$, but there are differences at $N_f = 10^6$, as can be seen from Fig. 3.

Reasons for the strong temperature dependence of fatigue resistance of aluminum alloys were discussed previously.[6] The superior fatigue resistance of 7075-T6 in the unnotched condition arises primarily from its higher static ultimate strength. The materials have only modest tensile ductilities, and no obvious plastic deformations were observed on the fatigue fracture surfaces of failed specimens in this study.

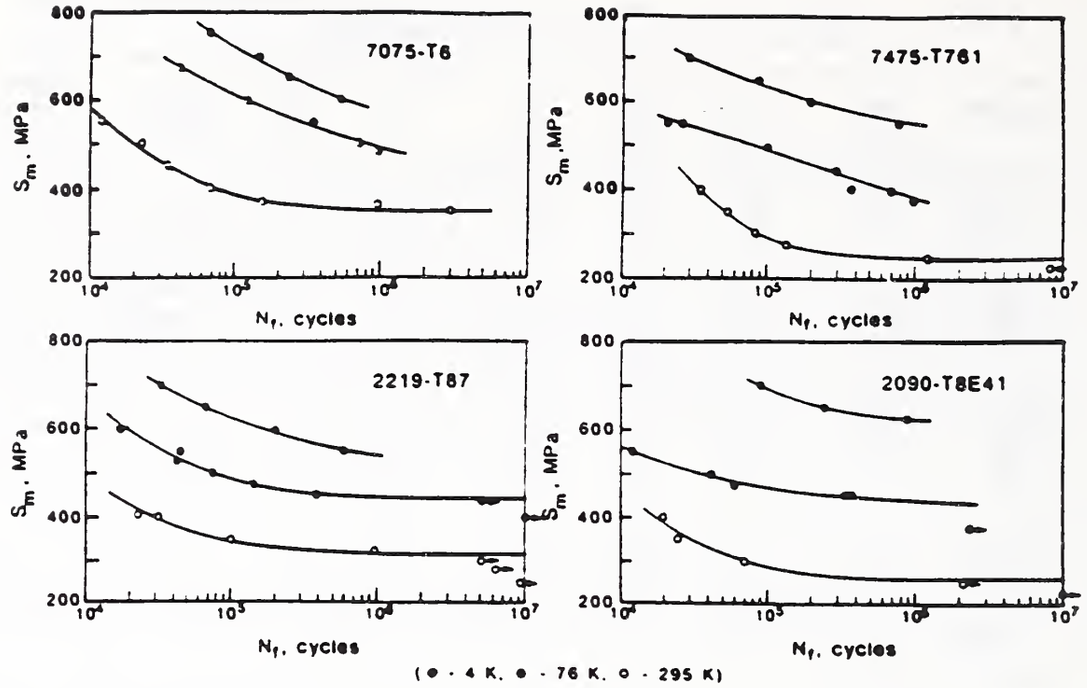

Figure 2. Fatigue life curves for high strength aluminum alloys.

Since static tensile strength is quite important, we compare the alloys on a normalized basis, using the ratio FS/UTS as a relative measure of fatigue resistance. Figure 5 shows that the relative fatigue resistance always increases with decreasing temperature. Whereas alloy 7075-T6 has the highest FS at all temperatures, it does not have the highest FS/UTS ratio at all temperatures; alloy 2090-T8E41 (not 7075-T6) has the highest relative fatigue resistance at 4 K (FS/UTS = 0.95, for a life of 10^5 cycles).

Notch Effect on Fatigue

Figure 6 shows the effect of the notch on S_m-N_f curves. Notching drastically decreases the fatigue lives of these alloys, but alloy 2090-T8E41 emerges with the highest notched specimen fatigue strength (NFS) for a

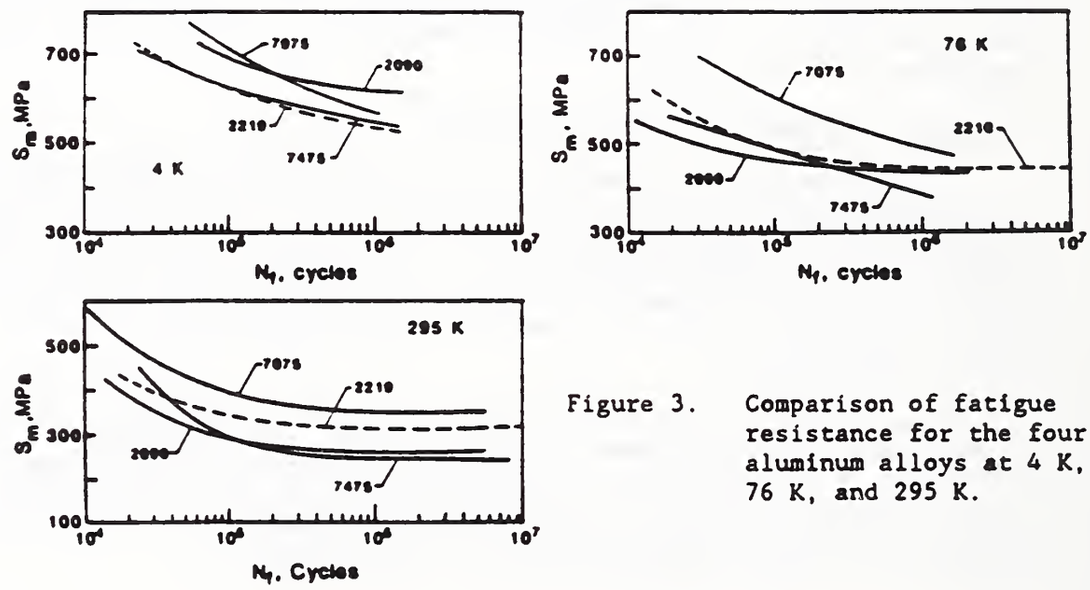

Figure 3. Comparison of fatigue resistance for the four aluminum alloys at 4 K, 76 K, and 295 K.

1146

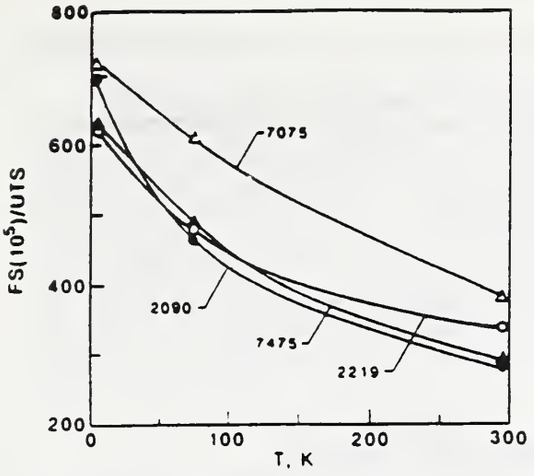

Figure 4. Temperature dependence of FS, at $N_f = 10^5$.

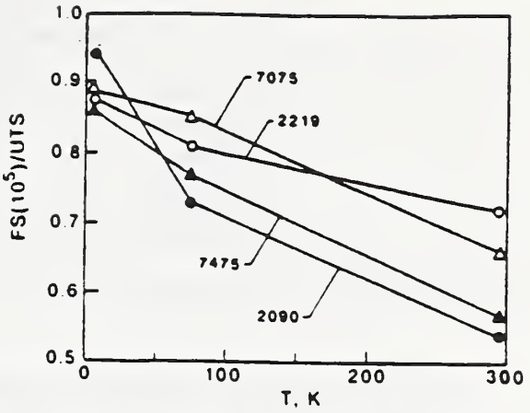

Figure 5. Fatigue strength, at $N_f = 10^5$, normalized by UTS.

life of 10^5 cycles. The fatigue notch sensitivity factor (q) can be used to rank the relative notch sensitivity of the alloys in fatigue:

$$q = \frac{K_f - 1}{K_t - 1}, \qquad (1)$$

Here, K_f = FS/NFS and K_t is the stress concentration factor for the notch. When q = 0, it means that the fatigue life of the material is entirely insensitive to the notch (FS = NFS). On the other hand, the fatigue life is notch sensitive to the degree that q approaches or exceeds 1. Table 2 lists our experimentally determined q and K_f values for comparison at 76 K and 10^5 cycles. Of all four alloys, 7075–T6 is most sensitive to the notch, and 2090–T8E41 is least sensitive. Thus, 2090–T8E41 is superior to the three other alloys on the basis of both absolute and relative notched specimen fatigue resistance.

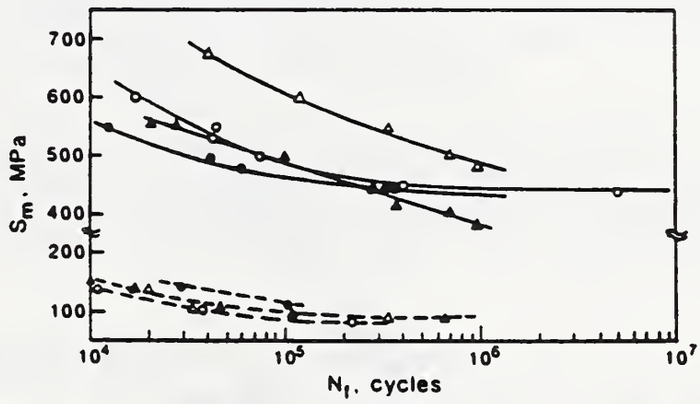

Figure 6. S-N curves of smooth and notched fatigue specimens for the four aluminum alloys at 76 K.

Table 2. Notch effects in terms of q and K_f (T = 76 K)

Alloy	q	K_f*
7075-T6	1.84	6.33
2219-T87	1.48	5.30
7475-T761	1.41	5.08
2090-T8E41	1.14	4.31

*K_f = FS(at 10^5)/NFS(at 10^5)

Fatigue Strength and Tensile Property Correlations

Smooth specimens. In Fig. 7, FS is plotted versus UTS for the four alloys using all data at 295, 76, and 4 K. With some scatter, we find a clear linear relationship between FS and UTS for the alloys at $N_f = 10^5$:

$$FS(10^5) = 1.42(UTS) - 409 \quad (MPa) \qquad (2)$$

This expression derives from a least squares fit, has a correlation coefficient of 0.96, and is rather precise; considering all the data including T = 295, 76, and 4 K, the predicted and measured FS values agree to ± 22% the agreement for 76 and 4 K data is ± 10%. Similar expressions for other lifetimes can be derived, such as that shown in Fig. 7 for 10^6 cycles. The capability of approximately predicting FS at 10^5 or 10^6 cycles from UTS values, which are more easily measured, is potentially important for alloy selection and screening purposes.

Notched specimens. Previously,[6] we discussed the fact that at 10^5 cycles the notched specimen fatigue strength ratio NFSR (NFS/NTS) is nearly constant (0.22 ± 0.01) for these four alloys. This implies that tensile tests of notched specimens, which are relatively easy to perform, may be used to predict the fatigue resistance of notched specimens at 10^5 cycles. More data are needed to confirm the value of the NFS/NTS ratio as a screening parameter for notched specimen fatigue, and to ascertain the range of applicability of this parameter for various alloys, temperatures, and stress levels.

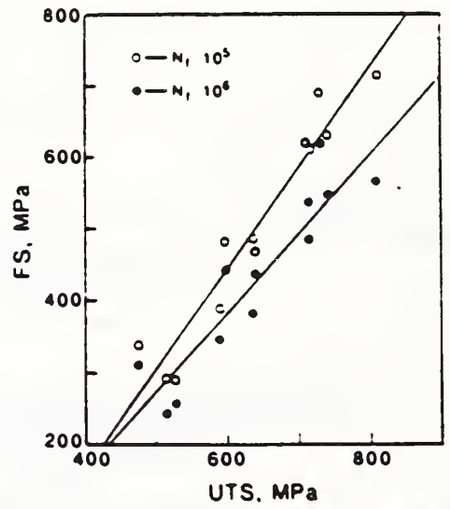

Figure 7. The relation between FS and UTS for the four aluminum alloys (4 - 295 K).

1148

Alloy Selection

Many aluminum alloys that remain ductile and tough at low temperatures might be used in cryogenic structures but each alloy has advantages and disadvantages that influence material selection for specific applications. Availability, weldability, and cost must always be considered in material selection for a practical application; yet, considering the mechanical properties alone we can conclude that none of the studied alloys is universally superior. For example, at 76 K, 7075-T6 offers the highest FS, YS, and UTS in the unnotched condition, 7475-T761 offers the highest tensile strength in the notched condition, and 2219-T87 offers the highest fracture toughness (judging from the NTS/YS ratio). At 4 K, alloy 2090–T8E41 offers the highest notched specimen fatigue strength and relative fatigue strength for the cycle life of interest.

Alloy 7075–T6 would be the best candidate for unnotched components when service is limited by cryogenic fatigue. However, alloy 2219–T87 is usually chosen for cryogenic aerospace applications because it is readily weldable and also has good fatigue resistance at 76 K and below. If notches are present and stress concentration factors are high, 2090–T8E41 may be preferred. For applications at 4 K requiring $N_f \geq 2.5 \times 10^5$ cycles, 2090-T8E41 is a good candidate for either smooth or notched components. Alloy 2090 is a relatively new material that offers special advantages: a 7% lower density, a 10% higher modulus, and lower fatigue notch sensitivity factor than conventional aluminum alloys. Additional tests of unrecrystallized 2090, or of other Al-Li alloys, are of interest for future studies.

CONCLUSIONS

1. For the unnotched condition, alloy 7075–T6 has the highest fatigue resistance among the studied alloys between 295 and 4 K. The rank of the other alloys varies with the test temperature and cycle life of interest.

2. For unnotched specimens, the FS increases strongly with decreasing temperature, but the temperature effect diminishes at lower stress levels. For lives of 10^5 or 10^6 cycles, we find useful linear correlations between FS and the UTS when the data at all three temperatures are pooled.

3. At 76 K, the fatigue resistances of all four alloys are substantially reduced by the notch; but the notched specimen fatigue strength of 2090-T8E41 is better than that of the other three alloys when the notched specimen fatigue values and fatigue notch sensitivity factors (q) are compared at 76 K and a life of 10^5 cycles.

4. For notched specimens of all four alloys, the ratio of the NFS (notched-specimen fatigue strength) at 10^5 cycles to the NTS (notched-specimen tensile strength) is nearly constant (0.22 ± 0.01), which suggests that it may be possible to predict the NFS from the NTS for high strength aluminum alloys, under certain specified conditions.

ACKNOWLEDGMENTS

This work was sponsored by the Superconducting Super Collider Central Design Group, Universities Research Association, and by the Department of Energy, Office of Fusion Energy.

REFERENCES

1. J.W. Morris, Jr., and J. Glazer, Mechanical Behavior of Aluminum Alloys at Cryogenic Temperatures, in: Cryogenic Materials ' 88, Vol. 2, Int. Cryo. Maters. Conf., Boulder CO, R.P. Reed, Z.S. Xing, and E.W. Collings, Eds., 1989, pp. 713-726.

2. C. Peters, K. Mirk, A. Wandestforde and C. Taylor presented at the Tenth International Conference on Magnet Technology, Boston, September 21–25, 1987.

3. R.L. Tobler and D.T. Read, Fatigue Resistance of a Uniaxial S-Glass/Epoxy Composite at Room and Liquid Helium Temperature, J. Compos. Mater. 10:32–43 (1976).

4. J.W. Kaufman, G.T. Sha, R.F. Kohn, and R.J. Bucci, in: Cracks and Fracture, ASTM STP 601, Amer. Soc. Test. Maters., Philadelphia, 1976, pp. 169–190.

5. R.L. Tobler, J.K. Han, L. Ma, R.P. Walsh, and R.P. Reed, Tensile, Fracture, and Fatigue Properties of Notched Aluminum Alloy Sheets at Liquid Nitrogen Temperature, in the proceedings of the fifth inter-international conference, "Aluminum-Lithium Alloys V", Williamsburg, VA, March 27-30, 1989, to be published.

6. R.L. Tobler, J.K. Han, and R.P. Reed, Fatigue Resistance of a 2090-T8E41 Aluminum Alloy at Cryogenic Temperatures, in: Cryogenic Materials '88, Vol. 2, 1988 Int. Cryo. Mater. Conf., Boulder, 1988, pp. 703-712.

1150

NIST-114A
(REV. 3-89)

U.S. DEPARTMENT OF COMMERCE
NATIONAL INSTITUTE OF STANDARDS AND TECHNOLOGY

BIBLIOGRAPHIC DATA SHEET

1. PUBLICATION OR REPORT NUMBER
NISTIR 3944

2. PERFORMING ORGANIZATION REPORT NUMBER

3. PUBLICATION DATE
September 1990

4. TITLE AND SUBTITLE

MATERIALS STUDIES FOR MAGNETIC FUSION ENERGY APPLICATIONS AT LOW TEMPERATURES-XIII

5. AUTHOR(S)

R.L. Tobler and R.P. Reed, editors

6. PERFORMING ORGANIZATION (IF JOINT OR OTHER THAN NIST, SEE INSTRUCTIONS)

U.S. DEPARTMENT OF COMMERCE
NATIONAL INSTITUTE OF STANDARDS AND TECHNOLOGY
Boulder, CO 80303

7. CONTRACT/GRANT NUMBER

8. TYPE OF REPORT AND PERIOD COVERED

9. SPONSORING ORGANIZATION NAME AND COMPLETE ADDRESS (STREET, CITY, STATE, ZIP)

Department of Energy
Office of Fusion Energy
Washington, D.C. 20545

10. SUPPLEMENTARY NOTES

Previous reports in this series: NISTIR 89-3931; NBSIR 88-3082; NBSIR 87-3067; NBSIR 86-3050; NBSIR 85-3025; NBSIR 84-3000; NBSIR 83-1690; NBSIR 82-1667; NBSIR 81-1645; NBSIR 80-1627; NBSIR 79-1609; NBSIR 78-884.

[ ] DOCUMENT DESCRIBES A COMPUTER PROGRAM; SF-185, FIPS SOFTWARE SUMMARY, IS ATTACHED.

11. ABSTRACT (A 200-WORD OR LESS FACTUAL SUMMARY OF MOST SIGNIFICANT INFORMATION. IF DOCUMENT INCLUDES A SIGNIFICANT BIBLIOGRAPHY OR LITERATURE SURVEY, MENTION IT HERE.)

This report contains the results of research to determine the properties of materials that may be used in cryogenic structures for the superconducting magnets of fusion energy power plants and prototypes. Its purpose is to facilitate their design and development. The program was developed jointly by the staffs of the National Institute of Standards and Technology and the Office of Fusion Energy of the Department of Energy; it is managed by NIST and sponsored by DOE. Research is conducted at NIST and at other laboratories through cooperative agreements with NIST.

Research results for 1989-90 are presented in technical papers under four headings that reflect the main program areas: Structural Alloys, Welding, Test Standards, and Technology Transfer. Objectives and research highlights are summarized in the introduction to each program area.

12. KEY WORDS (6 TO 12 ENTRIES; ALPHABETICAL ORDER; CAPITALIZE ONLY PROPER NAMES; AND SEPARATE KEY WORDS BY SEMICOLONS)

austenitic steels; cryogenic properties of materials; low temperature; mechanical properties; stainless steels; standards; structural materials; welds

13. AVAILABILITY

[XX] UNLIMITED

[ ] FOR OFFICIAL DISTRIBUTION. DO NOT RELEASE TO NATIONAL TECHNICAL INFORMATION SERVICE (NTIS).

[ ] ORDER FROM SUPERINTENDENT OF DOCUMENTS, U.S. GOVERNMENT PRINTING OFFICE, WASHINGTON, DC 20402.

[XX] ORDER FROM NATIONAL TECHNICAL INFORMATION SERVICE (NTIS), SPRINGFIELD, VA 22161.

14. NUMBER OF PRINTED PAGES
381

15. PRICE
A17

ELECTRONIC FORM